

# **Development and Testing of New Ring Spring Self-Centering Energy Dissipative (RS-SCED) Braces for Seismic Resilience of Buildings and Bridges**

by

**Ahmed Alaa El-din Hassan**

A thesis submitted to the

Department of Civil and Environmental Engineering

in partial fulfillment of the requirements for the degree of

**Doctor of Philosophy**

Ottawa-Carleton Institute for Civil and Environmental Engineering

Department of Civil and Environmental Engineering

Carleton University

Ottawa, Ontario

August, 2020

Ahmed Hassan, 2020

# Abstract

Self-Centering systems aim to eliminate or minimize residual drifts in structures leading to improved seismic performance and allowing immediate occupancy of structures during and post earthquakes, respectively. In this study a new compact Self-Centering Energy-Dissipative (SCED) brace is developed, designed, and experimentally tested. The new innovative compact high capacity ring spring SCED (RS-SCED) is a brace system that exhibits a nonlinear response with good energy dissipation and post-yield stiffness, while eliminating or minimizing residual drift after an earthquake.

Existing SCED braces typically rely on using prestressed tendons to achieve their self-centering capabilities. In conventional SCED braces, the tendon is required to be relatively long to achieve a large enough deformation capacity, resulting in SCED braces that are large in size. Similar SCED brace systems which do not rely on tendons to achieve their self-centering capability, tend to have a lower load capacity than conventional braces. Based on these constraints, the applicability of existing SCED braces is limited by size, as well as load and deformation capacity. The new high capacity compact ring spring SCED brace utilizes ring springs to provide a restoring force, while simultaneously dissipating energy through friction between ring spring units in the assembly. The new mechanism allows the brace to have a large deformation capacity without the need for a long tendon, resulting in a compact sized brace that can attain self centering behaviour during the earthquake response of a building for drift demands up to 4%, and potentially larger if necessary. The new RS-SCED brace has high load capacity with stable and repeatable hysteresis that makes them suitable for deployment in full scale building and bridge structures in high seismic regions.

Hybrid simulations are performed to evaluate the system level performance of the new brace in prototype structures. The hybrid simulation method allows for the realistic seismic assessment of critical structural components or subassemblies in a structure without the need to test the entire structure in a laboratory by combining experimental testing and numerical modelling together. In this study, a 4-storey building and a 3-span bridge with the new ring spring SCED brace are tested using hybrid simulations. The physical test substructure is the prototype compact high capacity ring spring SCED with a load capacity of 1400 kN and a deformation capacity of 160 mm. During the tests, the systems are subjected to a series of earthquake records with a wide range of frequency contents at different hazard levels.

In the new RS-SCED brace system, the seismic response of the structure can be improved through optimization of the brace design parameters, namely the brace pre- and post-activation stiffness, activation load, and deformation capacity. The optimization of these design parameters depends on the seismic demands on the structure, such as the storey drift and storey shear. Typical seismic design procedures rely on ductility and overstrength factors for simplified seismic analysis and design using an equivalent static force procedure. In this study, the FEMA P695 methodology is used to determine the ductility ( $R$ ), overstrength ( $\Omega_0$ ) and deflection amplification ( $C_d$ ) factors for seismic design of the proposed structural system. Two different levels of seismic hazard are examined for buildings with both short and long periods of vibration. To account for the variation in periods of vibration, the seismic responses of 2-, 4-, 8- and 12-storey steel framed buildings equipped with the new RS-SCED braces are examined. The combination of different building heights, bay sizes and seismicity levels led to the design of 12 different prototype building designs for the numerical analyses. Pushover analyses, as well as nonlinear dynamic time history analyses of the prototype buildings subjected to a suite of scaled ground motions are performed. The

calibration of the seismic design factors for the RS-SCED braced frame buildings, is based on optimization of the seismic performance of buildings by considering the peak storey drifts, residual drift and floor accelerations.

# Acknowledgments

First and foremost, all thanks belong to God the-all Mighty, Merciful, Compassionate, and Supportive for giving me the strength and resolve to complete this project.

I would then like to thank my supervisors Professor Jeffrey Erochko and Professor David Lau, both of which have invested tremendous time guiding, mentoring, and supporting me. Any success I had as a researcher or a teacher has been directly assisted whole heartedly by both of you.

I would also like to thank RingFeder Power Transmission, and in particular Edward Cole and Lars Jahnel for their technical support and providing the material for the project. I would also like to thank Dr. Keh-Chyuan Tsai, Dr. Murat Saatcioglu, Dr. Robert Langlois and Dr. Heng Khoo for taking the time to review this thesis and provide valuable feedback.

I also would like to extend a special word of gratitude for my dear friend Joshua Woods, his continuous support for the past 7 years has been relentless, he provided me with the advice, resources and training that I needed to complete this project.

I am also thankful for the support that I have received from faculty throughout my time at Carleton especially Dr. Juan Salinas, Dr. Yasser Hassan, Dr. Carlos Cruz-Noguez and Dr. Heng Khoo. I would also like extend my gratitude to the amazing, hard working, and often underappreciated laboratory and administrative staff at Carleton University including Stanley Conley, Jason Arnott, Kay Casselman, Pierre Trudel, Kenneth Akhiwu, and Stephen Vickers.

To the graduate and undergraduate students who dedicated their time to lend me a helping hand in my research, including Geoffrey Davidson, Said Said, Zhimeng Yu, and Omar El-Ghazal, you lent me your help when you did not need to, and for that I will be forever grateful. To my second family in the CU-MSA, I am grateful for an experience that has shaped me as a human being and gave me a fuller perspective of life outside academia.

Finally, I would like to reserve the most heartfelt thanks to my strong and supportive wife Nahda who has always been in my corner even during the toughest times, my brothers, Amr and Khaled, and my parents Alaa and Enas, who sacrificed everything for the sake of a better future for our family. Without all of you, there is no doubt in my mind that I would not have had the determination to finish this work.

# Table of Contents

Abstract.....	ii
Acknowledgments.....	v
Table of Contents.....	vii
Table of Figures.....	x
Chapter 1: Introduction.....	1
Chapter 2: Self-Centering Devices.....	6
2.1 Energy Dissipating Restraint (EDR) [38].....	7
2.2 Fluidic Self-Centering Device [40], [41].....	12
2.3 Friction Spring Seismic Damper [42], [43].....	15
2.4 Reusable Hysteretic Damping Brace (RHDB) and Self-Centering Friction Damping Brace (SFDB) [46], [47].....	17
2.5 Pretension SCED (PT-SCED) and High capacity SCED (HC-SCED) [26], [27].....	19
2.6 Telescoping SCED brace (T-SCED) and Dual Core Self Centering Brace (DC-SCB) [28], [48].....	23
2.7 Self-Centering Buckling Restrained Brace [50].....	28
2.8 Dual Tube Self Centering BRB [29].....	30
2.9 Cross-Anchored SC-BRB [30].....	33
2.10 Piston-Based Self-Centering (PBSC) Brace [52], [53].....	37
2.11 SMA Wire Self-Centering Dampers[54], [55].....	38
2.12 Pre-pressed Disc Spring SCED Brace (PS-SCED) [57].....	41
2.13 MR-SCB and Disc Spring SC-BRB [32], [58], [59].....	43
2.14 Assembled Self-Centering Brace (ASCB) [33].....	46
2.15 Summary of SCED devices.....	49
Chapter 3: Ring Springs.....	51
3.1 Characteristics of Ring Springs.....	54
3.1.1 High Capacity.....	54
3.1.2 High Weight Utilization Factor.....	56
3.1.3 Adjustable Spring Response.....	57
3.1.4 Hysteretic Response of Ring Springs.....	58
3.1.5 Load Rate and Temperature Independent.....	63

3.2 Utilization of Ring Springs in Seismic Isolation [42].....	64
3.3 Friction Spring Seismic Self-Centering Damper [45] .....	67
3.4 Use of Ring Springs as Seismic Dampers [63].....	74
3.5 Self-Centering Sliding Hinge Joint (SCSHJ) Connections [64], [65] .....	81
3.6 Rocking CBF with Double Acting Ring Springs [67].....	86
3.7 Spring-Based Piston Bracing (SBPB) [53].....	90
3.8 Summary .....	93
Chapter 4: Design of RS-SCED Brace and Testing Methodology .....	94
4.1 Design of the New Ring Spring SCED Brace .....	95
4.2 RS-SCED Brace Mechanism .....	99
4.3 SCED Brace Components.....	115
4.3.1 Ring Spring Assembly .....	117
4.3.2 Prestressing Steel Threaded Rod .....	120
4.3.3 Outer Tube, Slip-On Flange and Cover Plate .....	121
4.3.4 Prestressing Chair and Piston .....	123
4.4 Assembling the Brace .....	126
4.5 Secondary Fuse Mechanism .....	131
4.6 Experimental Test Setup .....	132
4.7 Instrumentation .....	136
4.7.1 Strains in Brace Components.....	137
4.7.2 Brace Deformation.....	139
4.7.3 Test Frame Deformations .....	141
4.8 Hydraulic Control and Data Acquisition .....	143
Chapter 5: Characterization of RS-SCED Brace Behaviour Through Experimental Testing ....	145
5.1 Frequency Dependence Test.....	145
5.2 ASCE 7-16 Loading Protocol .....	146
5.3 AISC 341-16 Testing Protocol.....	151
5.4 Capacity Test .....	153
5.5 Strain Gauge Measurements .....	154
5.6 Post-test RS-SCED brace conditions .....	157
Chapter 6: Hybrid Simulation of RS-SCED Brace.....	167
6.1 Previous Hybrid Simulation for Advanced Systems .....	168

6.2 Model Updating .....	172
6.3 Hybrid Simulation Architecture and Interface.....	174
6.4 Building Numerical Model .....	175
6.5 Comparison of Hybrid Simulation and Fully Analytical Model .....	184
6.6 Comparison of RS-SCED Braced Building to BRB-Braced Building .....	201
6.7 Bridge Analytical Modelling .....	212
6.8 Comparison of Bridge Hybrid Simulation to Numerical Modelling .....	220
6.9 Comparison of RS-SCED Retrofitted Bridge and Original Bridge .....	235
Chapter 7: Fragility Assessment and Seismic Design Factors.....	242
7.1 FEMA P695 Methodology.....	243
7.2 Building Archetypes .....	249
7.3 Non-Linear Building Models.....	253
7.4 Determining Ductility Factor $R$ .....	254
7.5 Determining overstrength factor, $\Omega_0$ .....	260
7.6 Comparison of Archetypal Building Response at Varying Hazard Levels .....	263
7.7 Summary.....	271
Chapter 8: Conclusions and Future Research .....	272
8.1 Conclusions.....	272
8.2 Recommendations for Future Research .....	276
References.....	278
Appendix A: Brace Drawings.....	293
Appendix B: Design of prototype building for Hybrid simulation and BRB structure .....	325
Appendix C: Seismic Analysis and design for FEMA P695 Archetype structures .....	330
Appendix D: Earthquake Record Suite and Scaling for FEMA P695 .....	349
Appendix E: FEM of RS-SCED Brace Components.....	354

# Table of Figures

Figure 1.1 Examples of buildings with residual deformations that typically leads to demolition [7] .....	3
Figure 2.1 Non-linear Hysteresis response of Typical vs Self-Centering SFRS [37] .....	7
Figure 2.2 Schematics and hysteresis of EDR [38] .....	8
Figure 2.3 (a) Triangular Lobed hysteresis of EDR, and (b) Double flag-shaped hysteresis loop of EDR [39] .....	9
Figure 2.4 3-storey bare model frame used for shake table test [39].....	10
Figure 2.5 Frame with Energy Dissipating Restraints [39] .....	11
Figure 2.6 View of EDRs installed at second level of frame [39].....	11
Figure 2.7 Schematic and dynamics of the Fluidic self-centering device [41].....	13
Figure 2.8 Temperature effect on response of fluidic damping device [41].....	14
Figure 2.9 Hysteresis of fluidic damping device under (a) quasi-static load, (b) 2.0Hz dynamic load, (c) 1.0Hz dynamic load, and (d) 0.5Hz dynamic load [41] .....	14
Figure 2.10 Friction Spring assembly consisting of 4 outer rings, 3 inner rings and 2 half inner rings [44] .....	15
Figure 2.11 Bi-Directional Ring Spring Cartridge [42].....	15
Figure 2.12 Seismic damper [45].....	16
Figure 2.13 Hysteresis of the Ring Spring Damper [45] .....	16
Figure 2.14 Mechanical Configuration of RHDB [46].....	17
Figure 2.15 Mechanical Configuration of SFDB [47].....	18
Figure 2.16 Hysteresis of experimentally-tested SFDB [47].....	18
Figure 2.17 Schematic of PT-SCED [26] .....	19
Figure 2.18 Schematic of HC-SCED [27] .....	20
Figure 2.19 Setup for quasi-static and dynamic testing of frame incorporating PT-SCED brace [26].....	22
Figure 2.20 HC-SCED test setup and instrumentation [27] .....	22
Figure 2.21 Sample Hysteresis of PT-SCED (left) and HC-SCED (Right) [26], [37] .....	23
Figure 2.22 T-SCED brace schematics [28] .....	24
Figure 2.23 Dual-Core SCB Schematics [48].....	24
Figure 2.24 Test frame used for testing the TSCED brace [28] .....	25
Figure 2.25 Sample Hysteresis of T-SCED brace [28].....	26
Figure 2.26 Test setup used for testing the DC-SCB [48].....	27
Figure 2.27 Sample Hysteresis Response of the DC-SCB [48].....	27
Figure 2.28 SC-BRB components [50].....	29
Figure 2.29 SC-BRB mechanics [50] .....	30
Figure 2.30 Hysteresis response of two different SC-BRB configurations [50] .....	30
Figure 2.31 Assembly of the Dual Tube SC-BRB [29].....	32
Figure 2.32 Mechanics of the Dual-Tube SC-BRB [29] .....	32
Figure 2.33 Hysteresis response of Dual Core SC-BRB at increasing levels of loading [29].....	33
Figure 2.34 Assembly steps for cross anchored SC-BRB [30].....	34

Figure 2.35 Schematics of one cross-anchored SC-BRB specimen [30].....	35
Figure 2.36 Mechanics of the cross-anchored SC-BRB [30] .....	35
Figure 2.37 Loading system for testing the cross-anchored SC-BRB [30] .....	36
Figure 2.38 Hysteresis of the cross-anchored SC-BRB [30] .....	36
Figure 2.39 Design of the PBSC brace [52] .....	38
Figure 2.40 Hysteresis of a PBSC [52].....	38
Figure 2.41 Schematic of SMA damper by Qiu [54] (Left) and Li [55] (Right).....	39
Figure 2.42 Hysteresis of Self-Centering dampers tested by Li [55] .....	40
Figure 2.43 Proposed SMA SC-BRB proposed by Kari [56].....	40
Figure 2.44 Schematics of PS-SCED brace [57] .....	41
Figure 2.45 Mechanics of the PS-SCED brace [57] .....	42
Figure 2.46 Sample Hysteresis of PS-SCED [57] .....	43
Figure 2.47 components of the MR-SCB [32].....	44
Figure 2.48 Sample hysteresis of MR-SCB [32] .....	45
Figure 2.49 Configuration of the Disc-Spring SC-BRB [59] .....	46
Figure 2.50 Hysteresis curves of equivalent brace specimens: a) BRB, b) SCB, c) SC-BRB [59] .....	46
Figure 2.51 Components of the ASCB [33].....	47
Figure 2.52 Hysteresis response of ASCB at increasing deformation demand [33] .....	48
Figure 3.1 Different stacking arrangements of disc Springs [61].....	53
Figure 3.2 Typical ring spring assembly consisting of 4 outer rings, 3 inner rings and 2 half inner rings [44] .....	54
Figure 3.3 Range of possible friction spring solutions [44] .....	55
Figure 3.4 Weight utilization factor for various types of springs [44] .....	57
Figure 3.5 Change in spring travel and spring loading stiffness with increasing number ring elements [44] .....	58
Figure 3.6 Ring spring elastic response with no friction [44].....	59
Figure 3.7 Additional friction forces on loading being applied [44] .....	59
Figure 3.8 Breaking friction forces upon unloading [44] .....	60
Figure 3.9 Typical idealized hysteresis diagram of a ring spring assembly [44] .....	61
Figure 3.10 Sample of complete spring travel diagram including pre-compression [44] .....	63
Figure 3.11 Ring spring Hysteresis obtained from quasi-static testing [42].....	64
Figure 3.12 Experimental and Computer simulation displacement response under dynamic testing [42].....	66
Figure 3.13 Pivotal rocking seismic isolation system subject to base excitation [42].....	67
Figure 3.14 Complete test rig assembly mounted on shaker table [42].....	67
Figure 3.15 Diagrammatic view of seismic damper [45] .....	68
Figure 3.16 Performance benchmark tests for Ring Spring Seismic damper [45] .....	69
Figure 3.17 Effect of excitation frequency on physical parameters defining the hysteretic behaviour of the damper danper [45] .....	70
Figure 3.18 Force displacement hysteresis of damper during earthquake records: Saguenay(Top), El Centro (middle), and San Fernando (bottom) [45].....	71
Figure 3.19 Test structure incorporating seismic damper [45] .....	72

Figure 3.20 Ring spring damper assembly and components [63].....	75
Figure 3.21 Ring spring damper setup in testing machine at University of Canterbury [63].....	76
Figure 3.22 Outline drawing of testing frame structure [63].....	77
Figure 3.23 Placement of a straight tendon relative to idealized tendon [63].....	78
Figure 3.24 Tendon-floor slab detail [63].....	78
Figure 3.25 Layout of the supplemental control system with the structure [63].....	79
Figure 3.26 (a) SHJ Layout, (b) SCSHJ and (c) Joint rotation [65].....	82
Figure 3.27 Layout of Ring Spring Cartridge (i) in neutral position, (ii) under positive moment and (iii) under negative moment [65].....	83
Figure 3.28 SCSHJ and SHJ Test setup [65].....	84
Figure 3.29 Loading Regimes: (a) SAC, (b) SAC_Dy, (c) EQ and (d) NF [65].....	86
Figure 3.30 Centralized Rocking Concentrically Braced Frame (CRCBF) system with Ring spring assembly [67].....	88
Figure 3.31 Bottom Storey of CRCBF test setup [67].....	89
Figure 3.32 Static and dynamic loading regimes for testing the bottom storey of CRCBF [67].....	90
Figure 3.33 Double Acting SBPB configuration [53].....	91
Figure 3.34 Response Spectra of scaled EQ records compared to Vancouver response Spectrum [53].....	92
Figure 4.1 Two braces in parallel added to frame with chevron brace configuration.....	96
Figure 4.2 Schematic representation of RS-SCED showing the brace mechanism.....	100
Figure 4.3 Schematic of brace mechanism at different loading states.....	101
Figure 4.4 Schematic of the brace at the first step of the hysteresis (no load).....	102
Figure 4.5 Schematic of the brace while loading in tension pre-activation of springs.....	103
Figure 4.6 Schematic of the brace while loading in tension post-activation of springs.....	104
Figure 4.7 Schematic of the brace while unloading in tension pre-activation of springs.....	105
Figure 4.8 Schematic of the brace while unloading in tension post-activation of springs.....	106
Figure 4.9 Schematic of the brace while loading in compression pre-activation of springs.....	107
Figure 4.10 Schematic of the brace while loading in compression post-activation of springs...	108
Figure 4.11 Schematic of the brace while unloading in compression pre-activation of springs.....	109
Figure 4.12 Schematic of the brace while unloading in compression post-activation of springs.....	110
Figure 4.13 Schematic of the brace at the final step of the hysteresis (no load).....	111
Figure 4.14 Dividing the brace into three segments to calculate the initial stiffness of the brace.....	113
Figure 4.15 Dividing the brace into four segments to calculate the tensile post-activation stiffness of the brace.....	114
Figure 4.16 RS-SCED Brace cross-section showing the brace components.....	115
Figure 4.17 RS-SCED brace (a) neutral position, (b) fully compressed and (c) fully extended.....	116
Figure 4.18 End plates inserted on both ends of the Ring Spring assembly.....	119
Figure 4.19 Fitting the End plate guide through the Ring Spring assembly.....	119

Figure 4.20 Assembly of Type 34000 Ring Springs used for the RS-SCED Brace.....	120
Figure 4.21 Threaded rod, nut and washer plate.....	121
Figure 4.22 Schematic diagram of Outer tube and cover plate.....	123
Figure 4.23 Schematic diagram of the prestressing chair and piston .....	125
Figure 4.24 Prestressing chair and piston used for the RS-SCED brace .....	125
Figure 4.25 Inserting Ring spring assembly inside the outer tube.....	126
Figure 4.26 Cover plate placed on top of the ring spring assembly .....	127
Figure 4.27 Threaded rod passing through the drilled hole in the bottom end plate .....	128
Figure 4.28 Adding a coupler on the threaded rod at the prestressing chair end.....	129
Figure 4.29 Prestressing setup used to prestress the steel rod .....	130
Figure 4.30 Gap closes as the ring spring assembly compresses to the activation force.....	131
Figure 4.31 Schematic diagram of test setup used for testing RS-SCED brace .....	133
Figure 4.32 Test setup used for this study at Carleton University structures lab .....	133
Figure 4.33 Aerial image showing the out-of-plane and lateral support system .....	134
Figure 4.34 Side view of the Out-of-plane and lateral support in experimental setup .....	135
Figure 4.35 Instrumentation plan.....	136
Figure 4.36 Plan view showing the exact location of the strain gauges used on different components of the brace.....	137
Figure 4.37 Strain gauges installed to the Outer Tube surface.....	138
Figure 4.38 Strain gauges used to measure strains for pistons .....	138
Figure 4.39 Strain gauges applied on a section of the threaded steel rod.....	139
Figure 4.40 Plan view showing the exact location of encoders and string pot measuring the brace deformation.....	140
Figure 4.41 Encoder used to validate the deformation measurement obtained from actuators.....	141
Figure 4.42 Sting pot measuring deformation between piston chair base plate and outer tube cover plate.....	141
Figure 4.43 Plan view showing the location of the 3 LVDTs used to measure the deformations of the test setup.....	142
Figure 4.44 Support block LVDT measuring sliding of concrete block.....	142
Figure 4.45 Out-of-plane LVDTs #1 (left) and #2 (right) .....	143
Figure 4.46 Computer station used for hydraulic control and data acquisition [75] .....	144
Figure 5.1 Hysteresis response of RS-SCED brace when loaded under different displacement rates .....	146
Figure 5.2 ASCE 7-16 loading protocol .....	147
Figure 5.3 ASCE 7-16 loading protocol pre-hybrid tests .....	148
Figure 5.4 ASCE 7-16 loading protocol post-hybrid tests.....	150
Figure 5.5 Comparison between pre- and post-hybrid testing results after adjusting the nut for gap formed .....	150
Figure 5.6 AISC 341-16 Loading protocol.....	151
Figure 5.7 AISC 341-16 loading protocol pre and post hybrid tests .....	152
Figure 5.8 Full cycle of loading at design drift level of 4% .....	153
Figure 5.9 Measured strain response for steel threaded rod .....	155

Figure 5.10 Measured strain response for steel piston tube.....	155
Figure 5.11 Measured strain response for outer tube.....	156
Figure 5.12 Measured strain response for piston chair legs.....	157
Figure 5.13 Location of localized damage observed on the end plates .....	157
Figure 5.14 Localized damage at inner edge of end plate .....	158
Figure 5.15 Damage along the length of the inner edge of end plate .....	159
Figure 5.16 Localized deformation as a result of frequent contact with the inner surface of outer tube .....	159
Figure 5.17 Location of localized damage at washer plate and spacer bearing plate.....	161
Figure 5.18 Damage at the bearing plate .....	161
Figure 5.19 Notch at the bearing plate caused by impact with the washer plate.....	162
Figure 5.20 Localized damage on the washer plate caused by impact with bearing plate .....	162
Figure 5.21 The use of an inner and outer guide on either end plate of the assembly.....	163
Figure 5.22 Proposed Inter-lapping of inner and outer guides .....	163
Figure 5.23 Minimal damage to the inner surface of the outer tube due to friction with end plates.....	164
Figure 5.24 No observed damaged to spacer plate and welds .....	165
Figure 5.25 Small gap between UHMW plastic and end plate indicate no damage to piston tube .....	165
Figure 5.26 Ring spring assembly grease after testing .....	166
Figure 5.27 No damage observed on the cover plate.....	166
Figure 6.1 Steel rocking frame hybrid test setup [83] .....	169
Figure 6.2 Damping devices real-time hybrid test setup [84].....	170
Figure 6.3 Model substructuring for hybrid simulation of SCED brace building [49].....	171
Figure 6.4 Substructure modules for model updating [91].....	174
Figure 6.5 Architecture of the hybrid simulation setup at Carleton University, adopter from Josh [75] .....	175
Figure 6.6 Plan view of prototype building used for the hybrid simulation .....	176
Figure 6.7 Elevation view of a braced frame of the building .....	177
Figure 6.8 Analytical model used for the hybrid simulation of the 8-storey building.....	178
Figure 6.9 Section of the building analytically modelled.....	178
Figure 6.10 Elevation view of BRB lateral load resisting system .....	180
Figure 6.11 Analytical model of the 8-storey building utilizing an equivalent BRB system.....	181
Figure 6.12 Northridge earthquake record.....	182
Figure 6.13 Kobe earthquake record.....	183
Figure 6.14 Loma Prieta earthquake record.....	183
Figure 6.15 ChiChi earthquake record.....	183
Figure 6.16 Comparison of force-deformation hysteretic response for the Northridge earthquake: (a) FOE, (b) DBE, and (c) MCE hazard levels.....	188
Figure 6.17 Comparison of force-deformation hysteretic response for the Kobe earthquake: (a) FOE, (b) DBE, and (c) MCE hazard levels.....	189
Figure 6.18 Comparison of force-deformation hysteretic response for the Loma Prieta earthquake: (a) FOE, (b) DBE, and (c) MCE hazard levels.....	190

Figure 6.19 Comparison of force-deformation hysteretic response for the ChiChi earthquake: (a) DBE, and (b) MCE hazard levels .....	191
Figure 6.20 Comparison of time-history deformation response of the brace for the Northridge earthquake: (a) FOE, (b) DBE, and (c) MCE hazard levels .....	192
Figure 6.21 Comparison of time-history deformation response of the brace for the Kobe earthquake: (a) FOE, (b) DBE, and (c) MCE hazard levels .....	193
Figure 6.22 Comparison of time-history deformation response of the brace for the Loma Prieta earthquake: (a) FOE, (b) DBE, and (c) MCE hazard levels.....	194
Figure 6.23 Comparison of time-history deformation response of the brace for the ChiChi earthquake: (a) DBE, and (b) MCE hazard levels .....	195
Figure 6.24 Comparison of roof drift of building response for the Northridge earthquake: (a) FOE, (b) DBE, and (c) MCE hazard levels.....	197
Figure 6.25 Comparison of roof drift of building response for the Kobe earthquake: (a) FOE, (b) DBE, and (c) MCE hazard levels .....	198
Figure 6.26 Comparison of roof drift of building response for the Loma Prieta earthquake: (a) FOE, (b) DBE, and (c) MCE hazard levels.....	199
Figure 6.27 Comparison of roof drift of building response for the ChiChi earthquake: (a) DBE, and (b) MCE hazard levels .....	200
Figure 6.28 Comparison of first floor hysteresis of RS-SCED and BRB systems (DBE hazard level - Record 12) .....	204
Figure 6.29 Comparison of first floor hysteresis of RS-SCED and BRB systems (MCE hazard level - Record 12) .....	205
Figure 6.30 Statistics of the maximum inter-storey drifts for both structural systems: a) 50% in 50-year, b) 10% in 50-year hazard, and c) 2% in 50-year hazard level.....	207
Figure 6.31 Statistics of the residual storey drifts for both structural systems: a) 50% in 50-year, b) 10% in 50-year hazard, and c) 2% in 50-year hazard level.....	209
Figure 6.32 Statistics of the peak floor accelerations for both structural systems: a) 50% in 50-year, b) 10% in 50-year hazard, and c) 2% in 50-year hazard level .....	211
Figure 6.33 Retrofit scheme adopted in the parametric study [98].....	212
Figure 6.34 Details of modelled bridge used for this study [98] .....	214
Figure 6.35 Plan view of the bridge retrofit scheme.....	214
Figure 6.36 3D Spine analytical model used for hybrid simulation .....	215
Figure 6.37 Fibre section model in OpenSees [98].....	216
Figure 6.38 3D Spine model used for analysis of non-retrofitted bridge .....	217
Figure 6.39 Scaling of Northridge earthquake record .....	218
Figure 6.40 Scaling of Kobe earthquake record .....	219
Figure 6.41 Scaling of Loma Prieta earthquake record .....	219
Figure 6.42 Scaling of ChiChi earthquake record .....	219
Figure 6.43 Hysteresis of RS-SCED brace for Northridge record scaled at the (a) Ottawa MCE, and (b) Victoria MCE hazard levels .....	221
Figure 6.44 Hysteresis of RS-SCED brace for Kobe record scaled at the (a) Ottawa MCE, and (b) Victoria MCE hazard levels.....	222

Figure 6.45 Hysteresis of RS-SCED brace for Loma Prieta record scaled at the (a) Ottawa MCE, and (b) Victoria MCE hazard levels .....	223
Figure 6.46 Hysteresis of RS-SCED brace for ChiChi record scaled at the (a) Ottawa MCE, and (b) Victoria MCE hazard levels .....	224
Figure 6.47 Time-History deformation of RS-SCED brace for Northridge record scaled at the (a) Ottawa MCE, and (b) Victoria MCE hazard levels .....	226
Figure 6.48 Time-History deformation of RS-SCED brace for Kobe record scaled at the (a) Ottawa MCE, and (b) Victoria MCE hazard levels.....	227
Figure 6.49 Time-History deformation of RS-SCED brace for Loma Prieta record scaled at the (a) Ottawa MCE, and (b) Victoria MCE hazard levels .....	228
Figure 6.50 Time-History deformation of RS-SCED brace for ChiChi record scaled at the (a) Ottawa MCE, and (b) Victoria MCE hazard levels .....	229
Figure 6.51 Bridge transverse drift response for Northridge record scaled at the (a) Ottawa MCE, and (b) Victoria MCE hazard levels .....	231
Figure 6.52 Bridge transverse drift response for Kobe record scaled at the (a) Ottawa MCE, and (b) Victoria MCE hazard levels .....	232
Figure 6.53 Bridge transverse drift response for Loma Prieta record scaled at the (a) Ottawa MCE, and (b) Victoria MCE hazard levels.....	233
Figure 6.54 Bridge transverse drift response for ChiChi record scaled at the (a) Ottawa MCE, and (b) Victoria MCE hazard levels .....	234
Figure 6.55 Effect of RS-SCED brace retrofit on longitudinal drift of bridge when subjected to MCE hazard level in Victoria, BC for: (a) Northridge, (b) Kobe, (c) Loma Prieta, and (d) ChiChi earthquake records .....	237
Figure 6.56 Effect of RS-SCED brace retrofit on transverse drift of bridge when subjected to MCE hazard level in Victoria, BC for: (a) Northridge, (b) Kobe, (c) Loma Prieta, and (d) ChiChi earthquake records.....	238
Figure 6.57 Effect of RS-SCED brace retrofit on base shear at bridge foundation when subjected to MCE hazard level in Victoria, BC for: (a) Northridge, (b) Kobe, (c) Loma Prieta, and (d) ChiChi earthquake records .....	240
Figure 6.58 Effect of RS-SCED brace retrofit on base moment at bridge foundation when subjected to MCE hazard level in Victoria, BC for: (a) Northridge, (b) Kobe, (c) Loma Prieta, and (d) ChiChi earthquake records .....	241
Figure 7.1 Illustration of seismic performance factors defined in ASCE 7-16 [101].....	244
Figure 7.2 Seismic performance factors as defined by FEMA P695 methodology [101].....	247
Figure 7.3 Elevation view of the building archetypes used for this study .....	251
Figure 7.4 Plan view of 25 bay archetype buildings.....	252
Figure 7.5 Plan view of 15 bay archetype buildings.....	252
Figure 7.6 Plan view of 9 bay archetype buildings.....	253
Figure 7.7 Effect of uncertainty on fragility curves [101].....	256
Figure 7.8 Effect of uncertainty on Acceptable Collapse Margin Ratios [101] .....	256
Figure 7.9 Fitted fragility curves for archetypes in performance group 1: a) Archetype 1, b) Archetype 2, and c) Archetype 3 .....	259

Figure 7.10 Fitted fragility curves for archetypes in performance group 2: a) Archetype 4, b) Archetype 5, and c) Archetype 6.....	259
Figure 7.11 Idealized static pushover analysis [101].....	261
Figure 7.12 Sample pushover curve for archetype 1 .....	262
Figure 7.13 Statistical response results of archetype 1 building at different seismic hazard levels seismic hazard levels: a) residual drift, b) peak floor drift, and c) peak floor acceleration.....	268
Figure 7.14 Statistical response results of archetype 2 building at different seismic hazard levels seismic hazard levels: a) residual drift, b) peak floor drift, and c) peak floor acceleration.....	269
Figure 7.15 Statistical response results of archetype 3 building at different seismic hazard levels seismic hazard levels: a) residual drift, b) peak floor drift, and c) peak floor acceleration.....	269
Figure 7.16 Statistical response results of archetype 4 building at different seismic hazard levels seismic hazard levels: a) residual drift, b) peak floor drift, and c) peak floor acceleration.....	270
Figure 7.17 Statistical response results of archetype 5 building at different seismic hazard levels seismic hazard levels: a) residual drift, b) peak floor drift, and c) peak floor acceleration.....	270
Figure 7.18 Statistical response results of archetype 6 building at different seismic hazard levels seismic hazard levels: a) residual drift, b) peak floor drift, and c) peak floor acceleration.....	270

# Chapter 1 : Introduction

The 1994 Northridge earthquake in the United states and the 1995 Kobe earthquake in Japan caused significant damage to the infrastructure in urban areas with tragic loss of life and economic losses that exceeded \$50 to \$100 billion USD [1], [2]. From the lessons learned from these two events, the academic and structural engineering community shifted their focus towards performance-based design methodology. In performance-based design, structure performance during and after a major seismic event is more predictable and reliable. Structures designed using performance-based methodology are required to meet certain performance criteria which are not only based on the structural integrity, but also include criteria that correlate to safety of occupancy and functionality of the structure after an earthquake. Most performance-based design criteria are based on the maximum inter-storey drift experienced by a structure. However, the use of residual drift as an important performance criterion in addition to the maximum inter-storey drift is demonstrated by a number of studies which focus on the effect of residual drift on building functionality, occupant comfort, rehabilitation cost and structural safety. The residual drift is defined as the permanent deformation that is sustained by the structure following a seismic event.

Studies by Kaga [3] and Seto [4] determined that the minimum inclination angle that can be perceived by building occupants is approximately 0.005 rad (0.5% drift). A survey of 100 residents in Ashiyra city conducted after the Kobe earthquake found that inclination angles as small as 0.005 to 0.006 rad (0.5-0.6% drift) were noticeable by building occupants, with residents complaining from physiological signs of discomfort such as dizziness, headaches and nausea. In addition, residents also reported functionality concerns such as cracking, poor performance of non-structural components, rolling objects and formation of gaps from which air can escape [5].

Another study by Iwata et al. [6] investigated the feasibility of rehabilitation and repair of steel framed structures based on the level of residual drift sustained by the structure. The study found that

rehabilitation of buildings with a residual drift greater than 0.5% was prohibitively costly after considering the losses due to both direct and indirect repair costs as well as the losses from building closure due to construction. This was also observed in the aftermath of the 1985 Mexico city earthquake and the 1995 Kobe earthquake where the residual (permanent) deformation was found to be the deciding factor in the decision to demolish a structure as shown in Figure 1.1 [7], this is especially true when the damage can lead to structural failure when subjected to a second event or an aftershock.

Other studies of non-structural systems through unidirectional wall system testing [8] and shake table tests [9] have found a strong correlation between significant damage to door systems and residual drift exceeding 0.5%, this seriously compromises safety and egress of occupants after an earthquake. A study by Erochko et al. [10] found that systems such as Buckling Restrained Brace Frames (BRBFs) and Special Moment-resisting frame (SMRF) experience residual drifts in the range of 0.5-1.2% under design based earthquake hazards. It was found that when the damaged structures were subjected to a second design level earthquake event, the structures would not exhibit the expected performance assumed under the design standard ASCE 7-05 [11] because of P-Delta effects that seriously compromise the building structural stability and safety. Typical advanced structural systems, such as BRBFs and SMRFs, were shown to exhibit residual drifts ranging from 0.3% to 1.8% when subjected to the hazard level of Design Based earthquake (DBE), but can reach as high as 2% to 4% under the hazard level of Maximum Credible Earthquake (MCE) and near fault earthquake events[10][12].

Self-centering systems, such as rocking wall systems [13]–[18] and self-centering moment resisting frames [19]–[24], are viable options for protection of structures from excessive residual drifts after major seismic events. Self-centering systems rely on a structural mechanism that can accommodate significant drift without yielding, thus allowing the building to return to its original position after a seismic event.



**Figure 1.1 Examples of buildings with residual deformations that typically leads to demolition [7]**

According to a survey of the existing building stock in Canada [25], 56% of the total floor space of commercial and institutional facilities was built prior to 1979 using old design standards that specified poor seismic detailing. This, coupled with the observed poor seismic performance of buildings designed with CSA 1977 or earlier codes, clearly indicates that there is an urgent need to improve performance of these existing deficient structures. The use of some self-centering systems, such as rocking walls or self-centering MRFs, may be a viable option for new construction, but they are not typically appropriate for rehabilitation of existing structures. This led the structural and research community to investigate alternative designs for self-centering braces which can be applied in rehabilitation of existing structures.

Although many developments to self-centering braces have been suggested and evaluated in the past [26]–[33], a need for compact self-centering braces with a large force and sufficient realistic deformation capacity still exists. However, the major challenge for the previously-developed devices is their ability to have a large load capacity coupled with a large deformation capacity. Even when these devices can provide sufficient load and deformation capacity, their required size and length is very large making them impractical to use in most structures. This

project presents the development and performance verification for a new innovative self-centering brace that has the double advantages of a high load and deformation capacity, while still maintaining a compact size compared to previously developed SCED braces. Previously developed SCED braces relied on aramid tendons with a peak strain of 1.8% resulting in the need for tendons in excess of 8 m in length to accommodate a high inter-storey drift demand of 4%. The proposed brace would accommodate the same level of drift demand with a spring that is only 1.2 m in length making it a feasible option for application in both new and existing structures. At this size, the brace can fit in most building bay sizes. The new Ring Spring Self-Centering Energy Dissipative (RS-SCED) brace utilizes ring springs to achieve the self-centering capability and energy dissipation behaviour through friction without the need for external friction fuses.

A brief outline of the thesis is summarized as follows:

Chapter 2 presents an extensive literature review on previous research and development of Self-Centering Energy Dissipative (SCED) devices, with particular attention to the load and deformation capacity of existing device designs. The review includes the testing methodology and techniques used to evaluate these braces.

Chapter 3 presents a detailed discussion of the ring springs and their characteristics, as well as a review of previous studies of ring springs in seismic applications of structural engineering.

Chapter 4 outlines the design, mechanism and components of the new RS-SCED brace developed for this project. The experimental setup, instrumentation and controls used for the evaluation of the brace are presented.

In Chapter 5, results of several characterization tests are presented. These tests aim to evaluate the predictability, durability, consistency, capacity, and rate dependency of the brace. In this phase of

the study, valuable insights on the component response characteristics of the RS-SCED brace and its components are discussed.

Chapter 6 presents the study of a total of 18 hybrid simulations conducted to evaluate the global response of different structures designed with the newly developed RS-SCED braces. The 18 hybrid tests involve testing an 8-storey steel building and a 3-span bridge with voided concrete deck. The earthquake records used are selected to represent different frequency contents including a near-fault earthquake record scaled to different seismic hazard levels.

Chapter 7 presents an extensive analytical study based on the FEMA P695 [34] methodology to quantify the appropriate seismic design factors, such as the ductility factor  $R$ , and overstrength factor  $\Omega_0$ , that are often used in equivalent static load procedure for seismic design of new buildings with the new RS-SCED brace as the main Seismic Force Resisting System (SFRS).

Chapter 8 summarizes the conclusions of this study and highlights some areas recommended for future research work.

# Chapter 2 : Self-Centering Devices

Self-Centering systems have been developed with the design goal of eliminating or significantly reducing the residual drift exhibited by a structure following an earthquake excitation. The main distinctive feature that separates self-centering systems from other Seismic Force Resisting Systems (SFRS) is the flag-shaped hysteresis it exhibits. This flag shaped response results in the structure returning to its initial zero displacement position as shown in Figure 2.1. However, due to this flag-shaped hysteresis, self-centering systems dissipate less energy (at most half) than other typical SFRSs, which exhibit a parallelogram shaped hysteresis. Since large-energy earthquakes tend to be characterized by only one or two maximum peaks in the excitation, the lack of energy dissipation is generally not a major disadvantage. Previous research has shown that Self-centering systems have similar maximum storey drift demand to that of a typical yielding SFRS [35], [36]. The Self-centering behaviour can be introduced into a structure through several possible configurations, such as rocking wall [13]–[18] and self-centering moment-resisting systems [19]–[24]. Another alternative that can accommodate localized deformations without the need for major modifications to the structural system is the use of self-centering devices, which can be either dampers or braces. This section presents a review of existing self-centering devices and their verification testing procedures and results.

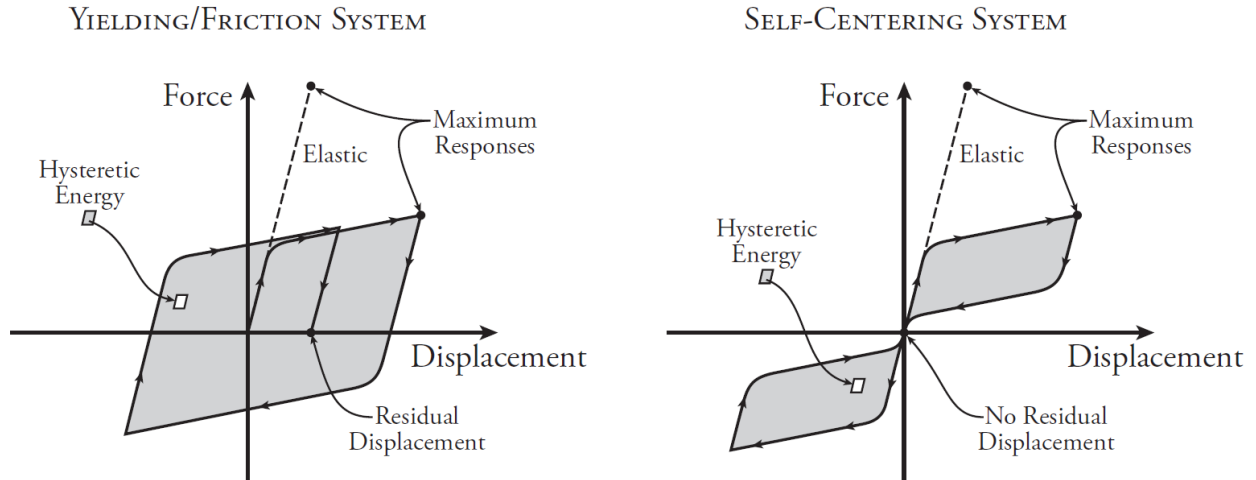
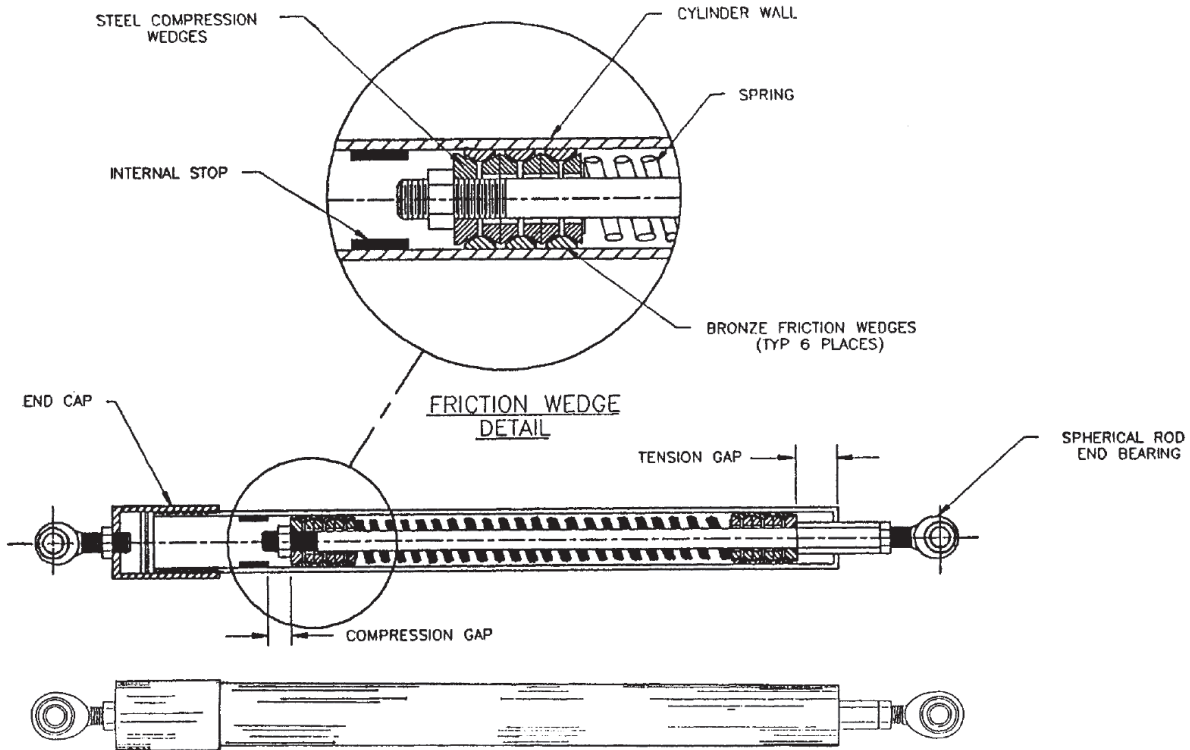


Figure 2.1 Non-linear Hysteresis response of Typical vs Self-Centering SFRS [37]

## 2.1 Energy Dissipating Restraint (EDR) [38]

An energy dissipating restraint (or EDR) is a self-centering bracing member that can be used in seismic retrofit of building structures [38]. A schematic showing the EDR and examples of the brace's hysteretic behaviour are shown in Figure 2.2 and Figure 2.3, respectively. The body of the brace consists of a steel cylinder that is connected to the end cap on the left end of the brace in the figure. The right end of the brace is connected to a rod which is housed within the cylinder. Two sets of friction wedges surround the rod at each of its two ends. These friction wedges provide energy dissipation through friction between the wedges and the outer cylinder. The two sets of wedges are separated by a coil spring. At the left end of the spring and friction wedges, there is a nut that forms a left stop for the friction wedges, whereas at the right end of the spring and friction wedges, the cross-section of the rod increases to provide a right stop for the wedges.



**Figure 2.2 Schematics and hysteresis of EDR [38]**

The EDR is designed so that it does not slip until an initial slip force is exceeded. The initial slip force is determined by the amount of initial compression force on the spring. As the initial spring force increases, the normal force between friction wedges and the cylinder wall increases, causing the friction force to increase. Controlling the initial slip force can be achieved by tightening or loosening the nut at the end of the rod. It is possible to use the EDR with no initial slip force, this can be achieved by tightening the nut so that the initial length of the spring is equal to its unloaded length. Having no initial slip force results in a triangular flag shape hysteresis as shown in Figure 2.3(a). In contrast, having an initial slip force results in the double flag-shaped hysteresis loop shown in Figure 2.3(b).

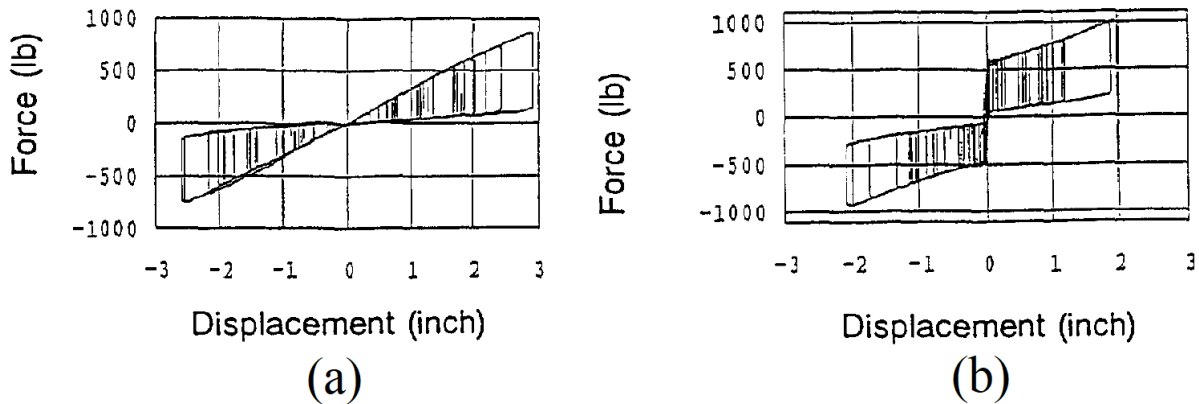
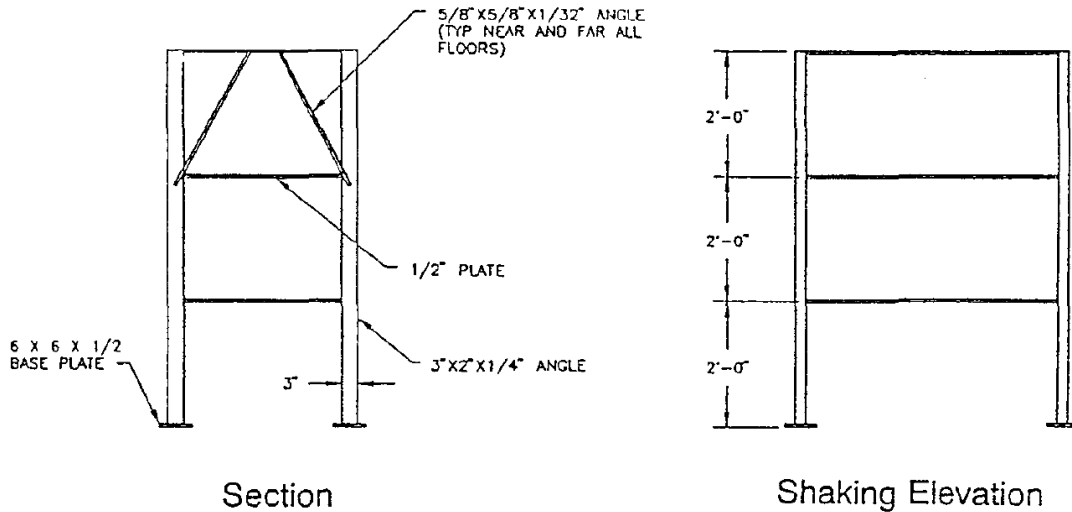


**Figure 2.3 (a) Triangular Lobed hysteresis of EDR, and (b) Double flag-shaped hysteresis loop of EDR [39]**

When the EDR is loaded in compression, the rod and spring are pushed to the left in the diagram, causing the spring to bear against the internal stop which compresses the spring between that internal stop and the enhanced cross section of the rod. When in tension, the rod and wedges shift to the right until the right friction wedges bear against end of the steel outer cylinder, compressing the spring between the nut and the right end of the outer cylinder.

A small-scale 3-storey steel frame was tested on a small shake table at the Earthquake Engineering Research Centre (EERC) at University of California, Berkley for evaluation of the EDR [38]. The model was a three-storey steel moment-resisting frame of all-welded construction. The model was 0.91 m x 1.22 m (3 ft x 4 ft) in plan and the total weight was 18.9 kN equally distributed between the floors [39]. The test program involved subjecting the 3-storey model to two earthquake ground motions. Two EDRs were mounted in each of the three stories of the model. Sketches of the model without and with the EDRs installed are shown in Figure 2.4 and Figure 2.5. Figure 2.6 shows the EDRs installed in the second level of the model. The experimental study also investigated the effect of changing the initial slip force on the acceleration, inter-storey drift and relative floor displacement of the structure. Results have shown that EDRs can reduce the inter-storey drift, relative displacement, and acceleration of the model structure. It was also shown

that an increase in the initial slip force reduced the inter-storey drift and relative displacement, while the effect of the slip force on the acceleration was less defined [39]. The highest recorded load confirmed by testing was about 50% of the floor weight (~ 3kN) with the highest inter-storey drift demand of 1.7%. Unfortunately, since the EDR relies on the stiffness of an axial coil spring, the concept does not scale well and therefore is not practical to design one with an axial capacity that is large enough to work in a full-scale structure. Instead, EDRs can be used as seismic dampers that can be installed in multiple frames to increase the damping in the structure.



Section Shaking Elevation  
 Figure 2.4 3-storey bare model frame used for shake table test [39]

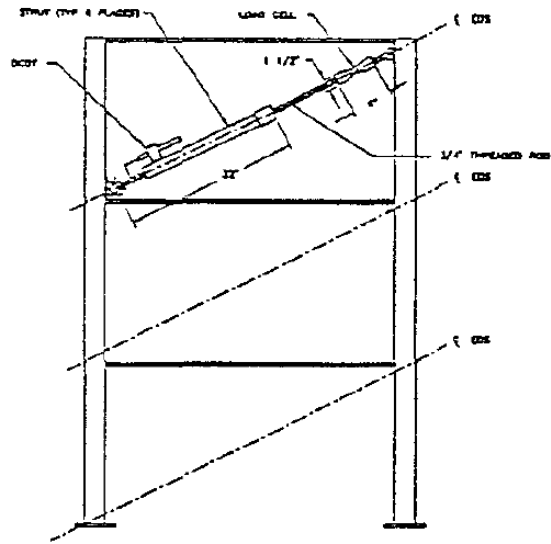


Figure 2.5 Frame with Energy Dissipating Restraints [39]

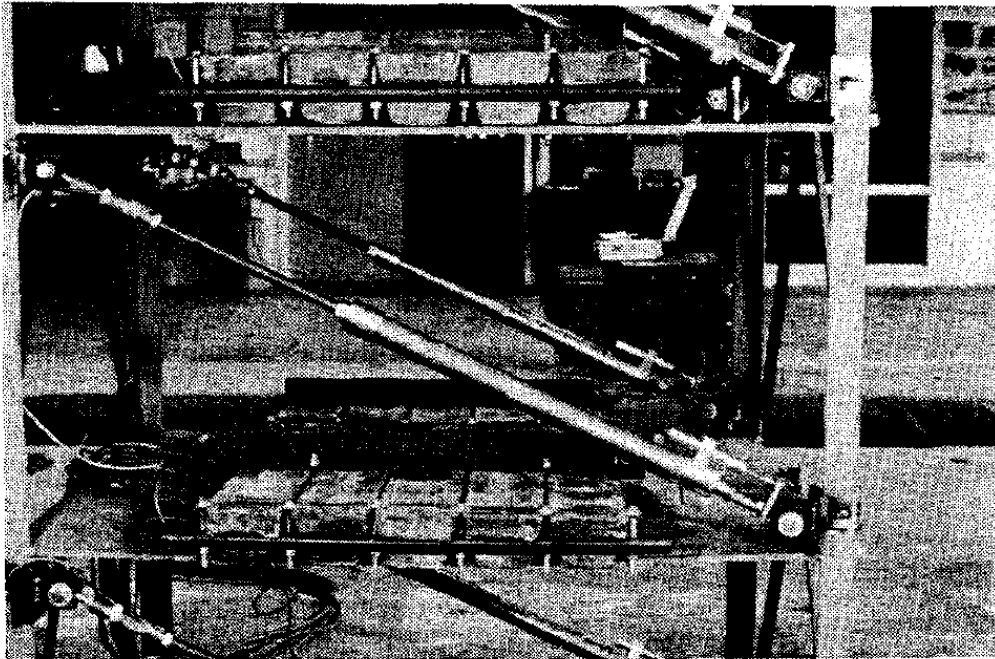


Figure 2.6 View of EDRs installed at second level of frame [39]

## 2.2 Fluidic Self-Centering Device [40], [41]

The fluidic Self-centering device [40] is a self-centering bracing member that was originally developed for the United States Military in the 1970s but was later adapted for use in combination with base isolation systems for civil engineering structures. The original device presented by Tsopelas and Constantinou [40] has a maximum axial capacity of only approximately 15 kN. However, the device has been scaled up recently to achieve an axial load capacity of 400 kN and an elongation capacity of 50 mm [41]. A schematic showing the fluidic self-centering device and its mechanics is shown in Figure 2.7.

Like the EDR, the body of the brace consists of a steel cylinder. Within that cylinder there is a compartment which contains a compressible silicone fluid. A piston head slides inside the fluid compartment separating it into two sides. The piston head contains orifices to allow the fluid to flow between the two sides of the compartment. The movement of this fluid as the piston head moves within the compartment creates a velocity-dependant viscous force in the brace. The restoring force in the system is provided by the compressible fluid. The piston rod is thick, so when the piston is pushed to the right side of the fluid compartment (as shown in the figure), the volume taken up by the rod increases, which compresses the fluid, providing a restoring force. Likewise, when the piston is pulled to the left, the volume taken up by the rod decreases. During assembly, the fluid is pre-compressed so that the pre-compression in the fluid must be exceeded before the piston can move.

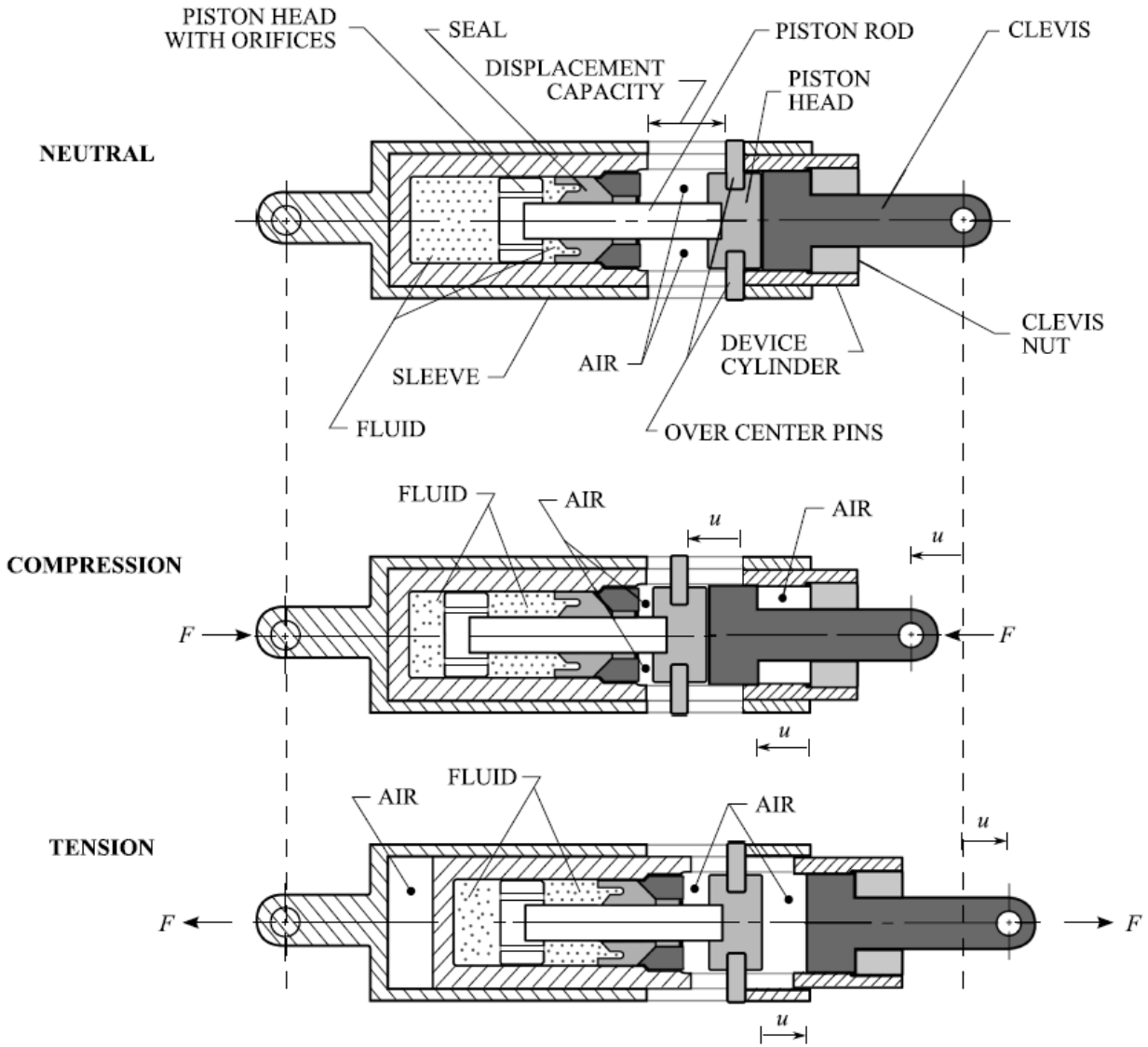


Figure 2.7 Schematic and dynamics of the Fluidic self-centering device [41]

The large fluidic self-centering devices were tested at the testing facility of Taylor Devices in North Tonawanda, New York [41]. The effect of temperature, loading rate and initial fluid compression were investigated. One device was tested quasi-statically up to an amplitude of 50 mm at 3 different temperatures. This affected the preload of the devices as shown in Figure 2.8. A second device was tested cyclically at different initial fluid compression pressures with an initial fluid pressure of 72.5 MPa. The device was loaded quasi-statically at an amplitude of 50 mm followed by 3 dynamic tests at varying loading rates. The hysteresis of the device at the varying

loading rates is shown in Figure 2.9. Due to the presence of the viscous fluid, the energy dissipation of the brace is highly dependent on the loading rate as shown in Figure 2.9. The device is also limited by its maximum load capacity of 400kN.

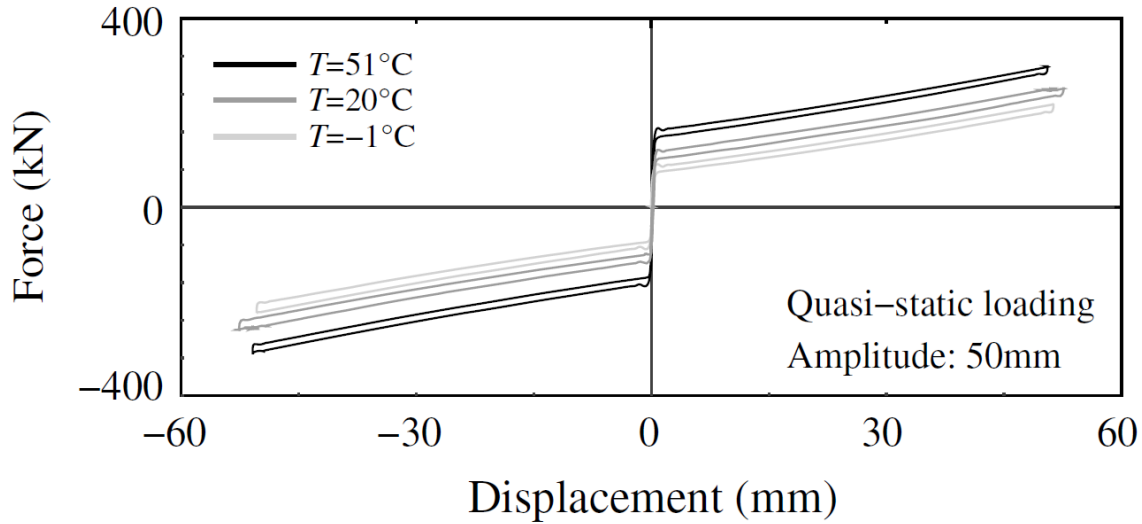


Figure 2.8 Temperature effect on response of fluidic damping device [41]

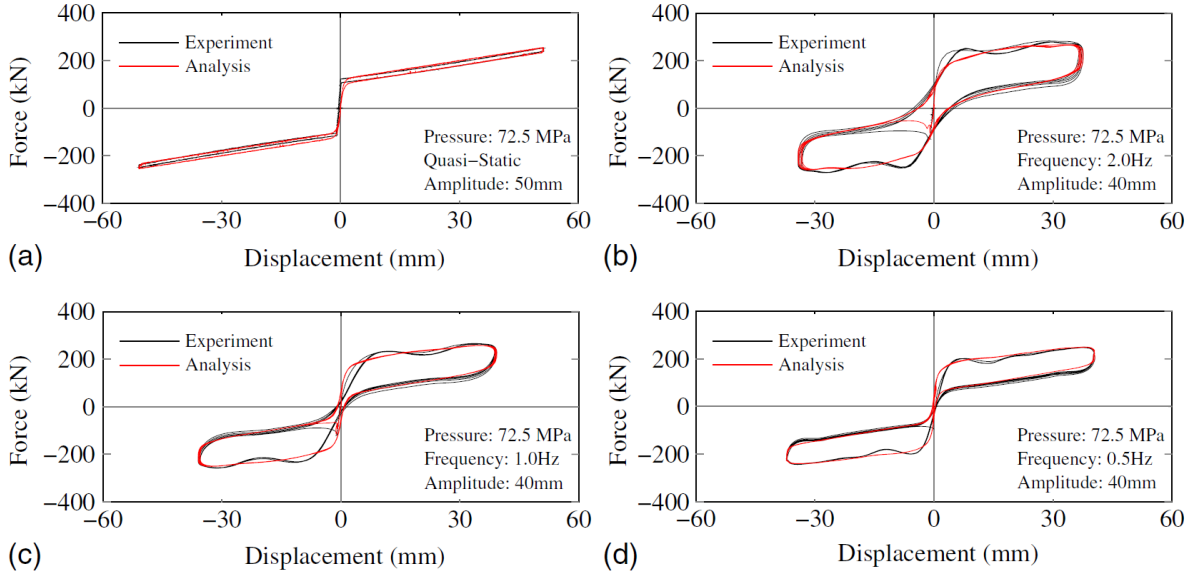


Figure 2.9 Hysteresis of fluidic damping device under (a) quasi-static load, (b) 2.0Hz dynamic load, (c) 1.0Hz dynamic load, and (d) 0.5Hz dynamic load [41]

### 2.3 Friction Spring Seismic Damper [42], [43]

The friction spring seismic damper is similar to the EDR in the sense that the restoring force is provided by a spring. However, this damper utilizes friction ring springs instead of a coil spring. The damper dissipates energy through friction between the ring spring contact surfaces rather than a separate friction wedge present in the EDR. A ring spring assembly comprises of individual inner and outer rings arranged in a columnar form as shown in Figure 2.10. When the spring column is axially loaded, the tapered surfaces slide against each other dissipating energy through friction. The schematics of two similar friction spring seismic dampers have been developed as shown in Figure 2.11 and Figure 2.12.

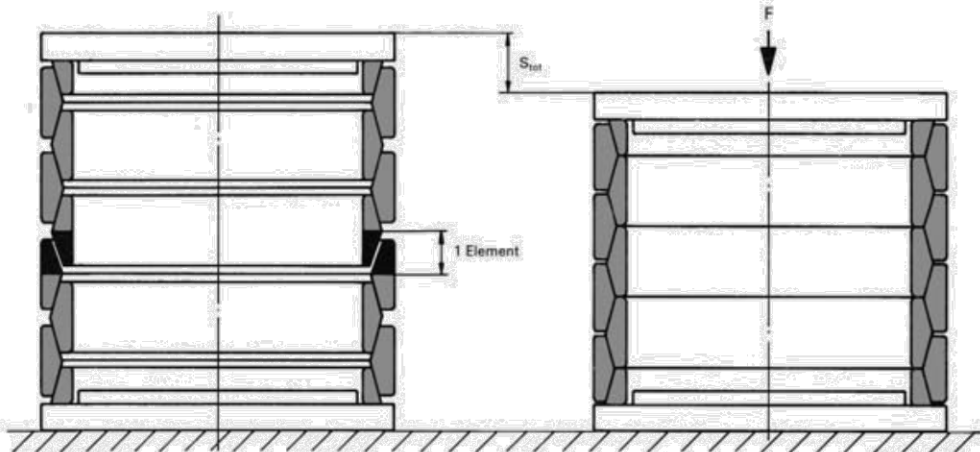


Figure 2.10 Friction Spring assembly consisting of 4 outer rings, 3 inner rings and 2 half inner rings [44]

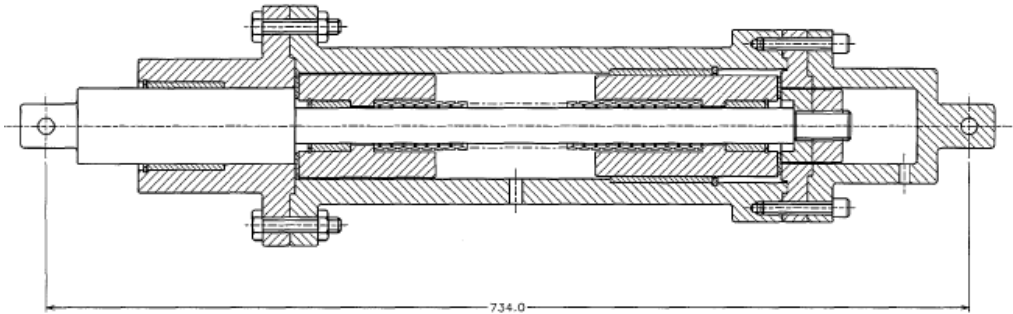


Figure 2.11 Bi-Directional Ring Spring Cartridge [42]

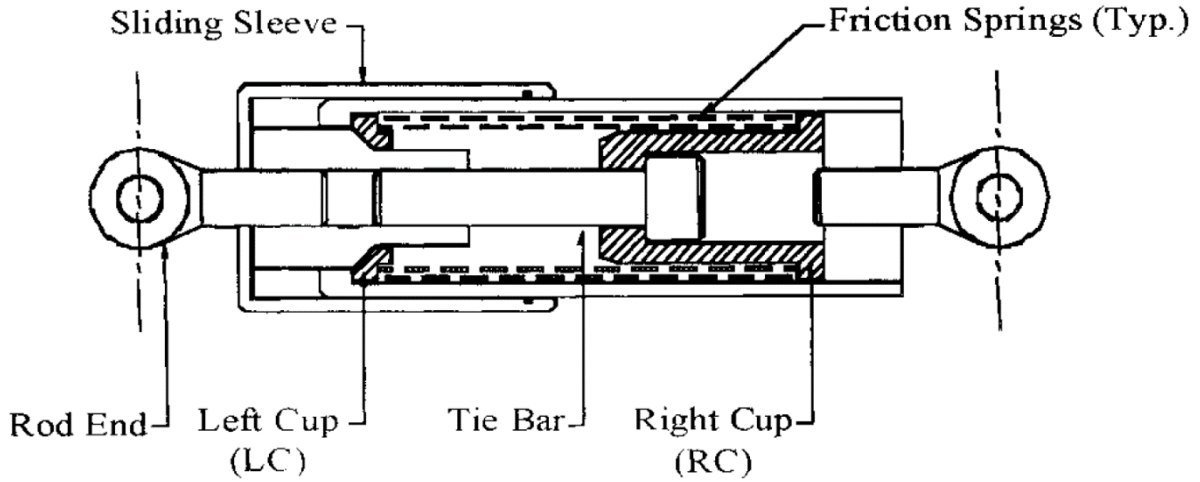


Figure 2.12 Seismic damper [45]

The seismic damper developed by Filiatrault et al. [45] was tested both cyclically as well as using shake table tests. Detailed discussion of this device response and test results is presented in Section 3.3. Despite the dampers having consistent hysteresis response as shown in Figure 2.13, the load capacity of these dampers was only about 100 kN and a deformation capacity of 25 mm, which limits the applicability of the dampers in large structural systems.

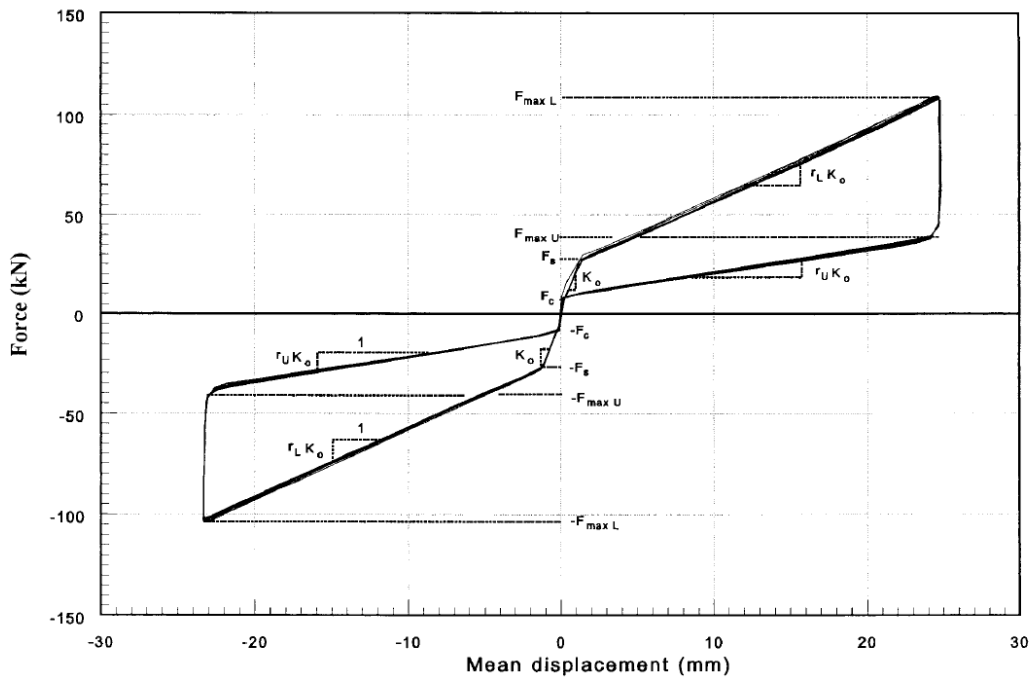


Figure 2.13 Hysteresis of the Ring Spring Damper [45]

## 2.4 Reusable Hysteretic Damping Brace (RHDB) and Self-Centering Friction Damping Brace (SFDB) [46], [47]

The reusable Hysteretic Damping Brace (RDHB) is a damping device with inherent Self-centering behaviour and enhanced energy dissipation capacity. The damping device relies on superelastic Shape Memory Alloy (SMA) strands made from superelastic Nitinol wire strands to both dissipate energy and provide a self-centering behaviour. The RHDB consists of two steel blocks that slide past each other as shown in Figure 2.14. Nitinol wire strands are attached to the two sliding blocks using anchor fixtures similar to the ones used for pre-stressing. Adjusting the volumes of the un-pretensioned and pretensioned wires allows the RHDB to achieve a self-centering hysteresis behaviour. The number of strands can vary to accommodate different force levels and different range of hysteretic behaviour.

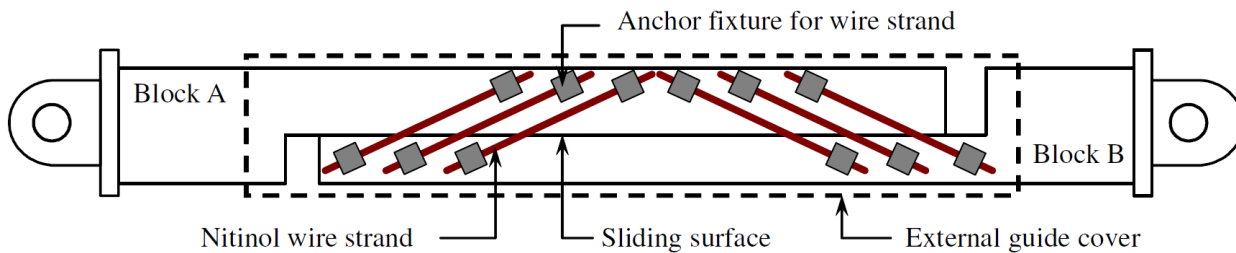


Figure 2.14 Mechanical Configuration of RHDB [46]

To enhance the energy dissipation capacity of this device, a third block can be added to introduce more friction surfaces. This new device with the added block is called the Self-Centering Friction Damping brace (SFDB) and is shown in Figure 2.15. By varying the tension of the bolts, the frictional force can be adjusted, allowing for more energy dissipation in the damper hysteresis. A scaled down prototype was cyclically tested on an MTS servo-hydraulic test machine at the loading frequency of 2 Hz. The cyclic test was conducted at three different levels of friction force. Figure 2.16 (d), (e) and (f) show the hysteresis of the frictional forces corresponding to the total brace hysteresis in Figure 2.16 (a), (b) and (c), respectively. The SFDB prototype achieved an

elongation of about 2.5% (equivalent to 18 mm) and an axial capacity of 12 kN. An analytical study of a full-scale brace with a length closer to 2 m showed the brace can achieve an axial capacity of 2000 kN and an elongation capacity of 3.6% (equivalent to 70 mm). However, scaling of the brace to this level may be cost prohibitive, limiting the applicability of the brace in large structures.

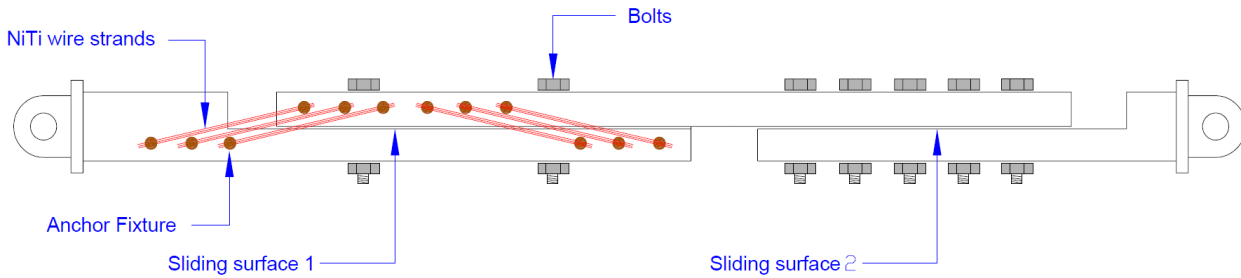


Figure 2.15 Mechanical Configuration of SFDB [47]

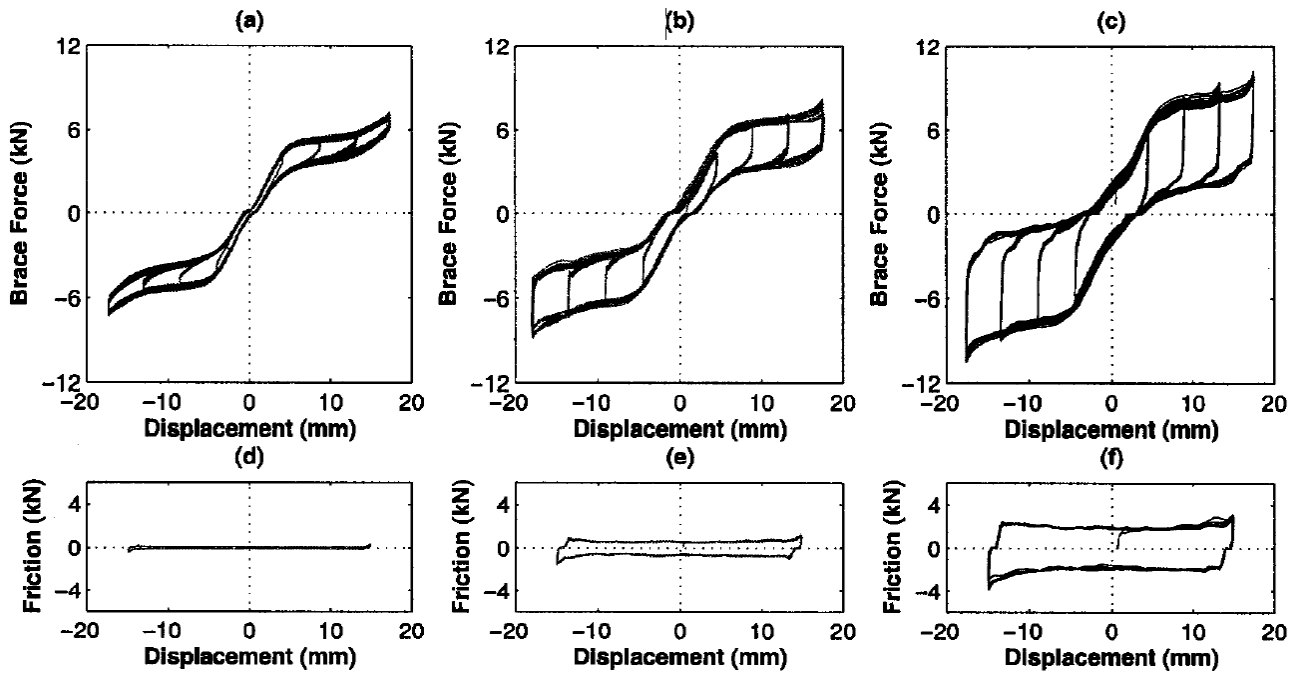


Figure 2.16 Hysteresis of experimentally-tested SFDB [47]

## 2.5 Pretension SCED (PT-SCED) and High capacity SCED (HC-SCED) [26], [27]

The pretensioned SCED brace is a self-centering device that utilizes pretensioned aramid tendons and friction dampers to provide self-centering and energy dissipation, respectively. The brace consists of two steel members of the same length which are fitted one inside the other concentrically. The PT-SCED was a proof of concept design with a limited load capacity which utilized rectangular tube members for both the inner and outer members, as shown in Figure 2.17.

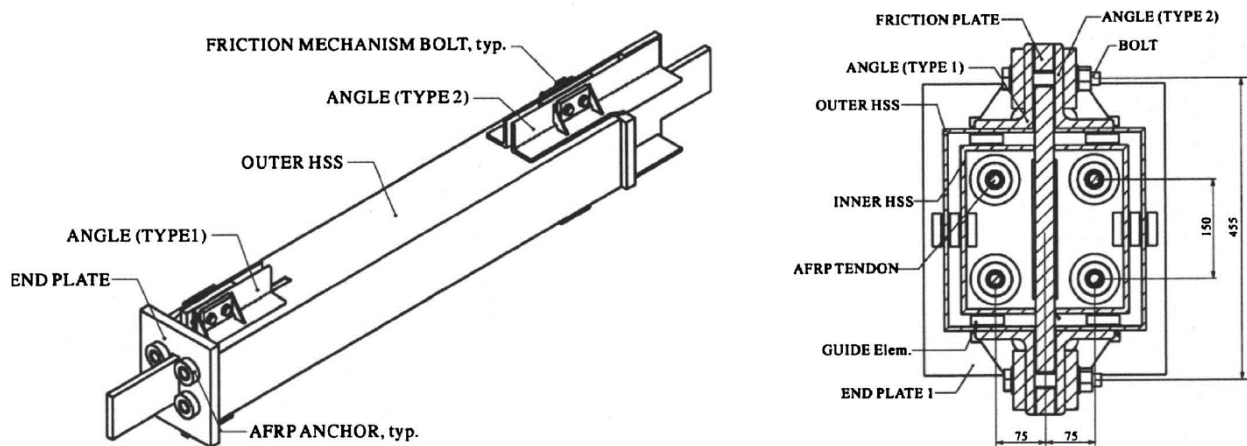
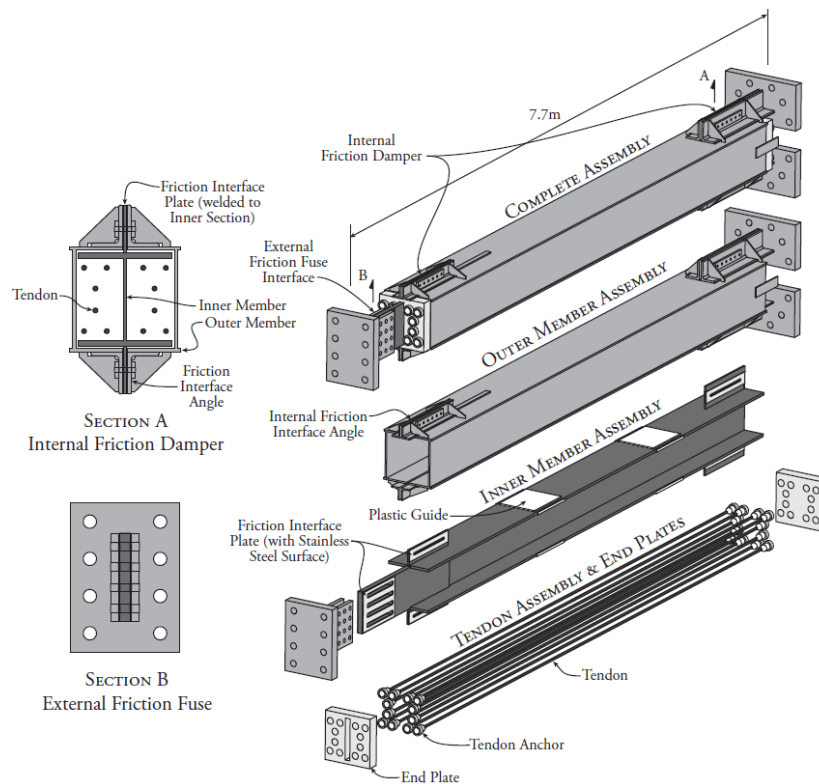


Figure 2.17 Schematic of PT-SCED [26]

The high capacity SCED (HC-SCED) utilized a WWF member as an inner member and a steel tube as an outer member as shown in Figure 2.18. In the HC-SCED, steel plates with stainless steel surfaces are welded to the outside surface of the inner member. The outer member is slotted at its ends to allow the motion of the welded steel plates relative to the outer member. At both ends of the outer member, pairs of back to back steel angles are welded to the outside surface with a gap in between them equal to the slot width. The outer member slots and the gap between the back to back steel angles, allow for the welded steel plates and stainless-steel surfaces to slide in between them when the inner and outer members move relative to each other. The steel angles have a recess to accommodate friction pads which creates a friction interface when in contact with the stainless-

steel surface. The friction caused by the movement of the outer and inner members creates friction at this interface, which provide energy dissipation to the hysteresis of the brace. High strength bolts are used to apply a normal force that controls the friction force at the friction interface. Aramid tendons are used to provide the self-centering restoring force in the brace. Two steel end plates are fitted on each end of the steel member assemblies. The Aramid tendons are pretensioned and anchored to the end plates. In addition, an external friction fuse is also introduced at the connection between the inner member and connecting frame to accommodate for extra deformation required to satisfy the drift demand of the structure as shown in Figure 2.18.



**Figure 2.18 Schematic of HC-SCED [27]**

As the brace undergoes compression, the inner member moves to the right pushing the right end plate to the right while the outer member moves to the left moving the left end plate to the left. This causes the plates to move apart putting the tendons under tension. When the brace is under tension the inner member moves to the left bearing against the left end plate which moves it to the

left while the outer member moves to the right bearing against the right end plate which moves it to the right. This once again moves the plates apart from each other causing the tendons to be under tension. Initially, the members move slightly relative to each other with an initial stiffness that is characterized by the parallel stiffness of both members and the tendon stiffness. Once the force exceeds the initial activation force, the members move in opposite direction relative to each other resulting in dynamic friction in the internal friction device. Once the brace reaches its load capacity the external fuse slips allowing for additional deformation capacity.

Full-scale testing was performed at the Structural Engineering Laboratory of École Polytechnique of Montreal using the 9 x 3.75 m test frame depicted in Figure 2.19. The frame was then subjected to a combination of reverse cyclic quasi-static and dynamic loading protocols. The frame was also subjected to real time inter-storey drift responses obtained from nonlinear dynamic analysis at the first-floor level of an eight-storey building incorporating the SCED bracing system subjected to three different ground motions. The capacity of the original PT-SCED was 800 kN. The HC-SCED improved the load capacity of the original PT-SCED to be comparable to that of a large Buckling Restrained brace. This was achieved by using larger members and more tendons. The inner member was also changed to a WWF section to improve the load transfer mechanism. The design capacity of the HC-SCED was 3800 kN. The HC-SCED brace was tested in the 12 MN load frame at École Polytechnique in Montréal. The test setup and instrumentation are shown in Figure 2.20. Both the PT-SCED and HC-SCED had an elongation capacity of 2% that can be increased to 4% with an external friction fuse. Sample hysteresis for the response of both braces is shown in Figure 2.21.

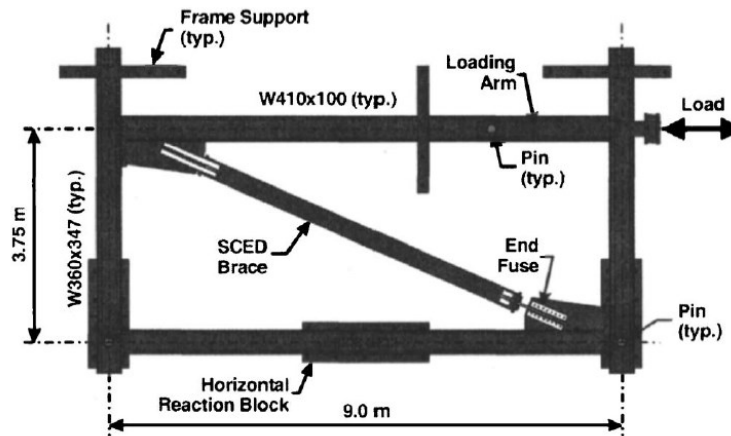
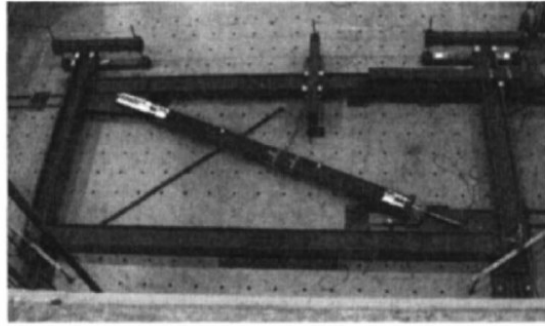


Figure 2.19 Setup for quasi-static and dynamic testing of frame incorporating PT-SCED brace [26]

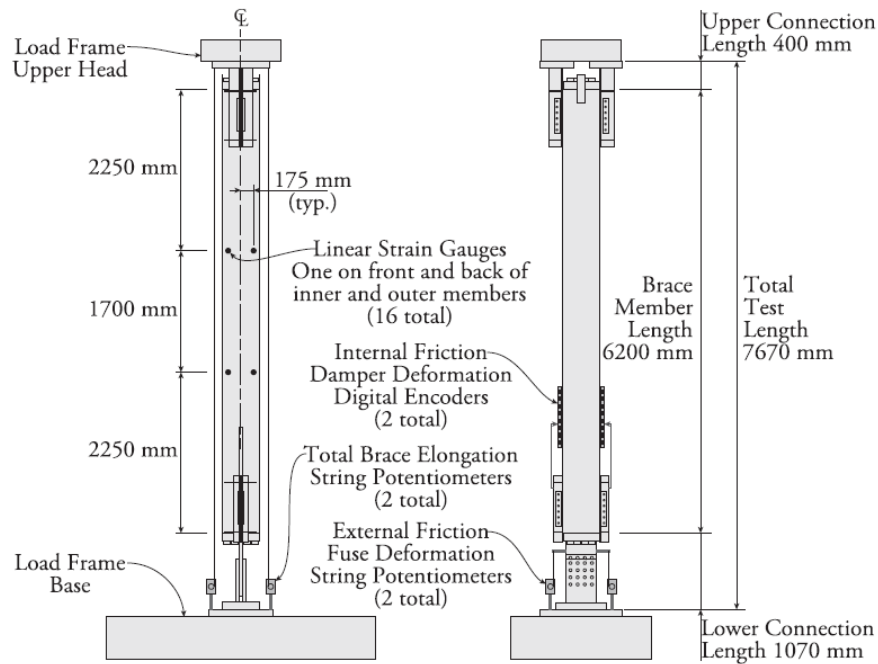


Figure 2.20 HC-SCED test setup and instrumentation [27]

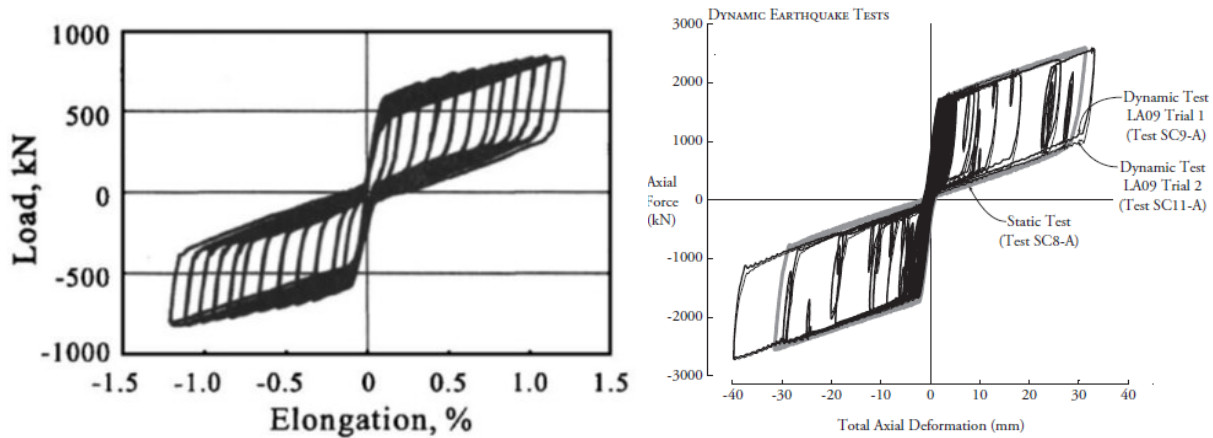


Figure 2.21 Sample Hysteresis of PT-SCED (left) and HC-SCED (Right) [26], [37]

## 2.6 Telescoping SCED brace (T-SCED) and Dual Core Self Centering Brace (DC-SCB) [28], [48]

Both the Telescoping SCED (T-SCED) brace and the Dual Core Self Centering Brace (DC-SCB) were designed to accommodate for a higher elongation capacity than the original PT-SCED and the HC-SCED braces but without the need of an external friction fuse. The major difference in these braces is the presence of an extra intermediate member as shown in Figure 2.22 and Figure 2.23. Even though only one intermediate member was added, it is possible to scale this concept and add two or three intermediate members. The addition of the extra member allows for doubling the elongation capacity of the brace.

Like the original SCED braces discussed in the previous section, the T-SCED brace uses aramid tendons and a friction device that consists of a friction interface angle welded to the outer member and a friction interface plate welded to the inner member. The DC-SCB brace uses E-glass Fibre Reinforced Polymer tendons with the same friction mechanism. In both applications, two sets of tendons were used. The first set of tendons is anchored to the inner end plates which bear against the inner and intermediate members. The second set of tendons is anchored to the outer end plates which bear against the intermediate and outer members. The inner and outer end plates can move

relative to each other. This concept means that both sets of tendons (the inner and the outer) experience the same strain while the elongation capacity of the brace is doubled.

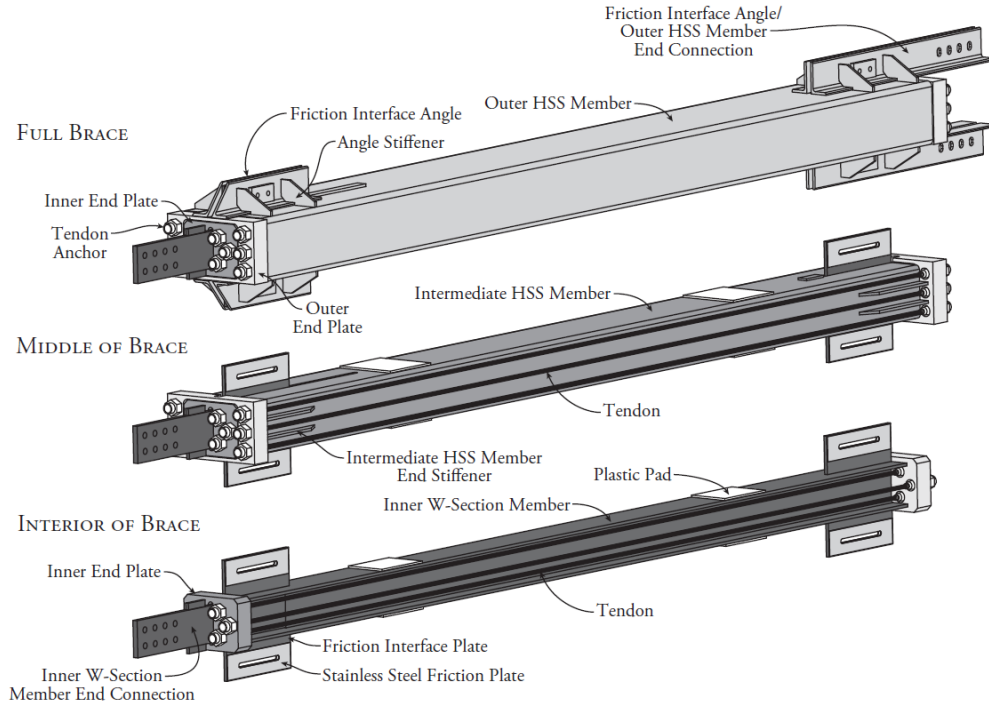
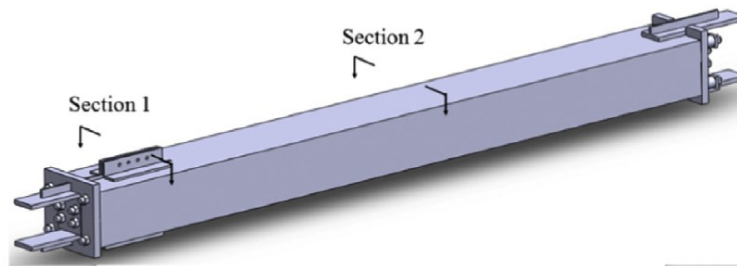
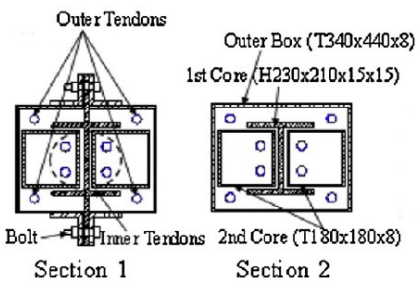


Figure 2.22 T-SCED brace schematics [28]



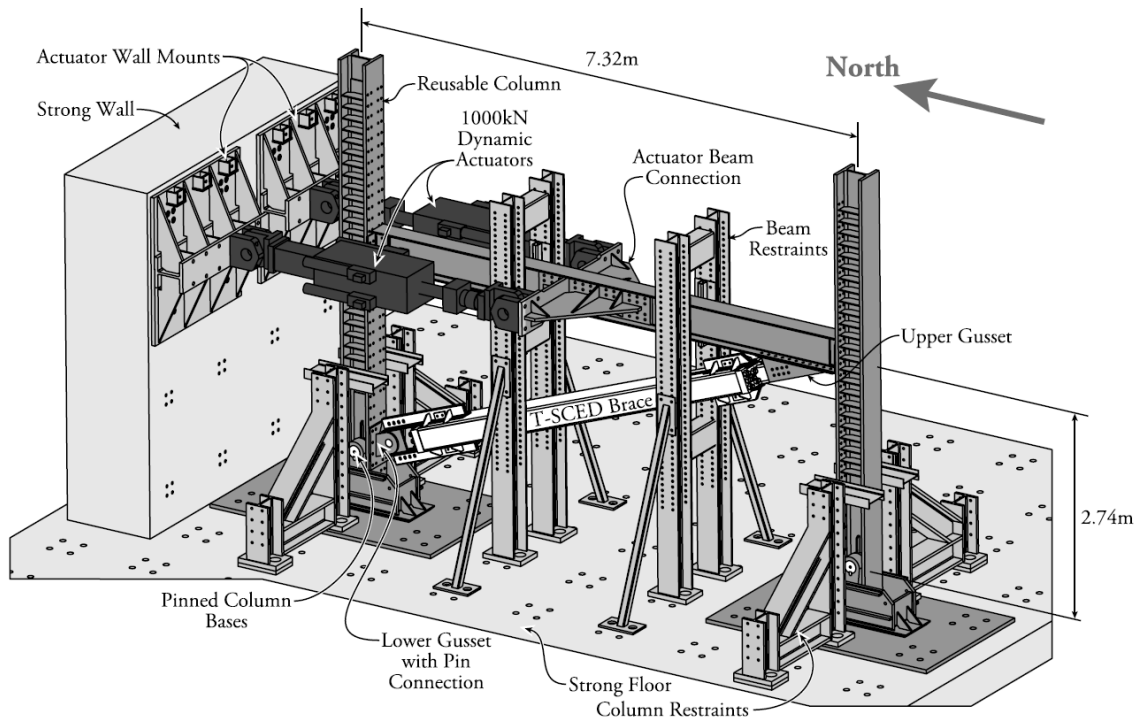
(a) Overall View



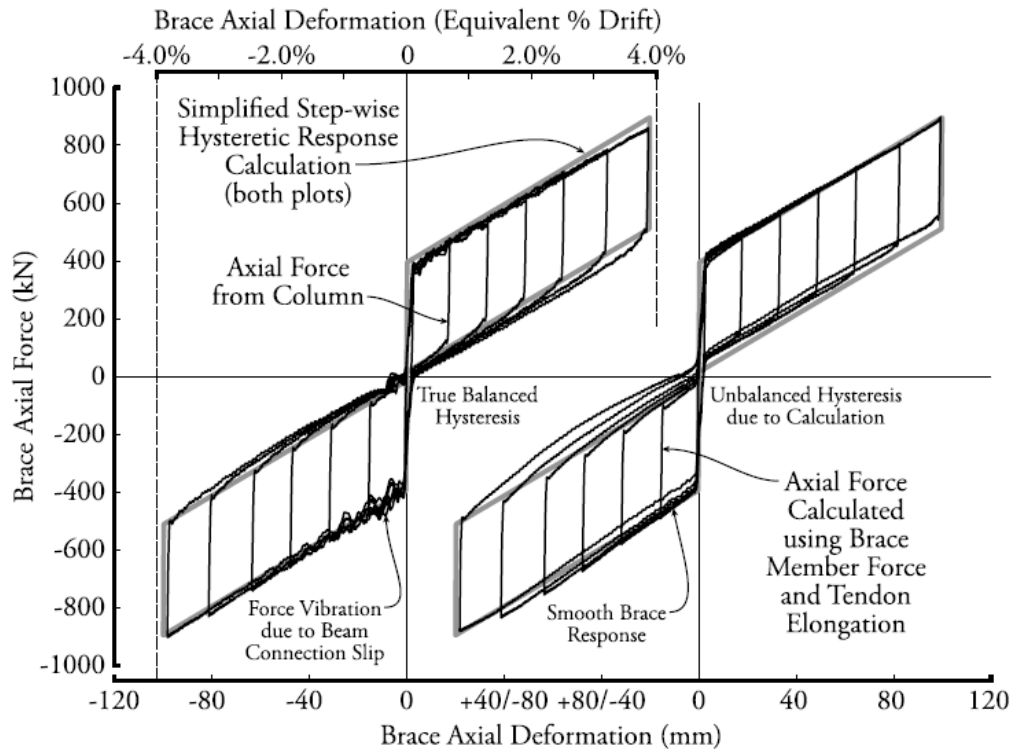
(b) Cross Section

Figure 2.23 Dual-Core SCB Schematics [48]

A full-scale reusable steel test frame with the T-SCED brace was tested in the structural laboratory at the University of Toronto using two dynamic 1000 kN actuators. The test setup is shown in Figure 2.24. The T-SCED brace was subjected to both static and dynamic protocol tests in addition to dynamic earthquake deformation records, most of which included equivalent lateral frame drift of 2% or greater. In addition, a separate hybrid testing program was conducted [49], which subjected the T-SCED brace to additional earthquake tests. The T-SCED was designed for a maximum load capacity of 820 kN and achieved a maximum elongation of 4.2%. The hysteresis of the T-SCED is shown in Figure 2.25.



**Figure 2.24 Test frame used for testing the TSCED brace [28]**



**Figure 2.25 Sample Hysteresis of T-SCED brace [28]**

Figure 2.26 shows the test setup for the DC-SCB, which included one steel box column pin-supported to the floor and attached to two 1000-kN hydraulic actuators. The brace was tested using quasi-static loading protocols at varying displacement rates depending on the level of drift. The DC-SCB was designed to have an axial load capacity of 1300 kN and achieved an elongation capacity of 2.6%. The hysteresis of the DC-SCB is shown in Figure 2.27.

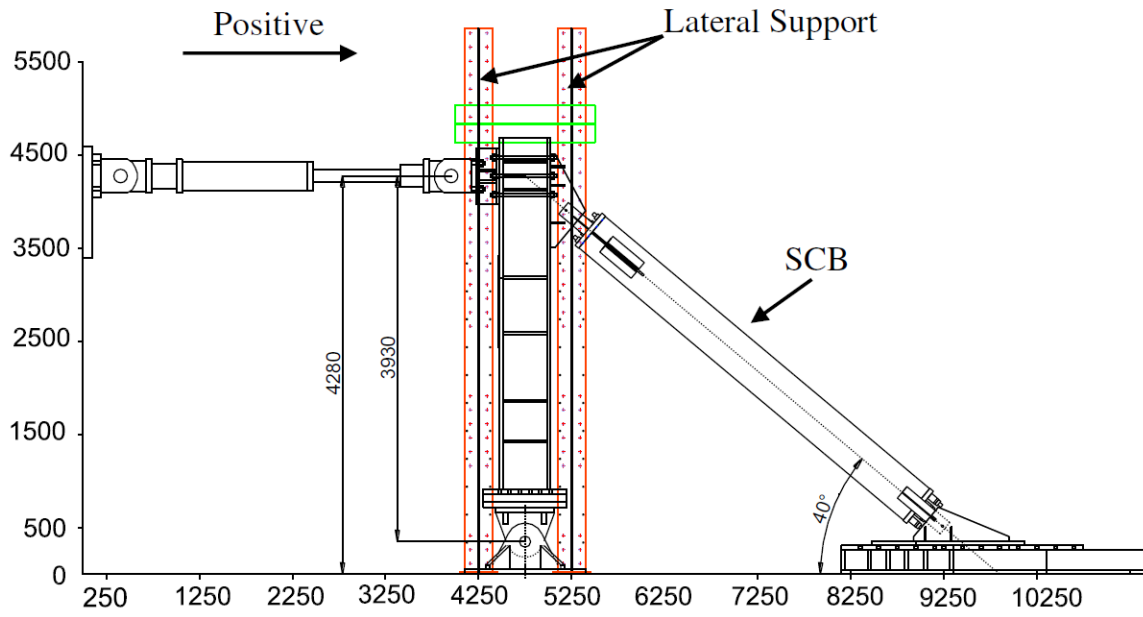


Figure 2.26 Test setup used for testing the DC-SCB [48]

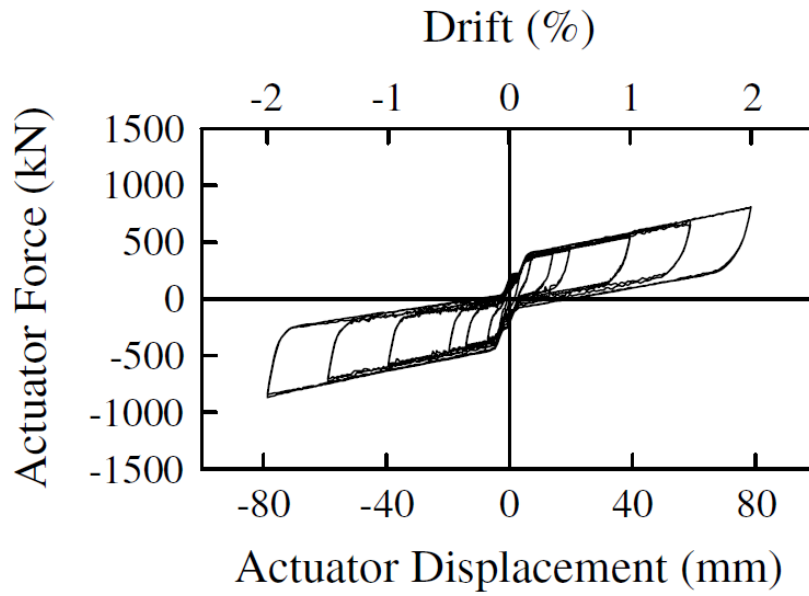


Figure 2.27 Sample Hysteresis Response of the DC-SCB [48]

## 2.7 Self-Centering Buckling Restrained Brace [50]

The Self-Centering Buckling Restrained Brace (SC-BRB) combines the self-centering behaviour of shape memory alloys (SMAs) and the energy dissipation of a Buckling Restrained Brace (BRB). The SC-BRB consists of three steel members, a steel BRB yielding core, SMA rods (NiTi SMA) and two steel end plates used for anchorage of the rods. A partially exploded view of the assembly is shown in Figure 2.28. The steel core is tapered along the length so that there is a yielding region in the center of the brace. As this core yields in tension and compression, it dissipates energy thus providing the majority the energy dissipation capacity of the brace. The inner tube is virtually unstressed and serves the sole purpose of preventing the buckling of the yielding and connection regions of the steel core. Concrete is placed between the inner tube and the steel core with a bond break and a small gap to allow for axial movements of the core. The middle tube is welded to the left end of the steel core (in the orientation shown in Figure 2.28) and slotted on the right end to allow for movement of the tube relative to the steel core. The outer tube is welded to the right end of the steel core (in the orientation shown in Figure 2.28). Anchorage plates are then added to both ends of the brace to anchor the SMA rods. The anchorage plates have cruciform-shaped slots that allow for unimpeded movement of the steel core. Finally, super elastic NiTi SMA rRods are pretensioned to clamp the two anchorage plates against the middle and outer tubes creating an initial compression. The full length of SMA rods is not required and can instead be coupled with high strength steel rods as shown in Figure 2.28.

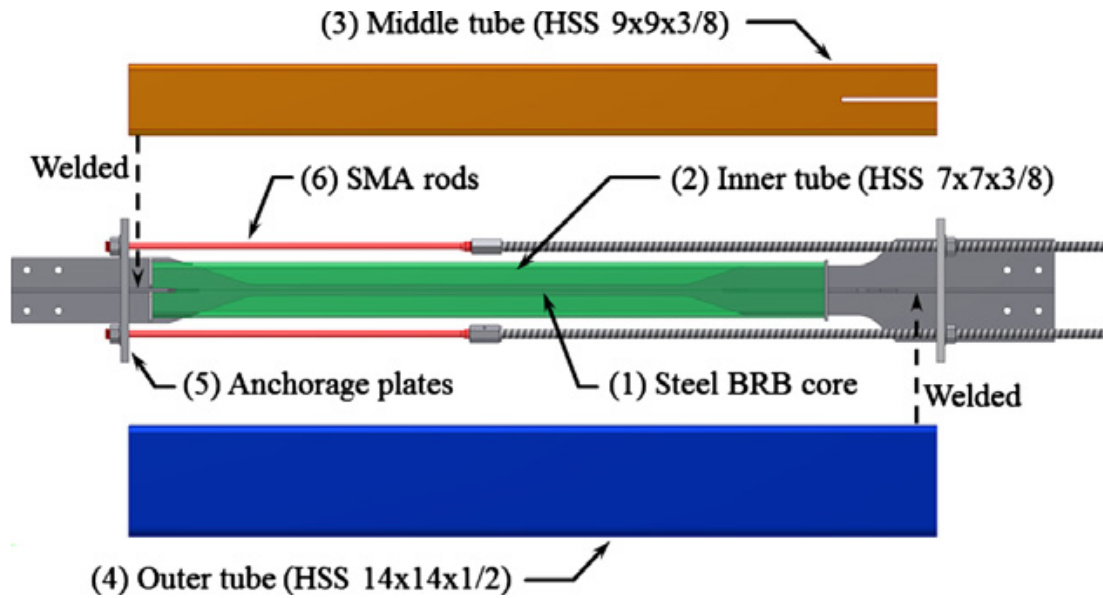


Figure 2.28 SC-BRB components [50]

The mechanics of the brace are designed to load the SMA rods in tension when the brace is under tension or compression. The mechanism of the SC-BRB is shown in Figure 2.29. The mechanics of this brace are very similar to those in the PT-SCED and HC-SCED described earlier. Two large-scale SC-BRB test specimens were designed based on the procedure outlined above. The braces were approximately half-scale as related to a typical mid-rise office building in a high seismic region such as western United States [50]. The specimens were tested in a 2.7 MN uniaxial servo-controlled hydraulic test frame, using a modified version of the BRB testing protocol specified in the AISC Seismic Provisions for Structural Steel Buildings (AISC 341). The SC-BRB behaviour was found to be robust, and the hysteresis behaviour of the brace showed that the residual deformation after load removal was 40%-60% of the maximum deformation of the brace. The residual deformation was attributed to a combination of BRB overstrength compared to yield strength, BRB strain hardening and loss of SMA pretension. Sample hysteresis of the SC BRB is shown in Figure 2.30.

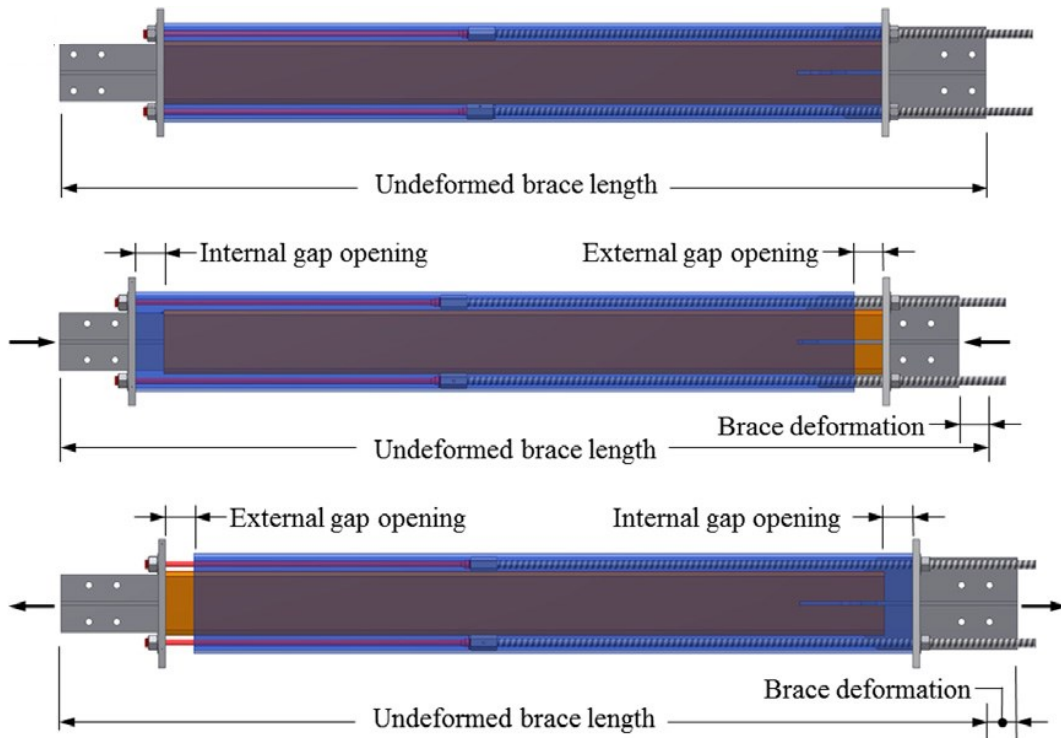


Figure 2.29 SC-BRB mechanics [50]

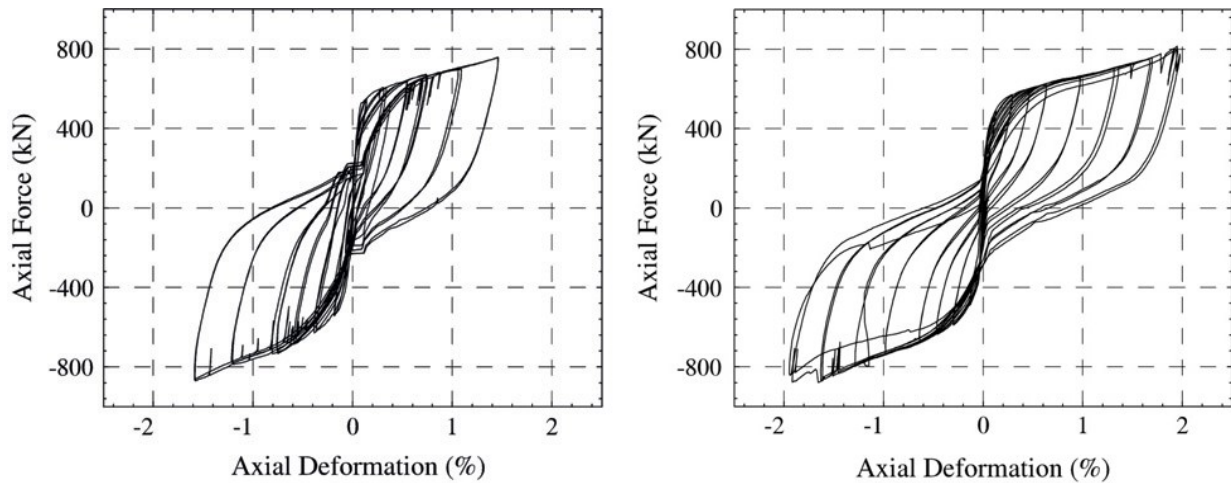
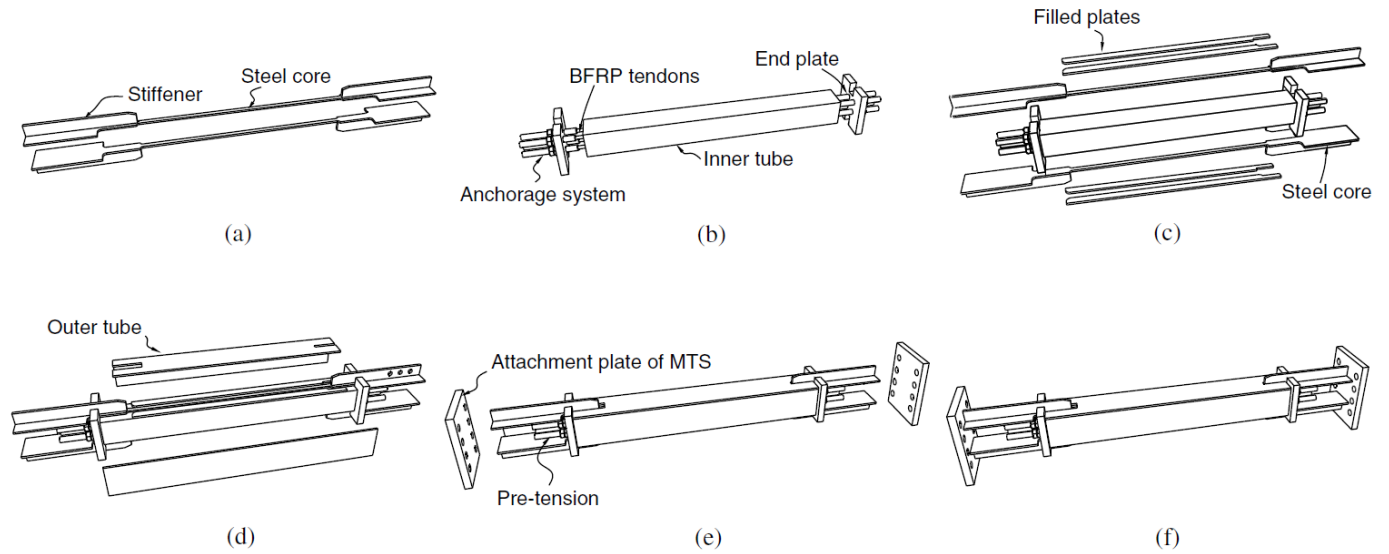


Figure 2.30 Hysteresis response of two different SC-BRB configurations [50]

## 2.8 Dual Tube Self Centering BRB [29]

The Dual Tube Self centering BRB had the main goal of simplifying the design of the SC-BRB developed by Miller et. al [50] in reducing the weight of the brace and fabrication costs. The Dual Tube SC-BRB also uses Basalt Fibre Reinforced Polymer (BFRP) tendons which have a lower cost than aramid and carbon fibres, while still having a lower elastic modulus and higher elastic

elongation than a prestressed steel strand. The main components of the Dual-tube SC-BRB are two steel tubes of equal lengths which fit into each other, two parallel steel core plates, two end plates at each end and BFRP tendons. The steel core is placed between the inner and outer tube thus restraining it from out of plane buckling. The steel cores are stiffened at both ends in the non-restrained region of the core to ensure the connection to the core are rigid (Figure 2.31a). The core is placed at both top and bottom surfaces of the inner tube. The two end plates are placed on both ends of the tube with the BFRP tendons passing through the middle of the tube (Figure 2.31b). The steel cores should be welded to the inner tube at one end of the tube (in this orientation it is the left end). To prevent in-plane buckling, two filled plates are welded to the outside of the inner tube on either side of each steel core (Figure 2.31c). The outer tube, which is made of two steel angles, is placed around the inner tube and the steel core, then welded together into a single tube (Figure 2.31d). After ensuring both tubes are bearing against the anchorage plates at both ends, the BFRP tendons are prestressed and fastened to the anchor plates (Figure 2.31e). The stiffeners at one end of the steel cores are then welded to the outside of the outer tube, and the stiffeners at the other end of the steel cores are welded to the inner tube. The stiffened steel core ends are then welded to the connecting plates to complete the assembly (Figure 2.31f). The brace is designed to allow for the steel core to yield in both tension and compression, while having the BFRP tendons always under tension. A schematic of the brace mechanics is shown in Figure 2.32.



**Figure 2.31 Assembly of the Dual Tube SC-BRB [29]**

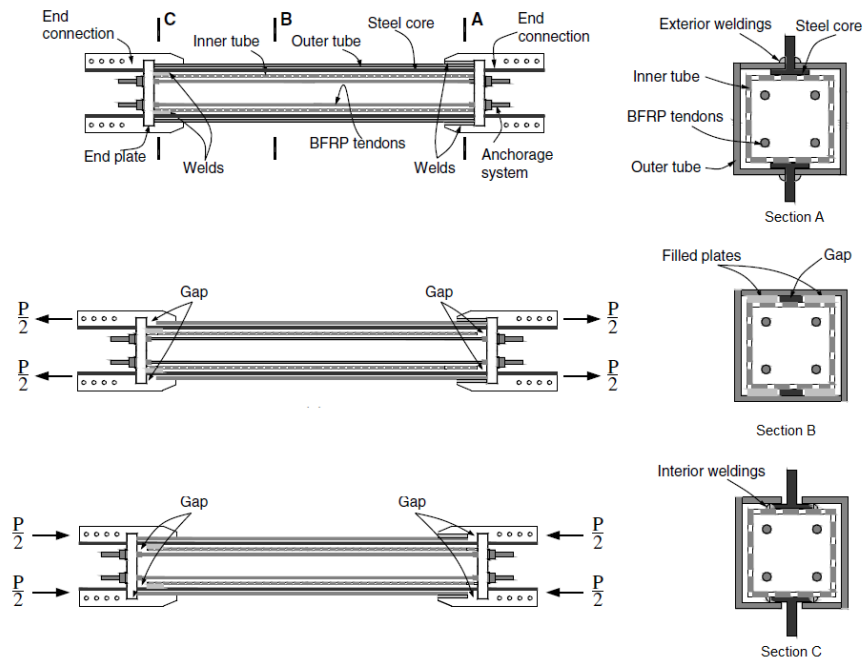


**Figure 2.32 Mechanics of the Dual-Tube SC-BRB [29]**

Quasi-static experiments were performed on all specimens using a 1000 kN MTS hydraulic testing apparatus in the Structural Laboratory at Southeast University [29]. The loading protocol for the experiment was determined according to the cyclic loading requirements for BRBs in the AISC seismic provisions for structural steel buildings [51]. The maximum axial capacity of the member tested was 750 kN with a maximum elongation of 1.3% (29.4 mm). The brace tended to

develop residual deformation even at low levels of loading mainly due to the yield hardening effect in the core plate. At around 1.2% elongation, the tendons started failing due to gradual rupture of the tendons causing degradation of the self-centering behaviour, and ultimately fracture of the steel core. A sample hysteresis of one of the tested Dual-Core SC-BRB is shown in Figure 2.33.

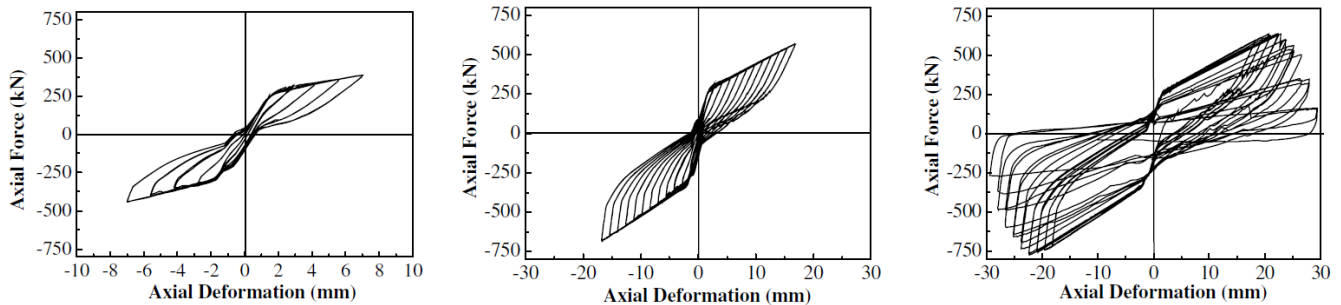
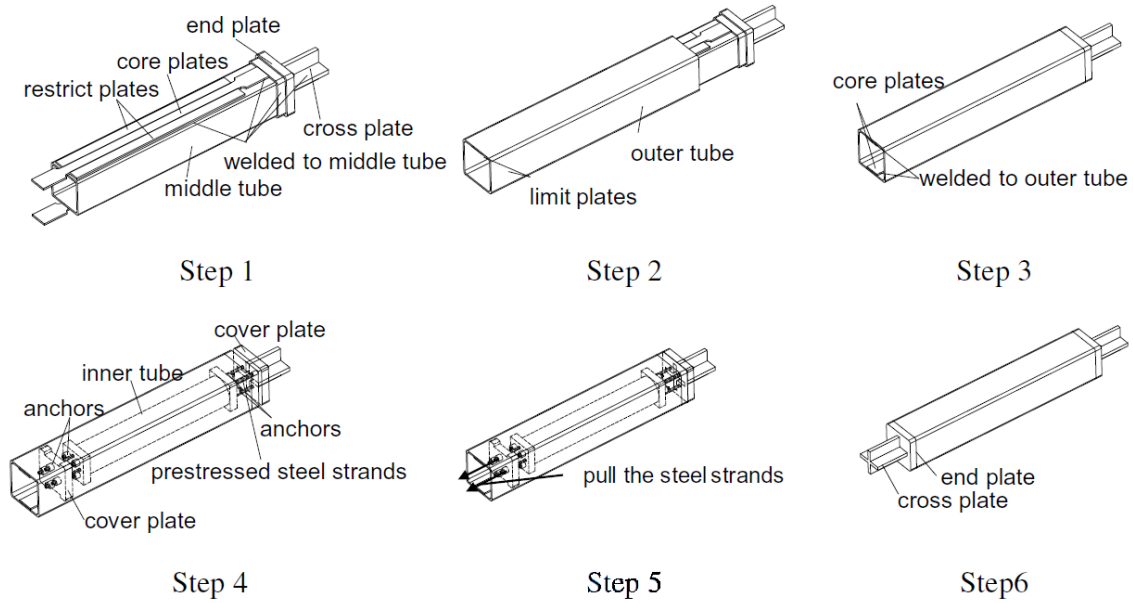


Figure 2.33 Hysteresis response of Dual Core SC-BRB at increasing levels of loading [29]

## 2.9 Cross-Anchored SC-BRB [30]

Wang [30] introduced a cross anchored SC-BRB that had the goal of using cross anchored prestressing mechanics (similar to the ones found in DC-SCB and T-SCED discussed in Section 2.6) to double the deformation capacity of a brace that uses steel prestressing tendons. The brace is designed to dissipate energy using a yielding buckling restrained steel core. This new cross-anchored SC-BRB consists of 3 steel tubes, 2 steel end plates, 4 steel cover plates and two yielding steel core plates. The main assembly stages are shown in Figure 2.34 and can be divided into 6 steps.



**Figure 2.34 Assembly steps for cross anchored SC-BRB [30]**

Step 1: the steel cores are welded onto the top and bottom surfaces of the middle tube. Restricting plates are also welded alongside the core plate to prevent out-of-plane buckling. The right end plate is welded to the right end of the middle tube (in orientation of the drawings) and a cross head is welded to the end plate (Figure 2.34a). Step 2: Limit plates are welded to the inside of the outer tube at a predetermined position (Figure 2.34b). Step 3: The middle tube is then inserted into the outer tube until its end is restricted from moving further due to the limit plates. Once the middle tube reaches its final position, the protruding portion of the core plate is welded to the inside of the outer tube (Figure 2.34c). Step 4: Cover plates are added to both ends of the inner tube, and then the inner tube is inserted into the middle tube. Another two cover plates are added to the brace, one of which bears against the right end plate and the other bears against the limit plates (Figure 2.34 d). Step 5: Four steel strands are prestressed and anchored between the right-most cover plate and the left inner tube cover plate. Another four steel strands are prestressed and anchored between the right inner tube cover plate and the left-most cover plate (Figure 2.34e).

Step 6: another end plate and cross plate are welded to the left of the outer tube (Figure 2.34f). The cross-anchored SC-BRB schematic and cross sections is shown in Figure 2.35. The mechanics of this cross-anchored SC-BRB are shown in Figure 2.36 and are very similar to those explained in Section 2.6.

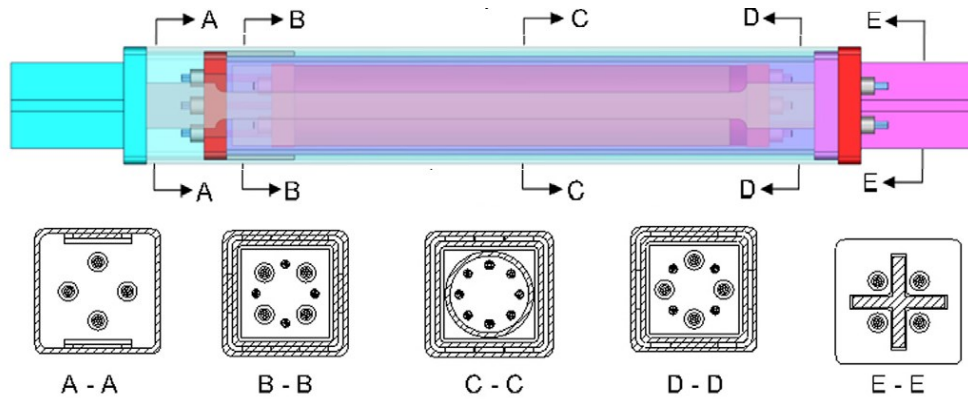


Figure 2.35 Schematics of one cross-anchored SC-BRB specimen [30]

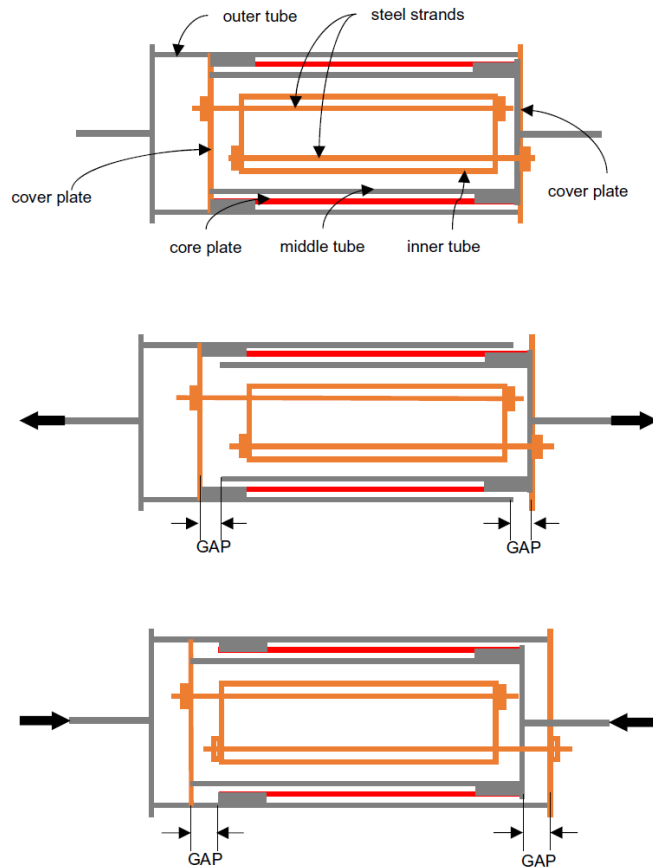


Figure 2.36 Mechanics of the cross-anchored SC-BRB [30]

Each specimen was tested by the loading system shown in Figure 2.37. Testing of the cross-referenced SC-BRB showed that the brace can reduce the residual deformations by about 75-85%, which is an improvement from the 50% reduction achieved by the Self-Centering BRB discussed in Section 2.7. The maximum load capacity of the brace was 1100-1200 kN in tension and 1530-1630 kN in compression. The increase of load capacity when the brace is under compression is attributed to the friction between the core plates and the tubes. The elongation capacity of the brace was around 1%. A sample hysteresis of the cross-referenced SC-BRB is shown in Figure 2.38.

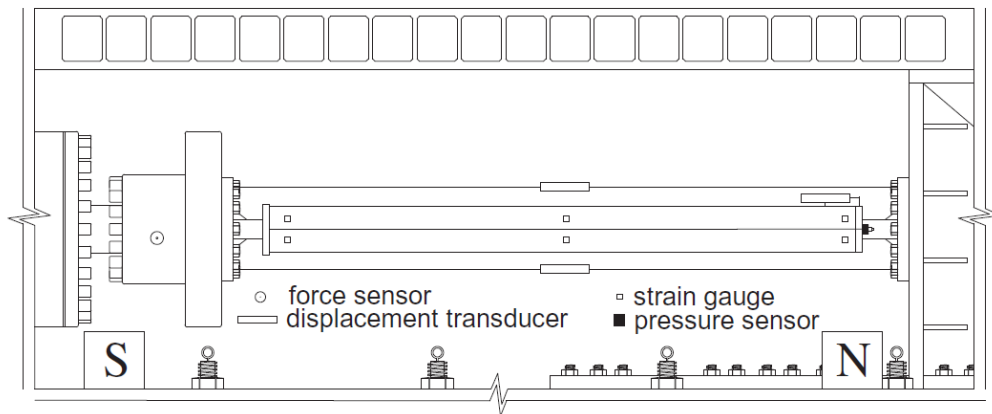


Figure 2.37 Loading system for testing the cross-anchored SC-BRB [30]

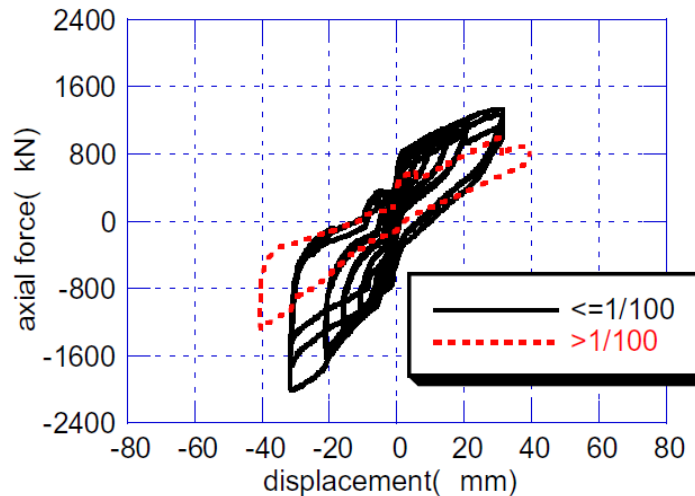


Figure 2.38 Hysteresis of the cross-anchored SC-BRB [30]

## **2.10 Piston-Based Self-Centering (PBSC) Brace [52], [53]**

Another design for a self-centering brace is the Piston-Based Self-Centering (PBSC) brace proposed by Haque [52]. In this design, a steel sleeve is used with front and back cap plates as shown in Figure 2.39. The back plate has an opening that allows for a shaft to move freely into and out of the sleeve. The front plate is attached to a hinge connection to restrain its movement. The brace shaft has a piston plate attached to its end which should also fit inside the sleeve and can move inside the sleeve. One set of SMA bars is connected to the back plate on one end and the piston plate on the other end, this set is called the back ties. Another set of SMA bars are connected to the front plate at one end and the piston plate on the other end, this set is called the front ties. At the initial state, the piston tube should be located at the center of sleeve with both the front and back ties having equal lengths. As the brace undergoes compression, the piston tube moves closer to the front cap causing the back ties to be under tension, the front ties become unstressed. When the brace undergoes tension, the piston tube moves towards the back cap causing the front ties to be under tension while the back ties become unstressed. The tension in the SMA bars provides both the energy dissipation and the self-centering characteristics of the brace. The volume between the piston plate and the front cap could be filled with high damping rubber to reduce the impact energy caused by sudden load reversals. A prototype was built and tested by Issa [53]. A combination of a quasi-static and dynamic reverse cyclic tests as well as a closed-loop dynamic test were conducted. All the tests were carried out at the Applied Laboratory for Advanced Materials and Structures (ALAMS) at the University of British Columbia (UBC)'s Okanagan campus. The scaled protocol achieved a total elongation of 0.65% (around 32 mm) with an axial capacity of 290 kN (Figure 2.40).

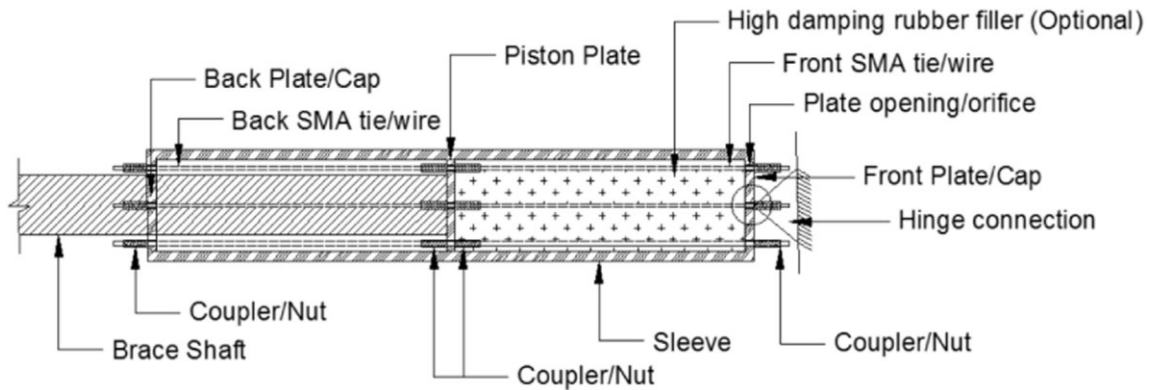


Figure 2.39 Design of the PBSC brace [52]

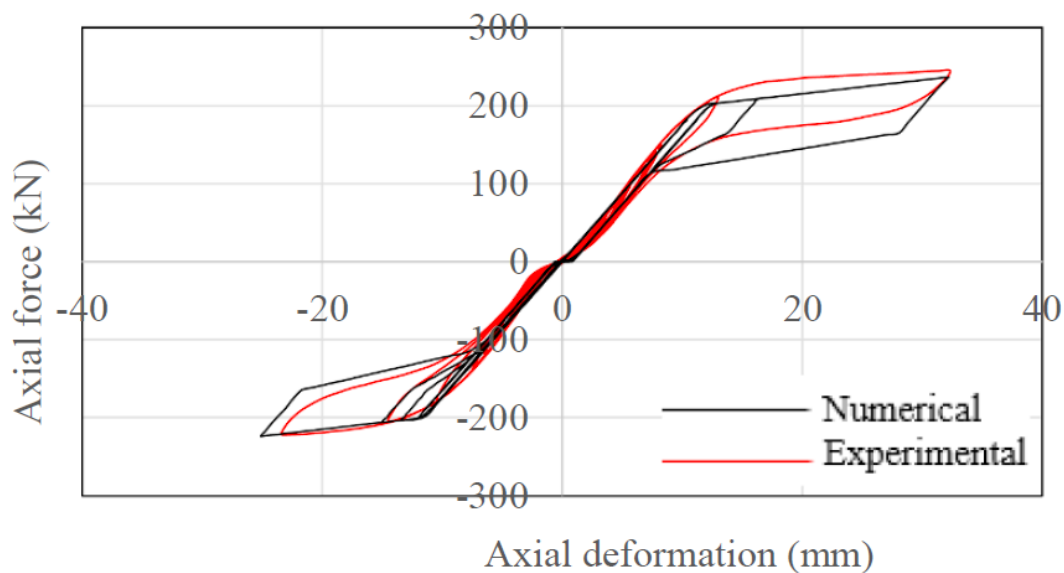
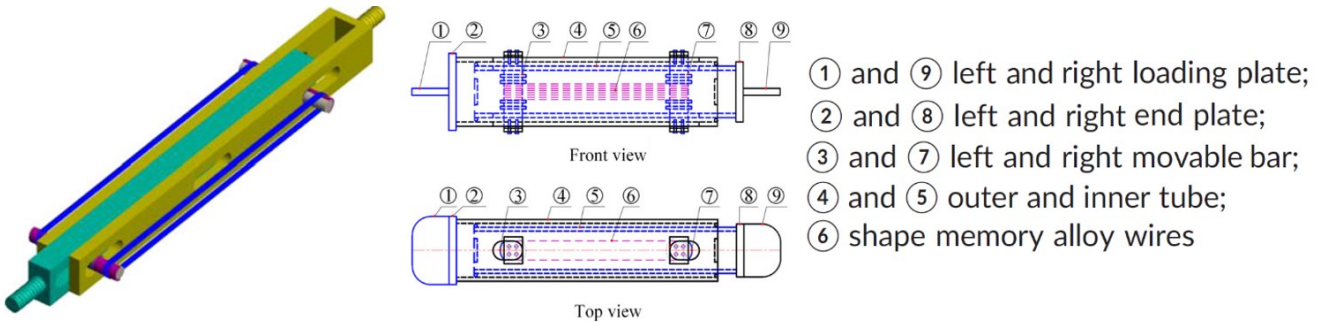


Figure 2.40 Hysteresis of a PBSC [52]

## 2.11 SMA Wire Self-Centering Dampers[54], [55]

Two different but similar SMA wire Self-Centering dampers have been proposed by Qiu [54] and Li [55]. In both those designs, the damper consists of an outer steel member and an inner steel member connected to a steel bracing member at both ends. The inner and outer steel members are slotted, and steel rods are placed in each slot. The rods can move inside the slot. Ni-Ti SMA wire strands are wrapped around the movable rods at a predetermined pretension level. Schematics of the prototypes from both designs are shown in Figure 2.41. As the damper is loaded in tension or compression the members slide relative to each other causing the rods to bear against the rod

moving them apart from each other. This in turn causes the SMA wires to be in tension which provides the self-centering component of the damper.



**Figure 2.41 Schematic of SMA damper by Qiu [54] (Left) and Li [55] (Right)**

To assess the seismic performance of the SMA-braced frame (SMABF) developed by Qiu [54], a series of shake table tests was conducted, in which the SMABF was subjected to ground motions with incremental seismic intensity levels. A 1/4 scaled frame was used for the shake table test. The test was conducted on a 3 m × 3 m unidirectional shake table housed in the Structural Dynamics Laboratory of The Hong Kong Polytechnic University. The SMA brace accommodated a maximum deformation of 50 mm.

To assess the SCB developed by Li et al. [55], an MTS 810 hydraulic servo-controlled fatigue testing machine was used. Several reverse cyclic quasi-static and dynamic tests were conducted at varying amplitudes and loading rates. A sample hysteresis of the largest tested damper in these two studies is shown in Figure 2.42. In order to increase the energy dissipation capacity of these dampers, an addition of a buckling restrained yielding steel core has been suggested by Kari [56]. Figure 2.43 shows the proposed prototype of the SMA wire damper with a yielding core. There has been no physically tested specimen of this proposed design to date.

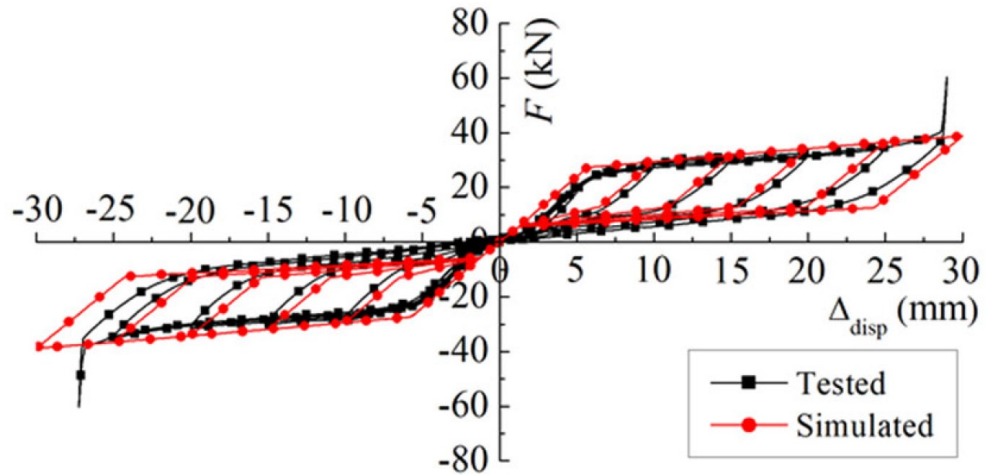


Figure 2.42 Hysteresis of Self-Centering dampers tested by Li [55]

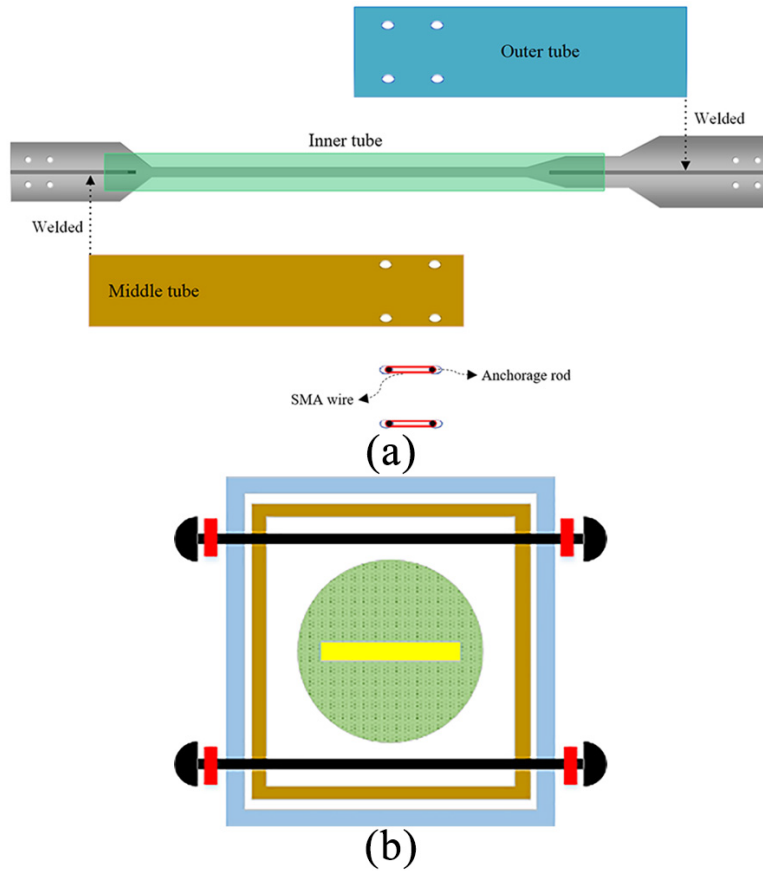


Figure 2.43 Proposed SMA SC-BRB proposed by Kari [56]

## 2.12 Pre-pressed Disc Spring SCED Brace (PS-SCED) [57]

Xu et al. [57] developed a new self-centering brace that utilizes a combination of disc springs and friction devices to provide self-centering and energy dissipative properties respectively. The ability of the disc springs to sustain large deformations without significant accumulation of residual deformation makes it possible for the brace to achieve good self-centering and deformability. However, due to the limited energy dissipation of the disc springs the inclusion of a friction device is necessary. The brace consists of 4 main components which are an inner tube, an outer tube, combinations of disc springs and friction devices. Figure 2.44 shows the assembly of the PS-SCED brace.

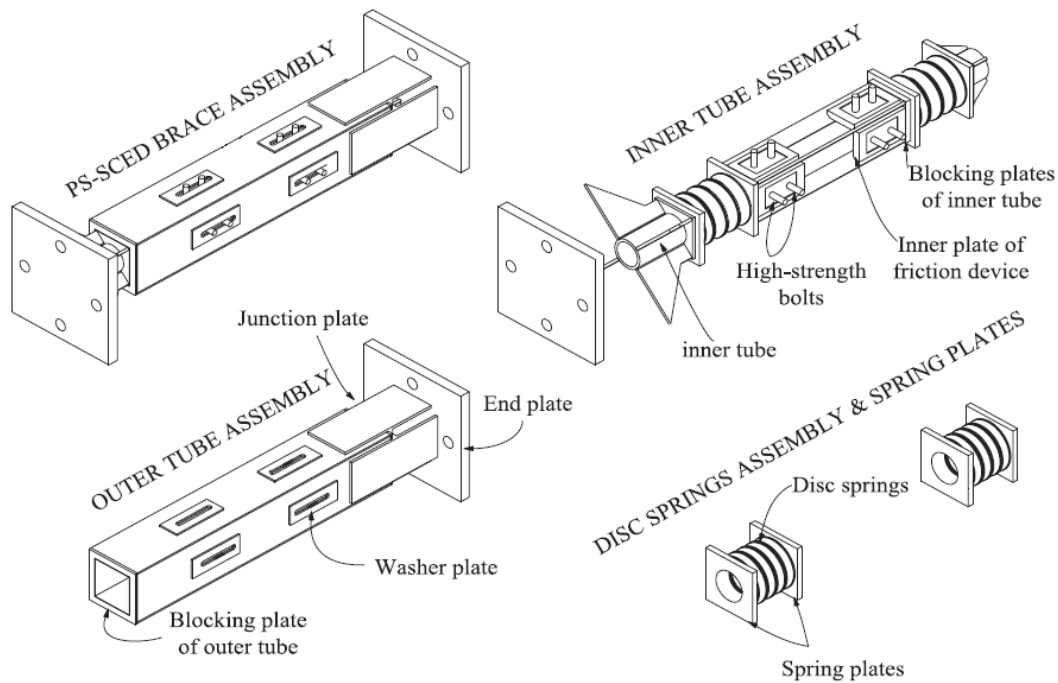
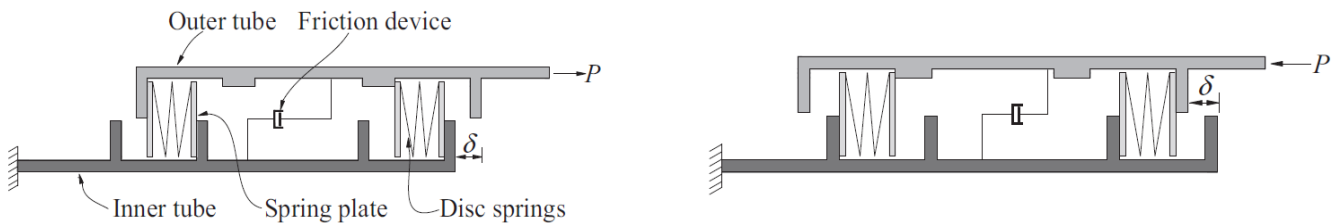


Figure 2.44 Schematics of PS-SCED brace [57]

Two different cross sections for the inner tube have been proposed, one of which is circular and the other is an X-shaped tube. These two cross sections identify the two tested specimens namely PS-SCED I and PS-SCED II, respectively. A steel box with protruding high strength bolts and

surface welded friction pads is attached to the middle of the inner tube by means of welding, as shown in Figure 2.44. A combination of 16-disc springs with spring plates is then added to both ends of the steel box. Blocking plates are welded to both ends of the inner tube, as shown in Figure 2.44, to provide a constant pre-pressed force to the disc springs. The outer tube is also equipped with blocking plates at the same locations of the blocking plates attached to the inner tube. Steel plates are welded to the inside of the outer tube and are in contact with the friction pads as the tubes move across each other. The outer tube has slots to allow for the protruding high-strength bolts to slide as the tubes move relative to each other. The bolts can be tensioned to provide varying normal force levels on the contact surfaces, thus providing different levels of friction and energy dissipation to the brace. To evenly distribute the normal force, washer plates are also added to the outside surface of the outer tube in the location of the friction devices. The outer tube is connected to an end plate by means of 4 junction plates. The PS-SCED brace is designed such that the pre-pressed springs are in compression whether the brace is loaded in compression or in tension. This is facilitated by means of the blocking plates attached to the inside of the outer tube and the outside of the inner tube. A diagram showing the mechanics of the PS-SCED brace is shown in Figure 2.45.



**Figure 2.45 Mechanics of the PS-SCED brace [57]**

The brace was subjected to several quasi-static reverse cyclic tests. Testing of the brace showed that the use of circular inner tube section improved the energy dissipation capacity and ductility. At low levels of loading, very limited residual deformations were observed. As the load increased,

the residual deformations increased, mainly due to the strain hardening effect of the inner and outer tubes. The average residual deformation for the brace was 7.7 mm, which accounts for 27.7% of the maximum target displacement of 28 mm. The maximum elongation of the brace was 1.67%, while the load associated with the maximum displacement was 1300 kN and 1110 kN for compression and tension, respectively. At the end of the tests, failure of the brace was initiated when the junction plates started to buckle. Accordingly, another prototype brace was designed in which the junction plates were reinforced to prevent buckling. In this new design, brittle failure occurred at the end of the tests due to fracture of the inner tube. A sample hysteresis of the tested specimen is shown in Figure 2.46.

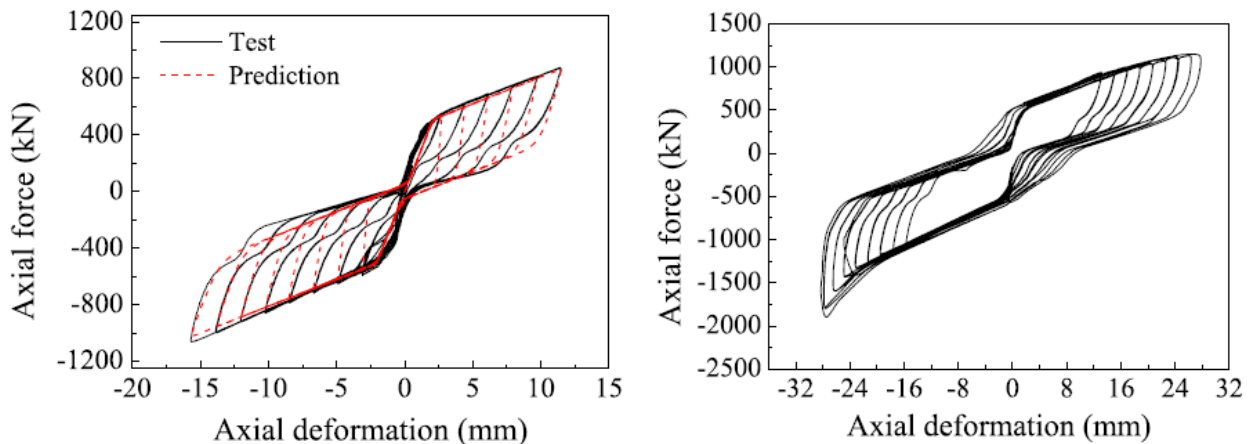
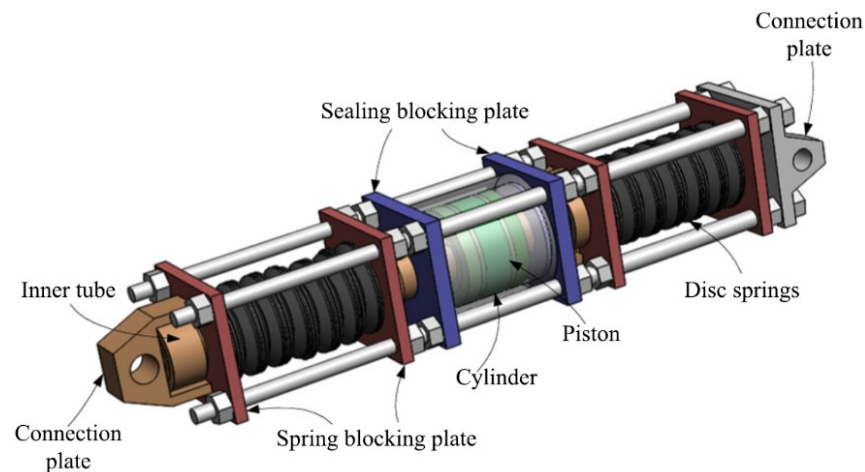


Figure 2.46 Sample Hysteresis of PS-SCED [57]

## 2.13 MR-SCB and Disc Spring SC-BRB [32], [58], [59]

Two other braces have been proposed and tested which have similar configuration to the PS-SCED described in the previous section. The magnetorheological self-centering brace (MR-SCB) consists of an inner tube that has a piston equipped with magnets on both ends attached to its center. The piston and magnets are situated in the middle of a cylinder filled with magnetorheological fluid (MRF) forming the main energy dissipation mechanism. The cylinder is

then sealed from both ends with sealing plates and sets of disc springs are attached to both ends of the cylinder like the PS-SCED as shown in Figure 2.47. Testing was performed on a damper testing machine at Beijing University of Technology [32]. The tests were conducted at varying frequencies and amplitudes of sinusoidal excitation. The response of the MR-SCB is dependent on three factors namely the post activation stiffness of the springs ( $k_2$ ), the activation load ( $p$ ) and the frequency of the motion. Higher stiffness and activation loads were found to reduce the residual deformation while a higher frequency was found to increase the residual deformation. The maximum elongation capacity of the MR-SCB was between 1.5% to 2% with the tested specimen capacity of approximately 400 kN. A sample hysteresis of the MR-SCB is shown in Figure 2.48.



**Figure 2.47** components of the MR-SCB [32]

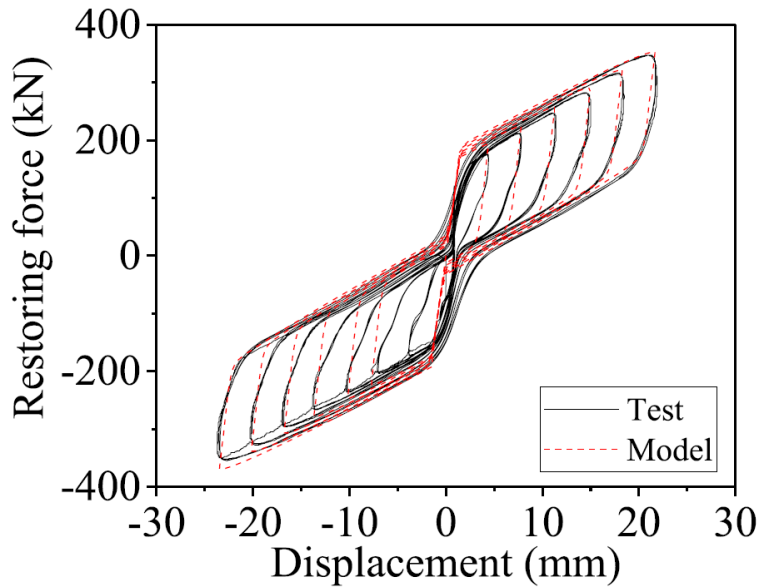


Figure 2.48 Sample hysteresis of MR-SCB [32]

The Disc Spring SC-BRB has similar layout to the PS-SCED with the exception that the inner tube encloses a steel core that is attached to both ends of the brace as shown in Figure 2.49. The steel core is designed to yield under both tension and compression allowing for the brace to dissipate energy. The presence of the yielding steel core resulted in a slight increase to the energy dissipation capacity of the pure SCB with no yielding core. To test the hysteresis of the SC-BRB, quasi-static cyclic tests were performed in the Key Laboratory of Urban Security and Disaster Engineering of Ministry of Education in Beijing University of Technology (BJUT), China [58]. The maximum elongation capacity observed was 1.75%. Hysteresis of the tested disc spring SC-BRB in comparison to a BRB and SCB of the same size are shown in Figure 2.50.

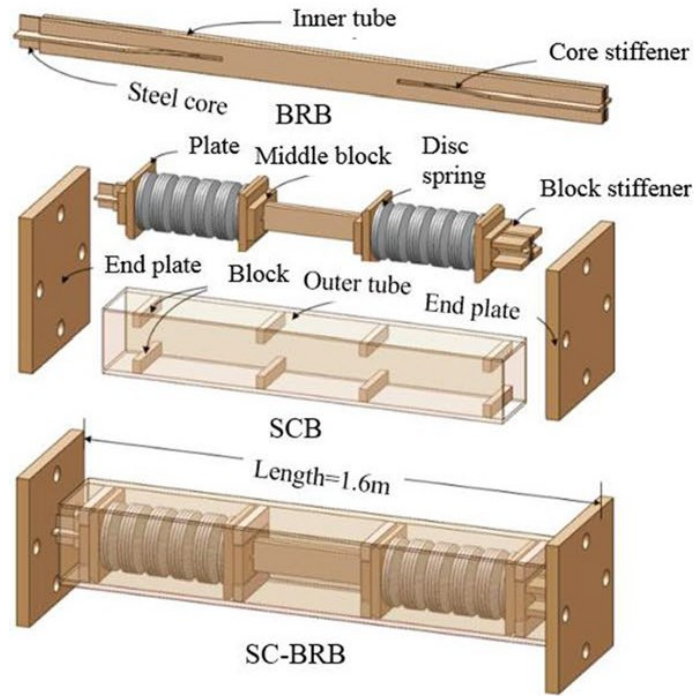


Figure 2.49 Configuration of the Disc-Spring SC-BRB [59]

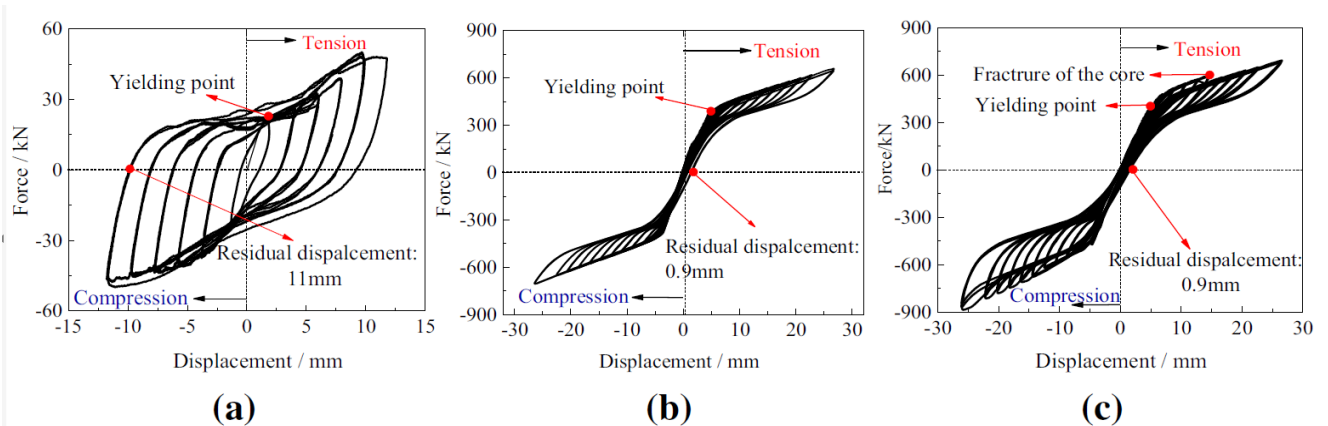
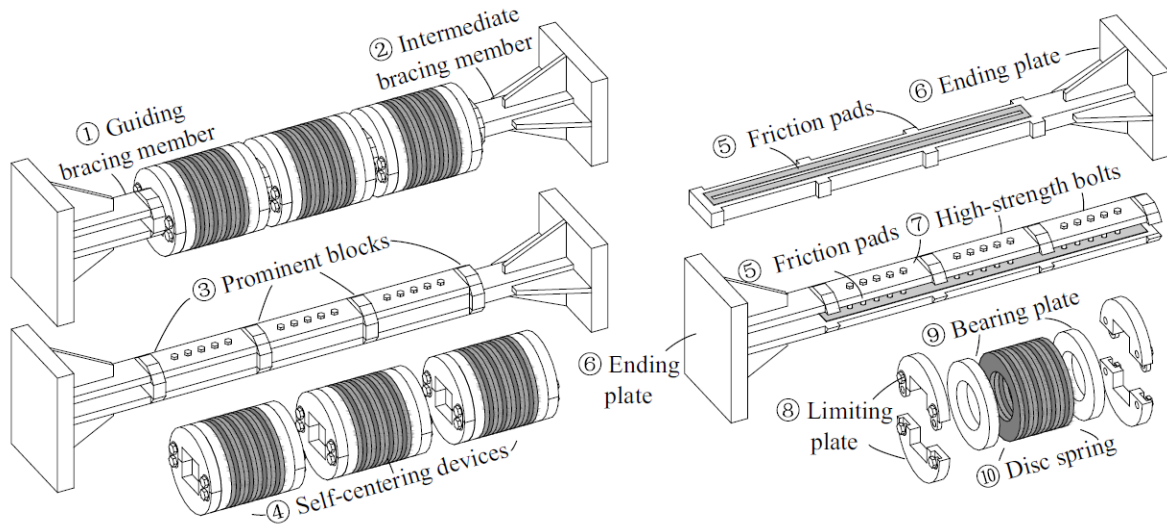


Figure 2.50 Hysteresis curves of equivalent brace specimens: a) BRB, b) SCB, c) SC-BRB [59]

## 2.14 Assembled Self-Centering Brace (ASCB) [33]

The main design objective for the assembled self-centering brace (ASCB) is to develop a self-centering brace with satisfactory seismic performance that can be easily assembled. The ASCB relies on disc spring assemblies to provide the self-centering needed for the seismic performance of the brace. The ASCB is composed of two steel bracing members and a combination of disc

spring sets with a pair of bearing and limiting annular plates for each set. The components of the ASCB is shown in Figure 2.51.



**Figure 2.51 Components of the ASCB [33]**

The first steel member is a pair of rectangular steel sections welded to an end plate, called a guiding bracing member. The other steel member, the intermediate bracing member, is designed to fit within and move freely relative to the guiding bracing member. The intermediate bracing member is slotted along its length and equipped with friction pads attached to its surface. The friction pad is in contact with the inner surface of the guiding bracing member forming a friction interface as the two members move relative to each other. High strength bolts, which pass through the two steel members, control the level of normal force between the surfaces, and thus controlling the friction force at the interface. Both the guiding and intermediate bracing members are designed with prominent blocks positioned at equal distances. Disc spring sets are placed in between these prominent blocks with a pair of bearing annular plates and pair of annular limiting plates on both ends of each set. The limiting plates have a rectangular opening that fits the cross section of the bracing members but not the prominent blocks. As the brace undergoes cyclic loading, the disc

springs are compressed between the prominent blocks as the bracing members move relative to each other.

A reduced scale prototype ASCB was manufactured and tested to failure in a quasi-static cyclic test. As shown in Figure 2.52, the response of the ASCB had a stable and repeatable flag-shaped response hysteresis. As the deformation demand increased past 1.3%, the load demand increased causing the bracing members to gradually yield. The yielding of the steel members resulted in cumulative residual drift with every increasing cycle. As the brace approached the maximum elongation capacity of 2%, the disc springs were compressed solid leading to an increase in the axial stress in the bracing intermediate member. This increase in load caused the intermediate bracing member to buckle. The axial capacity of the tested prototype was 800 kN.

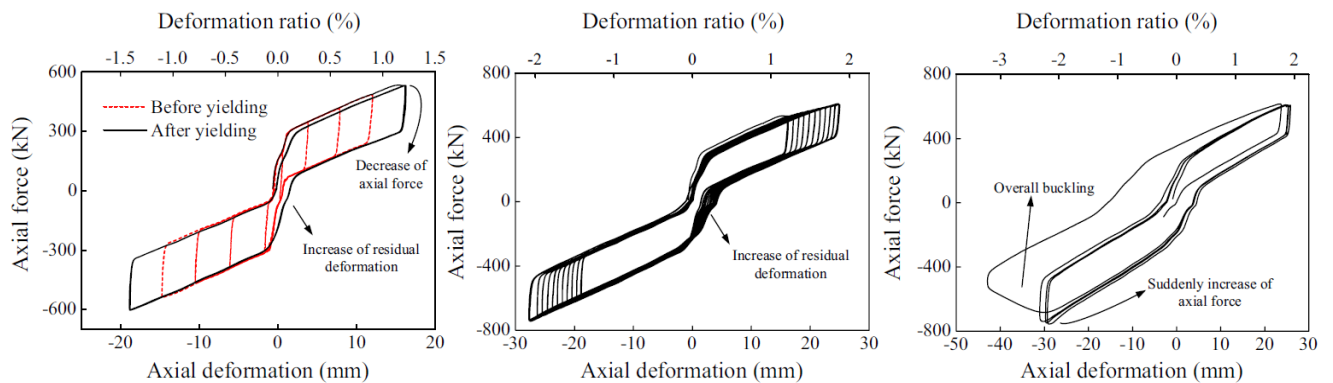


**Figure 2.52 Hysteresis response of ASCB at increasing deformation demand [33]**

## **2.15 Summary of SCED devices**

Table 2-1 summarizes the SCED devices (braces and dampers) discussed in this literature review. As evident in the previous sections, significant research has been dedicated to the development of Self-Centering Energy Dissipative devices. However, the major challenge for these devices is the ability to have a large load capacity coupled with a large deformation capacity. Even when these systems can provide sufficient load and deformation capacity, their required size and length is very large making them impractical to use in most structures. It is also notable that only a handful of studies investigated the dynamic effects of these devices on the rest of structure. This is traditionally done by performing shake table tests (which are usually limited by scale) or through hybrid tests (which was only conducted on the T-SCED brace). The new brace presented in this study addresses the need for developing a brace with large load and deformation capacity with a compact design that can practically be used for structures of varying sizes.

**Table 2-1 Summary of SCED braces and dampers**

<b>Brace</b>	<b>Self-Centering Component</b>	<b>Energy-Dissipation Component</b>	<b>Elongation capacity (Displacement/ Elongation rate)</b>	<b>Capacity of tested specimen</b>	<b>Testing procedure</b>
EDR	Coil spring	Friction	10.4 mm	3 kN	Shake table (scaled down)
Fluidic Self-Centering Device	Viscous fluid	Viscous fluid	50 mm	400 kN	Dynamic Cyclic only
Friction Spring damper	Ring Springs	Friction	25 mm	120 kN	Shake table and dynamic cyclic and record
SFDB	SMA wires	Friction	20 mm	12 kN	Dynamic cyclic only
PT-SCED	Aramid tendons	Friction	30 mm	800 kN	Quasi static and dynamic cyclic and record
			65 mm	(695 kN)	
HC-SCED	Aramid tendons	Friction	70 mm	3800 kN	Dynamic cyclic and record, shake table
			(140 mm w/fuse)		
T-SCED	Aramid Tendons	Friction	100 mm	820 kN	Dynamic cyclic, dynamic records and hybrid
DC-SCED	Steel tendons	Friction	80 mm	1300 kN	Dynamic cyclic only
SC-BRB	SMA rods	Yielding	60 mm	815 kN	Dynamic cyclic only
Dual Tube Self-Centering BRB	BFRP tendons	Yielding	30 mm	750 kN	Quasi-static cyclic only
Cross Anchored SC-BRB	Steel Tendons	Yielding	30 mm	1200 kN	Dynamic Cyclic only
PBSC	SMA rods	Yielding	32 mm	200 kN	Quasi static and dynamic cyclic and closed looped dynamic
PS-SCED	Disc Springs	Friction	30 mm	110 kN	Cyclic (Dynamic assumed)
MR-SCB	Disc Springs	MRF	25 mm	400 kN	Dynamic cyclic only
Disc Spring SC-BRB	Disc Springs	Yielding	30 mm	800 kN	Quasi static cyclic and record
ASCB	Disc Springs	Friction	30 mm	800 kN	Dynamic cyclic only

## Chapter 3 : Ring Springs

The previous chapter highlights the limitation of existing self-centering devices in terms of insufficient load or deformation capacity, as well as the large size that limits the applicability of such devices. The use of steel prestressing tendons to provide the restorative force in SCED braces has the limitation of having a limited elastic strain range of 0.2%, as a result, a long tendon is often required to allow for the building deformation to remain within the self-centering range of the brace. This typically results in large and impractical brace sizes. To overcome this challenge, several solutions have been studied and summarized in Chapter 2.

Some researchers suggested the use of other materials such as Aramid, Basalt Fibre Reinforced Polymers (BFRP), and Shape Memory Alloys (SMA). However, those materials are not commonly used for structural applications and have certain specific drawbacks. Aramid tendons [26]–[28] and Fibre Reinforced Polymers (Basalt or others) [29] are more brittle than steel creating a sudden failure mechanism for the brace. There has also been reports of anchorage failure for Aramid tendons [37], indicating that anchoring could be an issue for materials not traditionally used for prestressing of structural systems. Shape Memory Alloys are expensive and can be cost prohibitive when used for large SCED braces.

Another solution that has been studied is the use of spring systems to reduce the stiffness of the brace, such as the use of coil springs, ring springs or disc springs. In these applications, the braces are designed so that the spring stiffness contributes to the stiffness of the brace in series only after a certain activation load is exceeded. The low stiffness per unit length of the springs allow the brace to accommodate large deformations without the need for excessively long tendons.

However, coil springs have a low load capacity which limits their application to smaller self-centering damper applications.

Disc springs, in theory, can provide large enough load and deformation capacity. However, the resistance of the disc spring assembly is highly dependent on the number of stacked spring elements. A single commercially available disc spring element often cannot deform more than 7 mm. To achieve larger deformations, several elements need to be stacked in series as shown in Figure 3.1 (a). In addition, series stacks with single elements have the same load capacity as a single element. Single commercially available disc spring elements often do not have a load capacity larger than 500 kN. This load capacity can be increased by stacking elements in parallel as shown in Figure 3.1 (b). To achieve a load and deformation capacity appropriate for the use in large structures, a combination of parallel and series stacks can be used as shown in Figure 3.1 (c). This has the disadvantage of needing a very large number of elements to achieve the desired deformation and load capacity for structural applications, which can be cost prohibitive and impractical due to size limitations. This is evident by looking at developed devices utilizing disc springs discussed in Chapter 2 which had a maximum load capacity of 800 kN and a deformation capacity of 30 mm [32], [33], [57], [60]. In addition, the deformation of both the disc springs and coil springs do not dissipate much energy and often require the addition of a separate energy dissipation mechanism as discussed earlier in Chapter 2.

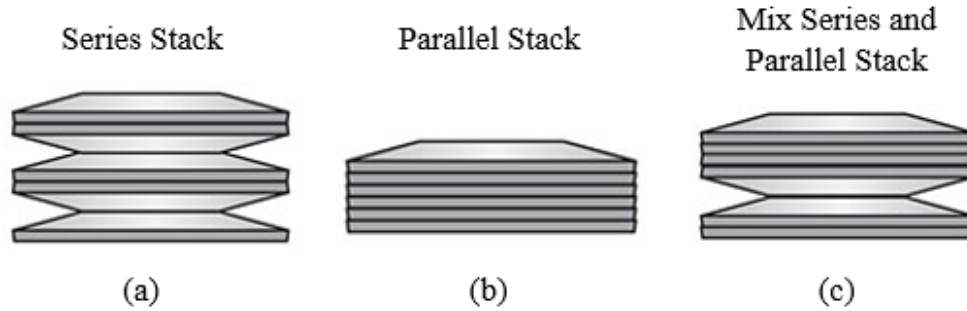


**Figure 3.1 Different stacking arrangements of disc Springs [61]**

Ring springs are frictional devices consisting of inner and outer rings that have tapered mating surfaces. As the spring assembly is loaded in compression, the assembly deforms axially due to the outer and inner rings being subjected to circumferential hoop stresses. The inner and outer rings undergo circumferential compression and tension, respectively. During this process, sliding occurs between the outer and inner rings along the conical friction surfaces as shown in Figure 3.2. The benefits of ring springs for structural applications include: high capacity, high work-to-weight ratio, low maintenance, flexibility of application and a response that is independent of loading rate. Ring springs also have the added advantage of being a passive energy dissipation device that dissipates energy through friction between the tapered surfaces of the springs. This means a brace utilizing ring springs does not necessarily require an additional energy dissipation mechanism, which is the case with most other SCED braces discussed previously. Due to these properties, some previous research studied the use of ring springs in earthquake engineering applications [42], [45], [62]–[67]. These studies investigated the use of ring springs either as a damper with lower load capacity, or as a rocking system which is difficult to implement in rehabilitation scenarios. In the current study, high-capacity ring springs are incorporated into a SCED brace. A review of previous research and the characteristics of ring springs are provided in this chapter.

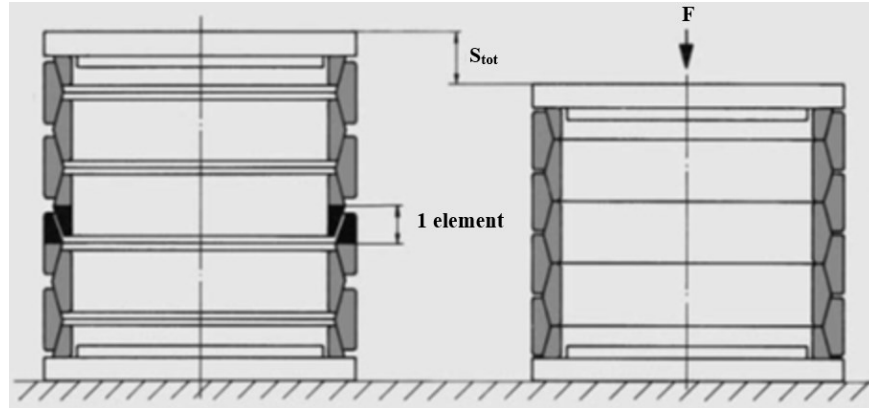


Figure 3.2 Typical ring spring assembly consisting of 4 outer rings, 3 inner rings and 2 half inner rings [44]

## 3.1 Characteristics of Ring Springs

This section lists several Ring Spring characteristics which make it an appealing component for incorporation into an efficient SCED brace.

### 3.1.1 High Capacity

One of the main advantages of ring springs is the high axial spring load that can be accommodated in each spring assembly. SCED braces require a capacity close to or greater than 1000 kN to be a viable option for practical design applications. This capacity is unattainable using coil springs, and attainable only through parallel stacking of disc springs. Ring Springs are manufactured from spring steel and can have a higher load capacity as the diameter increases. They also maintain the same load capacity irrespective of the number of elements used, unlike disc spring assemblies. For this study, the goal is to design a compact SCED brace that has a comparable capacity to other high capacity SCED braces but in a simple and more compact form. Based on a list of spring types manufactured by one of the primary manufacturers of these springs, Ringfeder Power Transmission, a few options are appropriate for use in the proposed SCED brace, as shown in Table 3-1. Certain custom-made ring springs with diameters of up to 800 mm can have a maximum load capacity of up to 8000 kN as shown in Figure 3.3; however, for this project

such capacity is not suitable especially considering the considerable increase in the size (diameter) of the spring.

**Table 3-1: List of common sizes of Ring Springs with large capacity suitable for SCED brace application [44]**

Spring Type	Terminal Force (kN)	Outer Diameter (mm)
24201	1000	247
26901	1250	274
30000	1000	306
32000	1200	326
34000	1450	346
35000	1400	356
40000	1800	407

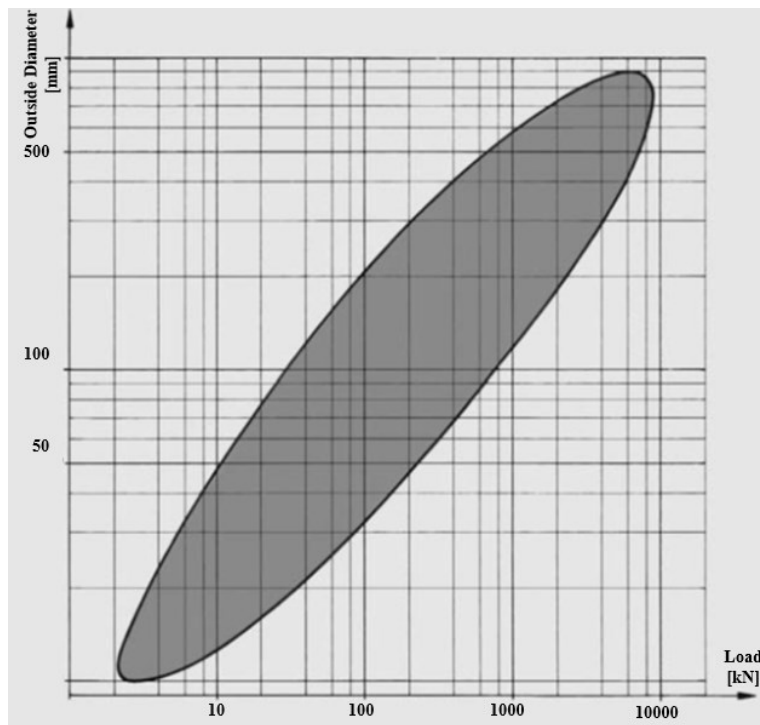


**Figure 3.3 Range of possible friction spring solutions [44]**

In addition, the ring springs are designed to be overload-safe, meaning the ring springs have a safety margin and do not get damaged in an exceptional case when the load exceeds the nominal load capacity. The reason for that is because as the spring is compressed up to its load capacity, the plane surfaces of the inner rings touch and form a rigid column effectively blocking it from travelling further. However, utilizing the spring assembly up to the maximum load capacity should

be avoided by design to protect the other elements of the brace (or the structure) from the steep rise in stiffness in the ring springs hysteretic behaviour. For this study, a readily available ring spring type is utilized and is found to be sufficient for the SCED brace application. However, it is worth noting that it is possible to use more than one spring assembly in parallel (i.e. a smaller ring assembly inside a bigger ring assembly) to increase the load capacity if a higher load capacity is required.

### 3.1.2 High Weight Utilization Factor

In seismic applications, added mass associated with the addition of seismic resistance elements can result in altering the seismic demand on a structure. This is of particular importance in rehabilitation applications. Therefore, it is preferred for the weight of rehabilitation devices to be as low as possible. To compare different springs, the ratio of spring work to weight, known as the weight utilization factor  $\eta_G$ , can be calculated. As shown in Figure 3.4, ring springs have a weight utilization factor that is superior to other common types of springs which have been previously used in SCED brace applications, such as the coil spring and the disc spring. The reason for this advantage is that the ring spring design allows for the efficient utilization of the materials by uniformly distributing the tensile and compressive circumferential stresses over the whole cross-sectional area. In contrast, other types of springs typically have the maximum stress occur only in the peripheral fibres, thus not fully utilizing the spring materials.

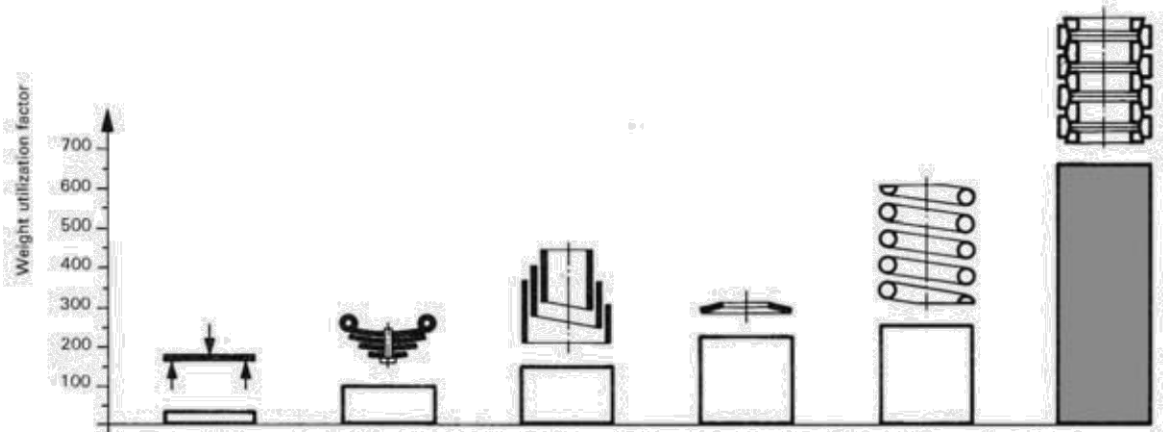


Figure 3.4 Weight utilization factor for various types of springs [44]

### 3.1.3 Adjustable Spring Response

One of the major benefits of using ring springs is the ability to adjust the response of the assembly by simply changing the number of rings as well as the lubrication of the rings in the assembly. As discussed earlier, each spring or spring type has a specific maximum load capacity  $F$  and spring travel per element  $S_e$ . The designer can choose to increase the total spring travel  $S_{tot}$ , by adding more ring elements to the assembly, as shown in Figure 3.5. This, in turn, also results in increasing the work done by the springs (and thus the energy dissipation) as well as decreasing the spring loading stiffness  $K_L$ . As such, the relations between the number of spring elements  $e$ , spring travel  $S_{tot}$ , loading stiffness  $K_L$ , and spring work  $W_{spr}$  can be expressed as follows:

$$S_{tot} = S_e e \quad \text{Equation 3-1}$$

$$K_L = F/S_{tot} \quad \text{Equation 3-2}$$

$$W_{spr} = F \times S_{tot}/2 \quad \text{Equation 3-3}$$

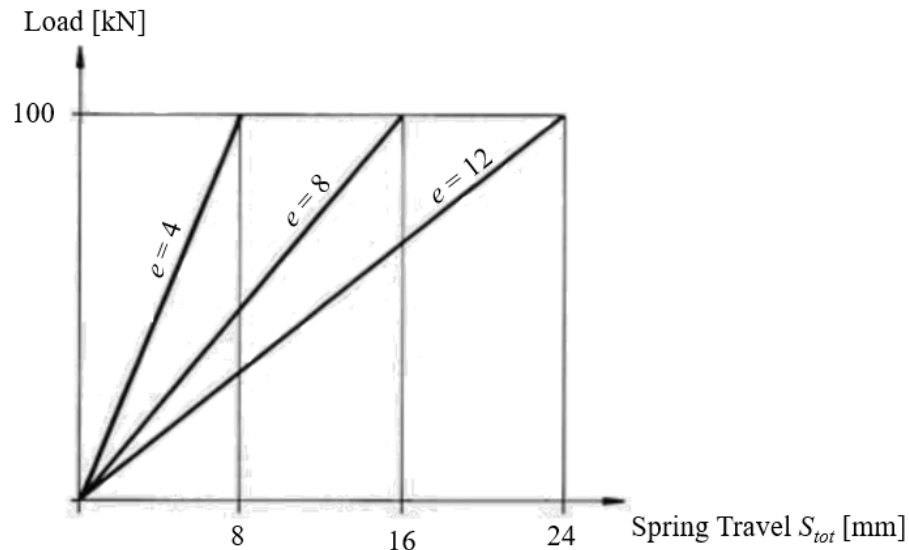


Figure 3.5 Change in spring travel and spring loading stiffness with increasing number ring elements [44]

Table 3-2: List of some Ring Spring types with load and travel capacity

Spring Type	Maximum Load Capacity $F$ (kN)	Travel per element $S_e$ (mm)
1800	5	0.4
2500	9	0.6
4200	26	1.0
6300	54	1.4
9000	100	2.0
10000	125	2.2
12400	200	2.6
16600	350	3.7
20000	510	3.9
22000	720	4.4
24201	1000	5.3
32000	1200	6.2
34000	1450	7.5

### 3.1.4 Hysteretic Response of Ring Springs

If one assumes a case where there is no friction acting on the taper faces of the rings, then there shall be a linear relationship between the total spring travel  $S_{tot}$ , and the elastic force in the springs

$F_{elast}$  as shown in Figure 3.6.

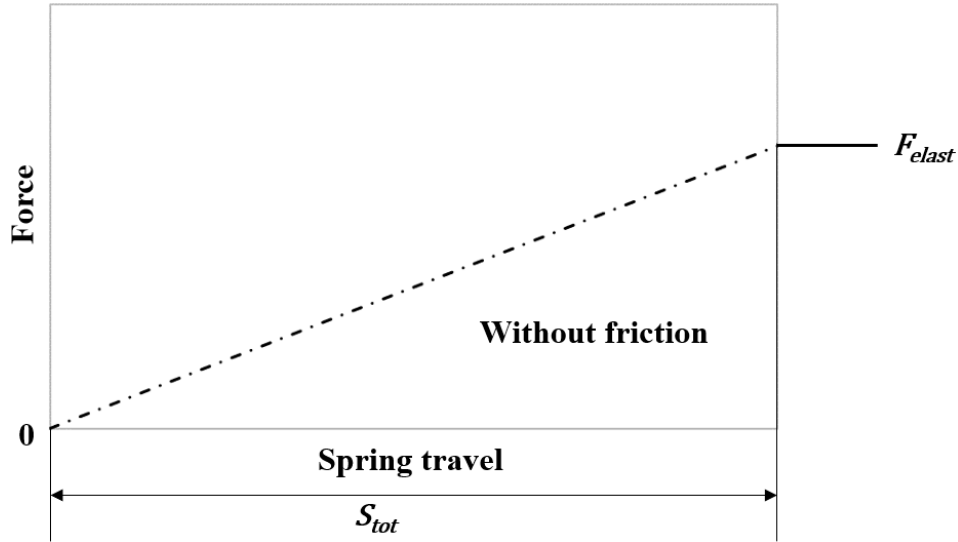


Figure 3.6 Ring spring elastic response with no friction [44]

As the force  $F_{elast}$  is being applied, the outer rings expand while the inner rings contract simultaneously. However, this motion of both rings against each other occurs while overcoming the frictional forces acting on the taper surface between the ring elements. The friction force  $R_1$  is proportional to the applied force  $F_{elast}$ , accordingly, we obtain a linear loading curve shown in Figure 3.7. The ratio of the frictional force  $R_1$  in proportion to the elastic force  $F_{elast}$  is dependent on the type of lubrication between the mating surfaces.

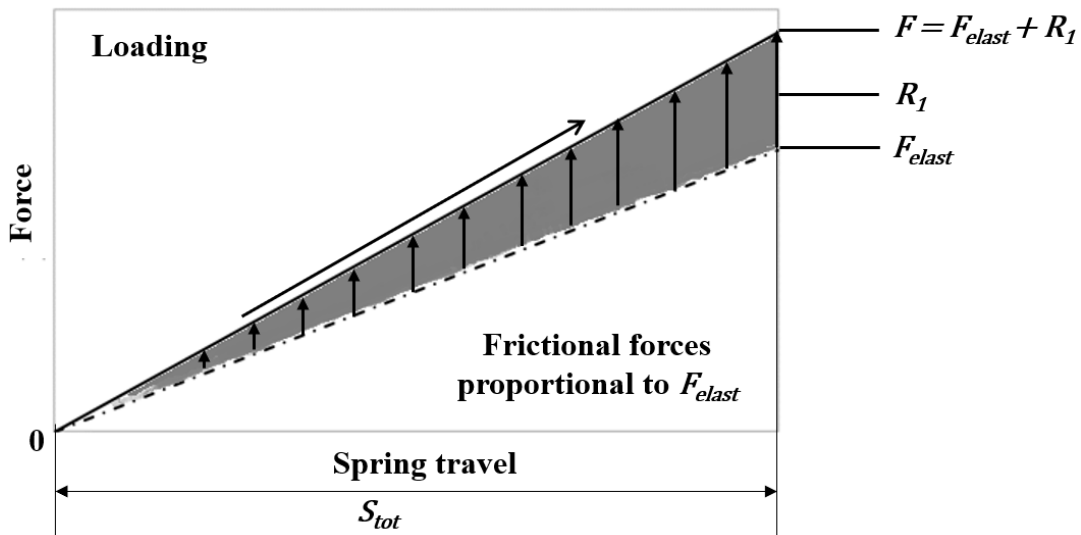


Figure 3.7 Additional friction forces on loading being applied [44]

The friction force  $R_1$  occurs in the direction opposite to the movement of the applied force  $F$ ; therefore, the applied force  $F$  is reduced back to  $F_{elast}$  when the spring momentarily stops at the onset of unload. During unloading, the friction force  $R_2$  counteracts the force  $F_{elast}$ ; thus the spring only starts to decompress when the external load is reduced to a value of  $F_R$  known as the recoil load as shown in Figure 3.8.

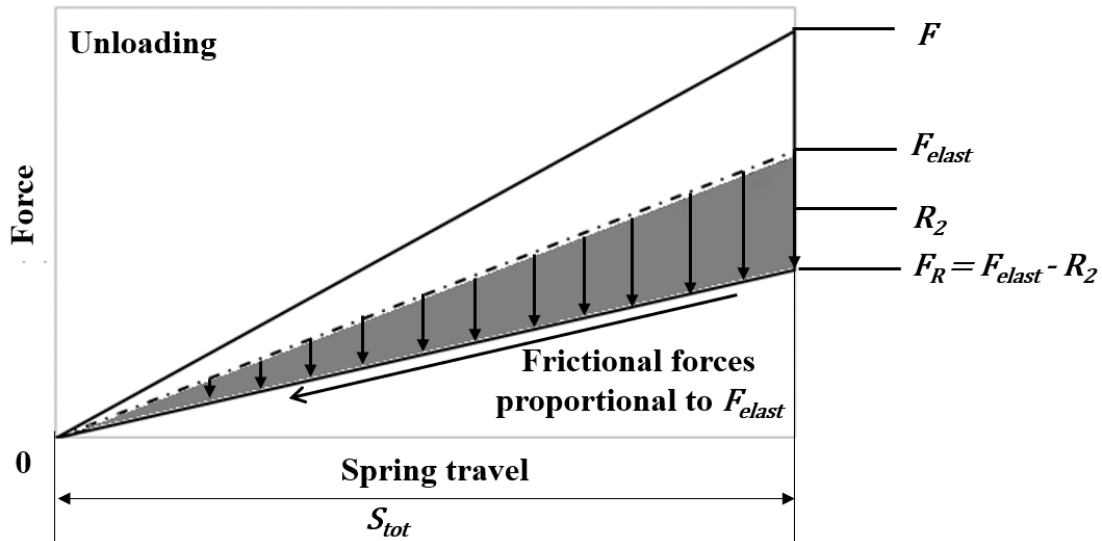


Figure 3.8 Breaking friction forces upon unloading [44]

A typical idealized closed loop hysteresis diagram of a spring assembly then becomes what is shown in Figure 3.9. During hysteretic cycling of the springs under compression, some of the energy is recovered while the rest of the energy is dissipated into heat energy due to friction. The dissipated energy can be controlled based on the lubrication used between the surfaces of the ring elements. The standard lubrication provided by manufacturer gives 66% damping which results in 66% of the total energy getting dissipated due to friction and 33% of the energy recovered. This ratio of dissipated energy to total energy is referred to as the damping ratio  $D$ .

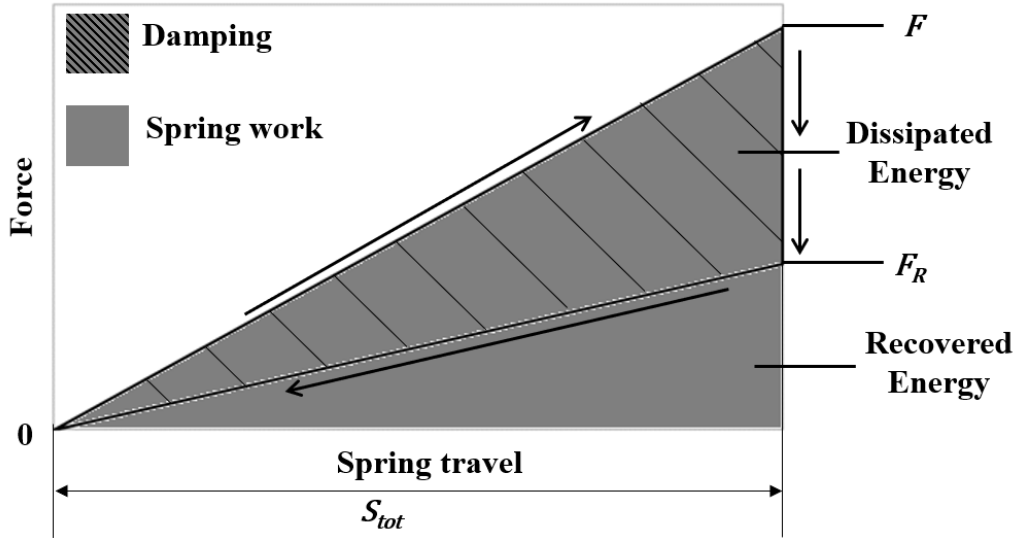


Figure 3.9 Typical idealized hysteresis diagram of a ring spring assembly [44]

Using the Damping ratio  $D$ , the Recoil force  $F_R$  can be determined using Equation 3-4.

$$F_R = F(1 - D) \quad \text{Equation 3-4}$$

As an example, in an assembly with the standard lubrication that provides 66% damping ratio  $D$ , the ratio between the maximum load  $F$  and a recoil load  $F_R$  is 3 to 1.

Similarly, the unloading stiffness  $K_u$  and loading stiffness  $K_L$  are directly related to the lubrication. Using the Damping ratio  $D$ , the unloading stiffness  $K_u$  can be determined using Equation 3-5.

$$K_u = F_R/S_{tot} = K_L(1 - D) \quad \text{Equation 3-5}$$

The ratio between the loading and unloading stiffness is once again 3 to 1 when the damping ratio  $D$  of 66% is used. The lubrication can be changed to provide a damping ratio  $D$  ranging from 35% to 65%. A higher damping ratio is desirable in earthquake engineering applications since it dissipates earthquake energy that would otherwise be imparted to the structure as strain energy, which leads to deformations in structural members, potentially resulting in structural damage.

In addition to the number of ring elements and the lubrication, another factor that affects the response of the ring spring assembly is the pre-compression of the springs. A typical hysteresis of a spring assembly with initial pre-compression is shown in Figure 3.10. To maintain the ring assembly's alignment, a level of pre-compression of the spring of at least 10% of the ring capacity should always be maintained. Thus, the spring assembly is locked in position until a load of equal magnitude is applied to the assembly to overcome the pre-compression load  $F_a$ . After this load is exceeded, the spring assembly deforms based on the loading stiffness  $K_L$  discussed earlier.

Due to the pre-compression of the springs, the available deformation capacity of the assembly  $S$  decreases from the full spring travel  $S_{tot}$  by a value of  $S_a$ , which corresponds to the spring travel at the pre-compression load  $F_a$ . The spring deformation capacity  $S$  can be calculated using Equations 3-6 and 3-7.

$$S_a = F_a / K_L \quad \text{Equation 3-6}$$

$$S = S_{tot} - S_a \quad \text{Equation 3-7}$$

In an earthquake engineering application, such as in a SCED brace, the initial pre-compression is not only important to maintain the stability of the spring assembly but also to prevent the brace from activating at a low load level, causing the building to sway unnecessarily and resulting in discomfort to occupants and possible high-cycle fatigue of building components. For example, it is important to ensure that the activation force of the SCED brace is higher than the load demand caused by wind loads. Even though the pre-compression of the springs would require the use of more spring elements to provide the same deformation capacity as a set of equivalent uncompressed springs, pre-compression is an essential step to ensure adequate structural performance.

When the ring spring assembly decompresses back to its initial precompressed condition, it retains a load referred to as  $F_d$  which can be calculated in a similar way to the recoil load  $F_R$ . The damping ratio  $D$  can be used to calculate the load present in the springs after decompression as follows:

$$F_d = F_a(1 - D) \quad \text{Equation 3-8}$$

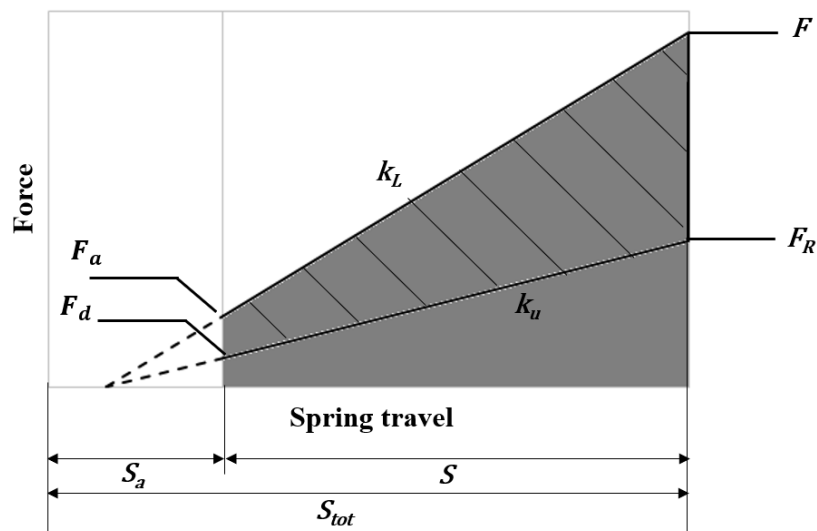


Figure 3.10 Sample of complete spring travel diagram including pre-compression [44]

### 3.1.5 Load Rate and Temperature Independent

When SCED braces are subjected to earthquakes with broad spectrum frequency content, elements with a hysteretic behaviour that is independent of loading rate and frequency give a more predictable local and global response behaviour of the structure. Frequency dependence tests performed by Filiatrault [45] examined the effect of loading rate on the hysteresis response of ring springs at different frequencies. The tests showed that the performance of the spring assembly is nearly independent of the loading frequency within the typical range expected during seismic events. SCED braces which are exposed to the environmental elements, such as those used on

bridges, ideally should also have a response that is independent of temperature. The properties and response characteristics of ring springs are consistent for temperature between  $-40\text{ }^{\circ}\text{C}$  and  $+80\text{ }^{\circ}\text{C}$  [44]. Considering that the springs are encapsulated within a steel tube and thus not directly exposed to the exterior environment, this range is sufficient for the springs to have a stable response year-round. The following discussion examines previous research done on the implementation of ring springs in self-centering structural applications.

### 3.2 Utilization of Ring Springs in Seismic Isolation [42]

The first published application of the utilization of ring springs for a structural seismic application was conducted by Hill [42] and it involved the design and testing of a bidirectional ring spring cartridge. The ring springs used had an axial load capacity of 20 kN. The spring cartridge was tested under a quasi-static loading protocol using a universal testing machine at the University of Canterbury at a loading rate of 15 mm/min and unloading rate of 5 mm/min. The results showed that the theoretical ring spring loading and unloading stiffnesses closely matched the calculated values for the ring spring stiffness as shown in the experimental hysteresis presented in Figure 3.11.

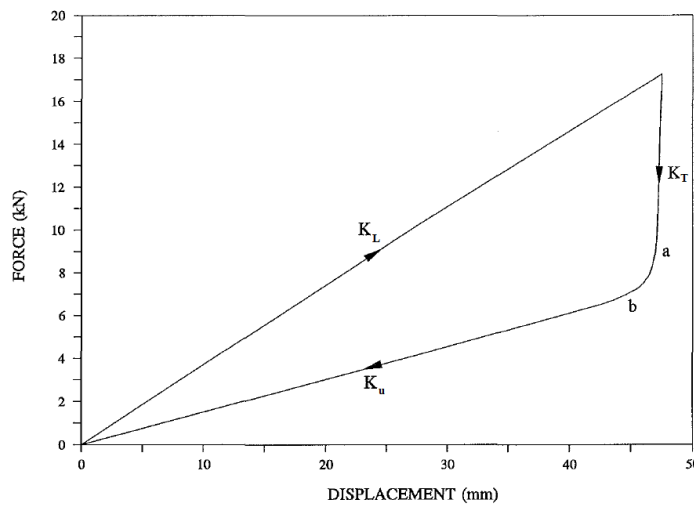


Figure 3.11 Ring spring Hysteresis obtained from quasi-static testing [42]

The testing also examined a transition stiffness  $K_T$  that acts during the transition between the spring loading stiffness  $K_L$  and the unloading stiffness  $K_u$ . In the idealized hysteresis presented earlier in Figure 3.9, this transition stiffness  $K_T$  in the unloading stage is assumed to be infinite considering an idealized state where the springs undergo no deformation as they unload until they overcome the breaking frictional forces. However, during testing, a very high stiffness of  $K_T = 17 \times 10^6$  N/m was observed, almost 50 times the initial loading stiffness  $K_L$ . The small deformations of the springs during this transitional stiffness are due to the release of stored strain energy within the springs.

As shown in Figure 3.11, the shift between the transition stiffness  $K_T$  and the unloading stiffness  $K_u$  was not abrupt and sharp as depicted in the ideal hysteresis shown in Figure 3.9. This can be attributed to the fact that some ring elements begin to slide before others due to manufacturing tolerances. This leads to rounding the corner of the transition between point  $a$  (in Figure 3.11), where the first ring elements begin to slide, and point  $b$  (in Figure 3.11), where all the ring elements are sliding. Although this transition from high stiffness to low stiffness may not be critical to the response of the brace, the stiffness from low stiffness back to a high stiffness is of special importance in earthquake engineering applications, particularly for self-centering systems. A sharp low to high stiffness transition could lead to overestimating peak floor accelerations in analytical modeling [68]. The effect of stiffness transitions on the new proposed RS-SCED brace is discussed in 6.5.

To experimentally evaluate the ring spring assembly under dynamic loading, a shake table test was conducted using the facility located at Industrial Research Ltd, Christchurch [42]. The input acceleration of the shake table as well as the acceleration and displacement of the rigid mass were measured during the experiment. Two sets of cartridge systems were tested, both pre-compressed

to 16% and 28% of their displacement capacity, respectively. The dynamic testing results were compared to computer simulation results and showed good agreement as shown in Figure 3.12.

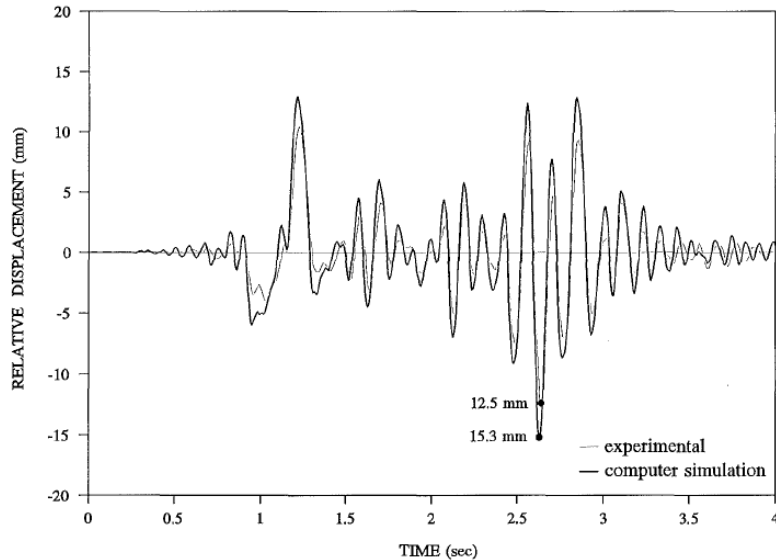


**Figure 3.12 Experimental and Computer simulation displacement response under dynamic testing [42]**

To evaluate the efficiency of using ring springs for seismic isolation of structures, Hill [42] proposed a pivotal rocking seismic isolation system (PR SIS) which incorporates ring springs to protect structures supported by columns during earthquakes. This system consists of a column with a base plate, supported with spring elements at both ends of the base plate as shown in Figure 3.13. An experimental prototype of the PR SIS was also tested using a shake table as shown in Figure 3.14. This multi-degree-of-freedom (MDOF) system was analytically modelled using the software package RUAUMOKO. Columns of different un-isolated vibration periods were subjected to 6 different earthquake records. It was found that the use of the PR SIS incorporating ring springs was capable of reducing the maximum bending moment of the column by a factor of 2 to 3 in most cases compared to the maximum bending moment in a fixed column [42]. The experimental results confirmed the numerical results obtained from the RUAUMOKO model.

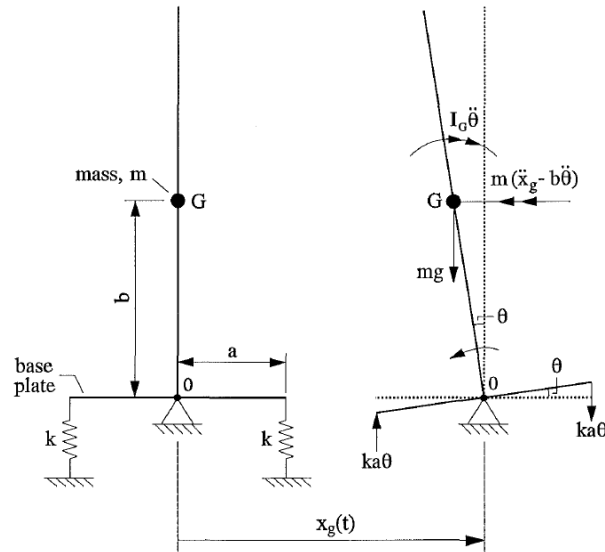


Figure 3.13 Pivotal rocking seismic isolation system subject to base excitation [42]

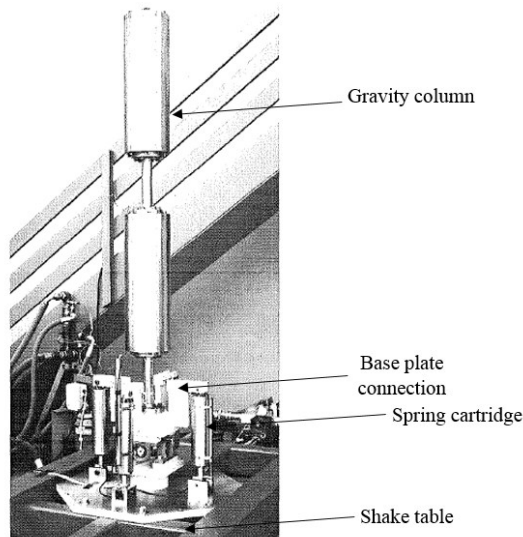
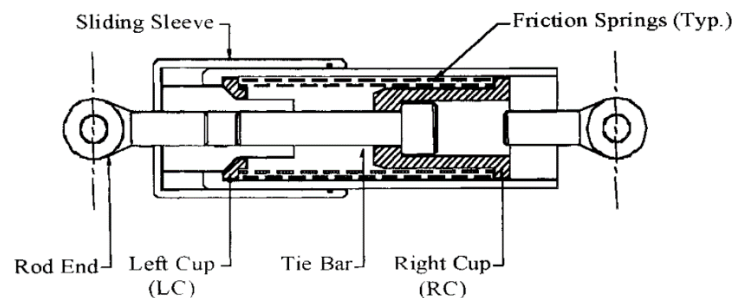


Figure 3.14 Complete test rig assembly mounted on shaker table [42]

### 3.3 Friction Spring Seismic Self-Centering Damper [45]

Filiatrault et al. [45] investigated the use of ring springs as seismic dampers in structures. A prototype damper with a force capacity of  $\pm 200$  kN and displacement capacity of  $\pm 50$  mm was used in this study. The unit had a center-to-center length between rod ends of 710 mm and an outer diameter of 165 mm. A diagram of the damper unit is shown in Figure 3.15. The spring stack is retained at its ends by the flanges of a pair of cups, the left cup (LC) and right cup (RC), identified

with hatch marks in the figure. Under an applied external compressive force on the left rod end, the LC compresses the rings in the axial direction while the tie-bar head slides in the slot toward the right. When the external force reverses direction and acts as a tension load, the RC is pulled by the tie-bar-head toward the left, and again, the friction springs are subjected to compression. The testing program for this study consisted of two phases. During the first phase, characterization tests were performed to evaluate the self-centering capabilities, stability, repeatability, and consistency of the damper. During the second phase, a shake table setup was used to perform an earthquake simulation on a half-scale moment resisting steel frame with and without the damper-bracing assembly, then comparing the results to numerical non-linear time-history dynamic analyses.



**Figure 3.15 Diagrammatic view of seismic damper [45]**

In the first phase of testing, 4 different characterization tests were performed on the seismic dampers using the earthquake simulator at Ecole Polytechnique in Montreal [45]. The first test performed was a performance benchmark test, based on the “Guideline for the Testing of Seismic Isolation and Energy Dissipating Devices” document prepared by the Highway Innovative Technology Evaluation Center (HITEC) [69]. The damper is subjected to 10 fully-reversed sinusoidal cycles at an amplitude of  $\pm 25$  mm (half the damper displacement capacity) and a frequency of 0.5 Hz. The results of the test were used to determine the number of cycles needed for the stabilization of the damper response, referred to as the shakedown cycles. The number of shakedown cycles for the damper was found to be 8 cycles, with only an 8% decrease in energy

dissipation per cycle between the first and eighth cycle. There was also very minimal decrease in maximum compression and tensile force (< 3%) within the first 10 cycles as shown in Figure 3.16.

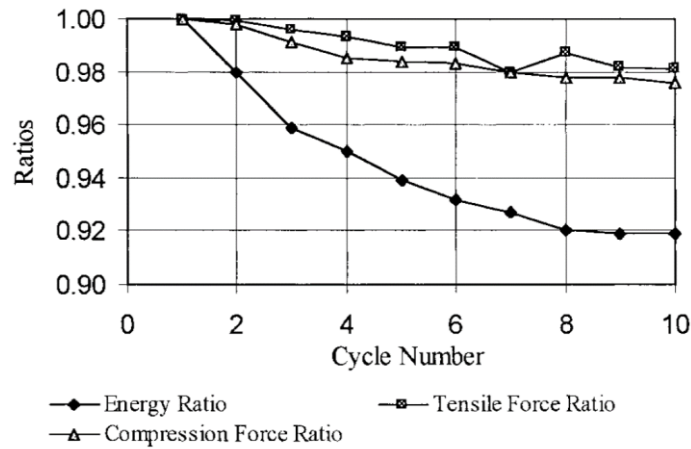


**Figure 3.16 Performance benchmark tests for Ring Spring Seismic damper [45]**

The second characterization test performed was a frequency dependency test in which the damper was subjected to three fully reversed sinusoidal cycles with an amplitude of  $\pm 25$  mm at varying frequencies of 0.05, 0.2, 0.5, 1.0 and 2.0 Hz. Five different physical parameters were compared to characterize the response, namely: the initial stiffness  $K_o$ , the loading stiffness  $r_l K_o$ , the unloading stiffness  $r_u K_o$ , the slip force  $F_s$ , and the recentering force  $F_c$ . The results obtained from this test indicated that the behaviour of the damper is very stable for all frequencies considered. It is worth noting that the large variance in the result of the initial stiffness  $K_o$  was attributed to the fact that it was calculated using very small deflections occurring over a short period of time. These conditions were very close to the limits of the transducers and data acquisition system. The results of the frequency dependency test are shown in Figure 3.17.

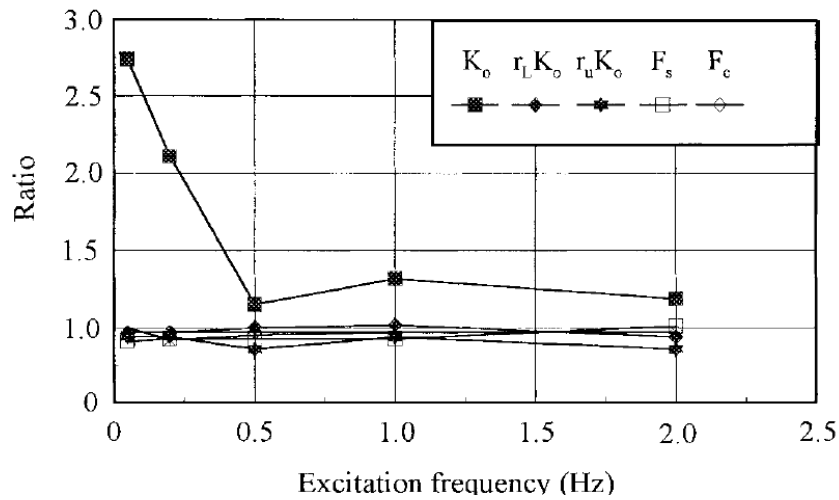


**Figure 3.17 Effect of excitation frequency on physical parameters defining the hysteretic behaviour of the damper [45]**

The third characterization test performed aimed to determine the dynamic performance characteristics of the damper under seismic excitations. The damper was subjected to three different historical earthquake ground motions with a wide range of frequencies. The records were scaled to impose  $\pm 25$  mm peak displacement for records with a lower frequency content and  $\pm 12.5$  mm for the earthquake record with a higher frequency content. The results of this test indicated that behaviour and performance of the damper are repeatable, reliable, and virtually independent of the seismic input. All the loading and unloading experienced by the damper followed the backbone curve of the force-displacement hysteresis as shown in Figure 3.18.

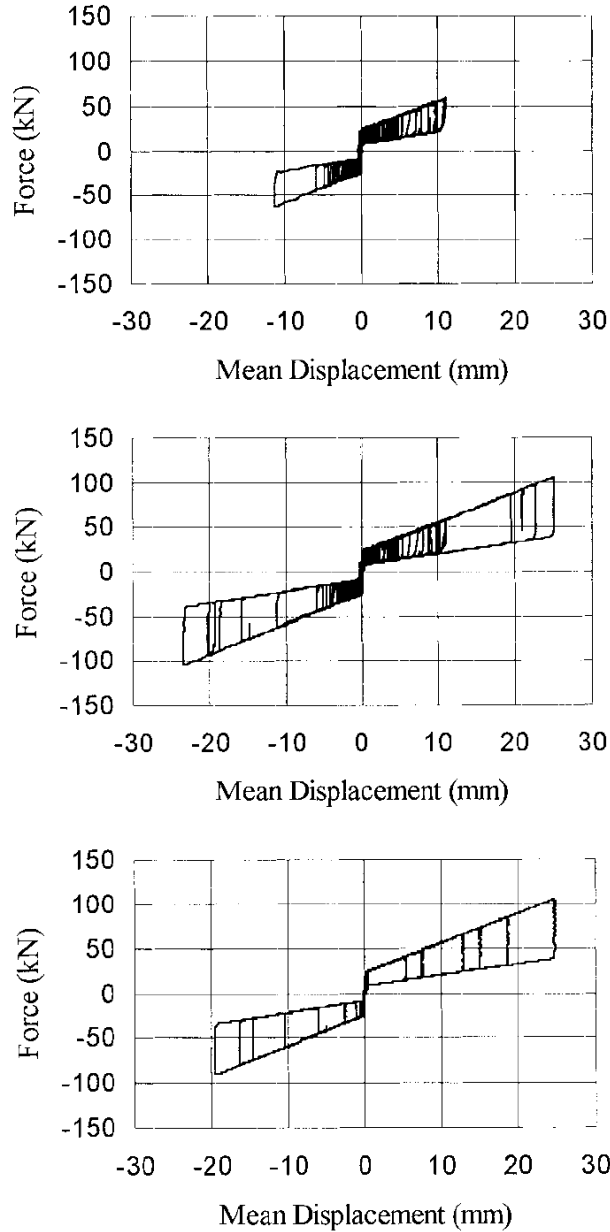


**Figure 3.18 Force displacement hysteresis of damper during earthquake records: Saguenay(Top), El Centro (middle), and San Fernando (bottom) [45]**

The last characterization test performed was a durability test in which the damper was subjected to 20 fully-reversed sinusoidal cycles with an amplitude of  $\pm 25$  mm and a frequency of 0.5 Hz to evaluate the performance of the damper in the event of multiple high-level aftershocks. The results of the durability tests indicated that degradation of the seismic damper is minimal with only a

maximum of 4% decrease in energy dissipation per cycle and less than 3% decrease in the peak force after 20 cycles [45].

In the second phase of testing, the seismic damper was tested in a tension-compression bracing configuration using an existing multipurpose steel frame on an earthquake simulator shake table as reported by Tremblay and Filiatrault [70]. The test setup with further details is shown in Figure 3.19 [45]. Four different seismic tests were conducted on the frame to allow for direct comparison between the seismic behaviour of the unbraced moment-resisting frame and the same frame retrofitted with the seismic damper. Two of the tests subjected the unbraced and braced frame to 100% of the 1940 El Centro earthquake (S00W component) while the other two tests subjected the frame to 200% of the same El Centro record component. These two intensities correspond to a Peak Horizontal Acceleration (PHA) of 0.33 g and 0.66 g. This record was chosen as it has been proven to cause the largest structural response amongst the three records considered during the characterization tests mentioned earlier and presented in Figure 3.18.

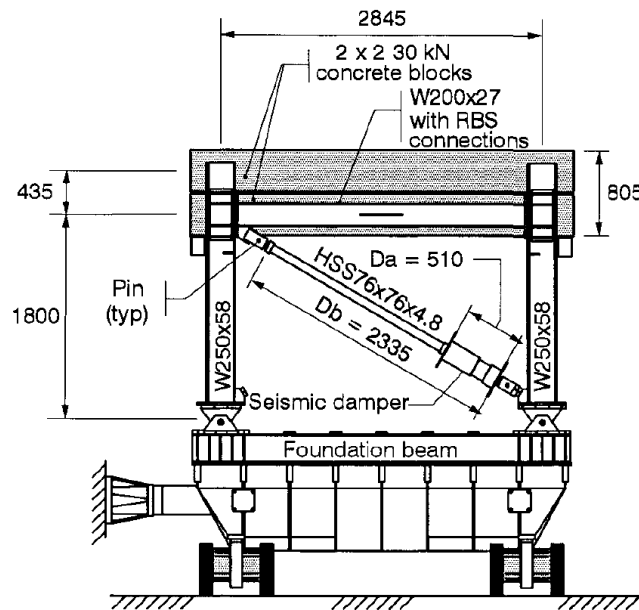


Figure 3.19 Test structure incorporating seismic damper [45]

The results of the tests showed that the seismic damper reduced the relative floor displacement under the two intensity levels of 100% and 200% by 50% and 38%, respectively. The damper reduced the peak floor acceleration by 30% under the 100% intensity level. However, the peak floor acceleration increased by about 33% under the 200% intensity level. This can be attributed to the yielding of the unbraced frame at this intensity level in addition to the restoring force adding to the yielding capacity of the braced frame. The seismic damper dissipated 20% and 40% of the energy imparted into the structure under 100% and 200% of the El Centro earthquake, respectively. A summary of these key results is presented in Table 3-3. The observed force-displacement hysteresis of the frame was again found to be stable, reliable and predictable, confirming the findings of the characterization tests. Finally, the braced frame was numerically modeled using dynamic analysis software RUAUMOKO and the results of the numerical analysis was compared to the experimental results. A good correlation both in amplitude and phase was observed between the experimental and numerical results.

**Table 3-3 Effect of retrofitting Steel MRF by Seismic Damper under 2 intensity levels [45]**

	<b>100% El Centro</b>	<b>200% El Centro</b>
Peak floor displacement	50% of unbraced	62% of unbraced
Peak floor acceleration	70% of unbraced	133% of unbraced
Energy dissipation/Total input energy	20%	40%

The results of this study proved the use of ring springs for self-centering dampers is adequate due to the reliability, repeatability, and predictability of its response. However, this study only focused on the use of smaller ring springs which are used primarily for the purpose of increasing the damping of the structure and not capable of restoring large structures to their initial position. Scaling of this design concept to achieve the load and deformation capacity needed for SCED

brace applications requires a new feasible design that can be constructed using commonly available structural shapes. Furthermore, a detailed full-scale testing of the scaled-up implementation of this concept, along with a parametric study that investigates the structure level response of structures using such braces, is necessary to determine the feasibility of using those braces as the main Seismic Force Resisting System (SFRS).

### **3.4 Use of Ring Springs as Seismic Dampers [63]**

Girges [63] investigated the use of low capacity ring spring cartridges as supplemental damping elements in structures. The prototype used for the tests had a tube with an outer diameter of 45.5 mm and a length of 229 mm. This tube enveloped 84 ring spring elements (42 outer rings and 41 inner rings and 2 half inner rings) with a capacity of 5 kN and 0.4 mm stroke per element. The tube was welded to an end plate on one side to be attached to the structure, while on the other side a steel piston rod, which was allowed to move within the tube, was connected to the other end of the structure. A schematic of the components of the ring spring damper used in this study is shown in Figure 3.20.

Position	Quantity	Nomenclature
1	42	Outer ring
2	41	Inner ring
3	2	Half inner ring
4	0.03kg	Special grease
6	1	Draw cup
7	1	Piston
8	1	Bar
9	1	Preloaded part
10	1	Tube
11	1	Base plate
12	1	fillet weld 4.5
13	1	Socket head cup screw
14	3	Socket head cup screw
15	1	Rod end
16	1	Hexagon nut

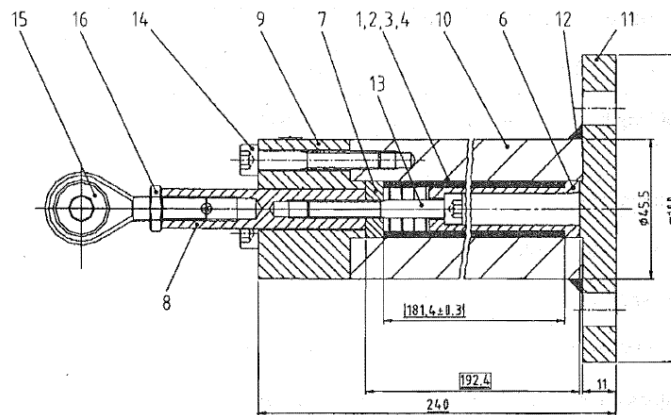
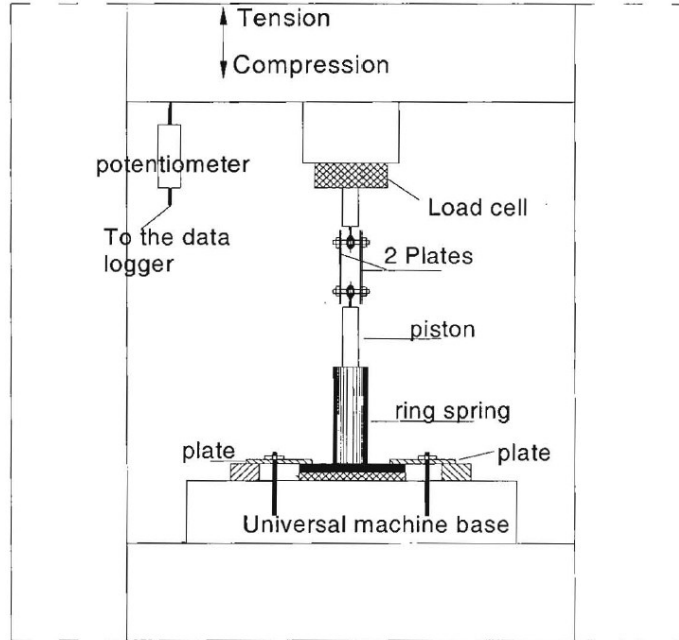


Figure 3.20 Ring spring damper assembly and components [63]

To determine the size and number of dampers required, computer analyses were carried out on a typical four storey structure with 15% inherent damping using computer program RUAUMOKO. The roof displacement of the typical structure with constant damping was compared to a frame with ring spring dampers. The frame with the dampers was designed to have the same roof displacement as the original inherently damped structure. The damper was pre-compressed to 10% of its capacity. The model structure was subjected to 3 earthquake excitations records, namely the NS component of the 1940 El Centro earthquake, a modified Taft S69E record and the Pacoima Dam ground accelerations. The tests were performed on each of the two prototypes built at the University of Canterbury. The test setup is shown in Figure 3.21. The results from those tests yielded consistent and repeatable results.



**Figure 3.21 Ring spring damper setup in testing machine at University of Canterbury [63]**

The dampers were also applied to a four storey, two-bay steel frame to evaluate their effectiveness as a supplemental control system in a structure. The steel frame was built using square hollow steel sections for the beams and column members. The connection between the beams and columns as well as floor and columns included replaceable steel plates acting as replaceable fuses in the structure. The stiffness of these fuses was designed to be much smaller than the rest of the frame to simulate stiffness degradation in concrete structures post cracking. Mass was added to the structure to achieve a period of vibration representative to that of a four storey concrete structure. The outline drawing of the frame structure is shown in Figure 3.22. Details of the connections and design of the testing structure can be found in the reference by Girges [63].

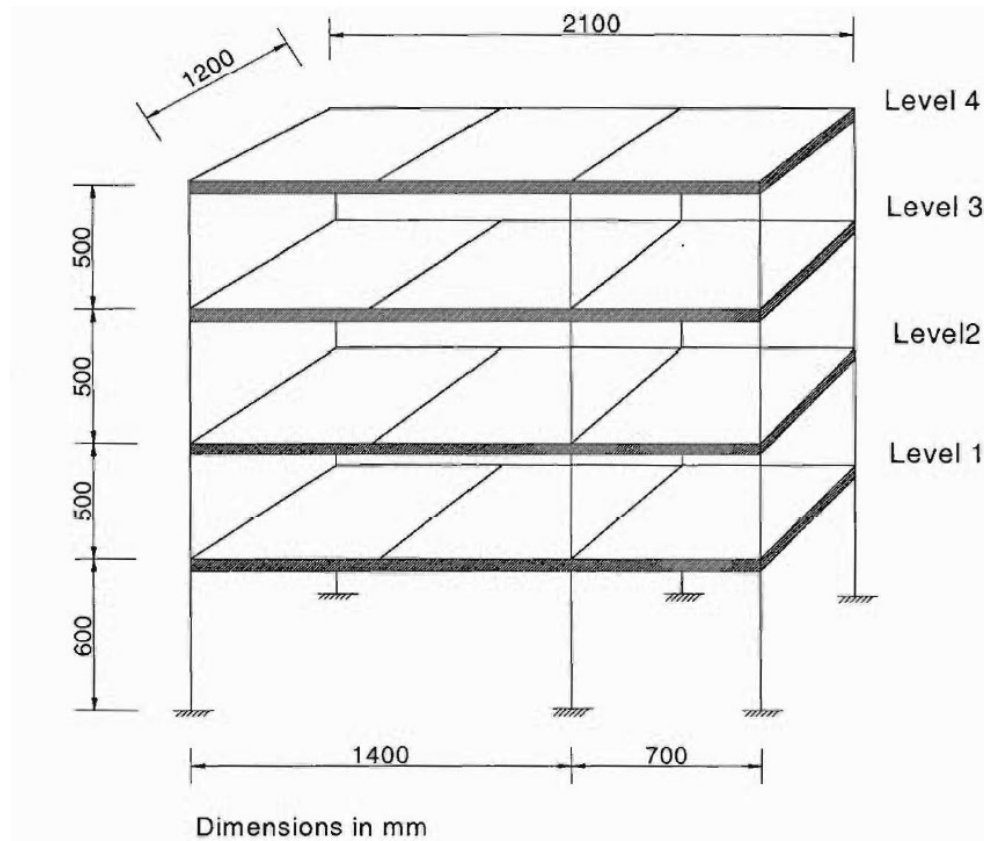


**Figure 3.22 Outline drawing of testing frame structure [63]**

To determine the optimal orientation and placement of the damper, the author proposed a new configuration referred to as the “load balancing damper-tendon system”. In this system the earthquake forces are to be balanced using a draped tendon coupled with a supplemental damping system. When properly designed, this system should, in theory, reduce the overturning moment and storey shear demands on structural elements. It is also intended to reduce the number of supplemental damping devices.

The placement of the tendon is determined through solving a tridiagonal matrix mainly composed of the ratio of floor-to-floor distribution of equivalent static applied earthquake loads. The simplest form of placement of this tendon is the placement of a straight tendon which optimizes the ideal moment resisted by the structure as shown in Figure 3.23. The damping forces

are transferred in the horizontal direction to the floor slabs using horizontal links as shown in Figure 3.24.

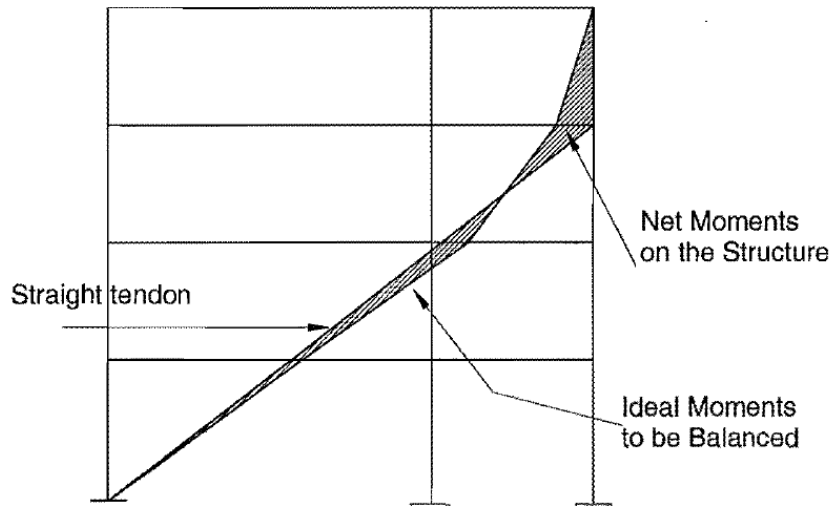


**Figure 3.23 Placement of a straight tendon relative to idealized tendon [63]**

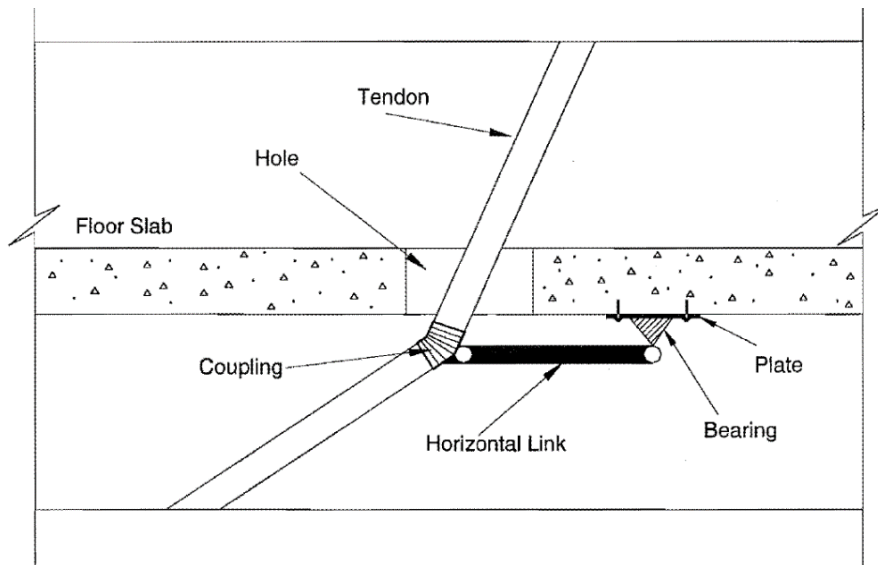


**Figure 3.24 Tendon-floor slab detail [63]**

In the experimental setup, a straight tendon that connected the base of the structure to the third floor was used. The first three floors were connected to the tendon-damper system using externally-mounted horizontal channel beams. On the first and second floors, horizontal links were used to transfer the damping forces from the tendon to the floors as shown in Figure 3.25. The

damper was connected to the tendon at the end and subsequently attached to the shake table. To connect the damper to the shake table, a simple pin connection fixed to the shake table floor was used. The horizontal links at the first and second floors utilized hollow structural steel sections to connect between the tendons and the channel beams.

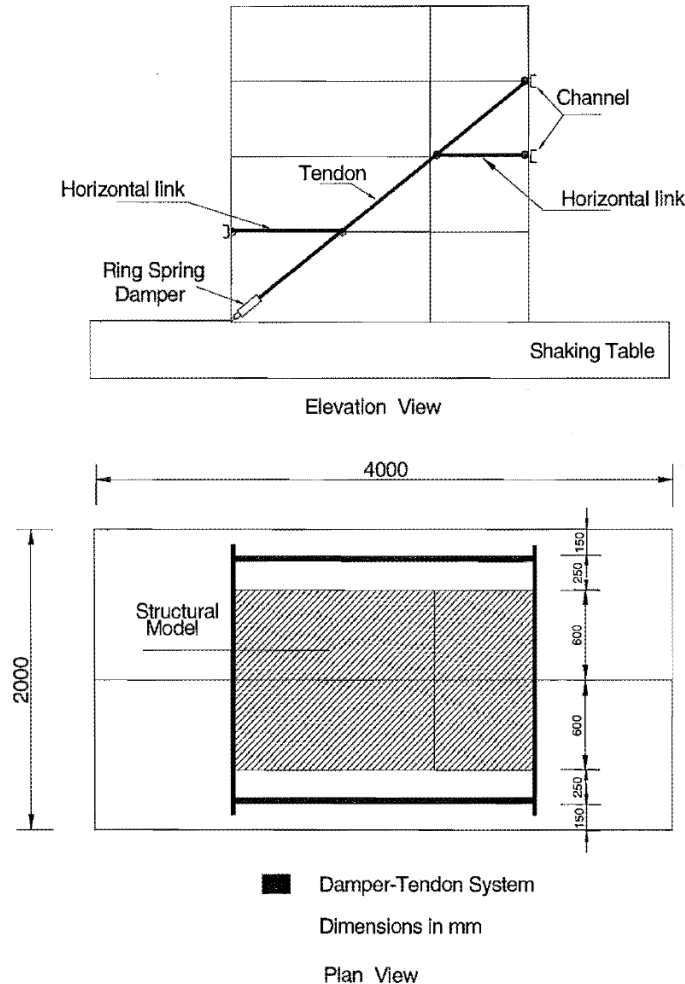


**Figure 3.25 Layout of the supplemental control system with the structure [63]**

A free vibration test was conducted on the frame with and without the supplemental control system to determine the period of vibration and damping ratio of the frame. The free vibration tests were done twice for each frame with different maximum initial roof displacements (5 mm and 6 mm). The natural period of vibration for the frame without the supplemental control system was

0.43 seconds with a damping ratio of 1.14%, meanwhile the period of vibration of the frame with the supplemental control system was 0.25 seconds with a damping ratio of 7.68%. The increase of stiffness caused by the introduction of the damper-tie supplemental control system resulted in the reduction of the spectral displacement by 84% from 0.032 to 0.005. Also, the increase in spectral acceleration due to the added stiffness was offset and overcome due to the added damping caused by friction of the ring springs which managed to reduce the spectral acceleration by almost half from 0.55 to 0.32.

**Table 3-4 Comparison of Testing frame dynamic properties after adding supplemental control system [63]**

	<b>Without Supplemental Control system</b>	<b>With supplemental control system</b>
Period of Vibration (s)	0.43	0.24
Damping Ratio (%)	1.14	7.68
Spectral Displacement	0.032	0.005
Spectral Acceleration	0.55	0.32

Two earthquake records with varying intensities were applied to the structure through the shake table with the supplemental control system being in place. The supplemental control system was then taken off and the same records at the same intensities were applied to the frame to evaluate the effectiveness of the system. The two records used were S69E Taft at intensities varying from 30% to 120%, as well as the NS component of the 1940 El-Centro earthquake at intensities varying from 10% to 120%. A total of 32 earthquake records were applied to the frame, split in half between the frame with and without the control system in place.

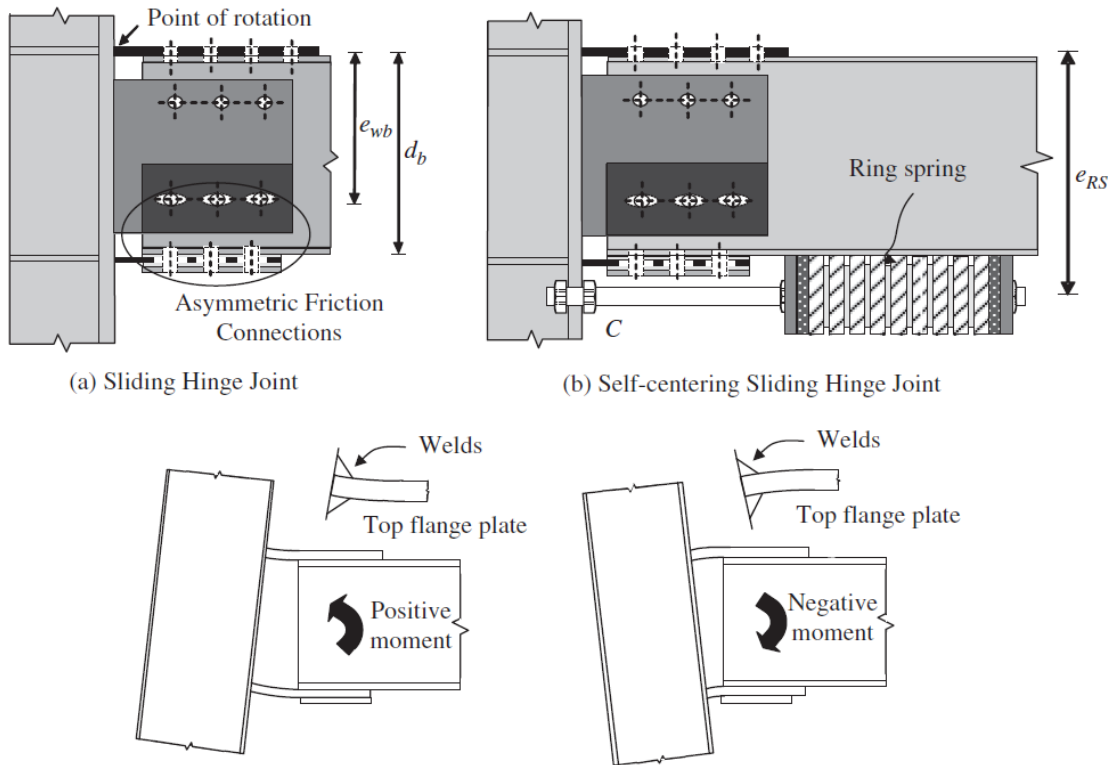
Both the maximum floor displacement and inter-storey drift were reduced by 40%-80% on average with the first floor showing the least reduction. The floor accelerations were also measured and did not show any increase when the supplemental control system was in place, in some cases reduction in the floor accelerations were observed when the supplemental control system was in place. This was due to the effect of the added damping and as evident by the spectral acceleration decrease shown above.

### **3.5 Self-Centering Sliding Hinge Joint (SCSHJ) Connections [64], [65]**

A self-centering sliding joint hinge connection was first proposed by Clifton [71] and later developed and tested by Khoo et al. [65]. The joint combines the self-centering and inherent energy dissipation capacity of ring springs with additional supplemental energy dissipation due to friction of the Asymmetric Friction Connection (AFC) [71]. The Asymmetric friction connection (AFC) is a beam to column connection typically used in moment resisting frames in which a rigid steel plate is bolted to the top flange of the beam and welded to the flange of the column. Similarly, the bottom flange of the beam is bolted to a steel plate that is welded to the flange of the column flange. However, the bottom flange plate is sandwiched between two steel shim plates made from high hardness abrasion resistant steel which allow for a smooth stable sliding behaviour. There is also a web plate that connects the column flange to the bottom of the beam web. The bottom web plate is designed in a similar way to the bottom flange plate with shim plates on both sides to allow for a smooth friction interface. The layout of this traditional AFC, referred to here as the Sliding Hinge Joint (SHJ) is shown in Figure 3.26(a). Both the bottom flange plate and the bottom web plate have slotted holes to allow for the sliding motion and facilitate the rotation to occur at the

joint by pivoting about the top interface only as shown in Figure 3.26(c), which minimizes frame expansion and damage to the floor slab.

To add the self-centering component to the typical SHJ connection, a steel tube housing a combination of pre-compressed ring springs is welded to the bottom flange of the beam as shown in Figure 3.26(b). To distinguish between the two types of AFC connections, the AFC connection that utilizes ring springs for self-centering is referred to as the Self-Centering Sliding Hinge Joint (SCSHJ) as opposed to the traditional Sliding Hinge Joint (SHJ).



(c) Joint rotation showing deformation of top flange plate (web plate not shown)

**Figure 3.26 (a) SHJ Layout, (b) SCSHJ and (c) Joint rotation [65]**

In the SCHJ, a steel rod in combination with steel nuts and end plates are utilized as a piston to compress the ring spring assembly as the frame deforms, as shown in Figure 3.27(i). When the beam is subjected to a positive moment, the gap between the column and the beam increases causing the steel rod to compress the ring spring assembly to the left towards the column as shown

in Figure 3.27(ii). When the beam is subjected to a negative moment the gap between the column and the beam decreases causing the steel rod to compress the ring spring assembly to the right away from the column as shown in Figure 3.27(iii).

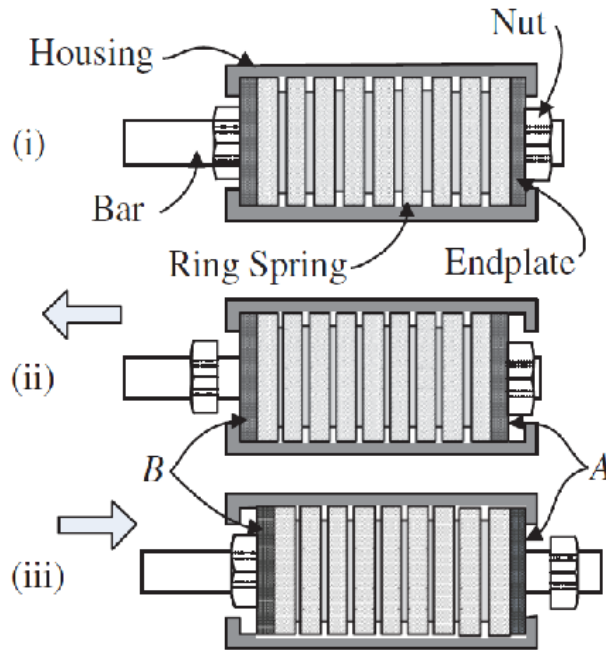
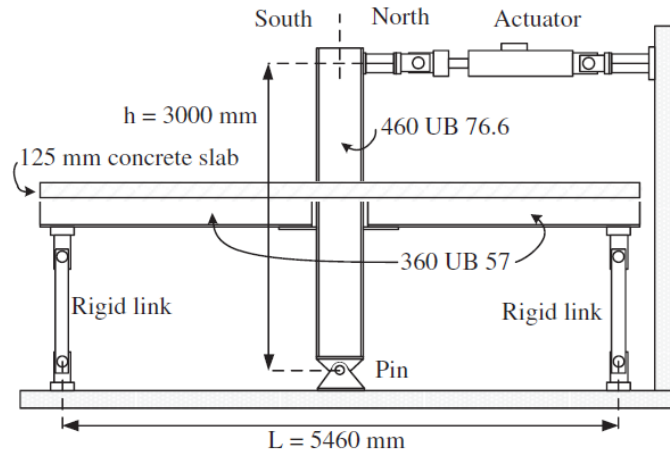


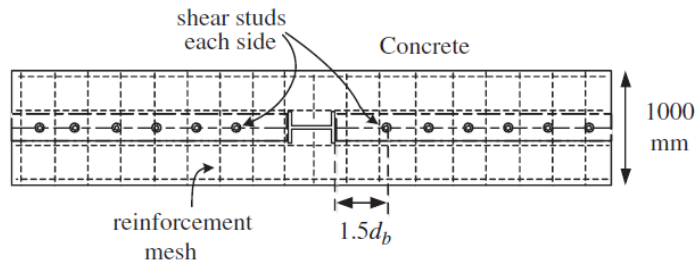
**Figure 3.27 Layout of Ring Spring Cartridge (i) in neutral position, (ii) under positive moment and (iii) under negative moment [65]**

To evaluate the effectiveness of the SCSHJ and SHJ, an eighth-floor section from the 10 storey Te Puni Village tower Building in Wellington, New Zealand was constructed in the laboratory. This structure was chosen to allow for comparison of the experimental results with the numerical results obtained from another analytical study [64]. As shown in Figure 3.28, vertically, the section constructed was from the mid-height of the floor below to the mid-height of the floor above, as well as from the midspan of the beam from either side of the column horizontally. A 1-meter wide segment of the concrete slab was also constructed cantilevering on both sides of the beam. The 125 mm concrete slab is connected to the beam using steel shear studs and contains a steel reinforcement grid. The frame was pinned at the bottom of the column preventing movement and allowing rotation. The frame was connected at the top to an actuator fixed to a strong wall. The

beams were supported by rigid links which were pinned at the bottom to the floor. This allowed lateral movement of the frame. Details of the design of the frame and joints can be found in the reference [65].



(a) Elevation View



(b) Plan View

**Figure 3.28 SCSHJ and SHJ Test setup [65]**

The frame was tested a total of 10 times, according to the testing protocols presented in Table 3-5. The frame tests were a combination of the frame with the AFC only referred to as Sliding Hinge Joint (SHJ), with both the ring spring Cartridge and AFC referred to as Self-Centering Sliding Hinge Joint (SCSHJ), or the Ring Spring Cartridge only referred to as Ring Spring Hinge Joint (RSHJ). The percentage of pre-compression in the springs was also varied to test different arrangements with three different levels of contribution to the moment capacity of the joint by the ring spring.

**Table 3-5 Testing plan for SCSHJ and SHJ [65]**

Test #	Joint type	Pre-compression of Ring Spring (%)	Loading protocol	Percentage of joint moment capacity developed by ring spring, $P_{RS}$ (%)
1	SHJ	0	SAC	0
2	SHJ	0	NF	0
3	SCSHJ	64.4	SAC	20.6
4	SCSHJ	56.7	SAC	40
5	SCSHJ	56.7	SAC_Dy	40
6	SCSHJ	56.7	EQ	40
7	SCSHJ	56.7	SAC	52.4
8	RSHJ	64.4	SAC	100
9	RSHJ	56.7	SAC	100
10	Typical			--

The tests were carried out under 4 different loading regimes. The first loading regime was the one recommended by the SAC [72] for steel MRF connection subassembly testing. In this loading regime, the frame is subjected to quasi-static loading cycles of symmetric drift to the frame. The SAC\_Dy regime is the same as the SAC displacement regime modified to consider dynamic rate of loading. The EQ loading regime is the loading protocol of applying displacement at the column location taken from analytical study of the same building performed under the maximum considered event [64]. The maximum considered event was the 1978 Tabas earthquake in Iran followed by the 1979 El Centro #6 imperial Valley earthquake. The NF loading regime was adapted from the recommendations of SAC [72] for near-fault protocol. The loading regimes are shown in Figure 3.29.

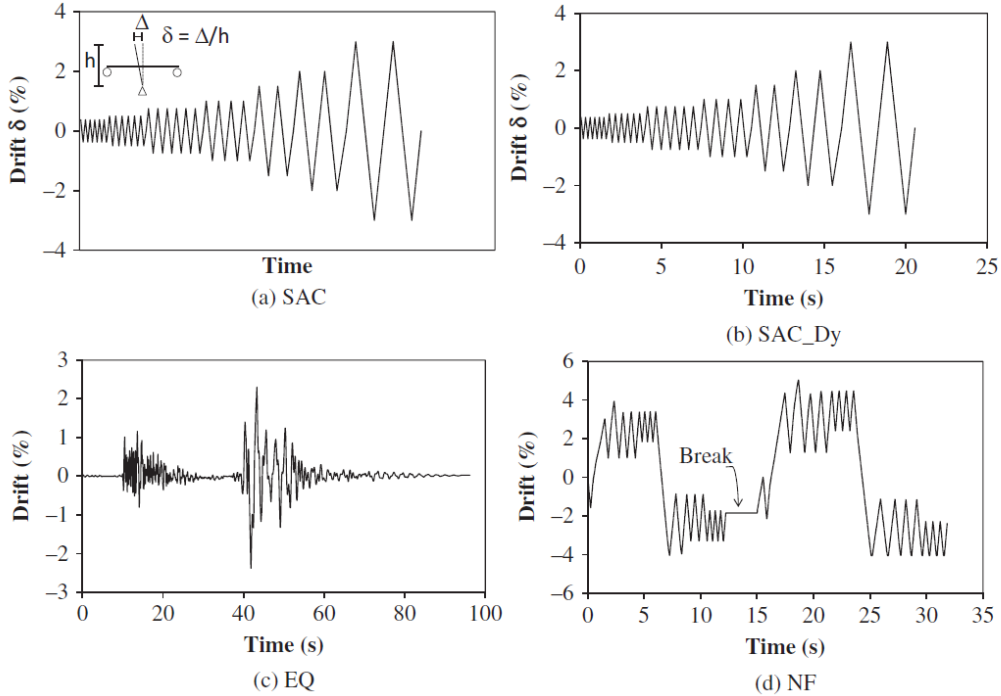


**Figure 3.29 Loading Regimes: (a) SAC, (b) SAC\_Dy, (c) EQ and (d) NF [65]**

Results from the test showed that as the percentage of the ring spring contribution to the moment capacity  $P_{RS}$  increases, the behaviour of the residual drift and final actuator loads improve. This led to the observation that there may be a need to increase the percentage of the moment capacity resisted by the ring springs  $P_{RS}$ , which could result in an increase in cost if implemented on a large scale especially considering the number of joints in a multi-storey building. The tests also found that there was negligible difference in results of the Ring Spring joints tested under dynamic load rating compared to those tested under quasi-static loading conditions.

### 3.6 Rocking CBF with Double Acting Ring Springs [67]

Gary et al. [67] proposed the use of ring springs in a centralized rocking concentrically braced frame (CRCBF) system. In a CRCBF system, the rocking causes the frame to rotate about the center which halves the magnitude of vertical movement of the frame corners thus minimizing the displacement compatibility issues with the attached floor slabs. The system relied on ring springs

at both corners of the CRCBF to dissipate seismic energy, while accommodating for the upward and downward movement. Below the columns of the CRCBF, two sets of ring springs with a 200 kN load capacity are placed inside a flanged cartridge to protect the springs from natural elements and dust. Two machined end plates are placed at both the top and bottom ends of the ring spring assemblies with the bottom end plate threaded. A threaded rod is centrally passed through the top end plate and ring springs, and threads into the threaded bottom end plate. The ring springs are then precompressed to 50% of their capacity and fastened using a clamping plate, which is then bolted to the flange of the cartridge as shown in Figure 3.30. The column base plate along with two hollow steel section (HSS) supports are seated on the top end plate of the ring springs and secured in position by means of the protruding threaded rod. When the column experiences compression, the column transfers the load to the HSS support which pushes the top end plate down compressing the column and thus transferring the load to the foundation. When the column experiences uplift, the threaded rods pull the bottom end plate upwards which compresses the ring springs against the cartridge flange.

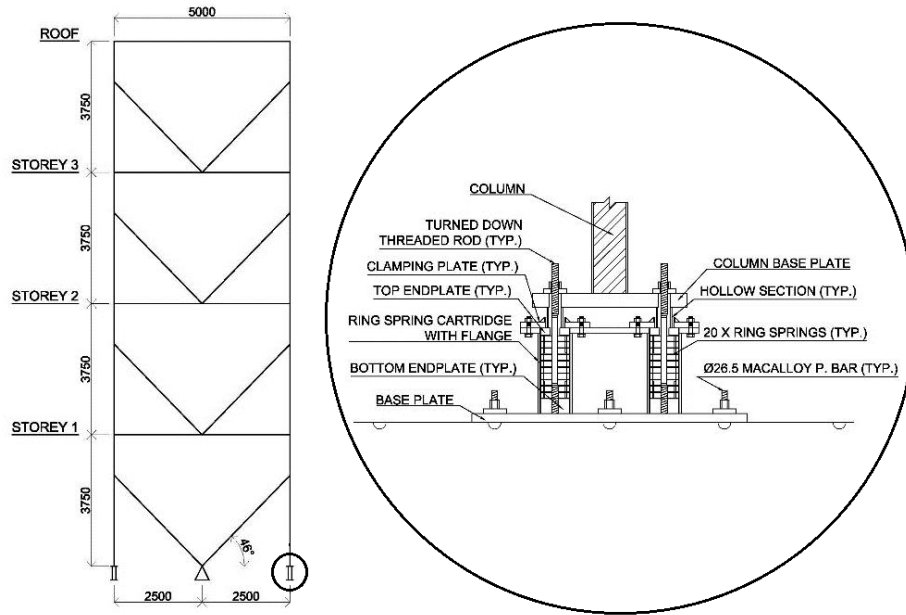


**Figure 3.30 Centralized Rocking Concentrically Braced Frame (CRCBF) system with Ring spring assembly [67]**

To test the efficiency of the CRCBF system, a four-storey office building in Wellington with the CRCBF as the main lateral force-resisting system was modeled in SAP 2000. The ring springs were defined as link element with the appropriate hysteresis properties. The building was subjected to both the original 1940 El Centro earthquake record and the same record scaled by a factor of two. A two-thirds scaled bottom storey of the CRCBF comprised of: a beam, a brace, a concrete filled HSS column, ring spring arrangement, central rocking pivot plate and a vertical post, was constructed for experimental testing in the laboratory, as shown in Figure 3.31. An actuator was used to apply displacement at the floor level.



**Figure 3.31 Bottom Storey of CRCBF test setup [67]**

Four different static cyclic and dynamic loading protocols were applied to the frame through the actuator as shown in Figure 3.32. The first regime was a uniform cyclic load with a slow rate of 0.5 mm/s. The second regime was a reverse cyclic load with decreasing amplitude and a faster dynamic rate of 20 mm/s. The third and fourth regimes were the displacement response of the first floor from a numerical analysis of the 4 storey building under both the original and scaled 1940 El Centro earthquake record. Test results showed that the hysteresis of the ring springs governed the response of the frame showing a stable and repeatable flag-shaped response. The hysteresis loops were also found to be consistent under all loading rates (quasi-static or dynamic) indicating that both the ring spring and the CRCBF response were independent of the loading rate. At the end of each test, the frame showed no residual drift proving the self-centering capabilities of the system. Also, through comparing the experimental results with analytical results of the brace it was noted that the distribution of the load between the two sets of springs was not uniform due to the rotation of the frame under rocking.

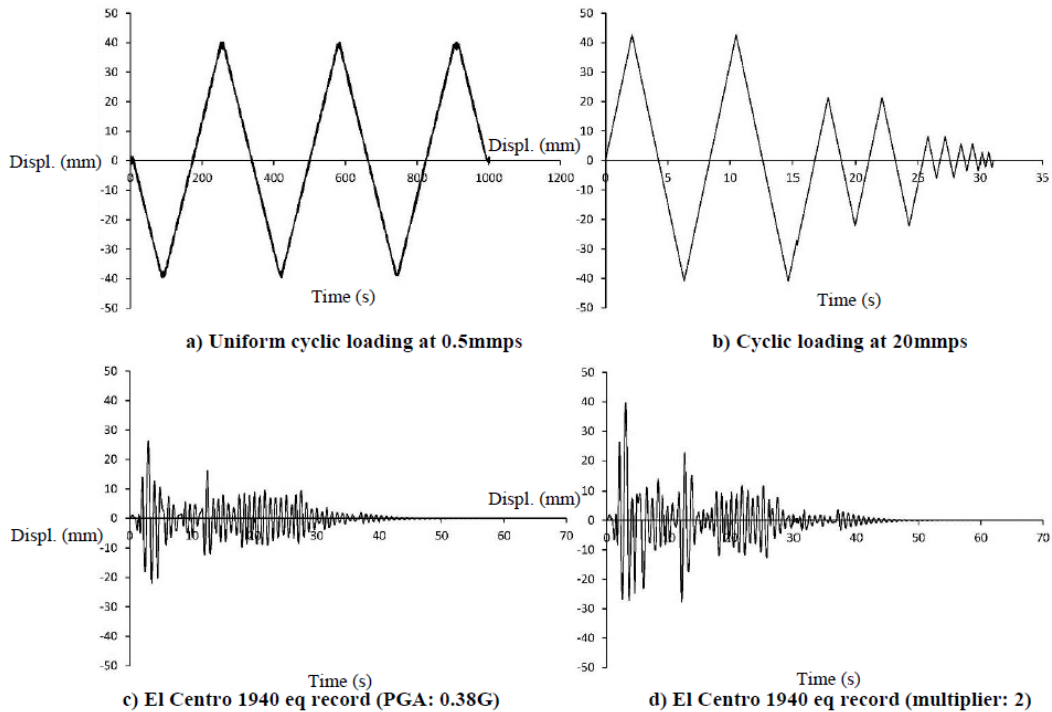
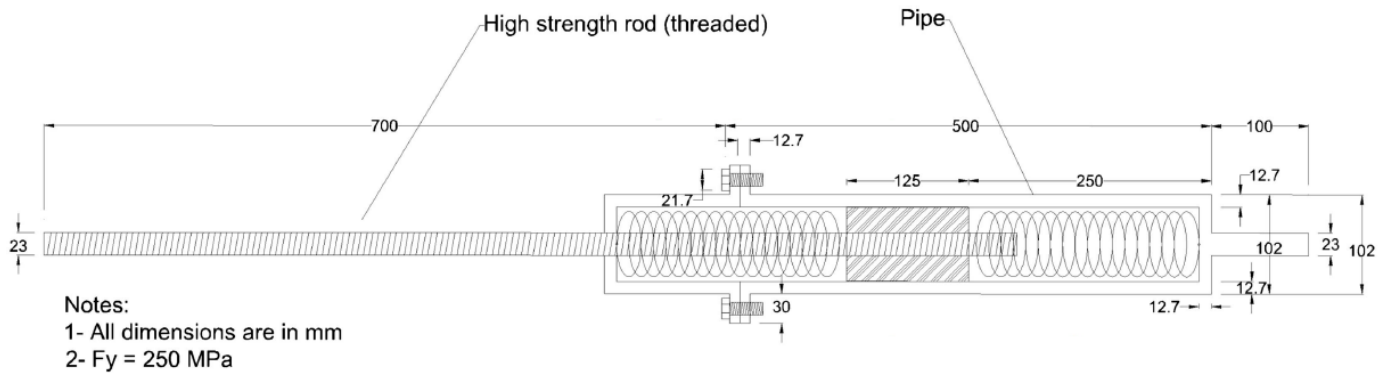


Figure 3.32 Static and dynamic loading regimes for testing the bottom storey of CRCBF [67]

### 3.7 Spring-Based Piston Bracing (SBPB) [53]

The Spring-based Piston Bracing (SBPB) was designed to be used mainly in chevron bracing configurations in buildings and relies on the use of friction ring springs for energy dissipation and recentering. The device is composed of 5 main parts namely the ring spring assembly, a holding cylinder, a piston, a locker, and bolts. Two prototypes were designed, one of which was a single acting ring spring in which ring springs only resist loads when the brace is under compression. The other configuration was a double acting ring spring in which ring springs resist both compressive and tensile forces from the brace. For the purpose of this review, only the results of the double acting configurations are discussed as it is more relevant to this study. The schematics for the design of the double acting ring spring brace is shown in Figure 3.33.



**Figure 3.33 Double Acting SBPB configuration [53]**

A threaded steel block moves left and right within the cylinder allowing for one of the two stacks of ring springs to always be in compression regardless of the type of load applied to the brace. It is worth noting however, that this design may not be the most efficient considering that only half of the ring springs are active at a time. The capacity of the ring springs used in this prototype was 65 kN (Type 7000). To investigate the cyclic behaviour of bracing members in CB frames, cyclic axial tests were conducted in the facilities of the Applied Laboratory for Advanced Materials and Structures (ALAMS) in the University of British Columbia (UBC). The bracing member was first subjected to quasi static loading and then an investigation of the effect of strain rate effect was conducted. The quasi-static loading tests were conducted in accordance with SAC protocol load history [72], which was previously discussed in 3.5, with a loading rate of 0.42 mm/sec. The results showed an excellent correlation with the predicted non-linear response of the system with stable, symmetric, repeatable loops with no residual deformation. The test was then repeated at varying loading rates of ~2, 5, 10, 50 and 100 times the rate of the quasi static test (0.42 mm/s). The hysteresis behaviour generated for the 5 increasing rates were almost identical, which is in line with observations made by other studies mentioned in the previous sections.

To evaluate the effectiveness of the SBPB system, a numerical analysis was conducted on a three-dimensional finite-element model for a sample structure using ETABS. The sample structure was a 4-storey office building located in Vancouver with a typical floor height of 3.8 m. The performance of the building was evaluated for a structural system with BRBs and compared to the performance of the same building with SBPB. The study used 20 far-field earthquake records which were scaled so that the median spectral acceleration of the set matched the maximum considered earthquake (MCE) spectral acceleration at the fundamental period of the structure. Figure 3.34 shows the Vancouver response spectrum according to NBCC [73], compared to the mean spectrum of the scaled records. The analyses showed that both the BRB and SBPB systems showed repeatable and stable responses with the clear distinction of the SBPB system resulting in no residual deformation. The floor acceleration for analyzed structures with BRBs was higher than the ones analyzed with SBPB. However, the maximum floor deformations exhibited by the building with BRBs were lower than those exhibited with building with SBPB. This was attributed to the low stiffness of the SBPBs compared to the stiffness of BRBs in this study.

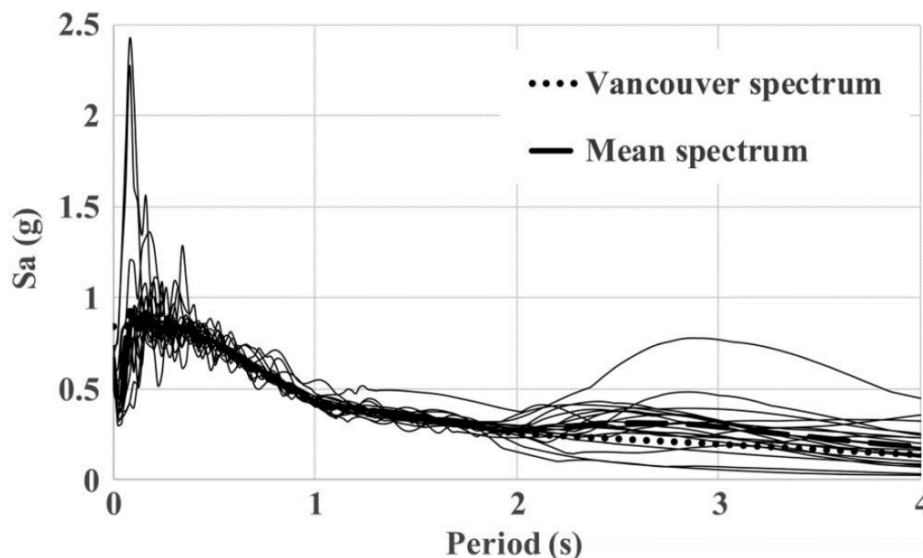


Figure 3.34 Response Spectra of scaled EQ records compared to Vancouver response Spectrum [53]

### 3.8 Summary

In this chapter, the characteristics of the ring springs and a literature review of some structural applications of ring springs were presented. One of the greatest advantages of ring springs are their versatility in terms of accommodating large loads and deformation based on the appropriate choice of ring sizes and number of elements in the assembly. Some other advantages include their high weight utilization ratio, load rate independence and temperature independence, all factors which are important in earthquake engineering applications. Ring springs are also capable of dissipating earthquake energy through friction, without the need for external energy dissipation mechanisms similar to the ones found in previously-developed SCED braces presented in Chapter 2. These advantages led to several studies which investigated different devices designed to utilize ring springs in earthquake engineering applications. Testing of these devices confirmed the repeatable and predictable hysteretic response of the ring springs, their loading rate independence, their energy dissipation, and excellent self-centering capabilities. However, most of these devices are limited in either their load capacity, deformation capacity, or both. Therefore, there exists a need for a new design that can be easily scaled and practical to construct yet capable of providing large load and deformation capacities. The next chapter discusses in detail a new design for a SCED brace that utilizes ring springs which can be constructed using readily available steel shapes, and has a force and deformation capacity comparable to other Seismic Force Resisting Systems (SRFS). Testing of the proposed brace, and, subsequently, the development of appropriate design factors for structures designed with the proposed brace system will be presented in the following chapters.

# Chapter 4 : Design of RS-SCED Brace and Testing Methodology

As discussed in Section 2.15, most SCED braces are limited in application by either their force or deformation capacity. SCED braces with a large load and deformation capacity require large size and length which presents challenges for implementing them in design of actual structures in engineering practice. Sections 3.2 to 3.7 summarize previous studies that utilized ring springs for a variety of self-centering systems. However, these implementations were either inadequate for use in large structures due to their load and deformation capacity; or impractical for rehabilitation applications due to disturbance caused by construction, which is the case with the CRCBF system. These issues limit the practical utilization of SCED braces in large structures such as high-rise buildings and bridges. The design objectives for the new RS-SCED (Ring Spring Self-Centering Energy Dissipative) brace are to: 1) achieve a large deformation capacity equivalent to at least 4% drift in a 4-meter-high bay, 2) achieve a load capacity that is in excess of 1000 kN to be on a comparable order of magnitude to other of lateral load resisting systems of large structures, 3) have a compact design which makes it easier to install the braces in both new construction and rehabilitation applications for existing structures, and 4) that can be fabricated using steel, a commonly used material in construction trusted by the engineering profession, using readily available section sizes.

The new design introduced in this chapter utilizes ring springs to provide both a large deformation and load capacities within a compact size. To evaluate the response characteristics of this brace both on its own and as the lateral load resisting systems in different structural systems, a full-scale prototype of the brace was designed, built and tested. The design of the brace, its mechanics as well as details of the testing setup are discussed in this chapter.

## 4.1 Design of the New Ring Spring SCED Brace

The ring spring SCED brace in this study is designed for a steel braced frame office building in Victoria, BC used for the hybrid simulation discussed in a later Section 6.4. The prototype building is an 8-storey building with plan dimensions of 35 m by 45 m, and an elevation of 32 m. The building has a typical floor height of 4 m and column spacing of 7 m. A chevron brace configuration is used for the braced frame as shown in Figure 4.1. In this configuration, two RS-SCED braces are placed horizontally acting in parallel under lateral loading. Since the braces are placed horizontally, this allows the ratio between the brace deformation  $\delta_b$  and floor deformation  $\delta_f$  to be equal to 1, which is higher than the ratio calculated for traditional diagonal brace configuration as shown in Equation 4-1.

$$\delta_b = \delta_f \cos \theta \quad \text{Equation 4-1}$$

where  $\theta$  is the angle of the brace relative to the horizontal. This is beneficial as it enables the full utilization of the brace deformation capacity in resisting the floor drift when compared to the traditional diagonal configuration for which  $\theta > 0$ .

Another advantage of using a chevron brace configuration is the ability to use two braces in parallel in a single frame which doubles the lateral load capacity of the frame. This configuration is not possible with previously designed large size SCED braces due to the space limitation of the horizontal layout configuration of the brace. This problem is resolved with the new compact design. The SCED braces are connected to the chevron brace and columns by means of true pins to ensure the brace resists axial loads only.

In this study, the prototype brace is designed to have the same load capacity as the largest commercially available ring spring that can fit within a readily available steel HSS section. This

design is chosen to validate the applicability and functionality of a brace with enough capacity to support multi-storey buildings and multi span bridges.

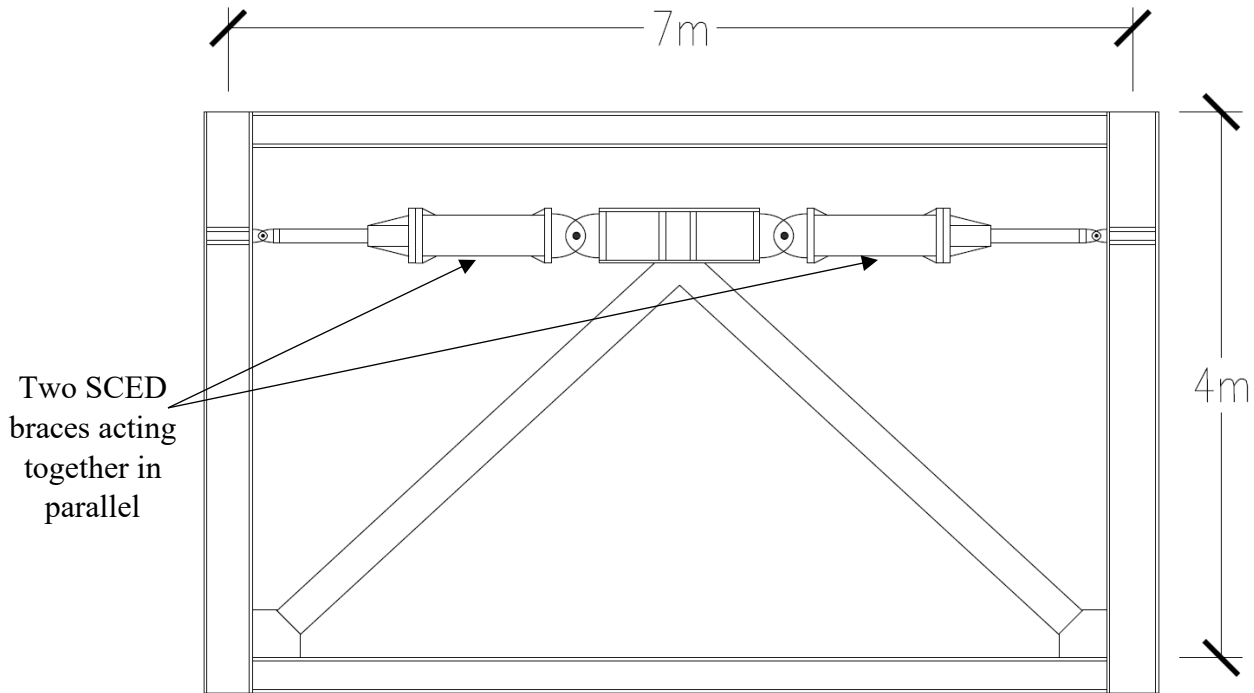


**Figure 4.1 Two braces in parallel added to frame with chevron brace configuration**

When designing a building using the new RS-SCED braces, an initial preliminary equivalent lateral load analysis is performed to determine the storey shear at each level. The design and analysis of the prototype office building for this study is discussed in later sections. The storey shear is divided by the number of braces per floor to determine the activation load  $P_a$  for each brace. To set this activation load, an initial pre-compression load of equal magnitude needs to be applied to the ring spring assembly of each brace. This pre-compression process is discussed in detail later in this chapter. The pre-compression of the ring springs is calculated as a percentage of the SCED brace ultimate load capacity  $P_u$  as follows:

$$PC (\%) = \frac{P_a}{P_u} > 10\% \quad \text{Equation 4-2}$$

The pre-compression of the ring springs  $PC$  should not be less than 10% to ensure that the ring assembly maintains its alignment [44]. A practical range for the pre-compression of the springs is usually between 20% to 30% to achieve the desired activation load  $P_a$ .

At low levels of load, below the activation load of the brace  $P_a$ , the SCED brace has a high stiffness which is governed by the sizes of steel sections used in the fabrication of the brace. At this stage of loading, deformation is minimal, which is important to ensure that the building does not deform under wind loads.

Once the applied load from an earthquake exceeds the activation load  $P_a$ , the ring springs elements start sliding against each other, causing the stiffness of the brace to be dominated by the spring loading stiffness  $K_L$  (See Section 3.1.3). The transition between the initial high stiffness and the post-activation low stiffness, allows the brace to achieve high deformation without a large increase in load that would otherwise result in yielding of steel elements in the brace.

The deformation capacity of each brace  $\delta_b$  is calculated based on the intended floor drift demand  $\Delta_f$ , the height of the relevant floor  $h$ , and the orientation of the brace relative to the floor  $\theta$ . The deformation capacity of the brace  $\delta_b$  is calculated as follows:

$$\delta_b = \Delta_f \times h \times \cos \theta \quad \text{Equation 4-3}$$

The deformation capacity of the brace  $\delta_b$  can be achieved by choosing the appropriate number of elements in the ring spring assembly  $e$  (See Section 3.1.3). The number of ring elements in the assembly can be calculated based on the deformation capacity of the brace  $\delta_b$  as follows:

$$e = \frac{\delta_b}{S_e \times (1-PC)} \quad \text{Equation 4-4}$$

where  $e$  is the number of elements in an assembly, and  $S_e$  is the deformation capacity of a single element.

The list of design parameters for the prototype ring spring brace designed for this study are shown in Table 4-1. The SCED brace ultimate load  $P_u$  is the maximum load capacity of the ring springs used in the assembly. For the prototype in this study, this corresponds to capacity of the largest commercially available ring spring that can fit in a commonly available steel shape, Ring Spring type 34000 provided by RingFeder. The target activation load of the SCED brace  $P_a$  is determined through the design of a prototype 8-storey office building with a 4 m typical floor height, designed for seismic design category D according to the ASCE 7-16 [74] and using the first floor storey shear demand. The storey drift demand  $\Delta_f$  of 4% is chosen to compare the response of this brace to other BRBs and SCED braces. This value is much larger than typical code drift limits and it represents a likely maximum drift when considering earthquake variability. Details of the design of this structure are presented in Section 6.4.

**Table 4-1: Ring Spring SCED design parameters**

<b>Parameter</b>	<b>Value</b>
SCED brace ultimate load ( $P_u$ )	1450 kN
Ring Spring Type	34000
SCED brace activation load ( $P_a$ )	406 kN
SCED brace pre-compression ( $PC$ )	28%
Storey Drift ( $\Delta_f$ )	4% (132 mm)
Floor height ( $h$ )	4 m
Orientation of the brace ( $\theta$ )	0°
Element Spring travel ( $S_e$ )	7.5 mm
Number of elements ( $e$ )	33
SCED brace deformation capacity ( $\delta_b$ )	169 mm

## 4.2 RS-SCED Brace Mechanism

The mechanism of the RS-SCED brace presented in this study, shown in Figure 4.2, is different from the mechanisms used by other large-scale SCED braces previously developed [26], [27]. This is because the new RS-SCED brace relies on compression of the ring spring assembly rather than the tension of the prestressing tendon to provide the restoring force and bring the brace back to its original configuration. The brace mechanism consists of 4 main elements: (1) a ring spring assembly that is precompressed with one end plate on each of its two ends, (2) a steel prestressing chair that has a steel piston that compresses the ring springs when the brace is under compression, (3) a steel threaded rod that transfers the load from the steel prestressing chair to the ring springs when the brace is under tension, and (4) an outer member that houses the ring springs and transfers the load to the rest of the structure.

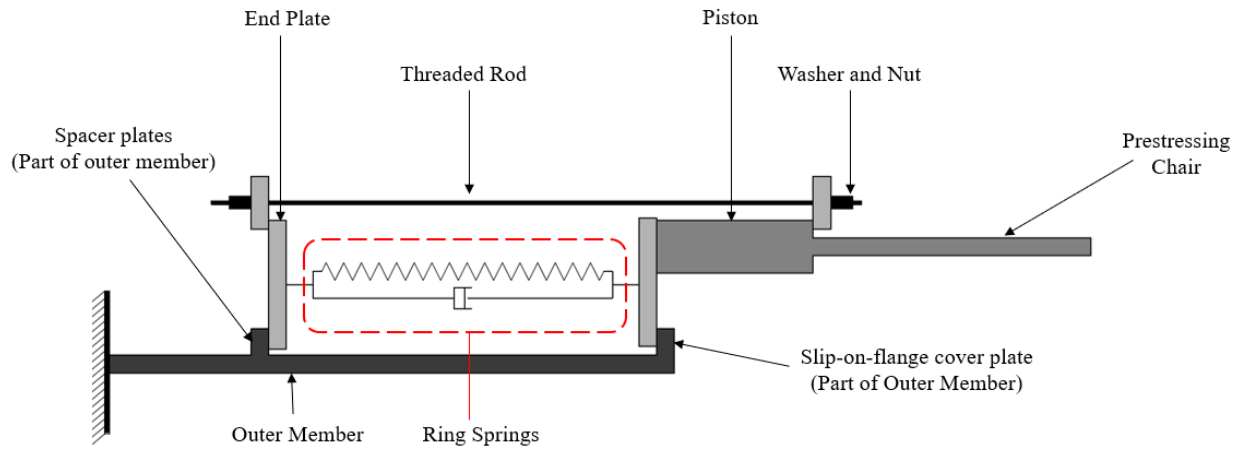


**Figure 4.2 Schematic representation of RS-SCED showing the brace mechanism**

Although the figure shows the ring springs to be adjacent to the outer member, the ring springs are usually fully housed inside the outer member. The ring spring assembly is contained and restrained from moving out of the outer member by means of a slip-on-flange cover plate on one end (the right end in the figure) and welded spacer plates on the other end (the left end in the figure). The slip-on-flange cover plate and the spacer plates are rigidly connected to the outer member and can be considered a part of the outer member, they are only separately identified here for explanatory purposes.

At one end of the brace (the right end in the figure), the structure is connected to the prestressing chair, and at the other end of the brace (the left end in the figure), the structure is connected to the outer member. The ring spring provides both stiffness and energy dissipation simultaneously when in motion (depicted by the spring and dashpot in the figure representing the behaviour of the ring springs). The interaction of the four main elements as shown in Figure 4.3, allows the brace to achieve a flag-shaped hysteresis behaviour.

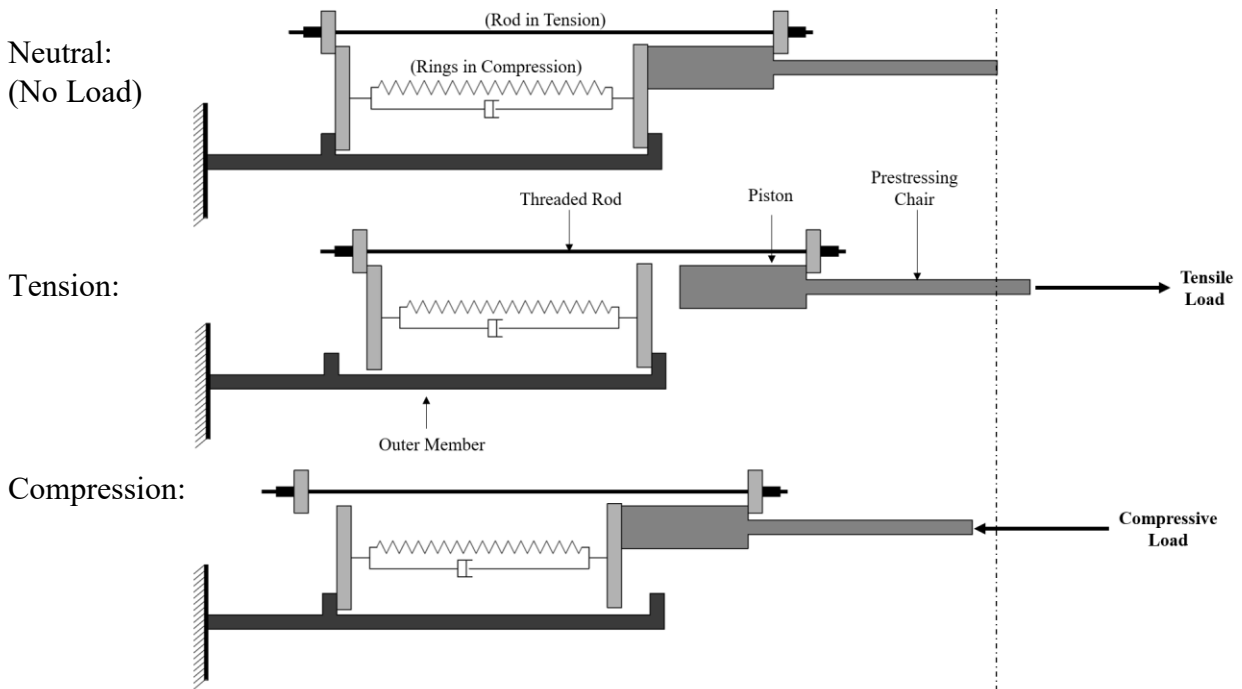
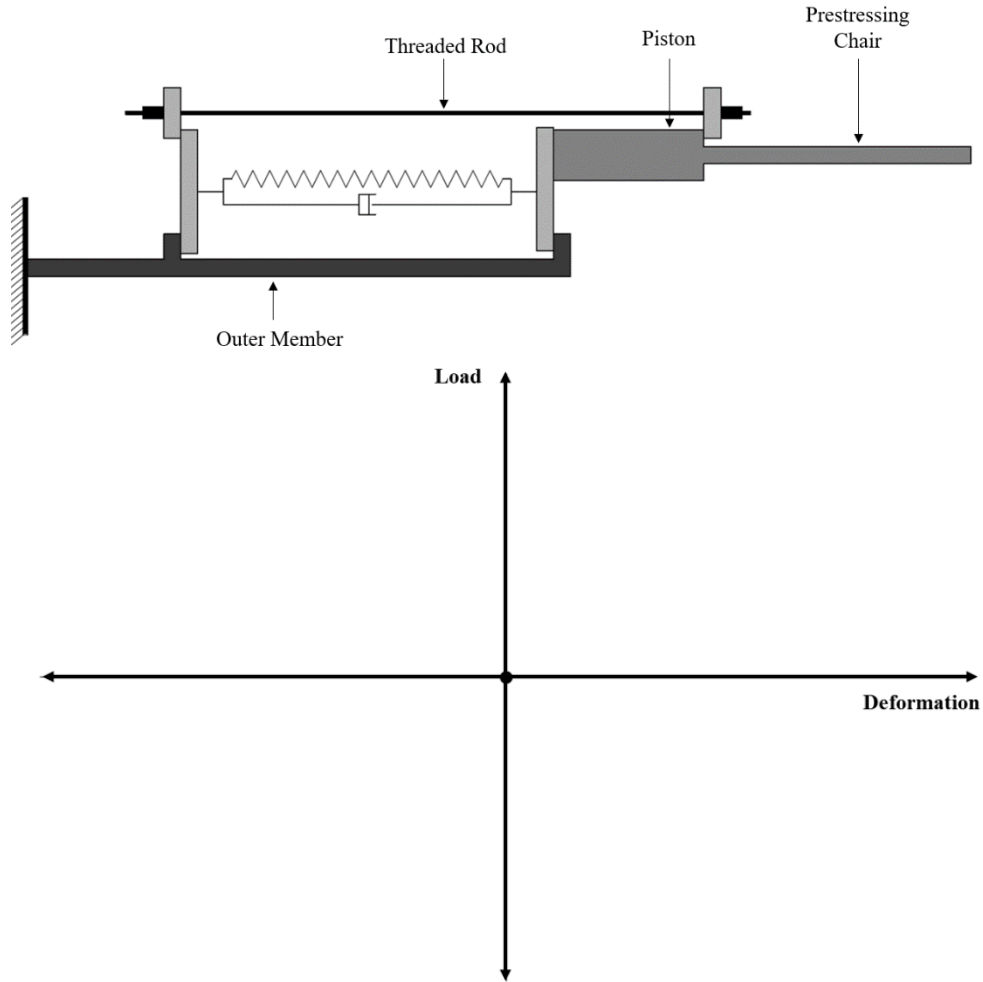


Figure 4.3 Schematic of brace mechanism at different loading states

Initially, the ring springs are precompressed by means of the threaded rod during the assembly (details of the assembly process will follow). Therefore, at its initial state (Figure 4.4), the piston along with the ring springs are both under compression while the steel threaded rod is under tension. The magnitude of this load is the equivalent to the intended activation load of the SCED brace  $P_a$ . Although the spacer plates and the slip-on-flange cover plate are both in contact with the ring assembly, neither of them is sustaining any significant load at this stage. Therefore, it is not anticipated that the outer member is loaded at this initial stage. Similarly, the prestressing chair is not loaded at this stage. Due to the arrangement of the brace components, the ring springs are compressed relative to their initial state regardless of whether the brace is in tension or in compression.



**Figure 4.4 Schematic of the brace at the first step of the hysteresis (no load)**

The initial stiffness  $K_i$  in the hysteretic response (Figure 4.5) is a result of all the elements deforming together until the tension force overcomes the initial pre-compression of the ring springs  $P_a$ , allowing the left end plate to separate from the outer member. Discussion of the determination of this stiffness will follow. After the initial compression force in the springs  $P_a$  is exceeded, the SCED brace is ‘activated’ and the stiffness of the brace is approximately equal to the stiffness of the ring spring loading stiffness  $K_L$ .

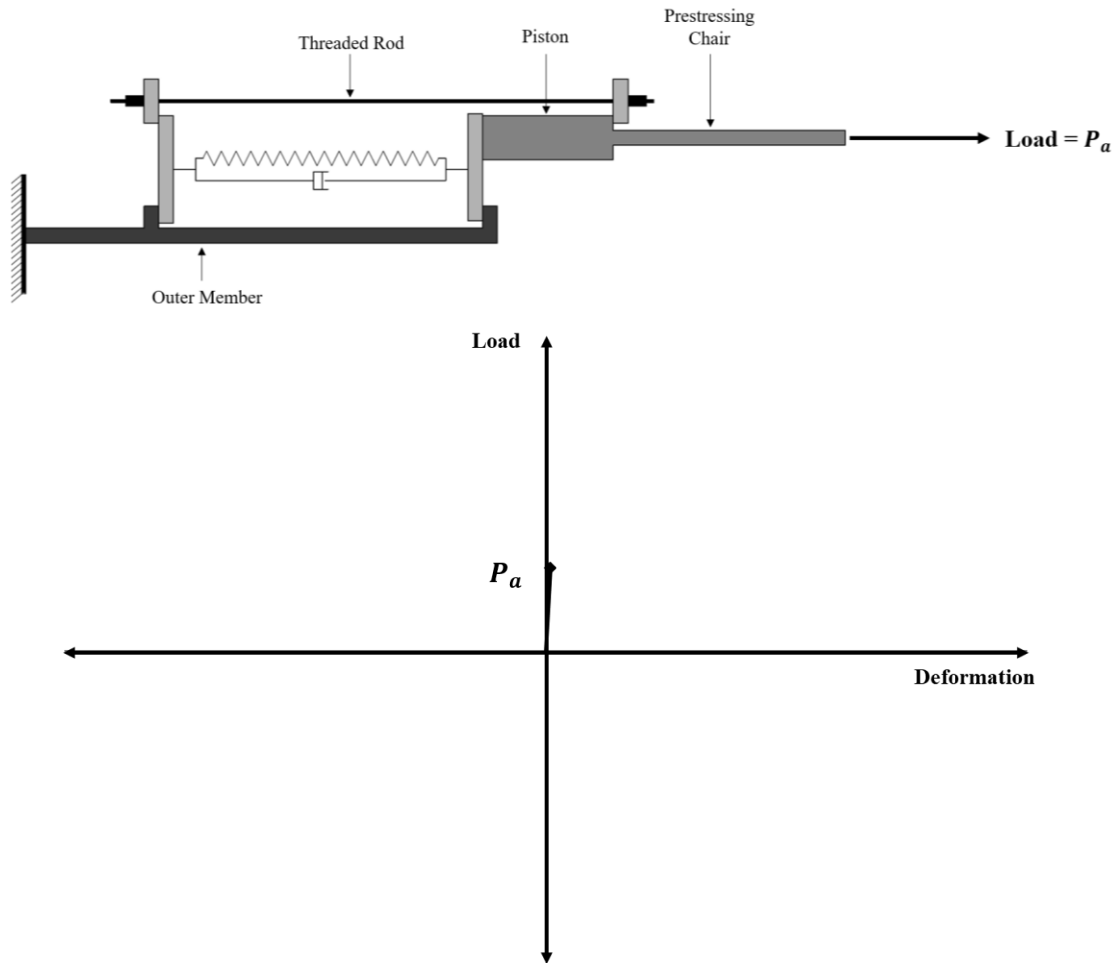


**Figure 4.5 Schematic of the brace while loading in tension pre-activation of springs**

When the brace is in tension (Figure 4.6), the prestressing chair moves to the right and abuts against the washer plate of the threaded rod. The threaded rod moves to the right pulling the left end plate to the right. This results in the ring springs getting compressed between the two end plates, since the right end plate is restrained from moving to the right by means of the slip-on-flange cover plate. The cover plate of the slip-on-flange transfers the load to the outer member which transfers it to the supporting structure of the brace. During this stage of loading, the piston tube as well as the spacer plates are not expected to carry any axial loads.

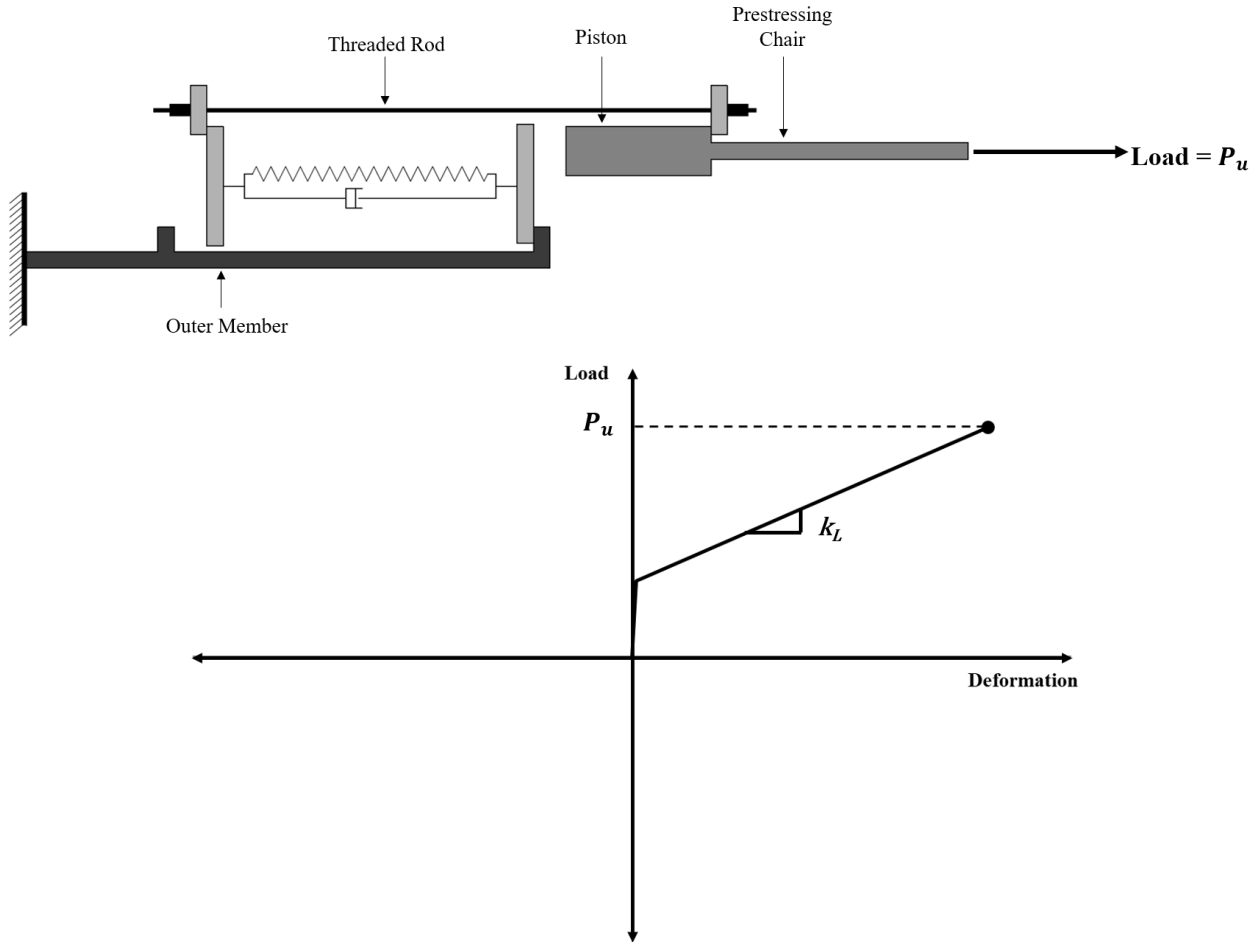
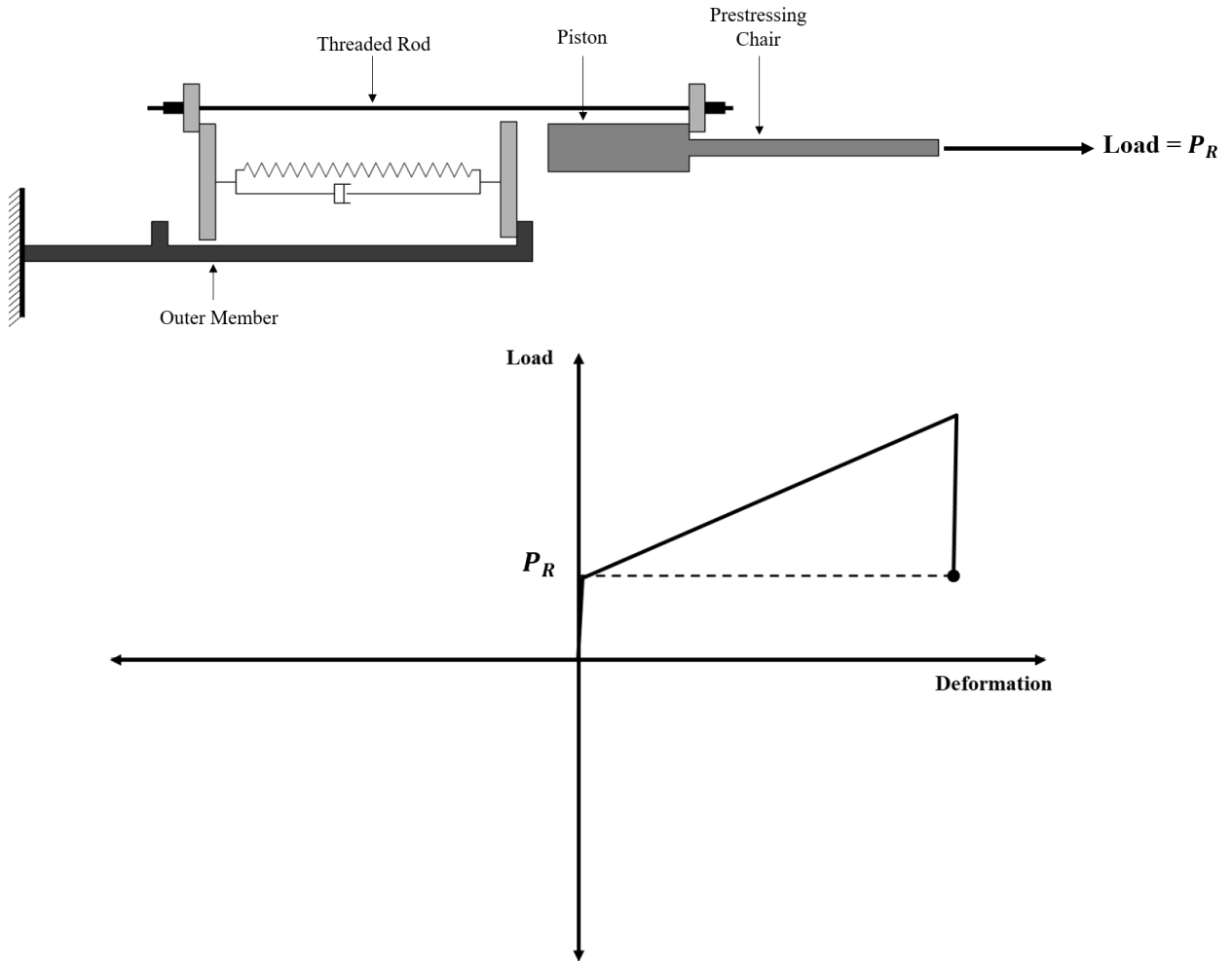


Figure 4.6 Schematic of the brace while loading in tension post-activation of springs

As the brace starts unloading, the ring springs are once again locked in position and does not decompress until the applied tension load decreases below the recoil load of the brace  $P_R$ . This is required to overcome the breaking friction force between the interlocked ring springs as described in detail in Section 3.1.4. During this stage, the stiffness of the brace is once again equal to the initial stiffness  $K_i$  as shown in Figure 4.7. Once the load drops below the recoil load  $P_R$ , the brace ‘reactivates’ and starts decompressing at a stiffness equal to the unloading stiffness of the ring springs  $K_u$ .



**Figure 4.7 Schematic of the brace while unloading in tension pre-activation of springs**

The springs continue to decompress until they reach their initial length. While the spring is decompressing, the stiffness of the brace is equal to the unloading stiffness of the spring  $K_u$ . When the spring decompresses to its initial length, the left end plate bears against the outer member via the spacer plates. When this occurs as shown in Figure 4.8, the load in the brace  $P_d$  should be equal to the load resisted by the ring springs post-decompression  $F_d$  defined earlier in Section 3.1.4 as a function of the activation load of the brace  $P_a$  and the pre-compression of the springs  $PC$ . At this stage, the brace stiffness returns to the initial stiffness until the brace fully unloads to the initial position as shown in Figure 4.8.

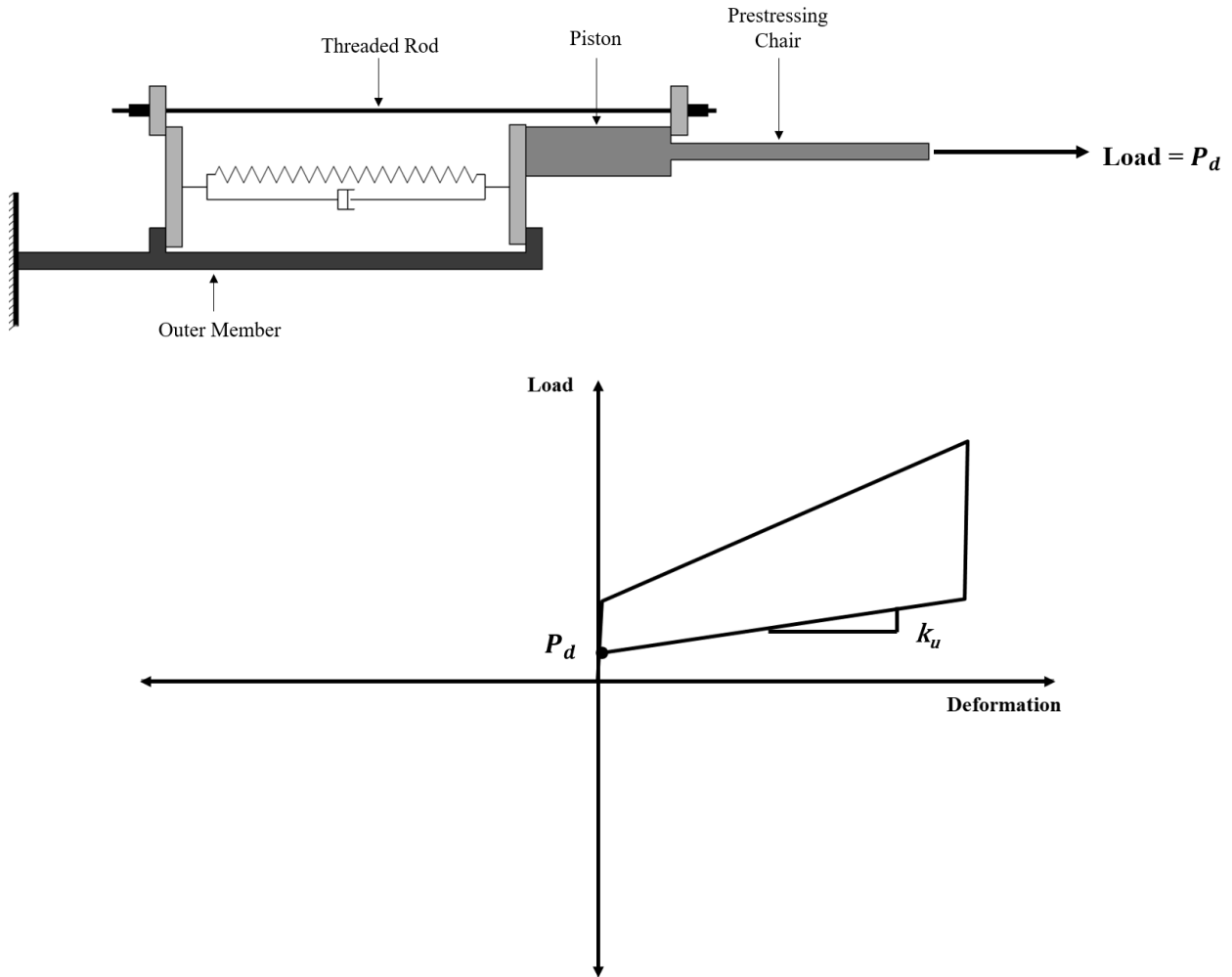


**Figure 4.8 Schematic of the brace while unloading in tension post-activation of springs**

When the brace is in compression (Figure 4.9), the piston bears against the right end plate moving it to the left. This results in the ring springs getting compressed between the two end plates since the left end plate is restrained from moving to the left by means of the spaced plates. The spacer plate then transfers the load to the portion of the outer member that is to its left which is then transferred to the rest of the structure. During this stage, the threaded rod does not carry any load and thus is free to slide. Most of the outer member and the slip-on-flange cover plate (the portion of the outer member to the right of the spacer plates) do not attract any load at this stage. Like in the tension cycle, the loading stiffness of the brace at the initial stage is equal to the initial stiffness  $K_i$ .

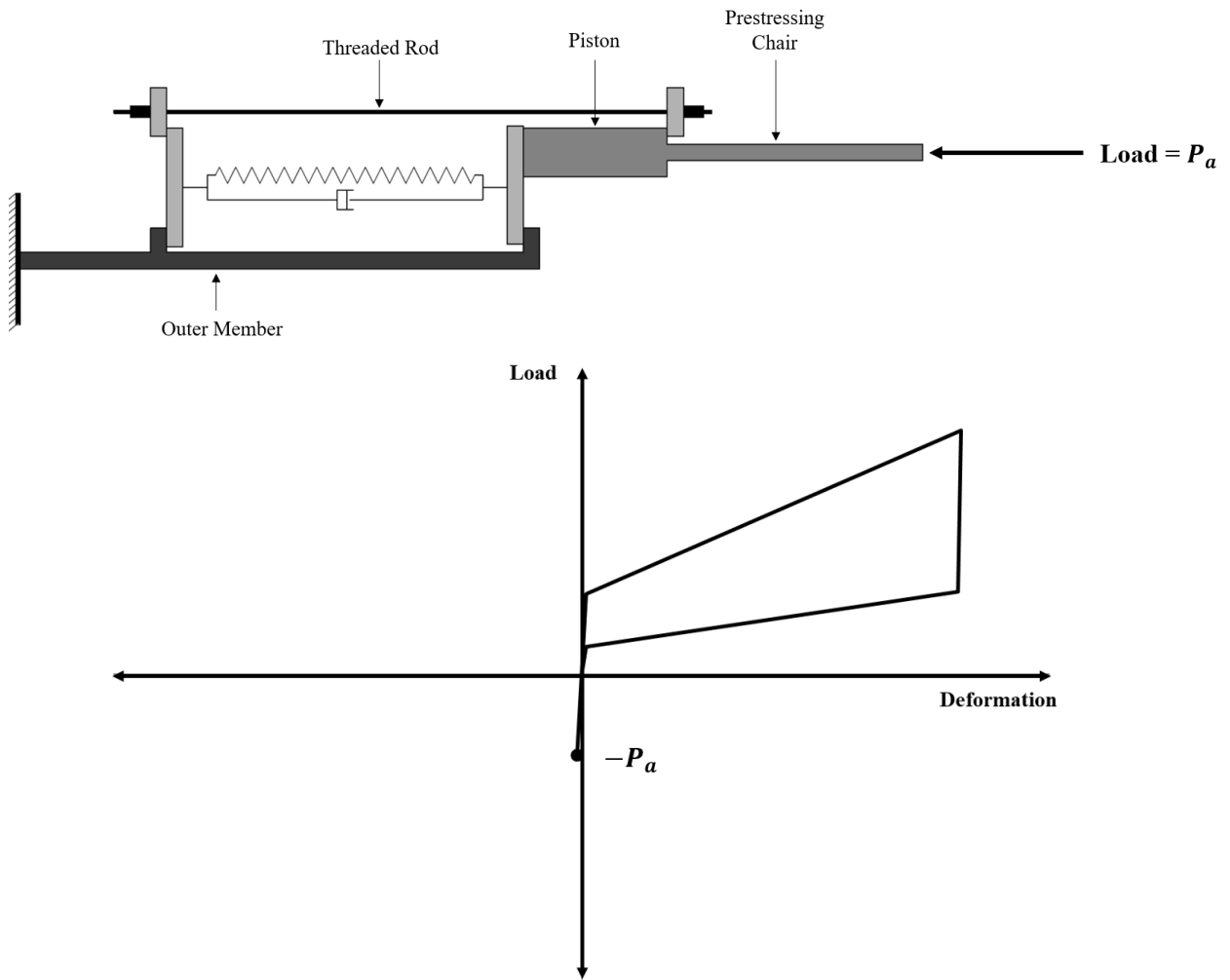


**Figure 4.9 Schematic of the brace while loading in compression pre-activation of springs**

Once the compressive load exceeds the activation load  $P_a$ , the point where the pre-compression in the springs is overcome, the stiffness of the brace at this stage is equal to the loading stiffness of the brace  $K_L$  as shown in Figure 4.10.

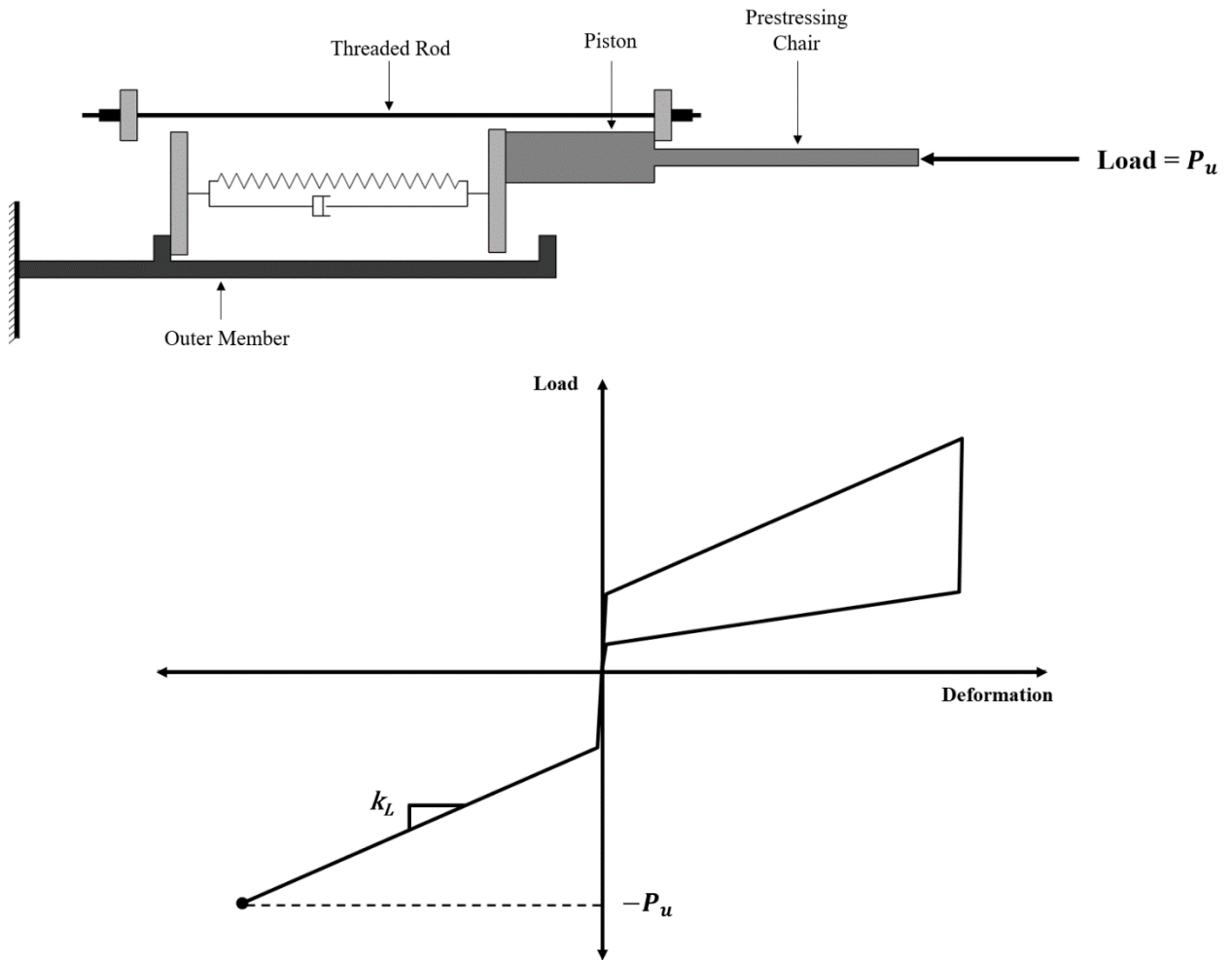
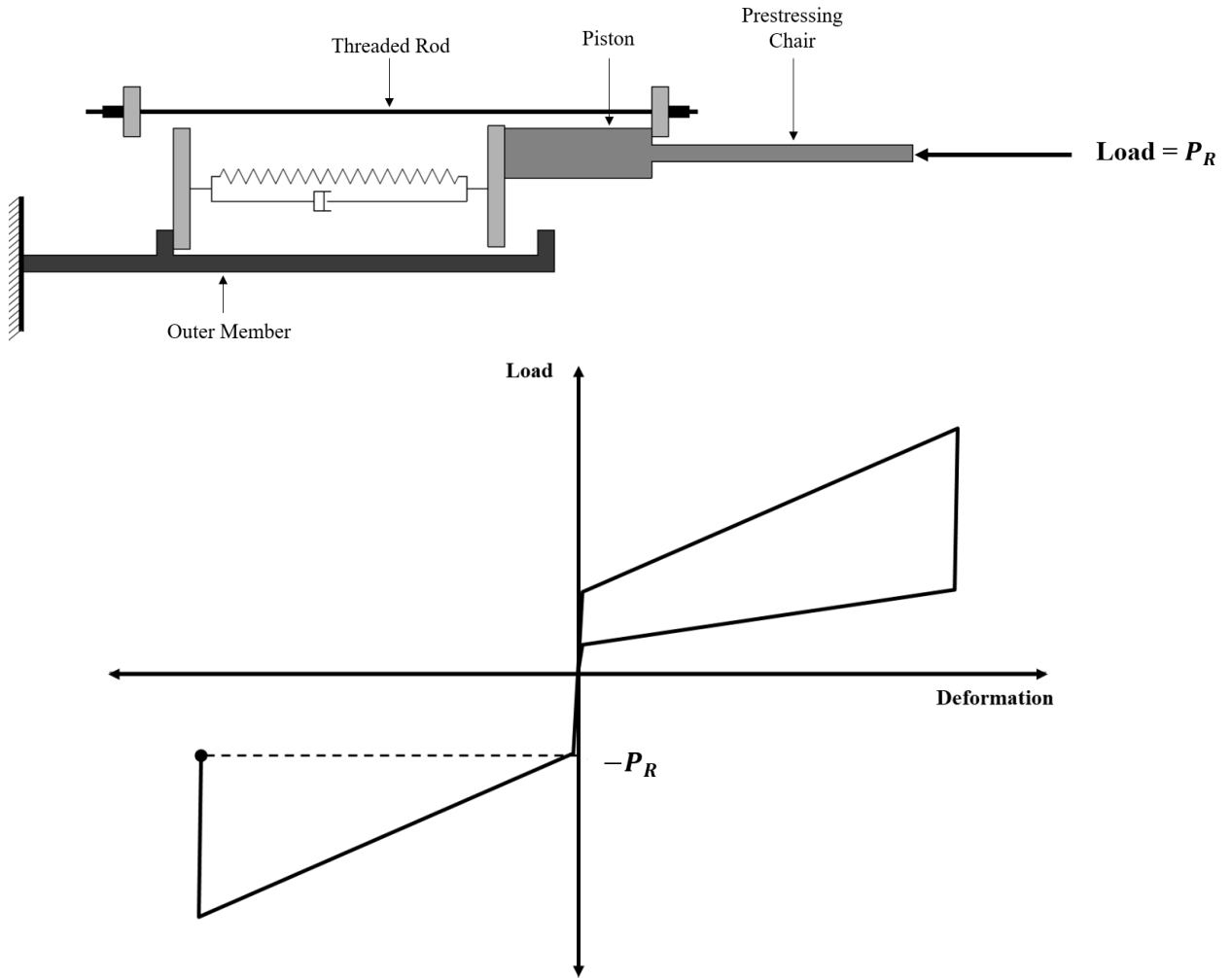


Figure 4.10 Schematic of the brace while loading in compression post-activation of springs

The unloading cycle in compression is similar to the unloading cycle of the tension cycle. The brace stiffness becomes the initial stiffness when unloading, until the load decreases past the recoil load  $F_R$  as shown in Figure 4.11.



**Figure 4.11 Schematic of the brace while unloading in compression pre-activation of springs**

Once the compressive load drops below the recoil load, the ring springs starts decompressing back to their initial length with the brace stiffness equal to the spring unloading stiffness  $K_u$  as shown in Figure 4.12.

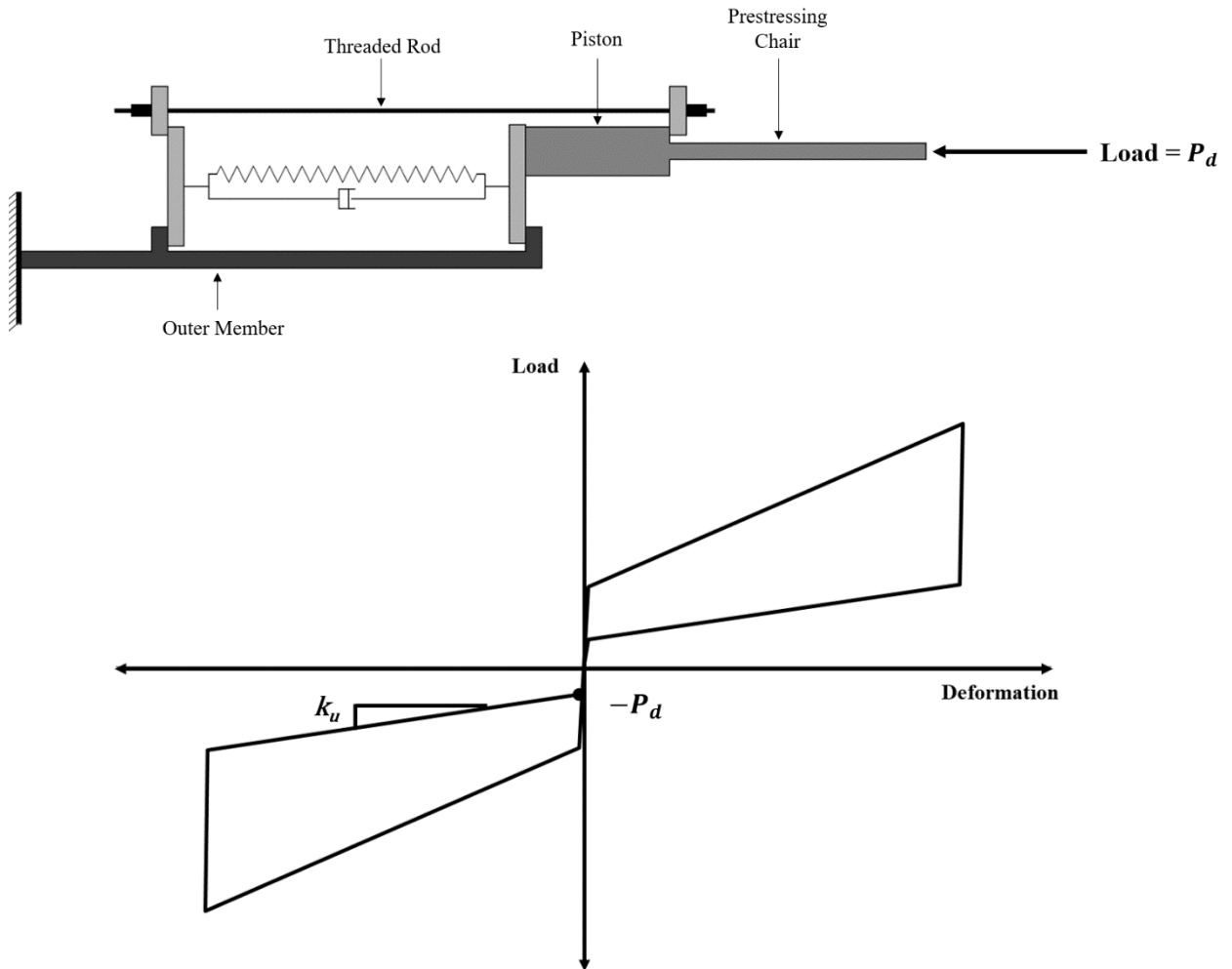
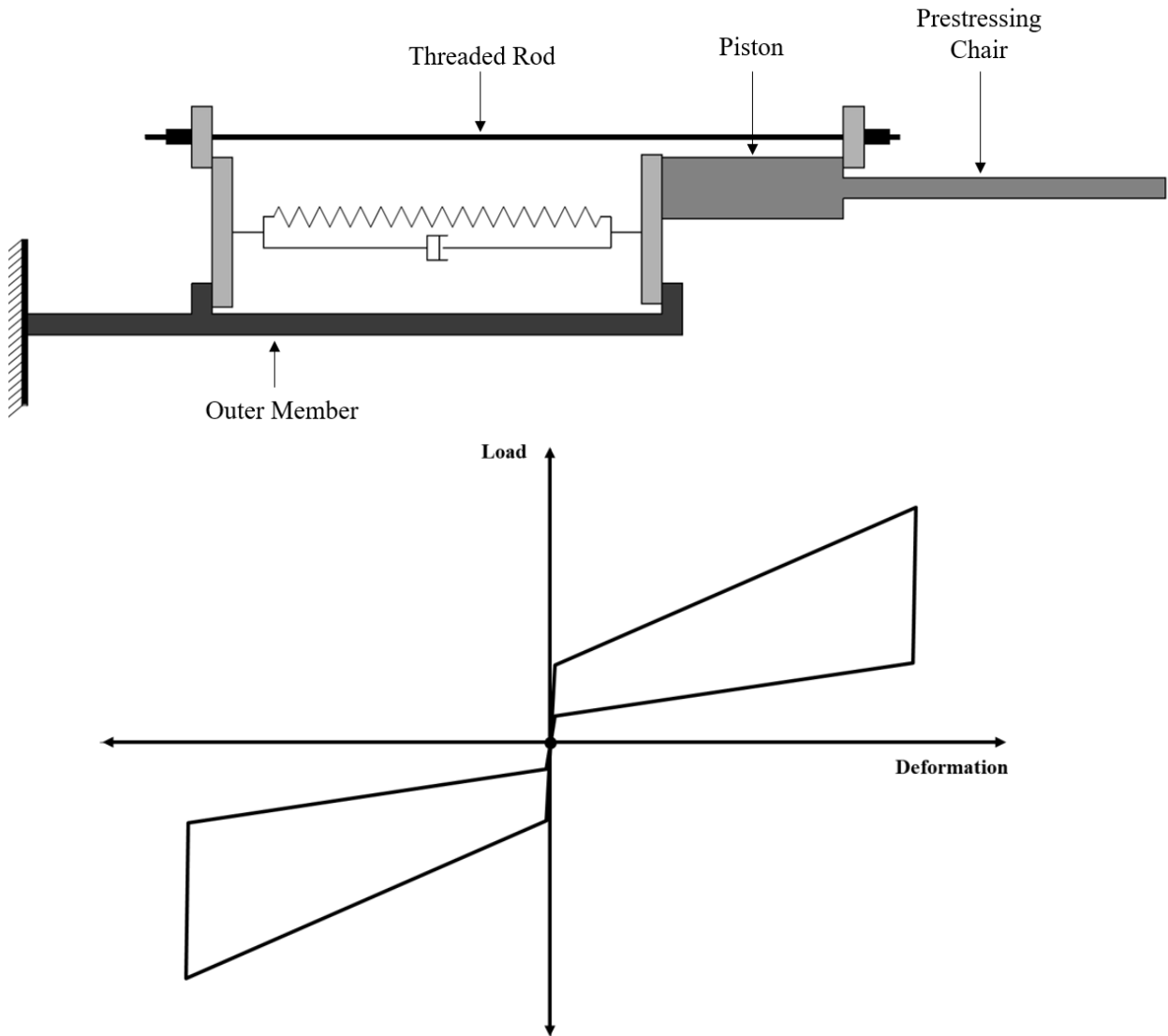


Figure 4.12 Schematic of the brace while unloading in compression post-activation of springs

The right end makes contact once again with the outer tube, the brace returns to the initial position with the initial brace stiffness  $K_i$  as shown in Figure 4.13.



**Figure 4.13 Schematic of the brace at the final step of the hysteresis (no load)**

As previously discussed, the initial brace stiffness in the hysteretic response  $K_i$  is caused by all the elements deforming together until the tension or compression force overcomes the initial pre-compression of the ring springs in the brace  $P_a$ , allowing the right or left end plate to separate from the outer member. After the initial compression force in the springs  $P_a$  is exceeded, the SCED brace is ‘activated’ and the stiffness of the brace is approximately equal to the stiffness of the ring spring loading stiffness  $K_L$ .

To calculate the initial stiffness of the hysteresis, the brace is divided into three segments which act in series. In the first segment, all the load is carried by the prestressing chair as shown in Figure 4.14 and thus the stiffness for this segment  $k_1$  can be calculated as follows:

$$k_1 = \frac{E_s A_c}{L_c} \quad \text{Equation 4-5}$$

where  $A_c$  and  $L_c$  are the cross-sectional area and the length of the chair, respectively, and  $E_s$  is the Young's modulus of steel. In the second segment, the load is being resisted by a segment of the threaded rod as well as the piston. The stiffness of this second segment is equal to the parallel sum of the two stiffnesses as follows:

$$k_2 = \frac{E_s A_r}{L_p} + \frac{E_s A_p}{L_p} = \frac{E_s}{L_p} (A_p + A_r) \quad \text{Equation 4-6}$$

where  $A_p$  and  $A_r$  are the cross-sectional areas of the piston and threaded rod respectively, and  $L_p$  is the length of the piston. In the third segment, the load is resisted in parallel by the threaded steel rod, the ring springs and the outer member. The stiffness of this third segment is usually much larger than the other two segments due to the very high stiffness of the ring springs and outer member when in a static position. The stiffness of this segment can be calculated as follows:

$$k_3 = \frac{E_s A_r}{L_o} + \frac{E_s A_{rs}}{L_o} + \frac{E_s A_o}{L_o} = \frac{E_s}{L_o} (A_r + A_{rs} + A_o) \quad \text{Equation 4-7}$$

where  $A_{rs}$  and  $A_o$  are the cross-sectional areas of the ring spring and outer members respectively, and  $L_o$  is the length of the outer member. When a tensile load is applied pulling the prestressing chair to the right, the initial stiffness of the brace is  $k_i$ , which is composed of the series sum of the stiffness of the three sections of the brace in series. The total initial stiffness of the brace  $K_i$  can be calculated as follows:

$$K_i = \frac{1}{\left(\frac{1}{k_1} + \frac{1}{k_2} + \frac{1}{k_3}\right)} \approx \frac{1}{\left(\frac{1}{k_1} + \frac{1}{k_2}\right)} \quad \text{Equation 4-8}$$

Since the stiffness of the third segment  $k_3$  is usually much larger than the other two segments, this term can typically be omitted in the calculation of the initial brace stiffness.

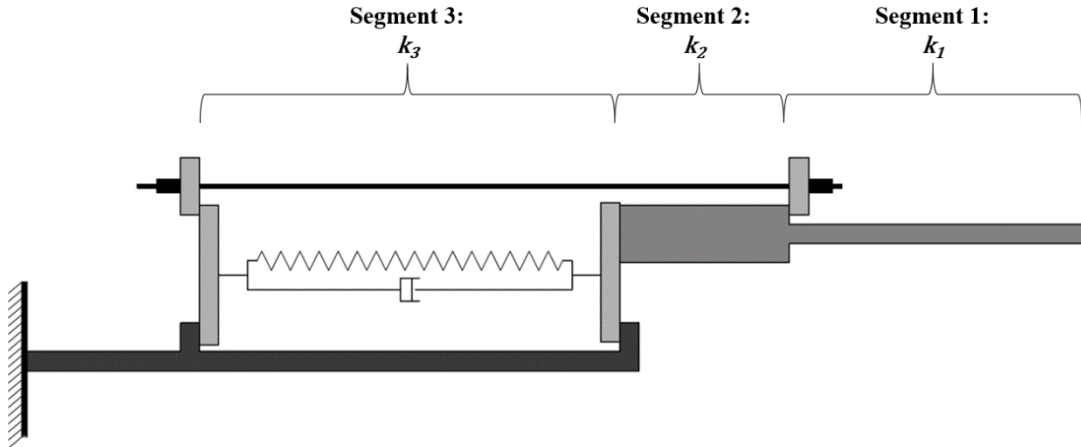


Figure 4.14 Dividing the brace into three segments to calculate the initial stiffness of the brace

To calculate the loading stiffness of the hysteresis during compression cycles, the stiffness of the third segment is slightly different since the rod and the outer tube do not carry any load. The stiffness of the third segment post-activation in compression  $k_{3LC}$  is equal to the loading stiffness of the ring spring assembly  $K_L$ . The total post-activation loading stiffness during compression  $K_{LC}$  can then be calculated as follows:

$$K_{LC} = \frac{1}{\left(\frac{1}{k_1} + \frac{1}{k_2} + \frac{1}{k_{3LC}}\right)} = \frac{1}{\left(\frac{1}{k_1} + \frac{1}{k_2} + \frac{1}{K_L}\right)} \approx K_L \quad \text{Equation 4-9}$$

Since the stiffness of the third segment  $K_L$  is much smaller than the other two segments, the total post-activation loading stiffness  $K_{LC}$  is dominated by the loading stiffness of the ring springs  $K_L$ .

The calculation of the loading stiffness of the hysteresis during tension cycles is slightly different since the load is transferred from the pre-stressing chair to the rod before it is transferred to the ring springs and then the outer tube. The brace can be divided into 4 segments as shown in

Figure 4.15 to calculate the total stiffness of the brace. The stiffnesses of the 4 segments can be calculated as follows:

$$k_{1LT} = k_1 = \frac{E_s A_c}{L_c} \quad \text{Equation 4-10}$$

$$k_{2LT} = \frac{E_s A_r}{L_p + L_o} \quad \text{Equation 4-11}$$

$$k_{3LT} = K_L \quad \text{Equation 4-12}$$

$$k_{4LT} = \frac{E_s A_o}{L_o} \quad \text{Equation 4-13}$$

The total post-activation loading stiffness during tension cycles  $K_{LT}$  can then be calculated as follows:

$$K_{LT} = \frac{1}{\left(\frac{1}{k_{1LT}} + \frac{1}{k_{2LT}} + \frac{1}{k_{3LT}} + \frac{1}{k_{4LT}}\right)} = \frac{1}{\left(\frac{1}{k_{1LT}} + \frac{1}{k_{2LT}} + \frac{1}{k_L} + \frac{1}{k_{4LT}}\right)} \approx K_L \quad \text{Equation 4-14}$$

Since the stiffness of the third segment  $K_L$  is much smaller than the other three segments, the total post-activation loading stiffness  $K_{LT}$  is once again dominated by the loading stiffness of the ring springs  $K_L$ . Therefore, the post-activation stiffness of the RS-SCED brace hysteresis would be equal to the loading stiffness of the ring springs in both compression and tensile cycles despite the difference in the load path between compressive and tensile loading.

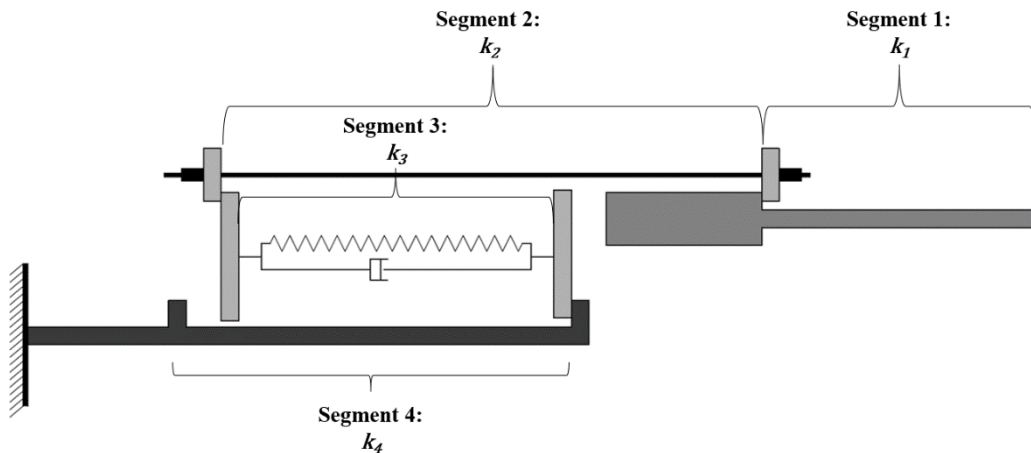


Figure 4.15 Dividing the brace into four segments to calculate the tensile post-activation stiffness of the brace

### 4.3 SCED Brace Components

This section discusses the main components of the RS-SCED brace. Figure 4.16 shows a cross section of the prototype RS-SCED brace designed and built for this study. The main components of the RS-SCED brace are the Outer member, threaded rod, the ring spring assembly, prestressing chair and piston tube, which are the same components described in the previous section.

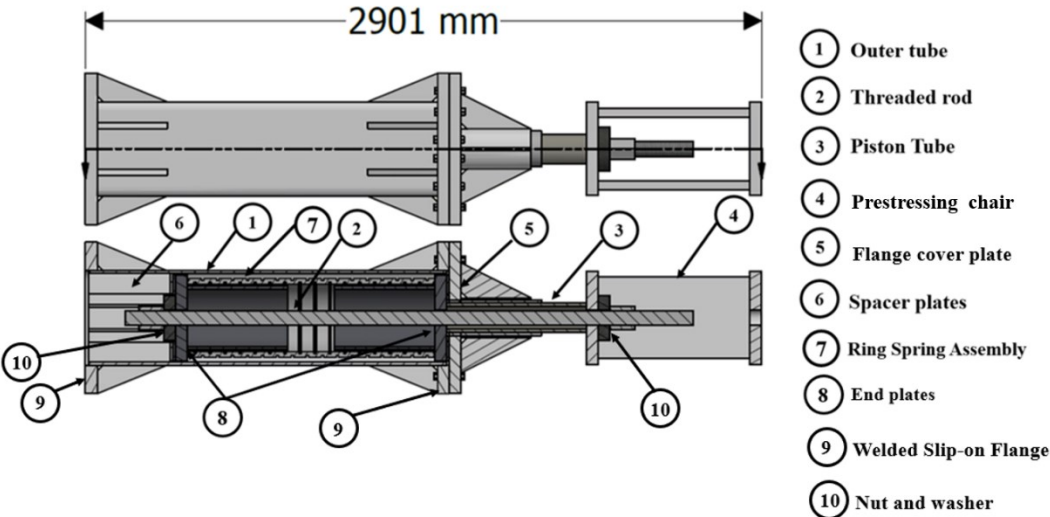


Figure 4.16 RS-SCED Brace cross-section showing the brace components

In the neutral state shown in Figure 4.17 (a), the two end plates are in contact with the outer tube via the spacer plates and the flange cover plate. The initial pre-compression of the spring assembly is applied through tensioning the steel threaded rod, anchored by means of nuts and washers to the left end plate at the left end and to the prestressing chair at the right end.

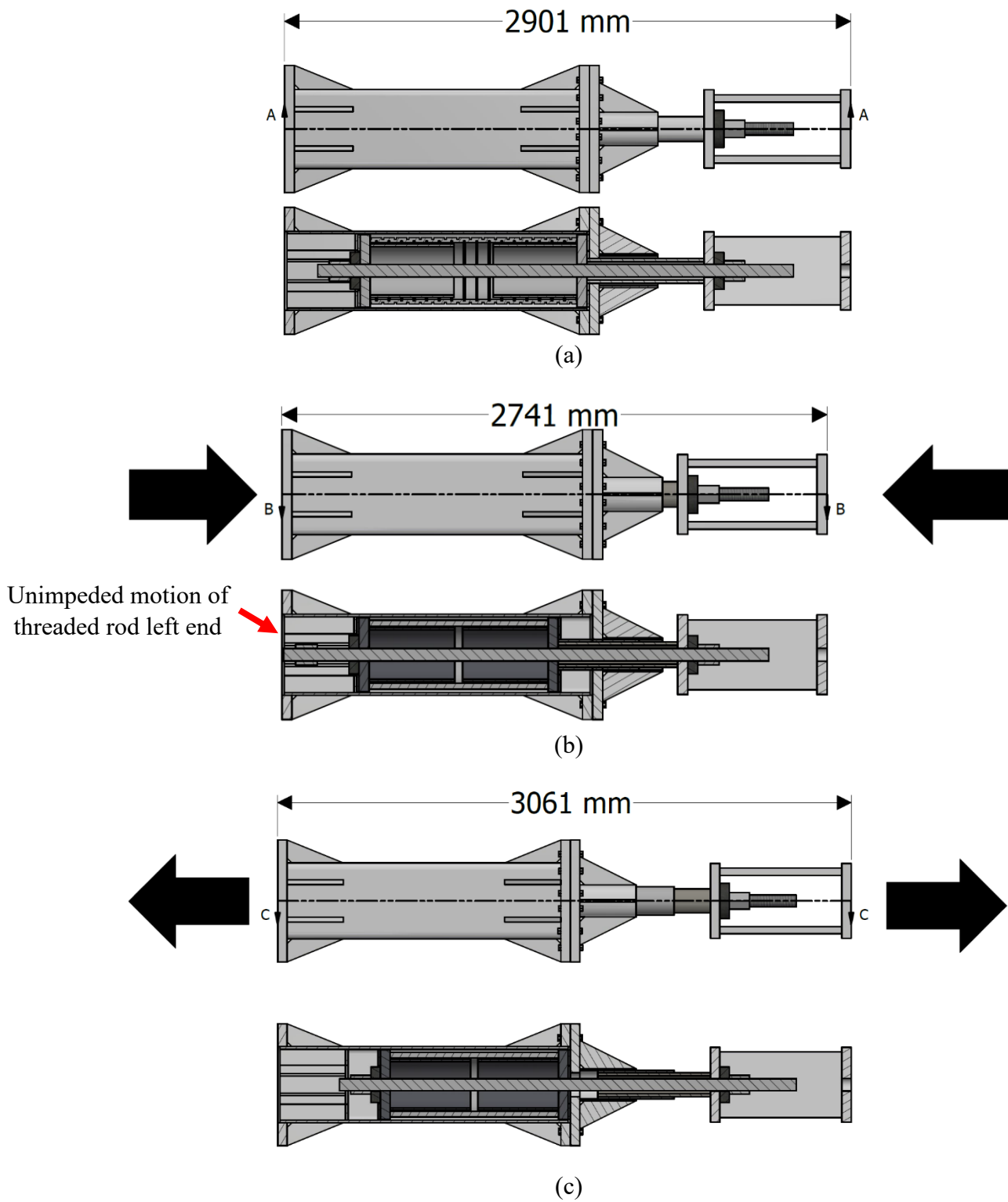


Figure 4.17 RS-SCED brace (a) neutral position, (b) fully compressed and (c) fully extended

In the compressed state, the prestressing chair moves to the left, pushing the right end plate to the left via the piston tube. The left end of the ring spring assembly is restrained from moving to the left by means of the spacer plates and are compressed as shown in Figure 4.17 (b). At this state, the prestressing threaded rod has no load and is free to slide. The spacer plates bearing against the left end plate need to be long enough to ensure there is enough distance between the left end plate and the end of the outer tube for the left end of the threaded rod and nut to move unimpeded.

Figure 4.17 (c) shows the brace loaded in tension. In this state the prestressing chair moves to the right. The threaded bar, which is anchored to the prestressing chair through a nut and a washer plate, is then moved to the right pulling the left end plate to the right as well. Since the ring spring assembly is restrained from moving to the right by means of the cover plate, the ring spring assembly gets compressed. The right end plate bears against the flange cover plate which then transfers the load to the slip-on flange, and eventually to the outer member and the rest of the structure. The following subsections discuss each individual component.

### 4.3.1 Ring Spring Assembly

The ring spring assembly is a column of outer and inner ring spring elements which are precompressed to a certain load determined in the design process. This pre-compression load is equivalent to the activation load of the brace  $P_a$ . The assembly used for this RS-SCED brace is shown in Figure 4.18. When a load applied to the springs is less than their pre-compression, the springs stay locked and do not compress. But when the springs sustain a load higher than their pre-compression, the assembly compresses further with a stiffness equal to the loading stiffness of the springs  $K_L$  discussed previously. It is recommended by the manufacturer to have half rings at each

end of the ring spring assembly to ensure a larger contact area between the springs and other components in the brace.

In the prototype brace designed for this project, the ring spring assembly is sandwiched between two 50.8mm (2") steel end plates which bear against the two half-ring elements at both ends of the ring spring assembly as shown in Figure 4.18. The end plates have a hole a bit bigger in size to the diameter of a steel threaded rod used as a prestressing tendon (discussed below). To ensure the ring spring assembly is aligned properly, each end plate has a 273 mm x 9.5 mm (10.75" x 3/8") hollow structural steel section welded to its inner surface to act as an inner guide for the ring assembly as shown in Figure 4.19. To minimize the friction from any incidental contact between the rings and the guide, the round HSS is jacketed with an ultra-high-molecular-weight (UHMW) polyethylene plastic sheet screwed to its outer surface. An image of the ring spring assembly used for the prototype brace is shown in Figure 4.20.

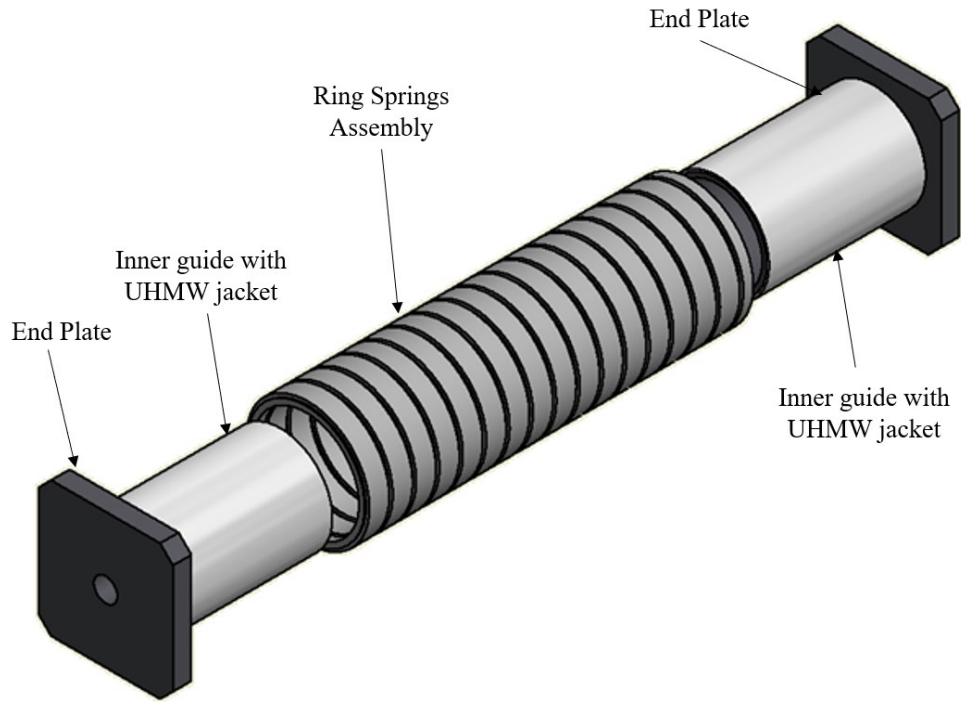


**Figure 4.18 End plates inserted on both ends of the Ring Spring assembly**



**Figure 4.19 Fitting the End plate guide through the Ring Spring assembly**



Figure 4.20 Assembly of Type 34000 Ring Springs used for the RS-SCED Brace

### 4.3.2 Prestressing Steel Threaded Rod

To facilitate the pre-compression of the ring springs and transfer the load between the brace components when the brace is in tension, a high-strength 2-1/4" (57 mm) threaded prestressing steel rod is used. Steel threaded rods are easy to prestress with a more predictable behaviour compared to other materials. To prestress the rod, a prestressing jack, another shorter threaded rod with the same diameter, and a coupler are used. The prestressing process is discussed below. Once the threaded rod is tensioned to the desired load, the nuts are screwed on tightly to maintain the tension in the rod and the compression in the ring springs. To ensure that the load transferred through the rod is distributed over a large bearing area at both anchored ends, two round washer

plates with a diameter of 7-1/2" (190 mm), are used to distribute the load from the nut to other members as shown in Figure 4.21. The threaded rod should be capable of resisting the full tensile load capacity of the RS-SCED brace  $P_u$  without yielding.

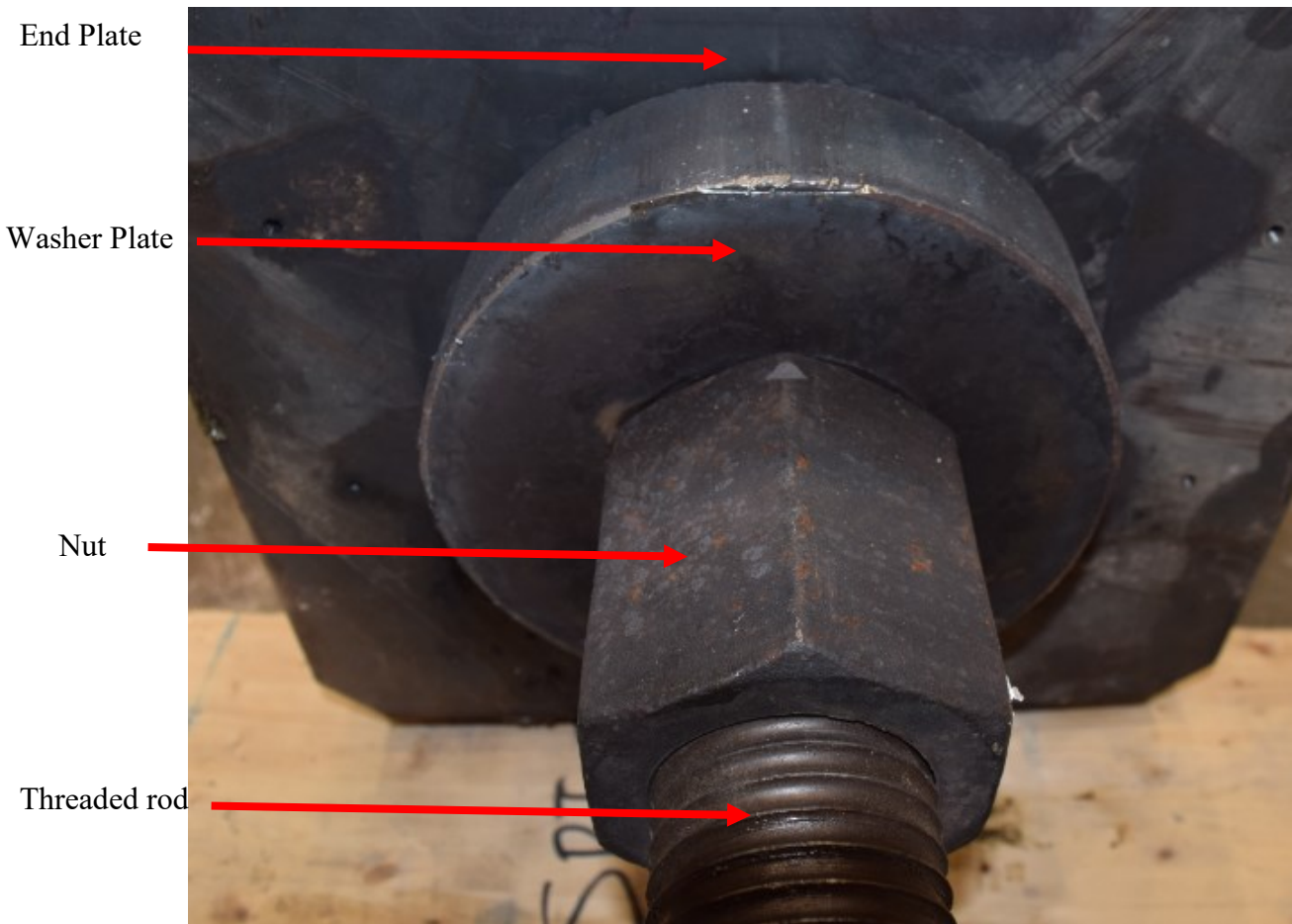


Figure 4.21 Threaded rod, nut and washer plate

### 4.3.3 Outer Tube, Slip-On Flange and Cover Plate

The Outer tube serves two purposes, it acts as a cartridge that protects and contains the ring spring assembly, and to transfer the loads from the ring spring assembly to the chevron brace. In the prototype design of the Ring Spring SCED brace, the outer tube is a Hollow square section of size 406 mm X 406 mm (16" x 16") with a wall thickness of 9.5 mm (3/8"). This is a commonly available size that can fit the chosen ring spring assembly.

The tube has slip-on welded flanges on both ends as shown in Figure 4.22, with one end bolted to the rest of the structure and the other end bolted to a cover plate. It is also important to ensure that the flange does not significantly bend due to the load in the bolts, hence, 1/2" stiffeners are welded between the outer tube wall and the slip-on flange.

At the right end of the tube, in Figure 4.22, the slip-on flange is bolted to a cover plate. The cover plate has a center hole that allows a piston tube (discussed below) to pass through and compress the springs when the brace is loaded in compression, while restraining the springs from exiting the tube when the brace is loaded in tension. The cover plate also has a welded guide tube that ensure the piston is aligned with the center of the brace while the brace is in motion. The load from the cover plate is transferred to the flange, and ultimately to the outer tube, by means of 16-1" bolts.

At the left end of the tube, in Figure 4.22, the slip-on flange is bolted to the rest of the structure at the left end of the brace, by means of 16 – 1" bolts. The inside of the tube at this end has welded spacer plates which ensure that the threaded rod has enough space to move freely when the brace is in compression. The spacer plates need to be designed to resist the compressive load without buckling. Also fillet welds for the spacer plate need to be designed to transfer the load in shear to the inside of the outer tube wall.

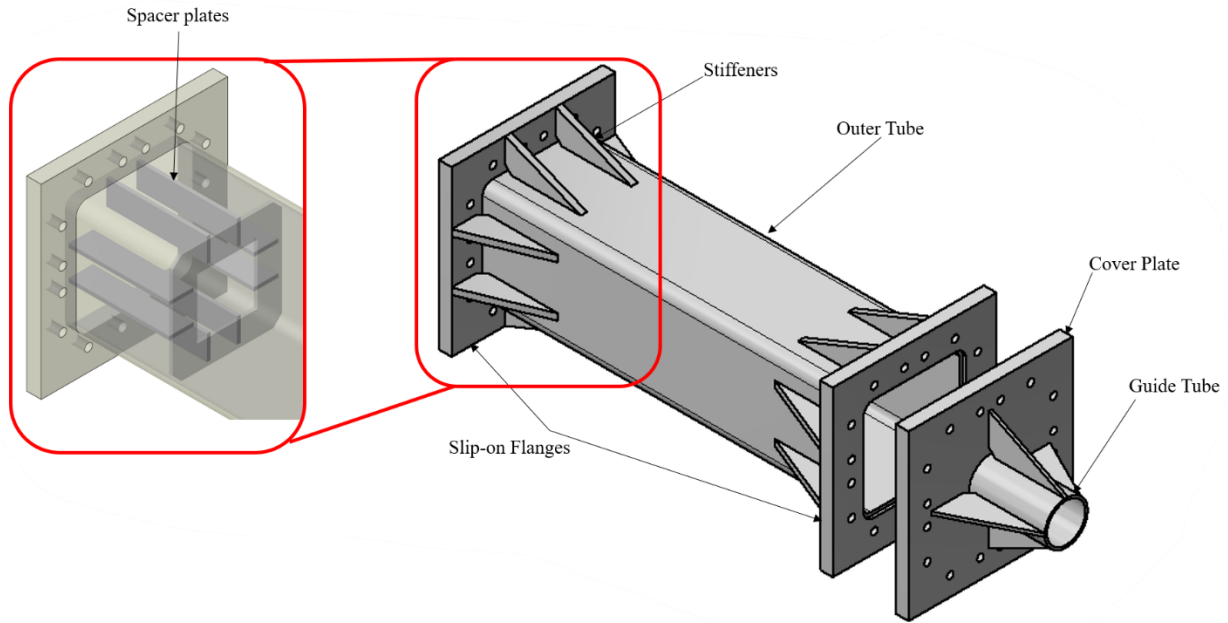


Figure 4.22 Schematic diagram of Outer tube and cover plate

#### 4.3.4 Prestressing Chair and Piston

In the prototype design for this project, a 127 mm (5") outer diameter drawn over mandrill (DOM) pipe with a wall thickness of 15.875 mm (5/8") is used as the piston that compresses the springs when the brace is in compression. A cylindrical sleeve made of UHMW plastic is screwed to the outside surface of the DOM tube once again to minimize friction between the tube and other brace components, namely the guide tube shown in Figure 4.22. Figure 4.23 below shows the piston DOM pipe and the UHMW jacket. The diameter of the piston tube has to be large enough to ensure that the bearing area is as far from the center of the end plate as possible such that it does not cause significant bending in the end plate.

The DOM pipe is welded to a 50.8 mm (2") steel plate, which is referred to as the chair base plate as shown in Figure 4.23. The chair base plate has a hole with the same diameter as the prestressing steel rod and is welded to two 38.1 mm (1-1/2") steel plates referred to as prestressing chair legs. The purpose of the chair legs is to provide enough clearance for a rod coupler to be

inserted during the prestressing process of the assembly. When the brace is under compression, the prestressing chair legs are under significant compressive load and thus it is important to ensure that the legs are designed to not buckle under this load.

The chair legs are welded to another 50.8 mm (2") steel plate which are referred to as the prestressing chair connection plate as shown in Figure 4.23. The chair connection plate has 8-1" (25.4 mm) bolt holes which are used to connect the brace to the rest of the structure at the right end of the brace, when the brace is in the same orientation as the one shown in Figure 4.16. The plate also has a larger hole at the center to allow for a steel rod with the same diameter as the prestressing rod to pass through and attach to the coupler during the prestressing process. Figure 4.24 shows an image of the prestressing chair and piston used in the prototype brace.

When the brace is under tension, the 8-1" bolts connected to the prestressing chair connection plate transfer the load to the rest of the brace. When the brace is in compression, the structure bears against the outside of the prestressing chair connection plate pushing it to the left. The load is transferred from the prestressing chair connection plate to the base plate through the prestressing chair legs. The chair legs are connected to the prestressing chair connection plate and base plate by means of all-around fillet welds at both ends.

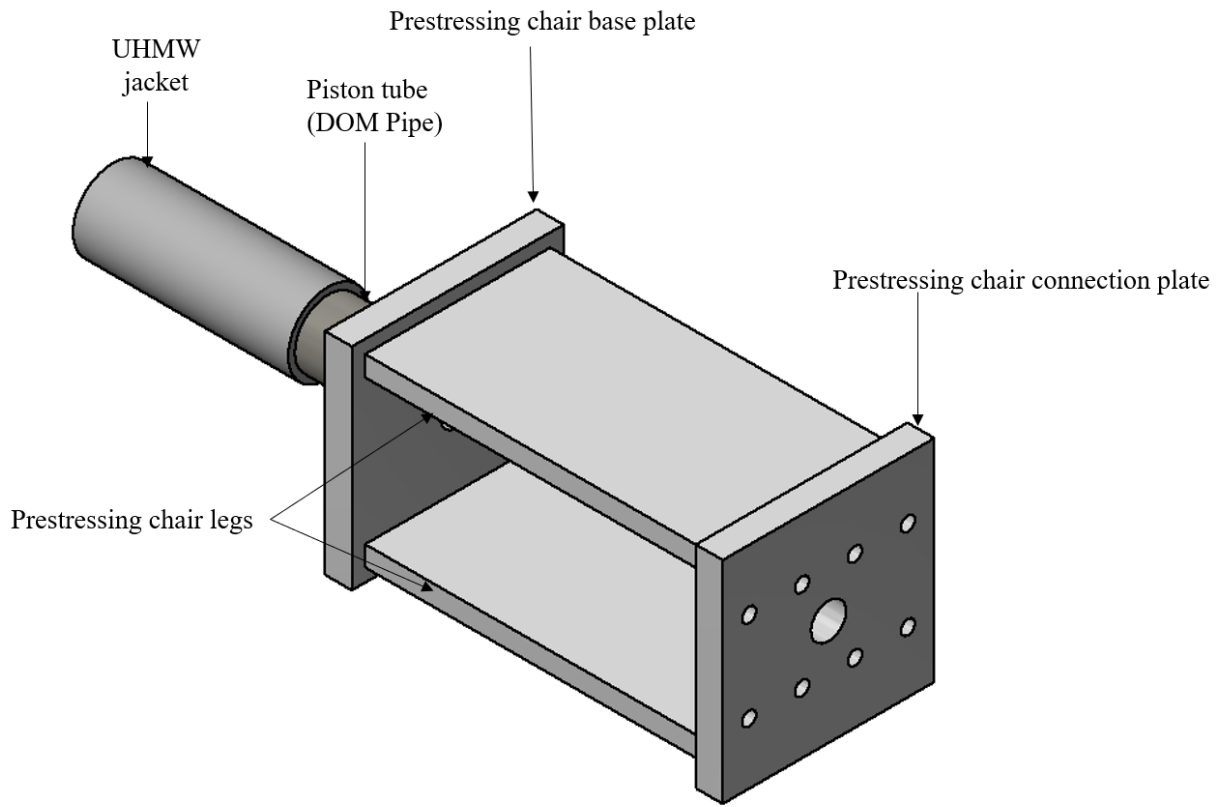


Figure 4.23 Schematic diagram of the prestressing chair and piston



Figure 4.24 Prestressing chair and piston used for the RS-SCED brace

## 4.4 Assembling the Brace

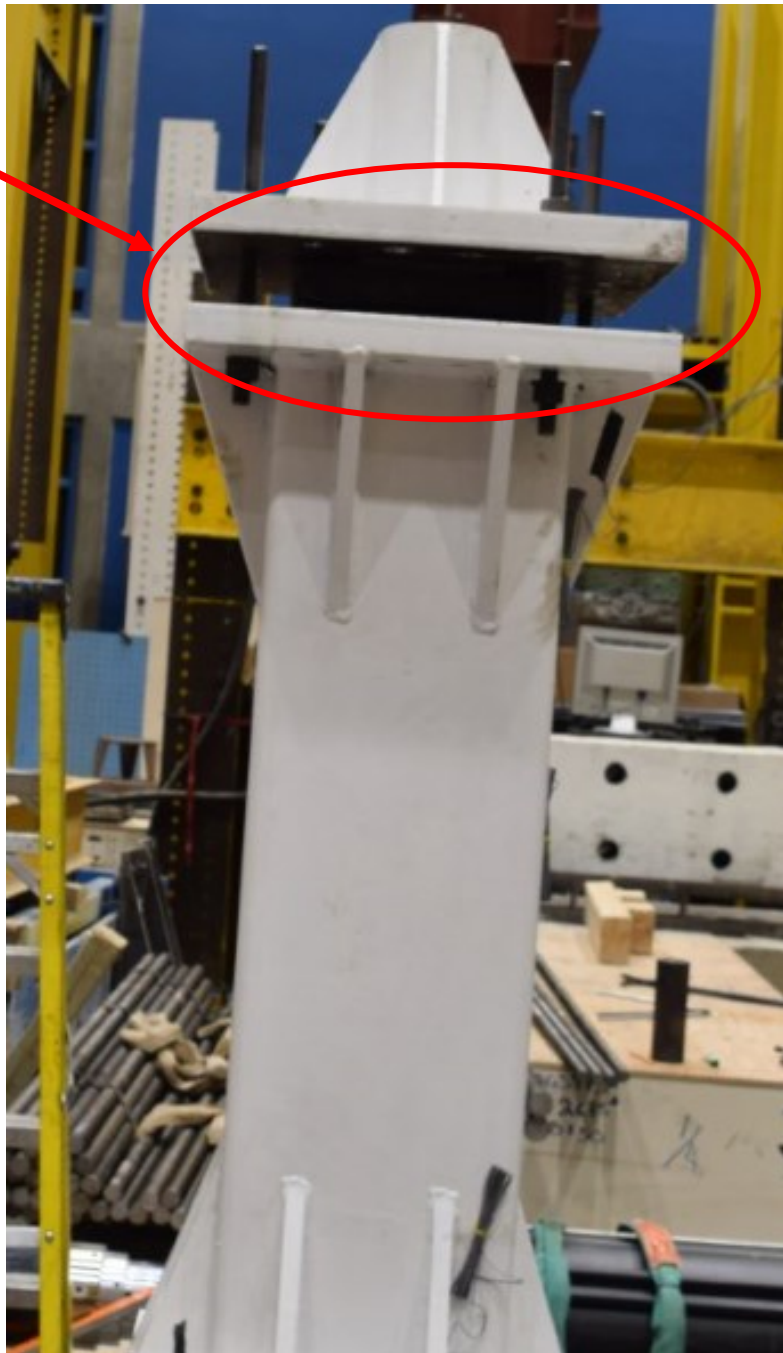
The first step in assembling the RS-SCED is to place the ring assembly into the outer tube. This step is completed more easily if the outer tube is placed vertically, as it allows the ring springs to be lowered in position by means of a crane. Therefore, the outer tube is rotated counter clockwise from the orientation shown earlier Figure 4.16 so that the left end of the tube (the end connected to the structure) is at the bottom, and the right end of the tube (the end connected to the cover plate) is at the top. This orientation is maintained throughout the assembly process. The ring spring assembly is lowered into position using a crane as shown in Figure 4.25. When in the final position, the ring spring assembly should be resting on the spacer plates.



Figure 4.25 Inserting Ring spring assembly inside the outer tube

The flange cover plate can then be placed on top of the ring spring assembly as shown in Figure 4.26. The surface of the end plate is initially protruding past the surface of the outer tube flange causing a gap between the cover and the flange. This gap is closed once the springs are compressed to the design pre-compression level.

Gap is closed after  
precompressing the  
springs



**Figure 4.26** Cover plate placed on top of the ring spring assembly

The next step is to thread the steel rod through the prestressing chair base plate hole and to add the washer plate and the nut so that one end of the rod is anchored to the prestressing chair base plate. The prestressing chair and the rod are then lowered into position. In this position, the piston tube free end bears against the surface of the top end plate with the rod threading through the hole in the lower end plate as shown in Figure 4.27.

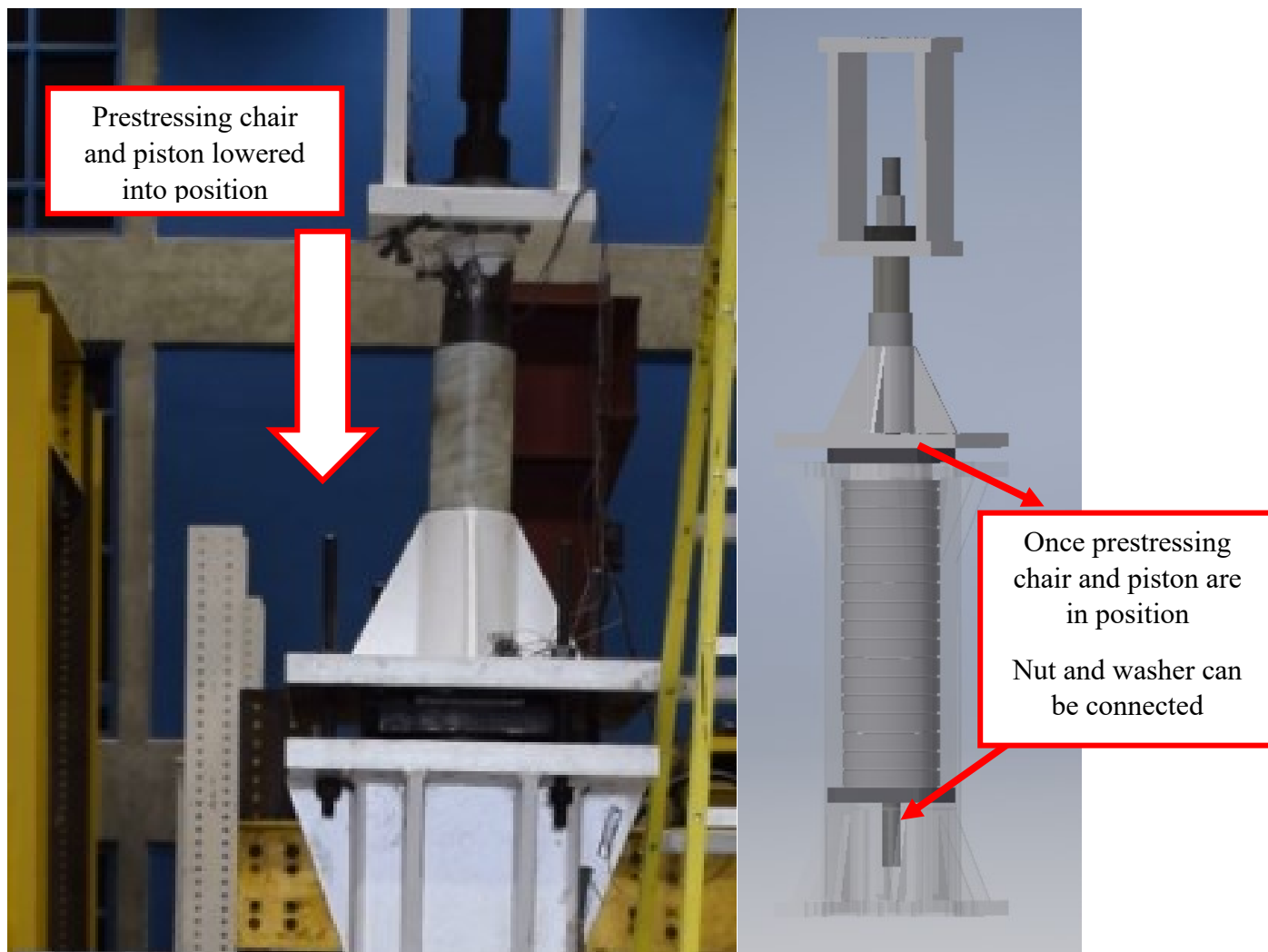


**Figure 4.27 Threaded rod passing through the drilled hole in the bottom end plate**

Once that step is done, a nut and washer plate should be added to the free rod end as shown in Figure 4.27. To prestress the rod (and precompress the springs) a coupler is threaded on the rod at the prestressing chair end as shown in Figure 4.28.

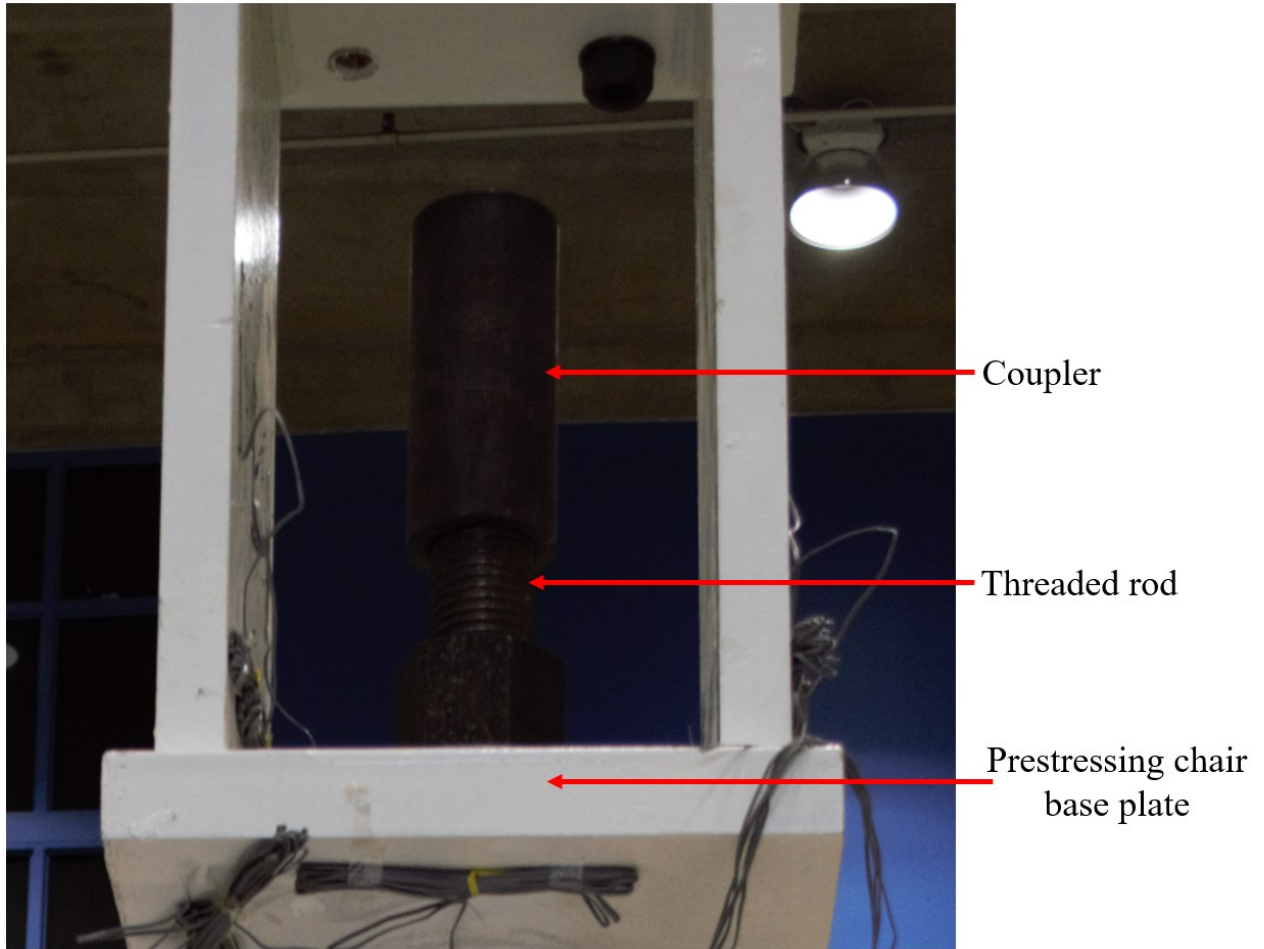


**Figure 4.28 Adding a coupler on the threaded rod at the prestressing chair end**

An additional rod with the same diameter is connected to the other side of the coupler. A prestressing jack is then placed on top of the prestressing chair connection plate. The rod should be long enough to pass through the hole in the prestressing chair connection plate, pass through the inner hole of the prestressing jack, and protrude out from the top of the prestressing jack with enough thread to be able to add another washer plate and nut as shown in Figure 4.29. The washer and nut bear against the top of the jack.

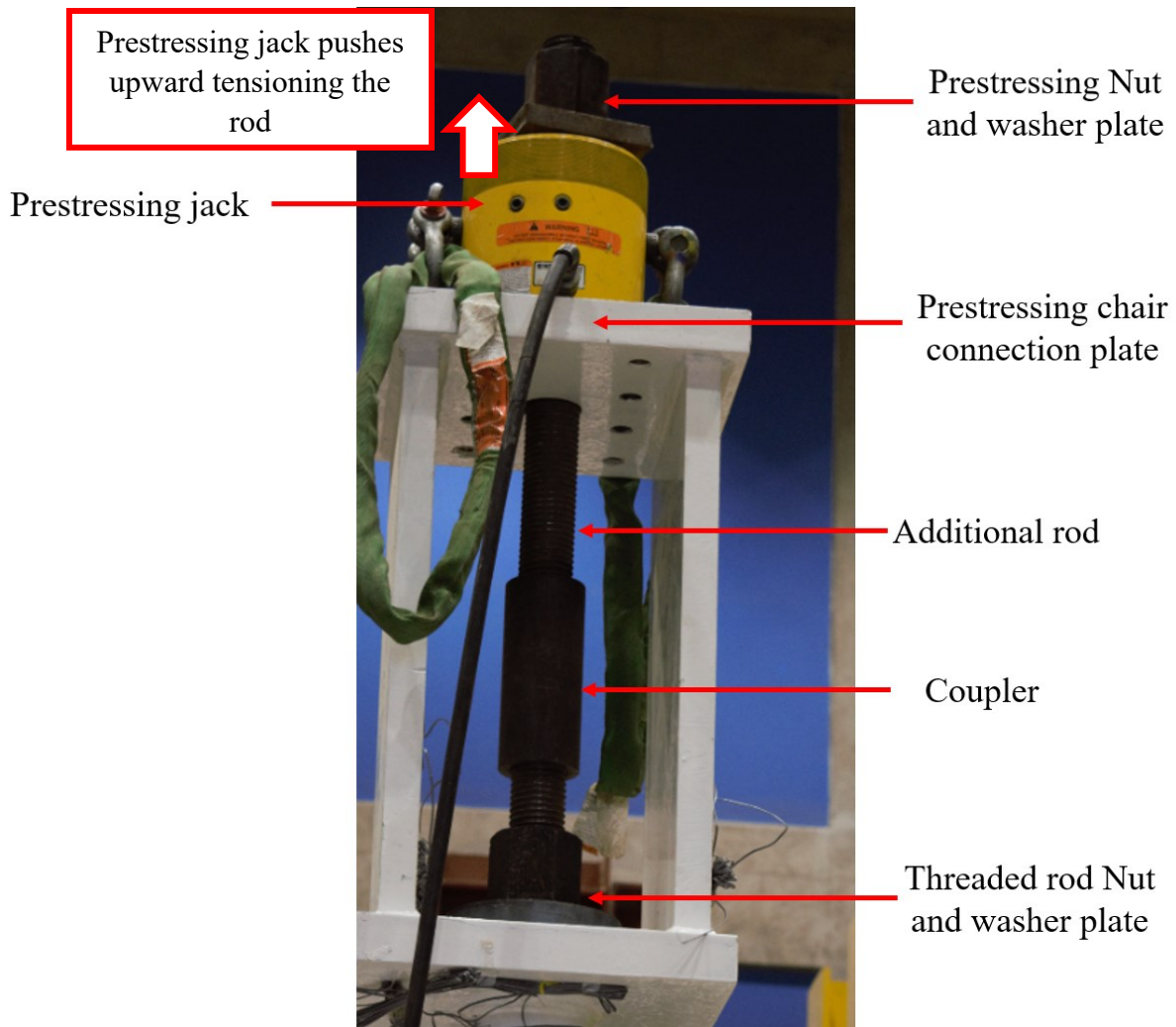


Figure 4.29 Prestressing setup used to prestress the steel rod

A hand pump is used to push the prestressing washer plate and nut upwards causing tension in the rod to increase. As the tension in the rod is increased, the piston compresses the springs until the gap closes (Figure 4.30), which indicates that the springs have reached their intended design activation load  $P_a$ . Finally, the threaded rod nut can be tightened to ensure that the pre-stressing of the rod/ pre-compression of the rings are maintained and then the bolts are used to connect the cover plate to the outer tube's flange. At this point the coupler, additional rod, prestressing jack and prestressing washer and nut can be removed.



**Figure 4.30 Gap closes as the ring spring assembly compresses to the activation force**

## **4.5 Secondary Fuse Mechanism**

When the brace reaches the maximum load capacity of the ring spring assembly, the ring spring becomes fully compressed and acts as a strong steel column which transfers the load in bearing. This then causes the stiffness of the brace to go back to the original initial stiffness which increases the load demand on all brace components risking the failure of the brace. This should be avoided in the design by ensuring sufficient deformation capacity of the brace by using sufficient number of spring elements in the assembly. However, in the unlikely situation where the deformation demand exceeds the design deformation, a secondary failure fuse mechanism should be provided to avoid exceeding the maximum compression load of the ring spring assembly. To facilitate this, the designer should choose a steel threaded rod that would initiate yielding at a load just below the maximum capacity of the ring spring assembly. This causes the steel rod to yield before the springs fully compress when the brace is in tension. Based on the configuration presented in Section 4.1,

in this study the braces are anticipated to be used in pairs, where one brace is loaded in tension while the other is loaded in compression, this design philosophy ensures that the brace pair does not reach the load capacity of the rings  $F$ , even under excessively high loads.

## 4.6 Experimental Test Setup

Figure 4.31 shows the experimental test setup in the Civil Engineering Structures laboratory at Carleton University. The RS-SCED brace is connected to a stiff reinforced concrete block by means of a steel link designed to simulate the connection of the RS-SCED brace to a stiff chevron brace in the proposed braced frame design. The reinforced concrete block is prestressed to the strong floor with a force large enough to ensure that the friction between the floor and the block prevents slip at the maximum RS-SCED brace load. The steel link is secured to the concrete block using steel threaded rods. The 3 m long steel beam shown in Figure 4.32 is used to apply axial load to the RS-SCED brace. The beam is used to simulate the column in the proposed configuration of the braced frame. The steel beam is bolted to the connection plate of the brace's prestressing chair and connected to two hydraulic actuators at its ends. Two MTS system series 244.51 hydraulic actuators with +/-1000 kN (225 kip) capacity and a +/-500 mm (+/- 20 in.) stroke are used to control the axial degree of freedom. These two hydraulic actuators are secured to the lab floor by means of two additional reinforced concrete blocks prestressed to the floor.

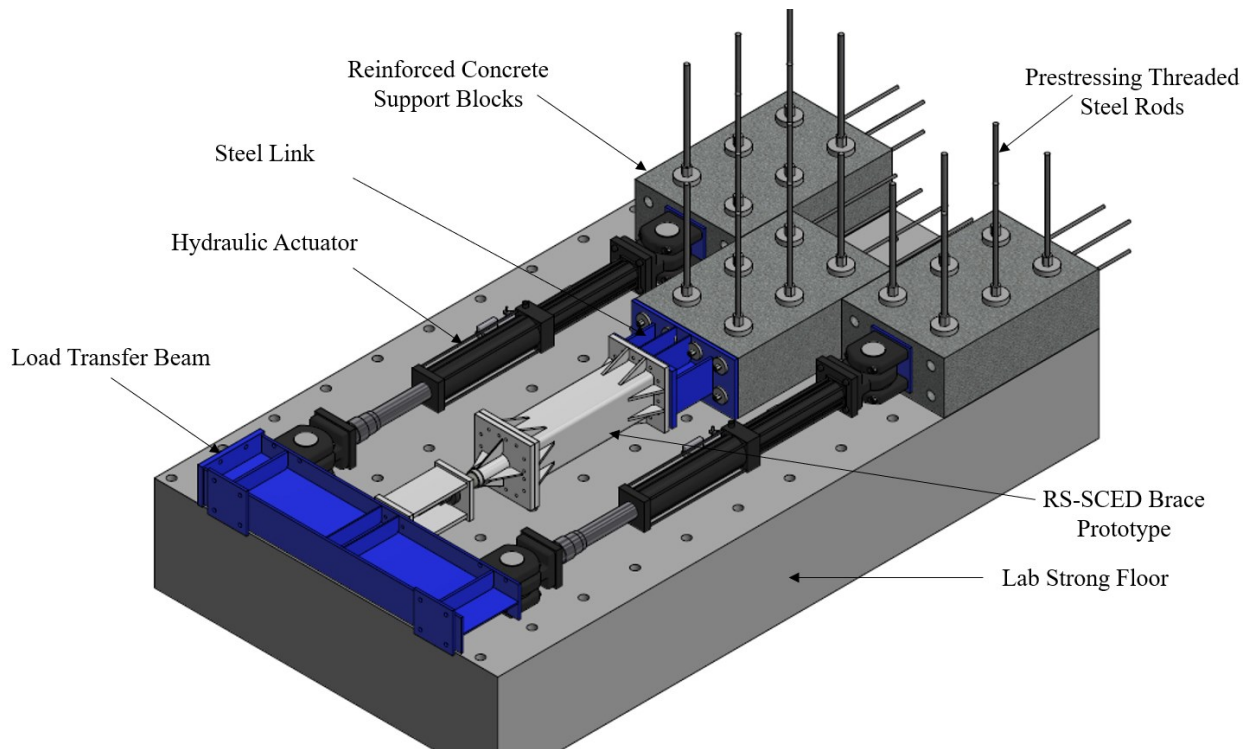


Figure 4.31 Schematic diagram of test setup used for testing RS-SCED brace

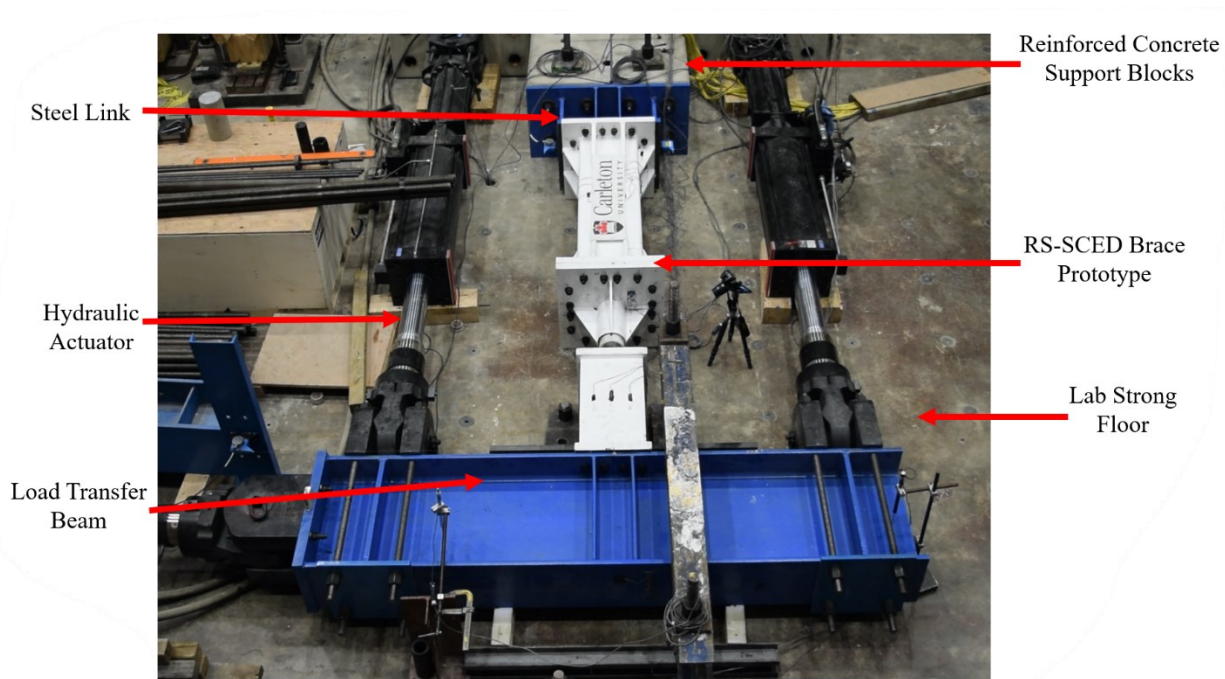
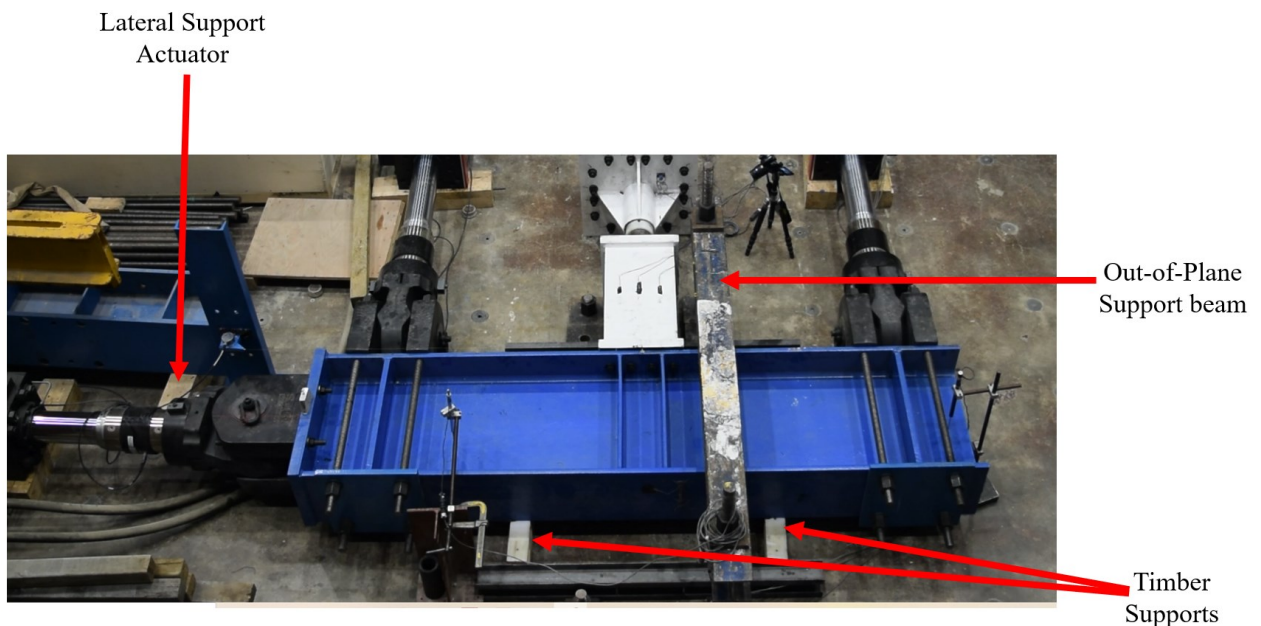


Figure 4.32 Test setup used for this study at Carleton University structures lab

Figure 4.33 and Figure 4.34 shows the lateral and out-of-plane support system used in the experimental setup to ensure that the brace is loaded only axially. The system is laterally supported

using an MTS series linear 24.60 T hydraulic actuator with +1000 kN/-600kN (+225/-146 kip) capacity and +/-150 mm (6 in.) stroke. This actuator is not used to control any of the brace degrees of freedom, rather it is used to ensure that the load transfer beam does not move laterally during the test. Accordingly, the actuator is placed parallel to the centerline of the load transfer beam and secured to the strong floor by large steel columns secured to the laboratory strong floor. The out-of-plane support system is comprised of two timber supports and an out-of-plane restraint beam. The load transfer beam slides on top of two timber supports that are topped with greased UHMW plastic sheets used to minimize the friction between the top of timber supports and the load transfer beam. In addition to the timber supports, an out-of-plane restraint beam is designed to restrain any potential out-of-plane displacement of the load transfer beam.



**Figure 4.33 Aerial image showing the out-of-plane and lateral support system**

Lateral Support Actuator

Out-of-plane Restraint Beam

Load Transfer Beam



Figure 4.34 Side view of the Out-of-plane and lateral support in experimental setup

# 4.7 Instrumentation

Figure 4.35 shows a summary of the instrumentation used to monitor the response of the brace, as well as any unintended deformations in the support system during testing. The three main response quantities measured in the tests are: (1) The strain of different brace components to validate the mechanism of the brace during different stages of loading, (2) an external brace deformation measurement that can validate the reading of the actuator displacement measured by the LVDT inside the actuator, and (3) any unintended deformation of the test frame such as out-of-plane displacement or sliding of the reinforced concrete support block. To measure these parameters, 21 strain gauges, 2 Encoders, a string pot and 3 LVDTs are used. The following subsections detail the instrumentation plan used in the experimental setup.

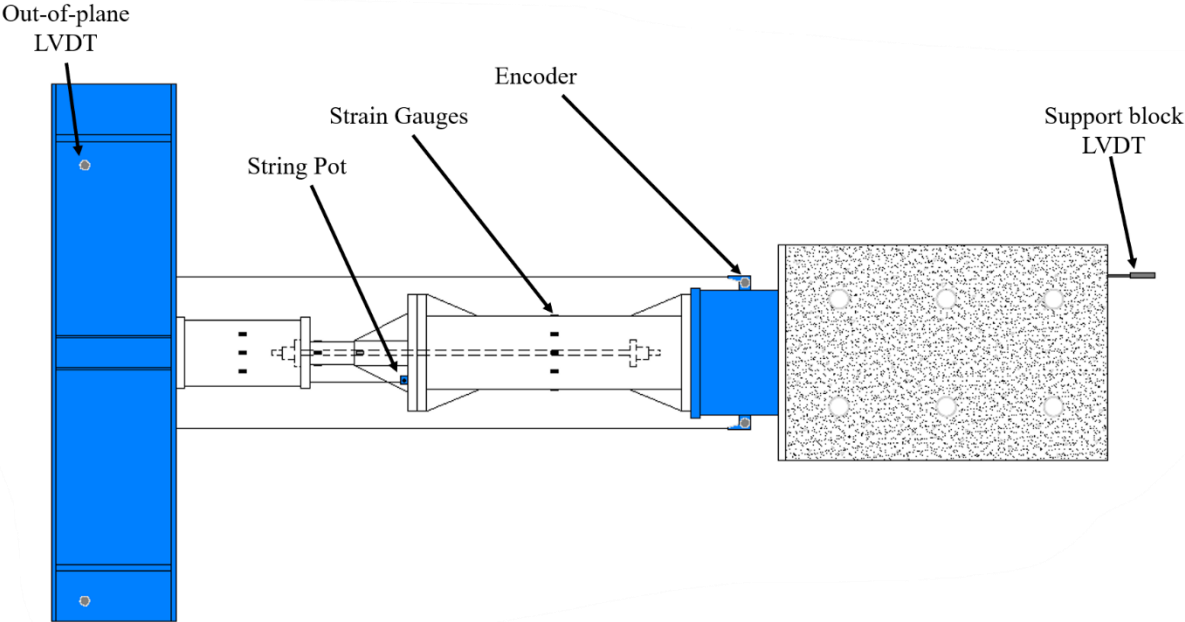
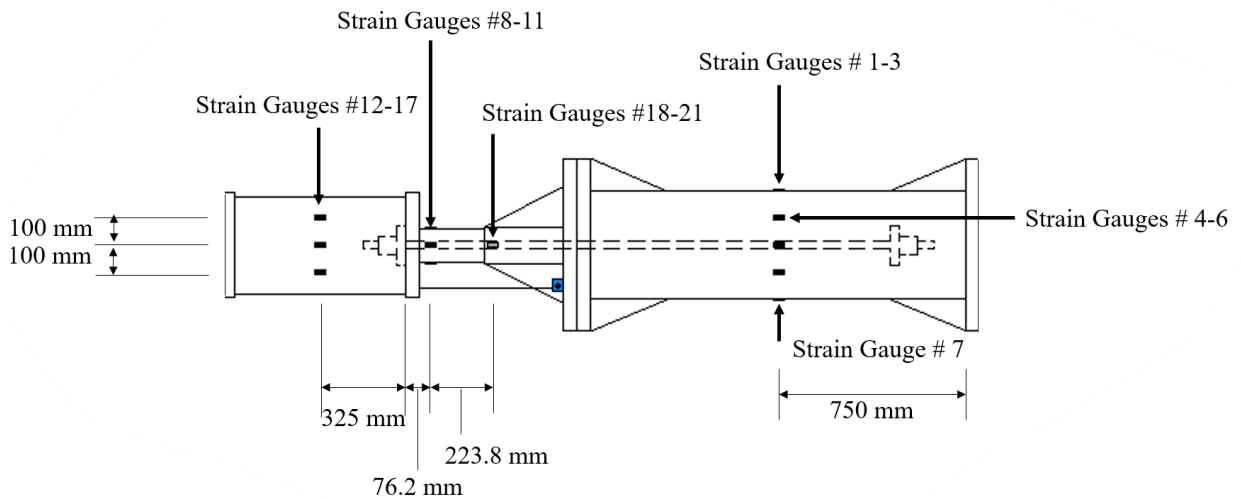


Figure 4.35 Instrumentation plan

## 4.7.1 Strains in Brace Components

A total of 21 strain gauges are used to monitor the strains in the different brace components during tests. The location and numbering of the strain gauges are shown in Figure 4.36.



**Figure 4.36 Plan view showing the exact location of the strain gauges used on different components of the brace**

A total of 7 strain gauges are used to monitor the strain in the outer tube as shown in Figure 4.36. Three strain gauges are applied on the top surface of the tube and another 3 strain gauges are applied at the far side of the tube with another strain gauge applied at the near side for comparison. Figure 4.37 shows an image taken from the near side of the brace showing strain gauges #1-3 and strain gauge #7. Strain gauges #4-6 are not visible as they are on the far side of the tube.

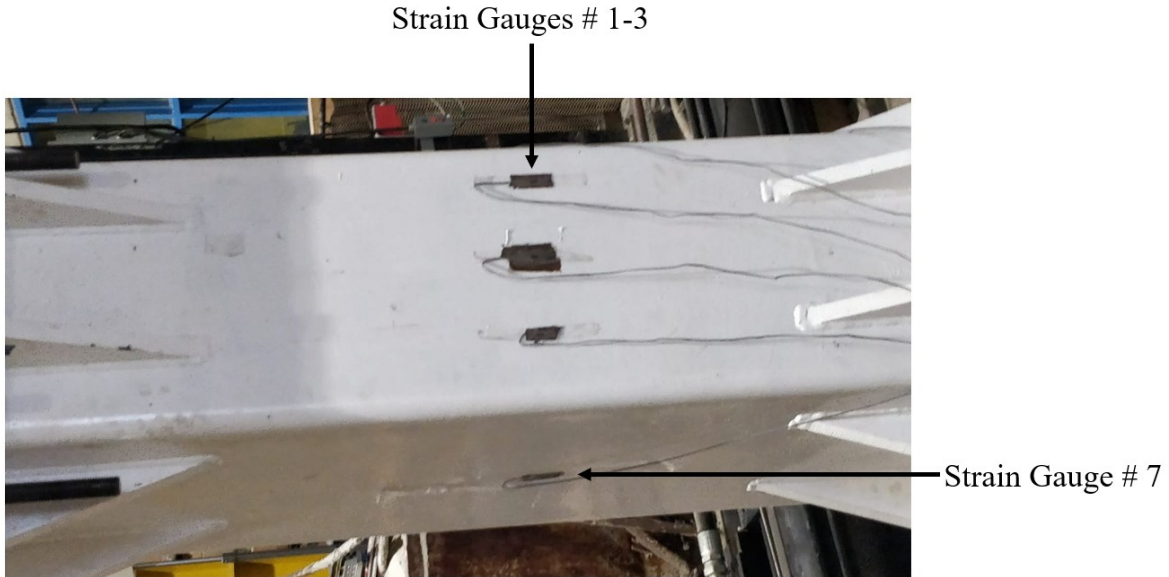


**Figure 4.37 Strain gauges installed to the Outer Tube surface**

Three strain gauges are used on each leg of the prestressing chair to monitor the strains on each leg as shown in Figure 4.38. Another 4 strain gauges are used to measure the strain in the DOM tube of the piston. The strain gauges on the DOM pipe are placed at the top, bottom and two sides of the outer surface of the pipe.

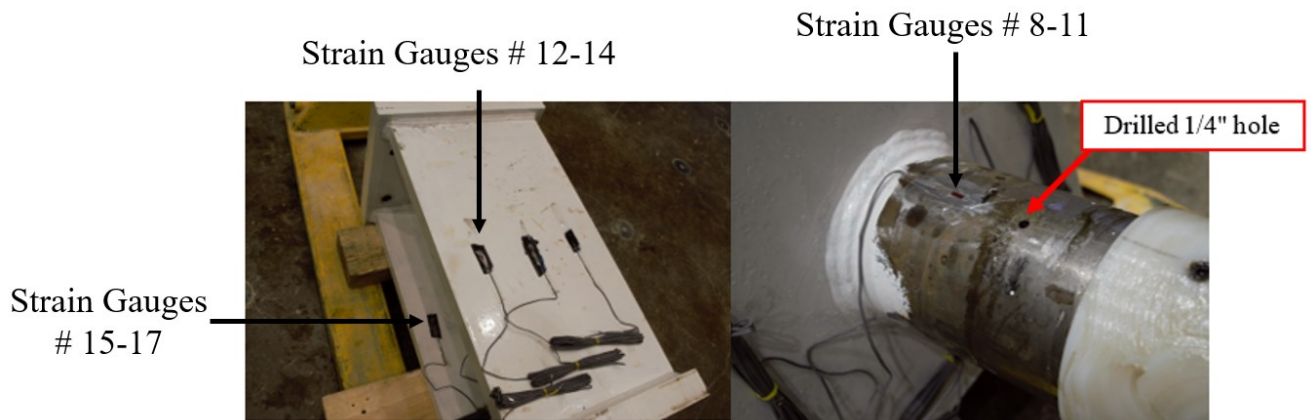


**Figure 4.38 Strain gauges used to measure strains for pistons**

To monitor the strain in the steel rod, a section of the rod is ground down to remove the threads and 4 strain gauges are used to measure the strain in the rod as shown in Figure 4.39. Figure 4.38

shows a small 1/4" hole is drilled through the DOM tube to allow for the strain gauge wires to be attached to the Data Acquisition (DAQ) system.

Strain Gauges # 18-21



Figure 4.39 Strain gauges applied on a section of the threaded steel rod

#### 4.7.2 Brace Deformation

The deformation of the brace in this test program is determined from the displacements measured by the actuators. However, during testing, it is expected that the displacements measured at the actuator heads relative to its starting position do not just include the actual deformation of the brace, but also include deformations resulting from the bending of the loading beam, as well as other small deformations within the connections. To measure the effect of these unintended deformations, externally-mounted displacement sensors are used, namely two encoders and a string pot. Figure 4.40 shows the exact locations of the encoders and the sting pot on a plan view of the experimental setup.

In this study, two Sick AFS/AFM60 SSI absolute encoders, shown in Figure 4.41, are attached to the steel link element to measure the deformation of the beam at the connection point between the brace and the beam. Although the theoretical displacement resolution of these encoders is

0.00076 mm, the maximum achievable resolution of the encoder is found to be 0.028 mm. This can be attributed to the inherent hysteresis in the wire draw mechanism, which is caused by the slack in the wire-draw cable during displacement measurements upon a reversal in the direction of the cable movement. In addition, a string pot is also used to measure the deformation between the piston prestressing chair and the outer tube cover plate as shown in Figure 4.42.

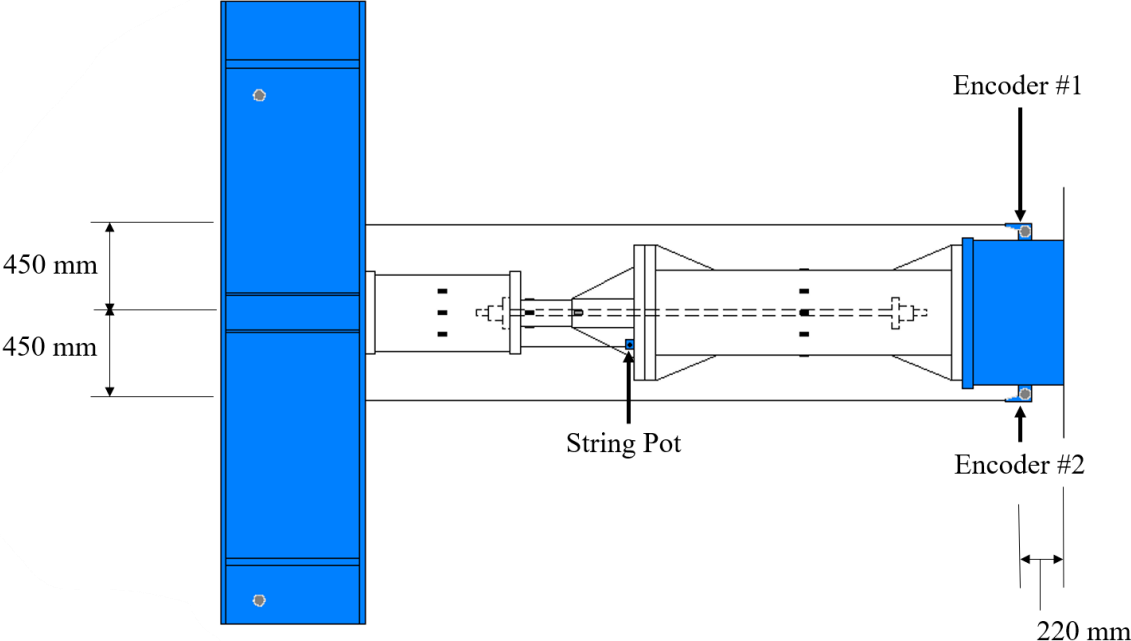


**Figure 4.40 Plan view showing the exact location of encoders and string pot measuring the brace deformation**

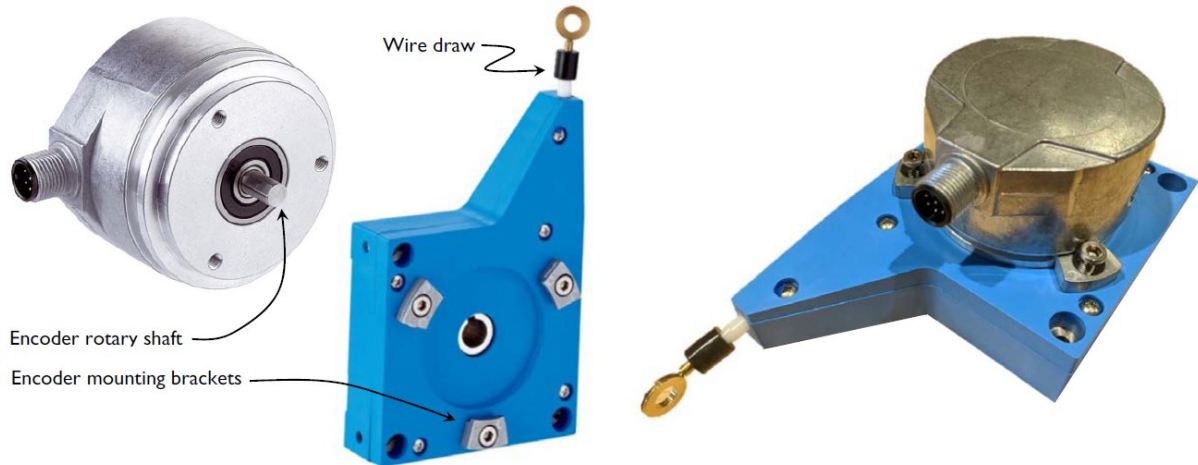


**Figure 4.41 Encoder used to validate the deformation measurement obtained from actuators**

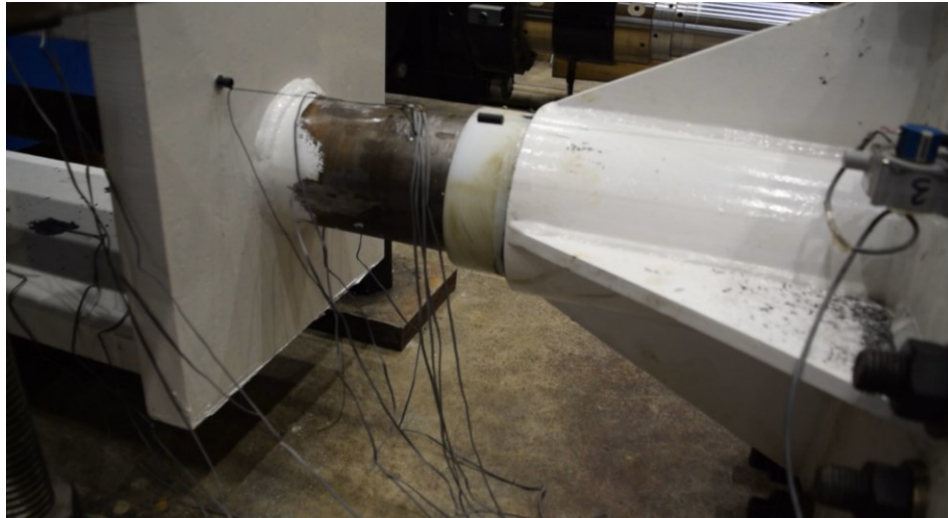


**Figure 4.42 Sting pot measuring deformation between piston chair base plate and outer tube cover plate**

### 4.7.3 Test Frame Deformations

To monitor any unintended deformations of the test frame, three LVDTs are used as shown in Figure 4.43. The first LVDT, shown in Figure 4.44, is used to monitor the sliding of the middle block in case the load on the brace exceeds the frictional force between the block and the strong floor. The other two LVDTs, shown in Figure 4.45, are used to monitor any out-of-plane deformation of the loading beam.

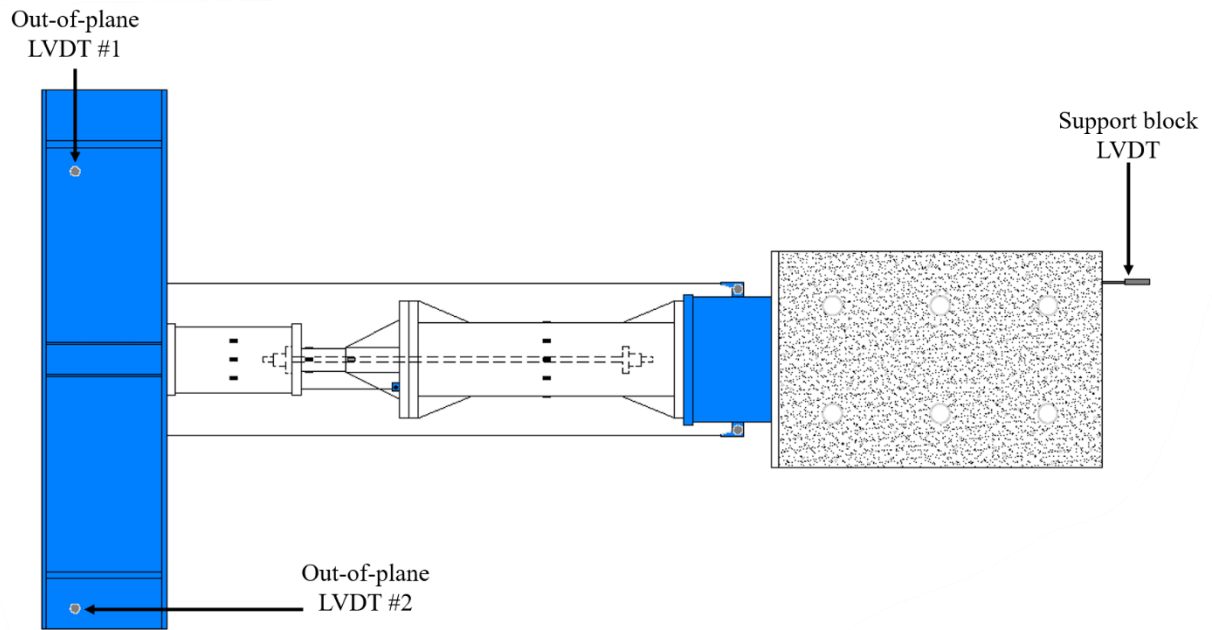


**Figure 4.43** Plan view showing the location of the 3 LVDTs used to measure the deformations of the test setup



**Figure 4.44** Support block LVDT measuring sliding of concrete block



Figure 4.45 Out-of-plane LVDTs #1 (left) and #2 (right)

## 4.8 Hydraulic Control and Data Acquisition

Figure 4.46 shows the hydraulic control and data acquisition computer station used for this experiment. Two different methods of control are used in this study depending on the phase of the test program. During the characterization testing phase of this study, a reversed cyclic loading protocol is prescribed using Multi-Purpose Elite (MPE) test suite of MTS 793 control software. MTS 793 sends the appropriate displacement command to the actuator through MTS FlexTest 100 controller by sending the appropriate command signal to the actuator servovalve for moving the actuator with the required displacement. The other control method is discussed in detail in Chapter 6 as part of the discussion regarding hybrid simulation of this study.

While the actuator displacement and forces are monitored through the MTS Flextest 100 controller, two 32-channel MTS FlexDAC data acquisition systems are used for data collection during the test. Data collection includes displacement measurements from the LVDTs used to monitor the deformation of the experimental test support structure, strain gauge readings used to

measure the strain in the brace components, encoder and string pot displacements measuring the brace deformation. Data acquisition is executed in MTS Multi-Purpose Elite (MPE), which runs parallel to the test procedure which can either run from MPE (for cyclic characterization tests) or MTS Csi (For hybrid tests).

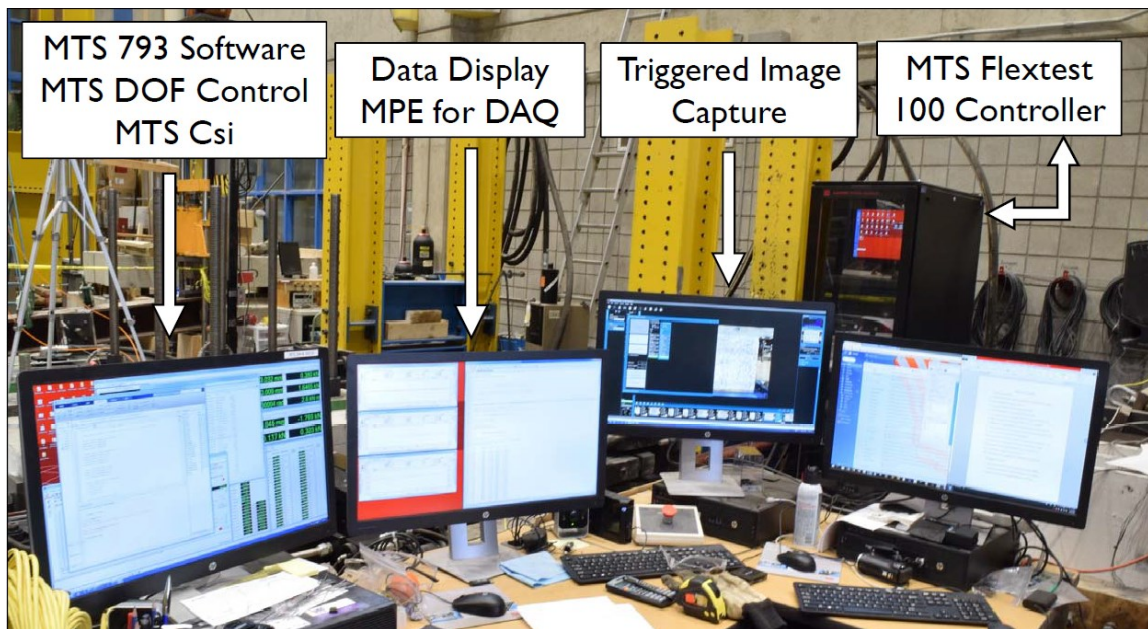


Figure 4.46 Computer station used for hydraulic control and data acquisition [75]

# Chapter 5 : Characterization of RS-SCED Brace Behaviour Through Experimental Testing

This chapter discusses the brace response characterization test program performed in this study. In the testing program, in addition to investigating the local response of different components of the RS-SCED brace (e.g. outer tube, threaded rod, piston tube, etc.), the hysteresis behaviour of the RS-SCED brace, its repeatability, durability and frequency dependence are investigated. The test program includes 4 different components, namely, the frequency dependence test, the ASCE 7-16 Protocol [74], the AISC 341-16 protocol [51] and the capacity test. In this chapter, the inter-storey drift is calculated based on a typical floor height of 4 m in the configuration previously presented in Section 4.1.

## 5.1 Frequency Dependence Test

The purpose of the frequency dependence test is to determine the dynamic performance of the new RS-SCED brace at different loading rates. The RS-SCED is subjected to 4 fully-reversed sinusoidal cycles of  $\pm 10$  mm displacement at maximum displacement rates ranging from 2 mm/s (0.06 Hz) to 45 mm/s (1.43 Hz). The hysteretic response recorded during the frequency dependence test is shown in Figure 5.1.

The frequency dependence test results show that the hysteretic response of the RS-SCED brace remains stable and repeatable at all displacement rates considered in this study. The RS-SCED brace self-centering behaviour and flag shaped hysteresis are found to be stable and consistent throughout all tests and they are not influenced by the displacement rate. The post-activation and pre-activation stiffnesses are found to be practically unaffected by the displacement rate. Similarly,

the activation load  $P_a$ , recoil load  $P_R$  and decompression load  $P_d$  observed remain stable and consistent at all displacement rates. These observations are consistent with findings from previous studies on self-centering ring spring devices discussed in Chapter 3.

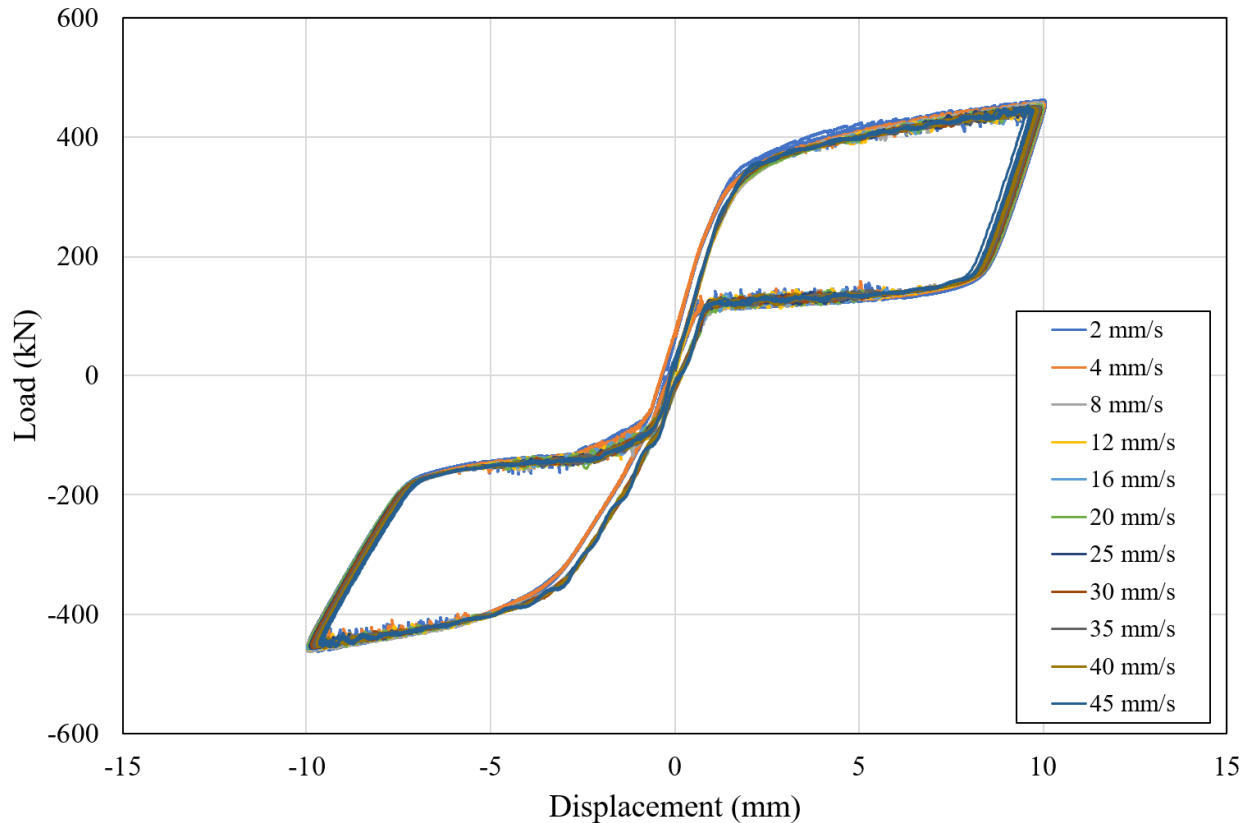
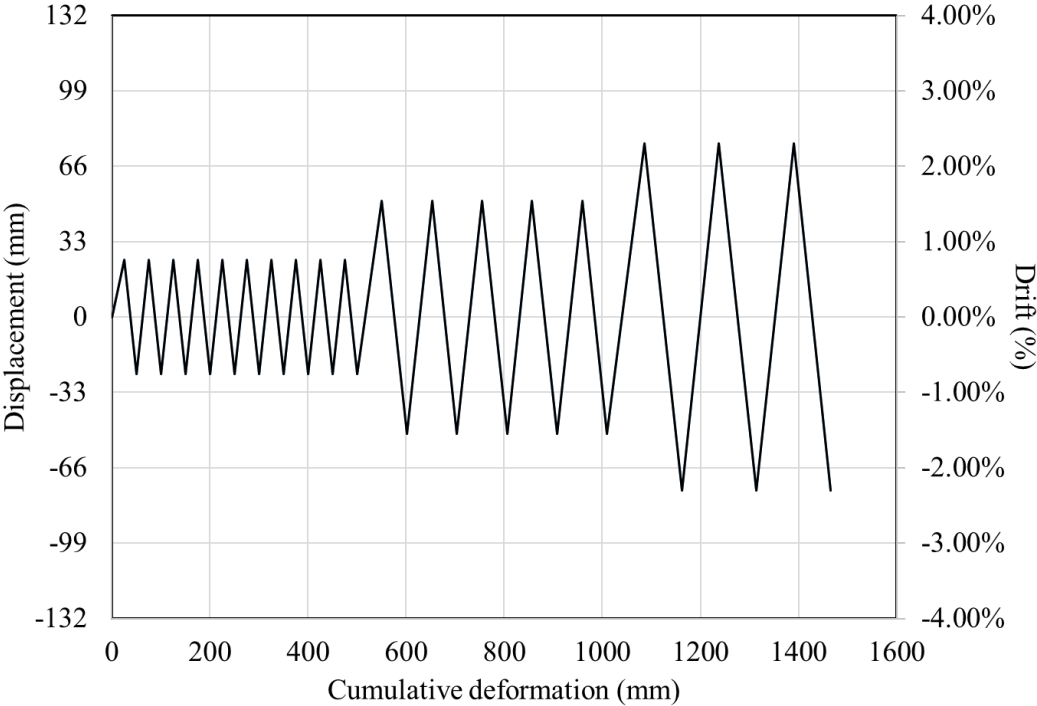


Figure 5.1 Hysteresis response of RS-SCED brace when loaded under different displacement rates

## 5.2 ASCE 7-16 Loading Protocol

The prototype test specified in Section 18.6 of ASCE 7-16 [74] is intended to confirm the force-velocity-displacement properties of damping devices and to demonstrate the robustness of individual devices under seismic excitation. ASCE 7-16, proposes using cycles of loading that simulate the drift demand on a structure subjected to a large earthquake that has a probability of exceedance of 2% in a 50-year period, commonly referred to as a Maximum Credible Earthquake (MCE). As shown in Figure 5.2, the ASCE 7-16 protocol consists of 10 cycles at 1/3 of the

maximum drift the structure is expected to experience during a large earthquake at the MCE hazard level. This is followed by 5 cycles at 2/3 of MCE hazard level drift and finally 3 cycles of the MCE hazard level drift. Numerical results from a parametric study were used to determine the drift level expected at the MCE hazard level for the 8-storey building structure used for the hybrid simulation, which is discussed in more detail in Chapter 7. Typically, the frequency at which the test is to be conducted is equal to  $1 / (1.5T_1)$ , where  $T_1$  is the first fundamental period of the structure. Alternatively, the test can be performed at any rate provided other separate tests are performed to examine the rate dependent effects. Given that an alternative set of tests were conducted to verify that the RS-SCED brace was not rate-dependent, the ASCE 7-16 loading protocol was applied at a rate of 15 mm/s.



**Figure 5.2 ASCE 7-16 loading protocol**

Figure 5.3 shows the hysteresis of the RS-SCED brace when loaded according to ASCE 7-16 protocol. The observed hysteresis is consistent with the theoretical response predicted and discussed in Section 4.2. The response is stable and repeatable for all 18 cycles. The pre- and post-

activation stiffnesses are consistent for all displacement demands with clearly-defined activation force  $P_a$ , recoil load  $P_R$  and decompression load  $P_d$ . The RS-SCED brace response also shows no residual drift with the brace fully capable of maintaining the self-centering behaviour throughout all of the cycles in the ASCE 7-16 loading protocol.

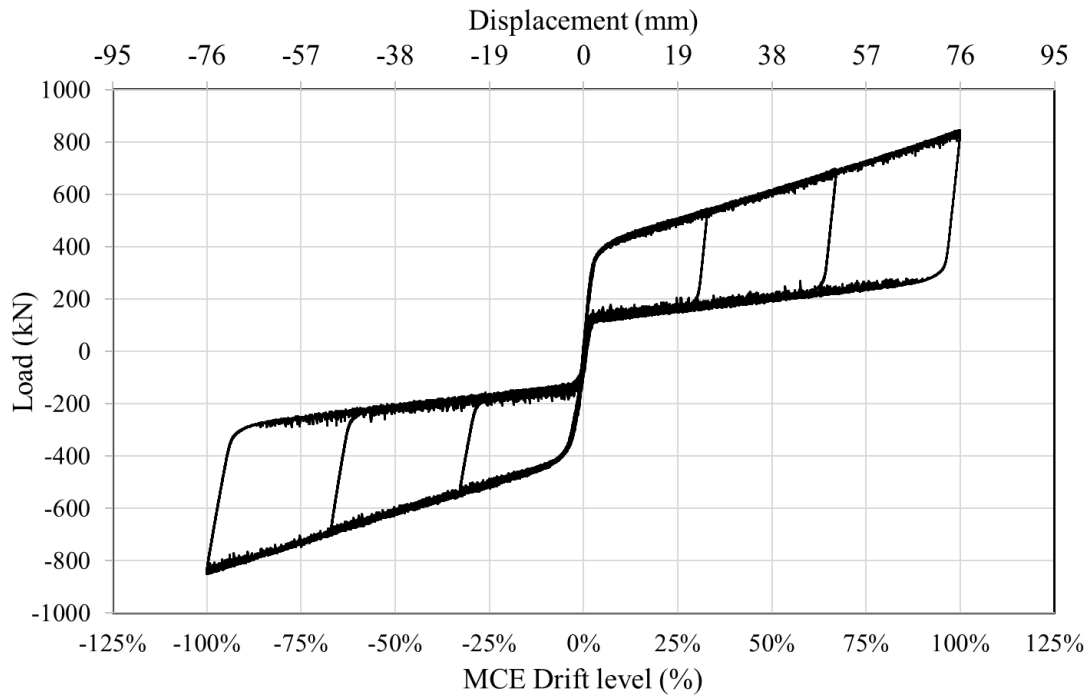


**Figure 5.3 ASCE 7-16 loading protocol pre-hybrid tests**

To check the durability of the RS-SCED brace, the ASCE 7-16 protocol was conducted for a second time upon the completion of the 19 hybrid simulations discussed in Chapter 6. Figure 5.4, shows the hysteresis of the RS-SCED when tested after the completion of the hybrid tests. Although the pre- and post-activation stiffnesses, as well as the activation force  $P_a$ , recoil load  $P_R$  and decompression load  $P_d$  remain consistent throughout the test, the hysteresis shows a gradual shift in the recoil position of the brace after every cycle. This is caused by the nut on the steel rod becoming a bit loose gradually after repeated cycles. This generated a gap between the nut on the end of the threaded rod and the end plate that is in contact with the spacer plates. In turn, this gap caused a delay between the point at which the brace reaches the neutral position and the end of the

threaded rod bearing against the end plate and initiating the tensile cycle. As the brace was subjected to more of these cycles the size of the gap increased causing the observed change in the hysteretic response behaviour.

To mitigate against the formation of the gap, the nut on the threaded rod was tightened to ensure that it once again bears against the ring spring assembly when the brace is at its neutral position. As shown in Figure 5.5, the hysteretic response of the RS-SCED brace after this adjustment is consistent with the original hysteresis and the results demonstrate that the full self-centering capacity is restored. To address this issue in the future, it is recommended that the threaded rod nut be locked in position either by adding a second nut or by tack welding the nut to the threaded rod.

The pre- and post- activation stiffnesses, activation force  $P_a$ , recoil load  $P_R$  and decompression load  $P_d$  are restored when comparing the adjusted hysteresis of the brace after significant testing with the original hysteresis before testing. Considering that the number of frequency tests, loading protocols and hybrid tests this brace experienced far exceeds the number of earthquake records that any brace would experience throughout its life cycle, the results demonstrate the durability and robustness of the RS-SCED when subjected to significant loading for a large number of cycles.

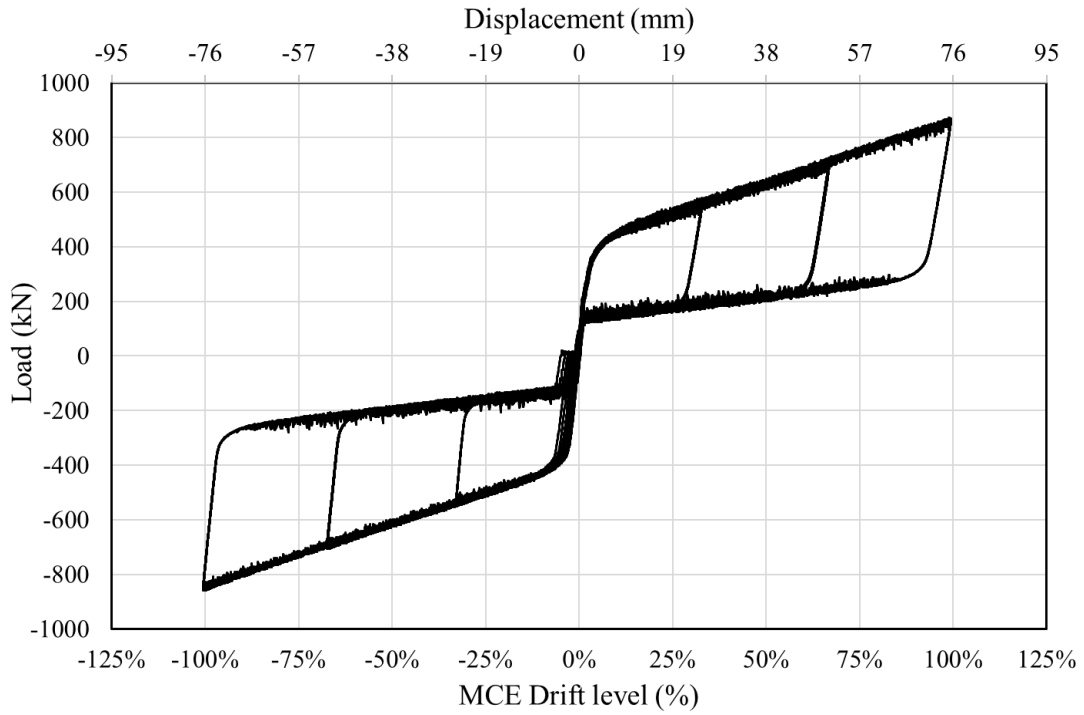


Figure 5.4 ASCE 7-16 loading protocol post-hybrid tests

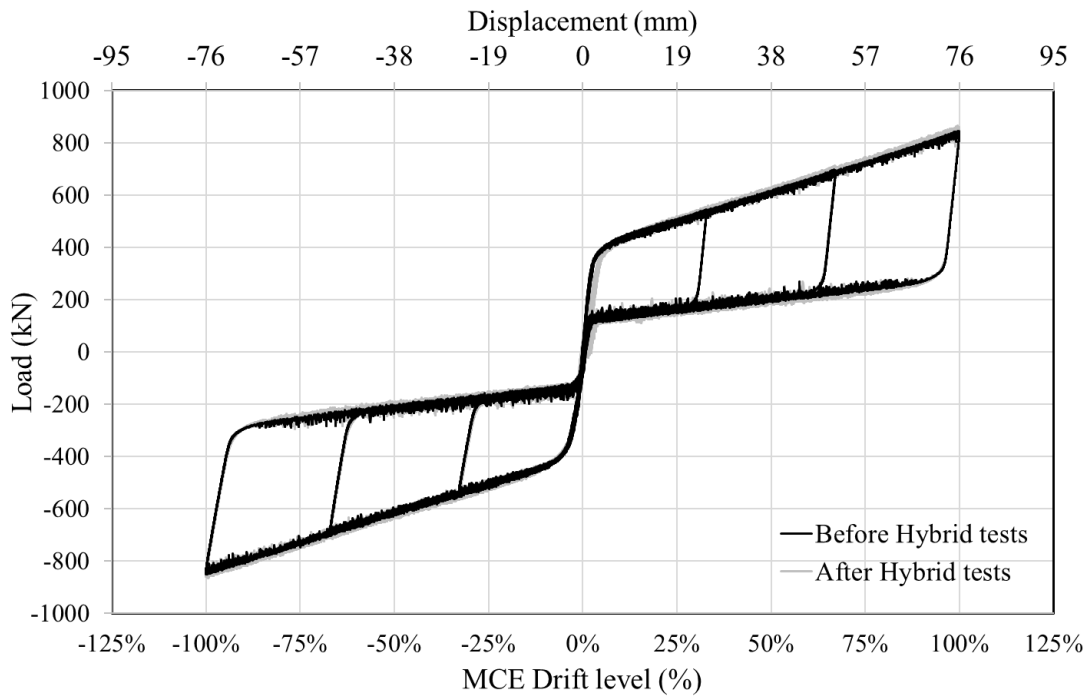


Figure 5.5 Comparison between pre- and post-hybrid testing results after adjusting the nut for gap formed

### 5.3 AISC 341-16 Testing Protocol

The purpose of the AISC 341-16 [51] cyclic testing protocol is to provide evidence that a buckling restrained brace (BRB) satisfies requirements for strength and inelastic deformation. Because the RS-SCED brace is designed to have similar force capacity and applications as a BRB, testing the RS-SCED brace using the AISC 341-16 loading protocol is helpful for assessing its performance. The AISC 341-16 loading protocol is a series of load cycles calculated as a function of the design storey drift  $\Delta_{bm}$ , which is equal to 1% for this series of tests as per AISC recommendations. As shown in Figure 5.6, the protocol includes two repeated cycles at increasing displacement levels increasing at increments of  $0.5 \Delta_{bm}$  up to 3% drift. There is no specified loading rate for the AISC 341-16 loading protocol, however, the effects of loading rate were examined in a separate series of tests described in Section 5.1.

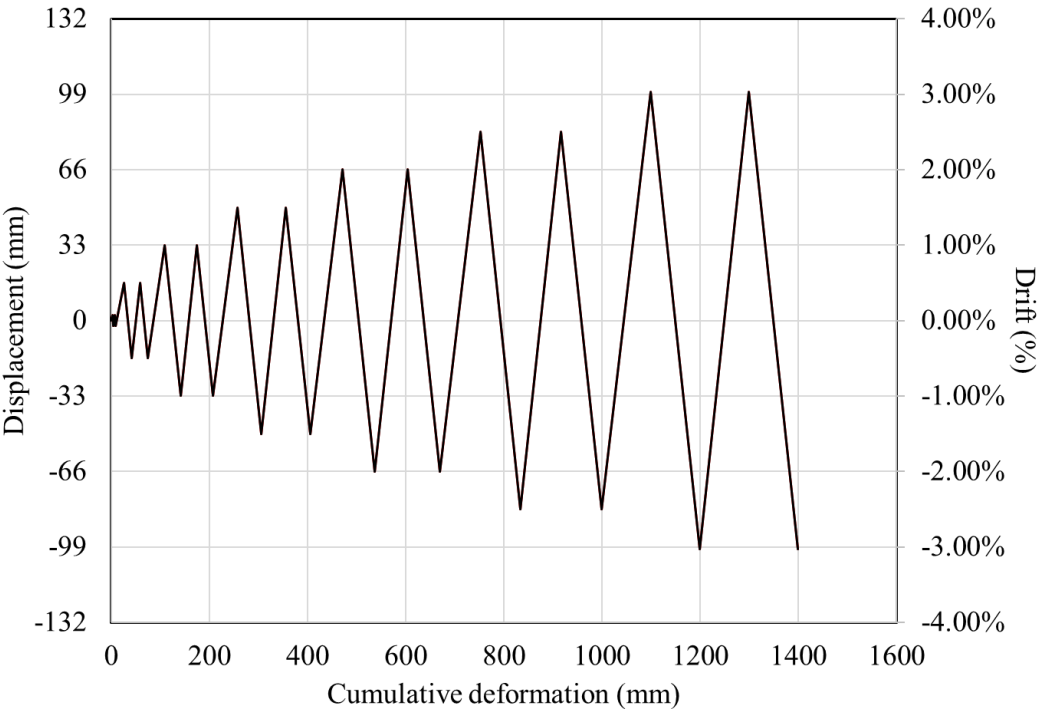
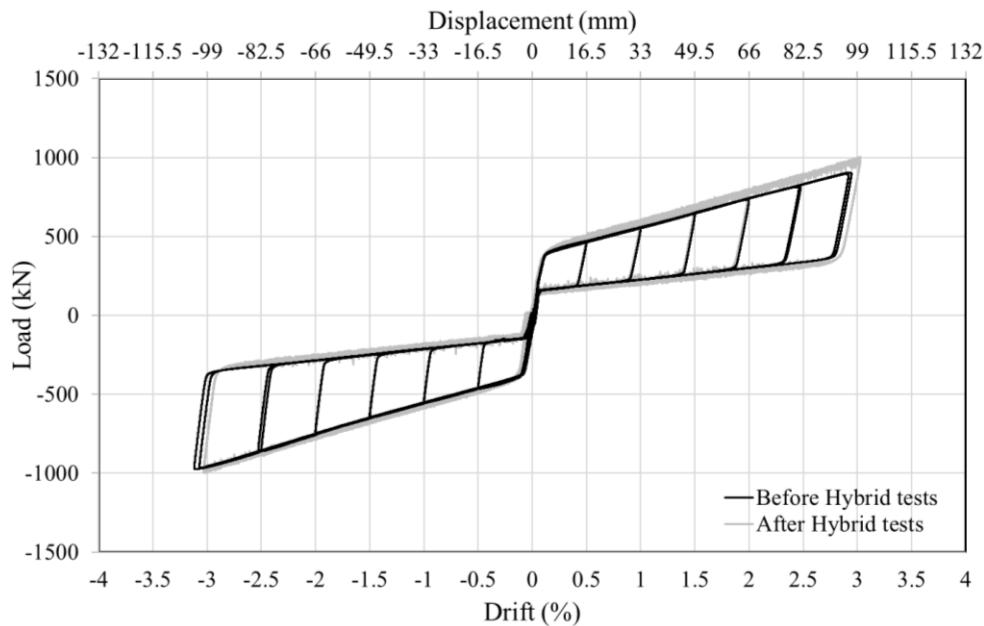


Figure 5.6 AISC 341-16 Loading protocol

As shown in Figure 5.7 , the force-deformation response of the RS-SCED brace is stable and repeatable at drift levels up to 3%. Similar to the results shown for the ASCE 7-16 protocol presented in the previous section, the initial and post-activation stiffnesses as well as the activation force  $P_a$ , recoil load  $P_R$  and decompression load  $P_d$  correlate well with the response predicted from the response of the ring spring assembly. It is evident from the hysteresis shown in Figure 5.5 and Figure 5.7 ,that there is no observable residual deformation even after being subjected to numerous cycles from both the ASCE and AISC loading protocols.. Also, the pre- and post-activation stiffnesses are highly consistent even at high load and deformation demands. The only other noticeable difference between the pre-hybrid test and post hybrid tests, was an increase in minor load fluctuation. This is mainly due to the slight increase in friction caused by frequent incidental contact between the bottom of the end plates and the inner surface of the outer tube. This is discussed in more detail in Section 5.6.



**Figure 5.7 AISC 341-16 loading protocol pre and post hybrid tests**

# 5.4 Capacity Test

In this study, the RS-SCED brace is subjected to a loading cycle in which the brace is loaded up to the design drift demand of 4%, which corresponds to 132 mm of axial deformation of the brace. This test is conducted to determine whether the brace can maintain its re-centering capacity at significant inelastic deformation and load demands. As shown in Figure 5.8, the RS-SCED is capable of maintaining stable hysteresis with a constant post-activation stiffness at a drift demand of 4% and a maximum load of 1200 kN. The RS-SCED maintains its self-centering behaviour showing no signs of residual deformation up to its maximum design capacity. It is worth noting this loading cycle did not load the brace to its ultimate capacity of 1400 kN at a deformation of 160 mm to avoid potentially damaging the brace prior to the hybrid testing program.

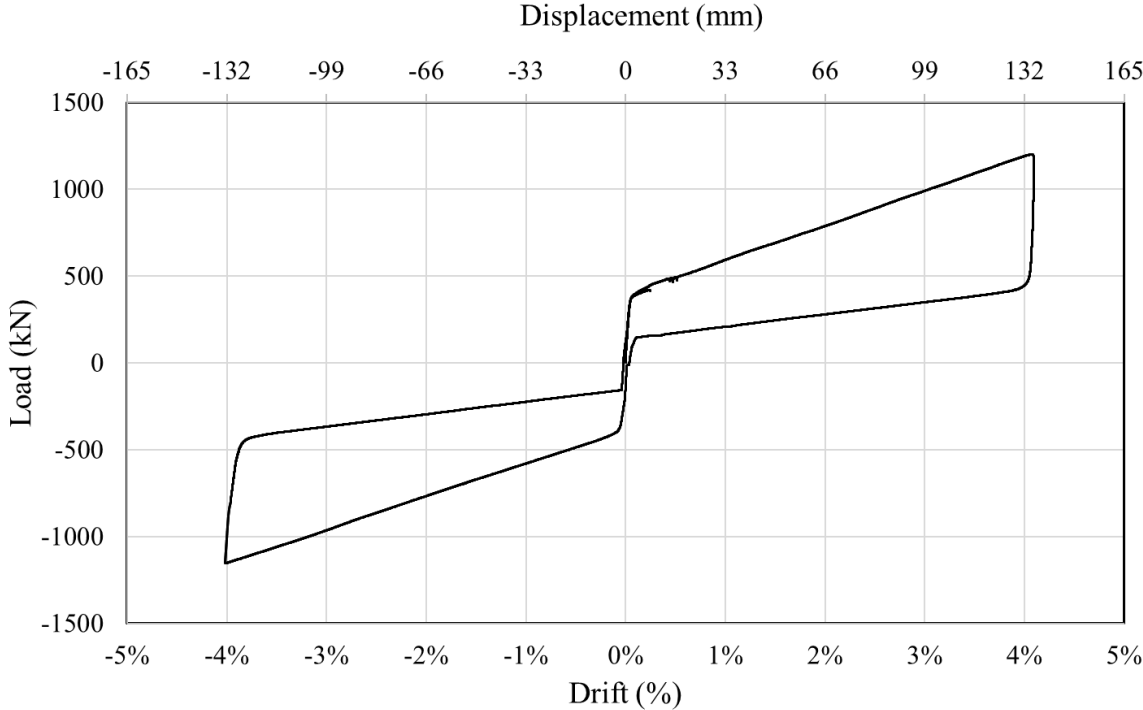
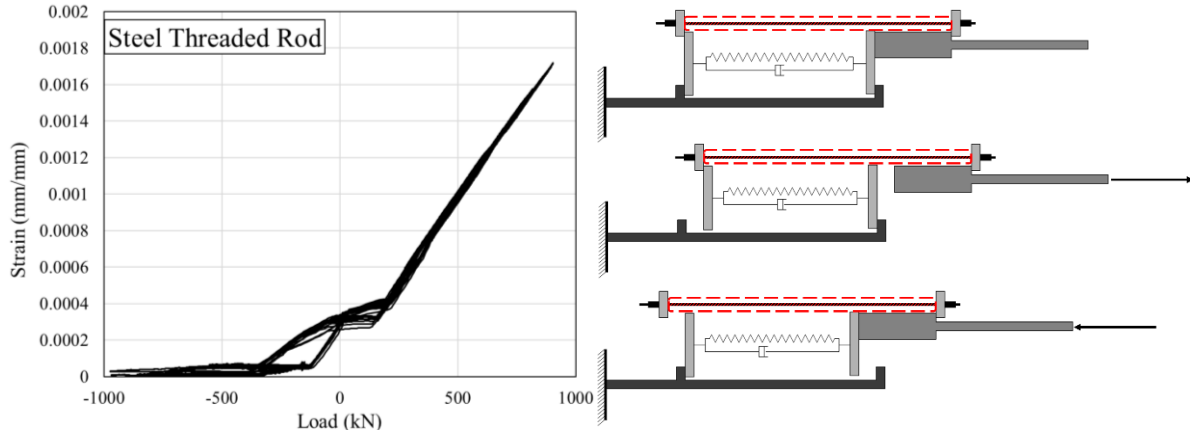


Figure 5.8 Full cycle of loading at design drift level of 4%

## 5.5 Strain Gauge Measurements

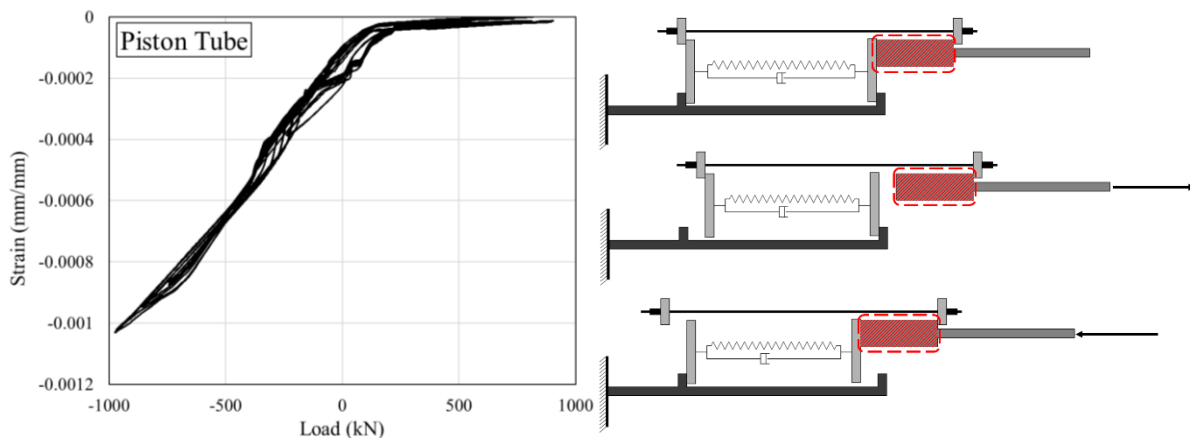
Another goal of the series of characterization tests is to validate the local response of the different brace components under its design load and multiple load cycles. Section 4.3 summarized the design load carried by all components of the RS-SCED brace at different loading stages. The average strains from the strain gauges mounted on the steel threaded rod, outer tube, piston tube and prestressing chair legs are plotted with respect to the applied external load on the RS-SCED to better understand the local behaviour of each of these components. The strain values used for these plots were collected from the AISC protocol test, results from other tests showed similar results.

Figure 5.9 shows the steel threaded rod strains during the testing of the RS-SCED brace. Initially, there is a tensile strain in the rod when the brace is in a neutral position with no external force applied to the brace. This is caused by the initial prestressing that is applied to the rod to precompress the ring spring assembly. When the RS-SCED is loaded in compression, the tensile strain decreases to zero when the brace reaches its activation load, more specifically when the threaded rod is no longer bearing on the end plate of the ring assembly. When the brace is loaded in tension the rod strain increases linearly and shows no signs of yielding in the rod as the measured strains remain well below the yield strain of the rod of 0.004 mm/mm according to the manufacturer. These results are consistent with the predicted behaviour discussed in Section 4.3.



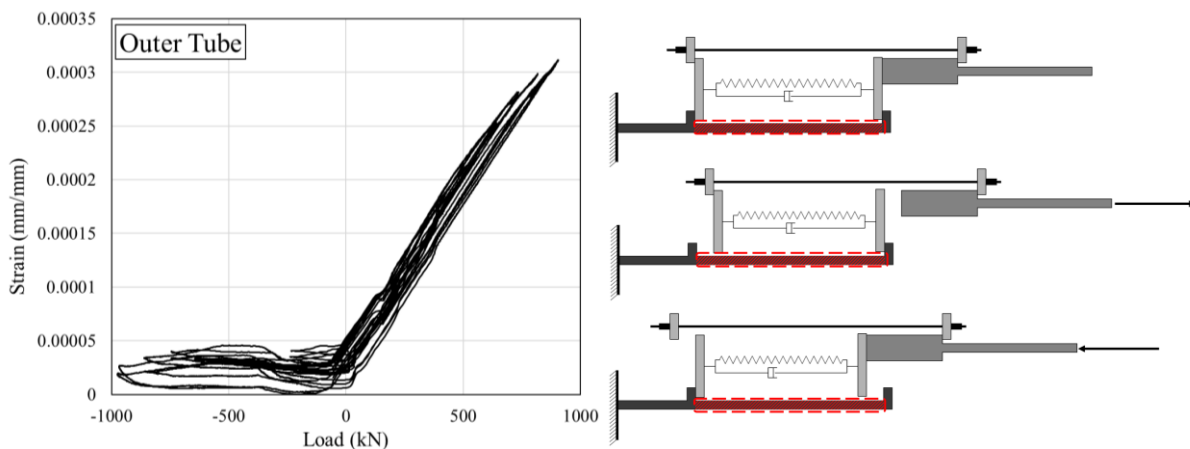
**Figure 5.9 Measured strain response for steel threaded rod**

Figure 5.10 shows the strain in the steel piston tube during the cyclic loading process of the RS-SCED brace. At the initial position, the tube has a compressive strain, indicating the compressive load that is resisted by the tube as it transfers the load between the end plate of the ring spring assembly on one end, and the prestressing chair base plate from the other end. When the brace is loaded in compression this strain increases linearly indicating no signs of yielding in the piston tube. As the brace is loaded in tension, the strain increases until it reaches zero and then stays at zero. This occurs when the ring assembly bears against the inside of the outer tube cover plate and no longer bears on the end of the piston tube. Once again this confirms the theoretical load path predicted in Section 4.3.



**Figure 5.10 Measured strain response for steel piston tube**

Figure 5.11 shows the strain sustained by the outer tube. Unlike the piston tube and the steel rod, the outer tube is not resisting any load when the brace is in the neutral position since the prestressing load is strictly resisted by the threaded rod, piston tube and ring spring assembly. The outer tube only shows a tensile stain when the RS-SCED is subjected to tensile loads, but no compressive strain when the brace is subjected to compressive loads. This is because in compression, the load is transferred from the prestressing chair, to the piston, to the ring spring assembly which is restricted from movement by means of the spacer plates. Therefore, only the end of the outer (along the welded edges of the spacer plates) will experience some compressive load.



**Figure 5.11 Measured strain response for outer tube**

Figure 5.12 shows the linear strain relation measured from the piston chair legs. The prestressing chair legs transfer the loads from the loading beam to the rest of the brace, either through the threaded rod when the brace is in tension or through the piston tube when the brace is in compression. Similar to the outer tube, the piston chair legs do not experience any initial strain as they are not part of the prestressing of the ring springs. All the strain vs applied load relations are linear indicating that the individual components do not yield and that the non-linearity and ductility of the RS-SCED brace is provided entirely by the change in length of the ring spring

assembly, which is critical to ensure that the RS-SCED does not have any residual deformation at the end of loading.

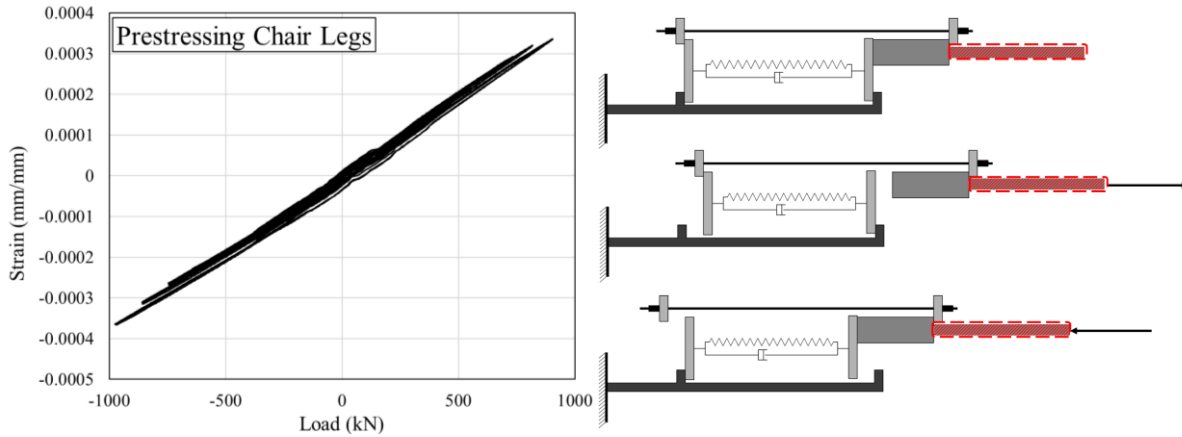


Figure 5.12 Measured strain response for piston chair legs

## 5.6 Post-test RS-SCED brace conditions

After all of the experimental testing, including the characterization and hybrid tests, the brace was closely inspected to identify and assess any localized signs of damage to the RS-SCED components. One of the more noticeable signs of minor localized damage was observed on the inner surface of the bottom edge of the end plates shown in Figure 5.13.

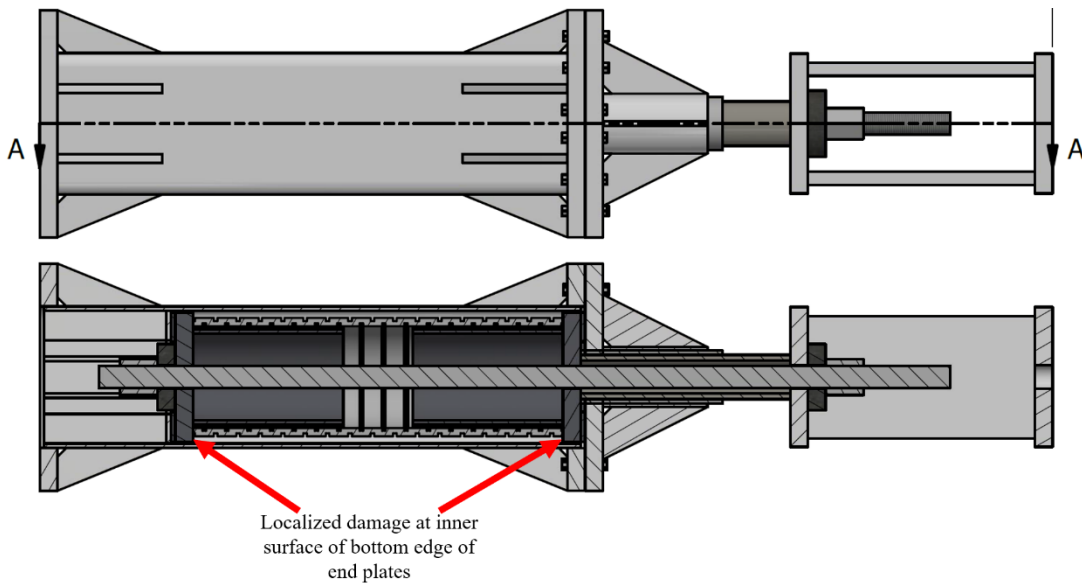


Figure 5.13 Location of localized damage observed on the end plates

As shown in Figure 5.14, Figure 5.15 and Figure 5.16, the inner edge shows some damage that is characterized by rounding of the edge of the endplate. As the end plate moves inside the outer tube while the ring spring assembly compresses, the inner edge of the end plate incidentally contacts the inner surface of the outer tube. One of the indicators of this friction is the fluctuation in the load hysteresis which was observed during the characterization tests discussed earlier in this chapter. It is worth noting that this effect was minimal at the start of the tests because the spring assembly was initially placed at the center of the outer tube with about 5 mm clearance between the endplate and the inner surface of the outer tube. However, under repeated cyclic loads, the ring spring assembly slowly settled down under its own self-weight resulting in the friction observed. This explains the gradual increase in the load fluctuations as the tests progressed. Distinct friction noises were also heard during testing in the laboratory. The sound got progressively louder and more frequent as the tests progressed, indicating the increase in friction associated with more settlement of the ring spring assembly under its own weight.



**Figure 5.14 Localized damage at inner edge of end plate**

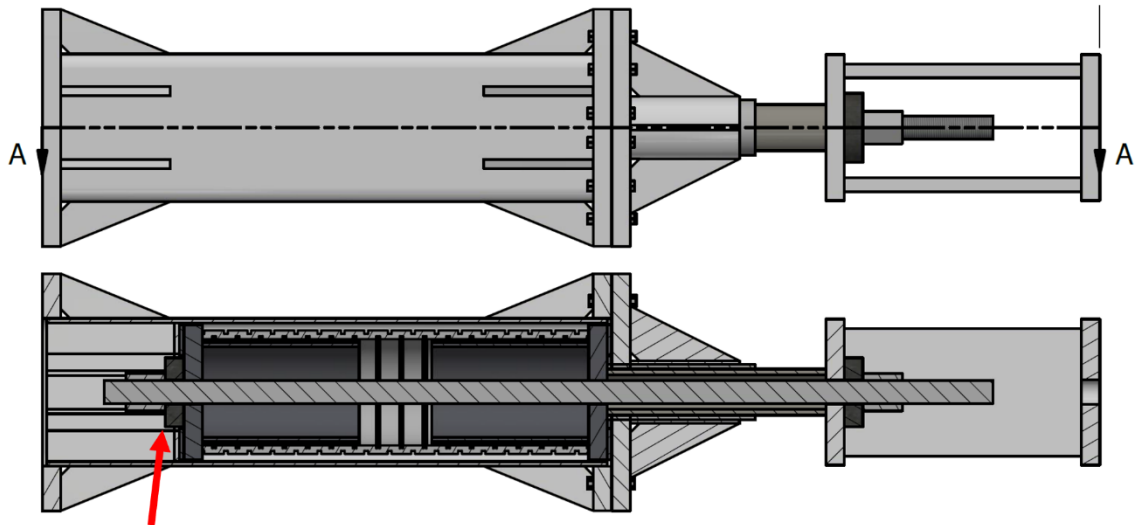


**Figure 5.15 Damage along the length of the inner edge of end plate**



**Figure 5.16 Localized deformation as a result of frequent contact with the inner surface of outer tube**

Another result of the settlement of the ring springs under their own weight is the formation of an impact region between the bottom of the washer plate and the space plate bearing plate as shown in Figure 5.17. This contact area resulted in the formation of a notched region observed on the bearing plate which was welded to the ends of the spacer plates as shown in Figure 5.18 and Figure 5.19. This also caused the washer plate to have some localized damage on its bottom edge as shown in Figure 5.20. To mitigate against the settlement of the ring springs, a sheet of UHMW low friction plastic could be added to the inner surface of the outer tube, or to the edges of the end plates. This would minimize the friction of any impact between the end plate and the outer tube, as well as ensure that the washer plate consistently moves through the opening between the spacer plates unimpeded. Another recommendation is to use inter-lapping inner and outer guides on the end plates at both ends of the ring spring assembly to ensure that the assembly is straight during the pre-compression stage of the assembly as shown in Figure 5.21 and Figure 5.22. This is also beneficial in pre-compressing the ring spring assembly as it was relatively difficult to keep the assembly straight during the process of initial pre-compression with only inner guides welded to the end plates.



Localized damage to washer plate due to contact with spacer plates

**Figure 5.17** Location of localized damage at washer plate and spacer bearing plate

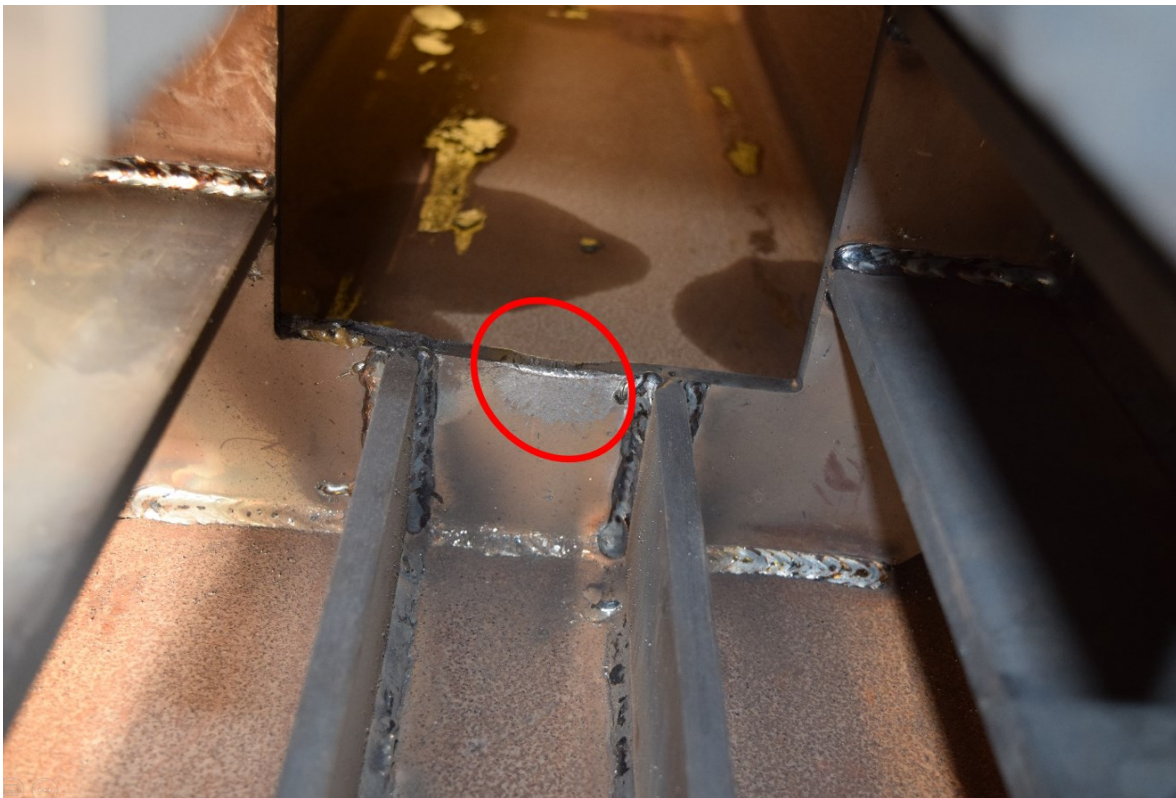


**Figure 5.18** Damage at the bearing plate



**Figure 5.19 Notch at the bearing plate caused by impact with the washer plate**



**Figure 5.20 Localized damage on the washer plate caused by impact with bearing plate**

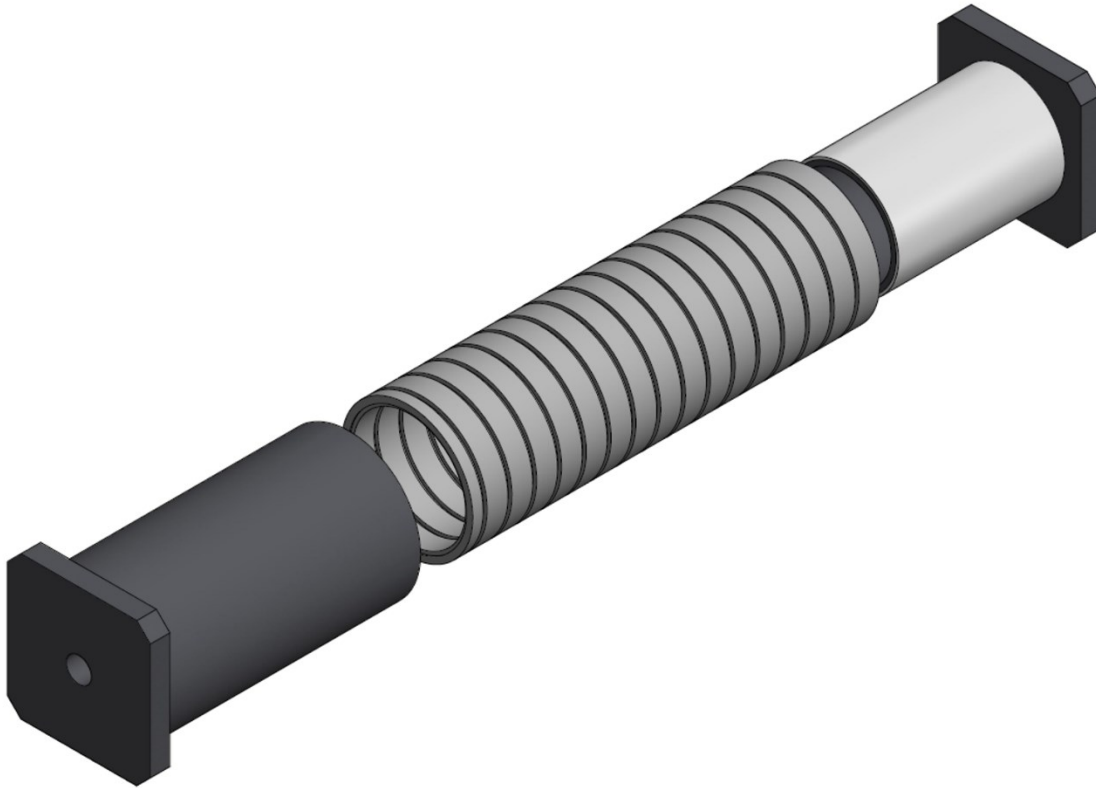


Figure 5.21 The use of an inner and outer guide on either end plate of the assembly

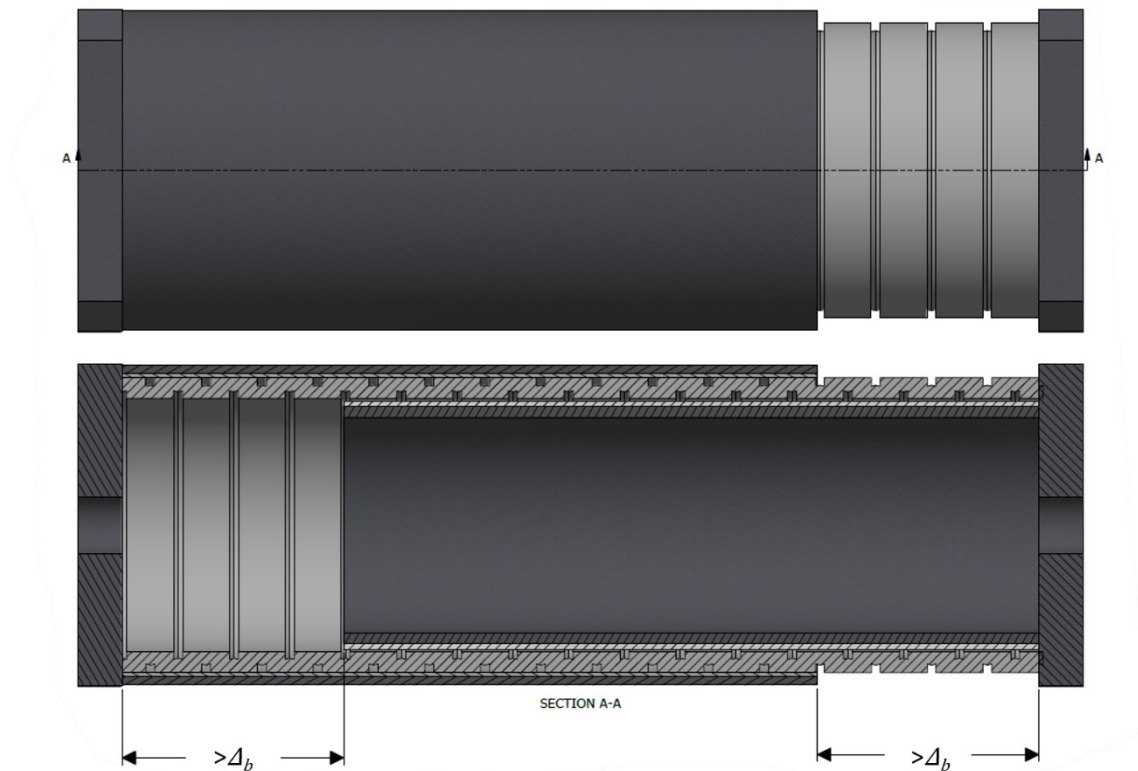


Figure 5.22 Proposed Inter-lapping of inner and outer guides

The inner surface of the outer tube suffered minimal damage due to friction with the end plate as shown in Figure 5.23. As the end plates slide along the length of the tube, they contact the inner surface of the outer tube at different points. This is in contrast to the localized nature of the impact on the inner edge of the end plates, hence the lower damage observed.



**Figure 5.23 Minimal damage to the inner surface of the outer tube due to friction with end plates**

The spacer plates showed no signs of damage after the test completion as shown in Figure 5.24. The same was also true for the piston tube, shown in Figure 5.25, which incurred minimal damage despite the large impact load that its end sustained with each compression cycle. The grease that was applied to the ring spring assembly was still on the surfaces of the ring springs after testing as shown in Figure 5.26. The consistency of the results between the pre- and post- hybrid test results of the AISC and ASCE protocols is likely in large part due to the grease applied to the spring, which ensures that the mating surface between the rings in the assembly provides the intended level of friction for energy dissipation. There was no damage observed on the cover plate as shown in Figure 5.27.

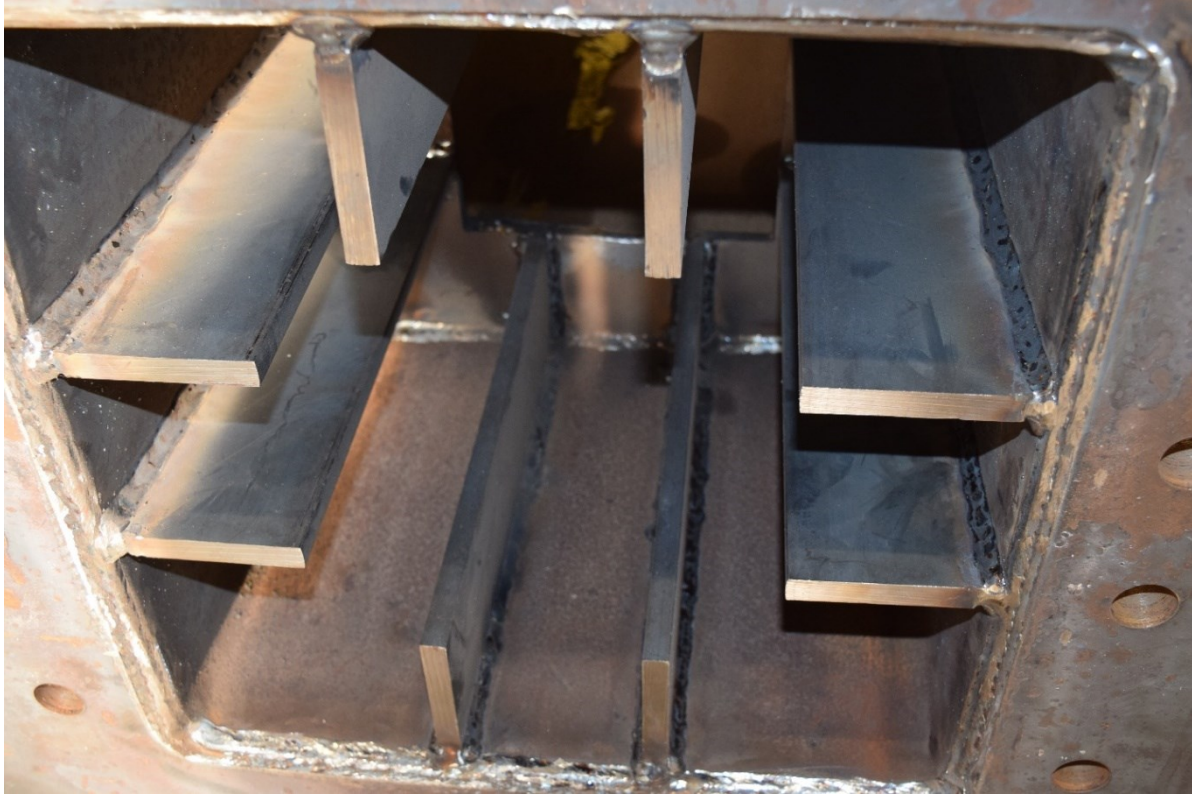


**Figure 5.24 No observed damaged to spacer plate and welds**



**Figure 5.25 Small gap between UHMW plastic and end plate indicate no damage to piston tube**



**Figure 5.26 Ring spring assembly grease after testing**



**Figure 5.27 No damage observed on the cover plate**

# Chapter 6 : Hybrid Simulation of RS-SCED Brace

Past studies have examined the behaviour of SCED braces under simulated seismic load. As discussed in Chapter 2, the majority of these studies were either quasi-static full-scale tests, or shake table tests involving scaled specimens. Quasi static full-scale tests have the limitation of not being capable of evaluating the effect of the brace response on the global system-level behaviour and performance of the structure. On the other hand, shake table tests are restricted by the test specimen size due to cost of construction and shake table capacity. In this study, a series of hybrid simulations are performed to evaluate the system-level performance of the new RS-SCED brace. The benefits of hybrid simulation include its ability to study the non-linear behaviour of a critical or complex structural component in detail in the laboratory through experimental testing, while at the same time capturing the system-level response of the full-scale structural system in a numerical model. This makes it feasible to determine the realistic behaviour and impact of the physically tested brace on the global response of the structure, without having the need to test the entire structure. To conduct a hybrid simulation, a substructuring approach is followed. In this approach, a structure is separated into experimental and analytical substructures in which the structural mass and damping effects are included in the analytical substructure. A discretized model of the analytical substructure is analyzed by a computer under the effects of static and/or dynamic loading. An earthquake ground acceleration time-history record is used as the input excitation for the model. At each discrete time step, a numerical integration technique is used to solve the equation of motion for the structure and to obtain a target displacement vector at the nodes that couples the analytical substructure with the physical substructure. By means of a middleware controller, static or dynamic hydraulic actuators apply one or more target displacements to the

physical substructure and the data-acquisition system comprising of several different measurement sensors and instruments including transducers and load cells record the restoring forces and achieved displacements. The restoring forces are fed back to the finite element software and into the equation of motion of the structure. The equation of motion is then solved again at the next time step and this process is repeated for the duration of the ground motion record.

To determine the effectiveness of the new RS-SCED brace, two numerical models are developed. The first model is an 8-storey office building designed for a site in Victoria, BC, which utilizes RS-SCED braces as the lateral load resisting system. To evaluate the performance of this new system, its response is compared to the response of an identical structure that uses BRBs as the seismic force resisting system (SFRS). The second model is a 3-span bridge designed for a site in Ottawa, ON that uses the RS-SCED braces as seismic dampers. To evaluate the performance of the bridge with the RS-SCED braces, the response of the bridge with and without the RS-SCED braces are compared. Additionally, the responses of fully-numerical models are used to verify the results obtained from the hybrid simulation.

## **6.1 Previous Hybrid Simulation for Advanced Systems**

Hybrid simulation has been used to evaluate the performance of conventional steel [76]–[79] and RC structures [80]–[82]. This section reviews previous applications of hybrid simulation to study the validity and performance of advanced self-centering structural systems. These systems include advanced braces and dampers as well as self-centering rocking structures. Dynamic testing is performed for systems that are rate-dependent to obtain realistic information on their performance, which cannot be reproduced using quasi-static hybrid simulation test methods.

Eatherton and Hajjar [83] validated the performance of a controlled rocking steel braced frame system using hybrid simulation. The tested frame specimen is a three-storey steel braced rocking frame, shown in Figure 6.1. The test frame is designed based on a prototype structure designed for the seismic hazard in Los Angeles, California. The goal of using hybrid simulation in that study is to demonstrate the global performance of the system under dynamic loading introduced to the system through real earthquake ground motion records. Hybrid simulation can simulate the second-order (P-Delta) effects from the gravity loads as well as the influence of the rest of the structure on the behaviour of the rocking frame. The P-Delta effects and the effect of ambient building resistance were modelled analytically in OpenSees and were linked to the experimentally-tested rocking frame using the UI-SimCore interface platform. The frame was subjected to the 1995 Kobe earthquake record to allow for comparison between other tests conducted at the E-Defense shake table test facility in Japan. Figure 6.1 shows a schematic representation of the hybrid simulation test setup. Results demonstrated the hybrid simulation was able to validate seismic performance of an innovative steel rocking wall structure.

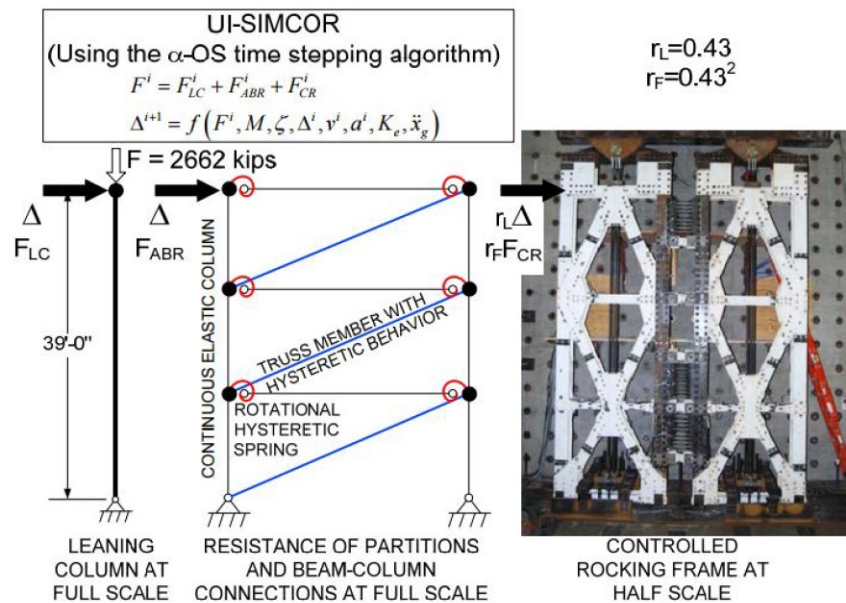


Figure 6.1 Steel rocking frame hybrid test setup [83]

A study by Karavasilis et al. [84] examined the use of large-scale real-time hybrid simulation to evaluate the effectiveness of supplemental damping devices for seismic hazard mitigation. In this study, because the damping devices proposed were rate-dependent, real-time testing was a necessity to accurately capture the performance of the dampers. The dampers were treated as experimental substructures, while the rest of the structure was modelled analytically. The method allowed repeated testing of the structure subjected to different input ground motions without the need to repair the damaged structure after each test. Figure 6.2 shows the analytical and experimental substructures for the real-time hybrid simulation. Real-time hybrid simulation proved to be an effective tool in analyzing the effects of the dampers on the peak floor velocities, floor accelerations, and floor spectra accelerations, something that could not be feasibly achieved without testing a full-scale structure on a shaking table, which would be time consuming and expensive.

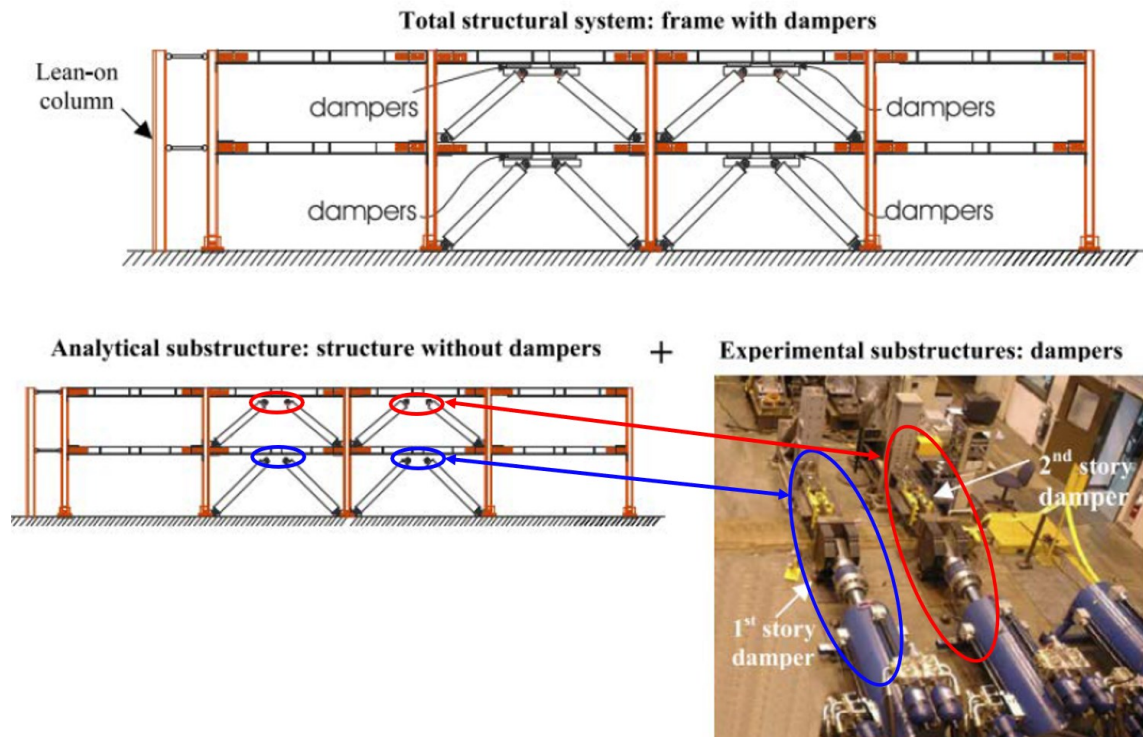


Figure 6.2 Damping devices real-time hybrid test setup [84]

Another advanced structural bracing system was studied by Kammula et al. [49] using the pseudo-dynamic test method. The study focused on a self-centering energy dissipative (SCED) brace developed to reduce residual drifts in steel structures following an earthquake and discussed in Section 2.6. A single T-SCED brace (see Section 2.6) in a steel frame formed the experimental substructure while the remaining 6-storey prototype structure was modelled analytically in the finite element software OpenSees. Figure 6.3 shows the analytical and experimental substructure used in the hybrid simulation for this study. The interface platform UI-SimCor developed by Kwon et al. [85] was used to connect the analytical and experimental substructures. Ultimately, hybrid simulation was shown to be a very effective tool in assessing the seismic performance of the SCED brace, allowing over 30 ground motions to be applied to the physical and analytical substructures. Given the number of tests that could be conducted on the physical specimen, results of the study were also used to develop seismic fragility functions of a structural system with SCED braces, demonstrating another unique capability of the hybrid simulation technique [49].

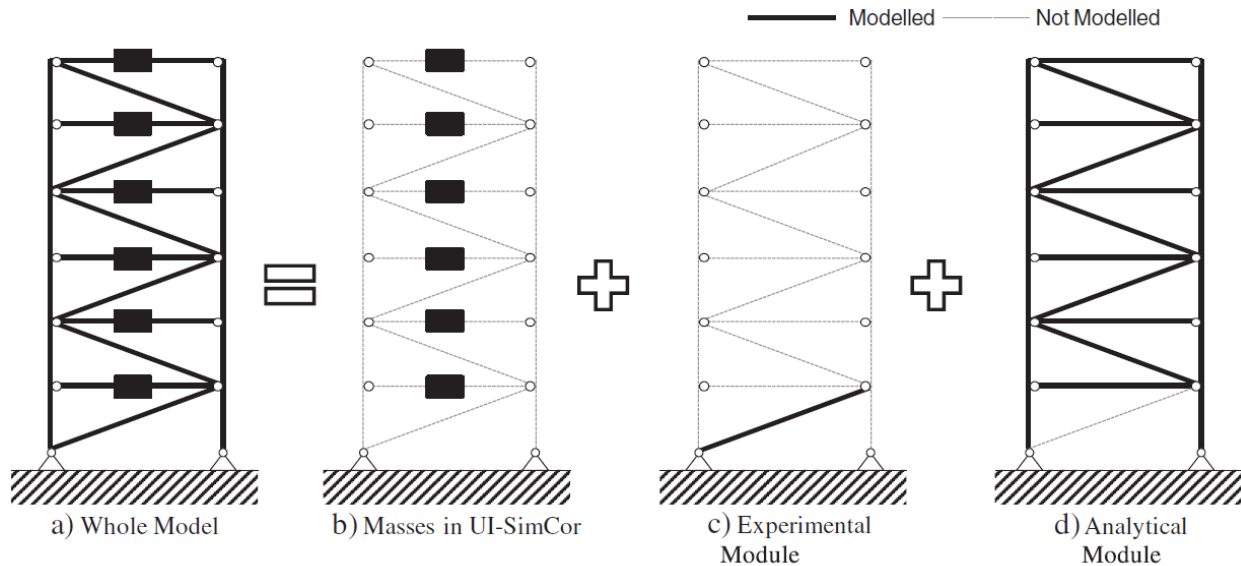


Figure 6.3 Model substructuring for hybrid simulation of SCED brace building [49]

## 6.2 Model Updating

In hybrid simulation studies, the modelled structures consist of many structural elements that form the seismic force resisting system (SFRS). For example, multi-storey braced buildings or multi-span bridges consist of several structural elements that collectively influence the global response of the structure. Because structural testing facilities have a limited quantity of testing equipment, only a few of the structural elements can be physically-represented in hybrid simulation as part of the experimental substructure. For example, only one element was physically represented out of nine [86], six [49], and three [87] main energy dissipation or lateral load resisting elements in previous studies. The largest number of physically represented elements, was three magneto-rheological dampers used in a three-storey structure simulation [88]. Hence, often times in PSD hybrid simulations, some of the elements in the seismic force-resisting system have to be part of the numerical substructure. This can only be avoided if there is enough number of actuators and specimens, which often times can be challenging.

With this limitation, a researcher has to determine which element is most appropriate for experimental testing while the remaining elements are analytically modelled. Often the most critical structural element should be tested since it would affect the most the response of the rest of the structure. In a multi-storey building, that would usually be an element at the base of the structure. With the approach that only the most critical nonlinear elements among a group of nonlinear components is physically tested, while the others are modelled numerically, there is a need for a procedure to improve the accuracy of the modelling of the nonlinear components in the numerical substructure based on the response and performance characteristic information of the test substructure obtained during the test in order to achieve the most accurate result in the system response of the entire structure.

To improve the accuracy of the numerically-modeled elements, a technique known as model updating was introduced. In model updating, the response of the experimentally-tested component is used to improve the accuracy of the numerical substructure. There are two main methods used for model updating.

In the first method, the elements modelled in the numerical substructure are assigned one material model with a number of parameters before the start of the simulation. The parameters of the material model are updated during the test at each step based on the results obtained from the experimental component. This method has the drawback of needing an accurate numerical material model before the start of the hybrid simulation, which can be a challenging task. Some of the model updating studies that used this method were presented by Hashemi et al. [89] and Shao et al. [90].

The second method is the one presented by Kwon [91] and shown in Figure 6.4 below. In this method, a predetermined number of numerical material models are chosen before the start of hybrid simulation. During the test, the experimental substructure results are used to calibrate proper weighting factors to each of the predetermined material models. The weighting factors are used to determine the weighted average for the numerical substructure material model. Like the first method, this method has a number of limitations including the high computational demands when there are a large number of parameters, making it inappropriate for real time hybrid simulation. Also, the accuracy of the model updating is dependant on proper choice of analytical models in advance of the hybrid simulation. Since model updating in hybrid simulation is still a research area in early stages of active development, it was considered but was not implemented in this study.

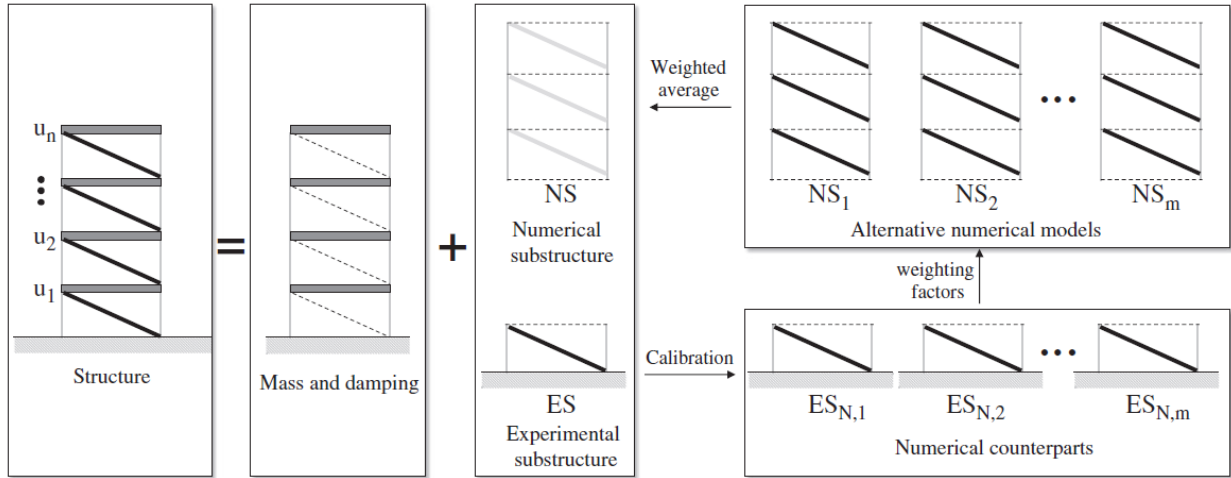


Figure 6.4 Substructure modules for model updating [91]

### 6.3 Hybrid Simulation Architecture and Interface

During the hybrid testing phase of this study, MTS computer simulation interface (MTS Csi), which runs inside the MTS 793 control software, is used to couple the numerical and experimental subassemblies in the laboratory. MTS Csi provides a programming interface for users to connect an MTS controller and communicate with MTS hardware through the MTS Csi application programming interface (API) [92]. MTS Csi maps specific DOFs in the hybrid model to specific control channels in MTS 793 and has a built-in predictor corrector. The predictor corrector ensures the brace is continuously loaded during the hybrid tests especially in between numerical steps. Figure 6.5 shows the complete architecture of hybrid simulation setup at Carleton University. Details of the hybrid simulation setup at Carleton University can be found in the reference by Woods [75].



system in the north-south (N-S) direction consists of four SCED braced frames located along the edges of the building as shown in Figure 6.6. The elevation view of the building is shown in Figure 6.7. A response modification coefficient factor  $R$  of 7 is used for the RS-SCED system, this is determined to be appropriate based on an extensive analytical study that utilizes the FEMA P695 methodology, which is discussed at length in Chapter 7.

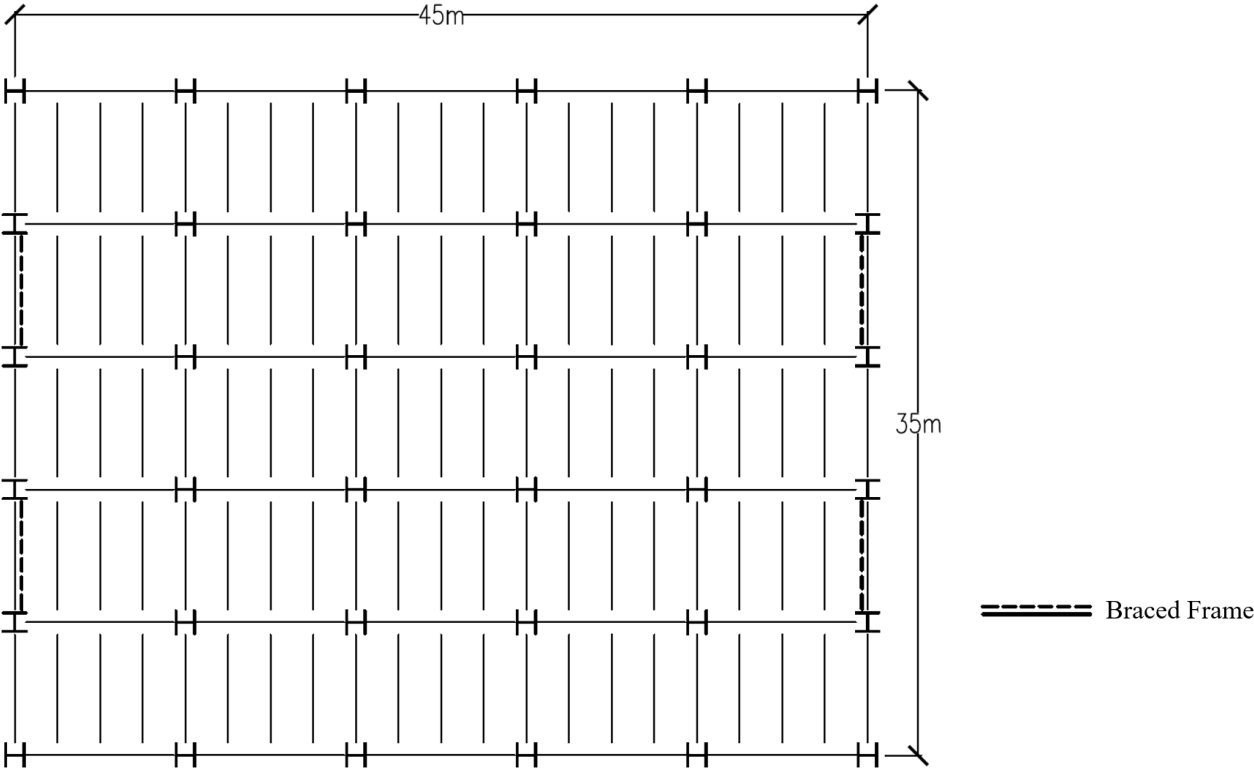
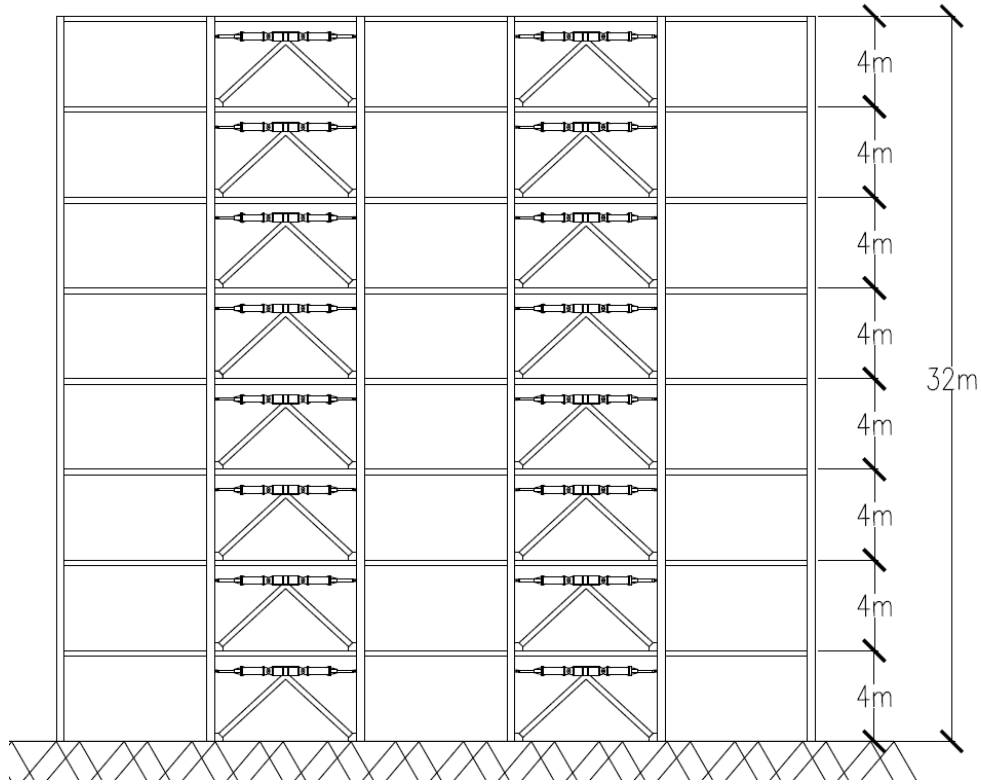


Figure 6.6 Plan view of prototype building used for the hybrid simulation



**Figure 6.7 Elevation view of a braced frame of the building**

For this study, the modelled structure response in the north-south direction is examined. In this direction, lateral loads are resisted by the RS-SCED braced frames located at the perimeter of the building. Beam-column connections are assumed to be pins in the design. Considering the symmetry of the structure, the effects of torsion are neglected both in design and analysis. Lateral loads are equally distributed between the four braced frames, allowing for a 2D analysis of each frame to be performed in lieu of three-dimensional analysis. Figure 6.8 illustrates the analytical model used for modelling a portion of the building, highlighted in Figure 6.9, using OpenSees. A leaning column is used to account for the P-Delta effects and is loaded vertically with the gravity loads from the tributary area equivalent to 1/4 of the building, minus the tributary weight that is directly supported by the braced frame. Accordingly, 1/4 the mass per floor is added to the nodes of the leaning column. The masses are assumed to be lumped at the floor levels. The mass is not to be confused with the weight of the structure as the mass accounts for the inertia effect in the

modal and time history analysis of the structure while the gravity load is necessary for accurately modelling the P-Delta effects on the structure response.

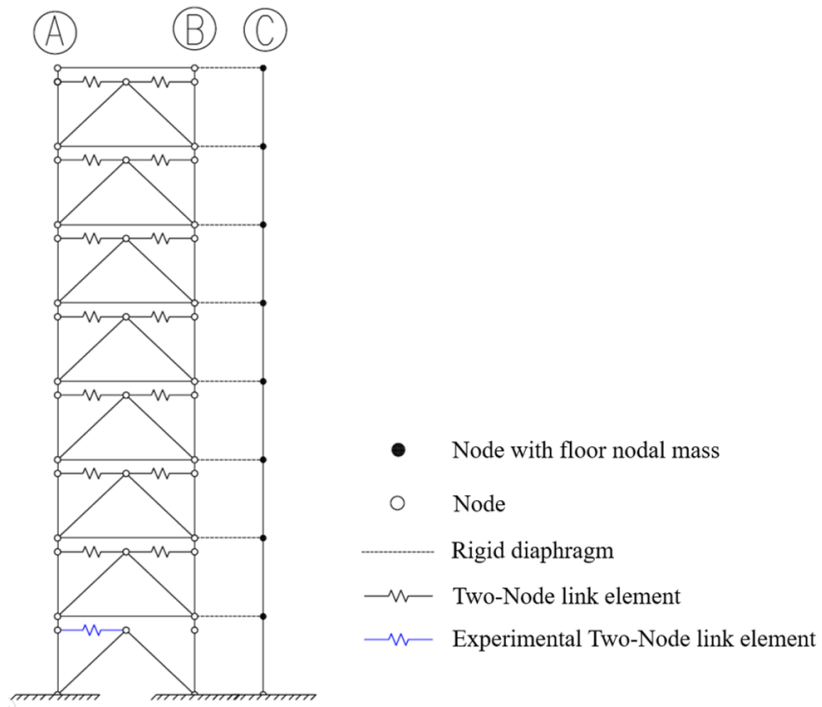


**Figure 6.8 Analytical model used for the hybrid simulation of the 8-storey building**

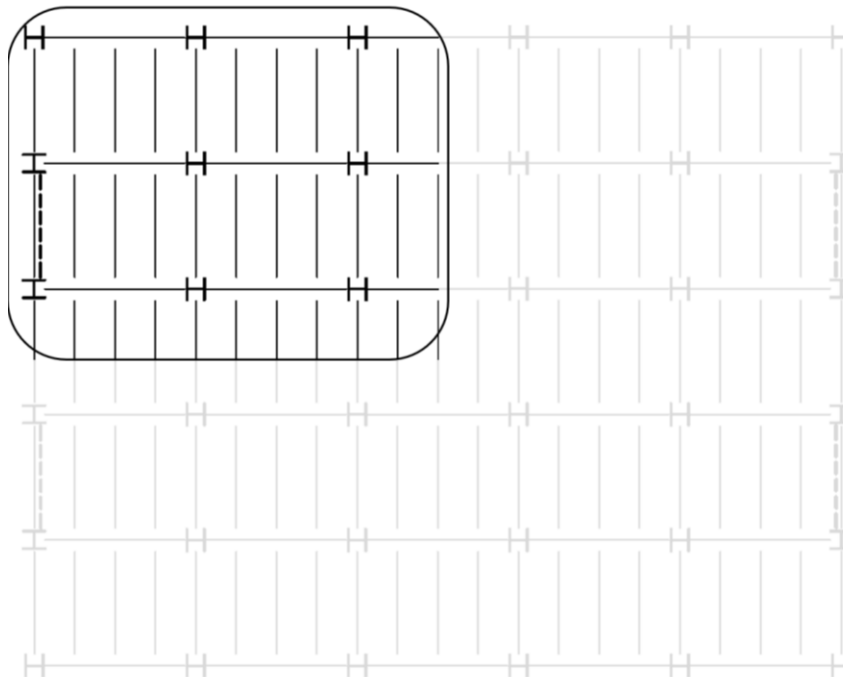


**Figure 6.9 Section of the building analytically modelled**

The leaning columns are connected to the main frame using rigid diaphragm constraints at each floor. The rigid diaphragm is modelled by constraining the horizontal displacement of all nodes for a given floor to the first node of that floor. In this hybrid simulation, the RS-SCED braces of the first floor SCED braced frame is experimentally tested in the physical substructure while the rest of the structure is analytically modeled in the numerical substructure. To link the analytical and experimental substructures, the interface software OpenFresco is used. An experimental Two-Node link element in OpenFresco is used to model the experimentally-tested RS-SCED brace in the first floor. Two-Node link elements with a special ring spring material model are used to model the RS-SCED braces at the floors above the first floor in OpenSees. The material model for the ring springs is written by the author and is a modified version of the original Self-Centering Material model developed by Erochko [93].

For comparison, an identical 8-storey structure is designed with BRBs. The design, loading, and member selection for this structure are presented in Appendix B. The elevation view of this building is shown in Figure 6.10 . The numerical model of the BRB system includes a leaning column to account for the P-Delta effects similar to the model used for the RS-SCED braced system. The BRBs are modelled using Two-Node link elements with Giuffre-Menegotto-Pinto (Steel02) constitutive material model from the OpenSees material library with a strain hardening ratio of 2%,  $R = 20$ ,  $CR1 = 0.925$  and  $CR2 = 0.15$ . A schematic of the numerical model used to analyze the building with BRB system is shown in Figure 6.11. The numerical analysis results of this structure is compared with the hybrid simulation results to evaluate the performance of the RS-SCED system. Rayleigh mass proportional damping of 2% based on the first and fifth modes is used for both numerical models. The use of initial stiffness proportional damping may produce large errors where large artificial viscous damping forces are generated due to the high initial

stiffness of the brace. These forces are the product of the deformational velocity multiplied by the initial stiffness and by the stiffness proportional damping constant. Therefore, when the damping is based on the initial stiffness, the best approach to avoid these artificial forces is to provide a stiffness proportional damping multiplier of zero for all yielding elements with artificially high initial stiffness [94].

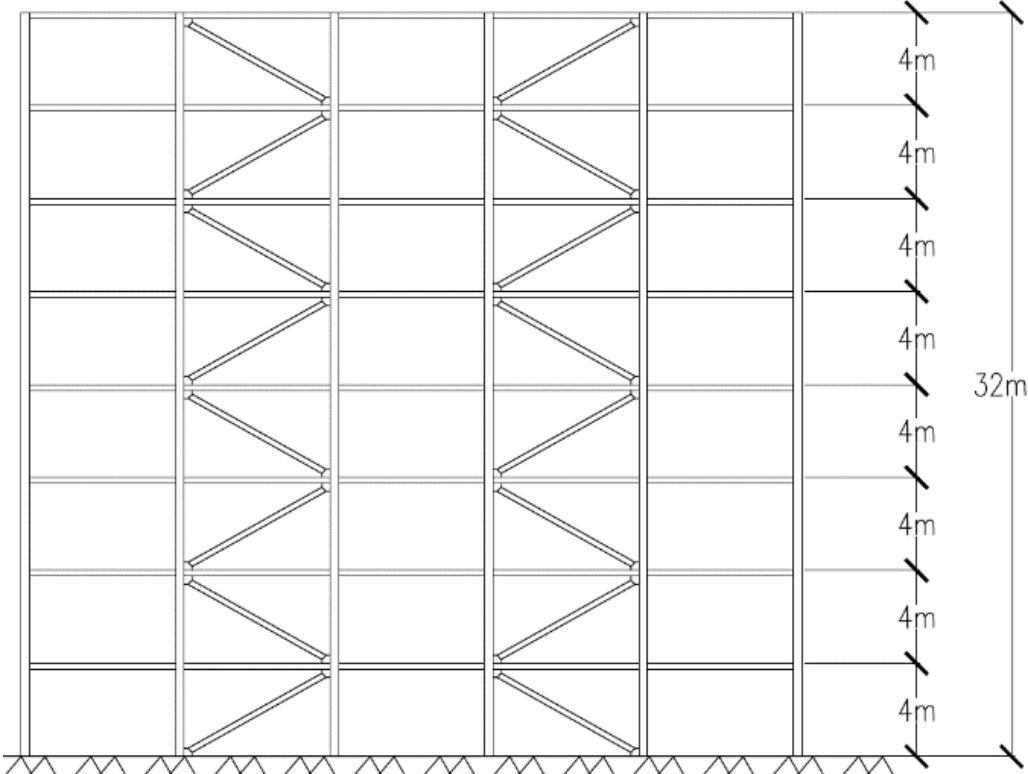


**Figure 6.10 Elevation view of BRB lateral load resisting system**

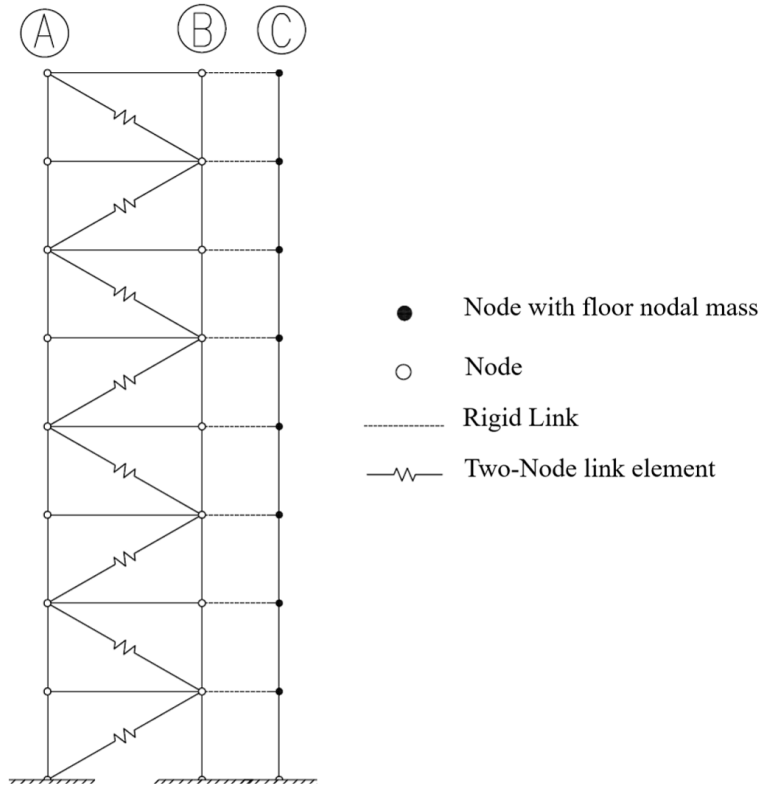


**Figure 6.11 Analytical model of the 8-storey building utilizing an equivalent BRB system**

Since the goal of the hybrid simulation is to evaluate the system level responses of the structures under a range of seismic hazard intensities, the structures are subjected to four different historical earthquake ground motions. These earthquake ground motions are chosen to cover a wide range of frequencies as expressed by the ratio (PHA/PHV) between peak horizontal acceleration (in g) to the peak horizontal velocity (in m/s) as shown in Table 6-1. Among the four earthquake records, one of the records (Chi-Chi) is a near-field record while the other three earthquake records are far-field records. The earthquake records are scaled so that the spectral acceleration at the first period of vibration of the structure ( $T_1 = 1.2$  s) matches or exceeds the response spectrum of the structure at that period for the Maximum Credible Earthquake (MCE) hazard level for Victoria BC. The MCE hazard level corresponds to a 2% probability of exceedance in a 50-year period. To examine the response of the structure at lower hazard levels, the earthquake records are also scaled to the Frequently Occurring Earthquake (FOE) and Design Based Earthquake (DBE) hazard levels; these

seismic hazards correspond to a 50% and 10% probability of exceedance in 50-years, respectively.

Figure 6.12 to Figure 6.15 show the scaled earthquake ground accelerations, as well as the response spectrum of the scaled records.

**Table 6-1 Unscaled earthquake record data and scaling intensity used for the hybrid simulation study**

Earthquake record	Intensity (Location)	PGA (g)	PGV (m/s)	PGA/PGV (g.s/m)	NF or FF
Northridge: Canyon Country-WLC	FOE, DBE & MCE (Victoria, Canada)	0.48	0.45	1.067	FF
Kobe: Shin-Osaka	FOE, DBE & MCE (Victoria, Canada)	0.24	0.38	0.632	FF
Loma Prieta: Capitola	FOE, DBE & MCE (Victoria, Canada)	0.53	0.35	1.514	FF
ChiChi: TCU 067	DBE & MCE (Victoria, Canada)	0.29	0.29	0.272	NF

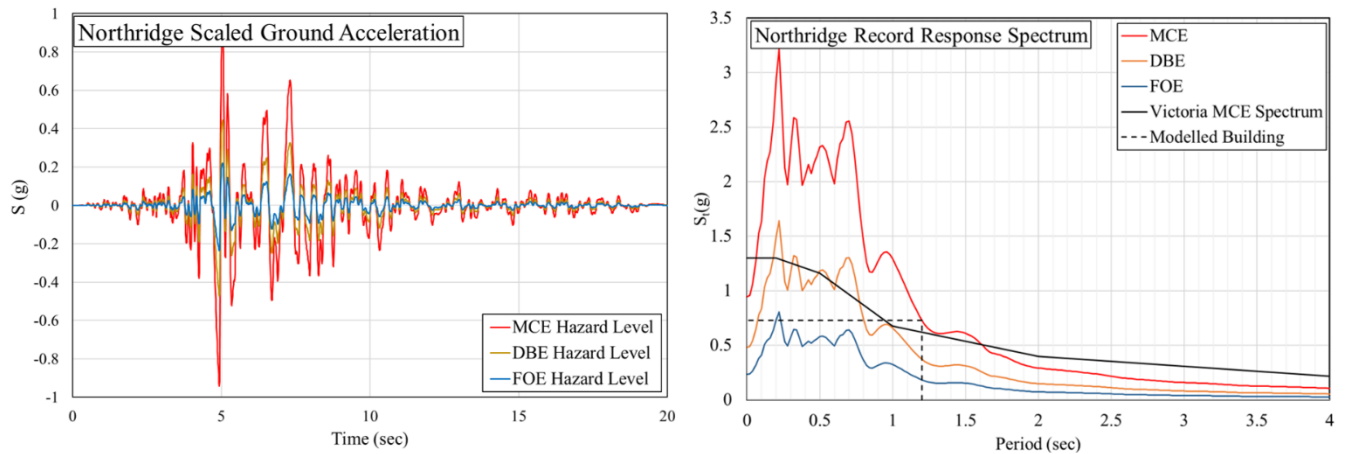


**Figure 6.12 Northridge earthquake record**

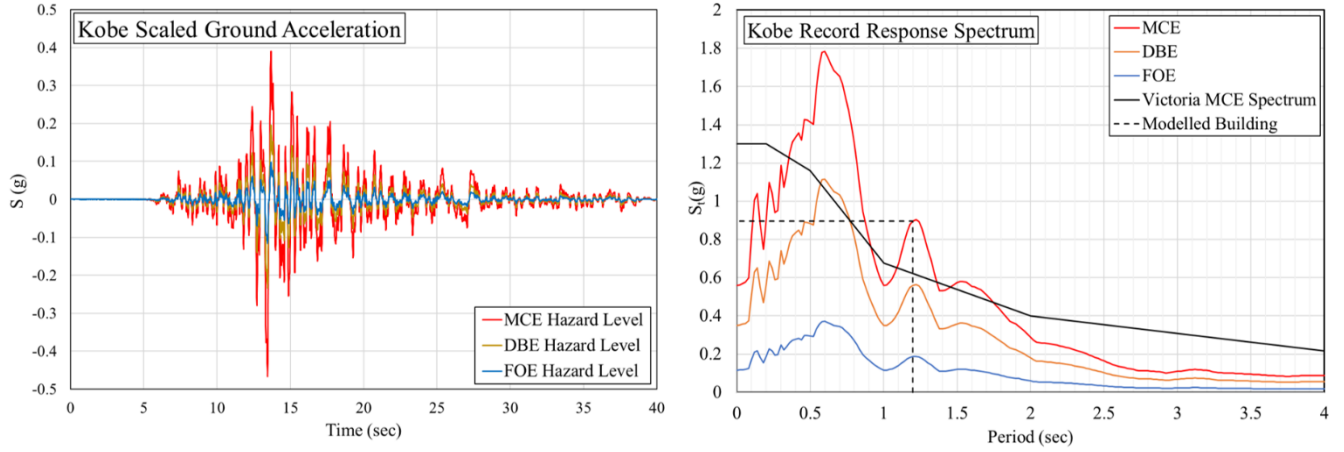


Figure 6.13 Kobe earthquake record

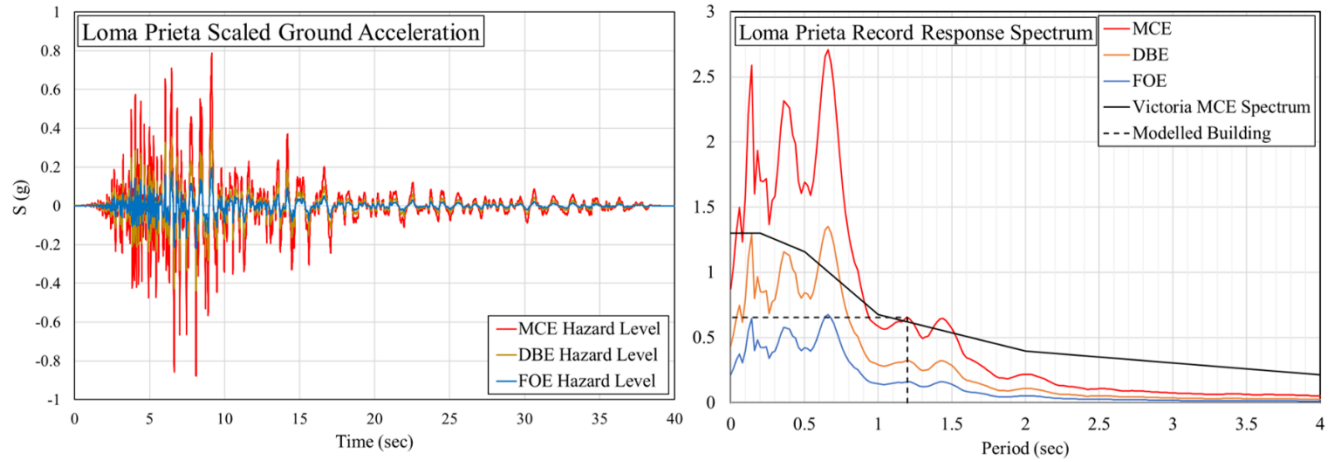


Figure 6.14 Loma Prieta earthquake record

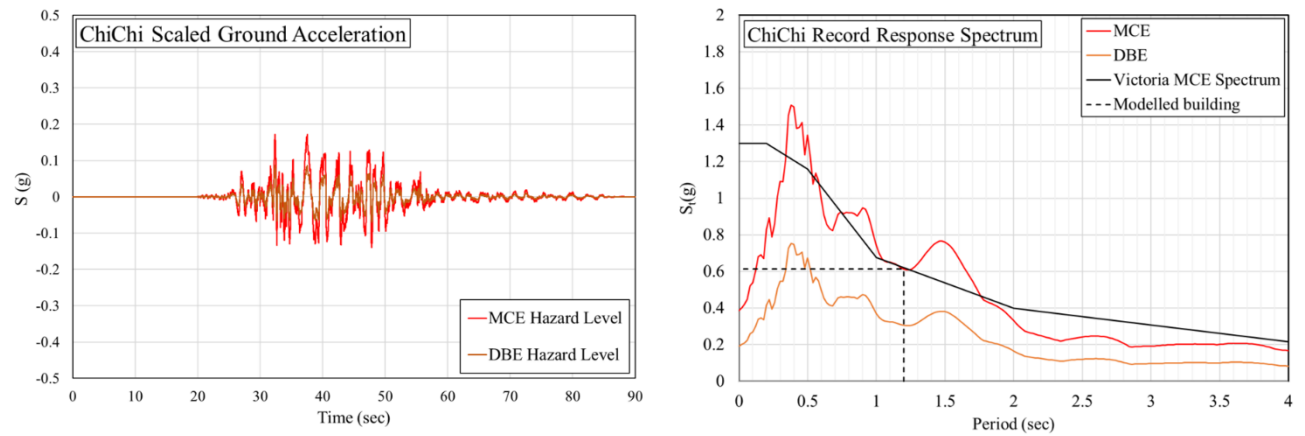


Figure 6.15 ChiChi earthquake record

## 6.5 Comparison of Hybrid Simulation and Fully Analytical Model

To evaluate the effectiveness of the numerical model in predicting the non-linear seismic response of a multi-storey building utilizing RS-SCED braces as the SFRS, this section compares the full-scale hybrid test results with the results from a fully-analytical finite element model. To compare the result of both systems, four different response parameters were evaluated at different hazard levels. The four response parameters chosen are the maximum first floor drift  $\Delta_1/h_s$ , the maximum first floor residual drift  $\Delta_{r1}/h_s$ , the maximum floor acceleration of the first floor  $a_{f1}$ , and the maximum roof drift  $\Delta_{roof}/h_{total}$ .

Table 6-2 summarizes the results obtained from the hybrid simulations and fully-analytical model for the 8-storey structure subjected to the Northridge, Kobe and Loma Prieta records at the frequently occurring earthquake (FOE) hazard level. The FOE hazard level is defined as the earthquake hazard with a 50% probability of occurrence in 50 years. The results show a good correlation between the analytical and the hybrid simulation results for all 4 parameters considered. For both the hybrid simulation and analytical modelling responses, the maximum inter-storey drift at the first-floor level is very low (less than 0.5%) with almost no residual drift of the structure subjected to all earthquake records. The structures also experienced a large first floor acceleration  $a_f$  for all three records. The high floor acceleration is the result of the high initial stiffness of the RS-SCED braces. The roof drift level is comparable in magnitude to the low first floor drift level.

**Table 6-2 Summary of results under 50% in 50 year hazard level**

Earthquake record at FOE hazard level	Northridge		Kobe		Loma Prieta	
	Hybrid Test	Analytical Model	Hybrid Test	Analytical Model	Hybrid Test	Analytical Model
$\Delta_1/h_s$	0.40%	0.38%	0.17%	0.18%	0.25%	0.22%
$\Delta_{r1}/h_s$	0.02%	0.03%	0.06%	0.00%	0.05%	0.01%
$a_{f1}$	0.52	0.51	0.40	0.41	0.53	0.68
$\Delta_{roof}/h_{total}$	0.34%	0.32%	0.45%	0.42%	0.31%	0.31%

Table 6-3 summarizes the analytical and hybrid simulation response for the 8-storey building structure subjected to the 4 records including the near field Chi-Chi record at the design base earthquake (DBE) hazard level. Once again, the analytical and hybrid simulation results showed great correlation for the maximum values recorded for all four response parameters under consideration. As expected, the structure experienced a higher inter-storey and roof drift compared to the earthquake records scaled to the FOE hazard level. There was a slightly higher residual drift observed compared to the FOE level, however, the maximum residual drift level did not exceed 0.1% for any of the records, maintaining the structure’s self-centering ability. The maximum floor acceleration recorded for the structure is higher than the accelerations recorded under the FOE hazard level due to the higher applied acceleration at the ground level.

**Table 6-3 Summary of results under 10% in 50 year hazard level**

Earthquake record at DBE hazard level	Northridge		Kobe		Loma Prieta		Chi-Chi	
	Hybrid Test	Analytical Model						
$\Delta_1/h_s$	1.09%	1.18%	0.81%	0.74%	0.57%	0.56%	0.51%	0.52%
$\Delta_{r1}/h_s$	0.06%	0.05%	0.09%	0.02%	0.08%	0.02%	0.01%	0.00%
$a_{f1}$	0.74	0.93	0.70	0.70	0.72	0.86	0.37	0.49
$\Delta_{roof}/h_{total}$	0.79%	0.82%	0.51%	0.52%	0.44%	0.50%	0.69%	0.67%

Table 6-4 summarize the results obtained from the hybrid simulation and fully-analytical model for all 4 records scaled to the maximum credible earthquake (MCE) hazard level, a hazard level associated with a seismic event with a probability of occurrence of 2% in 50 years. At this hazard

level, the results of the hybrid simulation and analytical model results continue to show good correlation for all 4 response parameters. Once again, the maximum inter-storey drift and the roof drift experienced by the structure at this hazard level are shown to be higher than the ones experienced by the structure when subjected to the FOE and DBE scaled records. At this hazard level, the maximum inter-storey drift is comparable to the design drift limit, which indicates that the design method achieved the intended outcome. This is to be expected due to the higher seismic demand on the structure at this hazard level. The residual drift of the structure at this higher seismic hazard level is the highest among all three hazard levels but still the highest residual drift at the first-floor level is only 0.11%. This indicates that the RS-SCED braces can maintain the self-centering capability even at this higher hazard level. The floor acceleration observed for the records scaled to the MCE hazard level is larger than the floor acceleration at the DBE and FOE hazard levels.

**Table 6-4 Summary of results under 2% in 50 year hazard level**

Earthquake record at MCE hazard level	Northridge		Kobe		Loma Prieta		Chi-Chi	
	Hybrid Test	Analytical Model						
$\Delta_1/h_s$	2.40%	2.34%	1.22%	1.17%	1.16%	1.23%	2.34%	2.45%
$\Delta_{r1}/h_s$	0.11%	0.09%	0.02%	0.02%	0.06%	0.01%	0.00%	0.01%
$a_{f1}$	1.10	1.13	1.10	1.10	0.93	1.02	0.60	0.71
$\Delta_{roof}/h_{total}$	1.76%	1.86%	0.71%	0.71%	0.91%	0.91%	1.34%	1.39%

Figure 6.16 to Figure 6.19 show the hysteretic response of the RS-SCED braces in the first floor for all 11 hybrid tests compared to the analytical model. The results show that the analytical model accurately predicts the pre- and post-activation response of the braces while capturing the full flag shape hysteresis of the brace. The activation force, post-activation stiffness, recoil load and decompression load measured in all 11 hybrid tests matched their design values. The major difference between the hybrid simulation and analytical model hysteresis response is the stiffness

transitions that occur each time the ring springs compress or decompress. The actual hysteresis of the RS-SCED braces, measured during the hybrid tests, show that the transition between: a) the initial stiffness to loading stiffness during activation, b) initial stiffness to unloading stiffness at the onset of decompression, and c) from the unloading stiffness back to the initial stiffness at the decompression load level unloading stiffness and initial stiffness during the decompression of the springs, are not sharp corners as assumed in the constitutive material model. This is because the ring springs within the assembly do not lock or unlock all at once but rather progressively start moving relative to each other resulting in a more gradual stiffness transition. This behaviour had been observed in previous studies discussed in Section 3.2. The sharp stiffness transition, used to model the flag shaped hysteretic behaviour of the brace in OpenSees, has been shown to typically result in the upper bound estimates of the acceleration, often resulting in overestimation of the system acceleration [68]. The stiffness transition that has the greatest effect on this overestimation is the transition from the unloading stiffness back to the initial stiffness of the brace which occurs when the applied load decreases to the decompression load.

Although the acceleration response was often accurately predicted as shown in Table 6-2 to Table 6-4, certain models showed the acceleration to be overestimated. This occurred when the structure was subjected to the Loma Prieta and the Chi-Chi earthquake records. The over estimation is attributed to the sharp stiffness transitions observed in the analytical hysteretic response shown in Figure 6.16 to Figure 6.19.

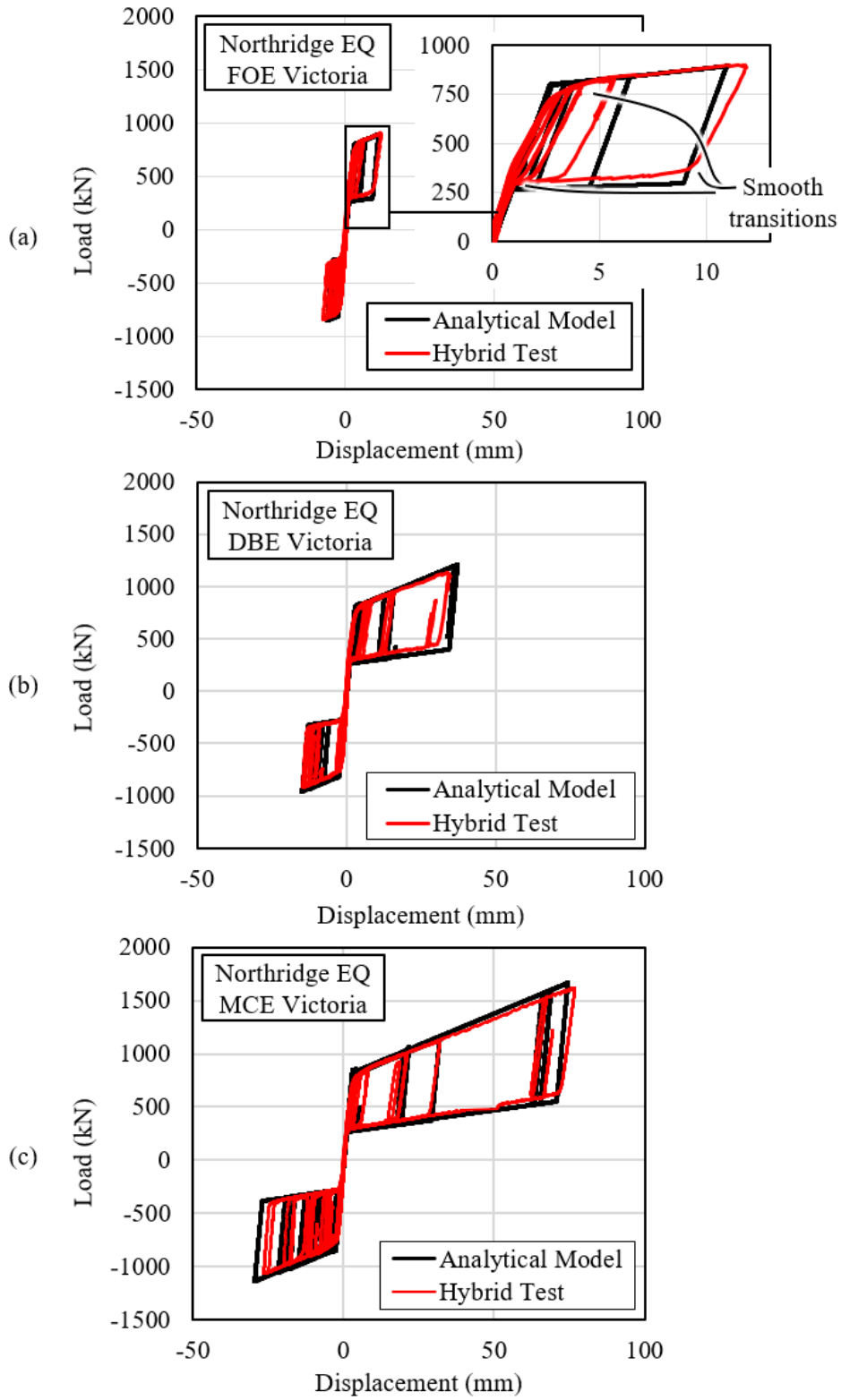
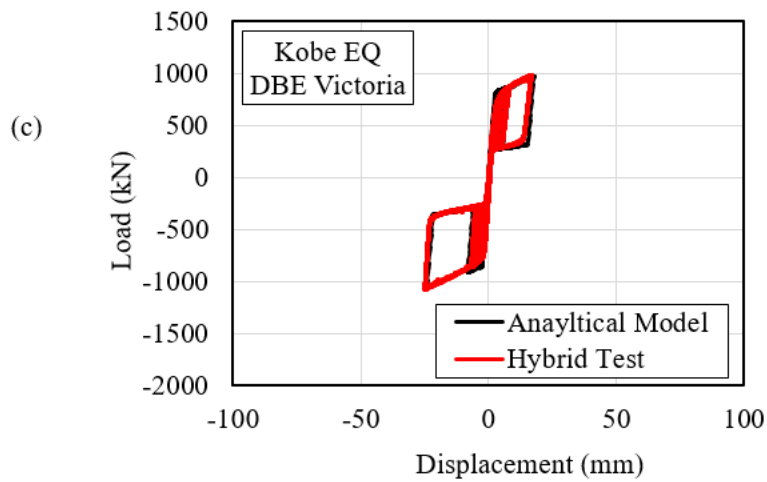
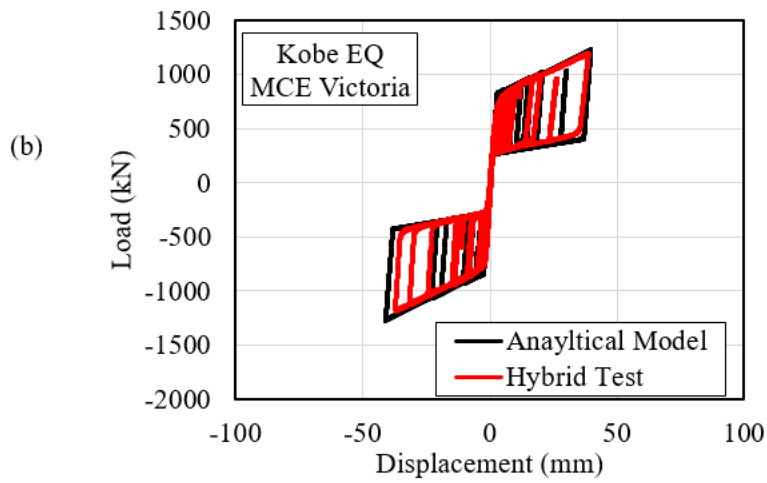
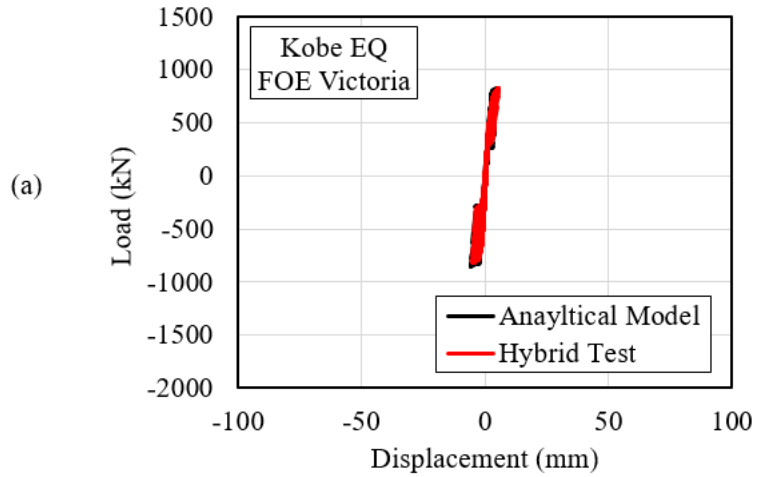


Figure 6.16 Comparison of force-deformation hysteretic response for the Northridge earthquake: (a) FOE, (b) DBE, and (c) MCE hazard levels



**Figure 6.17 Comparison of force-deformation hysteretic response for the Kobe earthquake: (a) FOE, (b) DBE, and (c) MCE hazard levels**

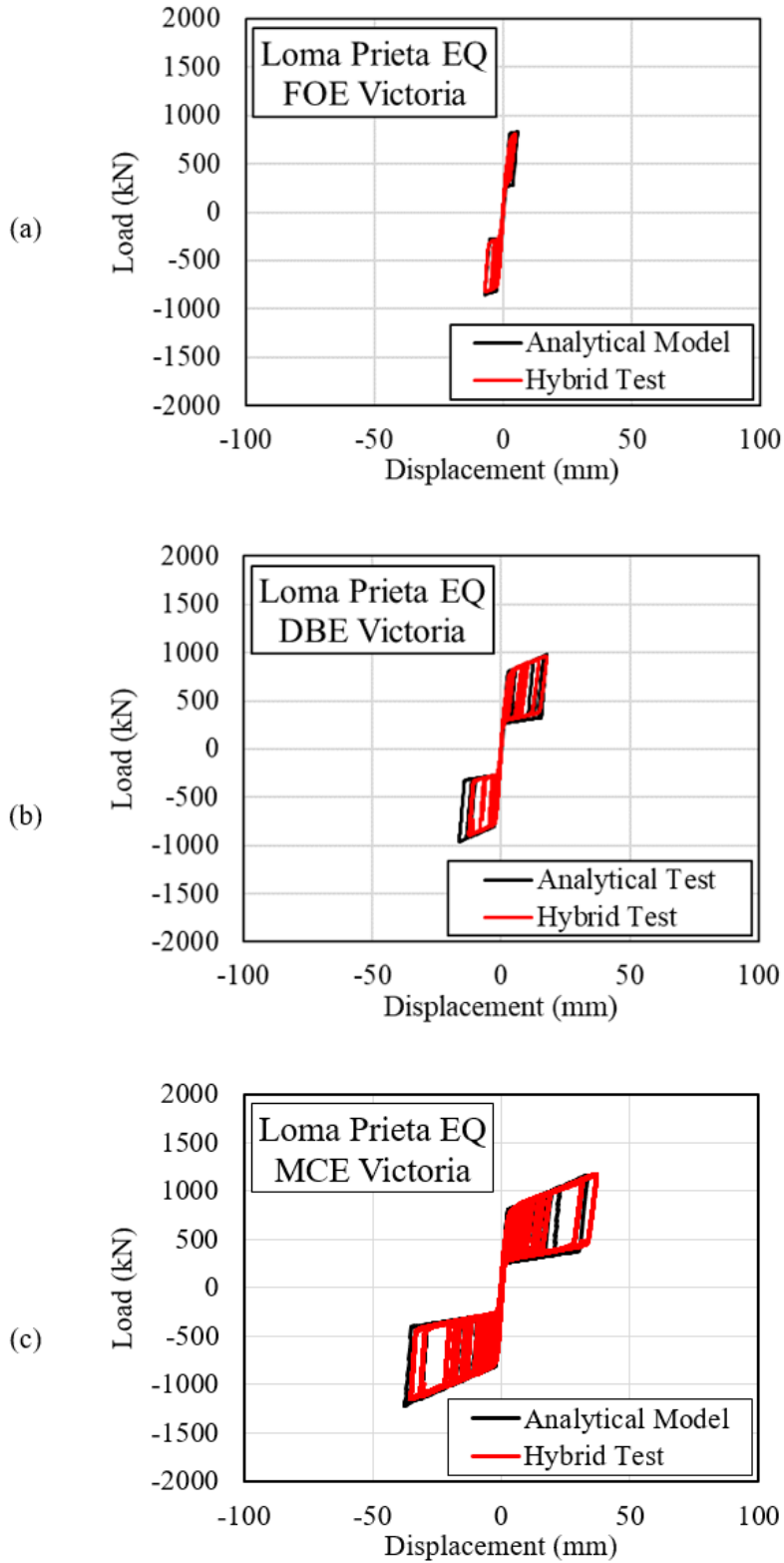
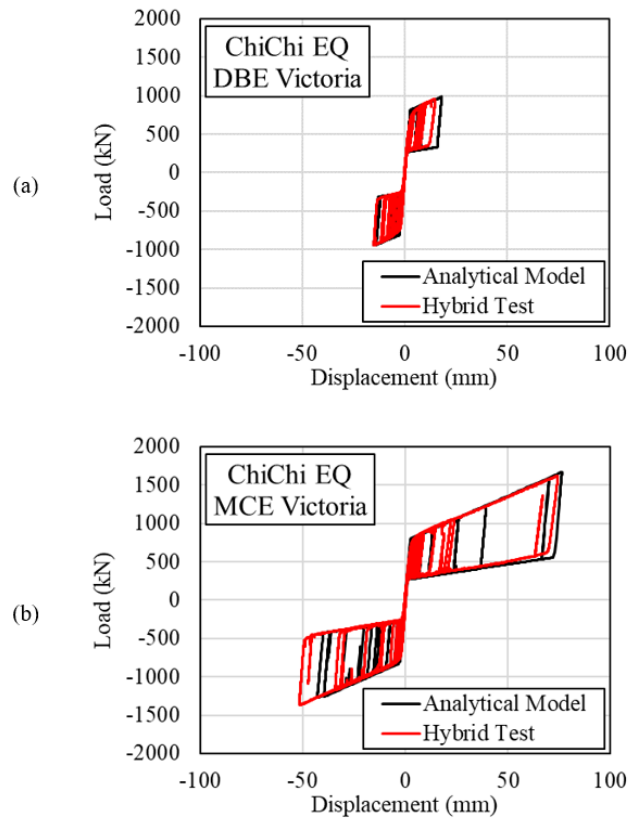


Figure 6.18 Comparison of force-deformation hysteretic response for the Loma Prieta earthquake: (a) FOE, (b) DBE, and (c) MCE hazard levels



**Figure 6.19 Comparison of force-deformation hysteretic response for the ChiChi earthquake: (a) DBE, and (b) MCE hazard levels**

Figure 6.20 to Figure 6.23 show the time history response of the first floor RS-SCED brace deformation obtained from the analytical model and hybrid simulations for all 11 tests conducted on the 8-storey structure. Similar to the hysteretic response, the brace deformation time history response predicted by the analytical model also correlated very well with the brace deformation time history response measured during the hybrid simulation, including at the peak of the responses. Despite having minor discrepancy in the prediction of some of the post peak response, especially under the Chi-Chi record scaled to the MCE hazard level, the analytical model accurately predicted the peak deformation of each response. Overall, the accuracy of the predicted time history of the RS-SCED brace deformation provides evidence to support the effective use of the proposed analytical model to calculate the response of RS-SCED braces under seismic loads.

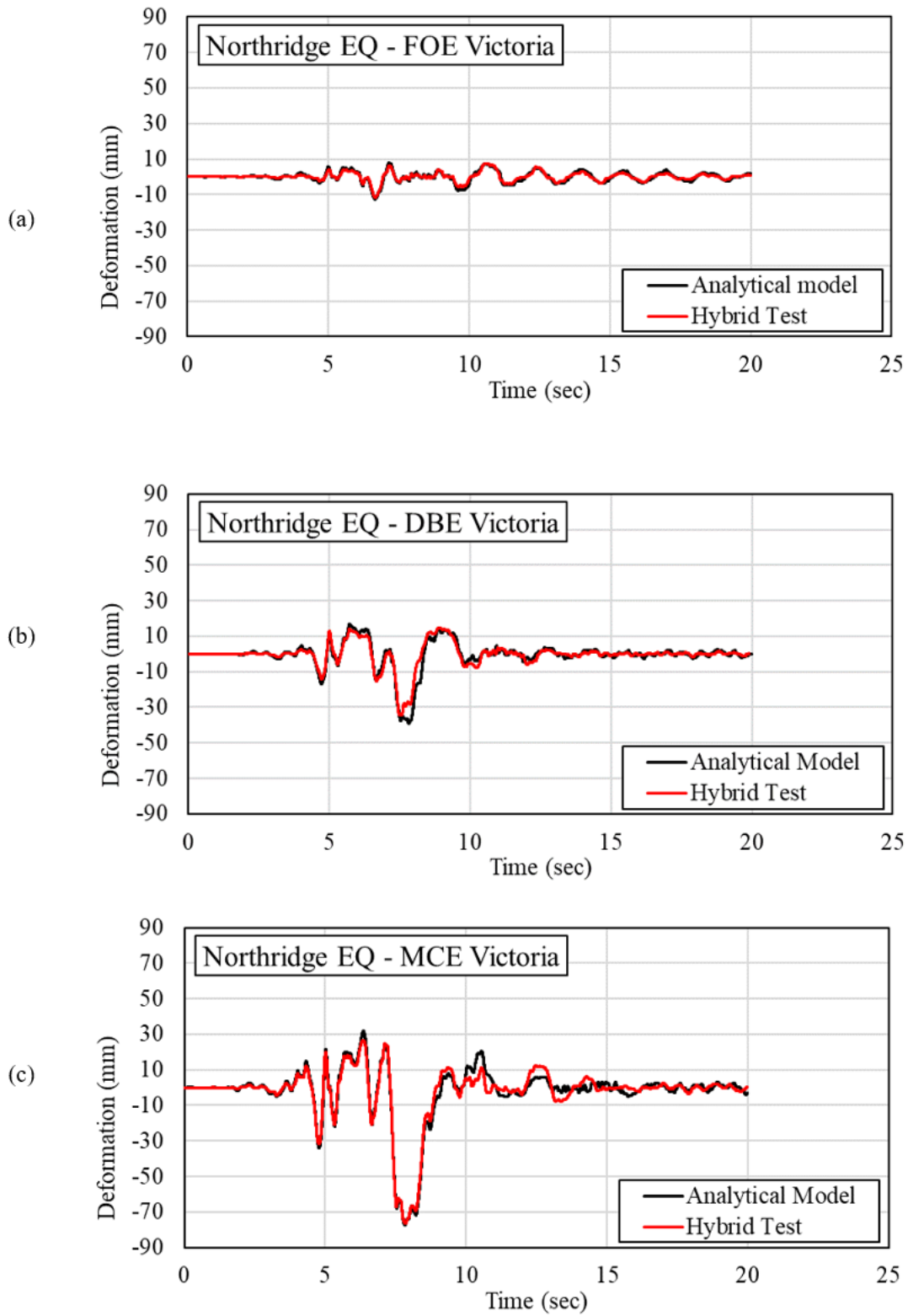


Figure 6.20 Comparison of time-history deformation response of the brace for the Northridge earthquake: (a) FOE, (b) DBE, and (c) MCE hazard levels

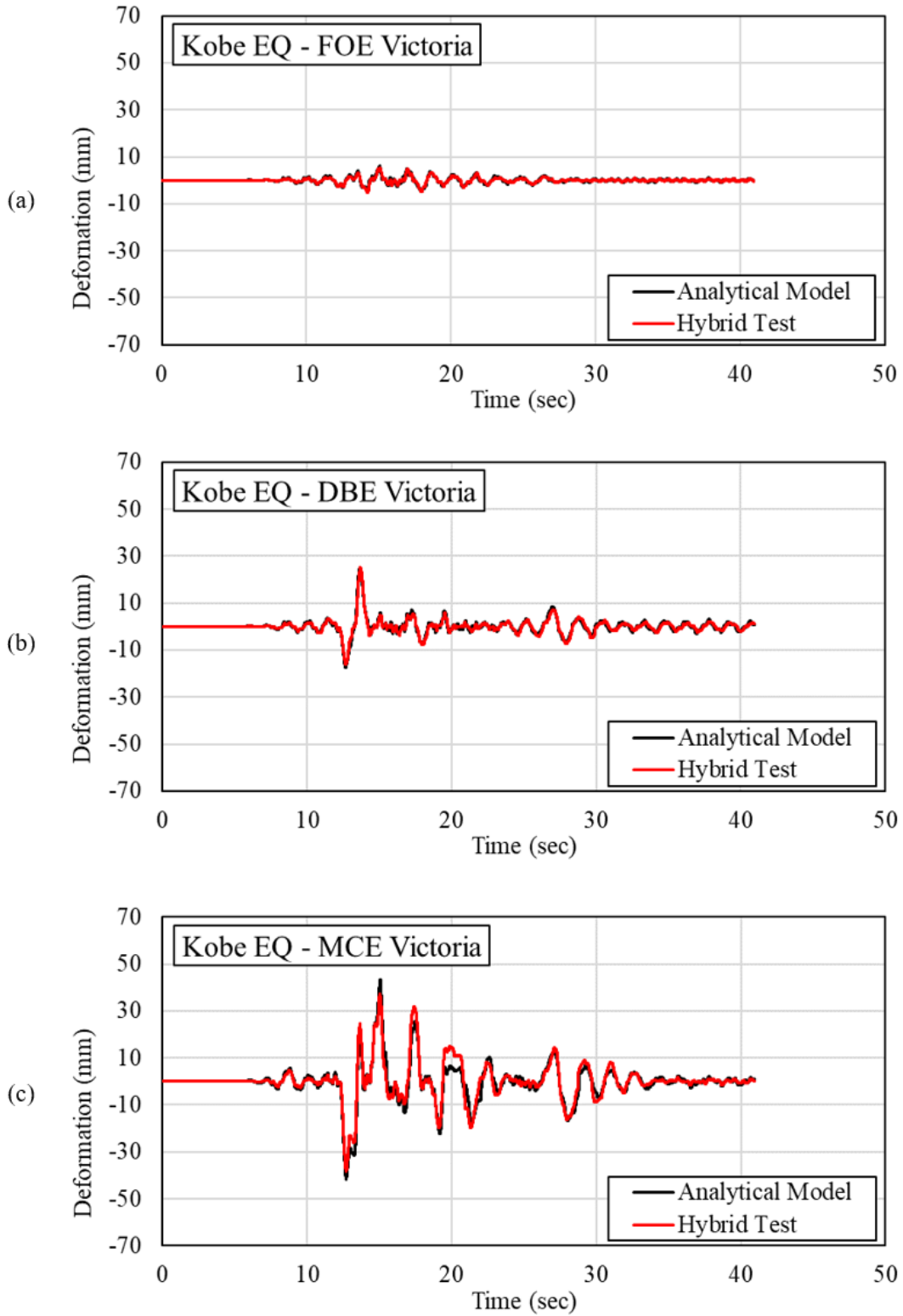


Figure 6.21 Comparison of time-history deformation response of the brace for the Kobe earthquake: (a) FOE, (b) DBE, and (c) MCE hazard levels

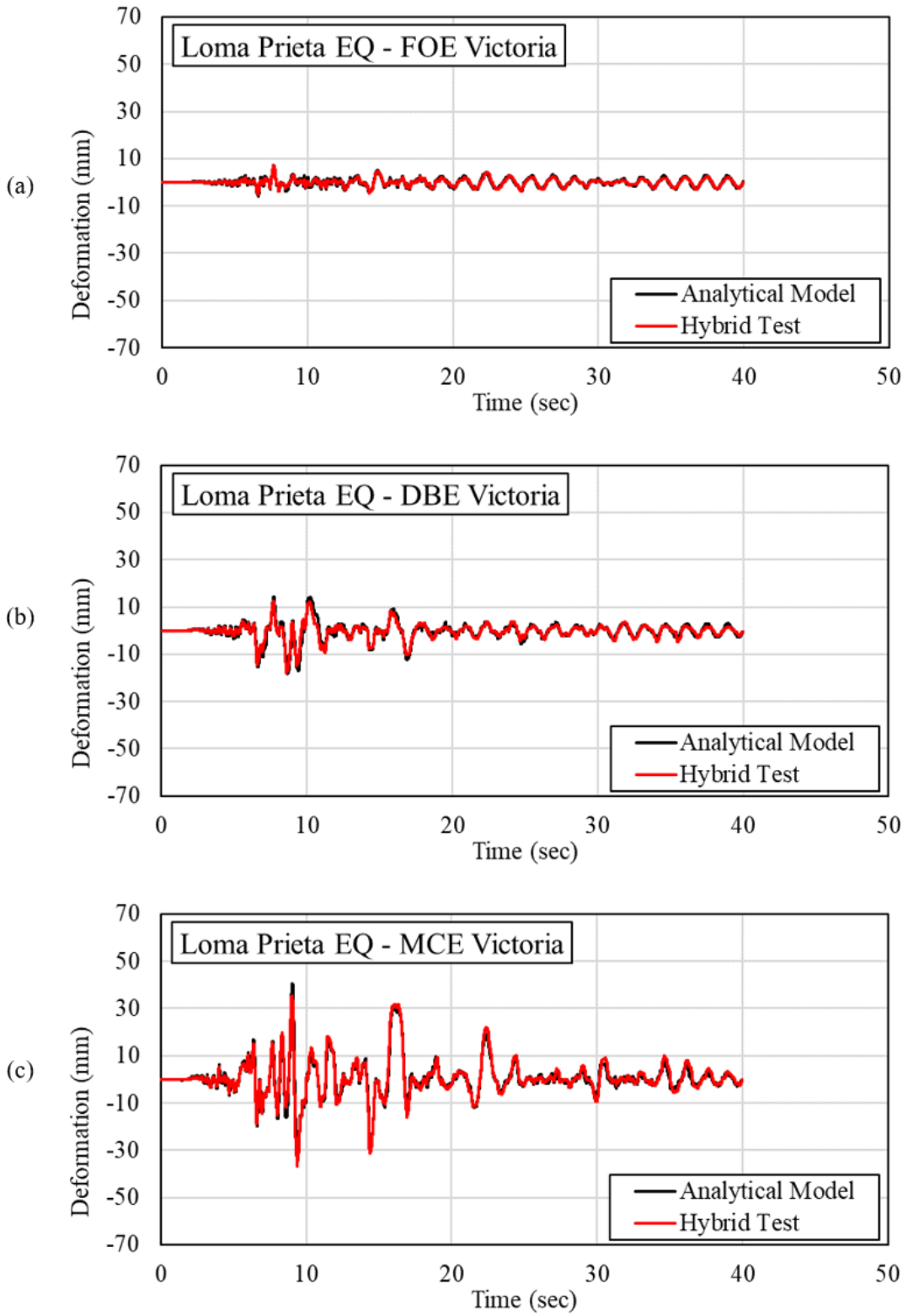
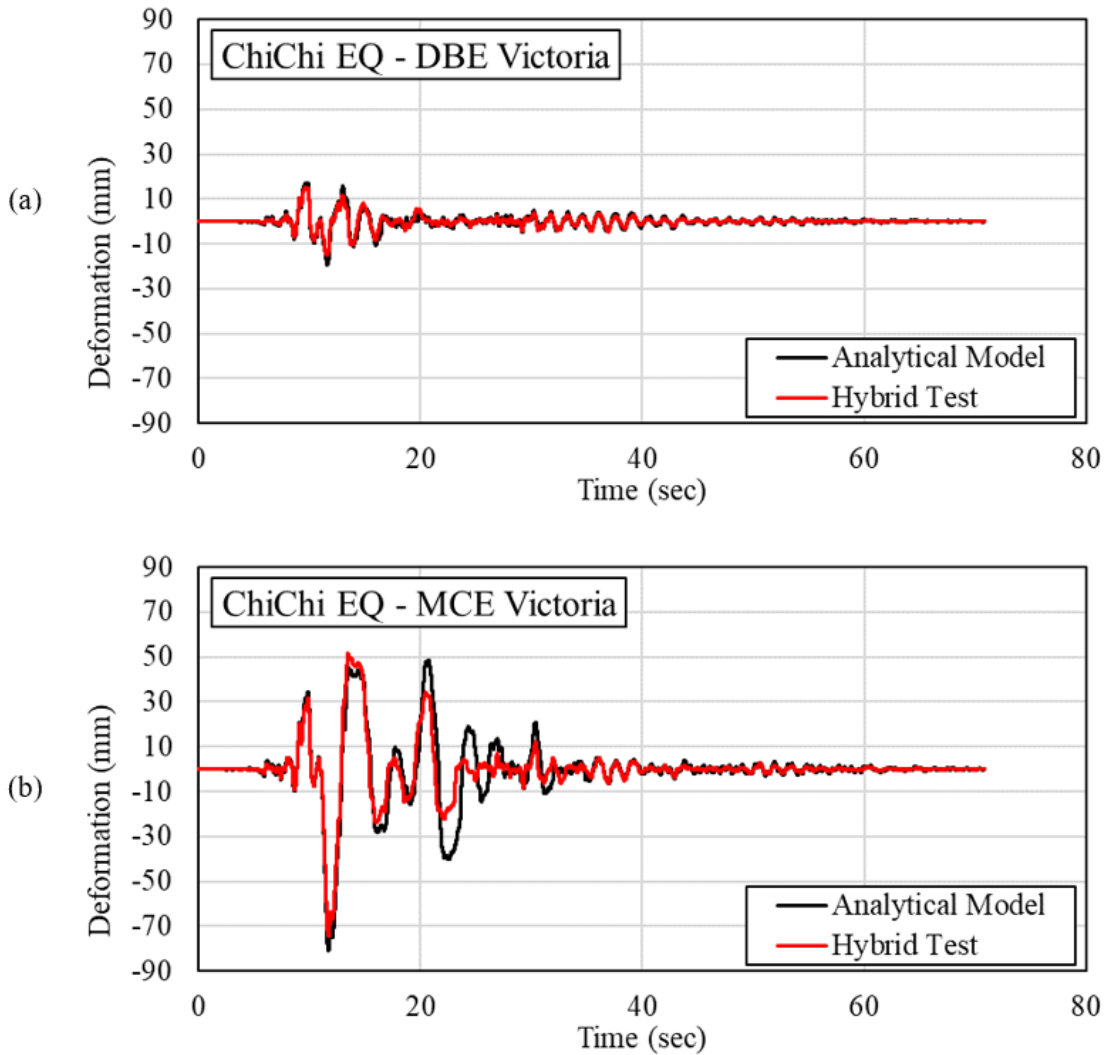


Figure 6.22 Comparison of time-history deformation response of the brace for the Loma Prieta earthquake: (a) FOE, (b) DBE, and (c) MCE hazard levels



**Figure 6.23 Comparison of time-history deformation response of the brace for the ChiChi earthquake: (a) DBE, and (b) MCE hazard levels**

Figure 6.24 to Figure 6.27 present the measured and the calculated roof drift response for the hybrid simulation and the analytical model. The Comparison of the roof drift response provides insight on the effect of the modeling of the RS-SCED braces on predicting the global response of the structural system, which is not possible when the investigation is focused only at the local component level such as the RS-SCED braces at the first floor of the structure. The analytical model shows very good agreement with the hybrid simulation with respect to roof drift. Similar to the first floor RS-SCED brace deformation time-history, the peak of the response was accurately

captured for all 11 tests even when the post peak response was not captured for some of the responses, namely the Northridge and Chi-Chi records scaled to the MCE hazard level. The correlation between the hybrid simulation and the analytical model shows that analytical modelling of the RS-SCED braces at the first-floor level does not negatively affect the prediction of the structure's global response.

Overall, the comparison of the analytical model and hybrid simulation results presented in this section validates the use of the analytical modelling technique proposed in the previous section. In the following section, this numerical model will be used to compare the response of this structure to the response of an equivalent 8-storey BRB braced structure.

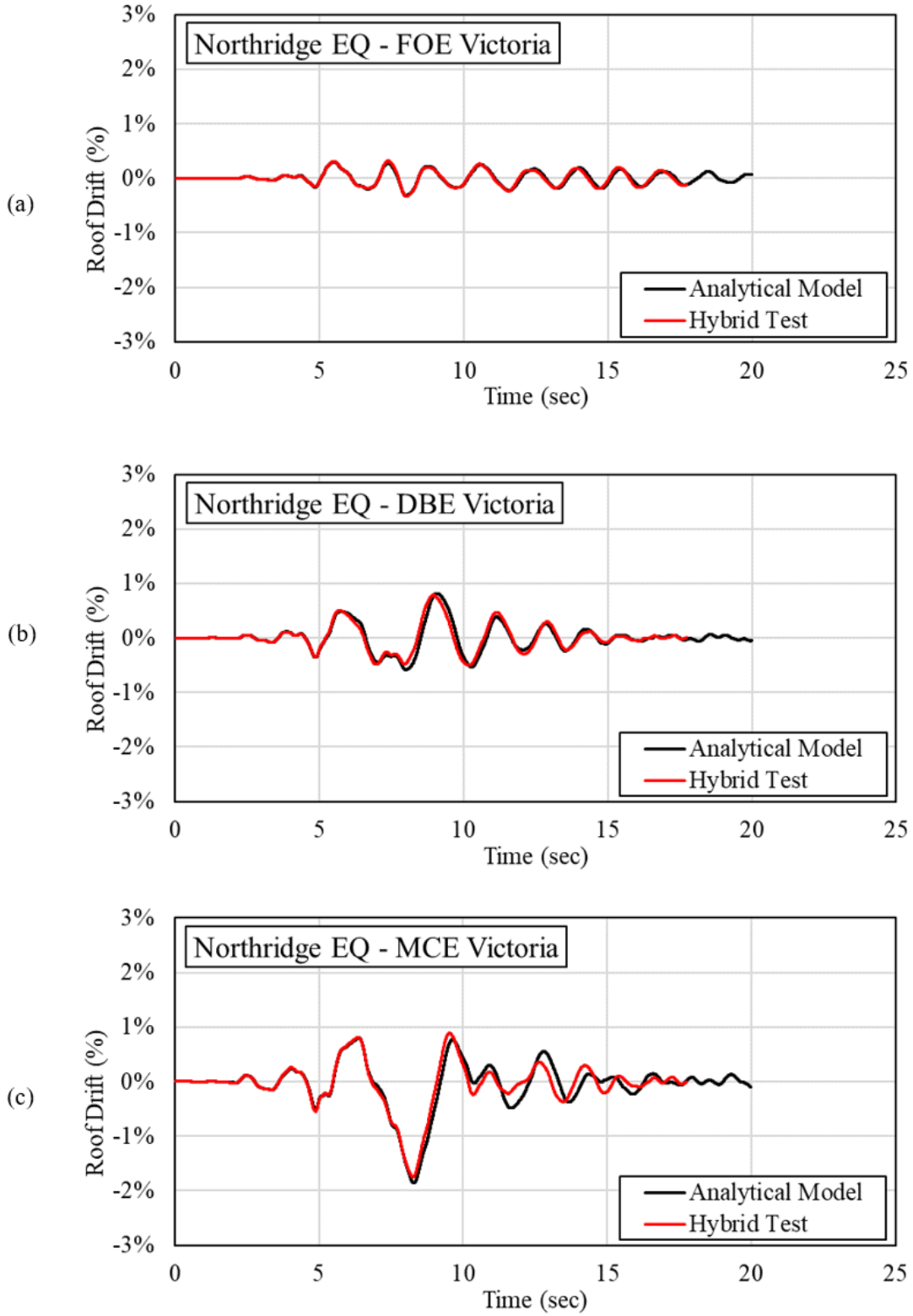


Figure 6.24 Comparison of roof drift of building response for the Northridge earthquake: (a) FOE, (b) DBE, and (c) MCE hazard levels

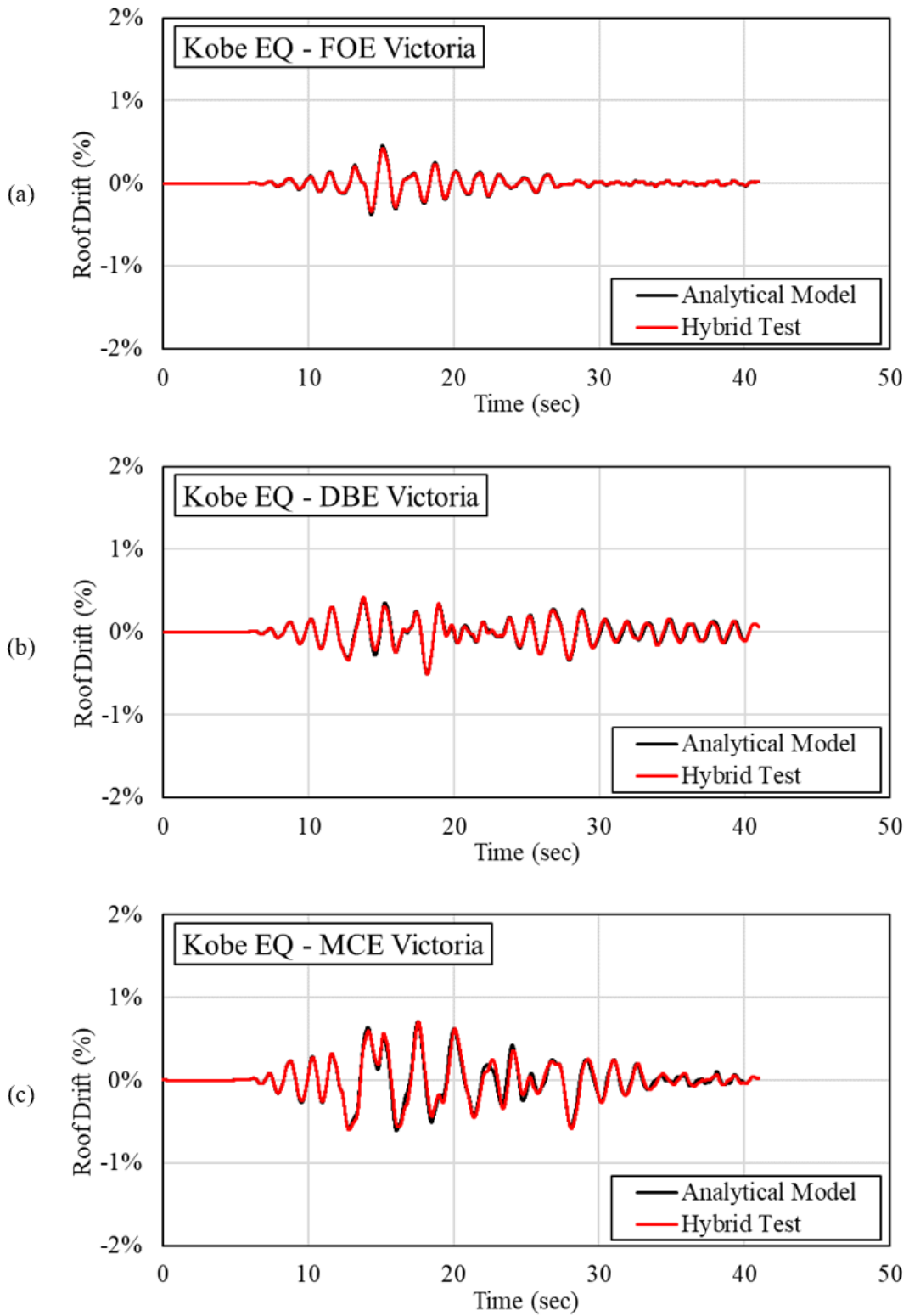


Figure 6.25 Comparison of roof drift of building response for the Kobe earthquake: (a) FOE, (b) DBE, and (c) MCE hazard levels

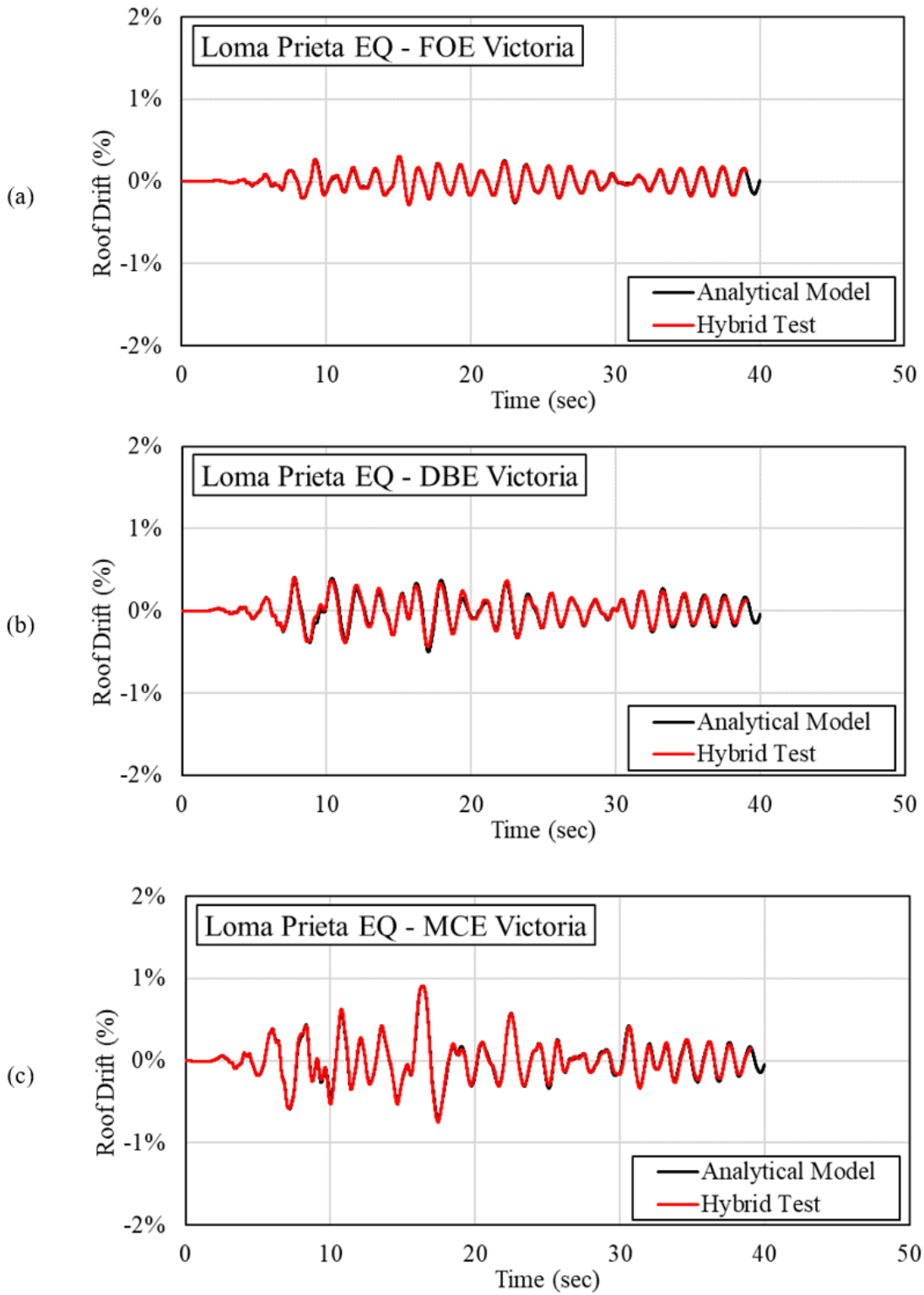
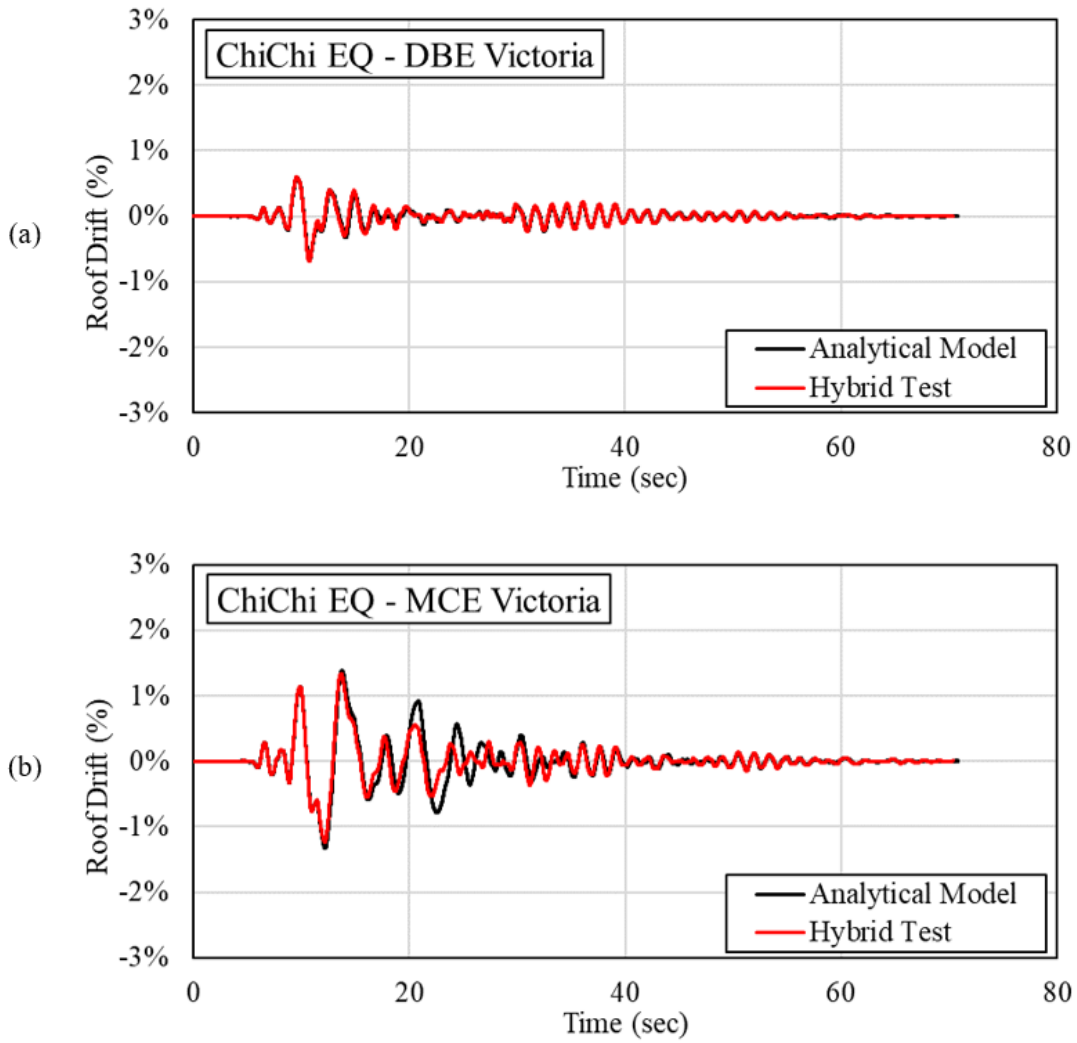


Figure 6.26 Comparison of roof drift of building response for the Loma Prieta earthquake: (a) FOE, (b) DBE, and (c) MCE hazard levels



**Figure 6.27 Comparison of roof drift of building response for the ChiChi earthquake: (a) DBE, and (b) MCE hazard levels**

## 6.6 Comparison of RS-SCED Braced Building to BRB-Braced Building

This section compares the seismic response of two prototype buildings subjected to a suite of 44 ground motion records scaled to the FOE, DBE, and MCE hazard levels. One prototype building is designed with the RS-SCED bracing system, while the second structure is designed with a BRB bracing system with details for both building designs presented in Appendix B. A comparison of their response will shed light on the benefits of the RS-SCED bracing system when compared to a more traditional high-performance bracing system. It is important to note that the conclusions derived in this section are based on the analysis of a single structure, to further understand the effect of using both systems, a detailed parametric analysis is needed. The purpose of this section is to determine whether the results are consistent with results from other parametric studies comparing the two systems conducted previously [36].

The numerical models for the RS-SCED braced system and the BRB system are subjected to a suite of 44 records scaled to 3 hazard levels, Frequently Occurring Earthquake (FOE), Design Based Earthquake (DBE) and Maximum Credible Earthquake (MCE). The earthquake record suite is adopted from FEMA P695 and can be found in Appendix D of this document. The method used to scale the records is based on the FEMA P695 methodology which is discussed in detail in Chapter 7. Rayleigh mass proportional damping of 2% for the first and fifth modes was used for both numerical models. The reason for using mass proportional damping is the same as the one discussed earlier in Section 6.4.

Three response parameters are examined to compare the global response of both the RS-SCED and BRB systems: a) The peak inter-storey drift at any floor  $\Delta/h_s$ , b) the highest residual drift at any floor  $\Delta_r/h_s$ , and c) the maximum floor acceleration at any floor  $a_f$ . Table 6-5 below

summarizes the 50<sup>th</sup> percentile (Median) and the 84<sup>th</sup> percentile of response values obtained from both systems at the FOE and DBE hazard levels when subjected to the full suite of records. The 84<sup>th</sup> percentile was chosen as it approximately corresponds to one standard deviation from the mean. The 50<sup>th</sup> percentile for response values obtained under the MCE hazard level are also presented. Under the MCE hazard level, the 84<sup>th</sup> percentile often indicates failure in more than 16% of the records for both systems, therefore, the 84<sup>th</sup> percentile under the MCE hazard level is not presented. This is consistent with findings from another study of SCED and BRB system comparative performance[36]. Since some of the scaled earthquake records result in collapse of the structure, defined as loss of structural integrity or an inter-storey drift exceeding 5% at any floor, the 84<sup>th</sup> and 50<sup>th</sup> percentiles were calculated using a statistical distribution model by Shome and Cornell [96] using Equation 6-1:

$$P_X(x) = P_C + P_{NC} \left[ 1 - \Phi_{NC} \left( \frac{\ln(x) - \ln(x_{m,NC})}{\delta_{NC}} \right) \right] \quad \text{Equation 6-1}$$

where  $P_X$  is the probability of parameter  $X$  exceeding a given value of  $x$  defined by the probability of collapse  $P_C$ , the probability of no collapse  $P_{NC} = 1 - P_C$ , the standardized cumulative normal distribution  $\Phi_{NC}$ , and the median and logarithmic standard deviations of the response parameter for the non-collapsed structures  $x_{m,NC}$  and  $\delta_{NC}$  respectively. Knowing  $P_C$ ,  $x_{m,NC}$  and  $\delta_{NC}$ , an iterative process is used to determine values of  $x_{84th}$  and  $x_{50th}$  which represent the 84<sup>th</sup> and 50<sup>th</sup> percentile for parameter  $X$  respectively.

**Table 6-5 Summary of the response for the RS-SCED and BRB systems**

Response parameter		FOE		DBE		MCE	
		(50% in 50 years)		(10% in 50 years)		(2% in 50 years)	
		RS-SCED	BRB	RS-SCED	BRB	RS-SCED	BRB
$\Delta/h_s$	50 <sup>th</sup> Percentile	1.15%	1.05%	2.26%	1.67%	3.14%	4.85%
	84 <sup>th</sup> Percentile	1.62%	1.49%	2.99%	2.67%	--	--
$\Delta_r/h_s$	50 <sup>th</sup> Percentile	0.01%	0.10%	0.01%	0.39%	0.02%	1.34%
	84 <sup>th</sup> Percentile	0.02%	0.35%	0.08%	0.85%	--	--
$a_f$	50 <sup>th</sup> Percentile	0.49 g	0.21 g	1.03 g	0.42 g	1.21 g	0.76 g
	84 <sup>th</sup> Percentile	0.80 g	0.29 g	1.19 g	0.56 g	--	--

The maximum inter-storey drift experienced by the structure with the RS-SCED brace system is similar for both structures at the FOE hazard level. The RS-SCED system shows a 50<sup>th</sup> percentile for maximum inter-storey drift of 1.15% compared to 1.05% for the BRB system at the FOE hazard level. At the higher DBE hazard level, the BRB system experienced a slightly better maximum inter-storey drift, with a median value of 1.67% compared to the median value of 2.26% for the RS-SCED system. In general, the high initial stiffness of the RS-SCED braces results in the structure having a shorter period of vibration, which may result in a higher seismic demand initially. Furthermore, due to the higher post-activation stiffness of the RS-SCED brace, the RS-SCED brace structure may have a lower period of vibration potentially resulting in higher seismic demand post-activation. In addition, the RS-SCED brace has a lower energy dissipation as shown in Figure 6.28, which can lead to increased drifts. The higher energy dissipation of the BRBs comes at the cost of residual drifts, which may not be as significant at this hazard level, but can be critical at higher hazard levels as shown in Figure 6.29.

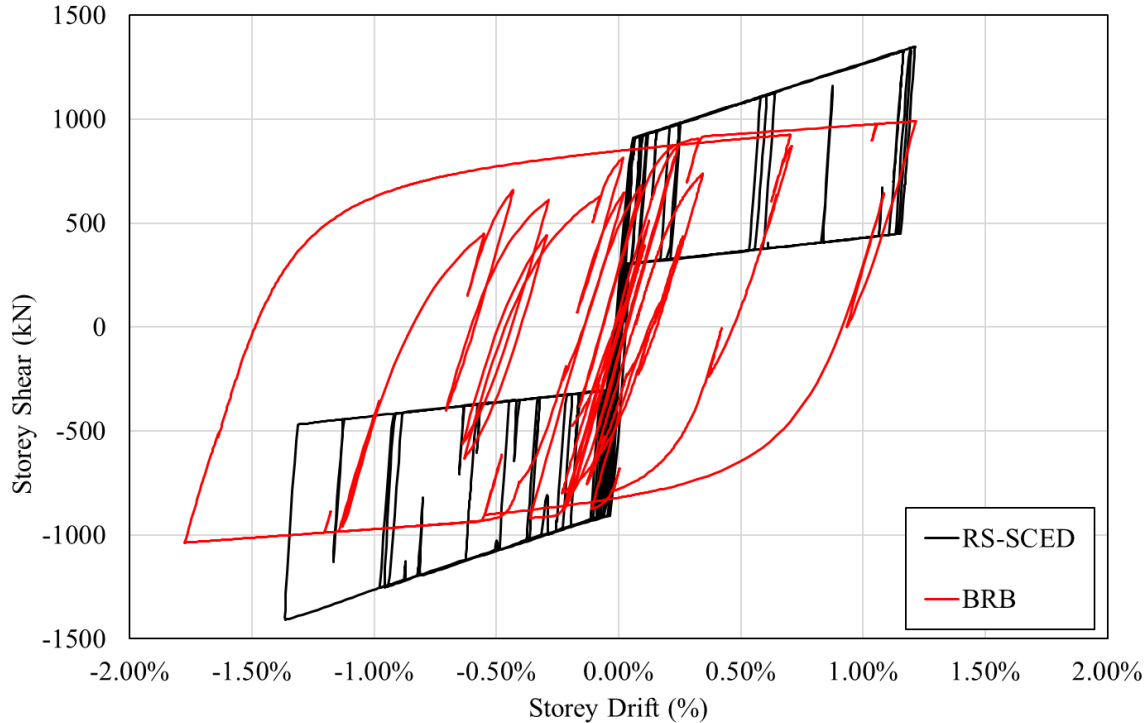


**Figure 6.28 Comparison of first floor hysteresis of RS-SCED and BRB systems (DBE hazard level - Record 12)**

At the higher MCE hazard level, the BRB system experiences a higher inter-storey drift when compared with the RS-SCED brace. At the MCE hazard level, the RS-SCED brace system 50<sup>th</sup> percentile of maximum inter-storey drift is 3.81% compared to 4.85% for the BRB system. This may be because at this hazard level, the BRB cores yielding cause the system to exhibit deformation biases, resulting in large residual drifts and progressively increasing drift as shown in Figure 6.29, this is especially at the lower floor levels which experience higher seismic load demands. Furthermore, the higher post-activation stiffness of the RS-SCED braces may also result in a better spread of activation across the height of the building, which can reduce drifts at lower floors compared to the drift concentrations at lower floors of the BRB structure.

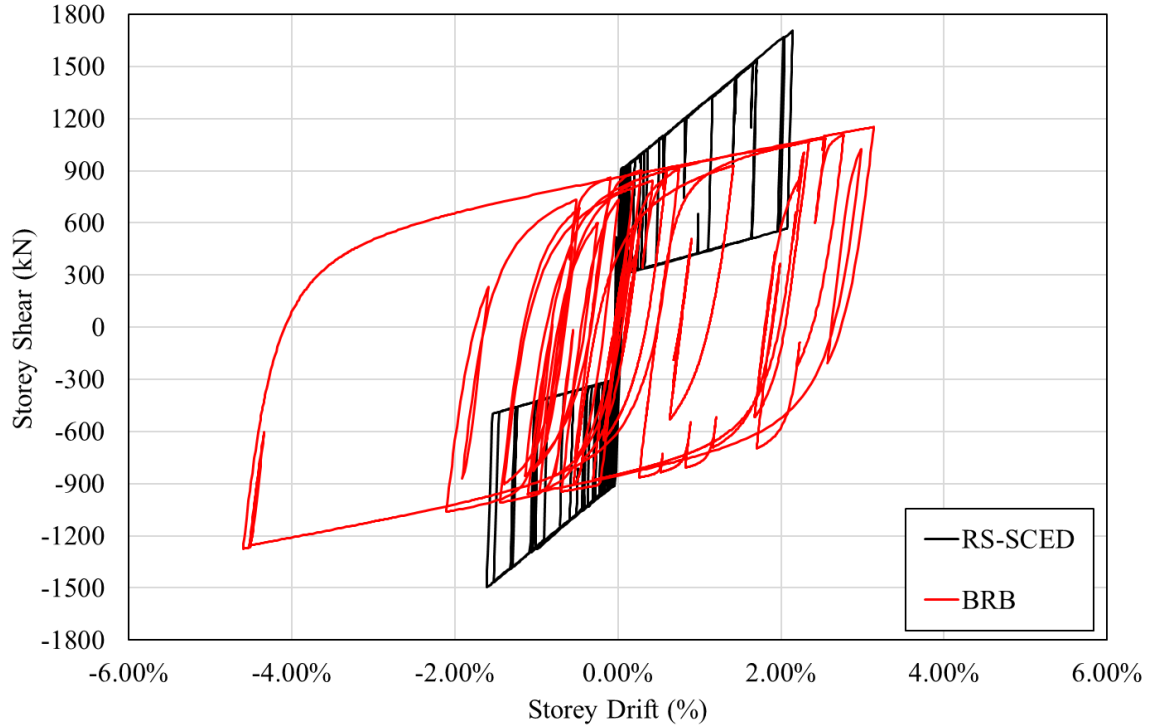


**Figure 6.29 Comparison of first floor hysteresis of RS-SCED and BRB systems (MCE hazard level - Record 12)**

The residual drift for the RS-SCED system is virtually zero even at the MCE hazard level. The median residual drift of the RS-SCED system was 0.01%, 0.02% and 0.03% at the FOE, DBE and MCE hazard levels, respectively. In comparison, the BRB system shows significantly higher residual drifts with median residual drift values of 0.10%, 0.39% and 1.34% at the FOE, DBE and MCE hazard levels. This significant difference between the two system is directly related to their energy dissipation mechanism and hysteretic response behaviour. In the RS-SCED brace, energy is primarily dissipated through friction between the rings in the ring spring assembly, while the self-centering component remains elastic, resulting in near-zero residual drifts even at very high drift demands. Accordingly, the resulting RS-SCED brace system flag shape hysteresis maintains the self-centering behaviour that eliminates the residual drift. In the BRB system, the energy is primarily dissipated in the form of strain energy caused by the yielding of the steel core. Once the

BRB core yields, the system sustains a residual drift that is directly related to the level of drift and load demand experienced by the BRBs.

The maximum floor acceleration in the RS-SCED system is higher than the BRB system. The median value for the maximum floor acceleration experienced by the RS-SCED system was 0.56 at the FOE hazard level, decreasing to 1.12 and 1.27 at the DBE and MCE levels. The BRB system has a median value for the maximum floor acceleration of 0.21, 0.42 and 0.76 at the FOE, DBE and MCE hazard levels, all of which are lower than the RS-SCED floor accelerations. The high floor acceleration of the RS-SCED system is due to their high stiffness compared to the BRBs. It is however important to remember that the floor acceleration predicted by the numerical model is likely an overestimation of the actual floor acceleration due to the reasons discussed in the previous Section 6.5.

To further understand the inter-storey drift response of both structural systems, the maximum inter-storey drift along the height of both structures is plotted for the records scaled to the three different hazard levels as shown in Figure 6.30. The calculated maximum inter-storey drift at the upper floors of the RS-SCED braced structure tend to be higher than at the lower floors. This could be caused by the use of the equivalent lateral force (ELF) procedure for the design of the structure which does not optimize the design of the braces in the structure. At the higher MCE hazard level, the lower floors of the BRB structure show significantly higher maximum inter-storey drift, predominantly because of significant yielding of the BRB cores. The yielding of the BRB cores results in residual drift after each large cycle which biases the response in future cycles. These drifts are especially concentrated at the lower levels where the seismic demand is highest.

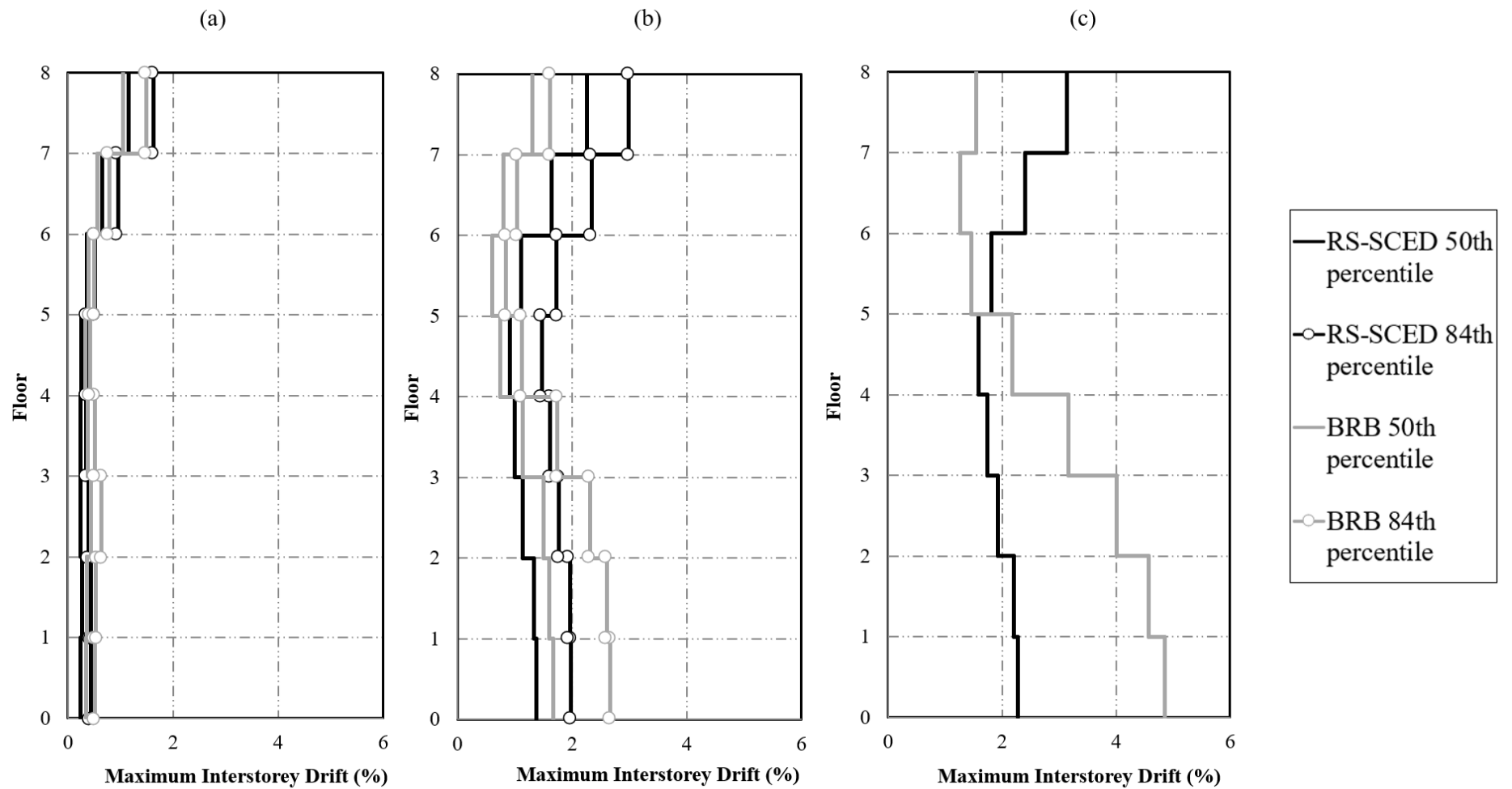


Figure 6.30 Statistics of the maximum inter-storey drifts for both structural systems: a) 50% in 50-year, b) 10% in 50-year hazard, and c) 2% in 50-year hazard level

Figure 6.31 shows the residual drift for the two structures when subjected to the three different hazard levels. At the FOE hazard level, both structures do not show significant residual drift at any floor level. At the DBE hazard level, significant residual drifts are experienced at the lower floors of the BRB building because of yielding of the BRB yielding cores, while little-to-no residual drift is observed in the RS-SCED structure. At the MCE hazard level, median residual drifts exceeding 0.5% is observed for the lower 5 floors of the structure. This level of residual drift would usually result in major discomfort to occupants and safety concerns caused by major non-structural damage [97]. In some cases, this residual drift would percept the structure as unsafe leading to demolition. Alternatively, the RS-SCED braced structure exhibits minimal residual drift along the height of the structure.

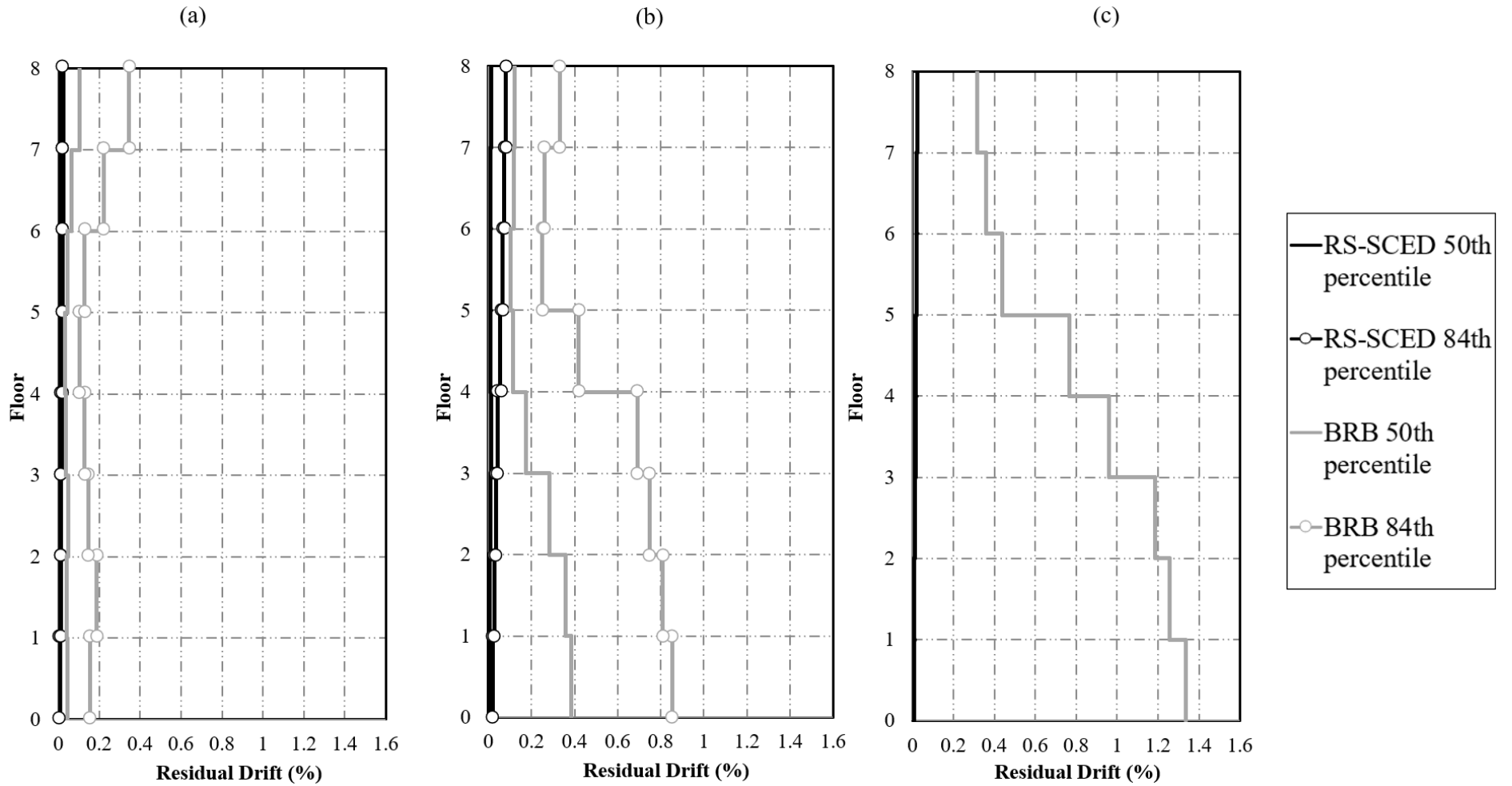


Figure 6.31 Statistics of the residual storey drifts for both structural systems: a) 50% in 50-year, b) 10% in 50-year hazard, and c) 2% in 50-year hazard level

Figure 6.32 shows the plots of floor acceleration along the height of the structure to examine the floor acceleration for both structural systems at different hazard levels. As discussed earlier, the floor acceleration of the BRB system is lower than the RS-SCED braced system due to the high initial stiffness of the RS-SCED braces. This is evident by examining the difference in the floor accelerations of the RS-SCED braced system along the height of the structure. The large RS-SCED braces located near the base of the structure have a high initial stiffness resulting in larger floor accelerations at the lower levels. At upper levels, the floor shear decreases resulting in a decrease in the size and stiffness of the RS-SCED braces. This in turn reduces the floor accelerations at the upper floors.

In summary, the RS-SCED system performance is superior to the BRB system in its ability to minimize the inter-storey drift and residual drift at high seismic hazard levels. This comes at the expense of higher floor accelerations and higher inter-storey drift compared to the BRB system at lower hazard levels. The RS-SCED system showed a significant reduction in inter-storey drift at the higher hazard level. The results presented in this section are consistent with findings from another parametric study that compared the performance of BRB system to a SCED brace system. The use of the RS-SCED brace almost eliminates the residual drift, allowing a structure to remain fully operational and occupied immediately after a major event, while reducing maintenance and rehabilitation costs.

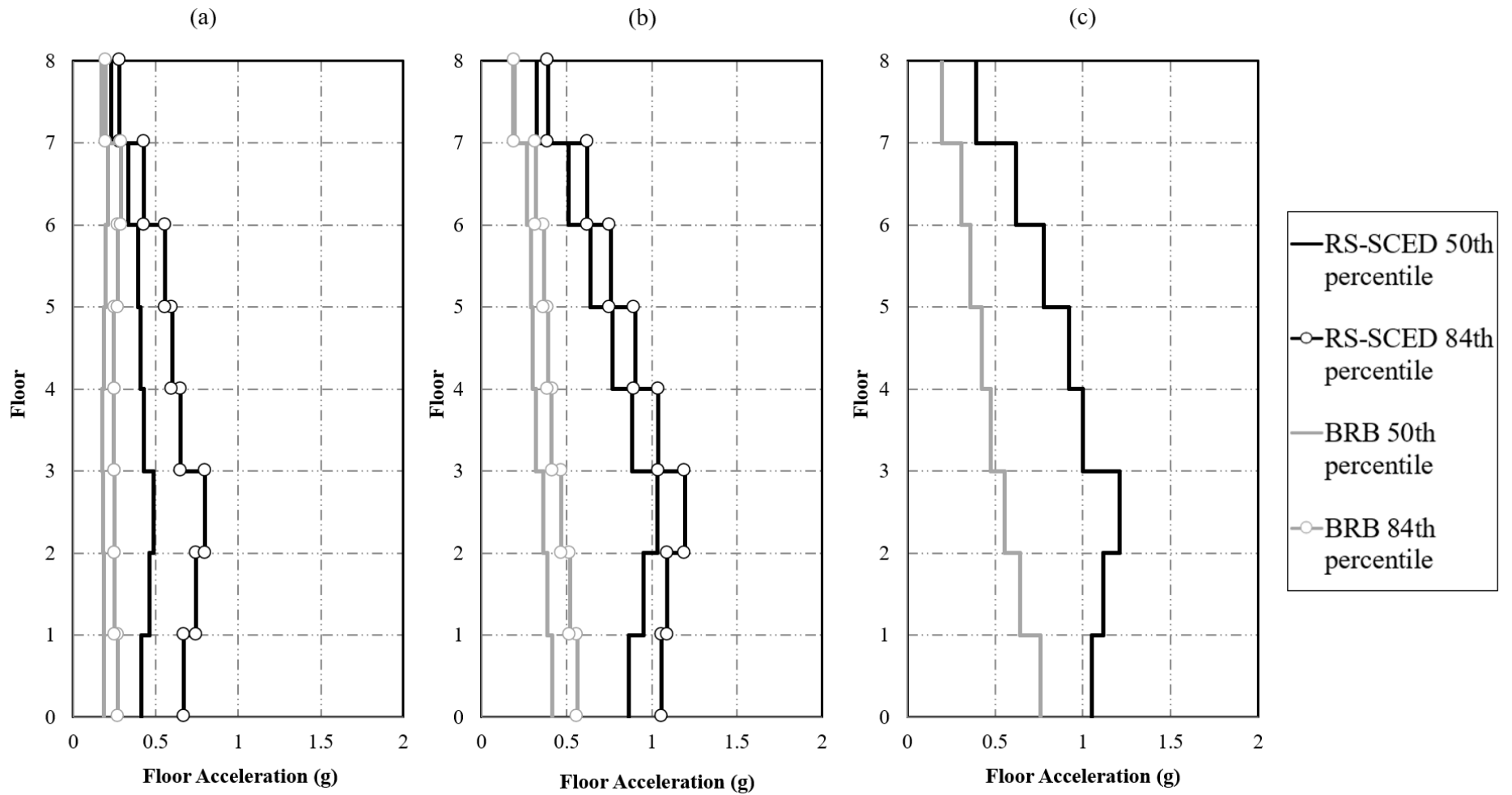


Figure 6.32 Statistics of the peak floor accelerations for both structural systems: a) 50% in 50-year, b) 10% in 50-year hazard, and c) 2% in 50-year hazard level

## 6.7 Bridge Analytical Modelling

Another objective of this study is to investigate the application of the new RS-SCED as a seismic damper for bridges in areas of moderate to high seismic hazard. A previous parametric study [98] investigated the use of SCED braces as seismic dampers for rehabilitation of bridges with various span lengths, number of spans and number of piers at each bent under both near-field and far-field record sets. The results of the parametric study showed that the SCED braces are effective for both far field and near field records but are particularly effective for the structures subjected to near-field ground motions. The retrofit scheme adopted for the parametric study consisted of two SCED braces at each end of the bridge in the longitudinal direction, and four braces in the transverse direction. The SCED braces in the transverse direction were located at each of the bridge's ends acting in pairs, with one on each edge of the bridges as shown in Figure 6.33. It is noted that Figure 6.33 shows a different bridge from the one adopted for this study, however, the retrofit scheme adopted for all bridges in the parametric study had the same retrofit scheme.

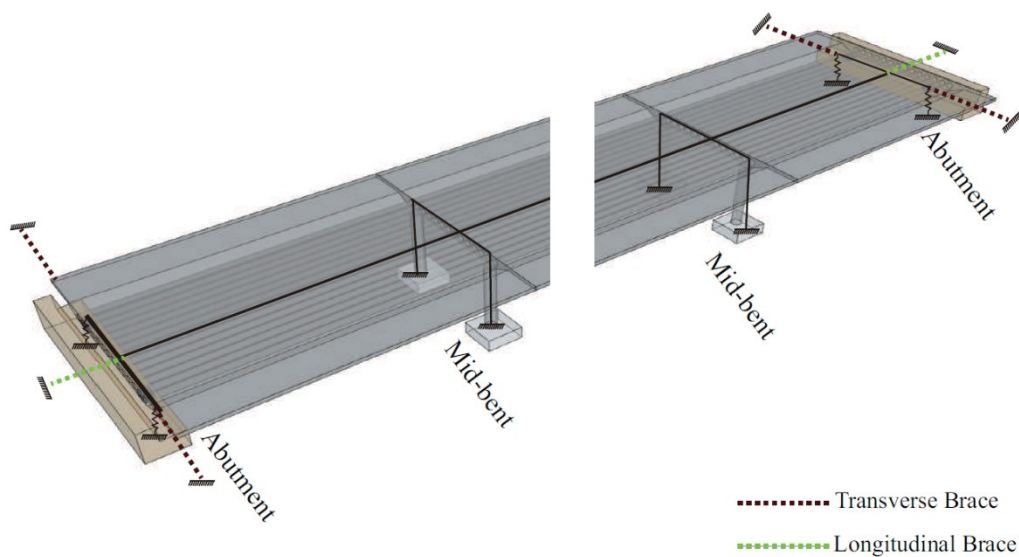
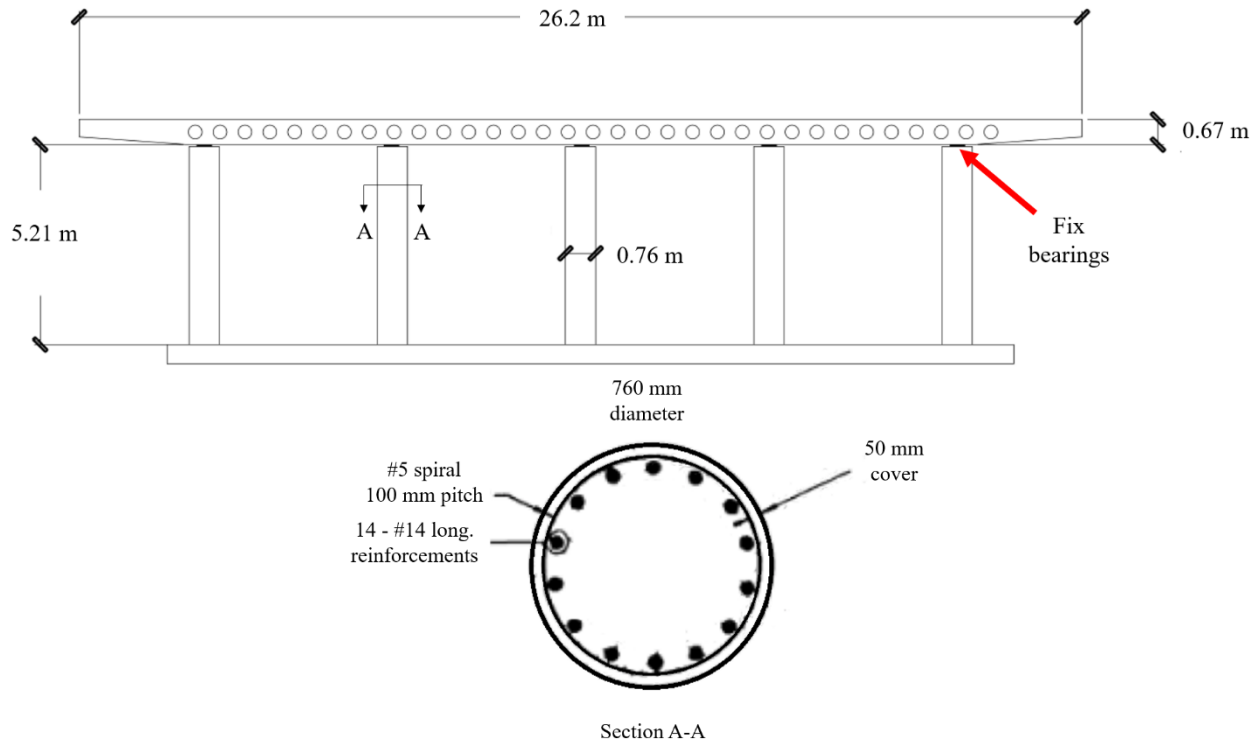


Figure 6.33 Retrofit scheme adopted in the parametric study [98]

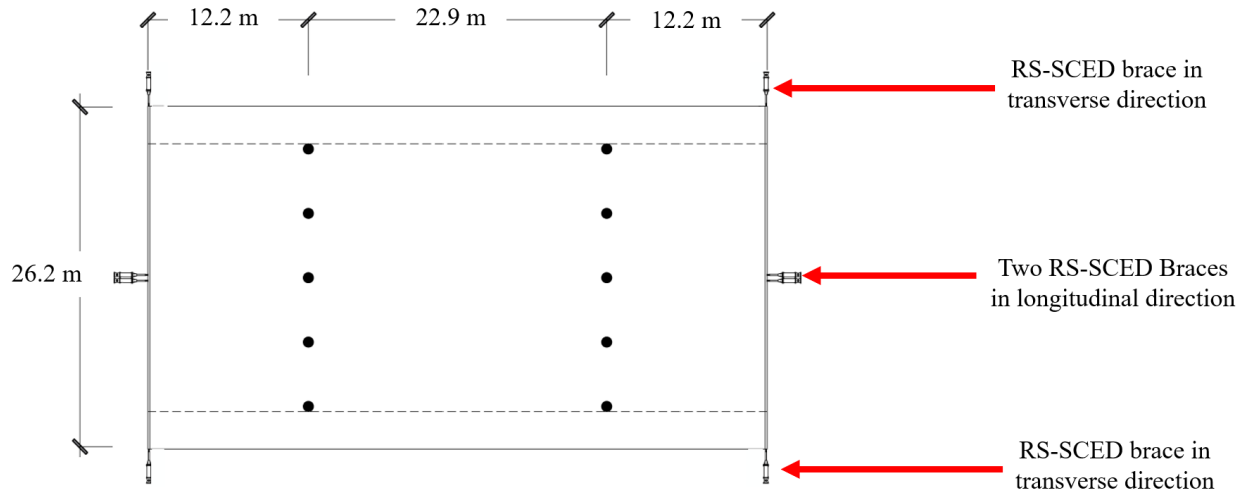
With the braces added to the structure, the peak displacement of the bridges was limited to within 60% of the original peak displacement. The residual displacement was eliminated or close to zero. The costs of the better performance were found to be the increased peak acceleration and velocity, and higher design load at the SCED brace connections. Despite the effectiveness of the previously proposed SCED in improving the seismic response of the bridges, the practicality of utilizing those SCED braces remained a challenge due to their length and large size. Alternatively, to overcome the size and length restrictions of the original SCED brace, the use of the more compact RS-SCED braces as retrofit scheme for a 3-span bridge built in Ottawa, Ontario, Canada is investigated by means of hybrid simulation.

Figure 6.34 shows the details of the bridge used for this study. The bridge was one of the bridges investigated in the parametric study discussed earlier [98]. This bridge is chosen because the load and deformation capacity needed for the SCED brace supporting this bridge closely matches the design criteria used for designing the prototype RS-SCED brace built in this study. The bridge has a voided concrete deck supported on 2 bents with 5 piers each. The bridge deck is supported by the piers by means of fixed bearings, which restrict any motion between the piers and the deck. At each end, the bridge is supported by seat-type abutments with exterior shear keys preventing movement in the transverse direction of the bridge.

The retrofit scheme for this bridge included adding 4 RS-SCED braces in the longitudinal direction (2 at each end along the centerline) and 4 RS-SCED braces in the transverse direction (1 at each corner oriented perpendicular to the centerline) to the original unretrofitted bridge as shown in the plan view shown in Figure 6.35.



**Figure 6.34 Details of modelled bridge used for this study [98]**



**Figure 6.35 Plan view of the bridge retrofit scheme**

A 3D OpenSees spine model with fixed supports at the base of the piers is used to analytically model the numerical substructure of the bridge as shown in Figure 6.36. Mass proportional Rayleigh damping of 5% is used to model the inherent damping in the bridge structure. To model the fixed bearings, rigid link elements are used to connect the top of the piers to the neutral axis of

the cross beam. The abutments are modelled using a spring abutment model to model the longitudinal response of the backfill and expansion joint, and the transverse response of the exterior shear keys. Details of the abutment modelling approach can be found in the reference by Cheng et. al [98]. When modelling the retrofitted bridge, a roller is used to model the boundary condition of the bridge in the longitudinal direction. The cross beam and spine are modelled as linear elastic beam column elements with the deck's gross section properties as per recommendations in Priestley et al. [99].

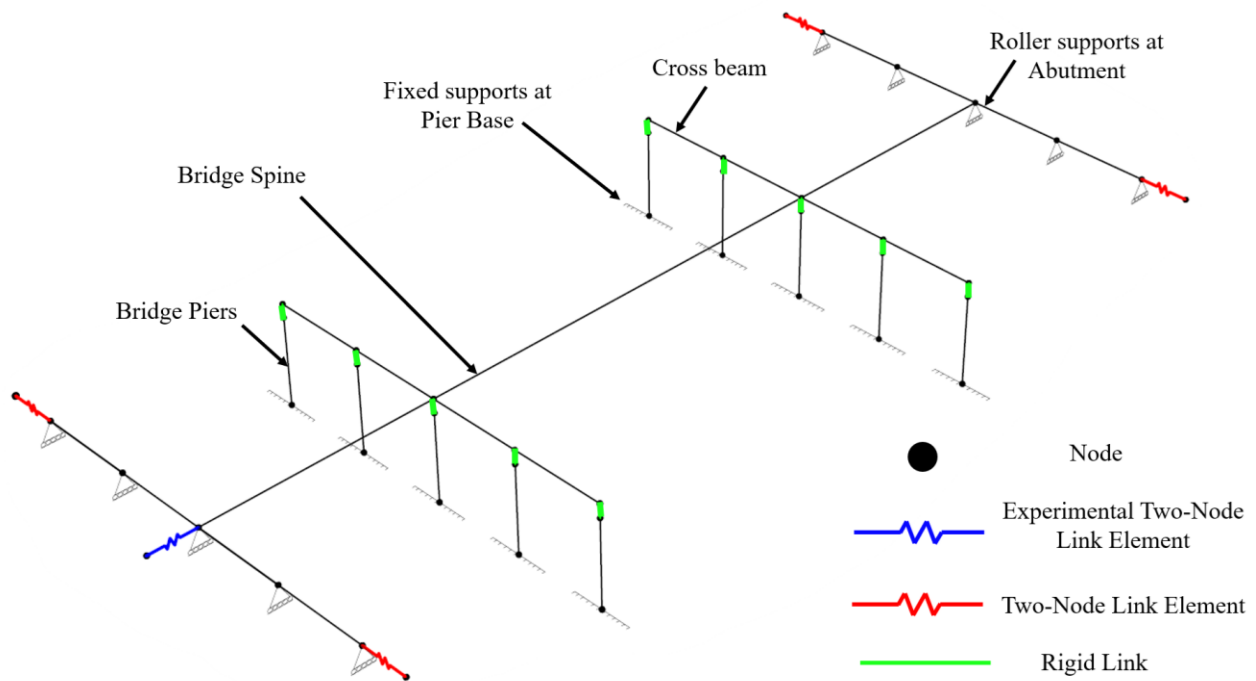


**Figure 6.36 3D Spine analytical model used for hybrid simulation**

The piers are modelled as non-linear beam column elements with fibre sections to capture their non-linear behaviour. A forceBeamColumn OpenSees element with 5 integration points is used to model the non-linear beam column, the number of integration points was determined through a sensitivity analysis in the reference [98]. The fibre section for the cross-section of the pier can be divided into three parts: confined concrete area, unconfined concrete area, and longitudinal bar

area as shown in Figure 6.37. The concrete region is discretized into smaller rings and wedges. The number of rings and wedges used for modelling was determined to be 10 rings and 10 wedges. The choice of this number is based on a sensitivity analysis presented in the reference [98]. The concrete fibres inside and outside of the confined region are modeled with different properties according to Mander's confined concrete model [100].

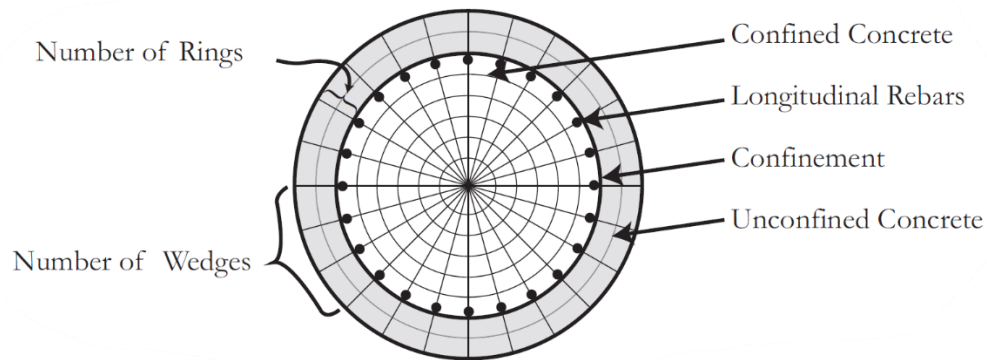


**Figure 6.37 Fibre section model in OpenSees [98]**

Modal analysis of the non-retrofitted bridge shows that the bridge is more flexible in the longitudinal direction. Hence, in this hybrid simulation, the RS-SCED braces oriented longitudinally are experimentally tested in the physical substructure while the bridge deck, piers and transverse RS-SCED braces are analytically modeled in the numerical substructure. Similar to the hybrid simulation of the prototype building discussed earlier, the longitudinal RS-SCED is modelled with an experimental Two-Node link element in OpenFresco while the transverse RS-SCED braces are modelled using Two-Node link elements in OpenSees. Due to the presence of 4 RS-SCED braces in the longitudinal direction, the feedback load measured using laboratory equipment is multiplied by a factor of 4 before being sent back to the numerical model. This is conducted under the reasonable assumption that there are no significant axial in-plane deformations along the bridge deck. The longitudinal RS-SCED braces do not experience axial

deformations caused by the bridge torsion about the vertical axis since the braces are located along the centerline of the bridge.

To evaluate the effectiveness of the retrofit scheme, the response of the retrofitted bridge is compared to the response of the bridge with no retrofit. To analyze the response of the non-retrofitted bridge, the Two-Node link elements are removed from the retrofitted analytical model as shown in Figure 6.38. The bridge is subjected to the same 4 records used for the building hybrid simulations shown in Table 6-6. For this study, the records are scaled to both the Ottawa MCE level and Victoria MCE response spectrum hazard levels as calculated in the NBCC 2015 [73]. The earthquake records are scaled such that their spectral acceleration at the first period of vibration of the structure matches the response spectrum of Ottawa or Victoria MCE levels as shown in Figure 6.39 to Figure 6.42. For the selected bridge, the first period of vibration is associated with the bridge swaying in the longitudinal direction.

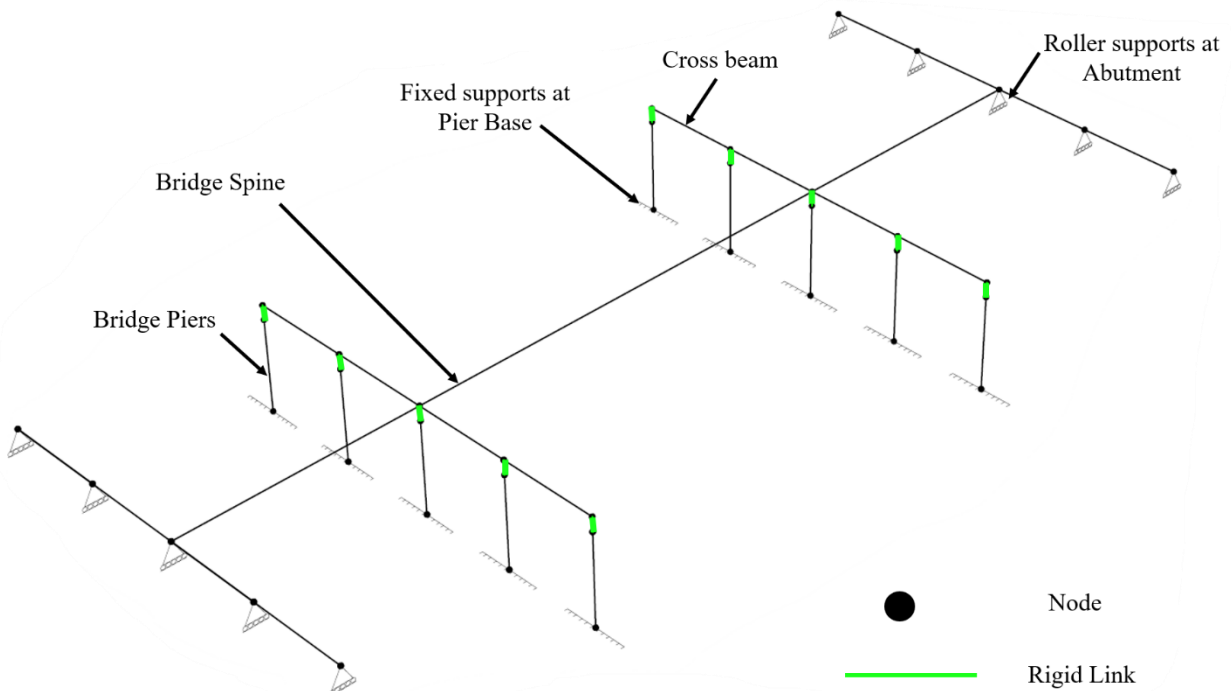
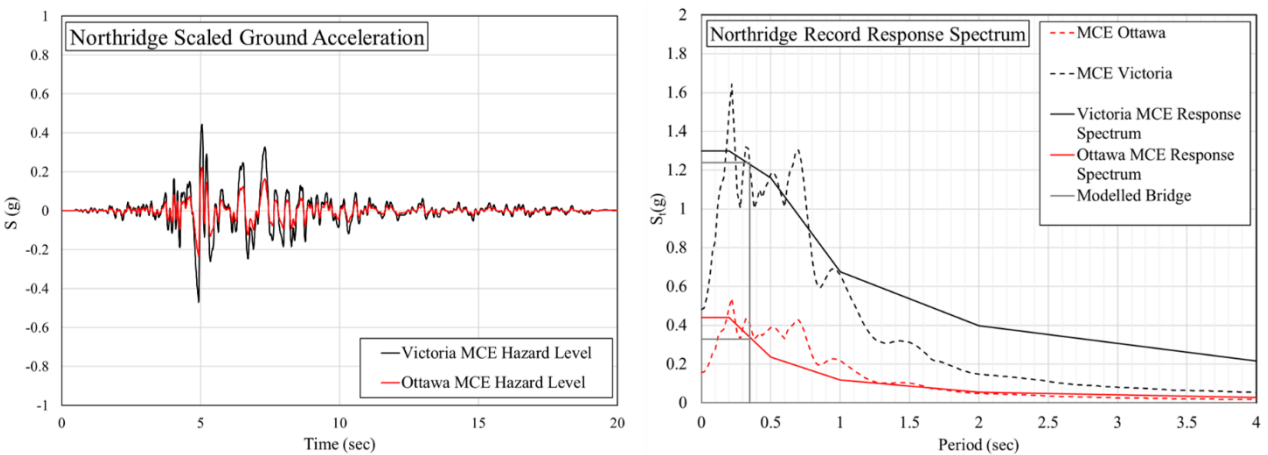


Figure 6.38 3D Spine model used for analysis of non-retrofitted bridge

**Table 6-6 Unscaled earthquake record data and scaling intensity for the bridge hybrid simulation study**

Earthquake record	Intensity	PGA (g)	PGV (m/s)	PGA/PGV (g.s/m)	Near Field (NF) or Far Field (FF)
Northridge: Canyon Country- WLC	50% (MCE Ottawa), 100% (MCE Victoria)	0.48	0.45	1.067	FF
Kobe: Shin-Osaka	100% (MCE Ottawa), 200% (MCE Victoria)	0.24	0.38	0.632	FF
Loma Prieta: Capitola	50% (MCE Ottawa), 150% (MCE Victoria)	0.53	0.35	1.514	FF
ChiChi: TCU 067	50% (MCE Ottawa), 100% (MCE Victoria)	0.29	0.29	0.272	NF



**Figure 6.39 Scaling of Northridge earthquake record**

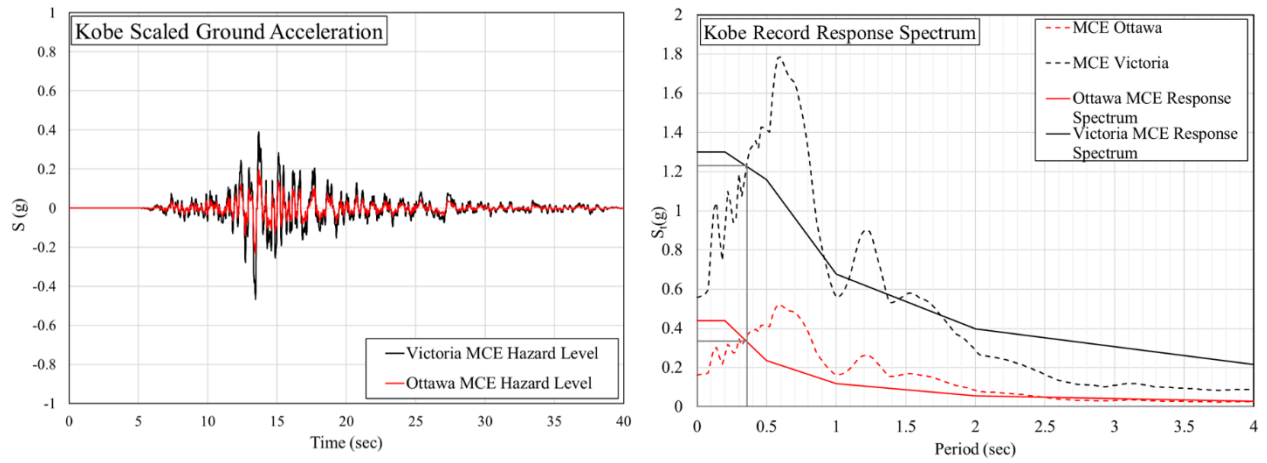


Figure 6.40 Scaling of Kobe earthquake record

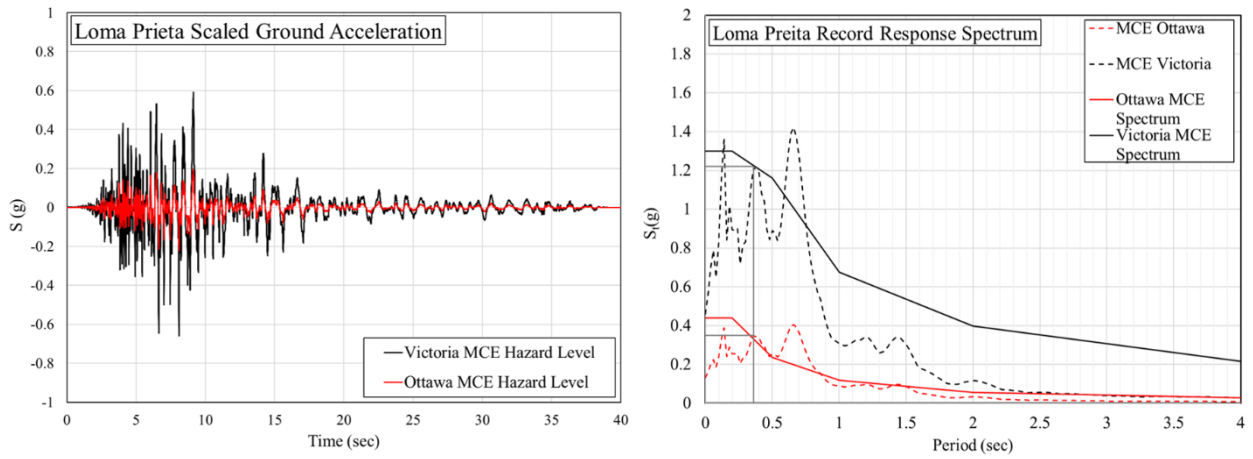


Figure 6.41 Scaling of Loma Prieta earthquake record

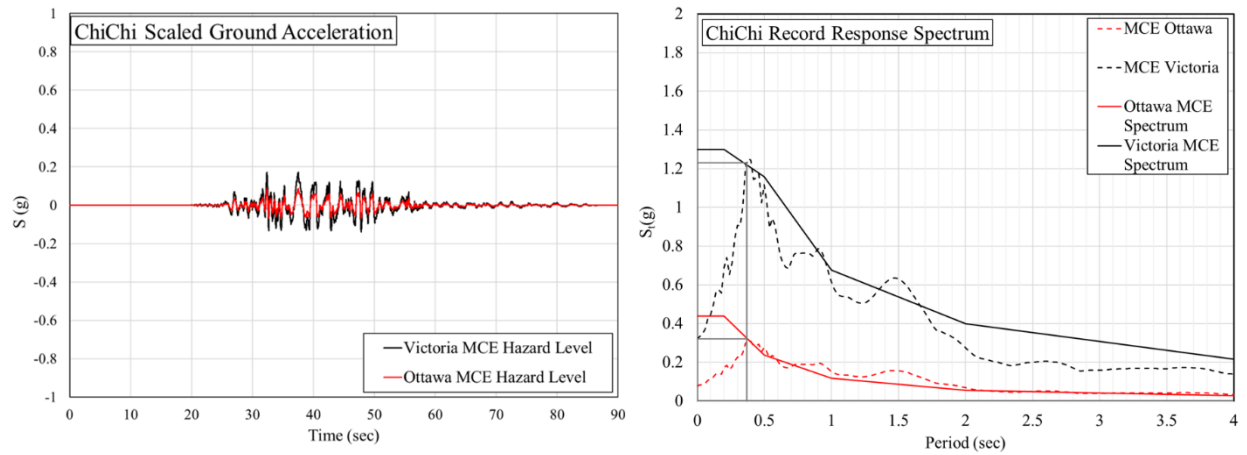
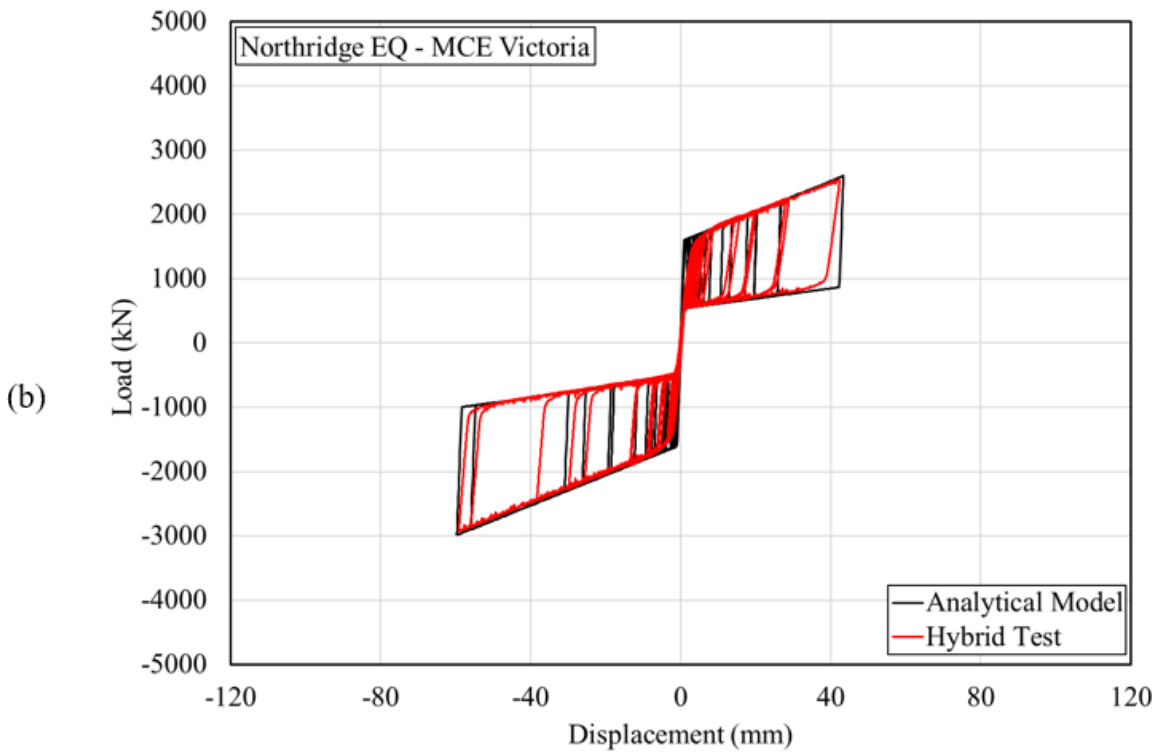
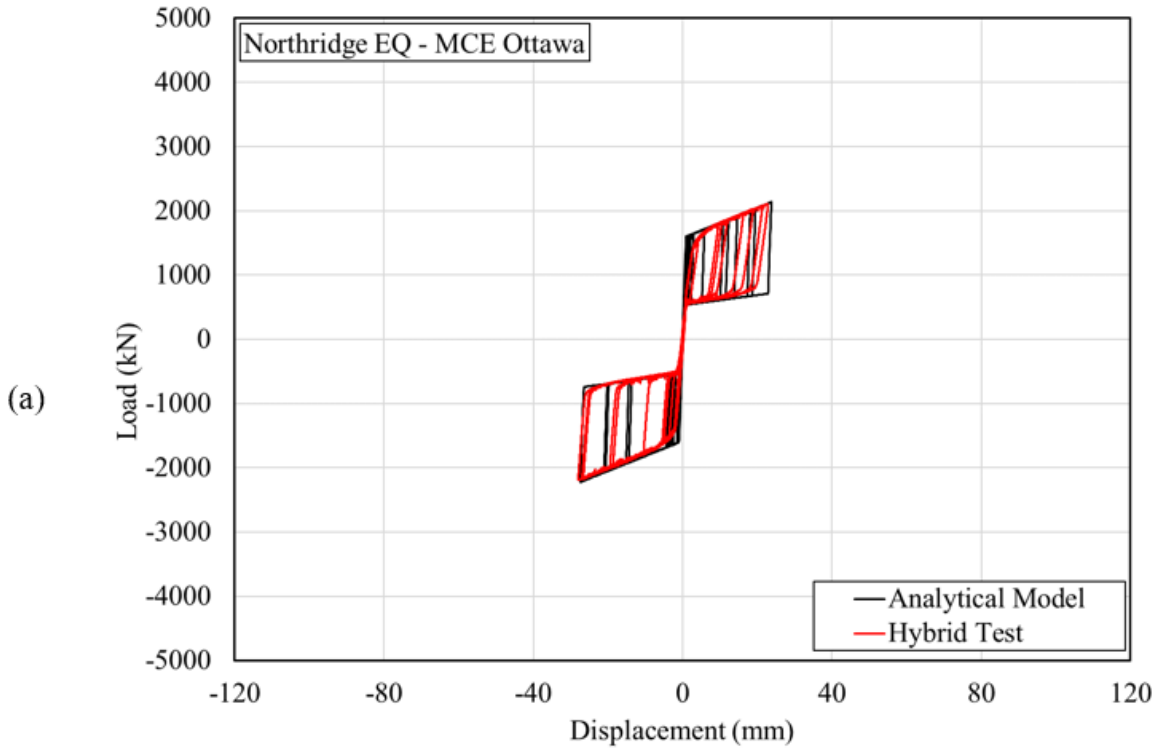


Figure 6.42 Scaling of ChiChi earthquake record

## 6.8 Comparison of Bridge Hybrid Simulation to Numerical Modelling

This section examines three response parameters to evaluate the numerical model used in modelling the RS-SCED brace bridge retrofit scheme which include the hysteresis of the RS-SCED brace in the longitudinal direction, the time history bridge deformation in the longitudinal direction, and the drift in the transverse direction. These responses are examined for the 4 described earthquake records scaled to the MCE seismic hazard level in Canada associated with the seismicity for Ottawa and Victoria.

The hysteretic response from the analytical model and the hybrid simulation are presented in Figure 6.43 to Figure 6.46. The results show very good correlation. The force values presented in the plots represent the sum of the forces in all 4 braces modelled in the longitudinal direction. The activation load  $P_a$ , recoil load  $P_R$  and decompression load  $P_d$  were consistent when comparing the results of the hybrid simulation and the numerical analyses. The initial stiffness  $K_i$  and post-activation loading stiffness  $K_L$  and unloading stiffness  $K_u$  were also accurately predicted by the numerical model. The force-deformation hysteretic response behaviour from the hybrid simulation results shows a gradual and smooth stiffness transition between the initial stiffness to post-activation stiffnesses in comparison to the sharp and abrupt stiffness transition in the theoretical model. This is consistent with the observations made in the previous section when analyzing the response of the prototype building structure with the RS-SCED bracing system.



**Figure 6.43 Hysteresis of RS-SCED brace for Northridge record scaled at the (a) Ottawa MCE, and (b) Victoria MCE hazard levels**

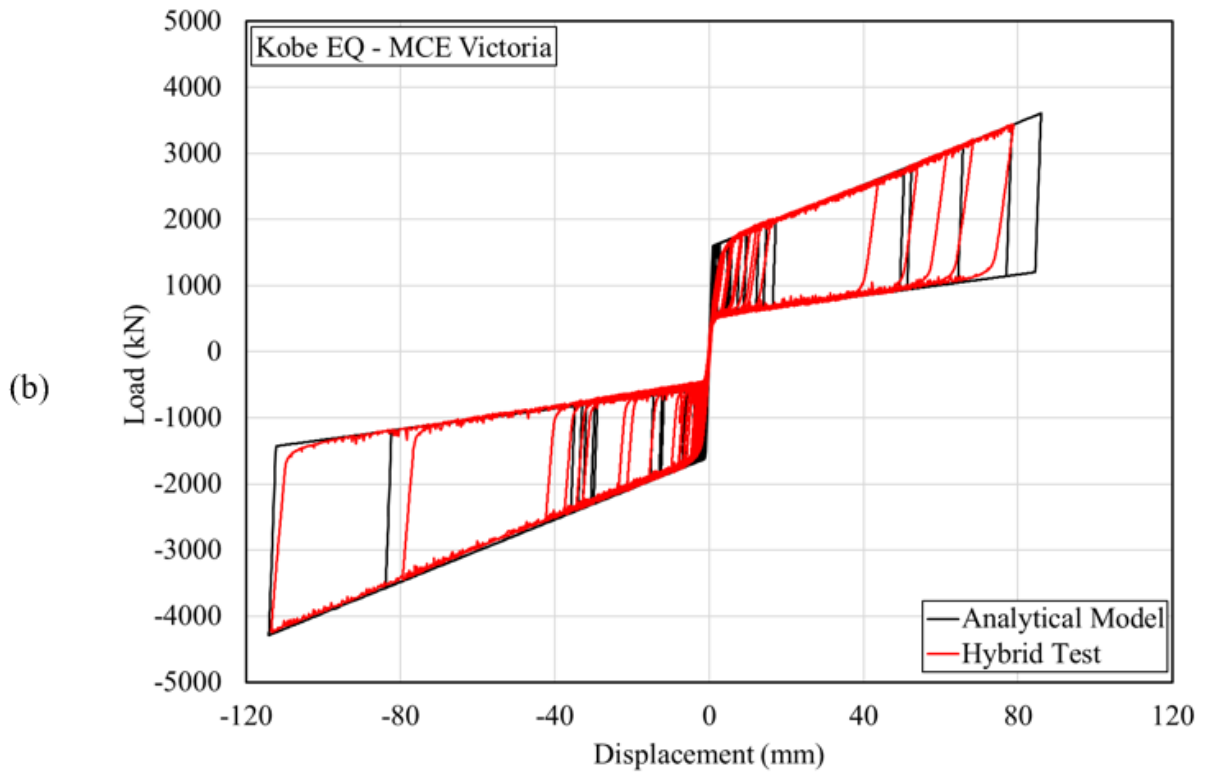
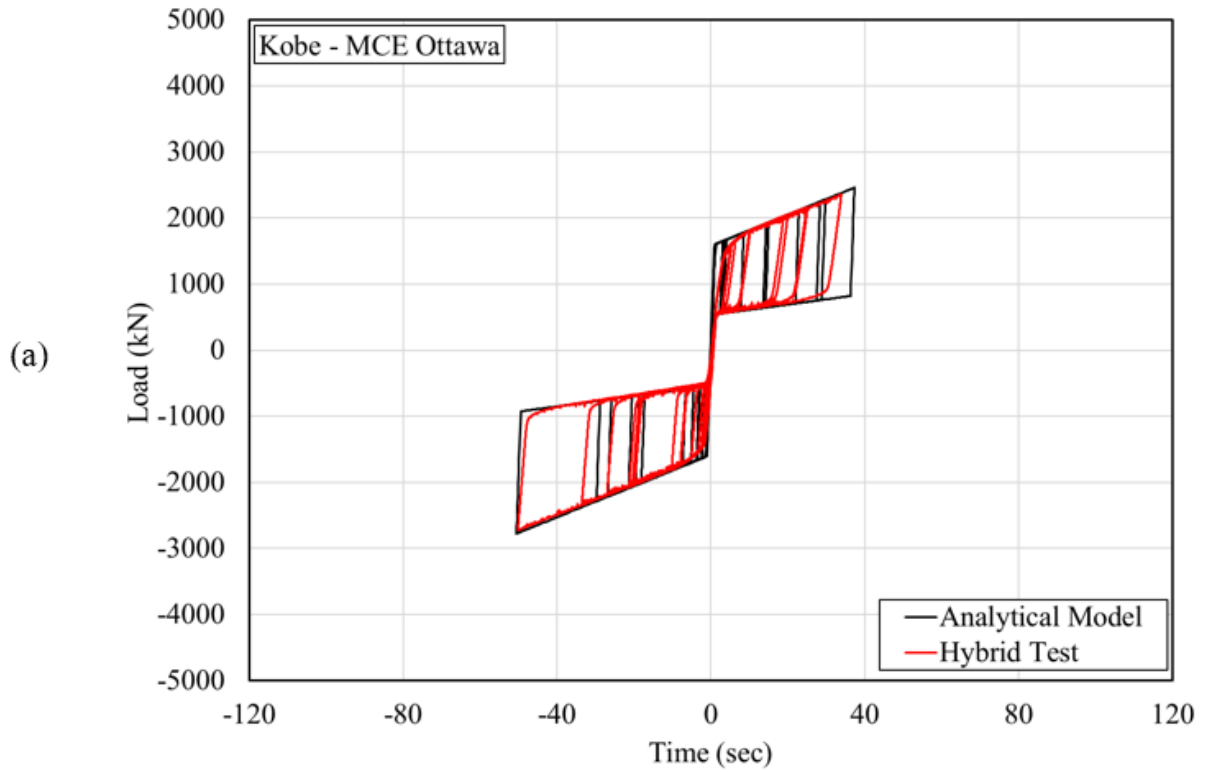


Figure 6.44 Hysteresis of RS-SCED brace for Kobe record scaled at the (a) Ottawa MCE, and (b) Victoria MCE hazard levels

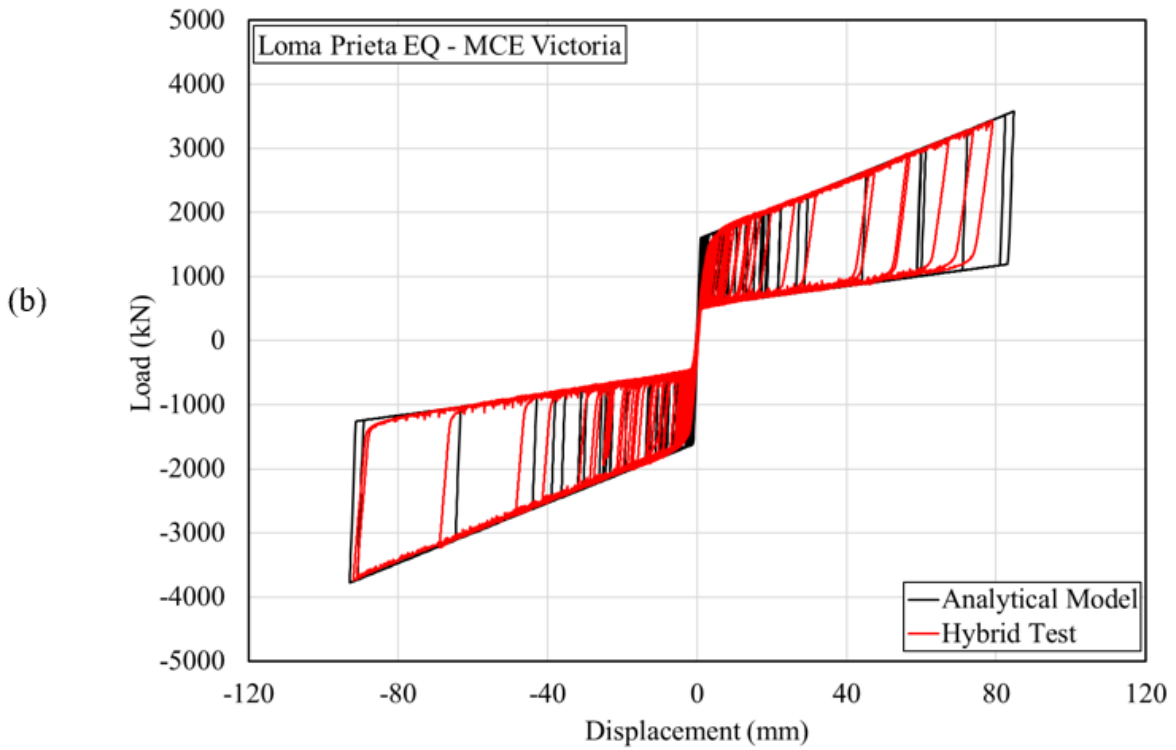
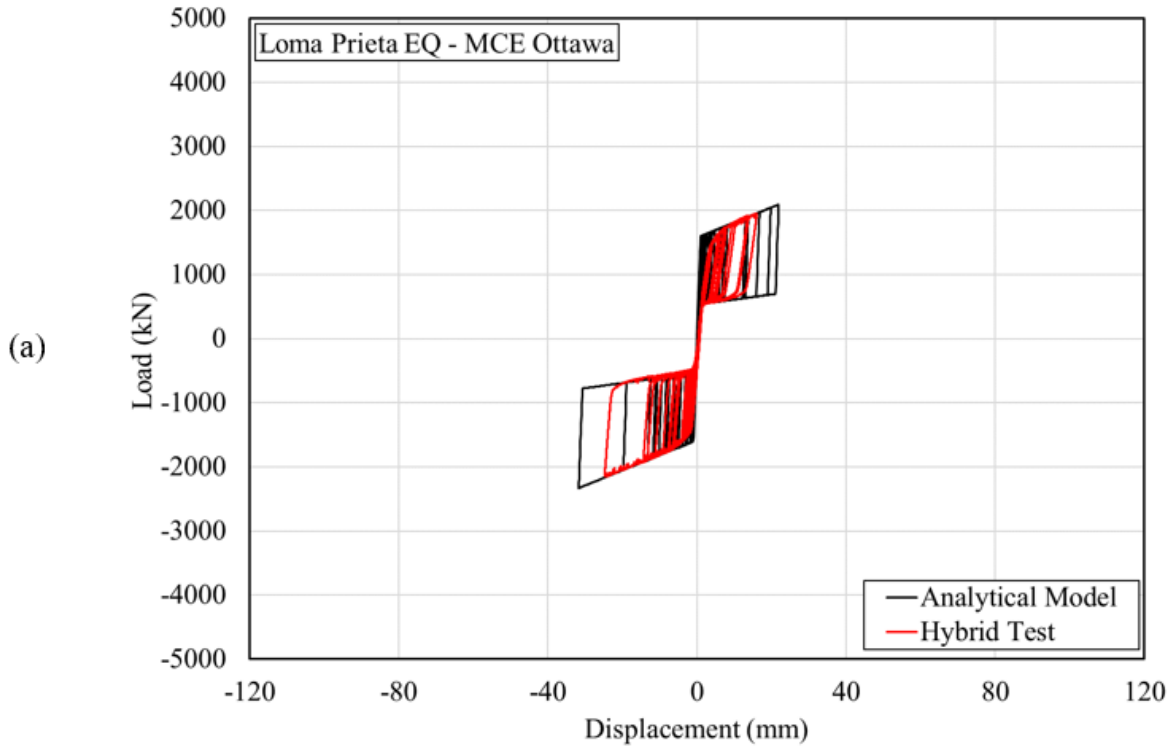


Figure 6.45 Hysteresis of RS-SCED brace for Loma Prieta record scaled at the (a) Ottawa MCE, and (b) Victoria MCE hazard levels

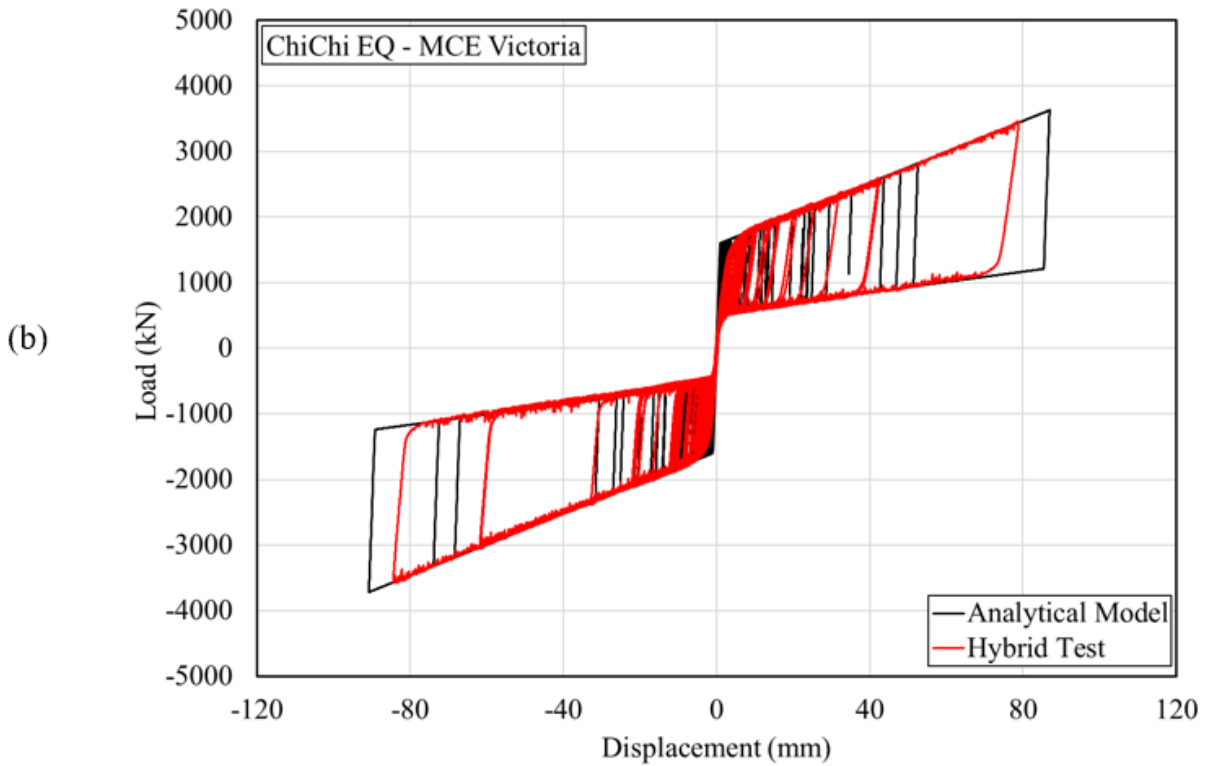
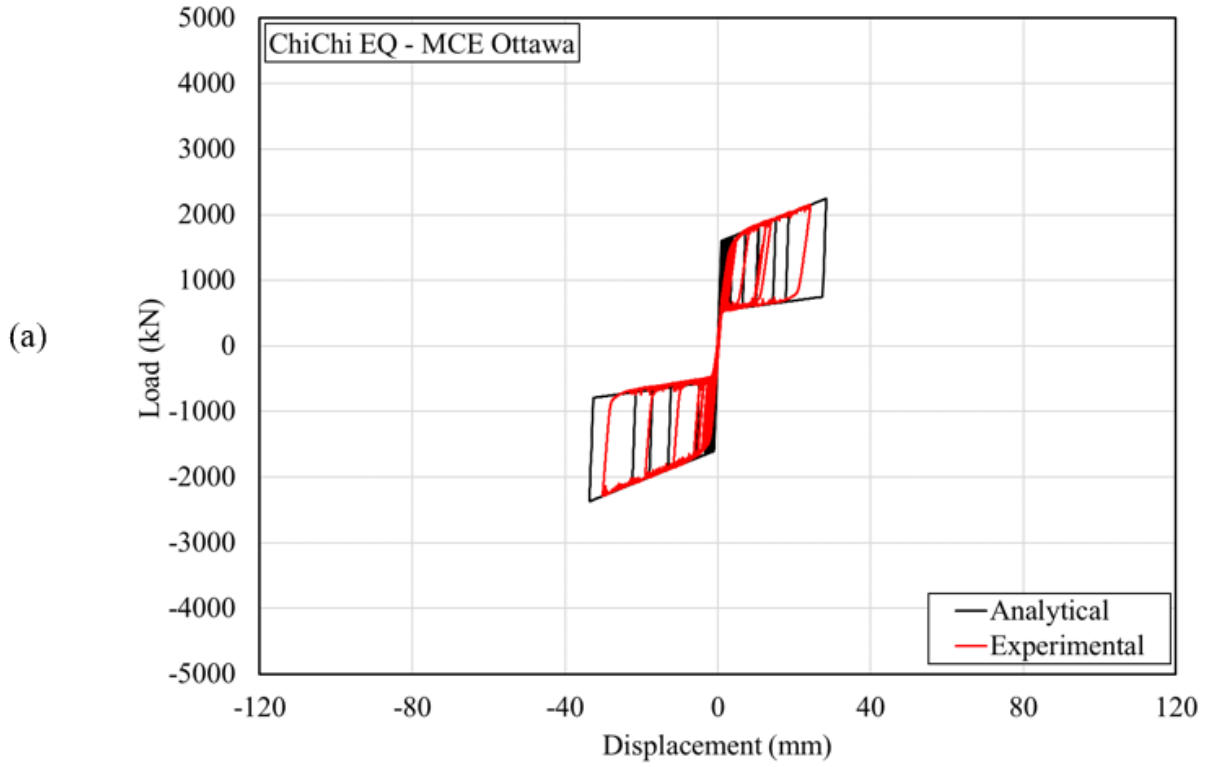


Figure 6.46 Hysteresis of RS-SCED brace for ChiChi record scaled at the (a) Ottawa MCE, and (b) Victoria MCE hazard levels

By comparing the longitudinal displacement-time history of the bridge from the hybrid simulation and numerical model, the influence of the RS-SCED braces on the global system-level response of the bridge can be evaluated. As shown in Figure 6.47 to Figure 6.50, the longitudinal deformation time history results of the analytical model correlate very well with the results obtained from the hybrid simulation for all the earthquake records investigated. This correlation was found both at the peak of the response as well as in the post peak response. The analytical model did not show the minor post peak longitudinal deformation discrepancy observed when analyzing the 8-storey building in Section 6.5, this is due to the higher Rayleigh mass damping used in modelling the bridge (5%) compared to the Rayleigh mass damping used in modelling the 8 storey steel structure (2%). This increased damping diminished the effect of the difference in stiffness transitions seen in the hysteresis of the braces.

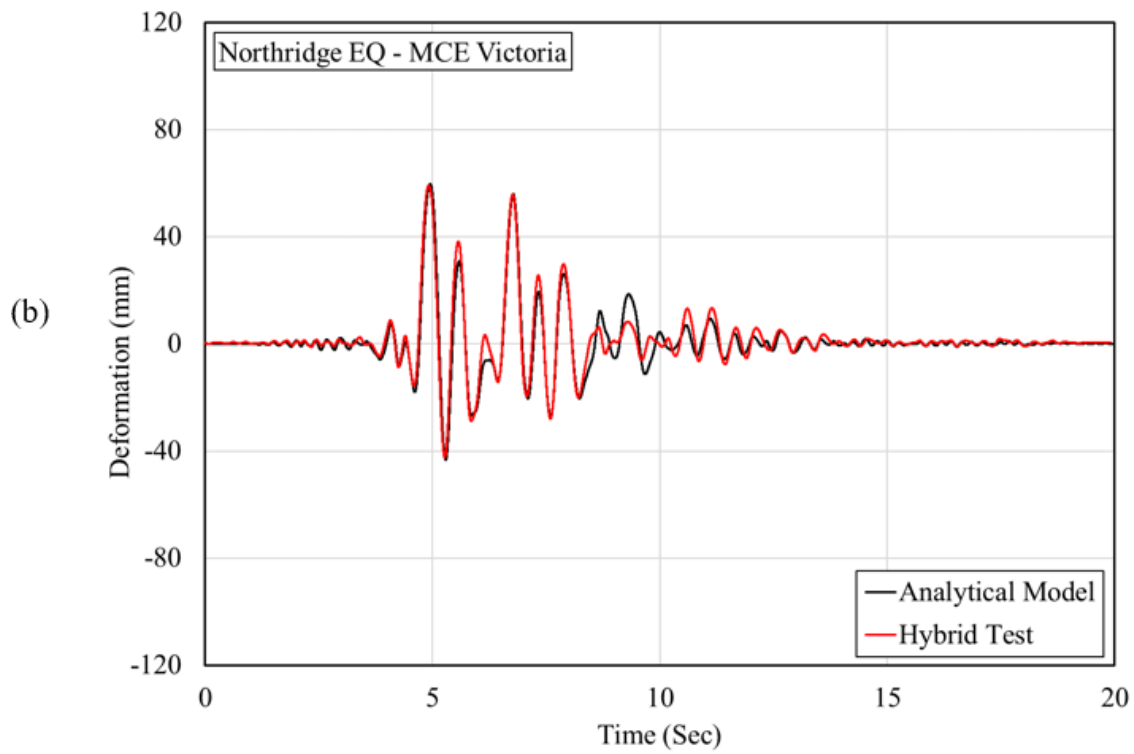
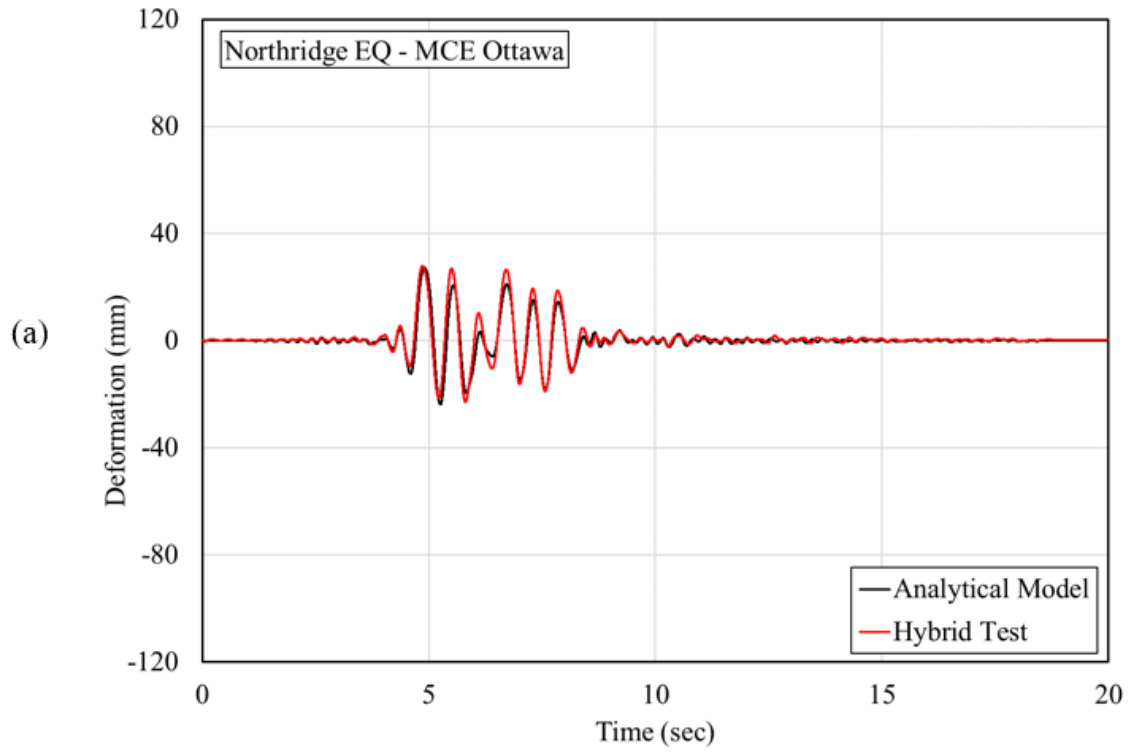


Figure 6.47 Time-History deformation of RS-SCED brace for Northridge record scaled at the (a) Ottawa MCE, and (b) Victoria MCE hazard levels

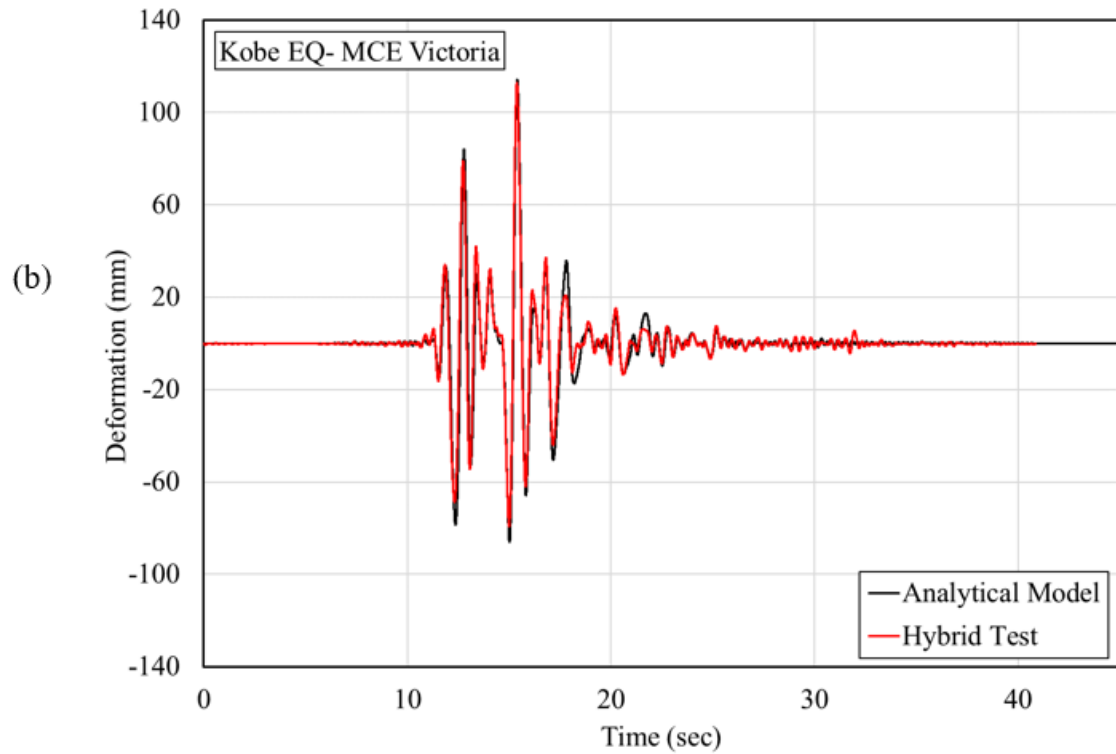
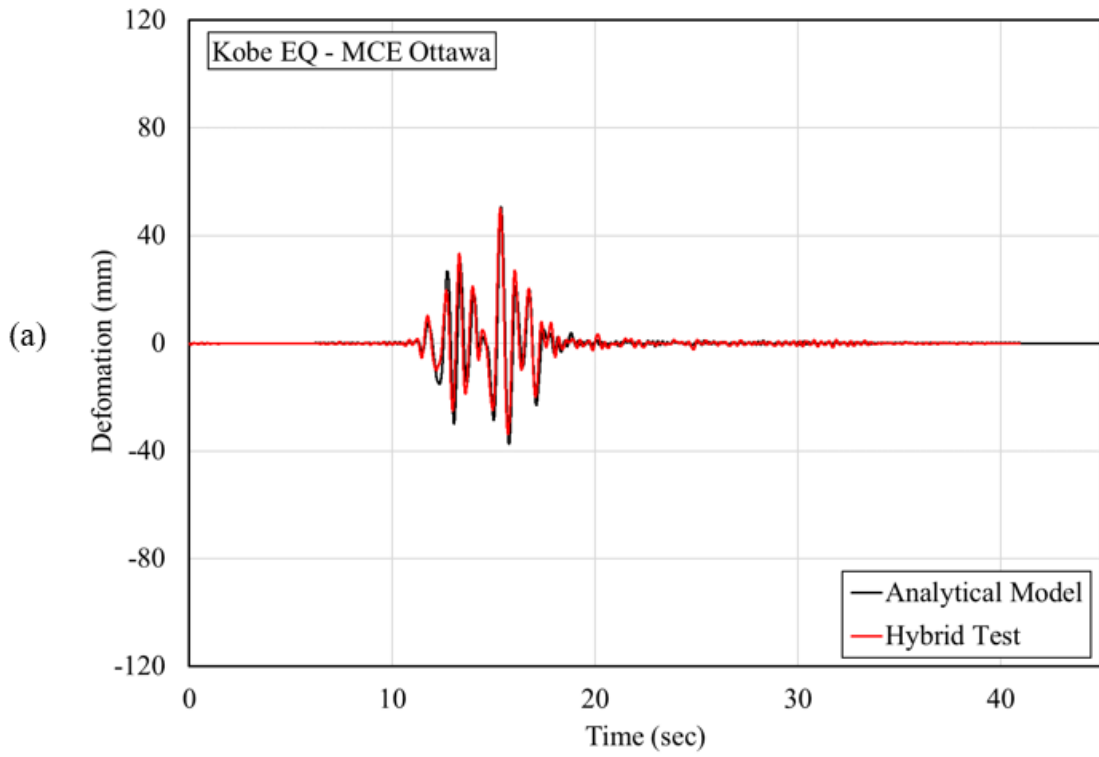


Figure 6.48 Time-History deformation of RS-SCED brace for Kobe record scaled at the (a) Ottawa MCE, and (b) Victoria MCE hazard levels

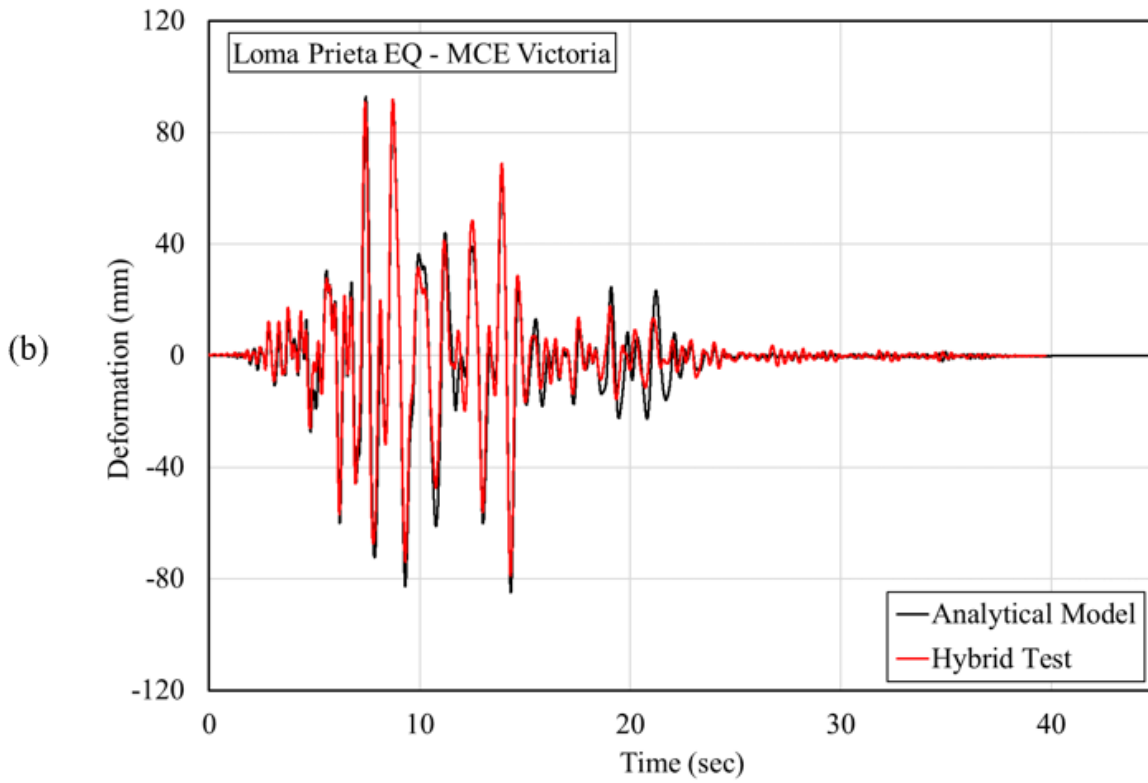
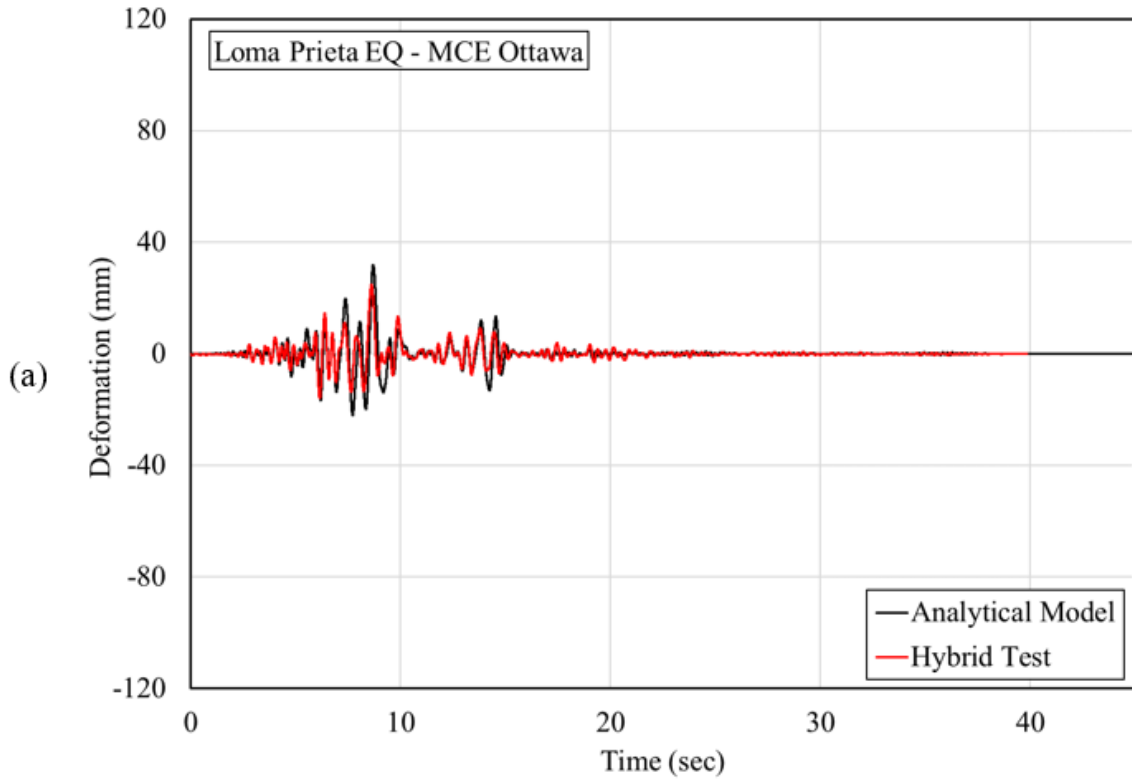


Figure 6.49 Time-History deformation of RS-SCED brace for Loma Prieta record scaled at the (a) Ottawa MCE, and (b) Victoria MCE hazard levels

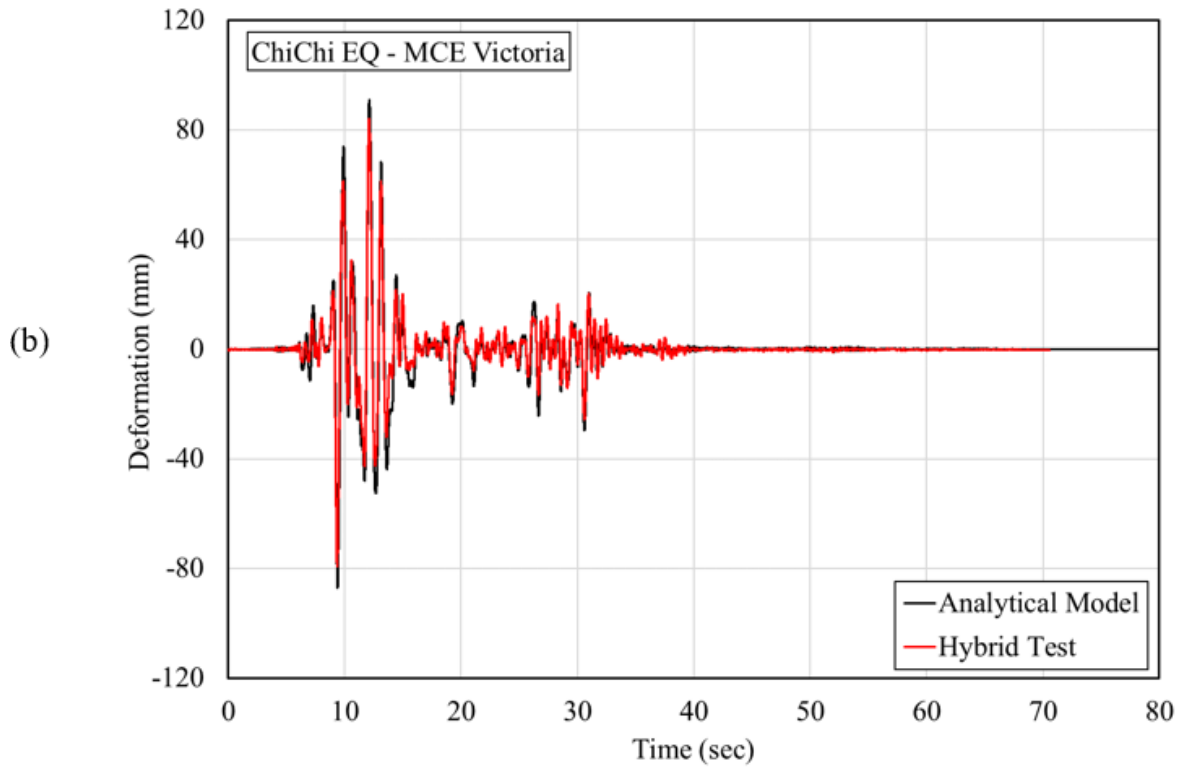
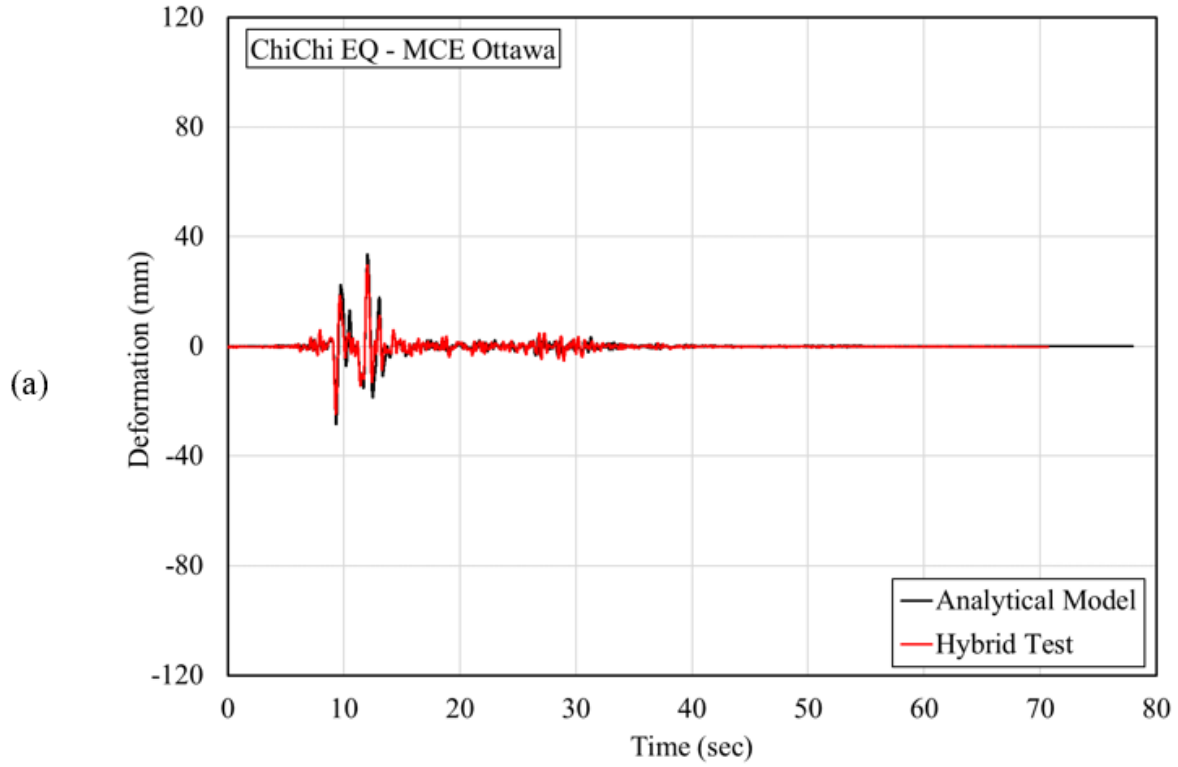
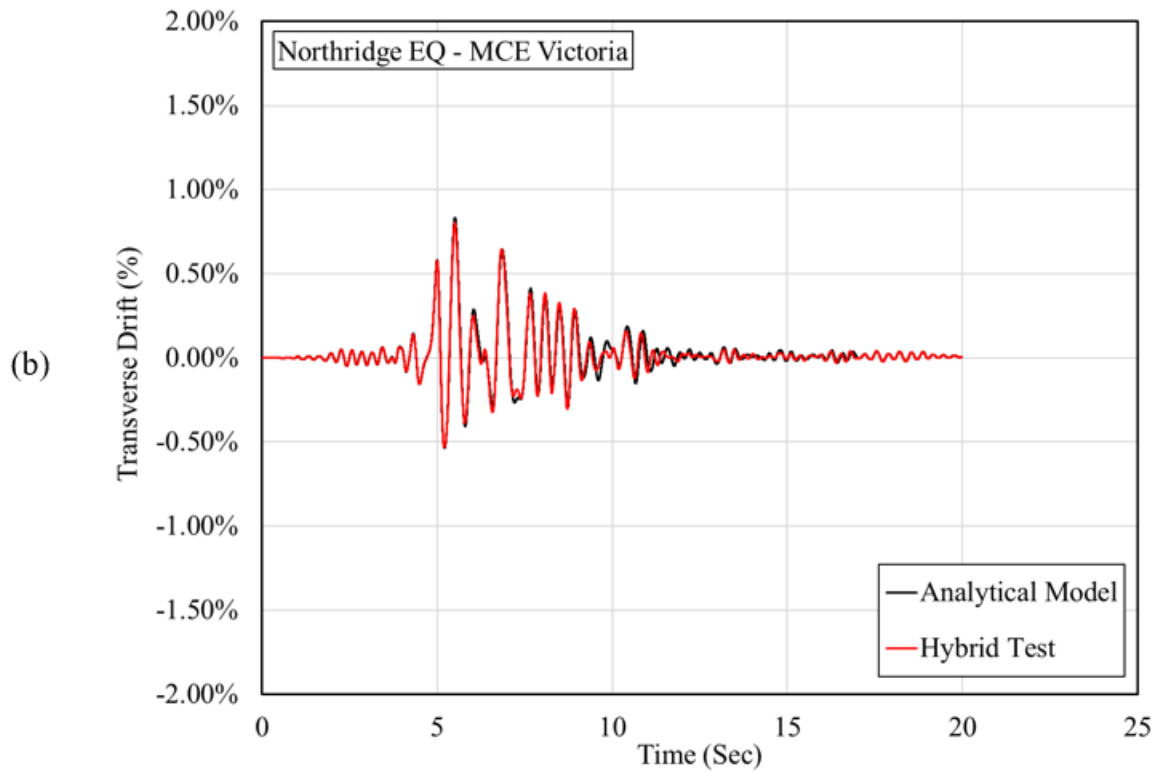
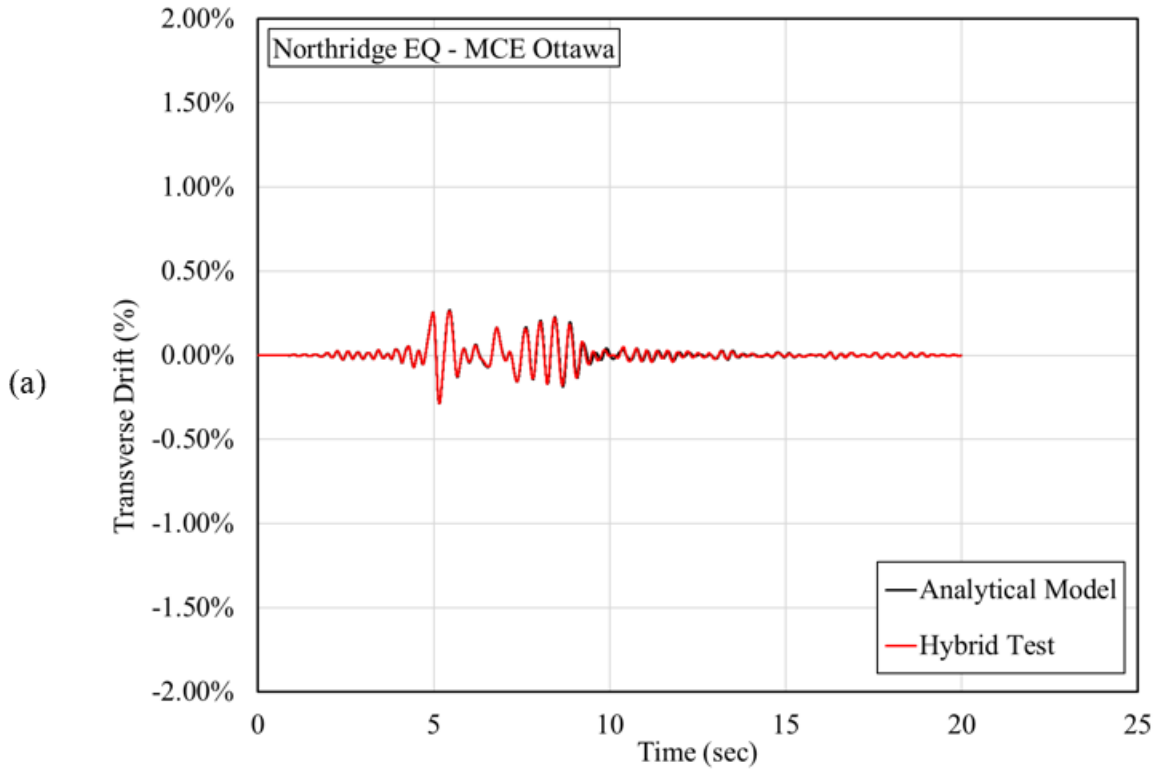


Figure 6.50 Time-History deformation of RS-SCED brace for ChiChi record scaled at the (a) Ottawa MCE, and (b) Victoria MCE hazard levels

Since the RS-SCED braces in the transverse direction were part of the numerical substructure in the hybrid simulation, the transverse drift deformation observed in the hybrid simulation is not expected to be different from the drift calculated from the analytical model. Also, the experimentally-tested RS-SCED brace elements oriented in the longitudinal direction are aligned with the centerline of the bridge section width to minimize any potential torsional effects about the vertical axis of the bridge. Nevertheless, the results are compared to determine if there are any torsional effects about the vertical axis of the bridge resulting from the numerical modelling of the longitudinal RS-SCED braces. As shown in Figure 6.51 to Figure 6.54, the transverse drift calculated from the analytical model correlated very well with the transverse drift observed for the hybrid simulation.

Overall, the comparison of the analytical model and hybrid simulation results presented in this section validates the use of the analytical modelling technique proposed for the modelling of bridge structures. The effect of using the RS-SCED braces on the seismic response of the bridge is accurately captured in the proposed analytical model. In the following section, this numerical model will be used to compare the response of this strengthening scheme to the original bridge structure.



**Figure 6.51 Bridge transverse drift response for Northridge record scaled at the (a) Ottawa MCE, and (b) Victoria MCE hazard levels**

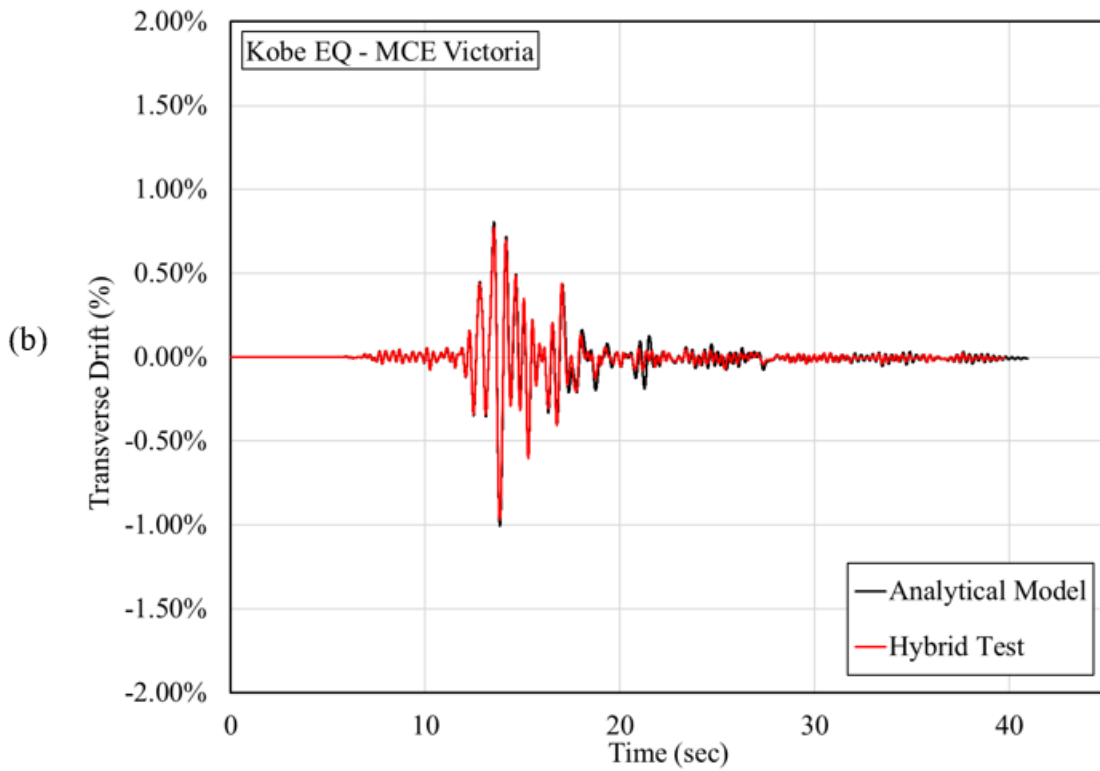
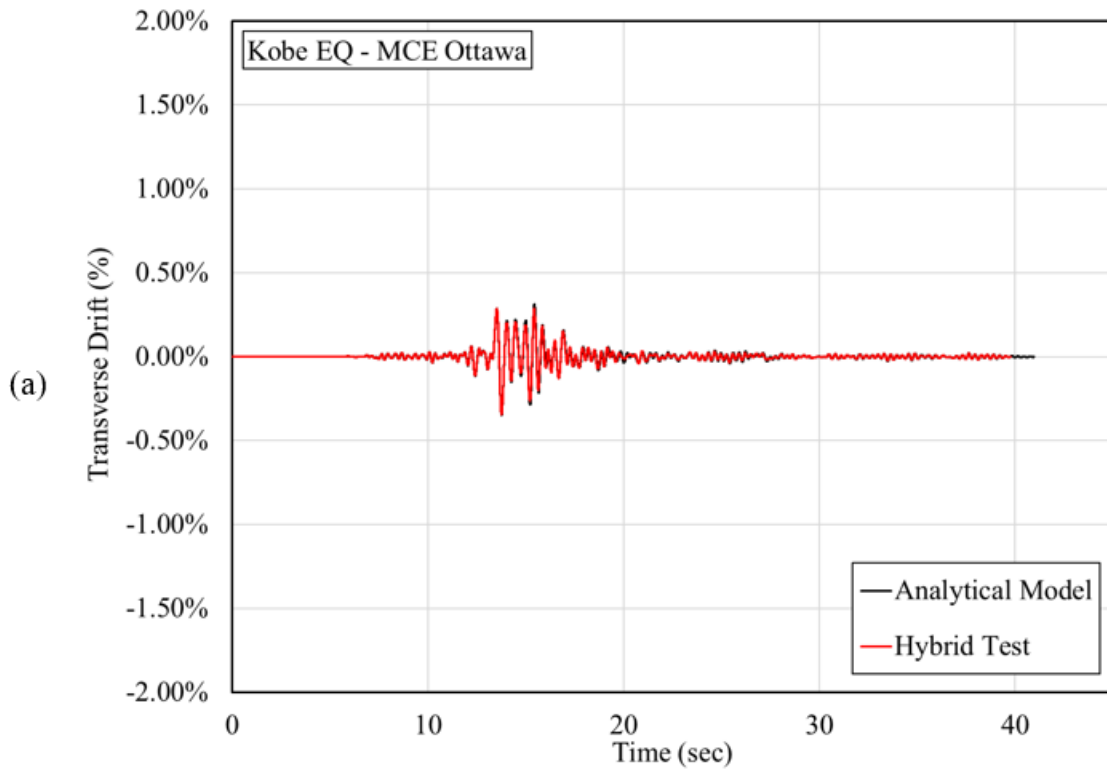


**Figure 6.52 Bridge transverse drift response for Kobe record scaled at the (a) Ottawa MCE, and (b) Victoria MCE hazard levels**

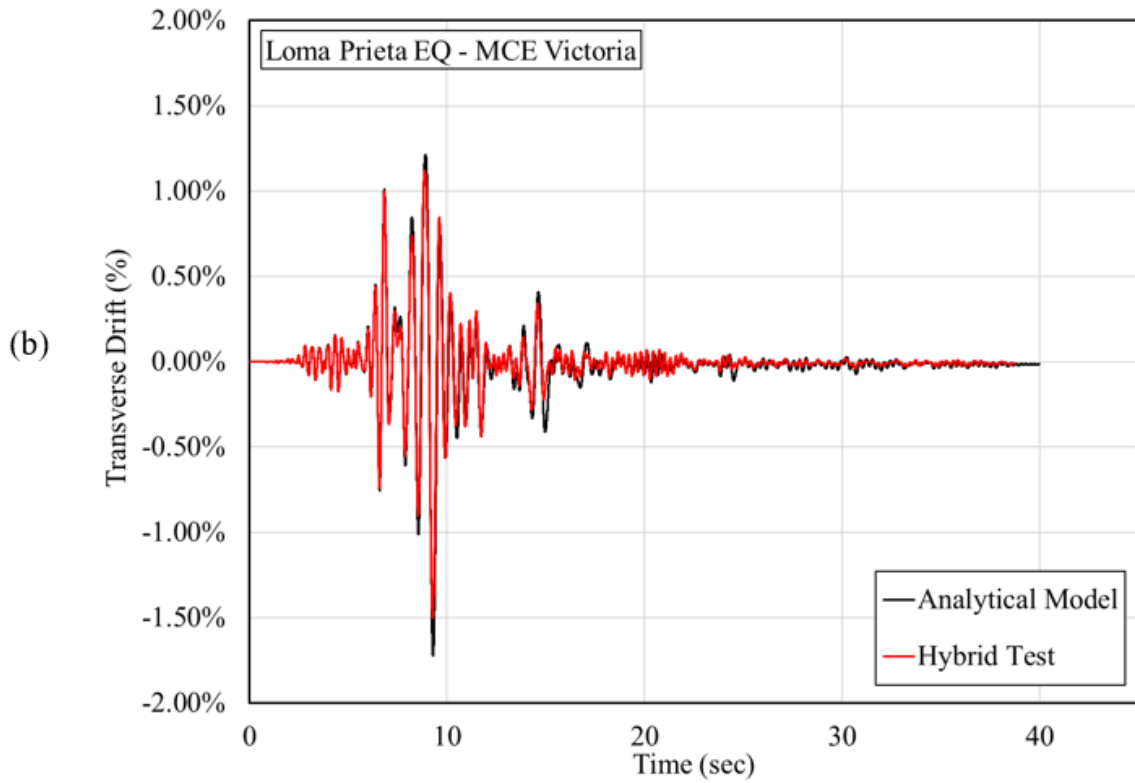
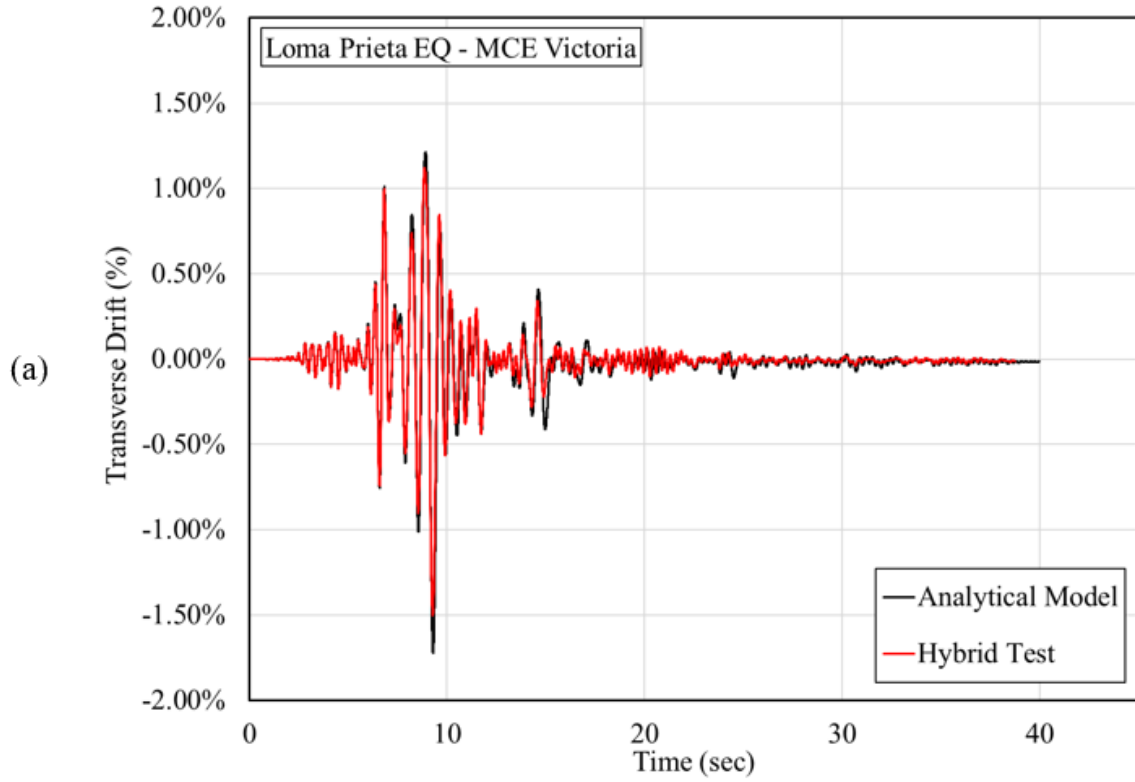


Figure 6.53 Bridge transverse drift response for Loma Prieta record scaled at the (a) Ottawa MCE, and (b) Victoria MCE hazard levels

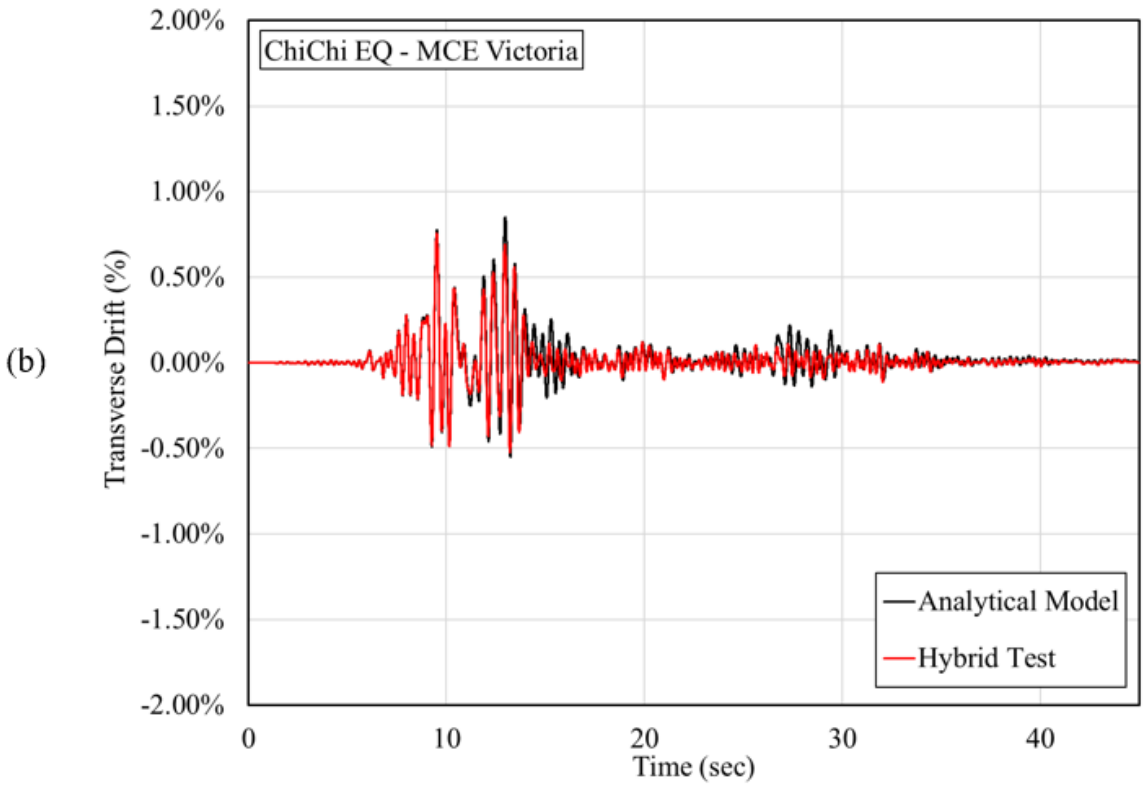
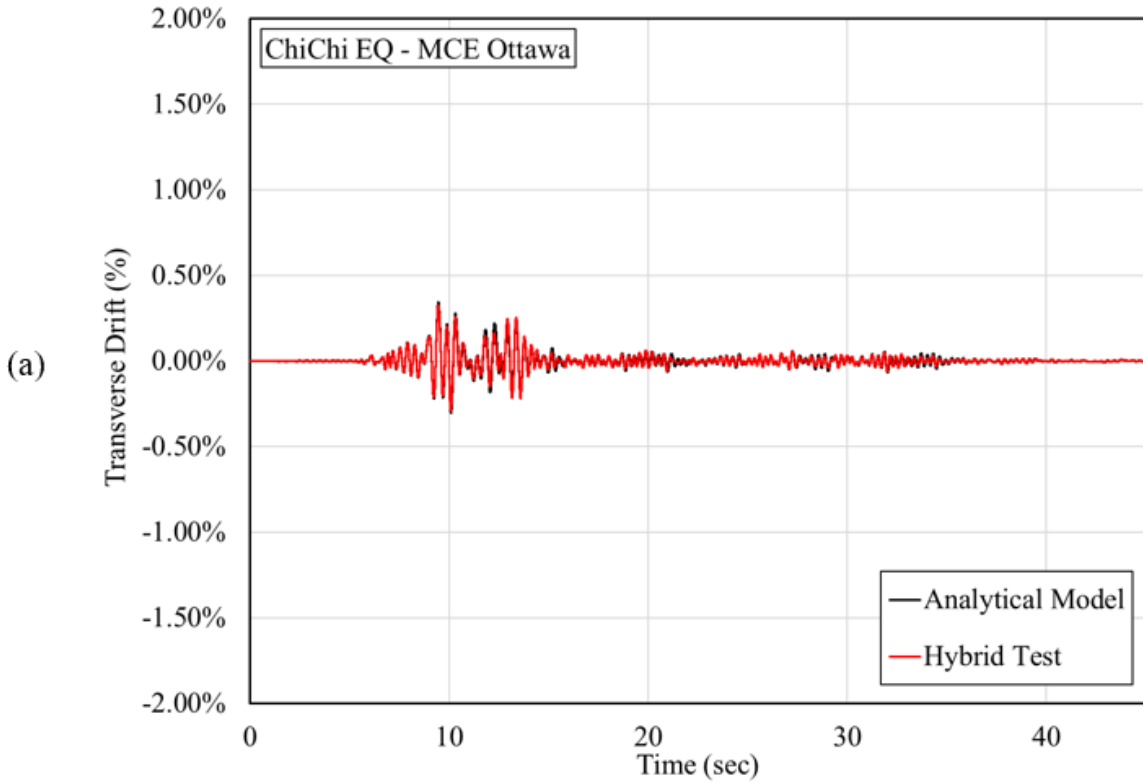


Figure 6.54 Bridge transverse drift response for ChiChi record scaled at the (a) Ottawa MCE, and (b) Victoria MCE hazard levels

## 6.9 Comparison of RS-SCED Retrofitted Bridge and Original Bridge

After validating the numerical model developed in the previous section, the goal of this section is to evaluate the effectiveness of the RS-SCED retrofit scheme on the three span bridge described in this study. The effectiveness of the RS-SCED brace is evaluated by comparing the response of both the original bridge and the bridge retrofitted with RS-SCED braces when subjected to all 4 records scaled to the Ottawa and Victoria MCE hazard levels. The longitudinal and transverse drift of the retrofitted and original bridges are compared to evaluate the influence of the RS-SCED brace on the vibration behaviour at the bridge deck level. In addition, the total moment and shear resisted at the base of the pier foundations is also compared for both bridges for the Victoria MCE scaled records, to evaluate any changes to the demand on the foundation caused by strengthening or retrofitting the bridge using RS-SCED braces.

As shown in Figure 6.55, the RS-SCED bridge is capable of reducing the maximum longitudinal drift especially under the higher seismic demand in Victoria, BC. The results also show that retrofit of the original bridge with RS-SCED braces also had a significant damping effect on the response of the structure, seen as the amplitude of the bridge displacements quickly returns to nearly zero following the peak displacements. This is directly related to the energy dissipation mechanism and design philosophy of bridge piers, which has traditionally designed the piers to remain elastic, to avoid damage that could result in significant damage and residual deformation which would require major repairs following a large earthquake. This design philosophy results in bridge structures that oscillate significantly through many cycles of very minimal yielding to dissipate the seismic energy introduced to the structure during a major event. This is evident by looking at Figure 6.55 where it is noticeable that even though RS-SCED retrofit does improve the

residual drift in most cases, the residual drift of non-retrofit bridges is still not significant. When the RS-SCED braces are introduced, they significantly increase the energy dissipation capacity of the whole system resulting in higher damping and less vibration during and after a seismic event. It is worth noting that this study focuses on validating the design and analytical modelling of the RS-SCED brace rather than proving the effectiveness of improving the seismic performance of bridges. A previous parametric study showed that the use of SCED braces significantly improves the residual drift of bridges subjected to high seismic hazard levels [98].

Similar observations are found for the drift in the transverse direction shown in Figure 6.56. The RS-SCED braces reduced the transverse drift at the bridge deck level significantly with a reduction in the residual drift. This effect was especially noticeable for the Loma Prieta record which had the highest peak ground acceleration and PGA/PGV ratio. The RS-SCED braces showed the ability to dampen the structural response post peak for the same reason discussed above.

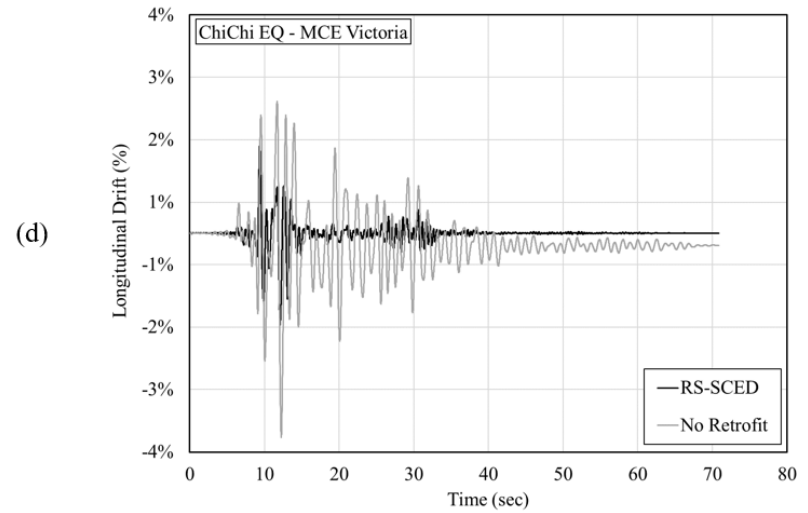
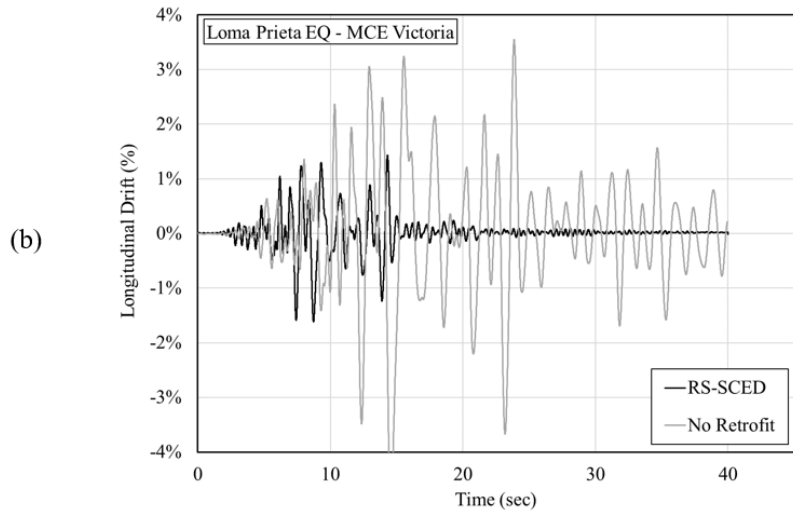
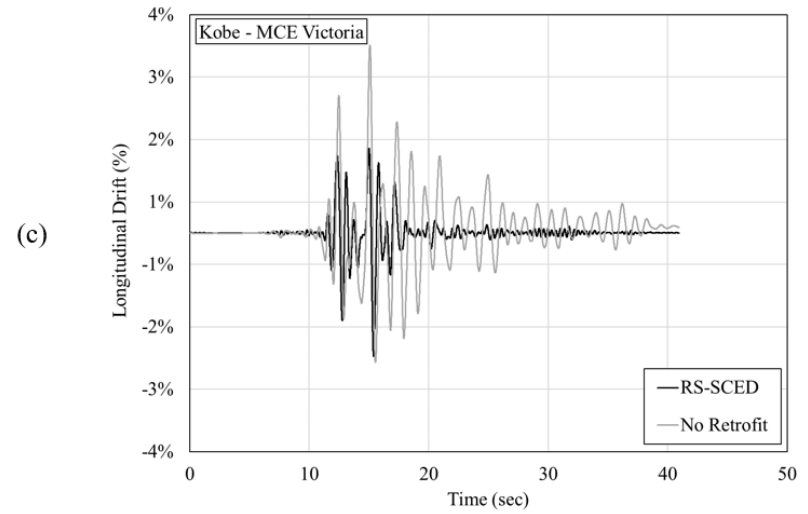
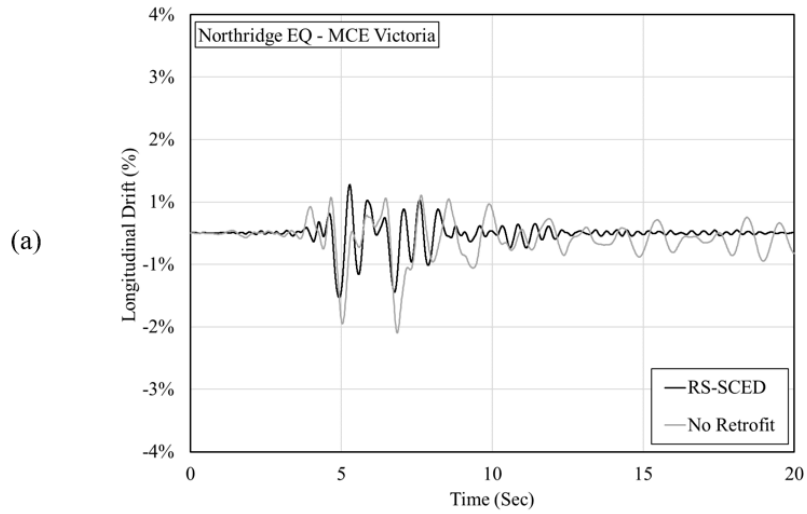


**Figure 6.55 Effect of RS-SCED brace retrofit on longitudinal drift of bridge when subjected to MCE hazard level in Victoria, BC for: (a) Northridge, (b) Kobe, (c) Loma Prieta, and (d) ChiChi earthquake records**

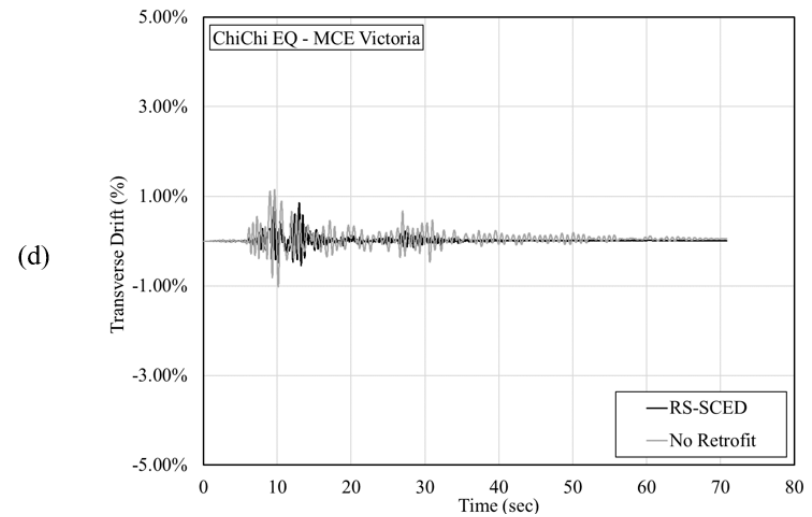
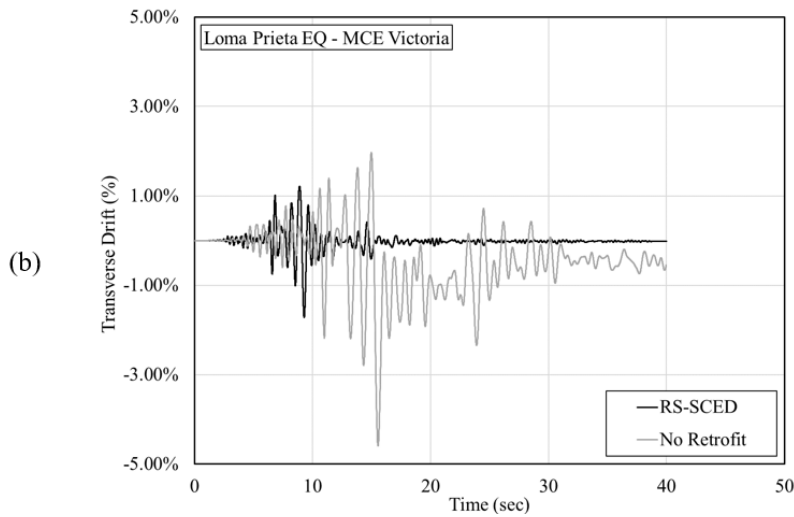
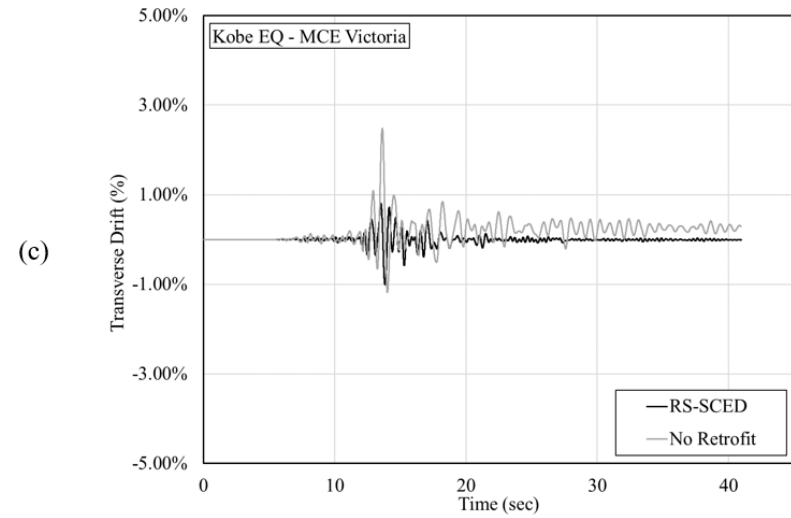
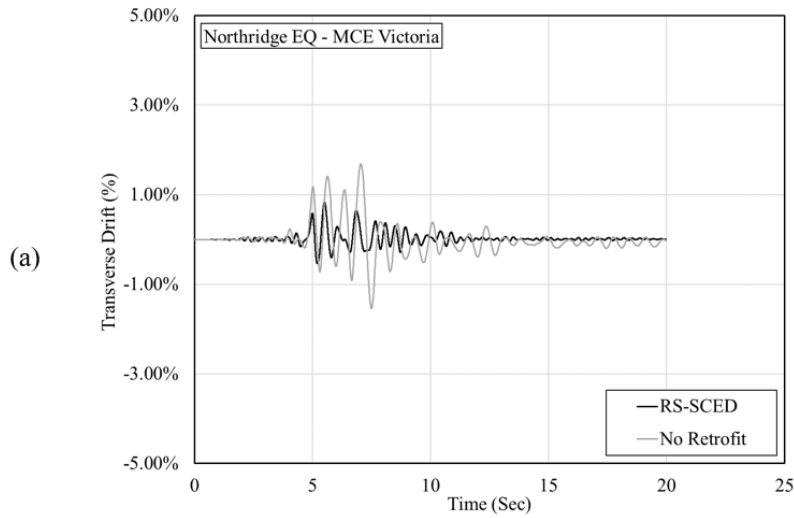


**Figure 6.56 Effect of RS-SCED brace retrofit on transverse drift of bridge when subjected to MCE hazard level in Victoria, BC for: (a) Northridge, (b) Kobe, (c) Loma Prieta, and (d) ChiChi earthquake records**

Another parameter that is investigated is the effect of the RS-SCED brace retrofit on the reactions at the base of the bridge piers for the higher seismic hazard level of Victoria MCE. As shown in Figure 6.57 and Figure 6.58, the RS-SCED retrofit either shows a similar level of peak shear and moment demands, or a reduction in demand in some cases, such as the case when the model is subjected to the ChiChi record. The damping effects of the RS-SCED braces is once again noticeable with the base shear and moment decreasing to near zero shortly after the peak of the response. The reason for the absence of significant reduction in the base shear and moment demand on the foundation, is the increased overall seismic demand caused by the higher stiffness of the overall structure, which results in a shorter period of vibration. This increase in demand is mainly resisted by the supports of the RS-SCED braces located at the abutments which are expected to have significantly higher demand than the non-retrofit backwall and shear key. However, the use of the retrofit scheme did not result in a higher demand on the foundation of the pier making it a viable retrofit scheme.

In summary, the RS-SCED brace retrofit scheme is found to be capable of reducing the maximum drift in both the longitudinal and transverse directions. The retrofit scheme also increases the energy dissipation and damping for the structure, reducing vibrations during and after the seismic event. The retrofit scheme does not increase the seismic demand on the bridge pier foundations, making it a viable option for seismic bridge retrofit and rehabilitation considering the lower cost and higher accessibility to the abutments as compared to the bridge pier foundations.

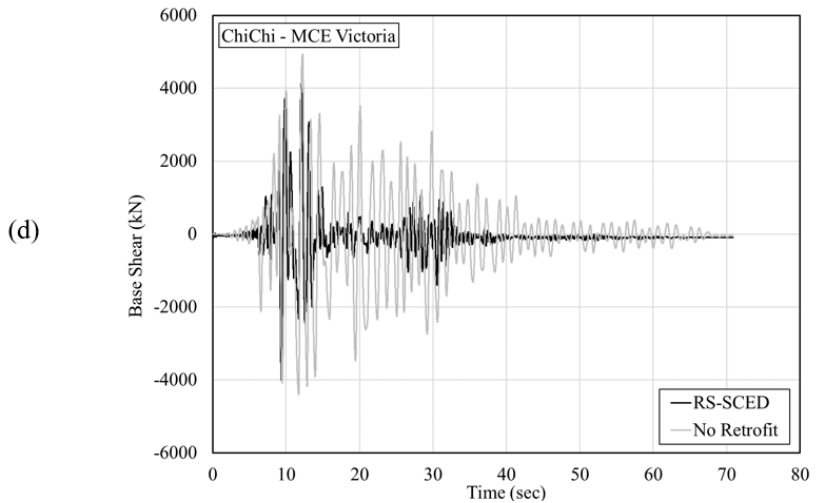
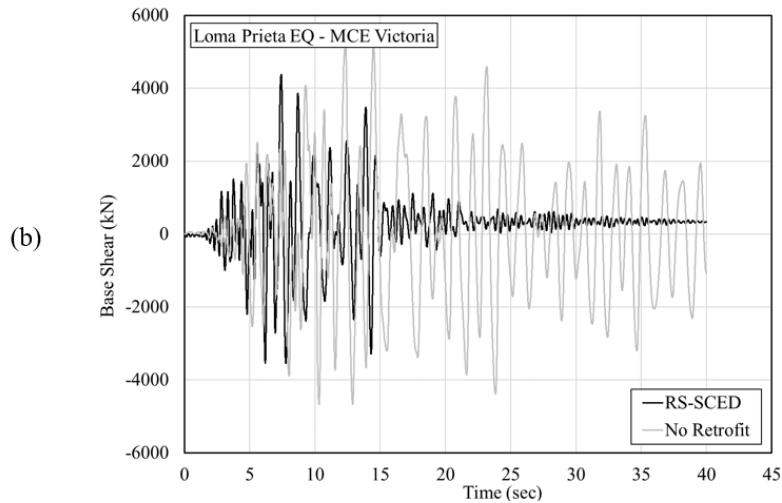
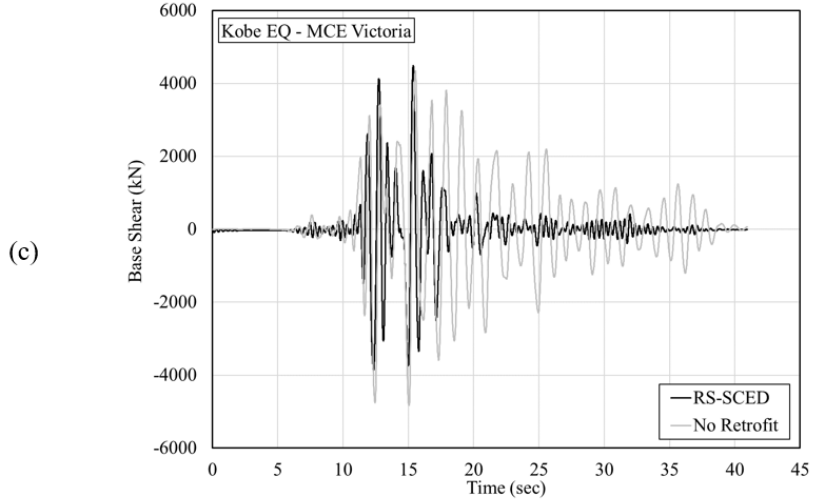
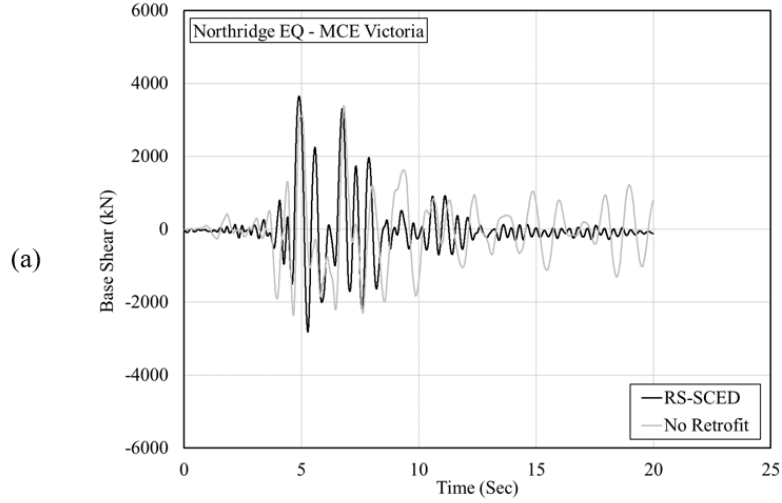


**Figure 6.57 Effect of RS-SCED brace retrofit on base shear at bridge foundation when subjected to MCE hazard level in Victoria, BC for: (a) Northridge, (b) Kobe, (c) Loma Prieta, and (d) ChiChi earthquake records**

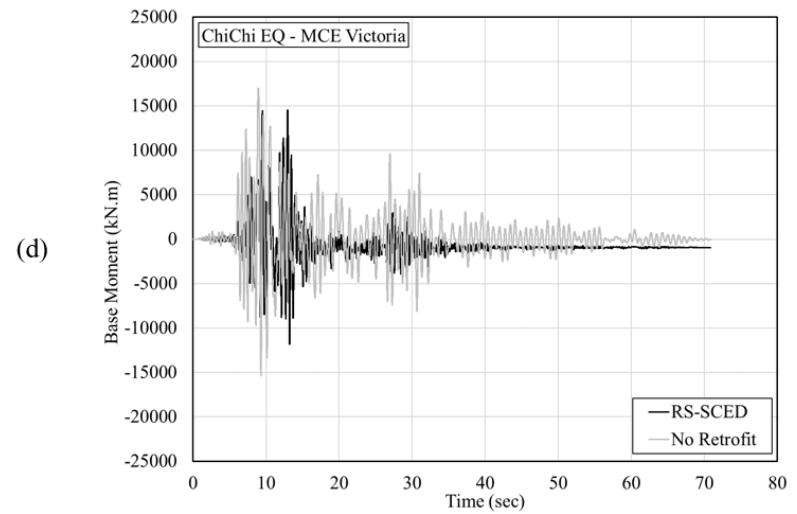
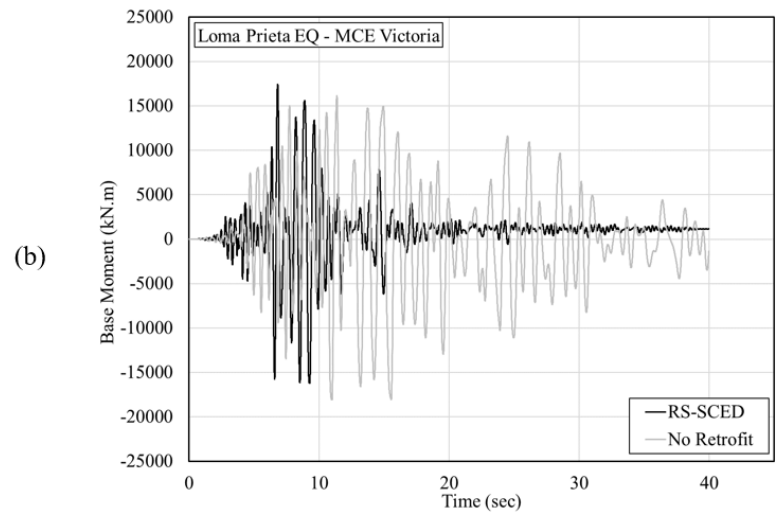
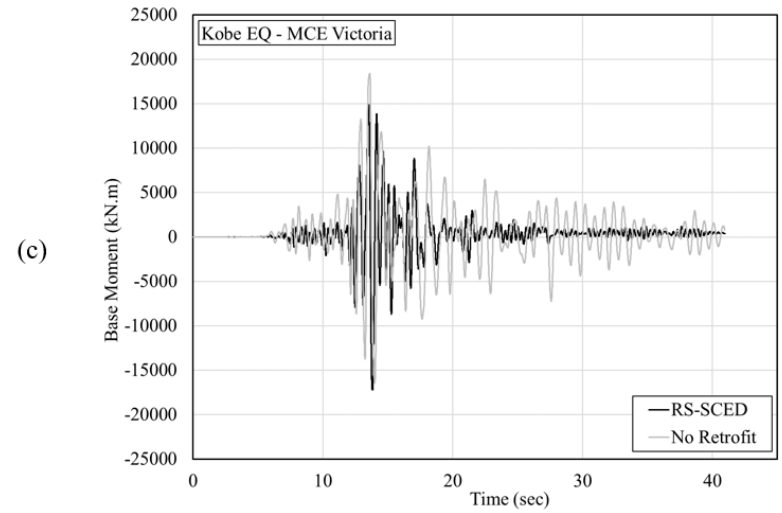
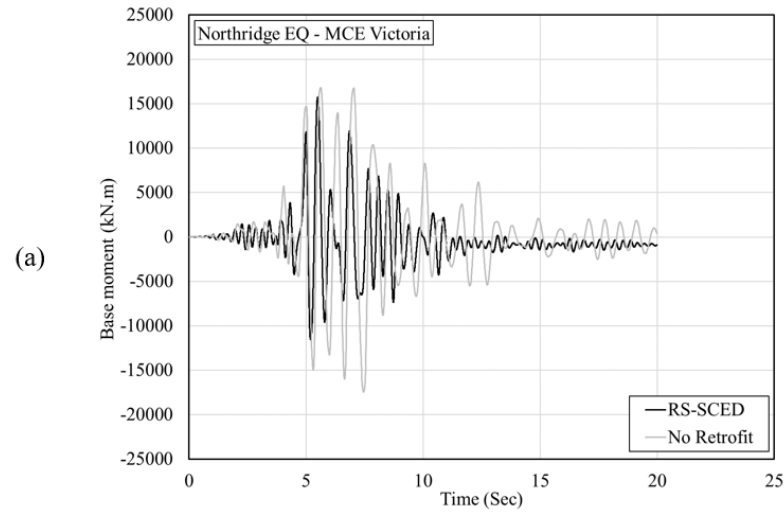


**Figure 6.58 Effect of RS-SCED brace retrofit on base moment at bridge foundation when subjected to MCE hazard level in Victoria, BC for: (a) Northridge, (b) Kobe, (c) Loma Prieta, and (d) ChiChi earthquake records**

# Chapter 7 : Fragility Assessment and Seismic Design Factors

The Equivalent Static Load procedure stipulated in building codes is based on the concept of converting the complicated nonlinear dynamic behaviour of a building structure under seismic loading to an equivalent linear problem. The design process starts with the selection of a basic seismic force resisting system for the structure. The code specifies a series of prescriptive requirements for structures based on each such system. These seismic design requirements are controlled through the assignment of a series of system response coefficients, which represent effect of material properties and design detailing on the seismic response of the selected system. Based on the linear dynamic response characteristics of the structure and these response coefficients, design lateral forces are distributed to the building's various structural elements using linear analysis procedures. The resulting member forces and structural deflections are calculated accordingly. As the codes have improved over the last several decades in how they address seismic design, there has been an expansion of code-approved seismic force resisting systems, with many individual systems classified by the type of detailing used. For each increment in detailing, response coefficients were assigned in the code, based largely on judgment and qualitative in comparison with the known response capabilities of other and existing systems. Since the existing seismic response coefficients for many different seismic lateral force-resisting systems were assigned, developed and evolved over the years without a consistent basis or framework process in the derivation of their values, there has been a need for a standard procedural methodology for the determination of the seismic response coefficients where the inelastic response characteristics and performance of typical structures designed to a set of structural system provisions could be quantified. Such a methodology needed to directly account for the potential variations in: structure

configuration of the designed structures, ground motions, and available laboratory data on the behavioural characteristics of prototypical structural elements.

To meet this need, the FEMA P695 [101] procedure was developed to establish a rational and consistent way to determine appropriate building system seismic performance and response parameters, namely  $R$ ,  $C_d$ , and  $\Omega_0$ , for the common linear seismic design methods as specified in the ASCE 7 [102] building code. The primary application of the procedure is to evaluate the earthquake performance of newly-developed structural systems. The procedure from P695 (herein referred to as the methodology) is used in this study to determine adequate response parameters for buildings with the newly-developed RS-SCED brace. It is worth noting that as of the time of this investigation, there is no equivalent Canadian methodology to the FEMA P695 procedure.

## 7.1 FEMA P695 Methodology

FEMA P695 methodology has the goal of determining appropriate design factors that can be used for the equivalent static method adopted in ASCE 7-16 [102]. Therefore, many of the design parameters in FEMA P695 and ASCE 7 have the same definition. However, some of the parameters are slightly modified to account for the fact that FEMA P695 methodology aims to analyze and evaluate seismic performance of new systems not identified in ASCE 7. Figure 7.1 presents an idealized pushover curve with the definitions of the three main seismic modification factors as per the ASCE 7-16, namely  $R$ ,  $C_d$  and  $\Omega_0$ . The term  $V_E$  represents the force level that would be developed in the seismic force resisting system (SFRS) if the system is to remain linearly elastic subject to the design earthquake. The term  $V_{max}$  represents the actual maximum strength of the fully yielded SFRS, while the term  $V$  represents the design base shear at the linear elastic limit of the SFRS. As shown in Equation 7-1,  $R$  is the ratio between the theoretical elastic base shear

$V_E$ , which would have developed had the building remained linearly elastic, to the design base shear  $V$ :

$$R = \frac{V_E}{V} \quad \text{Equation 7-1}$$

The overstrength factor  $\Omega_0$  represents the ratio between the actual maximum strength of the fully yielded SFRS, including any overstrength from material and construction, to the design base shear:

$$\Omega_0 = \frac{V_{max}}{V} \quad \text{Equation 7-2}$$

The term  $\delta_E/R$  represents the roof drift of the SFRS corresponding to the design base shear  $V$ , a level at which the system is assumed to still be in the elastic range. Conversely, the term  $\delta$  represents the assumed roof drift of the yielded system corresponding to design earthquake ground motion. A factor  $C_d$ , represents the ratio between the elastic deformation and the roof drift as a fraction of  $R$  as shown in Equation 7-3

$$C_d = \frac{\delta}{\delta_E} R \quad \text{Equation 7-3}$$

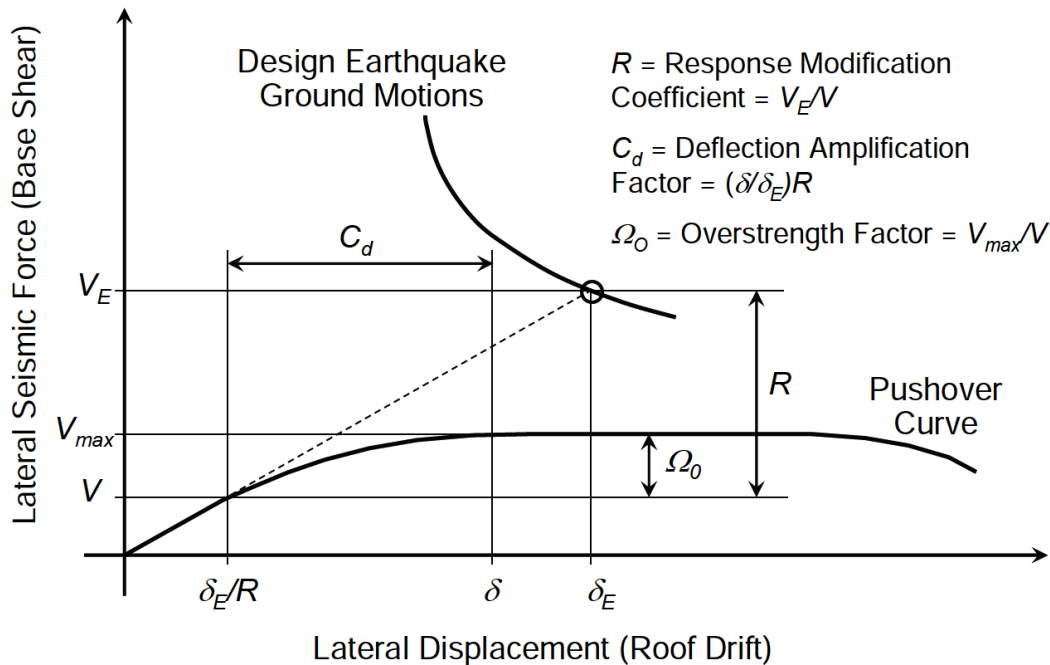


Figure 7.1 Illustration of seismic performance factors defined in ASCE 7-16 [101]

Figure 7.2 mirrors the pushover curve presented in Figure 7.1 using the spectral acceleration and displacement rather than lateral force and displacement (base shear and roof drift). The conversion to the spectral acceleration and displacement assumes that 100% of the effective seismic weight of the structure  $W$ , participates in the fundamental mode of the structure with the vibration period  $T$ . This is consistent with the assumption made in the equivalent lateral load procedure in ASCE 7 and shown in Equation 7-4 where  $C_s$  is the seismic coefficient.

$$V = C_s W \quad \text{Equation 7-4}$$

In Figure 7.2,  $S_{MT}$  represents the Maximum Credible Earthquake (MCE) spectral acceleration at the fundamental period of the structure if the system remained linearly elastic. The definition of the design-based earthquake (DBE) and the corresponding design spectral acceleration  $S_D$ , is defined in ASCE 7-16 (and FEMA P695) as two-thirds of the MCE spectral acceleration  $S_{MT}$ :

$$S_D = \frac{2}{3} S_{MT} \quad \text{Equation 7-5}$$

Based on the calculated  $S_D$ , the appropriate seismic coefficient can be calculated as follows:

$$C_s = \frac{S_{DS}}{R} \quad \text{when } T < T_s \quad \text{Equation 7-6}$$

and

$$C_s = \frac{S_{D1}}{T R} \quad \text{when } T > T_s \quad \text{Equation 7-7}$$

where  $T_s$  is the transition period, the period at which the constant acceleration part of the design response spectrum ends, and the constant velocity part of the spectrum begins. The period range between 0 s and the transition period  $T_s$  is referred to as the short period range. The transition period  $T_s$  is defined as:

$$T_s = \frac{S_{D1}}{S_{DS}} = \frac{S_{M1}}{S_{MS}} \quad \text{Equation 7-8}$$

Where  $S_{D1}$  and  $S_{M1}$  are the design and MCE spectral response acceleration parameter at a period of 1.0 s respectively, while  $S_{DS}$  and  $S_{MS}$  are the design and MCE spectral response acceleration parameters in the short period range, respectively. The values for  $S_{D1}$  and  $S_{DS}$  are determined based on the seismic design category for which the structure is designed and can be found in the original methodology (Table 5-1) [101]. In Figure 7.2,  $S_{max}$  represents the actual maximum spectral acceleration experienced by the structure after yielding.  $C_s$  on the other hand, represents the seismic base shear  $V$  normalized by the effective weight of the structure  $W$ . Therefore, the  $R$  factor can be expressed as a function of  $C_s$  and  $S_{MT}$  as follows:

$$1.5R = \frac{S_{MT}}{C_s} \quad \text{Equation 7-9}$$

The overstrength parameter  $\Omega$  is defined as the ratio of the maximum strength of the system after yielding to the design strength (normalized by  $W$ ) as follows

$$\Omega = \frac{S_{max}}{C_s} \quad \text{Equation 7-10}$$

The inelastic system displacement at the MCE level is defined as  $SD_{MT}$  which is equal to  $1.5C_d$  times the displacement corresponding to the design seismic acceleration  $C_s$ . Based on the Newmark rule and the assumption that the system has an effective damping approximately equal to 5%,  $C_d$  is determined to be equal to  $R$  under the FEMA P695 methodology. This definition of  $C_d$  is specific to the methodology and is not the same definition in ASCE 7-16 in which  $C_d$  is determined based on values of existing structural systems.

$$C_d = R \quad \text{Equation 7-11}$$

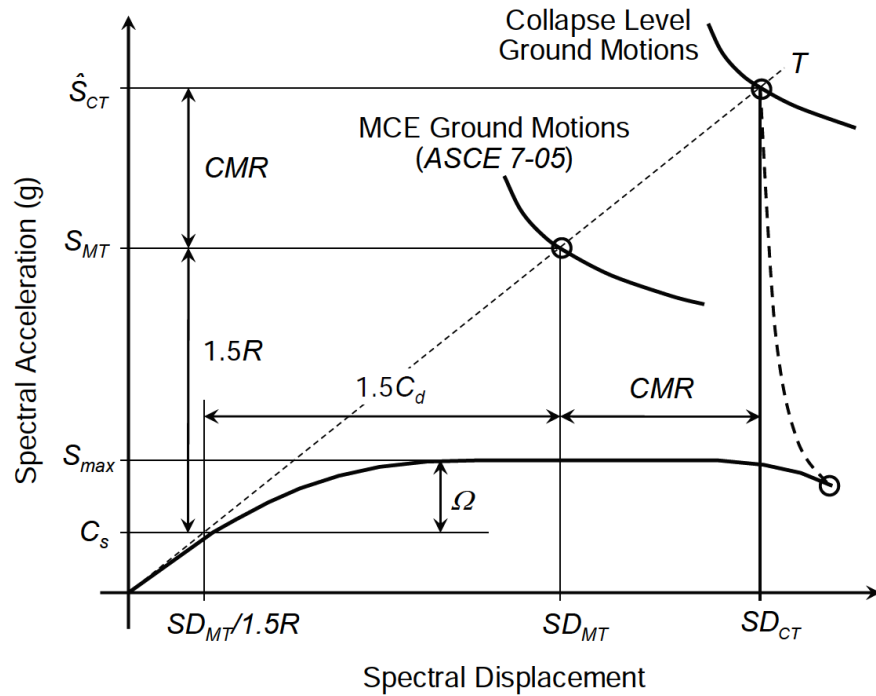


Figure 7.2 Seismic performance factors as defined by FEMA P695 methodology [101]

The methodology defines the collapse level ground motion as the intensity that would result in median collapse of the SFRS. Median collapse occurs when one-half of the ground motions in an earthquake suite are scaled to a certain intensity that causes a structure to have some form of life threatening collapse. The methodology does not specify what are the appropriate collapse criteria for the system being investigated. For this study, collapse is defined as the spectral acceleration where one of the following two collapse criteria occurred: (a) Structural instability/loss of structural integrity, or (b) a transient inter-storey drift of 5% or more occurs on any floor. The 5% limit on the inter-storey drift is adopted from the recommendation in FEMA 356 [103]. Another reason for choosing this value is the RS-SCED braces in this study are designed to accommodate 5% inter-storey drift before the steel rods start to yield. The residual drift performance of the buildings are compared against a separate limit of 0.5% on residual drift, however, this limit is not considered a collapse criterion since residual drift is not directly related to collapse. The limit on residual drift is based on the extensive study done on the permissible limit on residual drifts that

takes into account building functionality, construction tolerance and safety to occupants by McCormick et al. [97]. As shown in Figure 7.2, the median collapse level ground motions should cause higher spectral accelerations  $\hat{S}_{CT}$  than the MCE level ground motion spectral acceleration  $S_{MT}$  in order for the system performance to be considered adequate. The ratio between the Collapse level demand and the MCE level demand of the structure is defined as the Collapse Margin Ratio (*CMR*).

$$CMR = \frac{\hat{S}_{CT}}{S_{MT}} \quad \text{Equation 7-12}$$

In other words, the *CMR* can be thought of as the factor by which  $S_{MT}$  would need to be magnified to cause a collapse in the structure for half of the ground motions. Collapse of the SFRS, and inherently the *CMR*, is influenced by many factors such as ground motion variability, uncertainties in design, analysis and construction of the structure. To account for the uncertainty in the frequency content of the ground motions, an Adjusted Collapse Margin Ratio (*ACMR*) is defined in the methodology by a Spectral Shape Factor (*SSF*) as follows.

$$ACMR = SSF \times CMR \quad \text{Equation 7-13}$$

The spectral shape factor *SSF* depends on the fundamental period of the structure being investigated  $T$ , the period-based ductility  $\mu_T$ , and the applicable seismic design category. It is worth noting that each building that is investigated (defined as archetype in the methodology and explained further below) has a different period  $T$ , period-based ductility  $\mu_T$ , and SDC and thus will have different *SSF*. The methodology defines an acceptably low probability of collapse of a structure for MCE hazard level ground motions, given a certain level of uncertainty in the collapse fragility. Uncertainties in the collapse fragility are addressed by modifying the acceptable *ACMR* based on an assigned value for the total system uncertainty referred to as  $\beta_{TOT}$ . The evaluation of this uncertainty is discussed further in Section 7.4.

## 7.2 Building Archetypes

To account for the uncertainty due to variations in the characteristics of buildings, the methodology requires the analysis of a wide range of structures which are referred to herein as archetypes. Archetypes are grouped into different performance groups which reflect major differences in seismic load intensity, structural period, design gravity loads, configuration, and other factors. A minimum of 4 performance groups must be considered which are based on a combination of at least two seismic design levels and two period domains. The seismic structural period domain is based on distinction between short period structures ( $T < T_s$ ) and long period structures, and the seismic design level is based on the seismic design category used for design (from ASCE 7). Accordingly, in this study 2-, 4-, 8- and 12-storey buildings are investigated with varying numbers of 7 m x 9 m bays. Figure 7.3 shows the elevation of the archetypes considered in the study. Table 7-1 summarizes all the archetypes investigated in this study. The details of the design of each archetype including the different braces designed and the member sizes and loading of the archetypes are presented in Appendix C.

The archetypes for this study are designed according to ASCE 7-16 using the following approach: (1) First, the fundamental period of the structure is calculated. The period of the structure is a function of the building height and the structure type. Since this structural system is a newly proposed system, the FEMA P695 methodology suggests using the upper limit on calculated periods to calculate the structural demand. This is done by multiplying the approximate fundamental period  $T_a$  outlined in equation 12.8-7 in ASCE 7 by the appropriate coefficient for the upper limit on periods  $C_u$  in table 12.8-1 found in ASCE 7 [102]; (2) Following the calculation of the fundamental period, the design base shear of each structure  $V$  is calculated based on the seismic weight of each structure  $W$  and the seismic coefficient  $C_s$ . The seismic weight is calculated

by designing a typical steel composite floor with concrete filled steel deck designed to support office occupancy. The seismic coefficient is dependent on the seismic design category for which the archetype is being designed; (3) Base shear is vertically distributed to each floor based on floor weight and height according to equation 12.8-12 in ASCE 7-16 [102]; (4) The seismic force at each floor  $F_x$  is divided by the number of RS-SCED braces at each floor to determine the appropriate activation force  $P_a$  of the RS-SCED brace per floor; (5) The RS-SCED braces are designed according to the process outlined in Section 4.1. The geometry of the archetype structures and the 5% limit on inter-storey drift discussed in Section 7.1 are used to determine the deformation demand of the RS-SCED braces; and (6) The chevron brace and steel columns supporting the RS-SCED brace are then designed to resist the maximum load applied by the RS-SCED braces  $P_u$  to ensure building stability during the seismic response of the structure. Figure 7.4 to Figure 7.6 show the plan view of the modelled archetypes with the shaded area being the portion of the structure modelled analytically.

**Table 7-1 List of different building archetypes used for this study**

<b>Performance Group</b>	<b>Seismic Design Category</b>	<b>Archetype</b>	<b>Number of Floors</b>	<b>Number of Bays</b>	<b>Fundamental Period (s)</b>
1	D	1	12	25	1.77
		2	8	25	1.18
		3	4	25	0.61
		4	2	25	0.34
2	D	5	2	15	0.34
		6	2	9	0.34
		7	12	25	1.88
3	C	8	8	25	1.21
		9	4	25	0.67
		10	2	25	0.40
4	C	11	2	15	0.40
		12	2	9	0.37

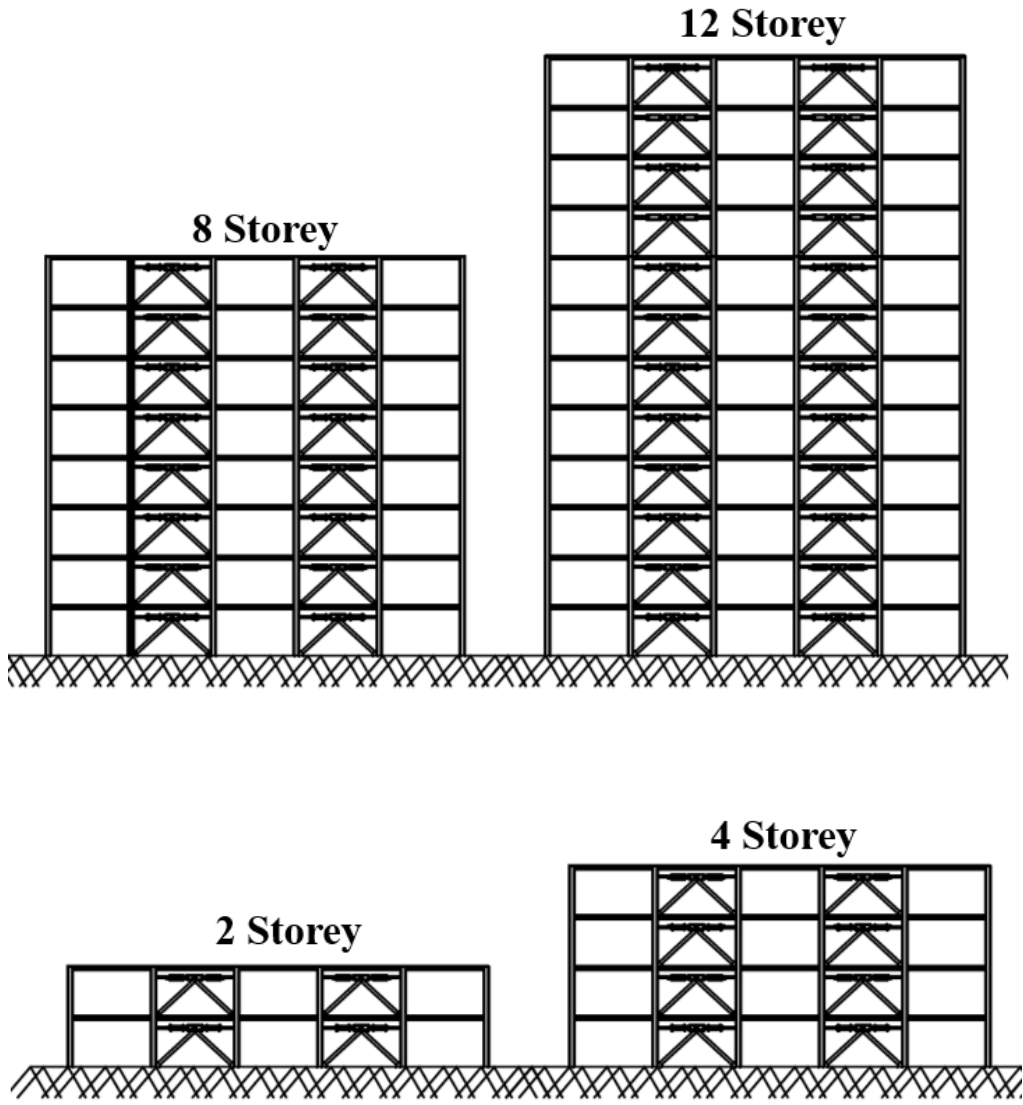
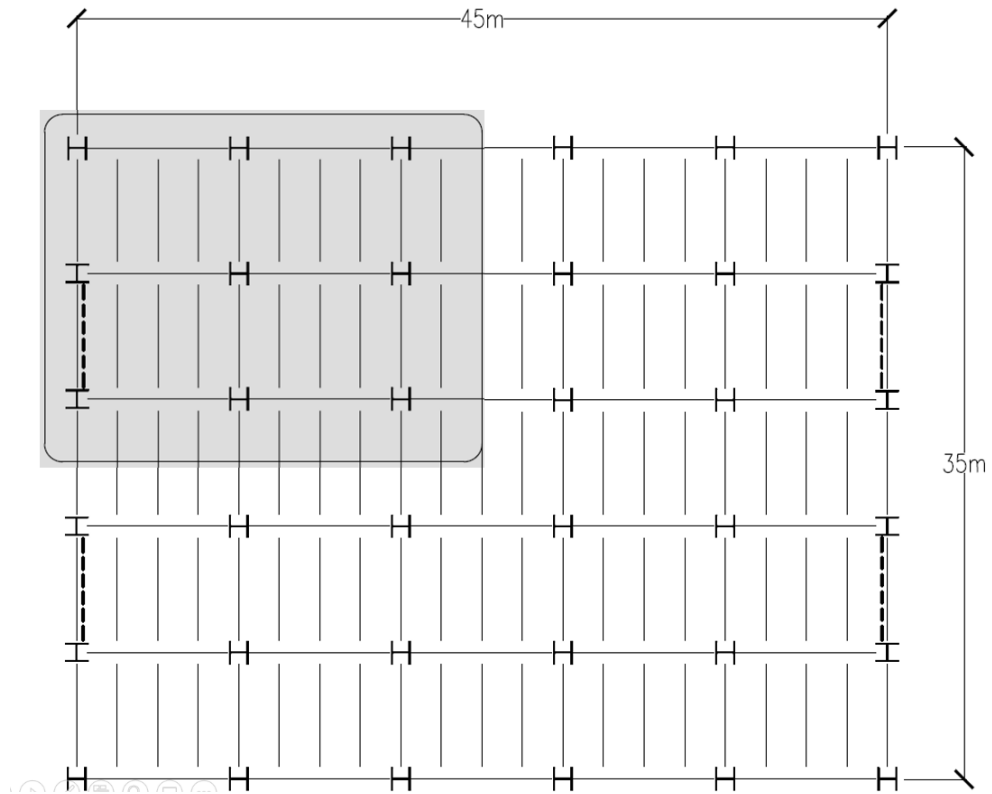
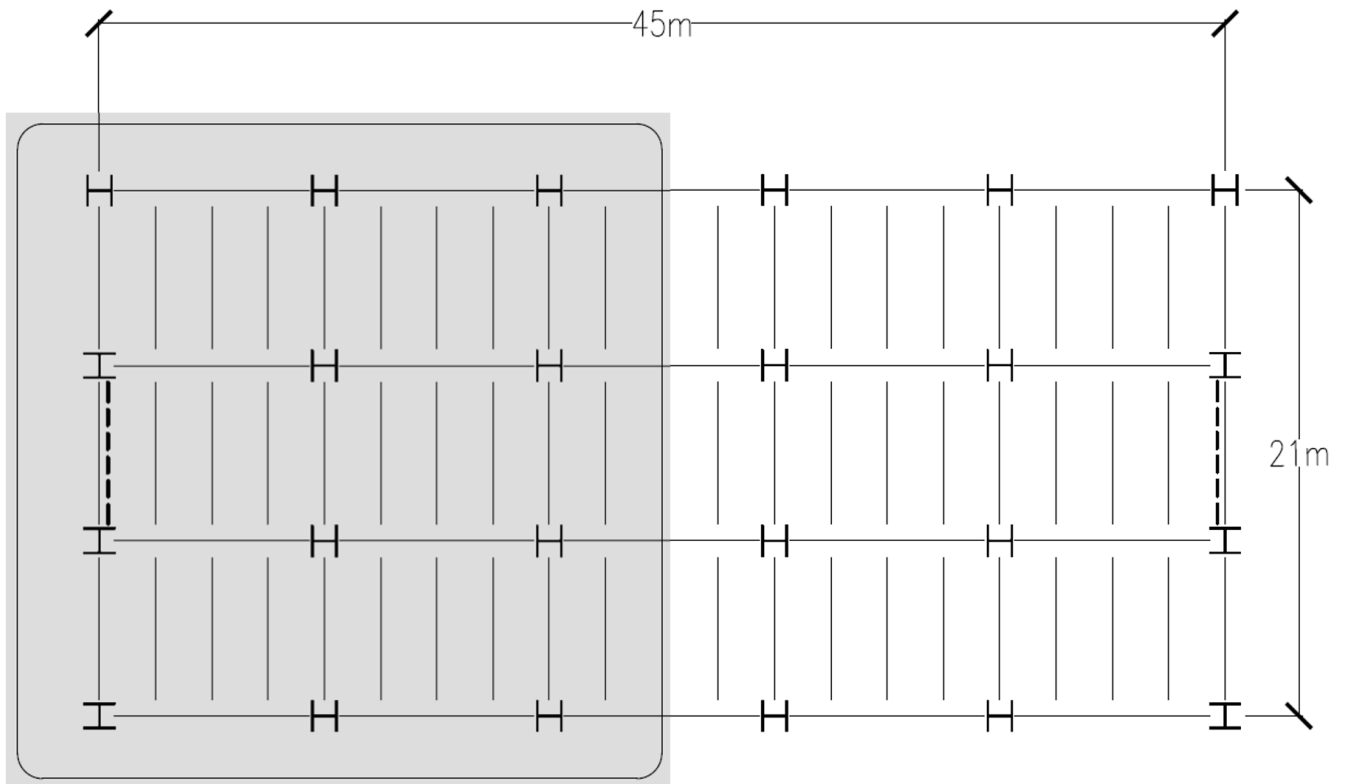


Figure 7.3 Elevation view of the building archetypes used for this study



**Figure 7.4 Plan view of 25 bay archetype buildings**



**Figure 7.5 Plan view of 15 bay archetype buildings**

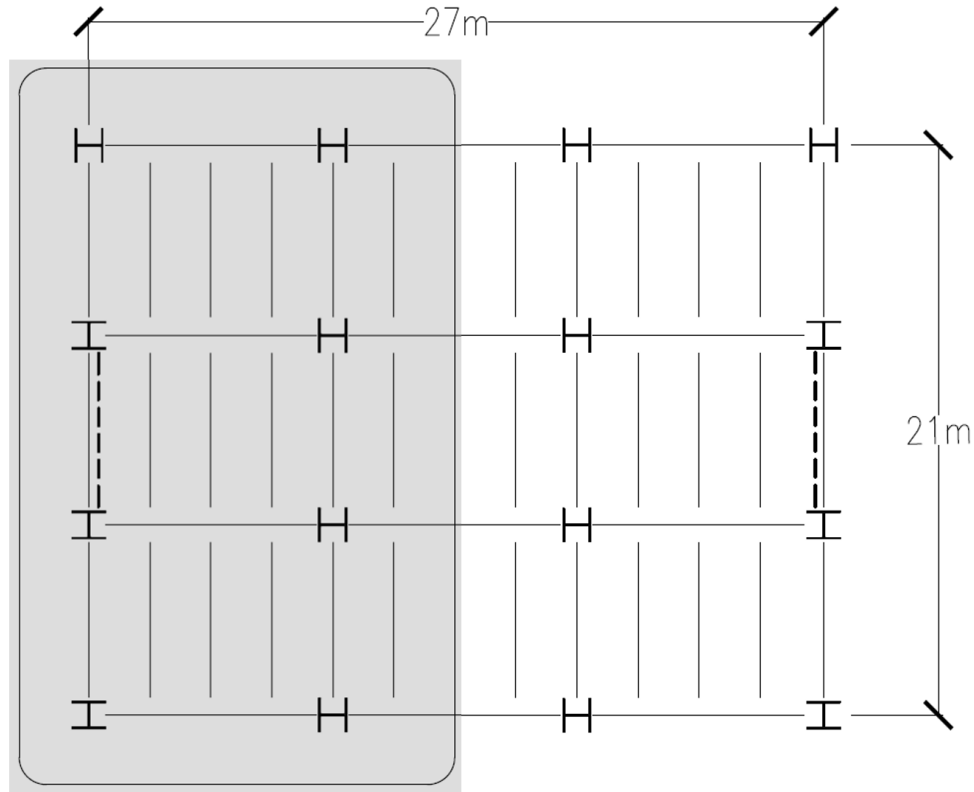


Figure 7.6 Plan view of 9 bay archetype buildings

### 7.3 Non-Linear Building Models

To conduct the analytical study required for the methodology, 12 non-linear models are developed in OpenSees based on the design of each archetype. The braced frame columns are modelled using distributed plasticity beam column elements, the beams and chevron braces are modelled using truss elements. The RS-SCED braces are modelled using Two-Node link elements with a material model specially developed for the ring spring behaviour. To account for the P-Delta effects, a leaning column is also included in the model and connected to the braced frame at each storey level by a rigid link. A nominal 5% Rayleigh inherent damping for the first two modes is assumed for the dynamic analysis in this study for the reasons discussed in Section 7.1. Based on this damping, the displacement amplification factor  $C_d$  would be equal to the  $R$  factor as determined from the non-linear dynamic analyses.

## 7.4 Determining Ductility Factor $R$

In the methodology, the  $R$  factor is determined in an iterative process. Initially, an arbitrary assumed value of  $R$  is used to design the building archetypes and then a partial incremental dynamic analysis (IDA) is performed. This is done through a process of fragmented scaling of the MCE hazard level, the methodology suggests at least 5 scaling levels to get an accurate representation of the fragility curve. The performance of each archetype structure, based on the achieved collapse margin ratio, is then evaluated to determine whether the initial  $R$  value is justified. If the performance is found to be inadequate, a lower  $R$  value should then be used, and the process is repeated until the performance of all archetypes is deemed acceptable.

To perform the incremental dynamic analysis, non-linear dynamic response of index archetypes is evaluated for a set of 44 predefined far field ground motions that are systematically scaled to increase their spectral acceleration until median collapse  $\hat{S}_{CT}$  is established. Median collapse is defined as the intensity at which half of the earthquake records result in collapse of a specific archetype. It is determined that only the archetypes designed under the higher seismic design category (i.e. SDC D) govern the collapse performance and the resulting  $R$  factor [104]. Thus, the IDA is only performed for Archetypes under performance group 1 and 2 (i.e. Archetype 1-6). The  $ACMR$  value is then determined for each archetype according to their Spectral Shape Factor ( $SSF$ ) using Equation 7-13.

In this Methodology, it is suggested that the probability of collapse due to Maximum Considered Earthquake (MCE) ground motions be limited to 10%. To quantify this criterion, the methodology defines  $ACMR_{10\%}$  as a lower limit on the acceptable collapse margin ratio. A system with a  $ACMR$  value below  $ACMR_{10\%}$  will have a probability of collapse greater than 10%. Each

performance group is required to meet this collapse probability limit, on average, recognizing that some individual archetypes could have collapse probabilities that exceed this value.

A limit of twice that value of collapse probability, or 20%, is suggested as a criterion for evaluating the acceptability of potential “outliers” within a performance group. This corresponds to an acceptable adjusted collapse margin ratio  $ACMR_{20\%}$ . All archetypes must have an  $ACMR$  value greater than  $ACMR_{20\%}$ , to ensure no outlier has a probability of collapse greater than 20% at the MCE hazard level.

Systems that have more robust design requirements, more comprehensive test data, and more detailed nonlinear analysis models, have less collapse uncertainty, and can achieve the same level of life safety with smaller collapse margin ratios (i.e. smaller values of  $ACMR_{10\%}$  and  $ACMR_{20\%}$ ). Higher uncertainty results in the fragility curve “getting flattened out” as shown in Figure 7.7. When taking this effect into account, it is necessary to have a higher  $ACMR$  to justify the same  $R$  value as shown in Figure 7.8.

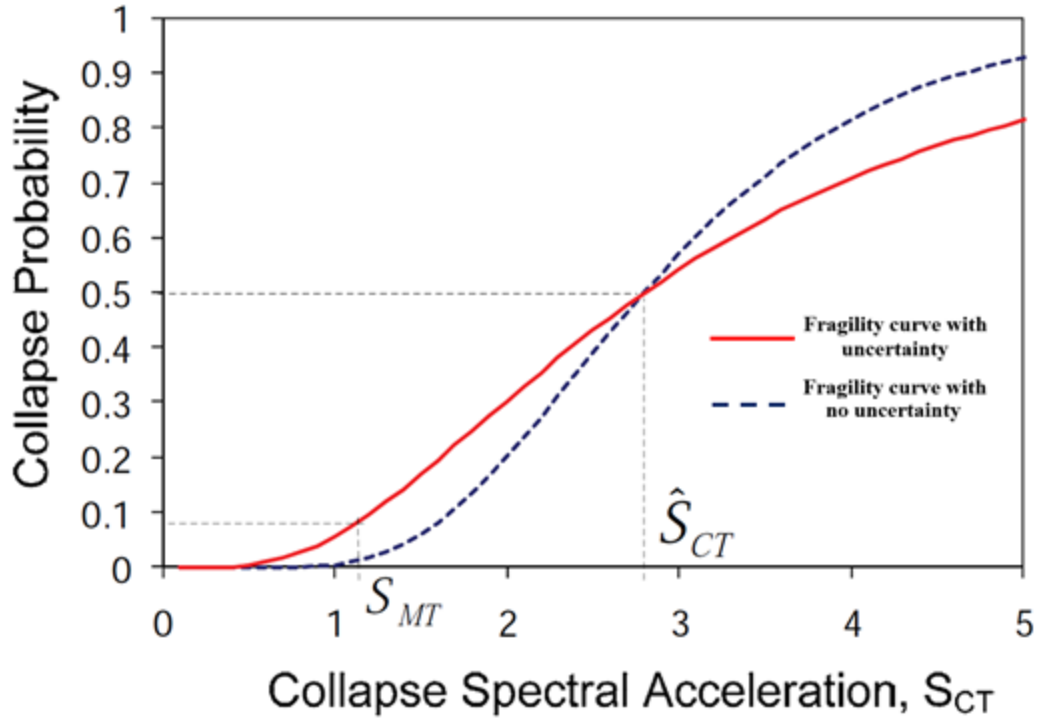


Figure 7.7 Effect of uncertainty on fragility curves [101]

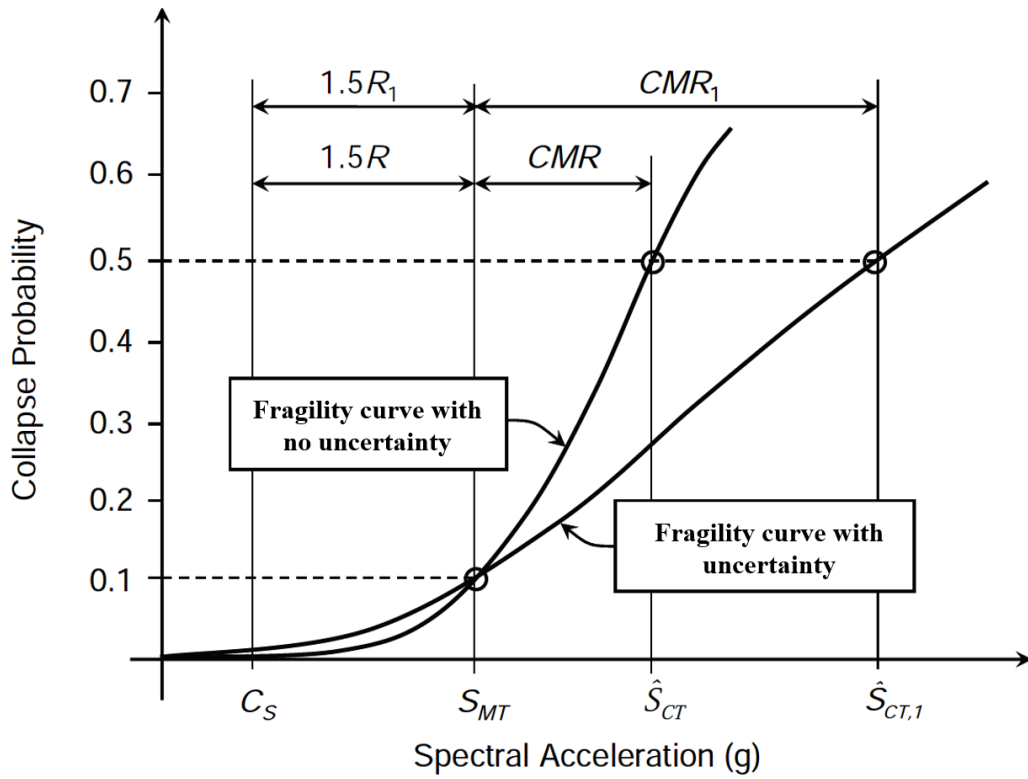


Figure 7.8 Effect of uncertainty on Acceptable Collapse Margin Ratios [101]

Total system collapse uncertainty is calculated based on a function of record-to-record (RTR) uncertainty, which is constant for all studies as long as the appropriate *SSF* factor and record set is used, design requirements-related (DR) uncertainty, test data-related (TD) uncertainty, and modeling (MDL) uncertainty. The record-to-record collapse uncertainty  $\beta_{RTR}$  is assigned a constant value of 0.4 based on the predetermined earthquake suite outlined in the methodology. Considering that the building is designed based on ASCE 7-16 requirements, and 12 different archetype structures studied, it is determined that the quality of design requirement is found to be rated as good, and thus the design requirements-related collapse uncertainty  $\beta_{DR}$  is equal to 0.2. Similarly, since the brace showed predictable and repeatable results when the full-scale prototype of the brace is tested under numerous protocols described in Chapter 5, the quality of the test data requirement is rated as good and is assigned a test data-related collapse uncertainty value  $\beta_{TD}$  equal to 0.2. And finally, considering that the hybrid simulation verified the analytical model approach of the building, and considering this modelling approach is common to academic and industry practice, as well as the fact that non-linear second order effects are modelled, the model quality is determined to also be rated as good. Therefore, the modelling -related collapse uncertainty  $\beta_{MDL}$  is equal to 0.2. Based on all these uncertainties, the total system collapse uncertainty is calculated according to Equation 7-14 and rounded to the nearest 0.025. Based on the calculation of the previously discussed uncertainty parameters, an appropriate value for the total system collapse uncertainty  $\beta_{TOT}$  is 0.525.

$$\beta_{TOT} = \sqrt{\beta_{RTR}^2 + \beta_{DR}^2 + \beta_{TD}^2 + \beta_{MDL}^2} \quad \text{Equation 7-14}$$

This collapse uncertainty results in an acceptable value of  $ACMR_{10\%} = 1.96$  and an  $ACMR_{15\%} = 1.72$ . Based on an *R* factor of 7.0, 5 of the 6 archetypes evaluated based on the previous process had an *ACMR* less than  $ACMR_{10\%}$  with only 1 archetype showing an *ACMR* less than  $ACMR_{15\%}$

as shown in Table 7-2 . This verifies the use of a ductility factor of 7.0 for the equivalent static force design procedure of structures with RS-SCED brace systems.

**Table 7-2 Evaluation of the ACMR of the archetypes designed using R=7.0**

<b>PG</b>	<b>SDC</b>	<b>AT</b>	<b>Period, T<sub>1</sub></b>	<b>SSF</b>	<b>CMR</b>	<b>ACMR</b>	<b>Archetype Exceeds Acceptable Collapse margin ratio of</b>
		1	1.77	1.61	1.450	2.33	10%
1	D	2	1.18	1.514	1.500	2.27	10%
		3	0.61	1.36	1.330	1.81	15%
		4	0.34	1.33	1.625	2.16	10%
2	D	5	0.34	1.33	1.625	2.16	10%
		6	0.34	1.33	1.625	2.16	10%

The fragility curves for the 6 archetypes examined are shown in Figure 7.9 and Figure 7.10. Since the methodology does not call for a full incremental dynamic analysis, (IDA) but rather a fragmented scaling at 5 or more levels, the fragility function fitting approach presented by Baker [105] is used to develop fragility curves.

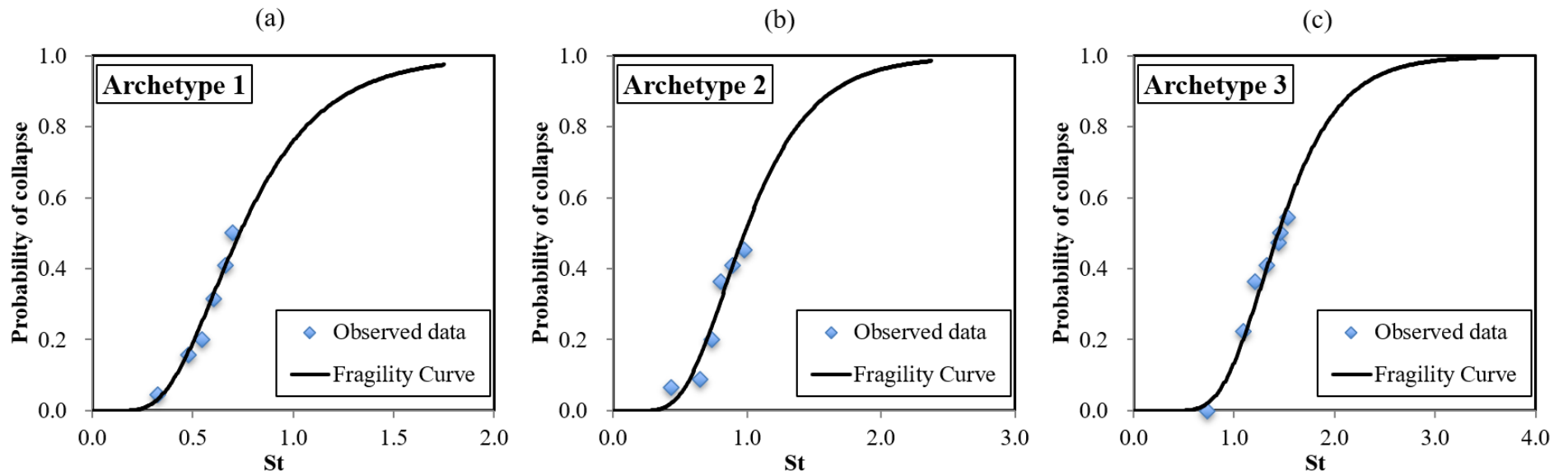


Figure 7.9 Fitted fragility curves for archetypes in performance group 1: a) Archetype 1, b) Archetype 2, and c) Archetype 3

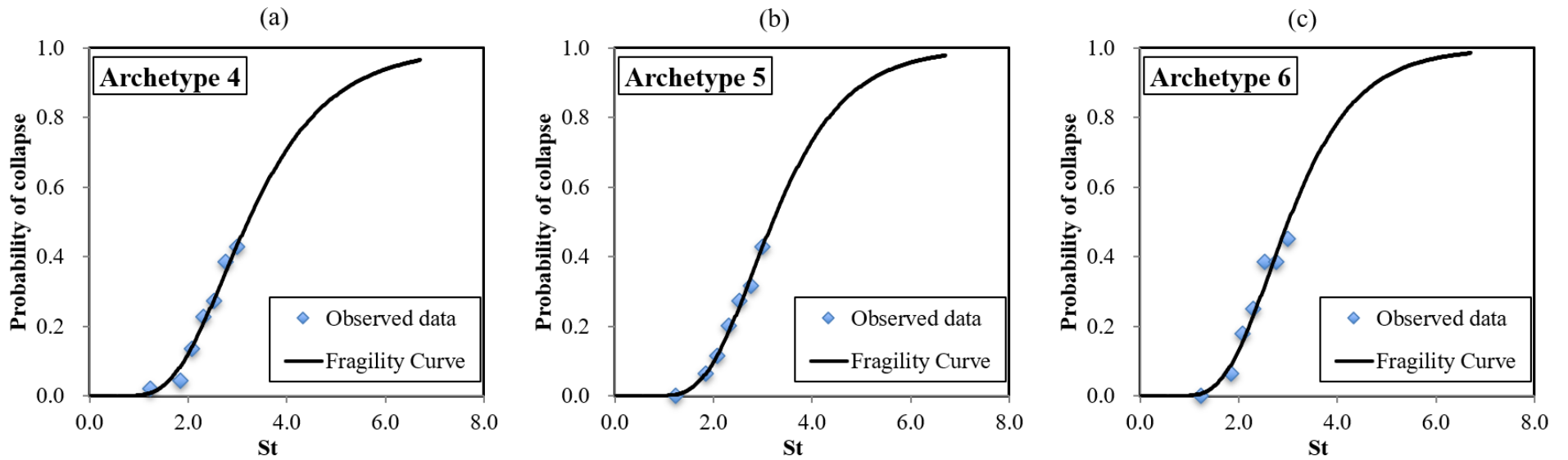


Figure 7.10 Fitted fragility curves for archetypes in performance group 2: a) Archetype 4, b) Archetype 5, and c) Archetype 6

## 7.5 Determining overstrength factor, $\Omega_0$

As specified in FEMA P695, a nonlinear static pushover analysis is used to quantify the overstrength factor  $\Omega_0$ . To do so, lateral forces  $F_x$  at each level  $x$  are vertically distributed proportional to the fundamental mode shape and floor mass of each archetype as follows:

$$F_x \propto m_x \phi_{1,x} \quad \text{Equation 7-15}$$

Figure 7.11 shows an idealized pushover analysis result with the definition of the maximum base shear capacity  $V_{max}$  and the ultimate roof displacement  $\delta_u$ . The ultimate displacement  $\delta_u$  is defined as the roof displacement reached by the structure after the structure loses 20% of its maximum strength ( $0.8 V_{max}$ ). The archetype specific overstrength factor  $\Omega$  can be calculated as the ratio between the maximum base shear  $V_{max}$  and the design base shear  $V$ :

$$\Omega = \frac{V_{max}}{V} \quad \text{Equation 7-16}$$

The period-based ductility  $\mu_T$  is calculated as the ratio between the ultimate roof displacement  $\delta_u$  and the effective yield roof displacement  $\delta_{y,eff}$  calculated as follows:

$$\mu_T = \frac{\delta_u}{\delta_{y,eff}} \quad \text{Equation 7-17}$$

$$\delta_{y,eff} = C_o \frac{V_{max}}{W} \left[ \frac{g}{4\pi^2} \right] (\max(T, T_1))^2 \quad \text{Equation 7-18}$$

$$C_o = \phi_{1,r} \frac{\sum_1^N m_x \phi_{1,x}}{\sum_1^N m_x \phi_{1,x}^2} \quad \text{Equation 7-19}$$

where  $T$  is the fundamental period is  $C_u T_a$  as defined in ASCE 7-16, is the  $T_1$  fundamental period calculated from eigenvalue analysis, and  $\phi_{1,r}$  is the first mode ordinates at the roof level.

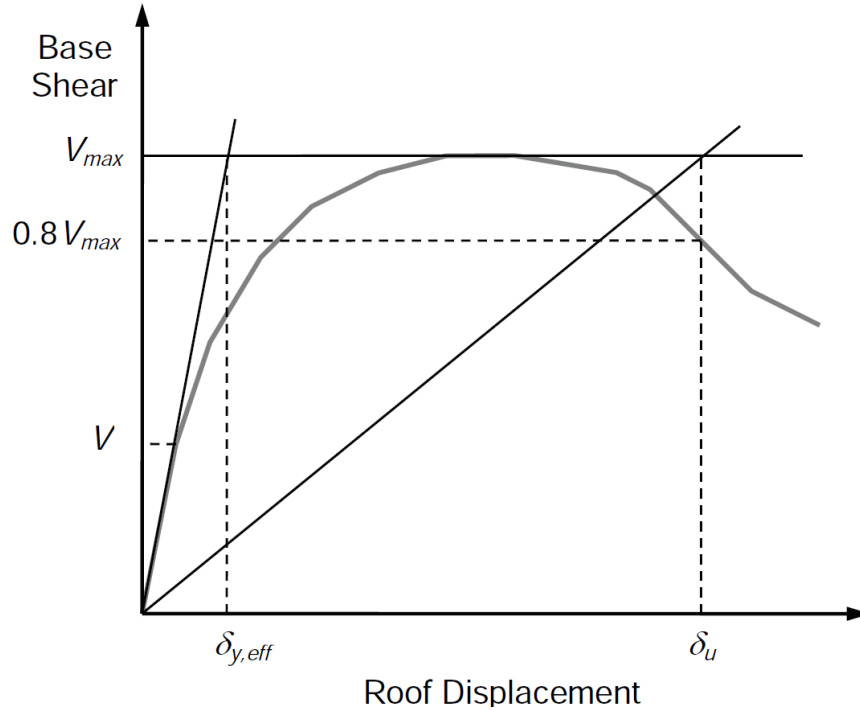


**Figure 7.11 Idealized static pushover analysis [101]**

The average value of archetype specific overstrength factor  $\Omega$  for each performance group are calculated. The system overstrength factor  $\Omega_0$  should not exceed any of the average values of  $\Omega$  for each performance group. However, practically this overstrength factor shall not exceed  $1.5 R$  or  $3.0$  whichever is smaller. Although studies have shown that the archetypes designed for the lower seismic design categories tend to govern the value of the overstrength factor [104], the pushover analysis for all archetypes is conducted in this study to offer extra validation to the modelling techniques and analysis used in this study.

A sample pushover curve from archetype 1 is shown in Figure 7.12 below. In this pushover curve, the base shear increases linearly up to a base shear  $V$ . At this base shear, the activation load in the bottom floor brace  $F_{a1}$  is exceeded and accordingly, the brace activates significantly changing the stiffness of the structure. At the peak of the structure response, the structure exceeds the drift capacity of the braced frames resulting in the steel tendons to progressively start yielding. Note that the roof drift at the peak of the response is 6.17%, which is higher than the design inter-

storey drift of 5% due to the deformation in the steel columns and chevron braces connected to the RS-SCEDs. Other archetypes show similar pushover analysis response.

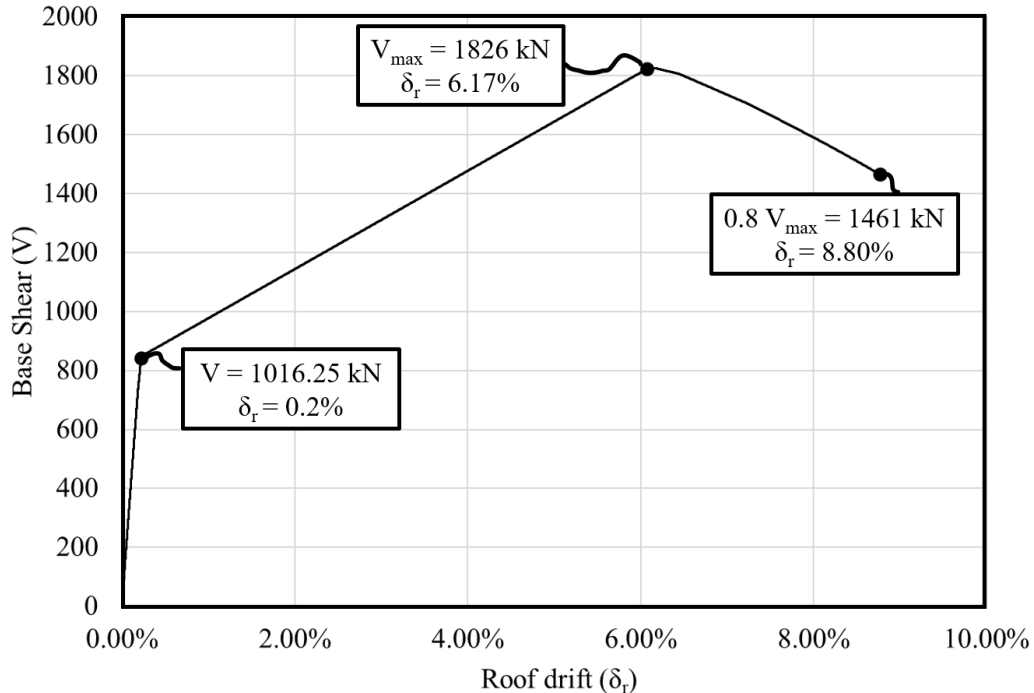


Figure 7.12 Sample pushover curve for archetype 1

As shown in Table 7-3, the highest performance groups designed under SDC C exhibited overstrength factors of  $\Omega > 3.0$  indicating that the use of a system overstrength factor  $\Omega_0 = 3.0$  is adequate for systems utilizing RS-SCED braces. It is also noticeable that the buildings designed under the higher seismic design category have lower values of seismic overstrength factors  $\Omega$ , indicating that the buildings designed under a lower seismic design category governed the system overstrength factor identification. This correlates with the findings in previous studies which followed the same methodology [104], and the recommendations of the methodology [101].

**Table 7-3 Performance evaluation of Archetypes under pushover analysis**

PG	SDC	AT	Period, $T_1$	$\Omega$	$\bar{\Omega}$
		1	1.77	1.80	
1	D	2	1.18	2.19	2.08
		3	0.61	2.26	
		4	0.34	2.71	
2	D	5	0.34	2.73	2.62
		6	0.34	2.42	
		7	1.88	4.07	
3	C	8	1.21	5.28	4.83
		9	0.67	5.15	
		10	0.40	5.24	
4	C	11	0.40	5.59	5.69
		12	0.37	6.24	

## 7.6 Comparison of Archetypal Building Response at Varying Hazard Levels

To investigate the global system-level behaviour of the RS-SCED braces as a seismic force resisting system (SFRS), the response of all 6 building archetypes designed under the seismic category D was investigated at three different scaled hazard levels, namely the FOE, DBE and MCE hazard levels. Three parameters are chosen to evaluate the global response of the structure: 1) the maximum inter-storey drift, 2) residual drift, and 3) floor acceleration. Considering that some structures may achieve the collapse criteria defined in Section 7.1, a statistical distribution model proposed by Shome [106] and presented in Equation 6-1 in Section 6.6, was used to calculate an adjusted 50<sup>th</sup> percentile for all 3 hazard level responses and an adjusted 84<sup>th</sup> percentile for the FOE and DBE hazard level responses. Table 7-4 summarizes the responses for all 6 archetypes at the three different hazard levels.

**Table 7-4 Response comparison for different building archetypes under varying seismic hazard levels**

Seismic Hazard Level	Response parameter	Percentile	Archetype #					
			1	2	3	4	5	6
<b>FOE (50% in 50 years)</b>	$\Delta/h_s$	50 <sup>th</sup>	1.11%	1.26%	0.71%	0.33%	0.31%	0.32%
		84 <sup>th</sup>	1.62%	1.78%	1.19%	0.64%	0.643%	0.61%
	$\Delta_r/h_s$	50 <sup>th</sup>	0.02%	0.01%	0.00%	0.00%	0.00%	0.00%
		84 <sup>th</sup>	0.06%	0.04%	0.01%	0.00%	0.00%	0.00%
	$a_f$	50 <sup>th</sup>	0.55	0.56	0.34	0.26	0.26	0.26
		84 <sup>th</sup>	0.88	1.09	0.49	0.36	0.35	0.37
<b>DBE (10% in 50 years)</b>	$\Delta/h_s$	50 <sup>th</sup>	1.92%	2.46%	2.28%	1.41%	1.30%	1.36%
		84 <sup>th</sup>	3.60%	3.81%	3.33%	2.47%	2.20%	2.37%
	$\Delta_r/h_s$	50 <sup>th</sup>	0.04%	0.02%	0.01%	0.00%	0.00%	0.00%
		84 <sup>th</sup>	0.30%	0.13%	0.02%	0.01%	0.01%	0.01%
	$a_f$	50 <sup>th</sup>	1.19	1.12	0.68	0.50	0.49	0.51
		84 <sup>th</sup>	1.86	1.53	0.86	0.64	0.63	0.65
<b>MCE (2% in 50 years)</b>	$\Delta/h_s$	50 <sup>th</sup>	2.63%	3.25%	3.47%	2.45%	2.38%	2.50%
	$\Delta_r/h_s$	50 <sup>th</sup>	0.09%	0.03%	0.03%	0.00%	0.00%	0.00%
	$a_f$	50 <sup>th</sup>	1.33	1.27	0.90	0.60	0.58	0.61

From the results in Table 7-4, it is evident that using RS-SCED braces results in an acceptable level of inter-storey drift regardless of the building archetype. The 84<sup>th</sup> percentile of the maximum inter-storey drift for all archetype buildings under the FOE hazard level did not exceed 2.0%, indicating an appropriate performance level for the structure under this low seismic hazard level. The 84<sup>th</sup> percentile for the maximum inter-storey drifts at the DBE hazard level does not exceed 4.0% for long period of vibration structures (Archetype 1-3) and less than 2.5% for short period of vibration structures (Archetype 4-6). The 50<sup>th</sup> percentile for the maximum inter-storey drift at the MCE hazard level was less than 3.5% for all building archetypes.

The RS-SCED braces also show an excellent self-centering ability for all the archetypes evident by the very low or non-existent residual drift in the structures investigated. The maximum residual drift for all building archetypes did not exceed 0.1% under any seismic hazard level. The maximum inter-storey drift and residual drift response of the structures indicate that all building archetypes with RS-SCED braces suffer minor damage to structural components, resulting in minimal rehabilitation cost and disruption to occupancy when the building is subjected to a MCE hazard level event, and almost no rehabilitation cost when the building is subjected to more frequent seismic events.

As shown in Table 7-4, the floor acceleration calculated for all building archetypes increases as the hazard level increases. At the MCE hazard level, the median value for peak floor accelerations is highest for archetype 1 structure (12-storey), with a peak floor acceleration of 1.33 g. The peak floor acceleration decreases as the structure gets shorter with 1.27 g for archetype 2 (8-storey), 0.9 g for archetype 3 (4-storey), and around 0.6 g for archetypes 4-6 (2-storey). This is due to the high stiffness of the RS-SCED braces located at the lower floors of the multi-storey long period structures compared to the smaller and less stiff braces in the short period structures. This could also be caused by the higher mode effects in the long period structures.

To understand the influence of building height on the seismic response of the proposed SFRS system, maximum inter-storey drift, inter-storey residual drift, and peak floor accelerations are compared for each of the building archetypes. As shown in Figure 7.13 to Figure 7.18, the maximum inter-storey drift is higher at the lower and upper floor levels for long period structures (Archetypes 1-3), with a smaller inter-storey drift at the middle floor levels of the structure. The high drift level near the base of the long period structures is attributed to the higher seismic demand due to the high cumulative floor shear. The seismic demand decreases along the height of the

structure resulting in smaller braced frame columns and smaller RS-SCED braces with lower activation forces when designed using the EFL procedure. However, at the upper levels of the structure, the RS-SCED braces are loaded up to their maximum capacity leading to overloading, and eventually yielding, of the steel columns in the braced frame under some of the . This in turn also leads to some residual drift at those upper floors as shown in Figure 7.13 to Figure 7.18. This could be because the storey shears used for the design of the braced frames is based on the EFL procedure which does not consider higher mode effects, which can be significant in this structural system. Also, the high post-activation stiffness of the RS-SCED brace could result in a better distribution of the seismic demand along the structure height leading to a higher storey shear at the upper floor than anticipated when using EFL analysis. Hence, using the EFL procedure does not result in the optimal design of the braces in the structure. The short period archetypes with two floors (archetypes 4-6) exhibit a larger inter-storey drift on the second floor compared to the first floor, as shown in Figure 7.13 to Figure 7.18, for the same reason.

As shown in Figure 7.13 to Figure 7.18, the floor acceleration at lower levels is higher due to the high stiffness and storey shear at base of the structures. Although this can result in unintended damage to non-structural components even when the structure is subjected to smaller more frequent seismic events, this can be mitigated by designing braces to have a more flexible connection between the RS-SCED and braced frame columns, which decreases the initial stiffness of the RS-SCED braced frame. When the brace was tested in the laboratory, the measured stiffness was much smaller than the theoretical stiffness due to the flexibility of the connections, indicating that the floor accelerations calculated are higher than the actual floor accelerations experienced by structures with RS-SCED braces. In design applications, the RS-SCED brace and braced frame column connections are specifically designed and modelled for each application to optimize the

building performance under all seismic hazard levels. This optimization process is not done for the fragility analysis and modeling of brace connection flexibility was not considered in this study. Alternatively, the stiffness used in modelling the RS-SCED braces is the theoretical stiffness calculated based on the axial stiffness of all components as discussed in Section 4.2.

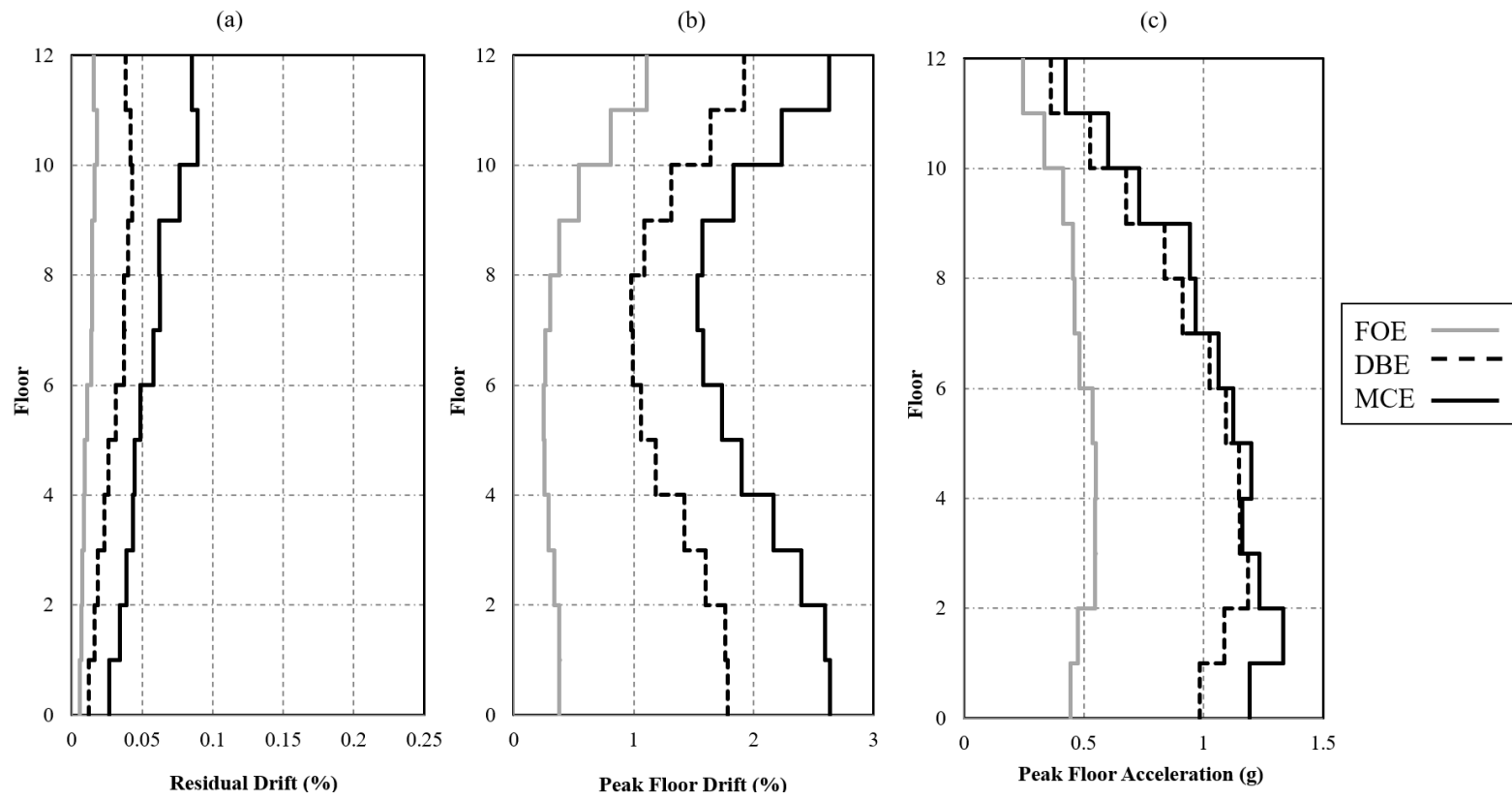


Figure 7.13 Statistical response results of archetype 1 building at different seismic hazard levels seismic hazard levels: a) residual drift, b) peak floor drift, and c) peak floor acceleration

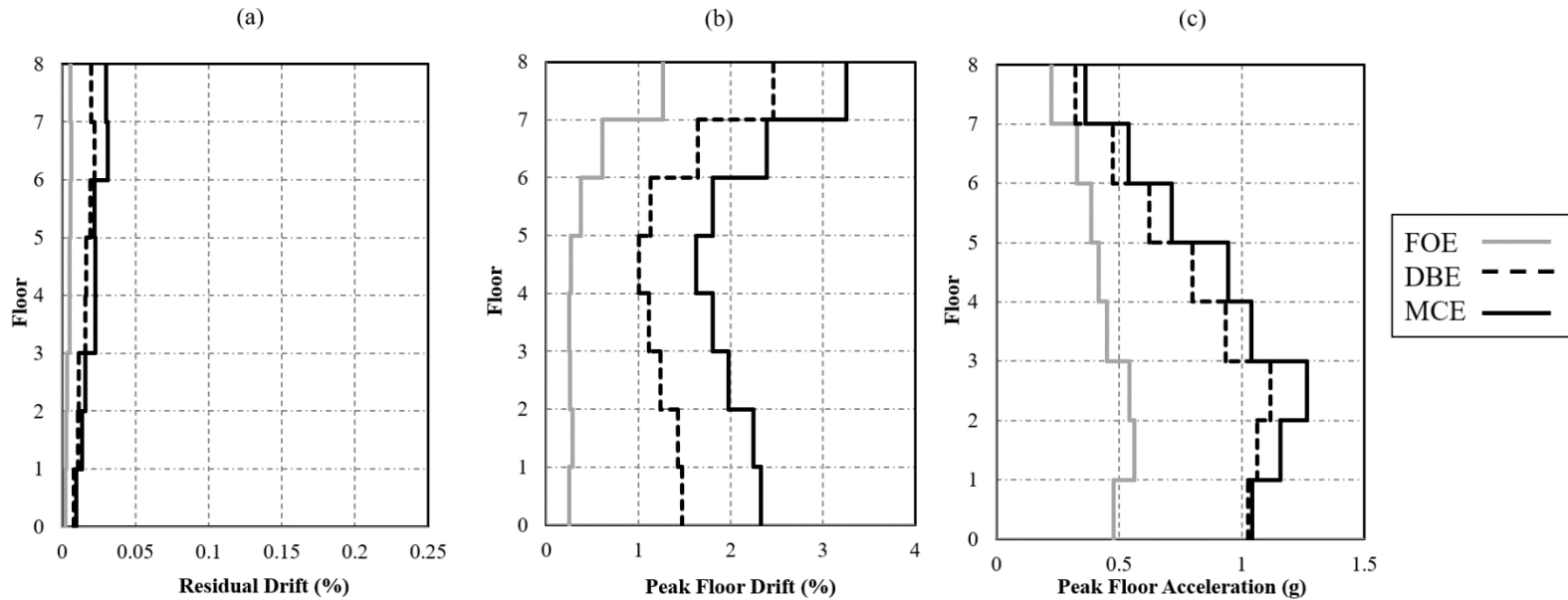


Figure 7.14 Statistical response results of archetype 2 building at different seismic hazard levels seismic hazard levels: a) residual drift, b) peak floor drift, and c) peak floor acceleration

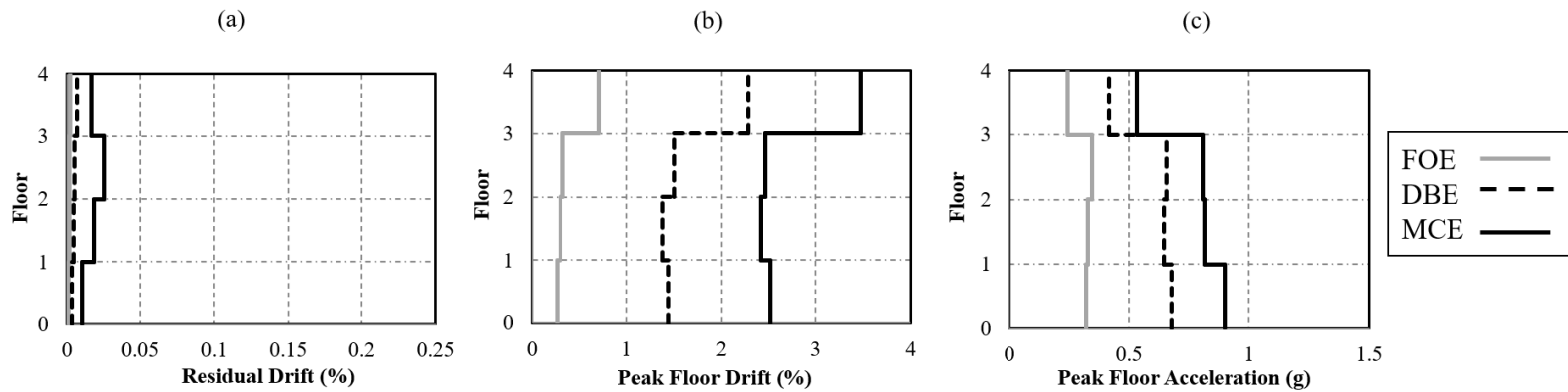


Figure 7.15 Statistical response results of archetype 3 building at different seismic hazard levels seismic hazard levels: a) residual drift, b) peak floor drift, and c) peak floor acceleration

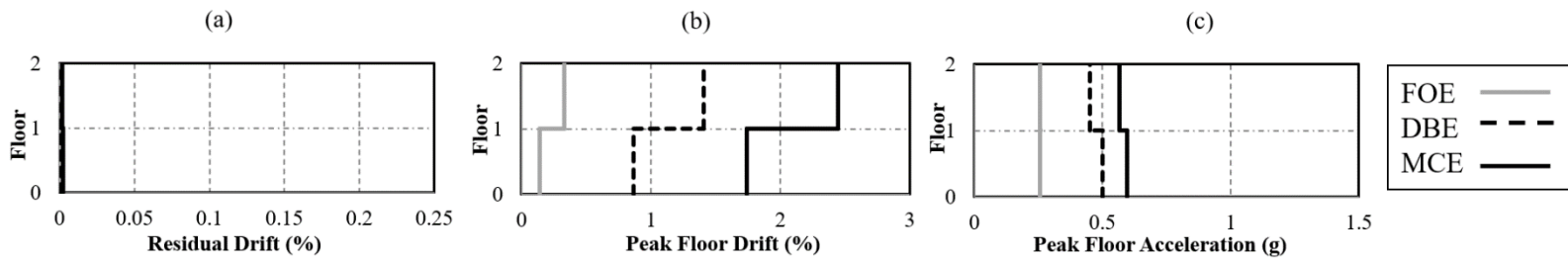


Figure 7.16 Statistical response results of archetype 4 building at different seismic hazard levels seismic hazard levels: a) residual drift, b) peak floor drift, and c) peak floor acceleration

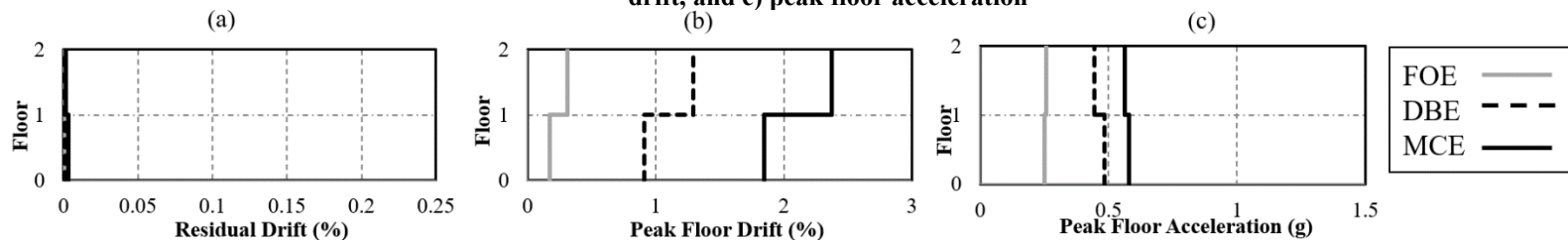


Figure 7.17 Statistical response results of archetype 5 building at different seismic hazard levels seismic hazard levels: a) residual drift, b) peak floor drift, and c) peak floor acceleration

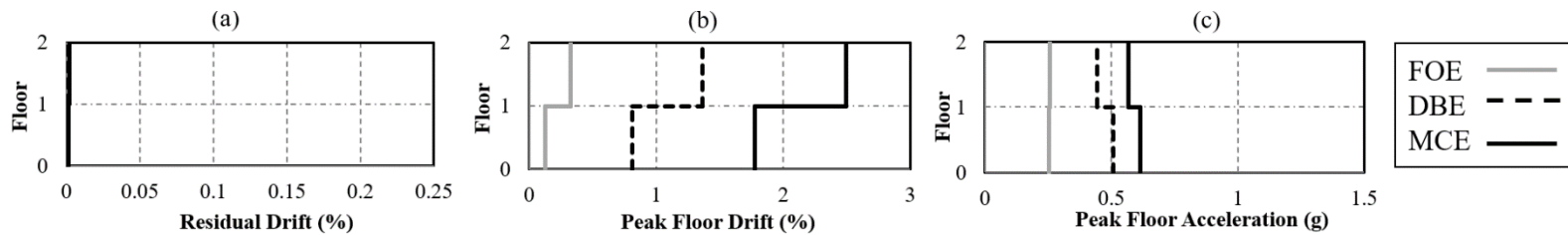


Figure 7.18 Statistical response results of archetype 6 building at different seismic hazard levels seismic hazard levels: a) residual drift, b) peak floor drift, and c) peak floor acceleration

## 7.7 Summary

In this chapter, a FEMA P695 study was undertaken to determine appropriate seismic response factors that can be used for the design of structures with RS-SCED braces. This process involves the design of 12 archetypal buildings with varying structural characteristics. The designed structures were then numerically modeled using software package OpenSees. The numerical modelling of the structures accounted for the geometric and material non-linearity of the structural response. The ductility factor  $R$  is determined based on a fragmented Incremental Dynamic Analysis (IDA). A ductility factor  $R$  and a deflection amplification factor  $C_d$  equal to 7 are determined to be appropriate for the design of structures with RS-SCED braces. To determine an appropriate overstrength factor  $\Omega_0$ , pushover analyses are performed on all archetype buildings. Based on the results of the pushover analyses, an overstrength factor  $\Omega_0$  of 3 is determined to be appropriate for structures with RS-SCED braces.

When investigating the effect of earthquakes at different hazard levels for the set of archetype buildings, the RS-SCED brace has shown to be capable of limiting the damage to structural components. This is evident by the low residual and maximum inter-storey drifts for all building archetypes, indicating that there is limited yielding in the rest of the SFRS. Optimizing the brace connection and detailing can be performed to ensure that the structure has a low floor acceleration that does not result in discomfort to building occupants and damage to non-structural components during frequent seismic events.

# Chapter 8 : Conclusions and Future Research

## 8.1 Conclusions

Major seismic events across the globe have caused tremendous economic losses but more importantly and tragically, significant loss of human life. Despite the benefits of many advanced seismic force resisting systems (SFRS) such as Buckling Restrained Braced Frames (BRBF) or ductile Moment Resisting Frames (MRF), these systems still exhibit large permanent deformation following a major earthquake. Permanent residual deformation to a building following an earthquake significantly affects the usability and safety of the structure, including damage to critical structural components or non-structural components. Furthermore, repair of these structures is time consuming and costly, requiring significant operational downtime resulting in additional economic losses. In many cases, it is more economically feasible to demolish and reconstruct a building exhibiting significant residual drift than it is to repair it. These challenges led to the development of self-centering systems including rocking walls and self-centering MRFs. However, the use of self-centering braces is a more appropriate option for rehabilitation of structures as it is less disruptive than installation of rocking wall or self-centering MRFs. Previously developed Self-Centering Energy Dissipative (SCED) braces had limited load capacity or were required to be very long to accommodate for large displacements, limiting their potential application in real structures. This study aimed to develop a new high-capacity SCED brace with a more compact design using ring springs, hence, the brace was named the Ring Spring Self-Centering Energy Dissipative Brace (RS-SCED).

The first phase of this study focused on the development and design of a full-scale brace with a capacity that is comparable to a BRB and that could be used in a multi-storey office

building. Accordingly, an RS-SCED brace was designed and built with a length of 3 m, a capacity of 1400 kN, and a deformation capacity of 165 mm. The brace was compact enough so that two such braces can be added to a single bay frame in a chevron bracing configuration. The RS-SCED brace was constructed and tested according to the ASCE 7-16 and the AISC 341-16 protocols for testing seismic dampers and buckling restrained braces, respectively. The results showed a repeatable, consistent, and predictable response that correlated with the theoretical force-deformation hysteretic response very well. The response of the brace remained consistent even after repeated testing and many loading cycles. The brace was also loaded cyclically at different frequencies to determine if its behaviour was rate dependent, and the results showed that the brace exhibits consistent pre- and post-activation stiffness and force over a wide range of load frequencies. During the tests, the brace was loaded upto a load and deformation of 1200 kN and 132 mm, respectively.

The second phase of this study investigated the system-level response of an 8-storey office building and a 3-span concrete voided deck bridge with RS-SCED braces. To accurately capture the nonlinear response of the proposed RS-SCED brace and its influence on the global system-level response of the prototype structures, 18 hybrid simulations were conducted. The structures were subjected to 4 different earthquake records which represented a wide range of frequency contents. The earthquake records used included one near-field earthquake record and 3 far-field earthquake records. The hybrid simulation results were compared with purely numerical models of both prototype building and bridge structures. To model the analytical structures, a new constitutive material was created in OpenSees to accurately represent the force-deformation response of the RS-SCED brace. Comparison of the system level response between the hybrid

simulation and the numerical analysis showed very good correlation for both the building and bridge structures.

To evaluate the effect of the RS-SCED brace on the 8-storey building, an equivalent building was designed with a BRB system. Both the RS-SCED braced building and the BRB building were then subjected to a suite of 44 earthquake records scaled to 3 different hazard levels to evaluate the response of both structures. The inter-storey drift, residual drift, and floor acceleration were the parameters chosen for this comparison. The following observations were made:

- The RS-SCED bracing system was found to minimize or even eliminate the residual drift even at high seismic demand. In comparison, the BRB system showed large residual drifts because of the yielding of the BRB cores and drift concentration at the lower floors.
- At high seismic demand, the RS-SCED braced system exhibited smaller inter-storey drifts when compared to the BRB system.
- The RS-SCED brace system exhibited higher floor accelerations compared to the BRB system because of the high initial stiffness of the braces. Some of this acceleration increase could have been artificially induced due to sharp stiffness transition between the pre- and post- activation stiffnesses in analytical models.
- The RS-SCED system is an effective alternative to a high-performance BRB system because it nearly eliminates residual drifts following a large seismic event.

To evaluate the effect of using RS-SCED braces on the 3-span bridge, the original bridge with no RS-SCED braces was analyzed under the same earthquake records and seismic hazard levels.

To compare the response of both the retrofitted and original structures, 4 different response parameters were evaluated: 1) drift in the longitudinal direction, 2) drift in the transverse direction, and 3) reaction shear forces and moments at the pier foundations. The following observations were made:

- The RS-SCED brace reduced the maximum drift both in the longitudinal and the transverse directions, which was particularly evident at the peak of the response
- The RS-SCED brace had a significant damping effect on the vibration of the structure, which resulted in significantly lower displacement amplitudes following the peak response.
- The shear forces and moments at the foundation of the piers were almost the same as the original bridge indicating that no increase in the capacity of the foundation was required. This comes at the cost of significant increase in the capacity of the backwall and abutments which support the RS-SCED braces.

The final phase of the study focused on the establishment of appropriate seismic design factors for use in simplified seismic design procedures. The FEMA P695 methodology was used to conduct an extensive analytical study to determine appropriate ductility factor  $R$ , over strength  $\Omega_0$ , and amplification factor  $C_d$  used in the equivalent seismic load design procedure used in the ASCE 7 [102]. Twelve different prototype structures with varying periods of vibration, sizes and regional seismic hazard levels were designed, This was followed by a series of pushover analyses and IDA. It was determined that a ductility factor of  $R = 7$ , amplification factor of  $C_d = 7$  and an overstrength factor of  $\Omega_0 = 3$ , were appropriate for the design of buildings with an RS-SCED brace system.

## 8.2 Recommendations for Future Research

This research has proven the feasibility and effectiveness of using the developed RS-SCED brace for new construction and rehabilitation of buildings and bridges. However, the development and improvement of this new system is still on going. The following list includes several recommendations for future investigation:

1. Testing of RS-SCED braces of various sizes and capacities, this study investigated a large capacity brace utilizing one of the largest commercially available ring spring sizes. However, smaller brace sizes may be required for some structures, indicating the need for testing smaller sized braces;
2. Studying and testing various RS-SCED brace connection details should be investigated. This is important as it can decrease the initial stiffness of the braced frame thus decreasing the floor acceleration;
3. Testing the possibility of using neoprene pads to minimize the sharp stiffness transition that was observed when the brace is unloading and transitioning from the post-activation stiffness back to the initial stiffness;
4. Hybrid simulations which simultaneously test multiple RS-SCED braces from multiple storey levels in a building. This may not be feasible in one laboratory facility, but an online hybrid simulation connecting multiple geographically distributed laboratories could be feasible. Model updating should also be investigated as the technology becomes more accessible in the future;
5. Real-time hybrid simulation or shake table tests can be completed to confirm the lack of rate dependent effects on the system level response of a structure;

6. A hybrid Incremental Dynamic Analysis (IDA) that can supplement the analytical IDA presented in this study;
7. A more wide-scale numerical IDA that would include different building materials and additional archetypal buildings, this may require a team effort with multiple researchers due to the large computational demand required.

# References

- [1] C. Comartin, M. Greene, and S. Tubbesing, *The Hyogo-ken Nanbu earthquake : Great Hanshin Earthquake Disaster, January 17, 1995 : preliminary reconnaissance report*. Oakland, California, 1995.
- [2] R. Eguchi, “Direct economic losses in the Northridge earthquake: a three-year post-event perspective,” *Earthq. Spectra*, vol. 14, no. 2, pp. 245–264, 1998.
- [3] K. Kaga, “Vestibular sensitivity and sense of inclination,” *J. Cogn. Sci. (Seoul)*, vol. 7, no. 1, pp. 16–22, 2005.
- [4] M. Seto, “Sensitivity and memory of body inclination (part 1) – Ability to restore to vertical position,” *Quilibrium Res.*, vol. 55, no. 5, p. 204, 1996.
- [5] M. Fujii, “Damage to an repair of foundations of residential buildings in liquefied areas inHygoken-Nanbu earthquake.,” *Soil Found.*, vol. 46, pp. 9–12, 2002.
- [6] Y. Iwata, K. Sugimoto, and H. Kuwamura, “Reparability limit of steel structural buildings: Study on performance-based design of steel structural buildings Part 2,” *J. Struct. Constr. Eng.*, vol. 588, pp. 165–172, 2005.
- [7] C. M. Ramirez and E. Miranda, “Significance of residual drifts in building earthquake loss estimation,” *Earthq. Eng. Struct. Dyn.*, vol. 41, no. 11, pp. 1477–1493, 2012, doi: 10.1002/eqe.2217.
- [8] M. Kato, “Seismic performance and damage evaluation of drywall partitions,” *J. Struct. Constr. Eng.*, vol. 614, pp. 139–146, 2007.

- [9] J. McCormick, Y. Matsuoka, P. Pan, and M. Nakashima, "Evaluation of Non-Structural Partition Walls and suspended ceiling systems through a shake table study," in *Proc. of the 2008 ASCE Structures Congress.*, 2008.
- [10] J. Erochko, C. Christopoulos, R. Tremblay, and H. Choi, "Residual Drift Response of SMRFs and BRB Frames in Steel Buildings Designed according to ASCE 7-05," *J. Struct. Eng.*, vol. 137, no. 5, pp. 589–599, 2010, doi: 10.1061/(asce)st.1943-541x.0000296.
- [11] ASCE, *Minimum design loads for buildings and other structures*. Reston, VA, 2005.
- [12] C. Fang, Q. Zhong, W. Wang, S. Hu, and C. Qiu, "Peak and residual responses of steel moment-resisting and braced frames under pulse-like near-fault earthquakes," *Eng. Struct.*, vol. 177, no. October, pp. 579–597, 2018, doi: 10.1016/j.engstruct.2018.10.013.
- [13] J. J. Ajrab, G. Pekcan, and J. B. Mander, "Rocking Wall–Frame Structures with Supplemental Tendon Systems," *J. Struct. Eng.*, vol. 130, no. 6, pp. 895–903, Jun. 2004, doi: 10.1061/(ASCE)0733-9445(2004)130:6(895).
- [14] L. Panian, M. Steyer, and S. Tipping, "An innovative approach to earthquake safety and concrete construction," *J. Post Tens. Inst.*, vol. 5, no. 1, pp. 7–16, 2007.
- [15] A. Wada, Z. Qu, H. Ito, S. Motoyui, H. Sakata, and K. Kasai, "Seismic retrofit using rocking walls and steel dampers," in *ATC/SEI Conf. on Improving the Seismic Performance of Existing Buildings and Other Structures*, 2009.
- [16] G. G. Deierlein, X. Ma, M. Eatherton, J. Hajjar, H. Krawinkler, and T. Takeuchi, "Collaborative research on development of innovative steel braced frame systems with controlled rocking and replaceable fuses," in *Proc., 6th Int. Conf. on Urban Earthquake*

- Engineering*, 2009, pp. 413–416.
- [17] Z. Qu, A. Wada, S. Motoyui, H. Sakata, and S. Kishiki, “Pin-supported walls for enhancing the seismic performance of building structures,” *Earthq. Eng. Struct. Dyn.*, vol. 41, no. 14, pp. 2075–2091, Nov. 2012, doi: 10.1002/eqe.2175.
- [18] B. Janhunen, S. Tipping, J. Wolfe, and D. Mar, “Seismic retrofit of a 1960s steel moment-frame high-rise using a pivoting spine,” in *Proc. 2012 Annual Meeting of the Los Angeles Tall Buildings Structural Design Council*, 2012.
- [19] M. M. Garlock, R. Sause, and J. M. Ricles, “Behavior and Design of Posttensioned Steel Frame Systems,” *J. Struct. Eng.*, vol. 133, no. 3, pp. 389–399, Mar. 2007, doi: 10.1061/(ASCE)0733-9445(2007)133:3(389).
- [20] A. I. Dimopoulos, T. L. Karavasilis, G. Vasdravellis, and B. Uy, “Seismic design, modelling and assessment of self-centering steel frames using post-tensioned connections with web hourglass shape pins,” *Bull. Earthq. Eng.*, vol. 11, no. 5, pp. 1797–1816, Oct. 2013, doi: 10.1007/s10518-013-9437-4.
- [21] A. S. Tzimas, A. I. Dimopoulos, and T. L. Karavasilis, “EC8-based seismic design and assessment of self-centering post-tensioned steel frames with viscous dampers,” *J. Constr. Steel Res.*, vol. 105, pp. 60–73, Feb. 2015, doi: 10.1016/j.jcsr.2014.10.022.
- [22] A. I. Dimopoulos, A. S. Tzimas, T. L. Karavasilis, and D. Vamvatsikos, “Probabilistic economic seismic loss estimation in steel buildings using post-tensioned moment-resisting frames and viscous dampers,” *Earthq. Eng. Struct. Dyn.*, vol. 45, no. 11, pp. 1725–1741, Sep. 2016, doi: 10.1002/eqe.2722.

- [23] A. S. Tzimas, G. S. Kamaris, T. L. Karavasilis, and C. Galasso, “Collapse risk and residual drift performance of steel buildings using post-tensioned MRFs and viscous dampers in near-fault regions,” *Bull. Earthq. Eng.*, vol. 14, no. 6, pp. 1643–1662, Jun. 2016, doi: 10.1007/s10518-016-9898-3.
- [24] F. Freddi, C. A. Dimopoulos, and T. L. Karavasilis, “Rocking damage-free steel column base with friction devices: design procedure and numerical evaluation,” *Earthq. Eng. Struct. Dyn.*, vol. 46, no. 14, pp. 2281–2300, Nov. 2017, doi: 10.1002/eqe.2904.
- [25] National Resources Canada, *Survey of commercial and institutional energy use: Buildings 2009*. Ottawa, 2013.
- [26] C. Christopoulos, R. Tremblay, H.-J. Kim, and M. Lacerte, “Self-Centering Energy Dissipative Bracing System for the Seismic Resistance of Structures: Development and Validation,” *J. Struct. Eng.*, vol. 134, no. 1, pp. 96–107, Jan. 2008, doi: 10.1061/(ASCE)0733-9445(2008)134:1(96).
- [27] J. Erochko, C. Christopoulos, and R. Tremblay, “Design, Testing, and Detailed Component Modeling of a High-Capacity Self-Centering Energy-Dissipative Brace,” *J. Struct. Eng.*, vol. 141, no. 8, p. 04014193, 2014, doi: 10.1061/(asce)st.1943-541x.0001166.
- [28] J. Erochko, C. Christopoulos, and R. Tremblay, “Design and Testing of an Enhanced-Elongation Telescoping Self-Centering Energy-Dissipative Brace,” *J. Struct. Eng.*, vol. 141, no. 6, p. 04014163, Jun. 2015, doi: 10.1061/(ASCE)ST.1943-541X.0001109.
- [29] Z. Zhou, Q. Xie, X. C. Lei, X. T. He, and S. P. Meng, “Experimental Investigation of the Hysteretic Performance of Dual-Tube Self-Centering Buckling-Restrained Braces with Composite Tendons,” *J. Compos. Constr.*, vol. 19, no. 6, p. 04015011, 2015, doi:

10.1061/(asce)cc.1943-5614.0000565.

- [30] H. Wang, X. Nie, and P. Pan, “Development of a self-centering buckling restrained brace using cross-anchored pre-stressed steel strands,” *J. Constr. Steel Res.*, vol. 138, pp. 621–632, 2017, doi: 10.1016/j.jcsr.2017.07.017.
- [31] L. Xu, X. Fan, and Z. Li, “Experimental behavior and analysis of self-centering steel brace with pre-pressed disc springs,” *J. Constr. Steel Res.*, vol. 139, pp. 363–373, 2017, doi: 10.1016/j.jcsr.2017.09.021.
- [32] L. H. Xu, X. S. Xie, and Z. X. Li, “A self-centering brace with superior energy dissipation capability: Development and experimental study,” *Smart Mater. Struct.*, vol. 27, no. 9, p. 95017, 2018, doi: 10.1088/1361-665X/aad5b0.
- [33] L.-H. Xu, X.-S. Xie, S.-Q. Yao, and Z.-X. Li, “Hysteretic behavior and failure mechanism of an assembled self-centering brace,” *Bull. Earthq. Eng.*, no. 0123456789, 2019, doi: 10.1007/s10518-019-00590-8.
- [34] ATC, “Quantification of building seismic performance factors,” *Fema P695*, no. June, p. 421, 2009.
- [35] C. Christopoulos, A. Filiatrault, and B. Folz, “Seismic response of self-centring hysteretic SDOF systems,” *Earthq. Eng. Struct. Dyn.*, vol. 31, no. 5, pp. 1131–1150, May 2002, doi: 10.1002/eqe.152.
- [36] R. Tremblay, M. Lacerte, and C. Christopoulos, “Seismic Response of Multistory Buildings with Self-Centering Energy Dissipative Steel Braces,” *J. Struct. Eng.*, vol. 134, no. 1, pp. 108–120, Jan. 2008, doi: 10.1061/(ASCE)0733-9445(2008)134:1(108).

- [37] J. A. . Erochko, “Improvements to the Design and Use of Post-Tensioned by Jeffrey A . Erochko A thesis submitted in conformity with the requirements for the degree of Doctor of Philosophy , Graduate Department of Civil Engineering , University of Toronto © Copyright by Jef,” 2013.
- [38] D. K. Nims, P. J. Richter, and R. E. Bachman, “The Use of the Energy Dissipating Restraint for Seismic Hazard Mitigation,” *Earthq. Spectra*, vol. 9, no. 3, pp. 467–489, Aug. 1993, doi: 10.1193/1.1585725.
- [39] I. D. Aiken, D. K. Nims, A. S. Whittaker, and J. M. Kelly, “Testing of Passive Energy Dissipation Systems,” *Earthq. Spectra*, vol. 9, no. 3, pp. 335–370, Aug. 1993, doi: 10.1193/1.1585720.
- [40] T. Tsopelas and C. Christopoulos, “Experimental and Analytical Study of a System Consisting of sliding Bearings and Fluid Restoring Force/ Damping Devices (NCEER-94-0014),” Buffalo, 1994.
- [41] S. Kitayama and M. C. Constantinou, “Fluidic Self-Centering Devices as Elements of Seismically Resistant Structures: Description, Testing, Modeling, and Model Validation,” *J. Struct. Eng.*, vol. 143, no. 7, p. 04017050, 2017, doi: 10.1061/(asce)st.1943-541x.0001787.
- [42] K. E. Hill, “the Utility of Ring Springs in Seismic Isolation Systems,” no. December, 1995.
- [43] R. Kar, J. H. Rainer, and A. C. Lefrançois, “Dynamic Properties of a Circuit Breaker with Friction-Based Seismic Dampers,” *Earthq. Spectra*, vol. 12, no. 2, pp. 297–314, May 1996, doi: 10.1193/1.1585881.

- [44] RingFeder, “RingFeder: Friction Springs,” Westwood, NJ, 2004.
- [45] A. Filiatrault, R. Tremblay, and R. Kar, “Performance Evaluation of Friction Spring Seismic Damper,” *J. Struct. Eng.*, vol. 126, no. 4, pp. 491–499, Apr. 2000, doi: 10.1061/(ASCE)0733-9445(2000)126:4(491).
- [46] S. Zhu and Y. Zhang, “Seismic behaviour of self-centring braced frame buildings with reusable hysteretic damping brace,” *Earthq. Eng. Struct. Dyn.*, vol. 36, no. 10, pp. 1329–1346, Aug. 2007, doi: 10.1002/eqe.683.
- [47] S. Zhu and Y. Zhang, “Performance Based Seismic Design of Steel Braced Frame System with Self-Centering Friction Damping Brace,” no. 1987, pp. 1–13, 2008, doi: 10.1061/41000(315)32.
- [48] C. C. Chou, Y. C. Chen, D. H. Pham, and V. M. Truong, “Steel braced frames with dual-core SCBs and sandwiched BRBs: Mechanics, modeling and seismic demands,” *Eng. Struct.*, vol. 72, pp. 26–40, 2014, doi: 10.1016/j.engstruct.2014.04.022.
- [49] V. Kammula, J. Erochko, O.-S. Kwon, and C. Christopoulos, “Application of hybrid-simulation to fragility assessment of the telescoping self-centering energy dissipative bracing system,” *Earthq. Eng. Struct. Dyn.*, vol. 43, no. 6, pp. 811–830, May 2014, doi: 10.1002/eqe.2374.
- [50] D. J. Miller, L. A. Fahnestock, and M. R. Eatherton, “Development and experimental validation of a nickel-titanium shape memory alloy self-centering buckling-restrained brace,” *Eng. Struct.*, vol. 40, pp. 288–298, 2012, doi: 10.1016/j.engstruct.2012.02.037.
- [51] AISC, “Seismic Provisions for Structural Steel Buildings,” *Seism. Provisions Struct. Steel*

- Build.*, p. 402, 2016.
- [52] A. B. M. R. Haque and M. S. Alam, “Hysteretic Behaviour of a Piston Based Self-centering (PBSC) Bracing System Made of Superelastic SMA Bars – A Feasibility Study,” *Structures*, vol. 12, no. June, pp. 102–114, 2017, doi: 10.1016/j.istruc.2017.08.004.
- [53] A. S. Issa and M. S. Alam, “Experimental and numerical study on the seismic performance of a self-centering bracing system using closed-loop dynamic (CLD) testing,” *Eng. Struct.*, vol. 195, no. August 2018, pp. 144–158, 2019, doi: 10.1016/j.engstruct.2019.05.103.
- [54] C. Qiu and S. Zhu, “Shake table test and numerical study of self-centering steel frame with SMA braces,” *Earthq. Eng. Struct. Dyn.*, vol. 46, no. 1, pp. 117–137, 2017, doi: 10.1002/eqe.2777.
- [55] R. Li, G. Shu, Z. Liu, and H. Ge, “Research and development of an innovative self-centering energy dissipation brace,” *Struct. Des. Tall Spec. Build.*, vol. 27, no. 15, pp. 1–16, 2018, doi: 10.1002/tal.1514.
- [56] A. Kari, M. Ghassemieh, and B. Badarloo, “Development and design of a new self-centering energy-dissipative brace for steel structures,” vol. 30, no. 6, pp. 924–938, 2019, doi: 10.1177/1045389X19828502.
- [57] L. H. Xu, X. W. Fan, and Z. X. Li, “Development and experimental verification of a pre-pressed spring self-centering energy dissipation brace,” *Eng. Struct.*, vol. 127, pp. 49–61, 2016, doi: 10.1016/j.engstruct.2016.08.043.
- [58] H. Dong, X. Du, Q. Han, H. Hao, K. Bi, and X. Wang, “Performance of an innovative self-centering buckling restrained brace for mitigating seismic responses of bridge structures

- with double-column piers,” *Eng. Struct.*, vol. 148, pp. 47–62, 2017, doi: 10.1016/j.engstruct.2017.06.011.
- [59] H. Dong, X. Du, Q. Han, K. Bi, and H. Hao, “Hysteretic performance of RC double - column bridge piers with self - centering buckling - restrained braces,” *Bull. Earthq. Eng.*, no. 0123456789, 2019, doi: 10.1007/s10518-019-00586-4.
- [60] S. Xiao, L. Xu, and Z. Li, “Seismic performance and damage analysis of RC frame–core tube building with self-centering braces,” *Soil Dyn. Earthq. Eng.*, vol. 120, no. January, pp. 146–157, 2019, doi: 10.1016/j.soildyn.2019.01.029.
- [61] Century Spring Corporation, “Disc Springs,” 2020. [Online]. Available: <https://www.centuryspring.com/products/disc-springs/>. [Accessed: 14-Jan-2020].
- [62] R. Kar, J. H. Rainer, and A. C. Lefrançois, “Dynamic properties of a circuit breaker with friction-based seismic dampers,” *Earthquake Spectra*, vol. 12, no. 2. pp. 297–314, 1996, doi: 10.1193/1.1585881.
- [63] N. Bishay-Girges, “Seismic protection of structures using passive control system,” p. 271, 2004.
- [64] H. H. Khoo, C. Clifton, J. Butterworth, G. MacRae, S. Gledhill, and G. Sidwell, “Development of the self-centering Sliding Hinge Joint with friction ring springs,” *J. Constr. Steel Res.*, vol. 78, pp. 201–211, 2012, doi: 10.1016/j.jcsr.2012.07.006.
- [65] H. H. Khoo, C. Clifton, J. Butterworth, and G. Macrae, “Experimental study of full-scale self-centering sliding hinge joint connections with friction ring springs,” *J. Earthq. Eng.*, vol. 17, no. 7, pp. 972–977, 2013, doi: 10.1080/13632469.2013.787378.

- [66] A. S. Issa, “Innovative spring & piston based self-centering bracing systems for enhanced seismic performance of buildings,” University of British Columbia, 2018.
- [67] S. Gary, G. Djojo, C. Clifton, and R. S. Henry, “Experimental validation of Rocking CBFs with Double Acting Ring Springs,” pp. 1–8, 2017.
- [68] L. Wiebe and C. Christopoulos, “Characterizing acceleration spikes due to stiffness changes in nonlinear systems,” *Earthq. Eng. Struct. Dyn.*, vol. 39, no. 14, pp. 1653–1670, Nov. 2010, doi: 10.1002/eqe.1009.
- [69] HITEC, “Guidelines for the testing of seismic isolation and energy dissipating devices,” 1996.
- [70] R. Tremblay and A. Filiatrault, “Seismic performance of steel moment resisting frames retrofitted with a locally reduced beam section connection,” *Can. J. Civ. Eng.*, vol. 24, no. 1, pp. 78–89, Feb. 1997, doi: 10.1139/196-084.
- [71] G. Clifton, *Semi-rigid Joints for Moment Resisting Steel Framed Seismic-Resisting Systems*. 2005.
- [72] SAC Joint Venture, “Loading histories for seismic performance testing of SMRF components and assemblies,” SAC Joint Venture, [Sacramento, Calif.], 2000.
- [73] NRCC (National Research Council of Canada), *National Building Code of Canada*, 2015th ed. Ottawa, 2015.
- [74] ASCE- American Society of Civil Engineers, *Minimum Design Loads and Associated Criteria for Buildings and Other Structures*, ASCE/SEI 7. Reston, VA: American Society of Civil Engineers, 2017.

- [75] J. E. Woods, “Advances in Retrofit and Testing of Reinforced Concrete Shear Walls : Part 1 - Seismic Retrofit of Deficient Walls with Fibre-Reinforced Polymer Sheets Part 2 - Building Scale Performance Evaluation using Hybrid Simulation by Advances in Retrofit and Test,” 2018.
- [76] T. Balendra, K.-Y. Lam, C. -n. Liaw, and S.-L. Lee, “Behavior of eccentrically braced frame by pseudo-dynamic test,” *J. Struct. Eng.*, vol. 113, no. 4, pp. 673–688, 1987.
- [77] P. B. Shing, O. S. Bursi, and M. T. Vannan, “Pseudodynamic tests of a concentrically braced frame using substructuring techniques,” *J. Constr. Steel Res.*, vol. 29, no. 1–3, pp. 121–148, 1994.
- [78] C. R. Thewalt and S. A. Mahin, “Non-planar pseudodynamic testing,” *Earthq. Eng. Struct. Dyn.*, vol. 24, no. 5, pp. 733–746, 1995.
- [79] F. Molina, G. Verzeletti, G. Magonette, P. Buchet, and M. Geradin, “Bi-directional pseudodynamic test of a full-size three-storey building,” *arthquake Eng. Struct. Dyn.*, vol. 28, no. 12, pp. 1541–1566, 1999.
- [80] P. Negro, E. Mola, F. J. Molina, and G. E. Magonette, “Full-scale psd testing of a torsionally unbalanced three-storey non-seismic RC frame,” in *Proceedings of the 13th World Conf. on Earthquake Engineering*, 2004.
- [81] V. Saouma, G. Haussmann, D.-H. Kang, and W. Ghannoum, “Real-time hybrid simulation of a nonductile reinforced concrete frame,” *J. Struct. Eng.*, vol. 140, no. 2, 2013.
- [82] C. A. Whyte and B. Stojadinovic, “Hybrid simulation of the seismic response of squat reinforced concrete shear walls,” 2013.

- [83] M. Eatherton, “Large-scale cyclic and hybrid simulation testing and development of a controlled-rocking steel building system with replaceable fuses.” ProQuest Dissertations Publishing, 2010.
- [84] T. L. Karavasilis, J. M. Ricles, R. Sause, and C. Chen, “Experimental evaluation of the seismic performance of steel MRFs with compressed elastomer dampers using large-scale real-time hybrid simulation,” *Eng. Struct.*, vol. 33, no. 6, pp. 1859–1869, 2011, doi: 10.1016/j.engstruct.2011.01.032.
- [85] O.-S. Kwon, N. Nakata, A. Elnashai, and B. Spencer, “A FRAMEWORK FOR MULTI-SITE DISTRIBUTED SIMULATION AND APPLICATION TO COMPLEX STRUCTURAL SYSTEMS,” *J. Earthq. Eng.*, vol. 9, no. 5, pp. 741–753, 2005, doi: 10.1142/S1363246905002158.
- [86] B. M. Phillips and B. F. Spencer Jr., “Model-based feedforward-feedback actuator control for real-time hybrid simulation.(Author abstract),” *J. Struct. Eng.*, vol. 139, no. 7, p. 1205, 2013, doi: 10.1061/(ASCE)ST.1943-541X.0000606.
- [87] O. Mercan and J. M. Ricles, “Experimental studies on real-time testing of structures with elastomeric dampers.(Author abstract)(Report),” *J. Struct. Eng.*, vol. 135, no. 9, p. 1124, 2009, doi: 10.1061/(ASCE)0733-9445(2009)135:9(1124).
- [88] R. Christenson, Y. Lin, A. Emmons, and B. Bass, “Large-Scale Experimental Verification of Semiactive Control through Real-Time Hybrid Simulation,” *J. Struct. Eng.*, vol. 134, no. 4, pp. 522–534, 2008, doi: 10.1061/(ASCE)0733-9445(2008)134:4(522).
- [89] M. J. Hashemi, A. Masroor, and G. Mosqueda, “Implementation of online model updating in hybrid simulation,” *Earthq. Eng. Struct. Dyn.*, vol. 43, no. 3, pp. 395–412, Mar. 2014,

doi: 10.1002/eqe.2350.

- [90] X. Shao, A. Mueller, and B. A. Mohammed, “Real-Time Hybrid Simulation with Online Model Updating: Methodology and Implementation,” *J. Eng. Mech.*, vol. 142, no. 2, p. 04015074, Feb. 2016, doi: 10.1061/(ASCE)EM.1943-7889.0000987.
- [91] O. Kwon and V. Kammula, “Model updating method for substructure pseudo-dynamic hybrid simulation,” *Earthq. Eng. Struct. Dyn.*, vol. 42, no. 13, pp. 1971–1984, 2013, doi: 10.1002/eqe.2307.
- [92] A. H. Schellenberg, S. A. Mahin, and G. L. Fenves, “Advanced Implementation of Hybrid Simulation. PEER Report 2009/104,” *Test*, no. November, p. 286, 2009.
- [93] J. Erochko, “OpenSEES SelfCentering Material Model.” 2012.
- [94] F. A. Charney, “Unintended Consequences of Modeling Damping in Structures,” *J. Struct. Eng.*, vol. 134, no. 4, pp. 581–592, Apr. 2008, doi: 10.1061/(ASCE)0733-9445(2008)134:4(581).
- [95] R. Tremblay, M. Lacerte, and C. Christopoulos, “Seismic Response of Multistory Buildings with Self-Centering Energy Dissipative Steel Braces,” *J. Struct. Eng.*, vol. 134, no. 1, pp. 108–120, 2007, doi: 10.1061/(asce)0733-9445(2008)134:1(108).
- [96] N. Shome and C. A. Cornell, “Structural seismic demand analysis: Consideration of collapse,” *8th ACSE Spec. Conf. Probabilistic Mech. Struct. Reliab.*, no. 3, pp. PMC2000-119, 2000.
- [97] J. McCormick, H. Aburano, M. Ikenaga, and M. Nakashima, “Permissible Residual Deformation Levels for Building Structures Considering both Safety and Human

- Elements,” *14th World Conf. Earthq. Eng.*, p. 8, 2008.
- [98] X. Cheng, J. Erochko, and D. T. Lau, “Improving the seismic performance of existing bridge structures using self-centering dampers,” *16-th World Conf. Earthq. Eng.*, 2017.
- [99] M. J. Nigel Priestley, F. Seible, and G. M. Calvi, *Seismic design and retrofit of bridges*. New York: Wiley, 1996.
- [100] J. B. Mander, M. J. Priestley, and R. Park, “Theoretical Stress-strain Model for Confined Concrete,” *J. Struct. Eng.*, vol. 114, no. 8, pp. 1804–1826, 1988.
- [101] Applied Technology Council, “Quantification of building seismic performance factors,” *Fema P695*, no. June, 2009.
- [102] ASCE, *Minimum Design Loads and Associated Criteria for Buildings and Other Structures*. Reston, VA: American Society of Civil Engineers, 2017.
- [103] ASCE- American Society of Civil Engineers, “Prestandard and Commentary for the Seismic Rehabilitation of Buildings,” *Rehabil. Requir.*, no. 1, pp. 1–518, 2000.
- [104] NEHRP Consultants Joint Venture, “Evaluation of the FEMA P-695 Methodology for Quantification of Building Seismic Performance Factors (NIST GCR 10-917-8),” *Natl. Inst. Stand. Technol. ...*, 2010.
- [105] J. W. Baker, “Efficient analytical fragility function fitting using dynamic structural analysis,” *Earthq. Spectra*, vol. 31, no. 1, pp. 579–599, 2015, doi: 10.1193/021113EQS025M.
- [106] N. Shome, “Probabilistic seismic demand analysis of nonlinear structures.” ProQuest Dissertations Publishing, 1999.

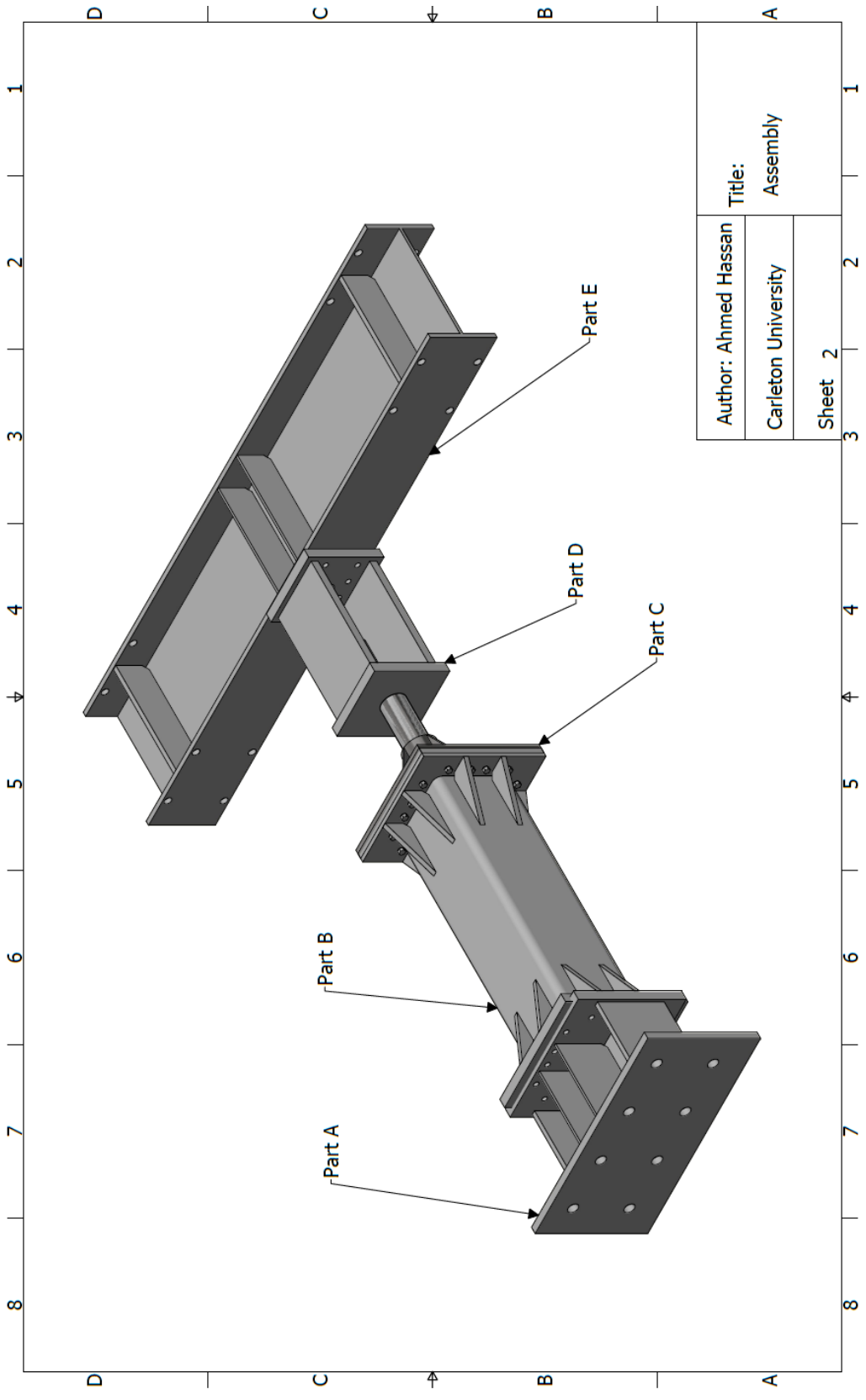


# Appendix A: Brace Drawings

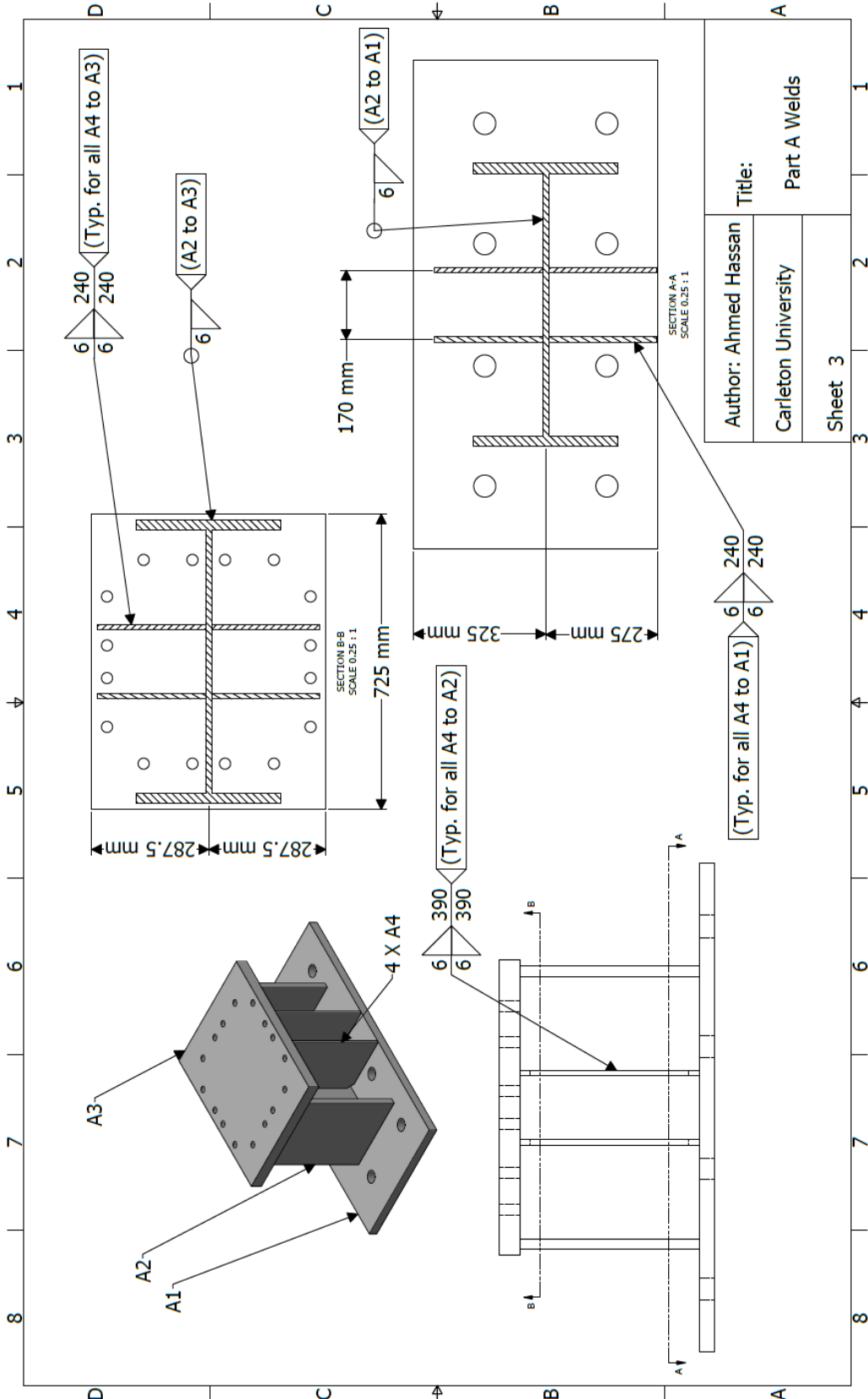
Part	Sub Part	Number Required	Notes	Steel Grade
A	A1	1	W690X217 Stiffeners	300W
	A2	1		350W
	A3	1		300W
	A4	4		300W
B	B1	1	HSS 406X406X13 Slip-On Flange Stiffeners	350W
	B2	2		300W
	B3	16		300W
	B4	8		300W
	B5	1		300W
C	C1	1	DOM pipe 6.75" OD and 0.375" wall thickness Stiffeners	C1026
	C2	1		300W
	C3	4		300W
D	D1	1	DOM pipe 5" OD and 0.625" wall thickness W690X217 Stiffeners	300W
	D2	2		300W
	D3	1		300W
	D4	1		C1026
E	E1	1	W690X217 Stiffeners	350W
	E2	4		300W
	E3	4		300W
	E4	1		300W
F	F1	2	HSS 273X13 Note: 8 parts are required	300W
	F2	2		350W
G	--	8		300W

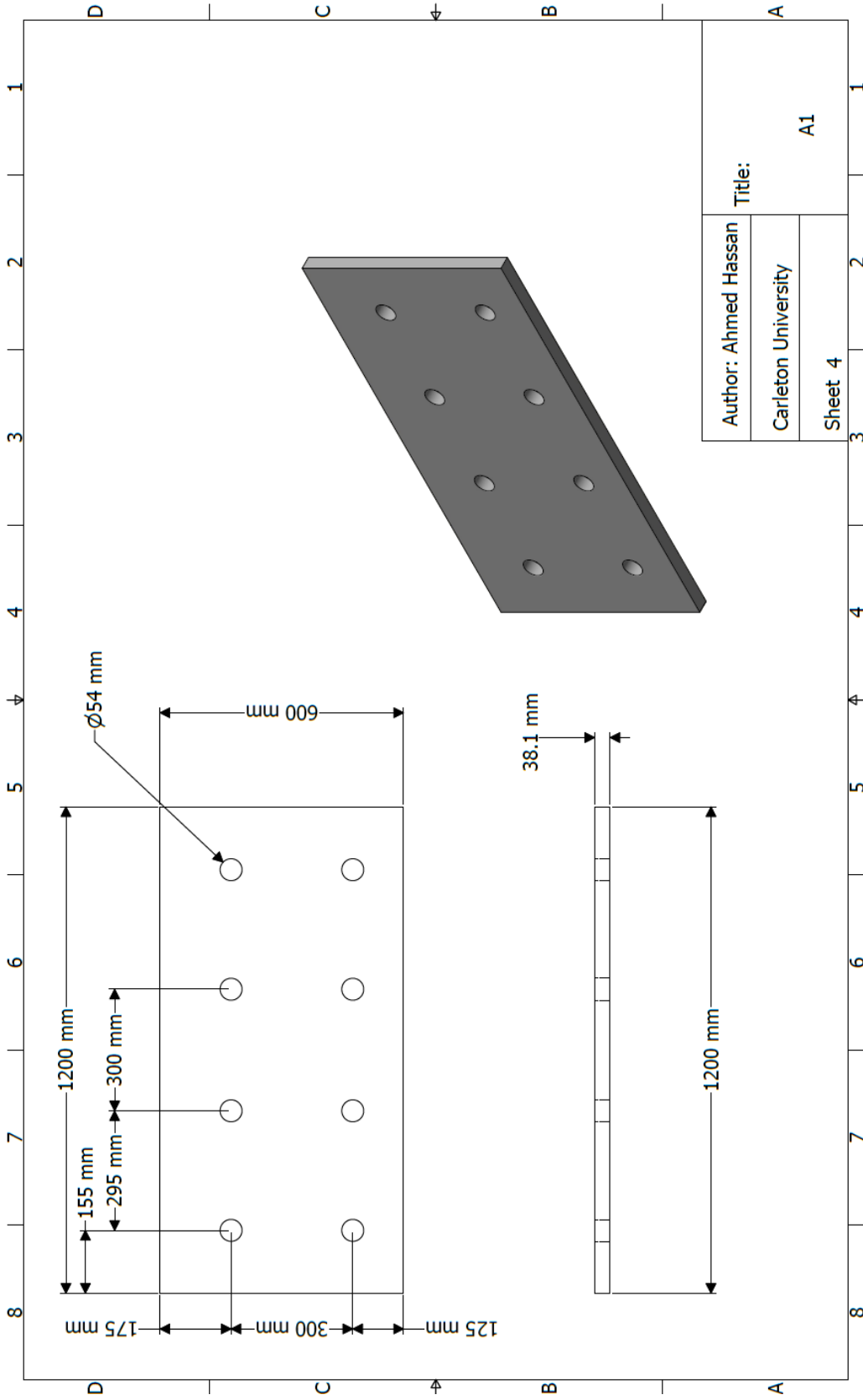
Author: Ahmed Hassan  
 Carleton University  
 Sheet 1

Title:  
 Schedule of Parts

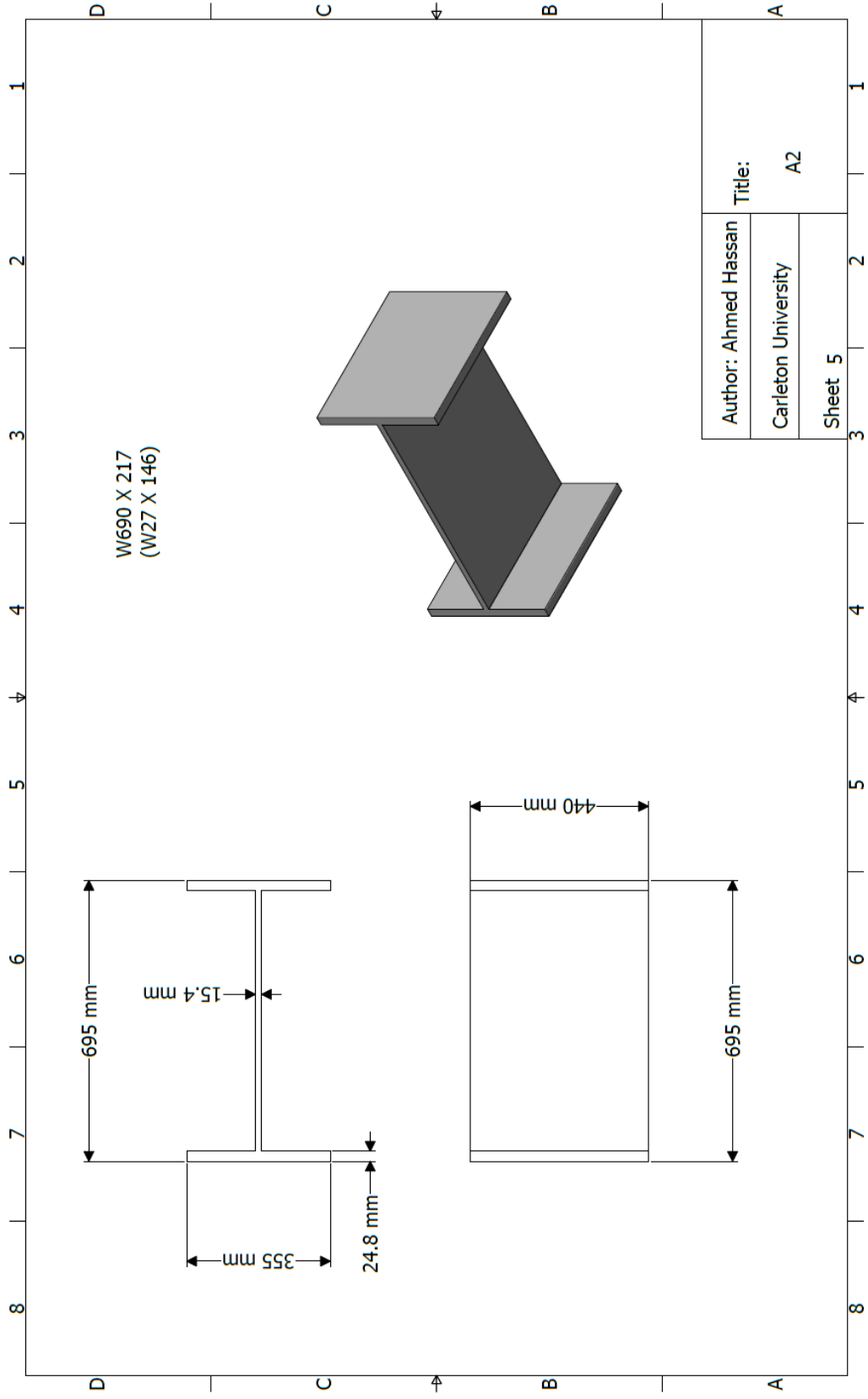


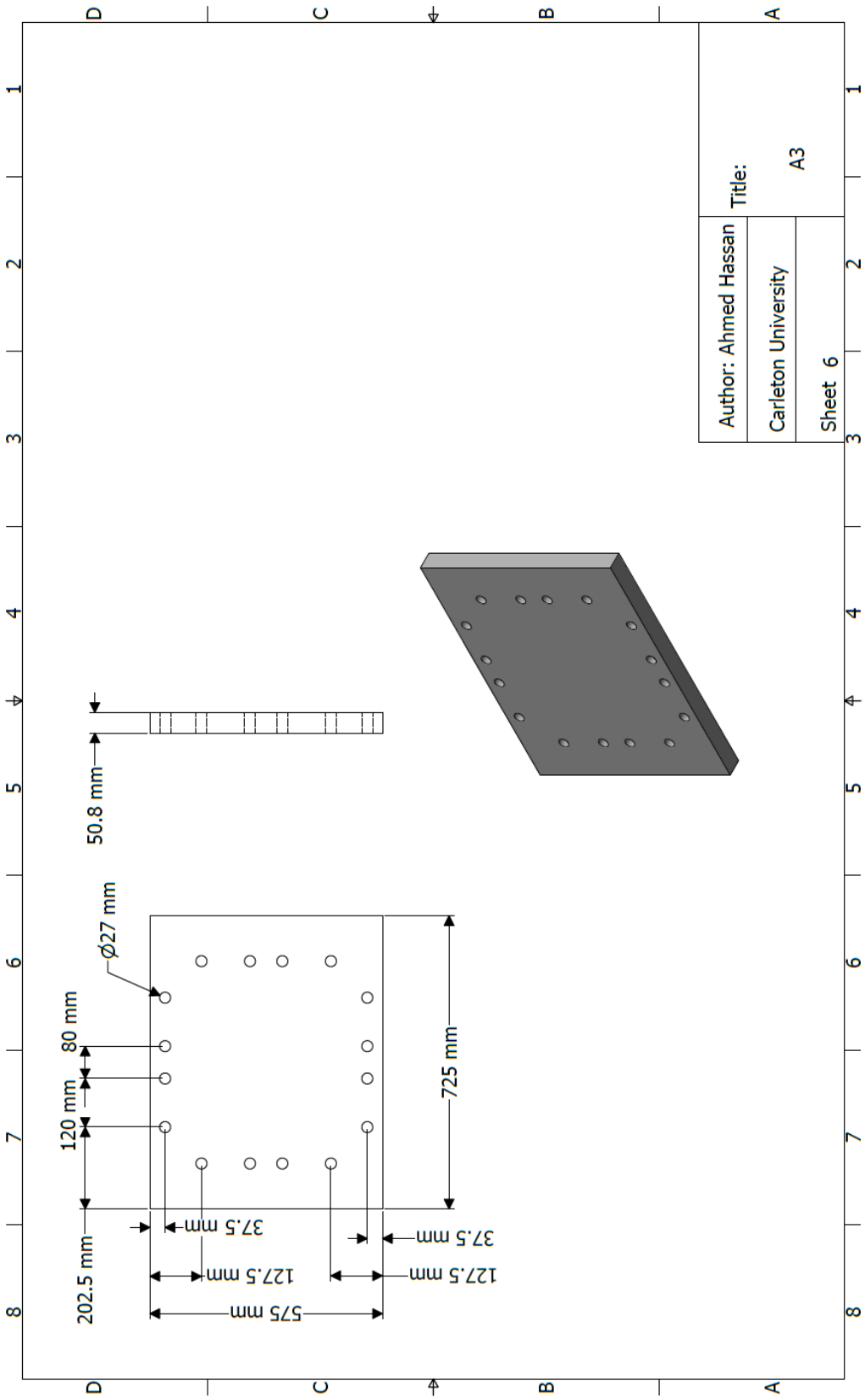
Author: Ahmed Hassan	Title: Assembly	
Carleton University		
Sheet 2	2	1



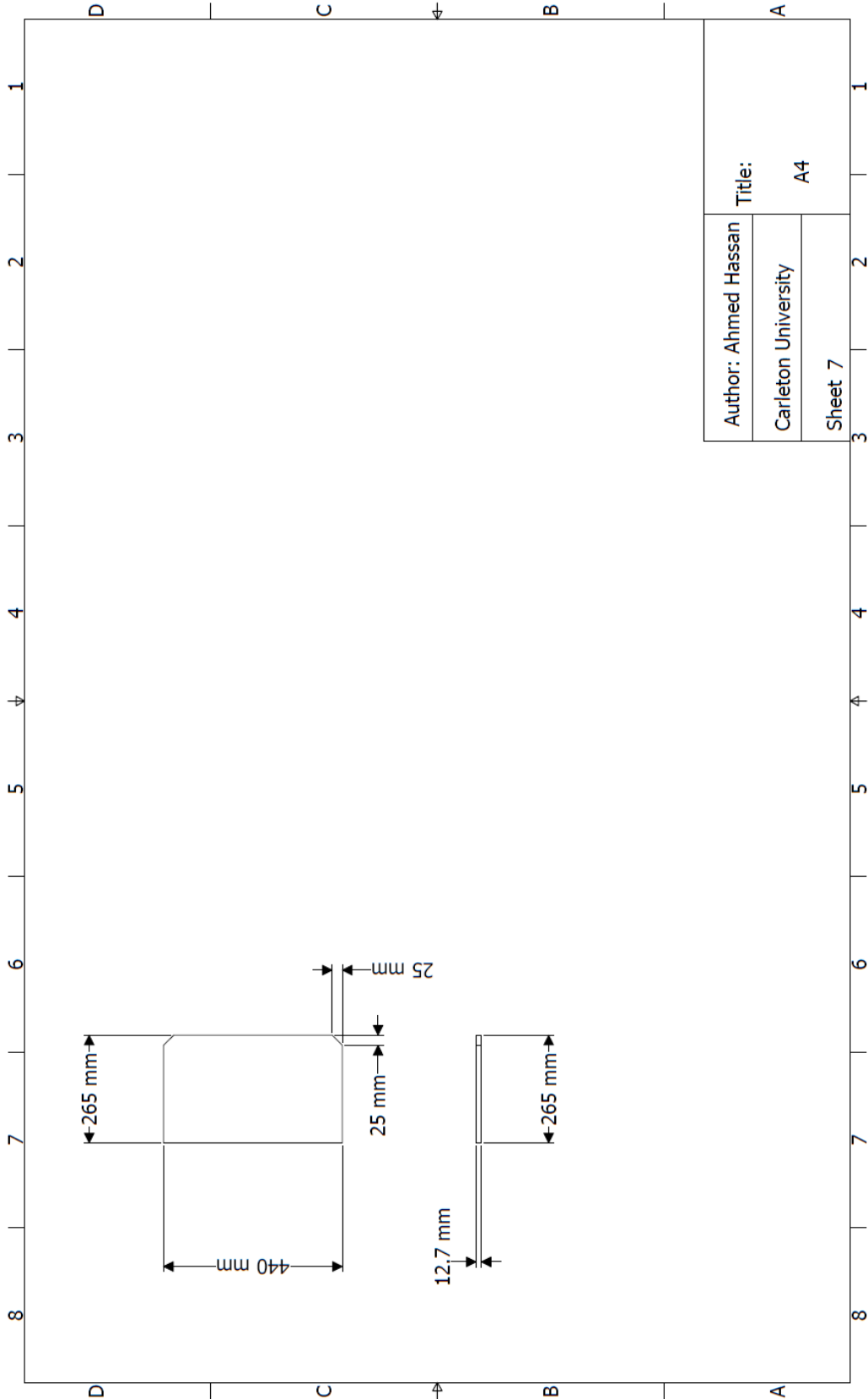


Author: Ahmed Hassan	Title:	
Carleton University	A1	
Sheet 4	2	3

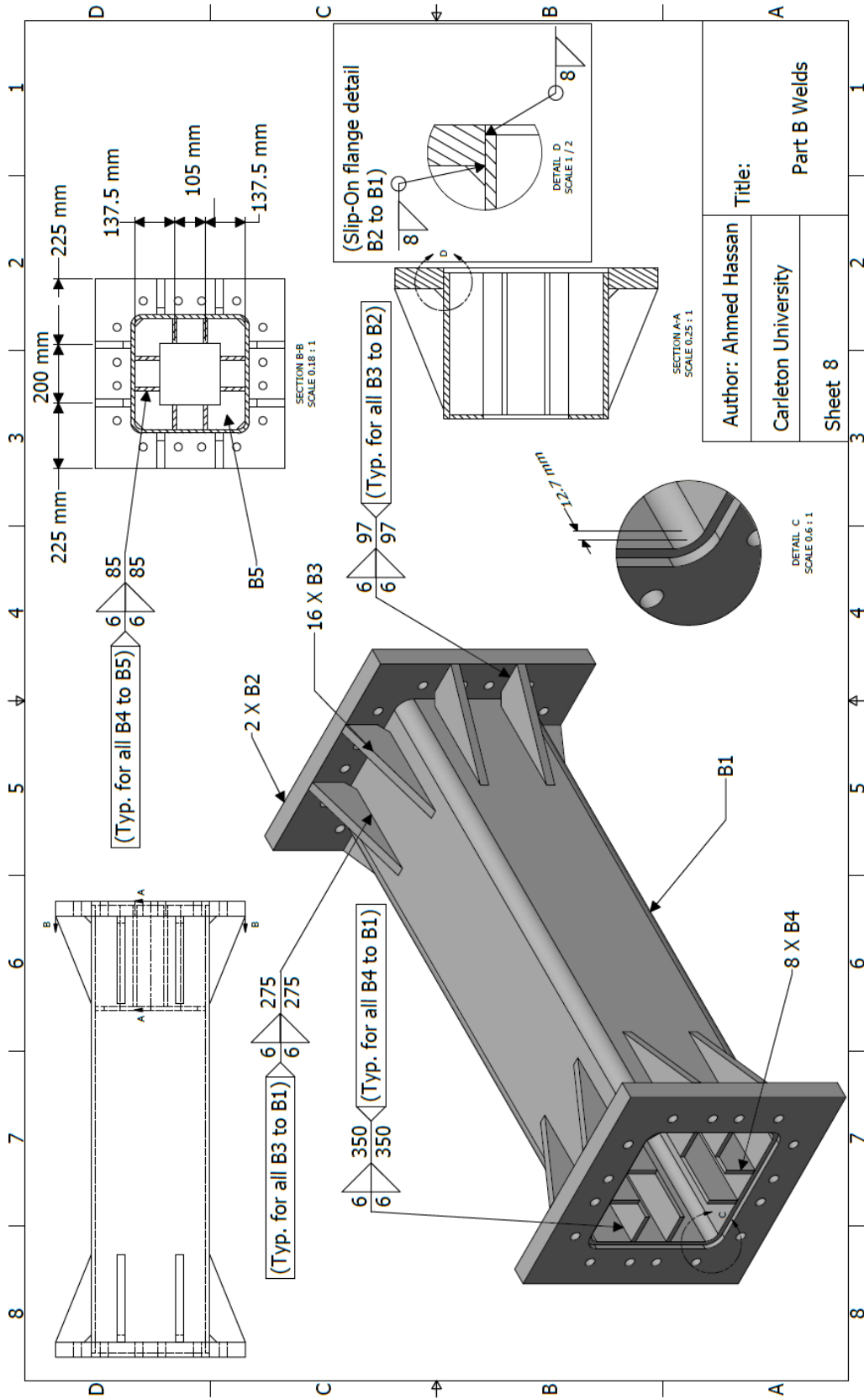


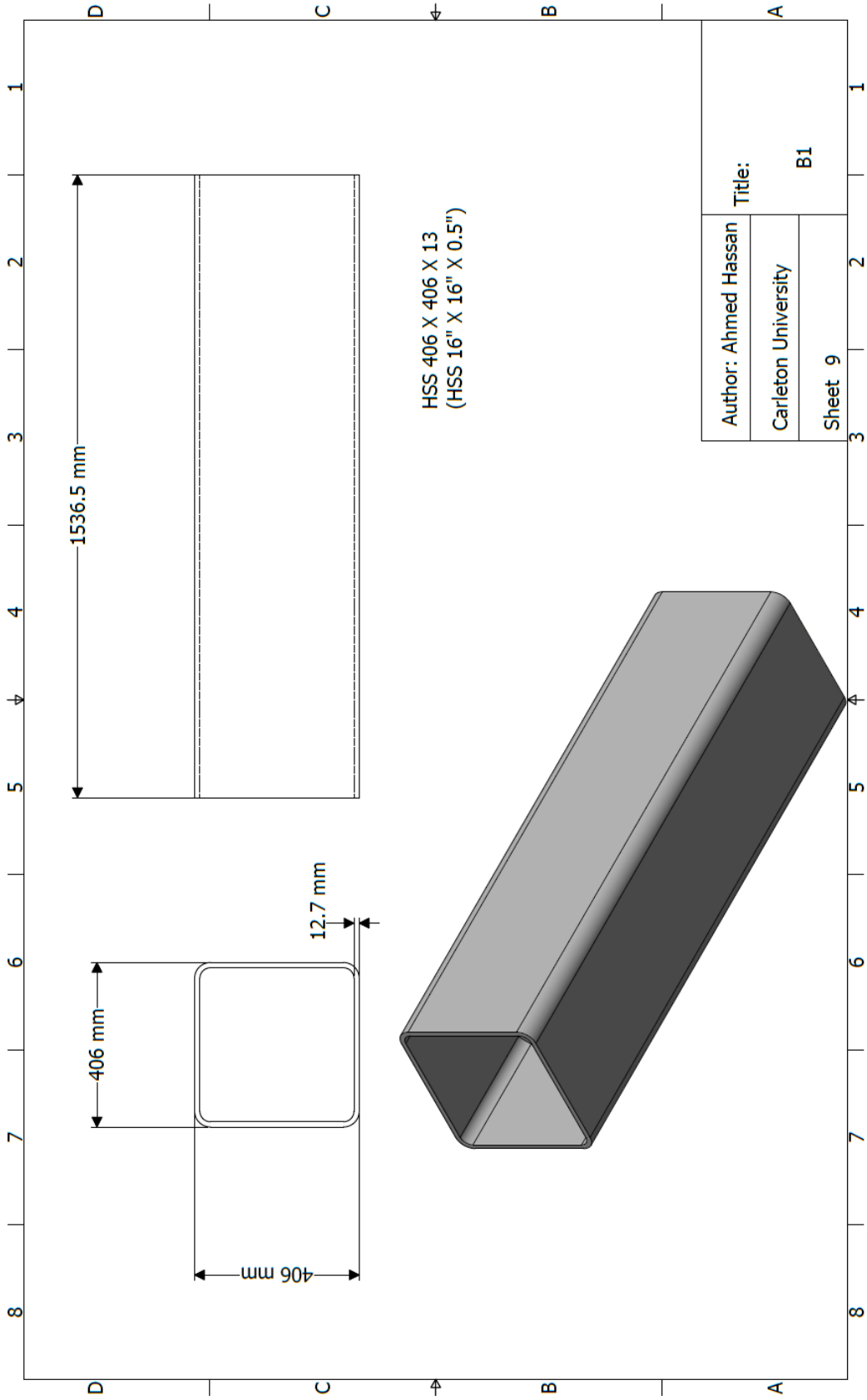


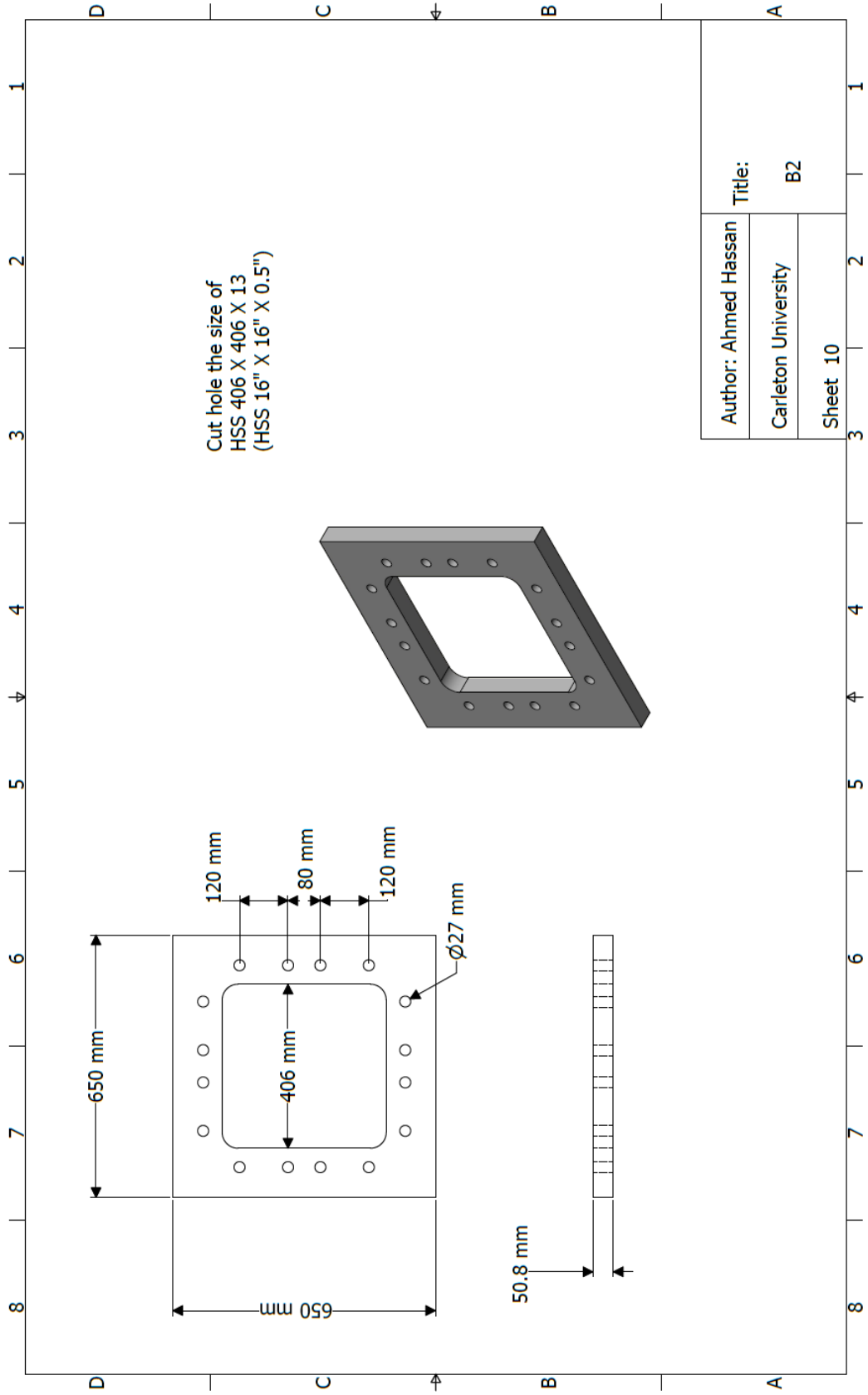
Author: Ahmed Hassan	Title:	
Carleton University	A3	
Sheet 6	2	1

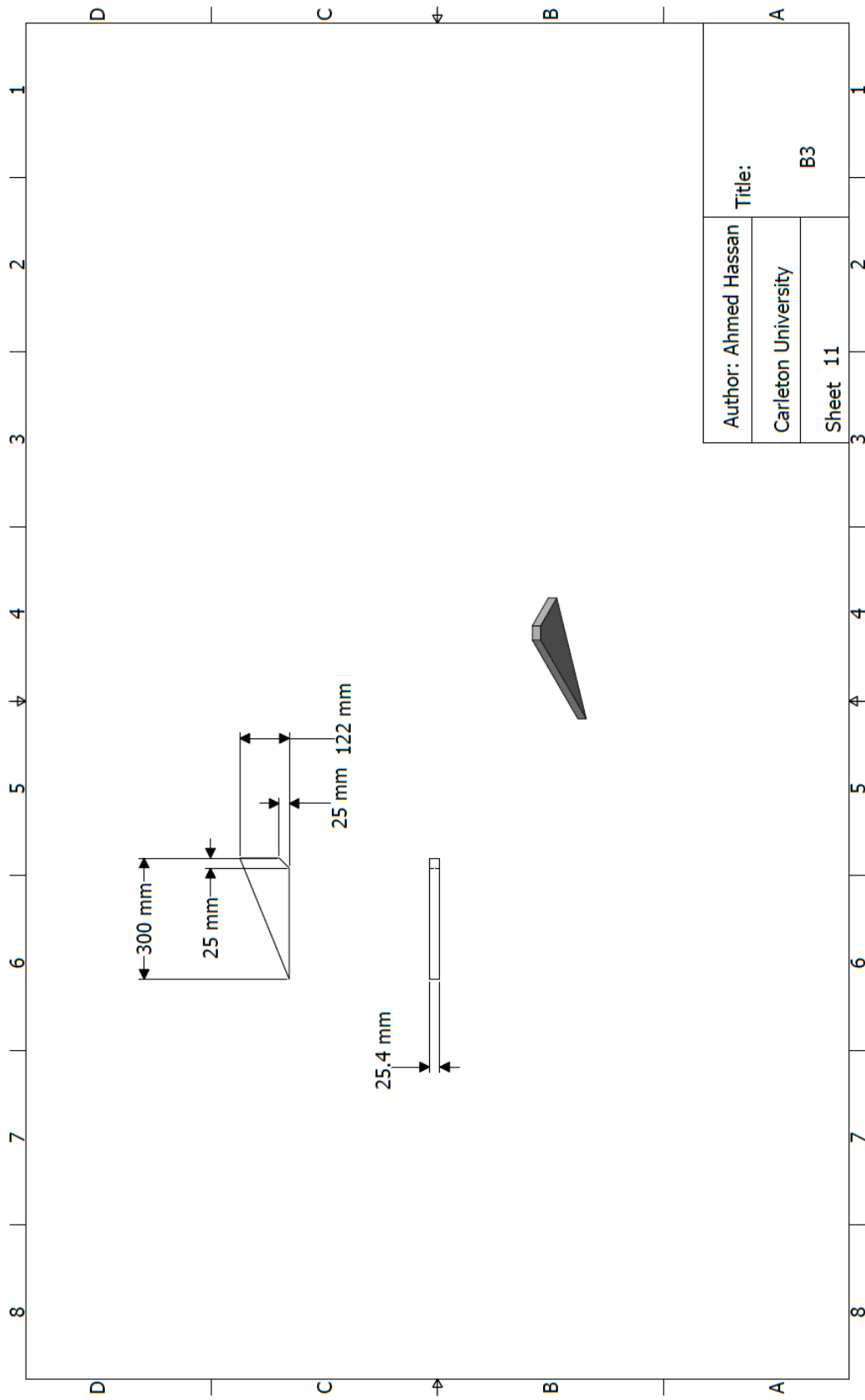


Author: Ahmed Hassan	Title:
Carleton University	A4
Sheet 7	

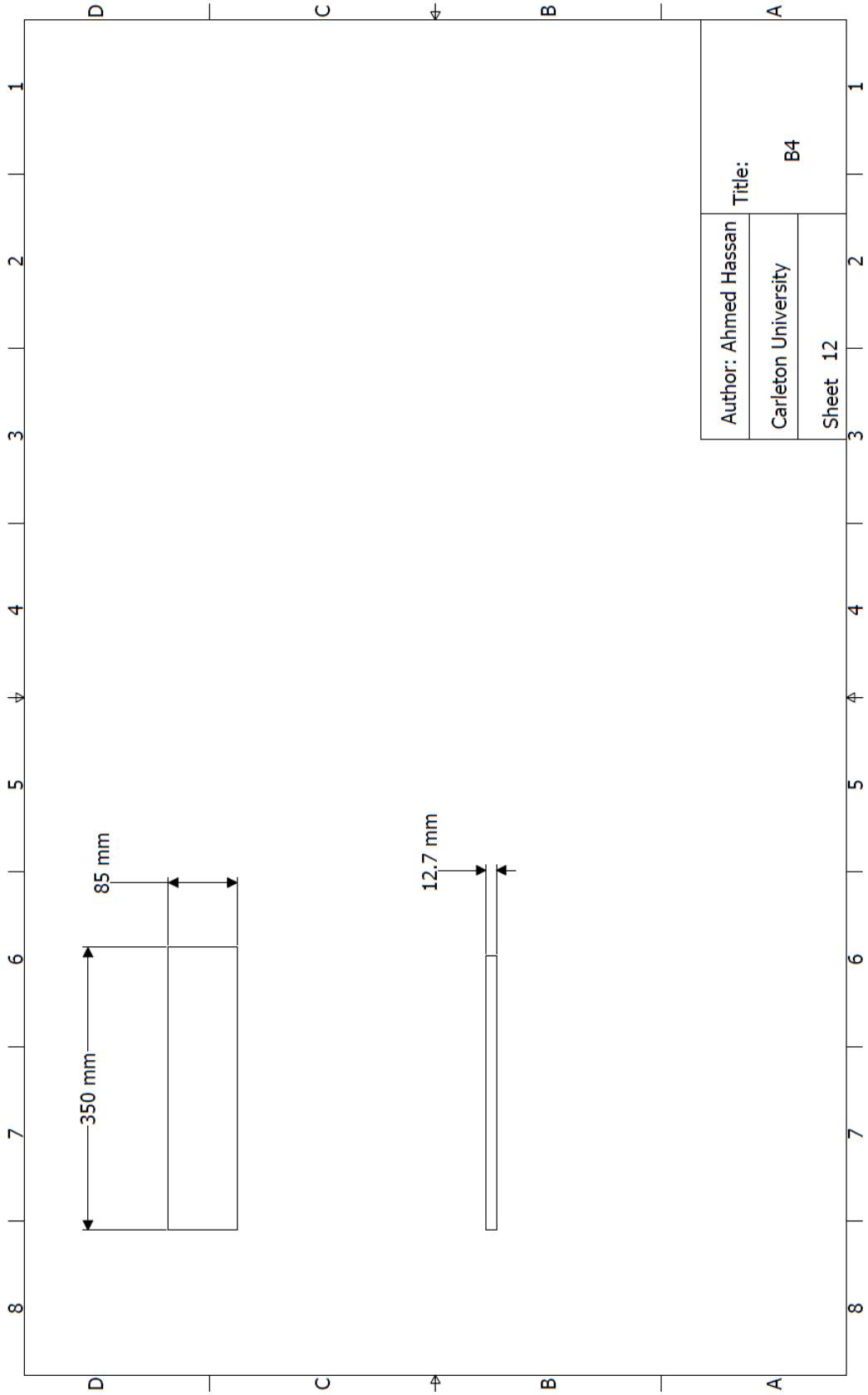


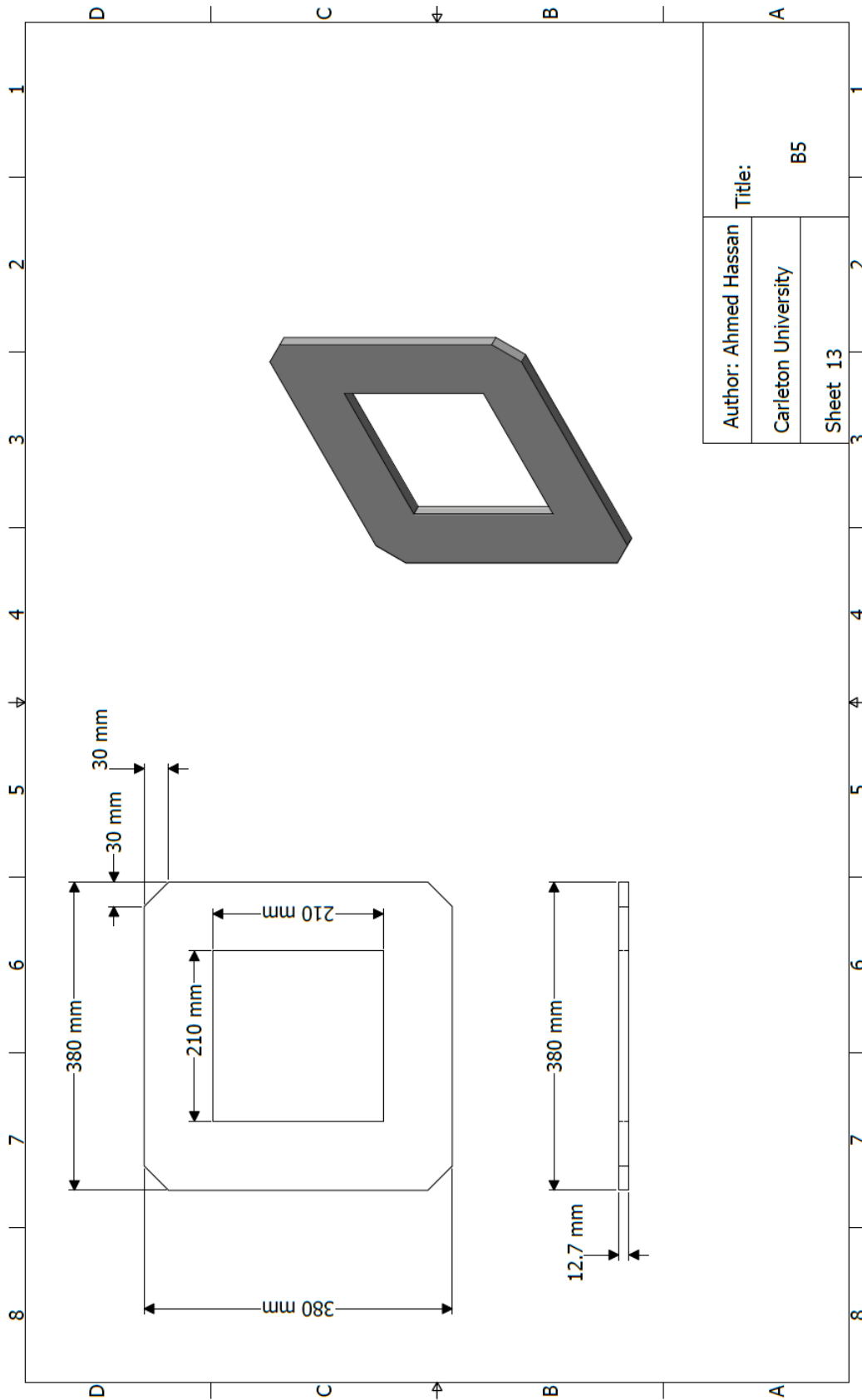


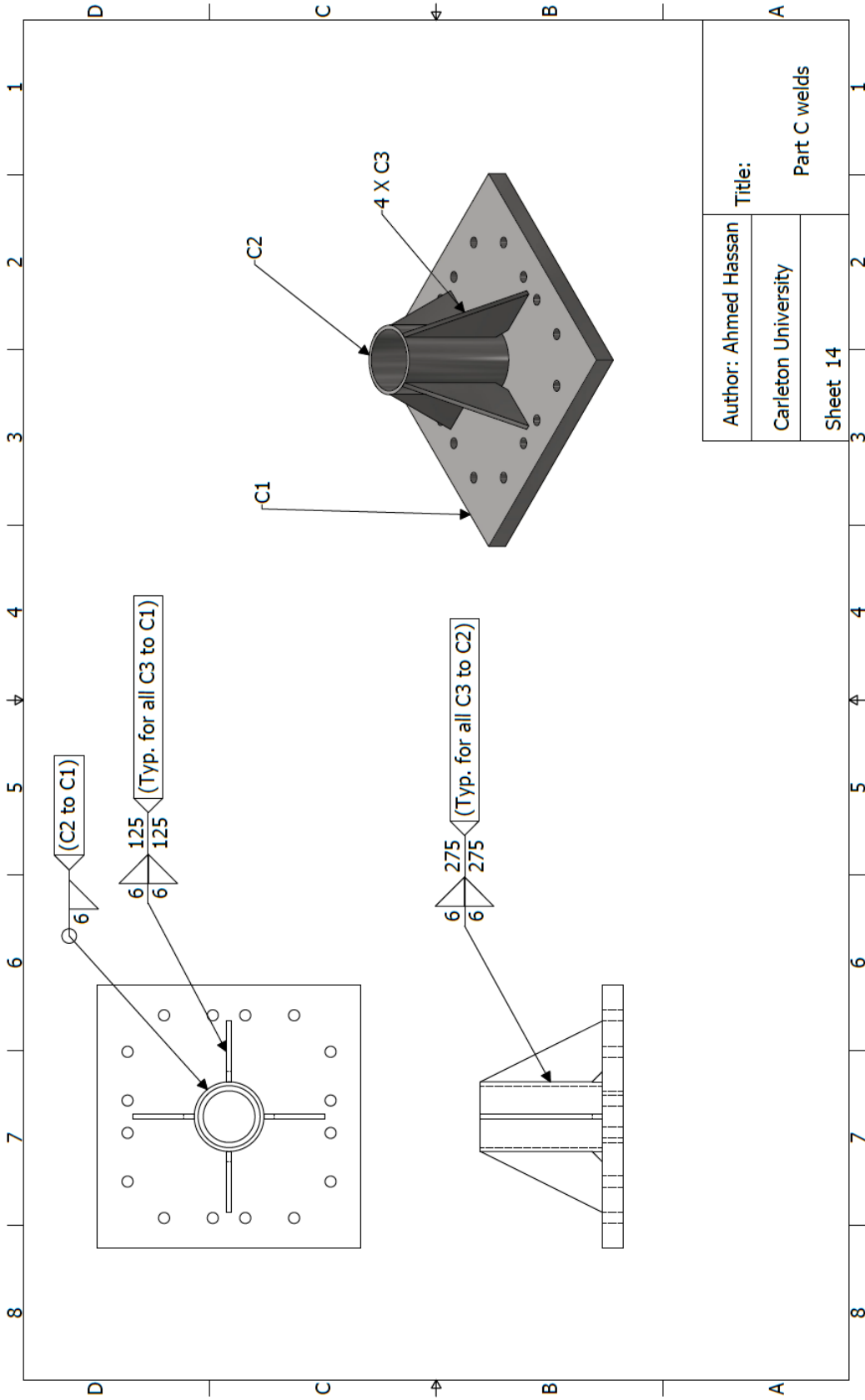




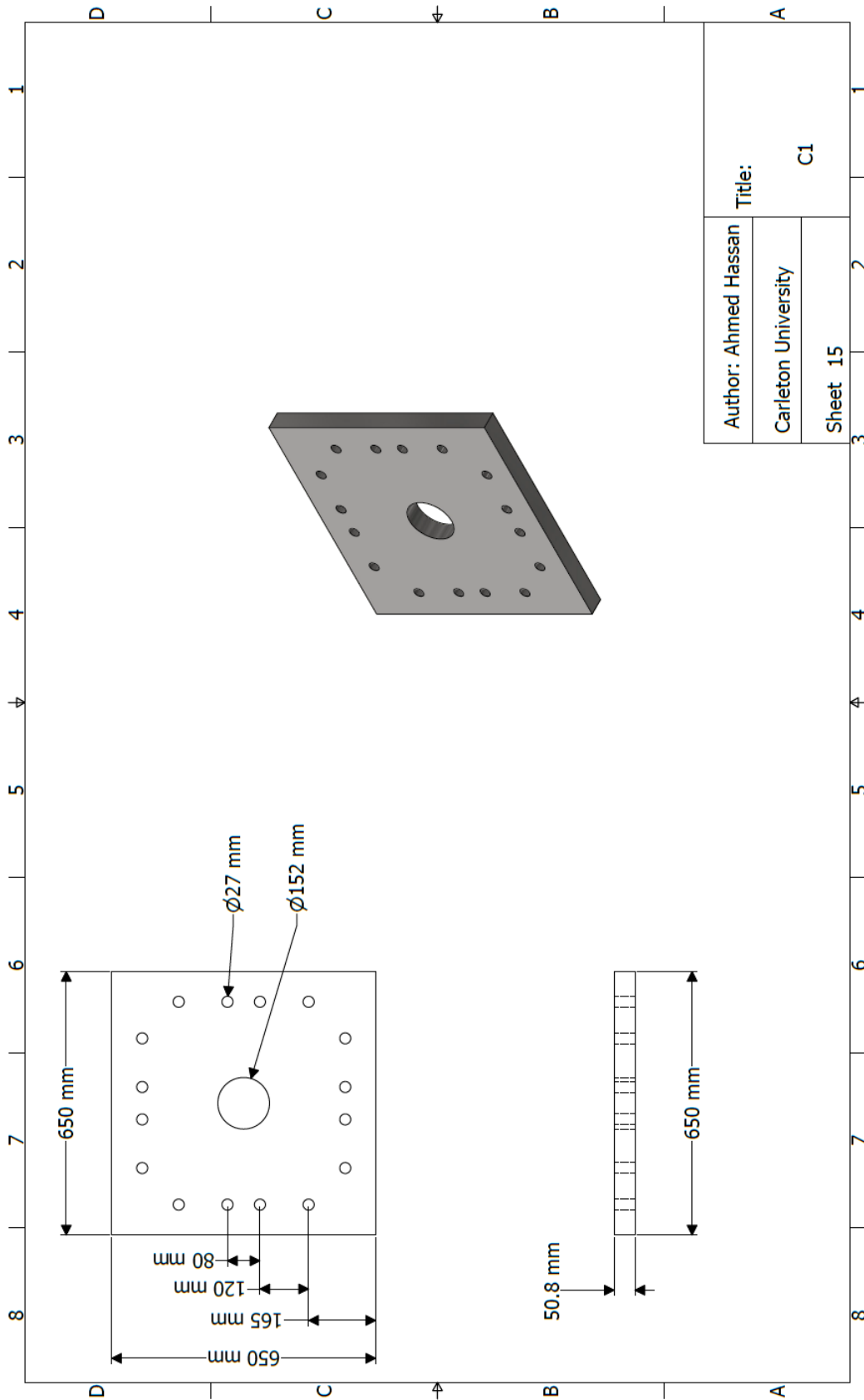
Author: Ahmed Hassan	Title:	
Carleton University	B3	
Sheet 11	2	3

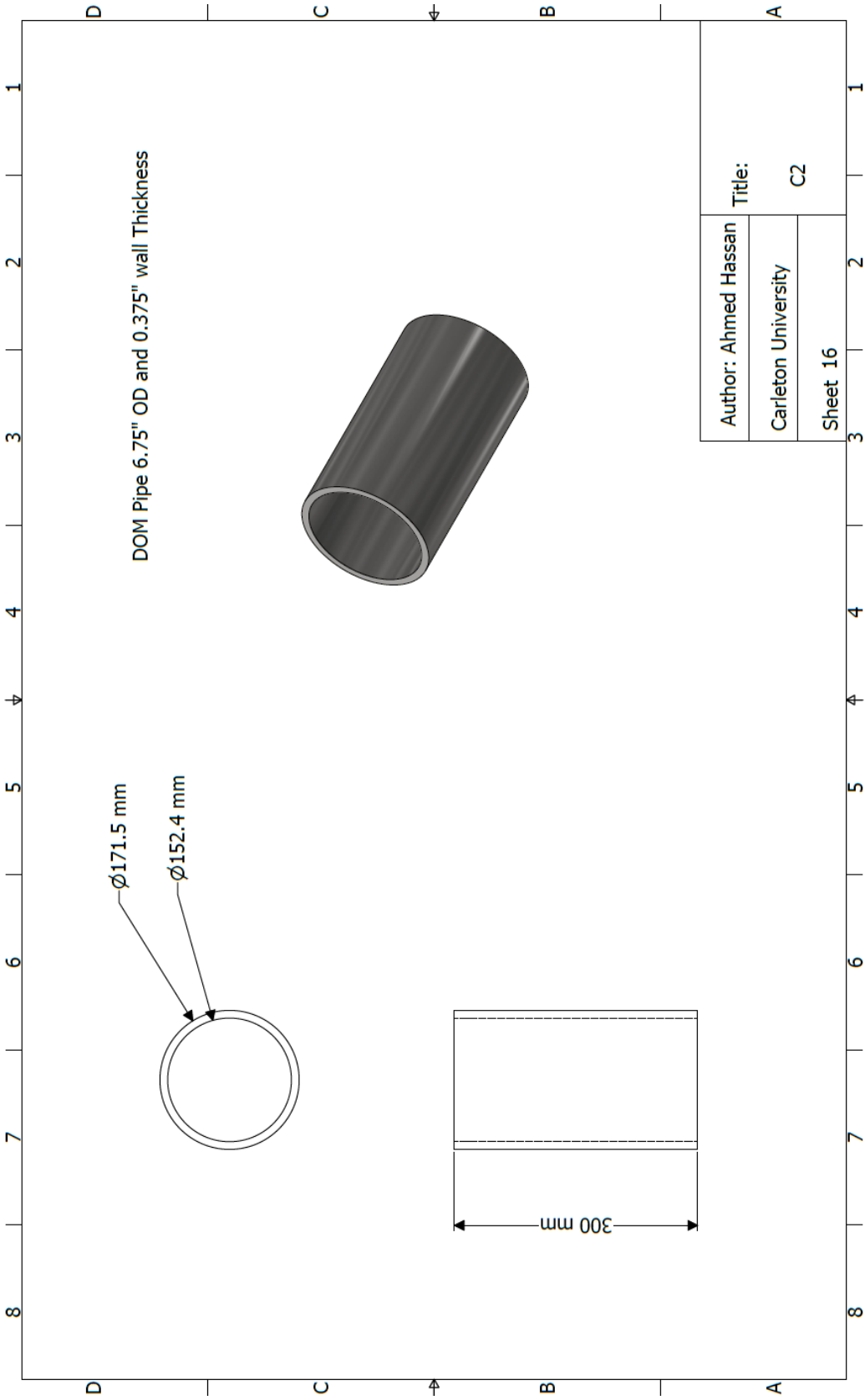


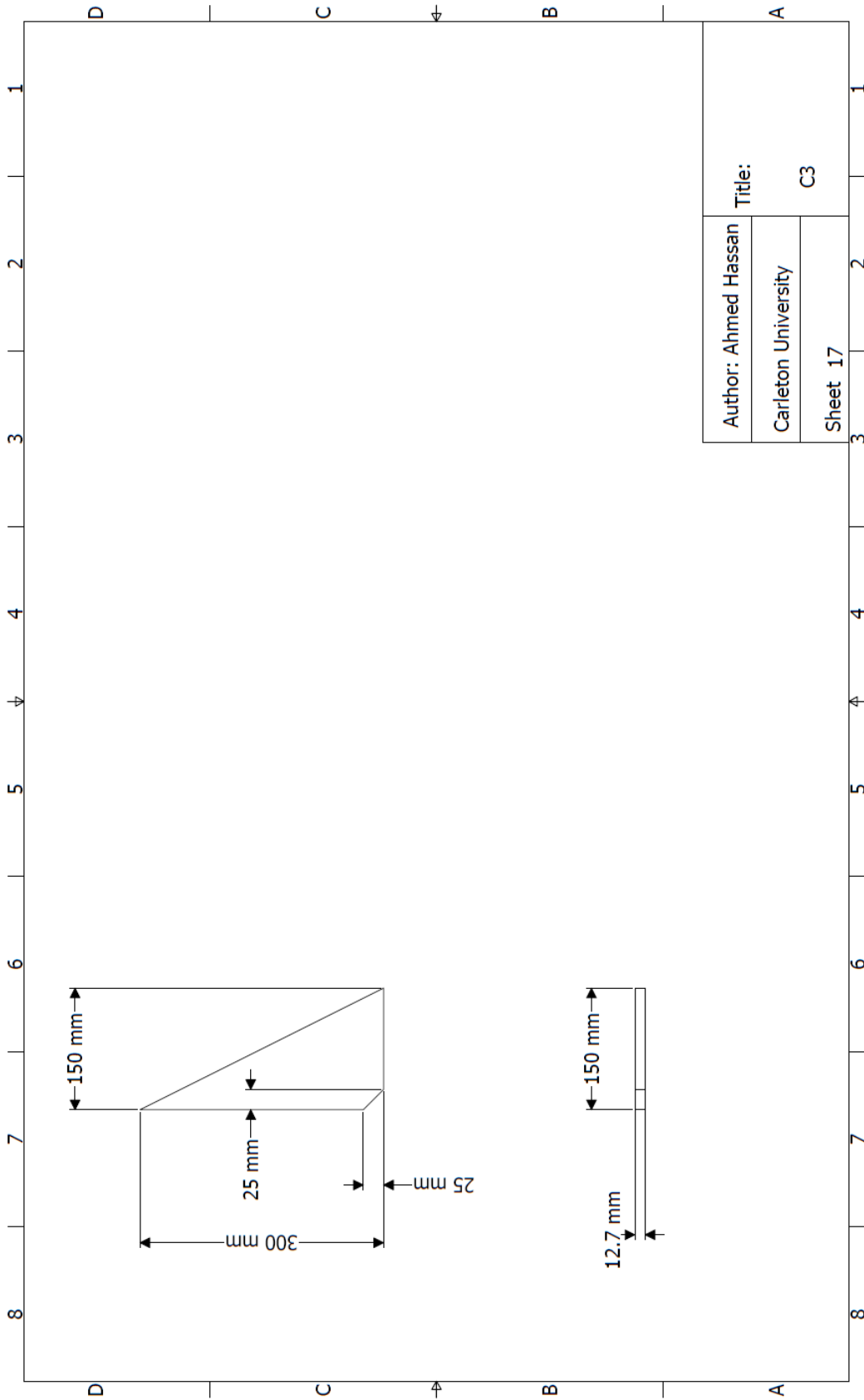


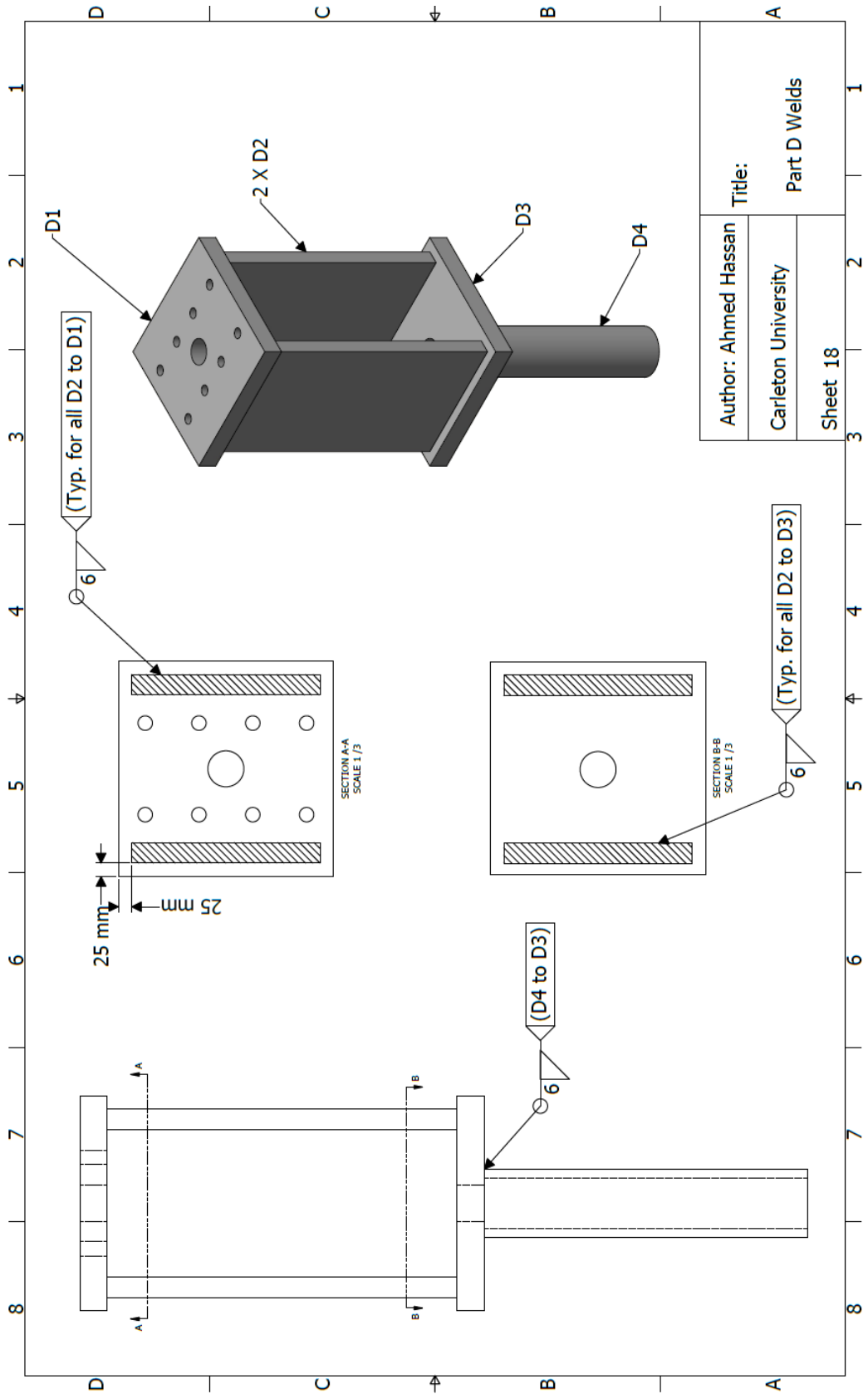


Author: Ahmed Hassan	Title:	
Carleton University	Part C welds	
Sheet 14		

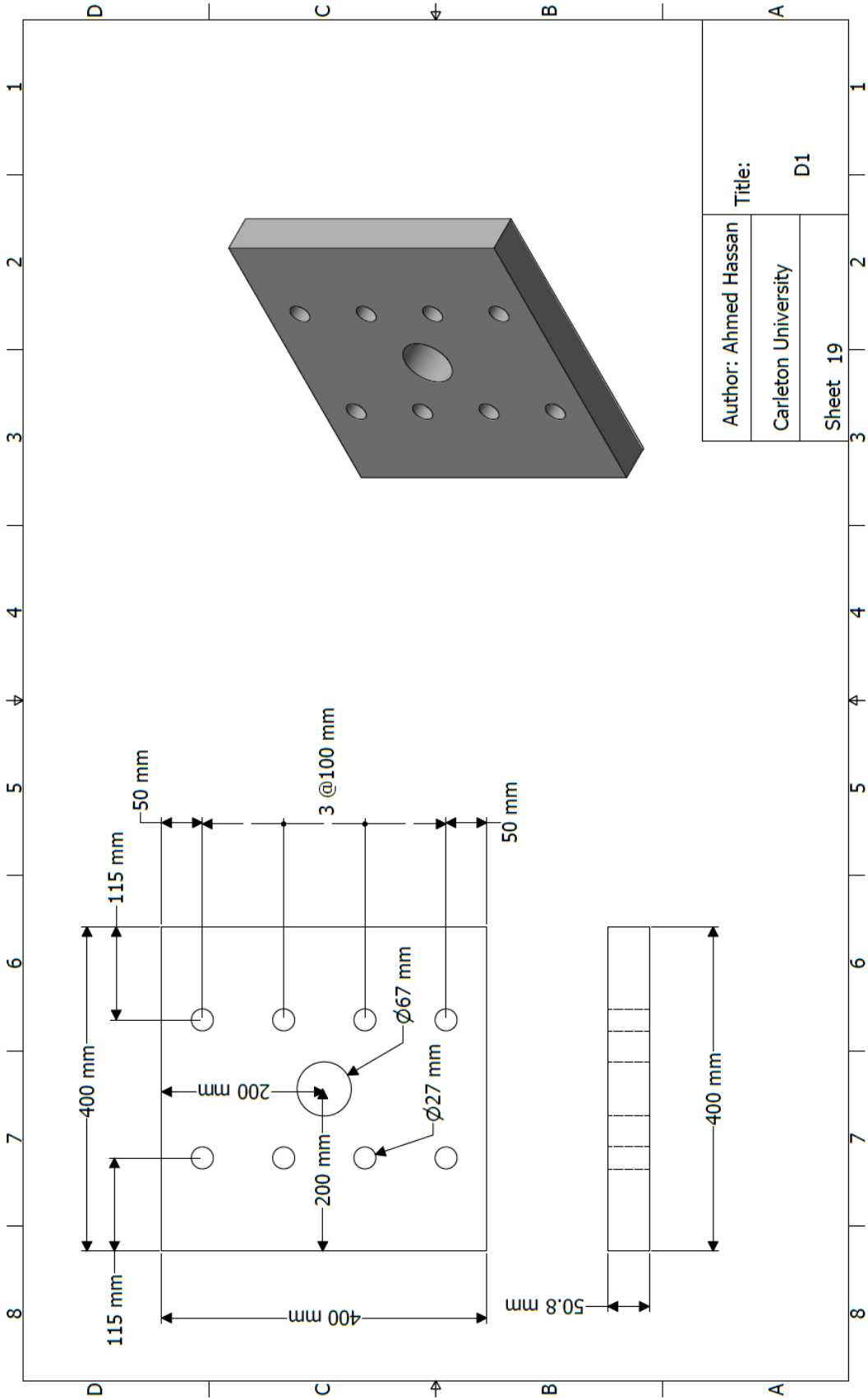


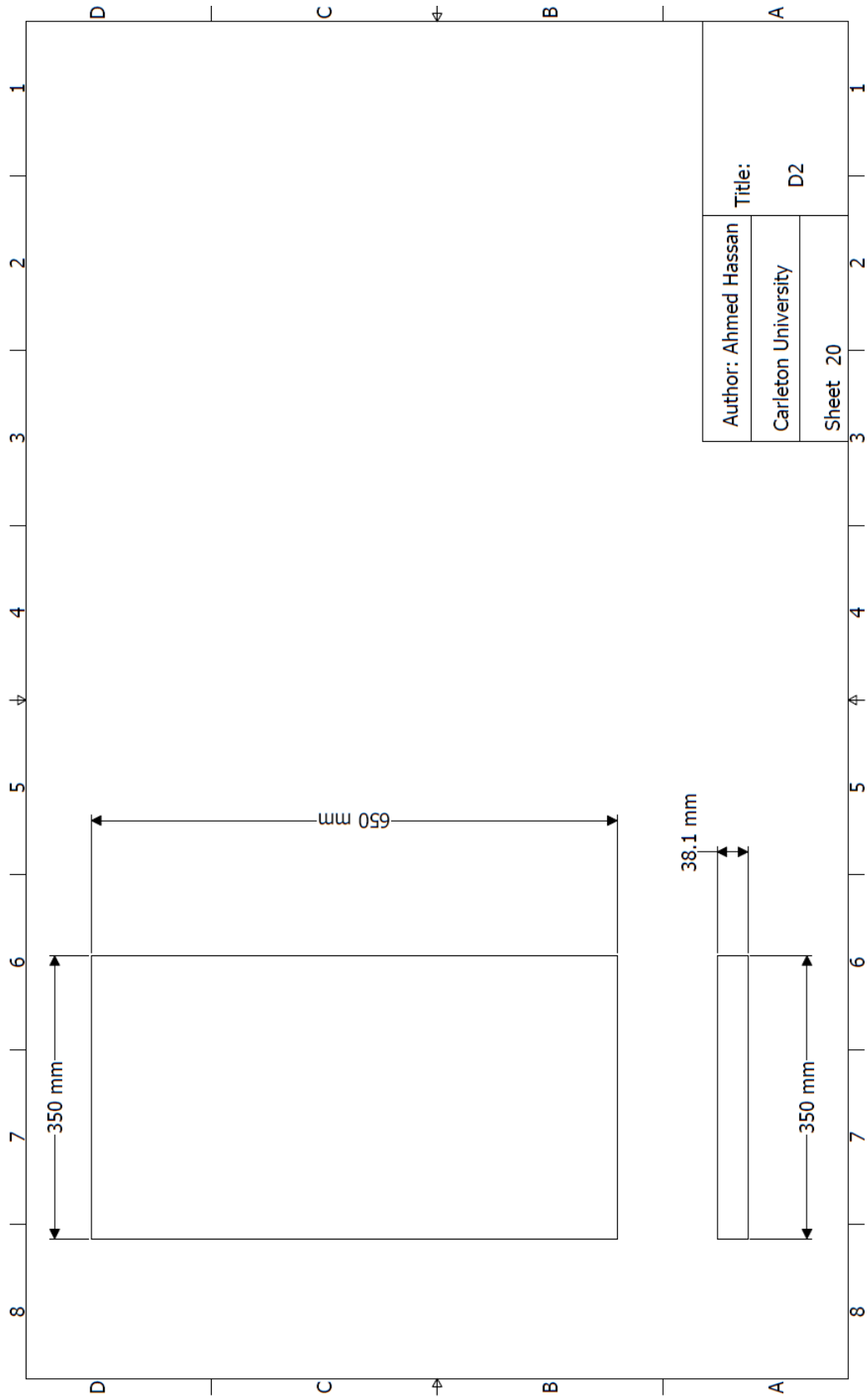




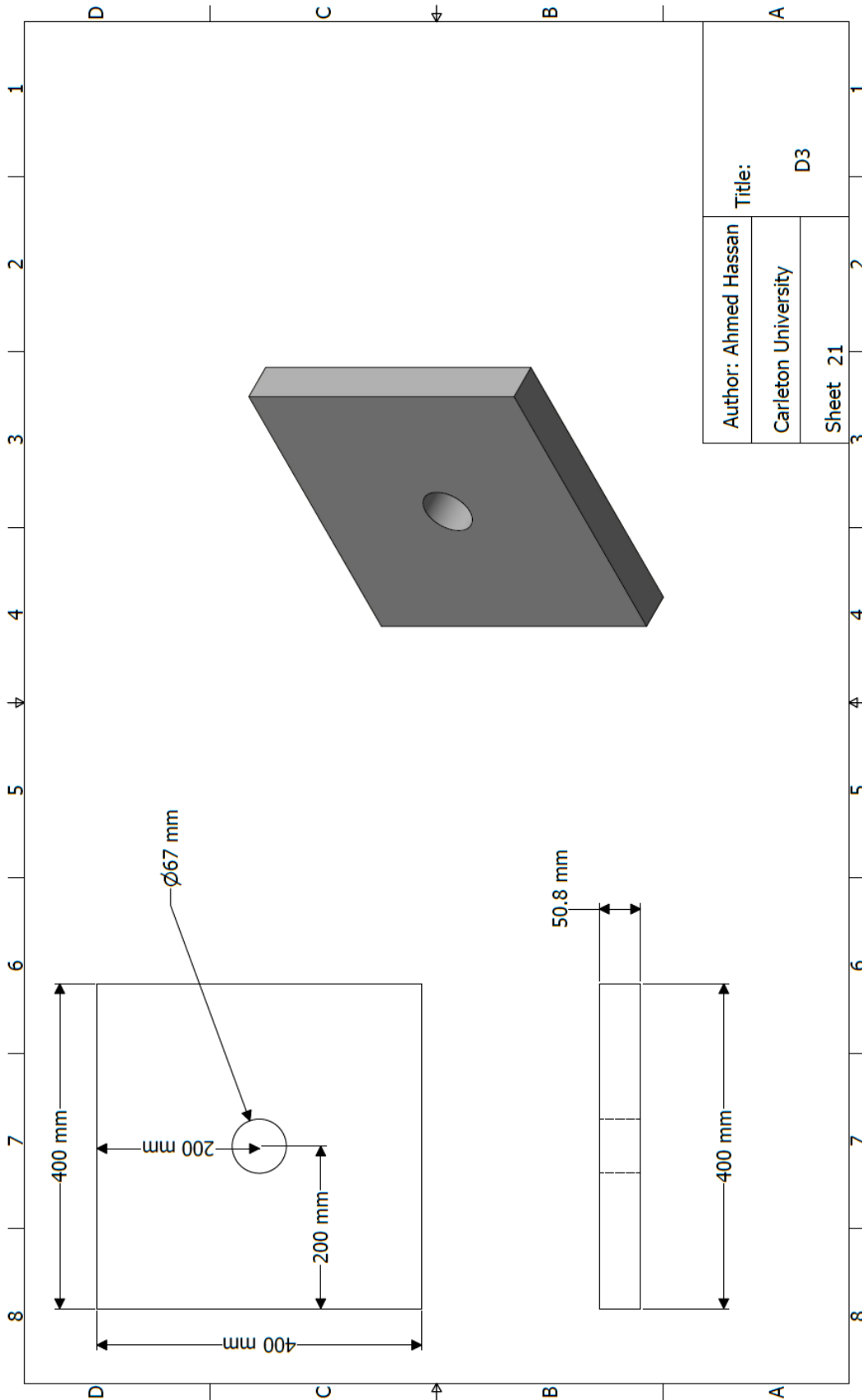


Author: Ahmed Hassan	Title:
Carleton University	Part D Welds
Sheet 18	

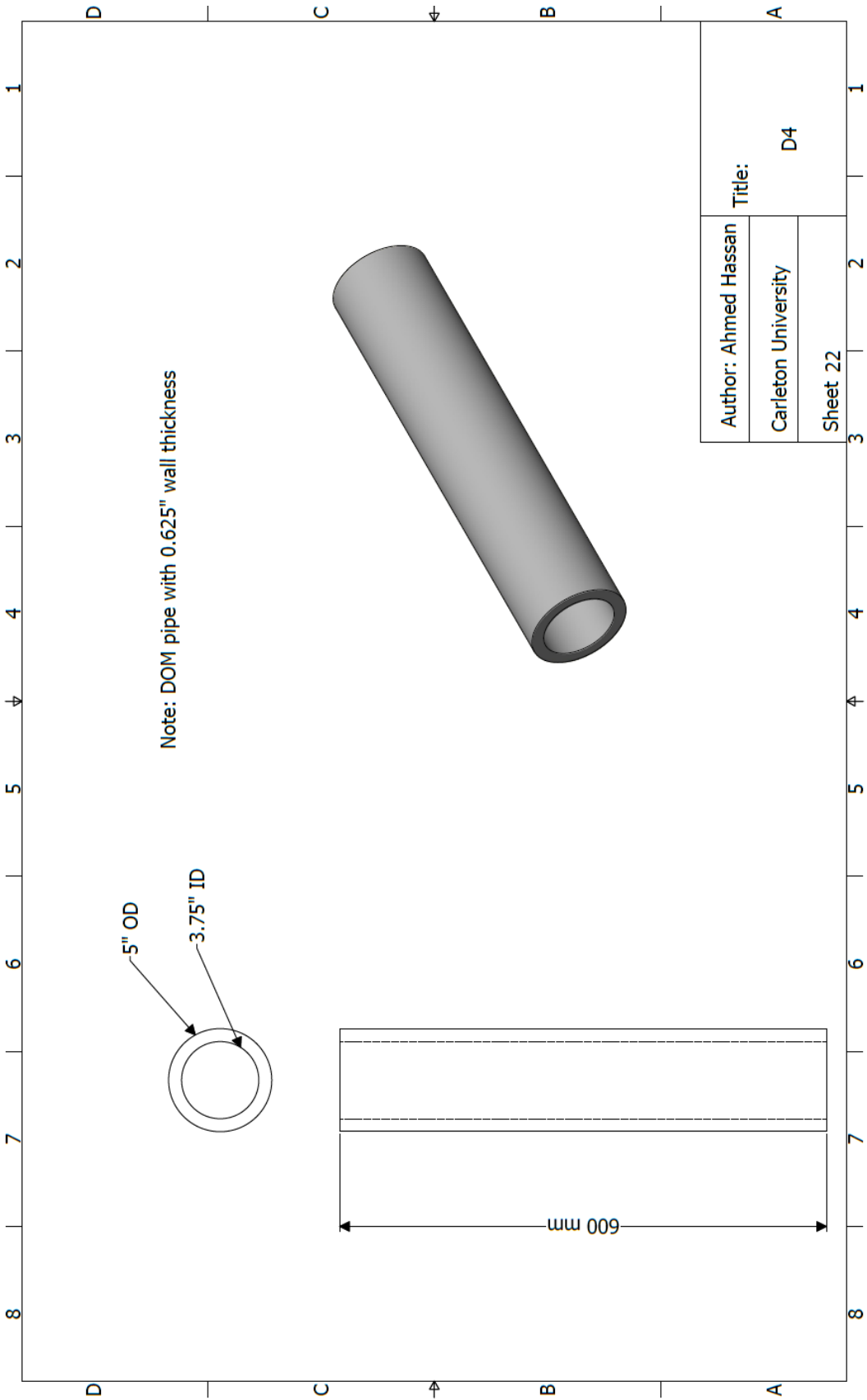


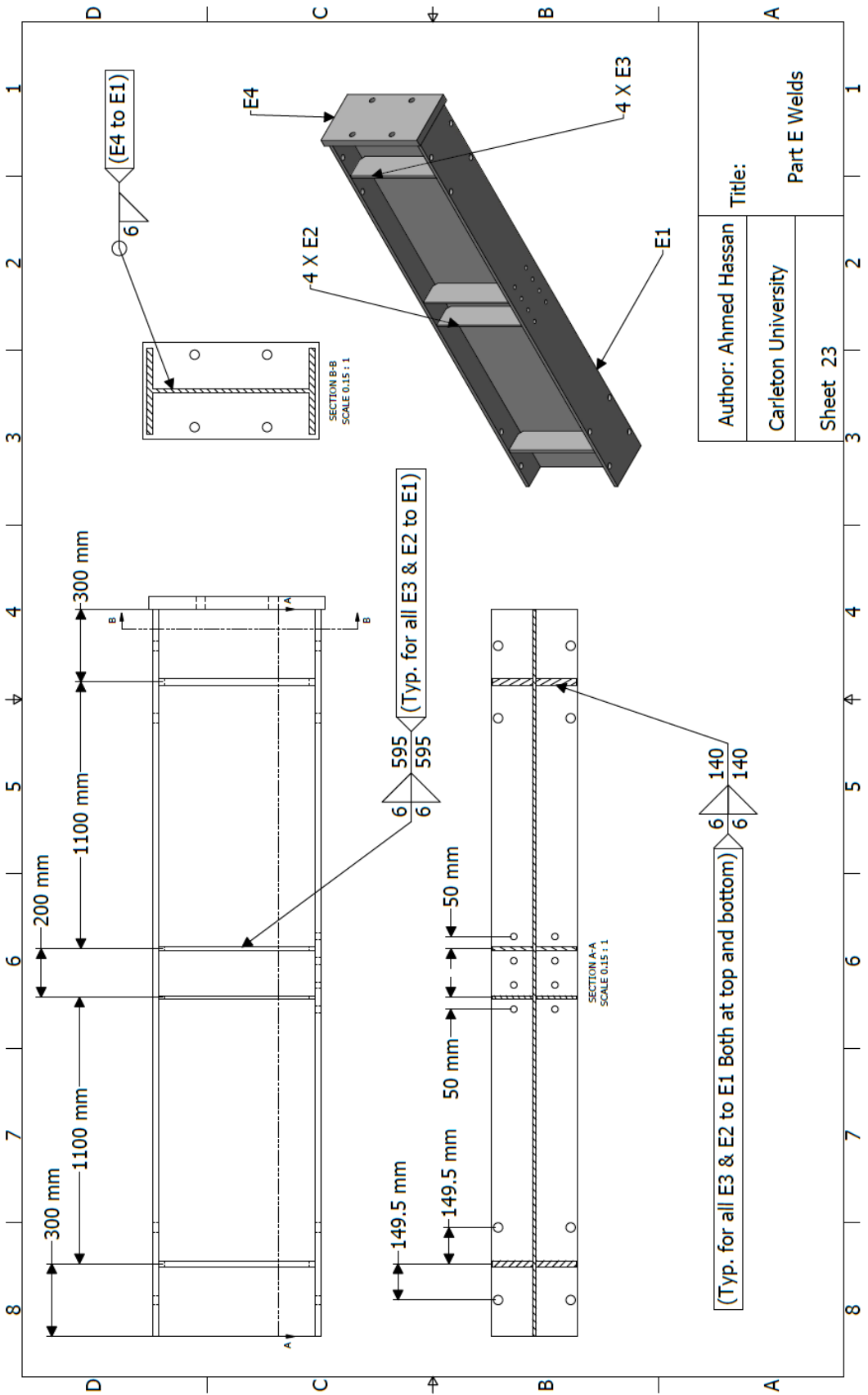


Author: Ahmed Hassan	Title:
Carleton University	D2
Sheet 20	

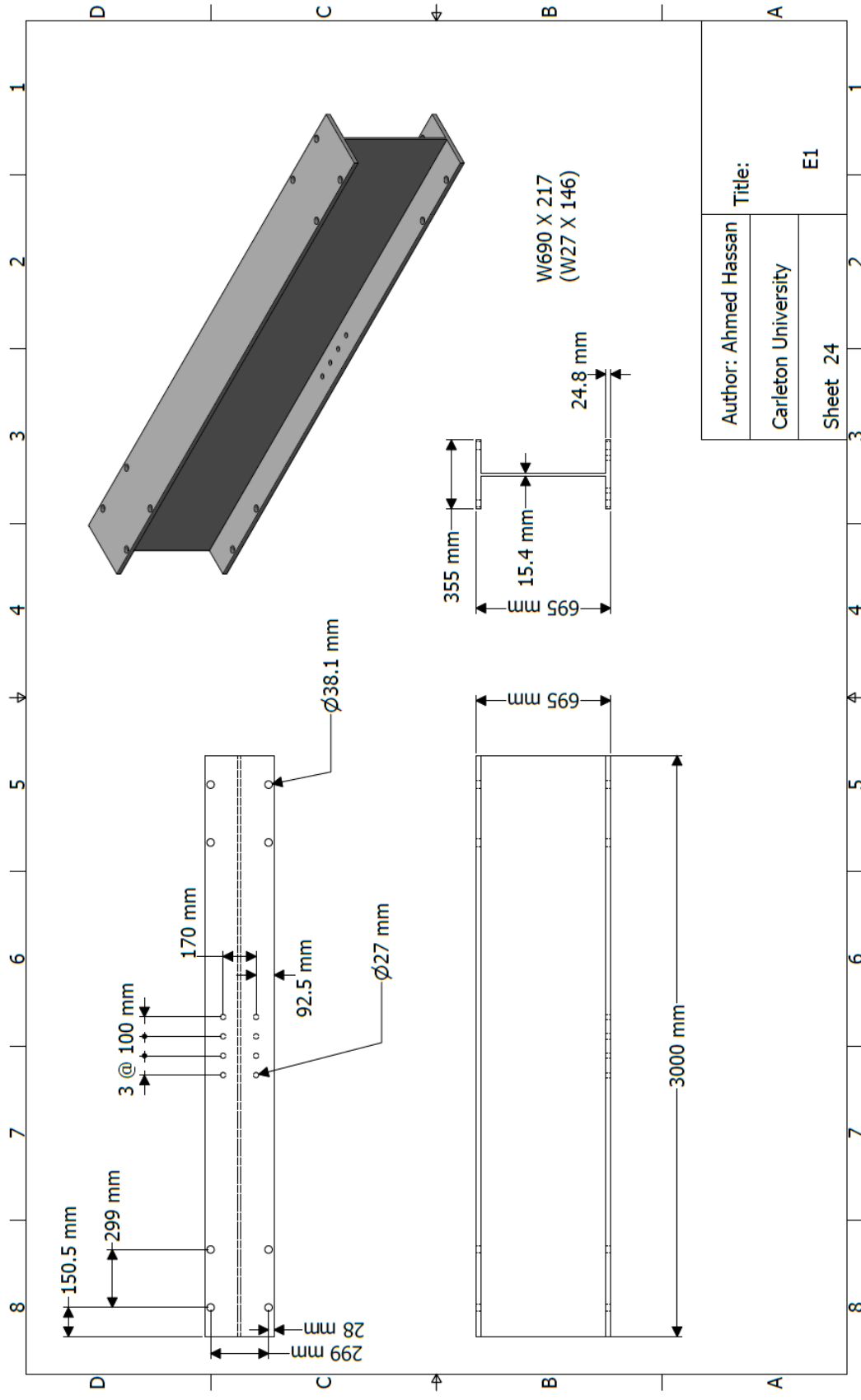


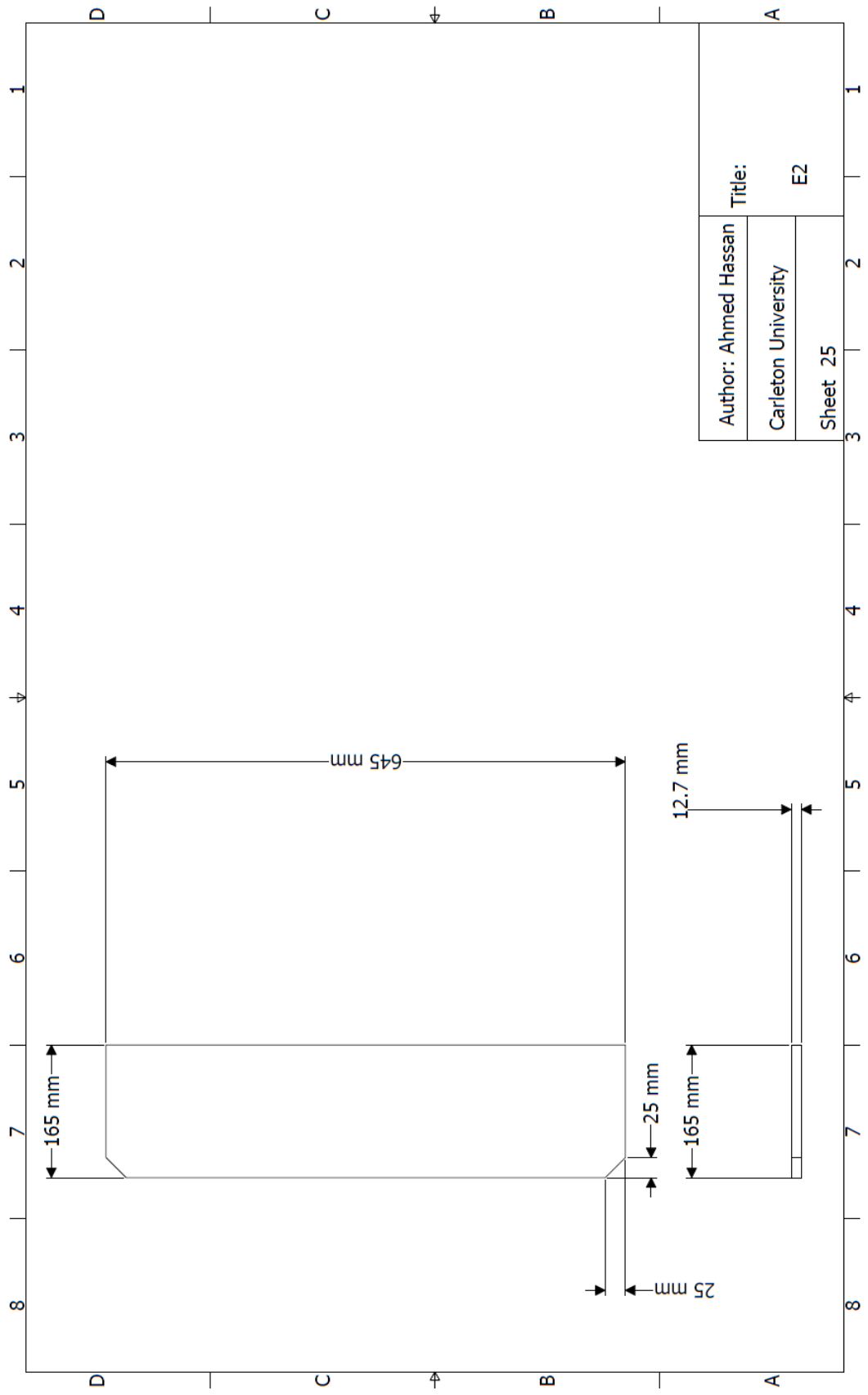
Author: Ahmed Hassan	Title:	
Carleton University	D3	
Sheet 21	2	1



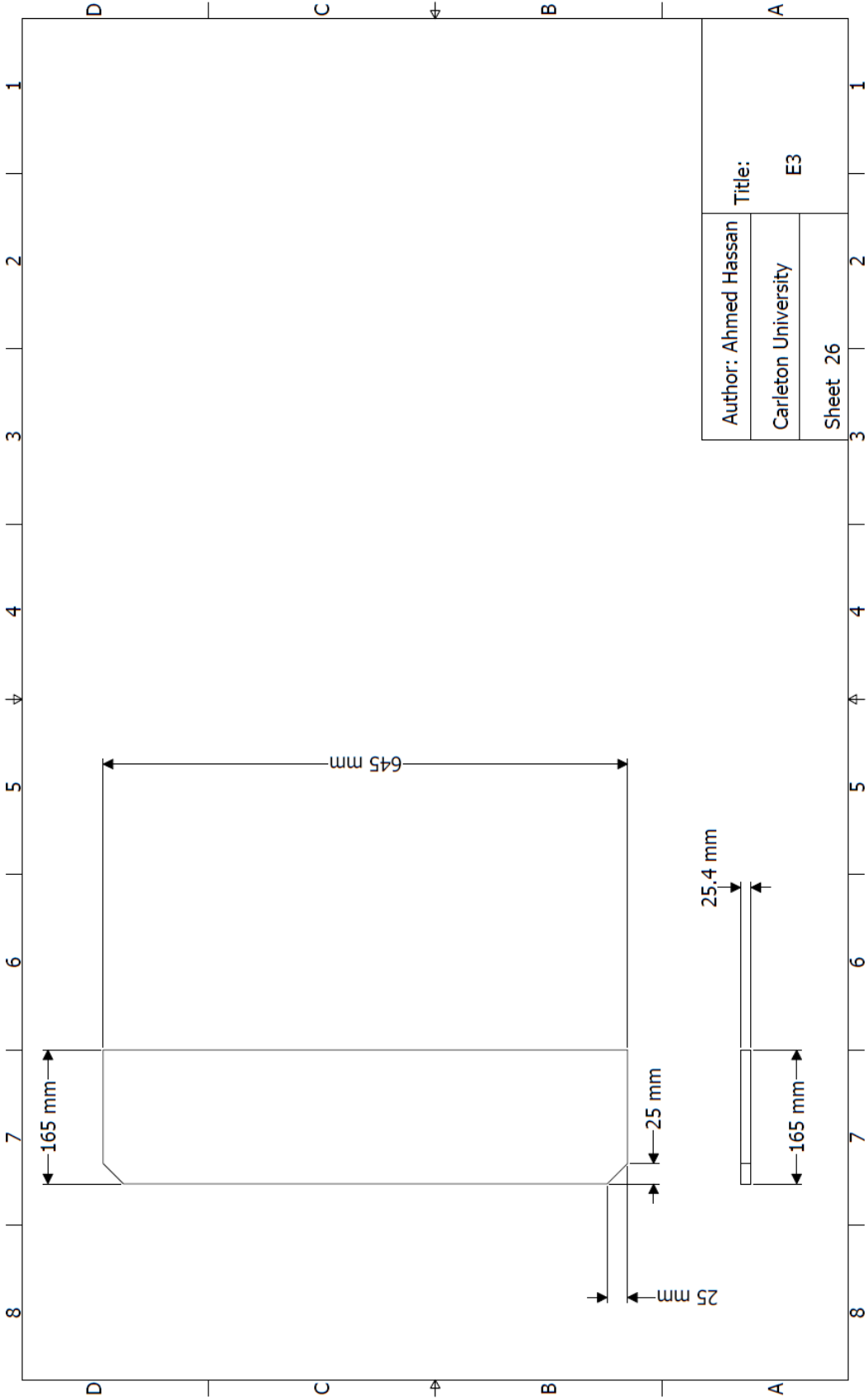


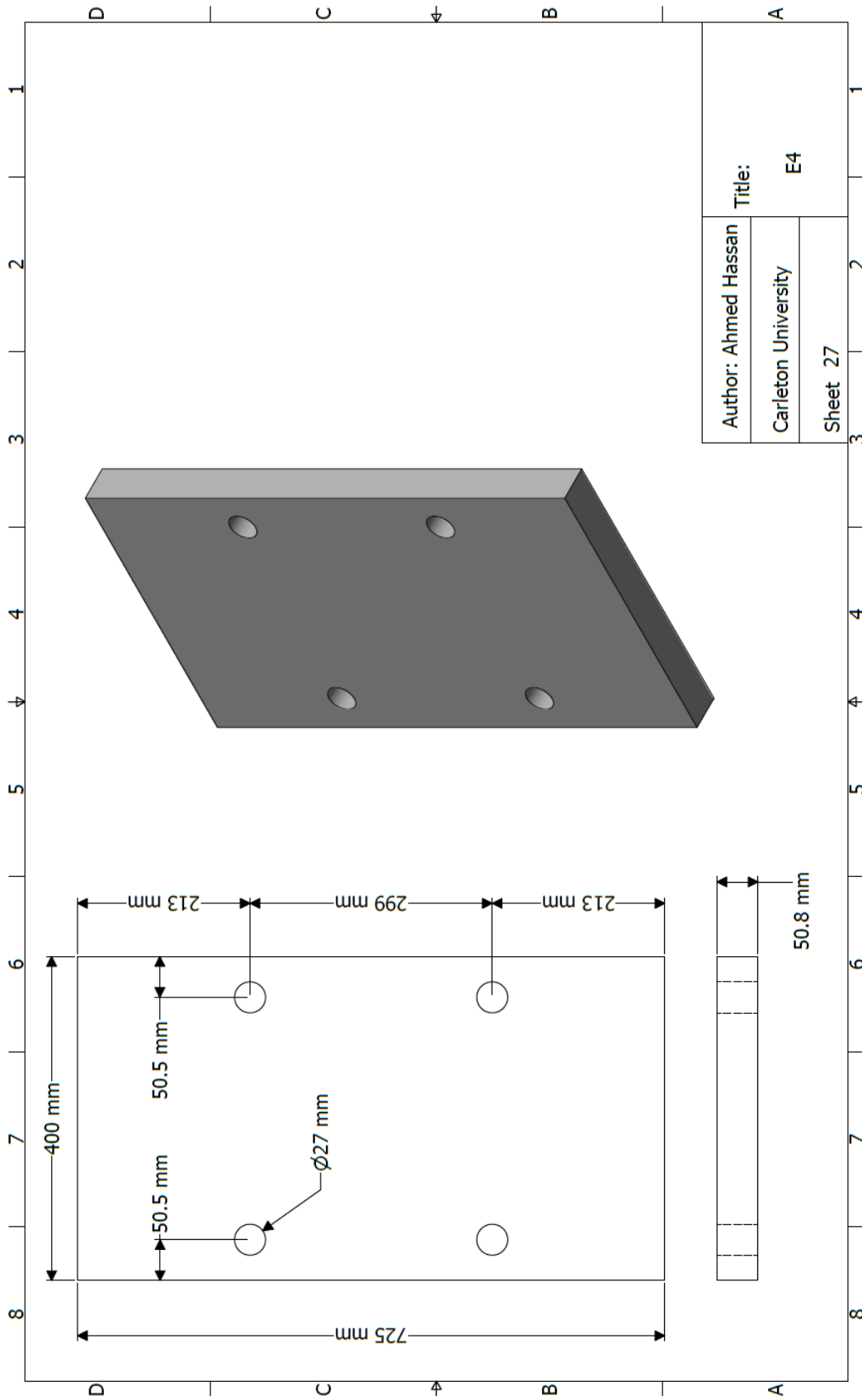
Author: Ahmed Hassan	Title:	
Carleton University	Part E Welds	
Sheet 23	1	2



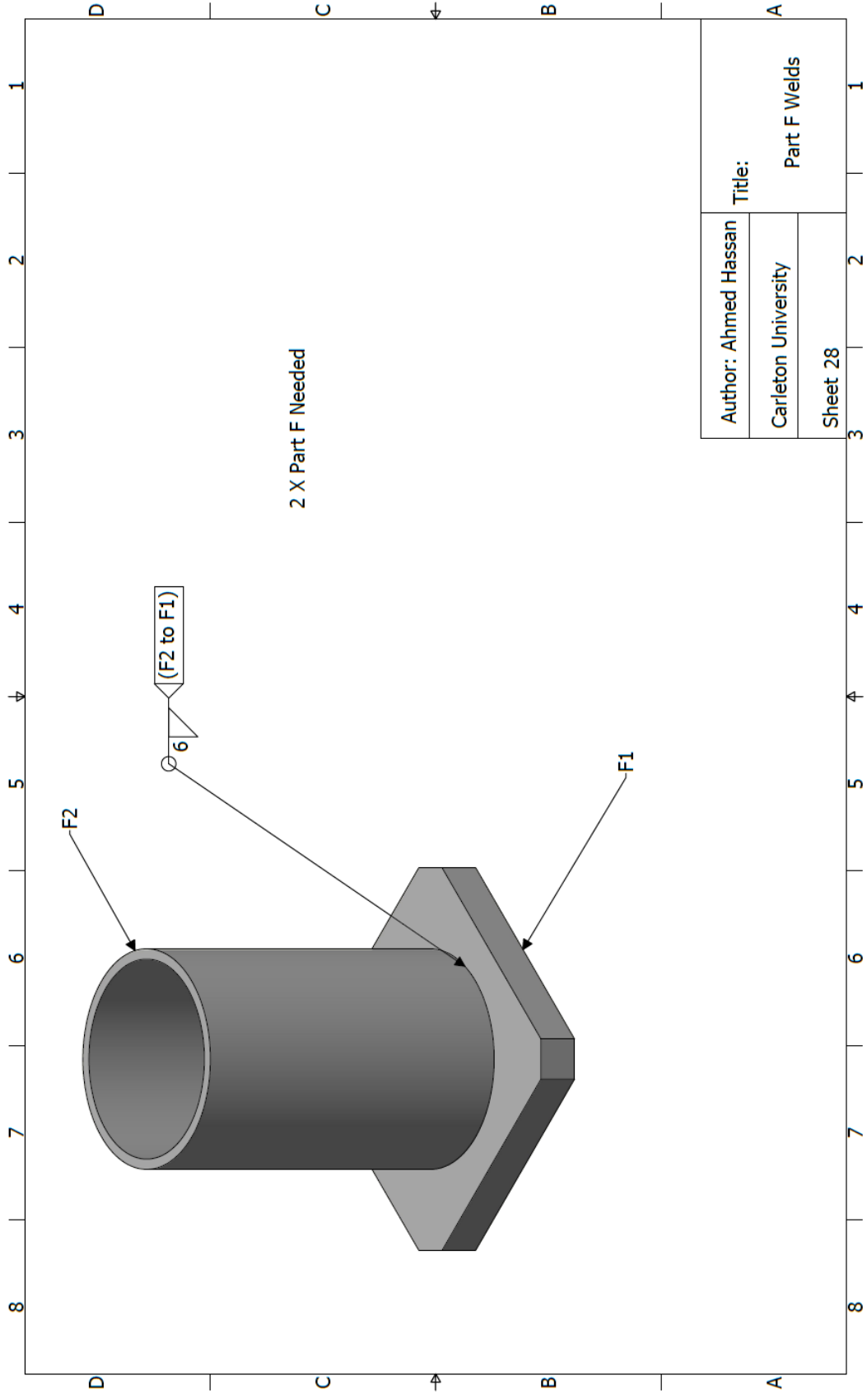


Author: Ahmed Hassan	Title:
Carleton University	E2
Sheet 25	

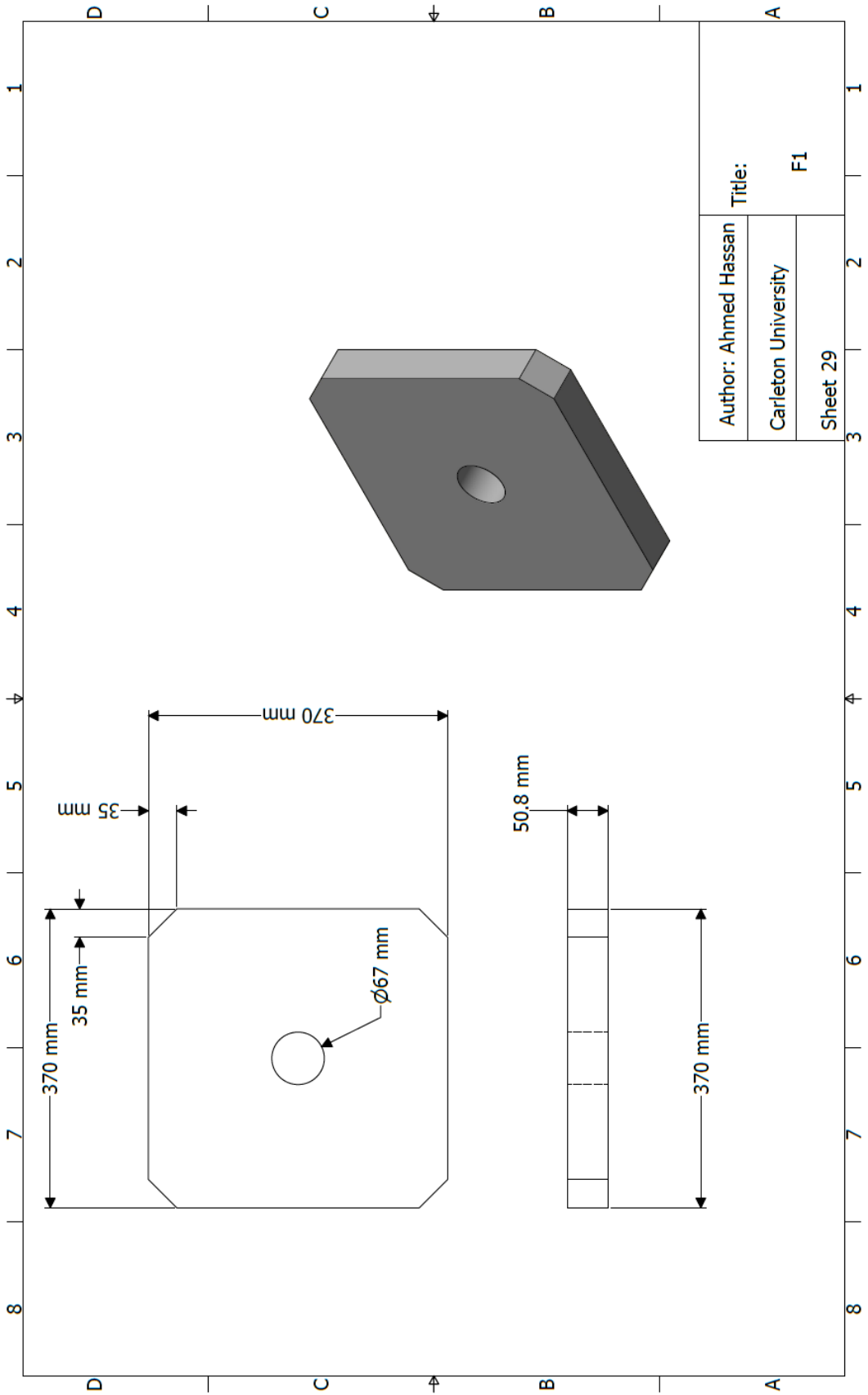


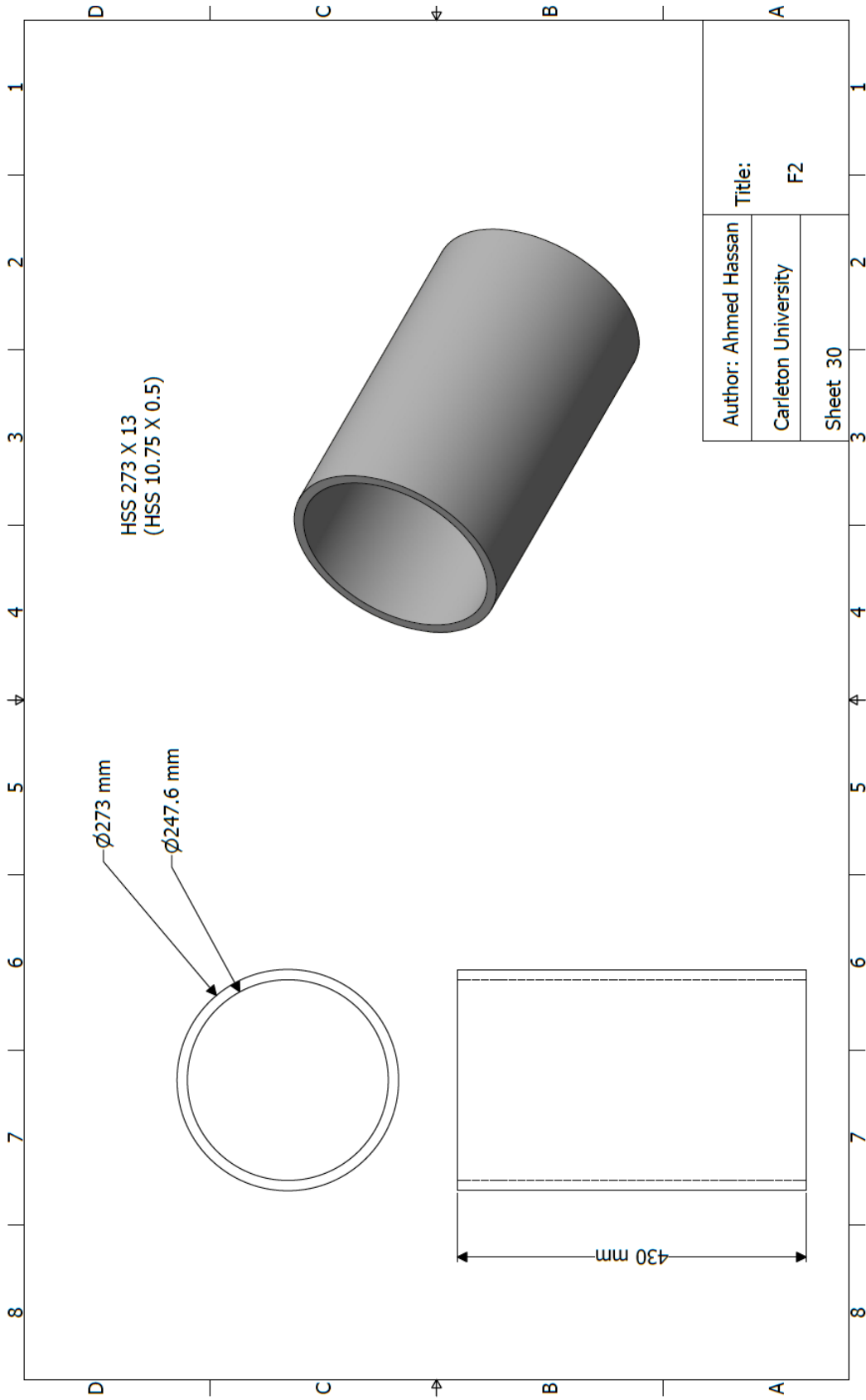


Author: Ahmed Hassan	Title: E4	
Carleton University		
Sheet 27		

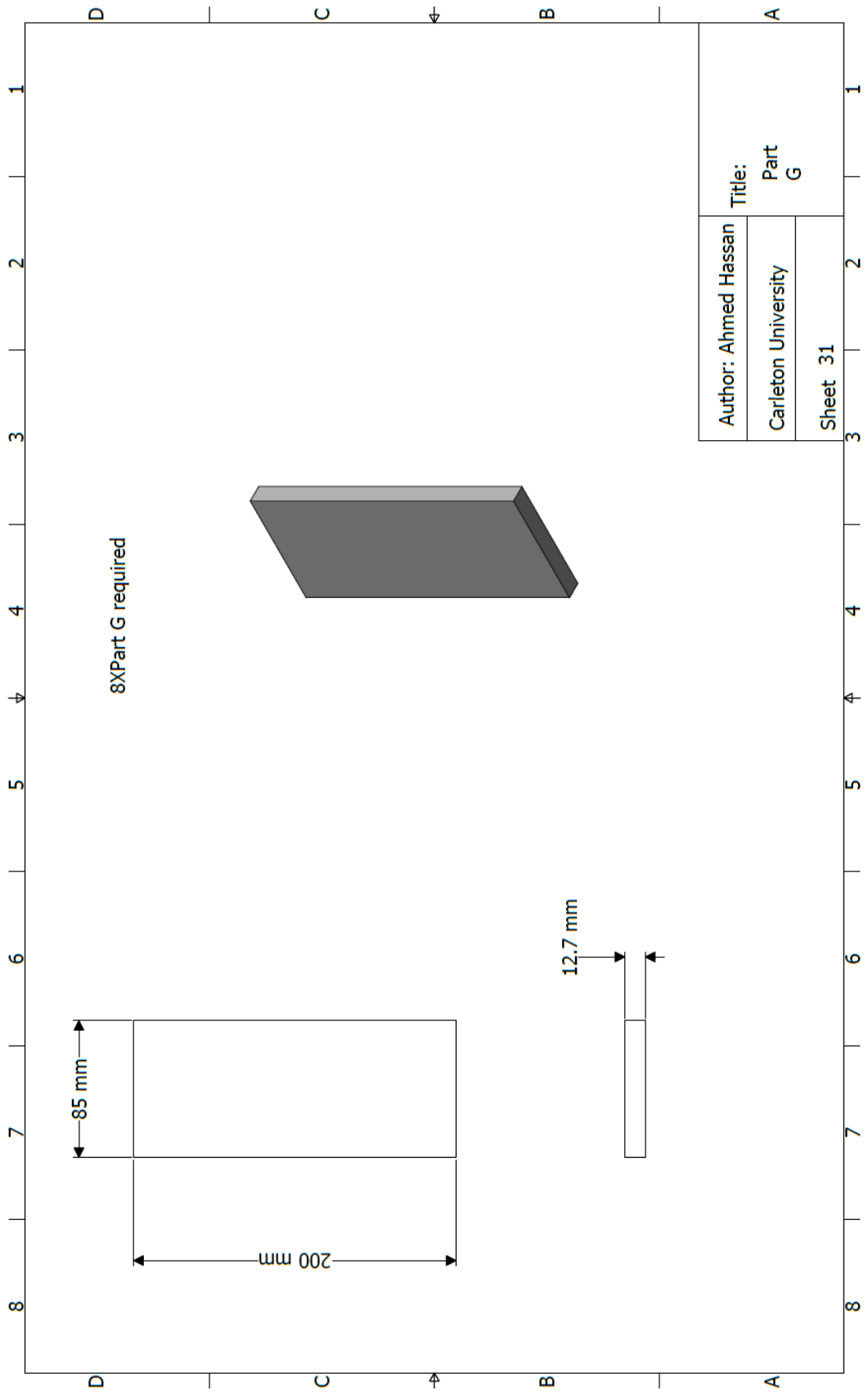


Author: Ahmed Hassan	Title:		A
Carleton University	Part F Welds		1
Sheet 28	2	3	4





Author: Ahmed Hassan	Title:
Carleton University	F2
Sheet 30	





## Appendix B: Design of prototype building for Hybrid simulation and BRB structure

RS- SCED Brace Parameters for Different RS-SCED Brace Sizes							
RS-SCED brace	Ring Type (from RingFeder)	Number of rings	Activation load range (kN)	PC (%)	Initial Stiffness (kN/mm)	Post-activation stiffness (kN/mm)	Ultimate Load capacity (kN)
A	34000	33	430-480	30-33	1407	5.9	1450
B	26901	33	315-420	25-33.6	641	5.1	1250
C	26200	50	215-305	25-35	531	3.6	860
D	19600	55	150-210	25-35	313	2.5	600
E	16600	70	90-140	18-40	138	1.4	350
F	14000	80	44-90	18-35	70.4	1.0	250

**Dynamic properties and Response spectrum analysis for 8 floor  
building designed according to ASCE 7**

<b>Dynamic properties and response Spectrum</b>	
<b>h</b>	32
<b>R</b>	7
<b>S<sub>s</sub></b>	1.5
<b>S<sub>I</sub></b>	0.6
<b>F<sub>a</sub></b>	1
<b>F<sub>v</sub></b>	1.5
<b>S<sub>Ms</sub></b>	1.500
<b>S<sub>M1</sub></b>	0.900
<b>S<sub>Ds</sub></b>	1.000
<b>S<sub>D1</sub></b>	0.600
<b>T<sub>s</sub></b>	0.600
<b>T<sub>L</sub></b>	8
<b>T<sub>max</sub></b>	1.377
<b>S<sub>MT</sub></b>	0.654
<b>C<sub>u</sub></b>	1.4
<b>C<sub>t</sub></b>	0.0731
<b>x</b>	0.75
<b>C<sub>s</sub></b>	0.062
<b>k</b>	1.438

**Equivalent Force Distribution of Earthquake load on the structures**

<b>Level</b>	<b><math>h_x</math> (m)</b>	<b><math>W_x</math> (kN)</b>	<b><math>W_x h_x^k</math> (kN-m)</b>	<b><math>F_x</math> (kN)</b>	<b><math>V_{story}</math> (kN)</b>	<b><math>V_{brace}</math> (kN)</b>
RF	32	5355	783169.2	733.6	0.0	N/A
R7	28	7560	912428.6	854.7	733.6	183
R6	24	7560	730968.5	684.7	1588.4	397
R5	20	7560	562341	526.8	2273.1	568
R4	16	7560	407942.2	382.1	2799.9	700
R3	12	7560	269699.1	252.6	3182.0	796
R2	8	7560	150514.9	141.0	3434.7	859
R1	4	7560	55534.16	52.0	3575.6	894
GR	0	0	0	0	3627.7	907
		<b>Total</b>	<b>3872598</b>	<b>3627.7</b>		

RS-SCED Braced Building									
Floor	Loading			Interior Column	Edge Column	Corner Column	Braced Frame Column	Chevron Brace	RS-SCED Brace
	Dead	Snow	Live						
8	2.8	3.0	--	W200x42	W200x36	W200x36	W310x107	127x127x9.5	E
7	4.8	--	2.4					178x178x8	D
6	4.8	--	2.4	W250x80	W200x42	W200x36	W310x129	203x203x13	C
5	4.8	--	2.4					305x305x9.5	B
4	4.8	--	2.4	W310x107	W250x73	W200x59	W360x216	305x305x9.5	B
3	4.8	--	2.4					305x305x13	A
2	4.8	--	2.4	W310x158	W310x86	W200x59	W360x347	305x305x13	A
1	4.8	--	2.4					305x305x13	A

BRB Building											
Floor	Loading			Interior Column	Edge Column	Corner Column	Braced Frame Column	BRB Core (L=4300m, $\sigma_y=350$ MPa)			
	Dead	Snow	Live					Activation Load (kN)	Area (mm <sup>2</sup> )	Initial Stiffness (kN/mm)	Post-activation Stiffness (kN/mm)
8	2.8	3.0	--	W200x42	W200x36	W200x36	W310x107	183	524	24.4	0.49
7	4.8	--	2.4					397	1135	52.8	1.06
6	4.8	--	2.4	W250x80	W200x42	W200x36	W310x129	568	1624	75.5	1.51
5	4.8	--	2.4					700	2000	93.0	1.86
4	4.8	--	2.4	W310x107	W250x73	W200x59	W360x216	796	2273	106	2.12
3	4.8	--	2.4					859	2453	114	2.28
2	4.8	--	2.4	W310x158	W310x86	W200x59	W360x347	894	2554	119	2.38
1	4.8	--	2.4					907	2591	121	2.42

## Appendix C: Seismic Analysis and design for FEMA P695 Archetype structures

	A	B	C	D	E	F
1		$S_T$ (g)				
2	T(sec)	Category C	Category D			
3	$S_s$	0.55	1.5		h	48
4	$S_1$	0.132	0.6		R	7
5	$F_a$	1.36	1			
6	$F_v$	2.28	1.5			
7	$S_{Ms}$	0.748	1.500	$S_{Ds}$	0.499	1.000
8	$S_{M1}$	0.301	0.900	$S_{D1}$	0.201	0.600
9	$T_s$	0.402	0.600			
10	$T_L$	6	8			
11	$T_{max}$	2.000	1.866			
12	$S_{MT}$	0.151	0.482			
13	$C_u$	1.5	1.4			
14	$C_t$	0.0731	0.0731			
15	x	0.75	0.75			
16	$C_s$	0.014	0.046			
17	k	1.750	1.683			

Seismic Analysis of Archetype 1 and 7

	A	B	C	D	E	F
1		$S_T$ (g)				
2	T(sec)	Category C	Category D			
3	$S_s$	0.55	1.5		h	32
4	$S_1$	0.132	0.6		R	7
5	$F_a$	1.36	1			
6	$F_v$	2.28	1.5			
7	$S_{Ms}$	0.748	1.500	$S_{Ds}$	0.499	1.000
8	$S_{M1}$	0.301	0.900	$S_{D1}$	0.201	0.600
9	$T_s$	0.402	0.600			
10	$T_L$	6	8			
11	$T_{max}$	1.475	1.377			
12	$S_{MT}$	0.204	0.654			
13	$C_u$	1.5	1.4			
14	$C_t$	0.0731	0.0731			
15	x	0.75	0.75			
16	$C_s$	0.019	0.062			
17	k	1.488	1.438			

Seismic Analysis of Archetype 2 and 8

	A	B	C	D	E	F
1		$S_T$ (g)				
2	T(sec)	Category C	Category D			
3	$S_s$	0.55	1.5		h	16
4	$S_1$	0.132	0.6		R	7
5	$F_a$	1.36	1			
6	$F_v$	2.28	1.5			
7	$S_{Ms}$	0.748	1.500	$S_{Ds}$	0.499	1.000
8	$S_{M1}$	0.301	0.900	$S_{D1}$	0.201	0.600
9	$T_s$	0.402	0.600			
10	$T_L$	6	8			
11	$T_{max}$	0.877	0.819			
12	$S_{MT}$	0.343	1.099			
13	$C_u$	1.5	1.4			
14	$C_t$	0.0731	0.0731			
15	x	0.75	0.75			
16	$C_s$	0.033	0.105			
17	k	1.189	1.159			

**Seismic Analysis of Archetypes 3 and 9**

	A	B	C	D	E	F
1		$S_T$ (g)				
2	T(sec)	Category C	Category D			
3	$S_s$	0.55	1.5		h	8
4	$S_1$	0.132	0.6		R	7
5	$F_a$	1.36	1			
6	$F_v$	2.28	1.5			
7	$S_{Ms}$	0.748	1.500	$S_{Ds}$	0.499	1.000
8	$S_{M1}$	0.301	0.900	$S_{D1}$	0.201	0.600
9	$T_s$	0.402	0.600			
10	$T_L$	6	8			
11	$T_{max}$	0.522	0.487			
12	$S_{MT}$	0.577	1.849			
13	$C_u$	1.5	1.4			
14	$C_t$	0.0731	0.0731			
15	x	0.75	0.75			
16	$C_s$	0.055	0.176			
17	k	1.011	1.000			

Seismic Analysis of Archetypes 4-6 and 10-12

RS- SCED Brace Parameters							
RS-SCED brace	Ring Type (from RingFeder)	Number of rings	Activation load range (kN)	PC (%)	Initial Stiffness (kN/mm)	Post-activation stiffness (kN/mm)	Ultimate Load capacity (kN)
A	34000	33	430-480	30-33	1407	5.9	1450
B	26901	33	315-420	25-33.6	641	5.1	1250
C	26200	50	215-305	25-35	531	3.6	860
D	19600	55	150-210	25-35	313	2.5	600
E	16600	70	90-140	18-40	138	1.4	350
F	14000	80	44-90	18-35	70.4	1.0	250

Archetype 1									
Floor	Loading			Interior Column	Edge Column	Corner Column	Braced Frame Column	Chevron Brace	RS-SCED Brace
	Dead	Snow	Live						
12	2.8	3.0	--					178x178x8	D
11	4.8	--	2.4	W200x71	W200x52	W200x46	W360x79	178x178x8	D
10	4.8	--	2.4					203x203x13	C
9	4.8	--	2.4	W200x100	W200x71	W200x52	W360x162	305x305x9.5	B
8	4.8	--	2.4					305x305x9.5	B
7	4.8	--	2.4	W250x167	W200x100	W200x71	W360x216	305x305x9.5	B
6	4.8	--	2.4					305x305x13	A
5	4.8	--	2.4	W310x179	W250x101	W200x86	W360x347	305x305x13	A
4	4.8	--	2.4					305x305x13	A
3	4.8	--	2.4	W310x202	W250x131	W200x100	W360x509	305x305x13	A
2	4.8	--	2.4					305x305x13	A
1	4.8	--	2.4	W360x314	W250x167	W250x101	W360x744	305x305x13	A

	A	B	C	D	E	F	G	H	I	J	K	L	M	N	O	P
1	<b>Archetype 1</b>															
2	Level	$h_x$	$W_x$	$W_x h_x^k$	$F_x$	$V_{story}$	$V_{brace}$	Brace	$S_t$	$K_1$	$K_2$	$F_{max}$	$P_{col}$	Column	$F_a$	$A_{Chev}$
3		(m)	(kN)	(kN-m)	(kN)	(kN)	(kN)	Type	(mm)	(kN/mm)	(kN/mm)	(kN)	(kN)	Size	(kN)	(mm <sup>2</sup> )
4	RF	48	5355	3618447	613.7	0.0	N/A	N/A	N/A	N/A	N/A	N/A	N/A	N/A	N/A	N/A
5	R13	44	7560	4412463	748.4	613.7	153.42	D	209	313	2.50	600	578.1		76.7	5240
6	R10	40	7560	3758473	637.4	1362.1	340.52	D	172	313	2.50	600	1244.4	W360X79	170.3	5240
7	R9	36	7560	3147714	533.9	1999.5	499.88	C	169	531	3.60	860	2463.3		249.9	9260
8	R8	32	7560	2581656	437.9	2533.4	633.34	B	183	641	5.10	1250	3745.1	W360X162	316.7	11000
9	R7	28	7560	2062006	349.7	2971.2	742.81	B	172	641	5.10	1250	5556.4		371.4	11000
10	R6	24	7560	1590777	269.8	3321.0	830.24	B	164	641	5.10	1250	7408.9	W360X216	415.1	11000
11	R5	20	7560	1170405	198.5	3590.8	897.69	A	170	1407	5.90	1450	9765.1		448.8	14400
12	R4	16	7560	803939	136.4	3789.3	947.32	A	165	1407	5.90	1450	12144.7	W360X347	473.7	14400
13	R1	12	7560	495374.7	84.0	3925.6	981.40	A	163	1407	5.90	1450	15008.8		490.7	14400
14	R1	8	7560	250350.1	42.5	4009.6	1002.41	A	161	1407	5.90	1450	17882.7	W360X509	501.2	14400
15	R1	4	7560	77960.11	13.2	4052.1	1013.02	A	160	1407	5.90	1450	21227.8		506.5	14400
16	GR	0	0	0	0	4065.3	1016.33	A	160	1407	5.90	1450	24574.4	W360X744	508.2	14400
17			Total	23969565	4065.3											
18																
19																
20									Number of bays in X		5					
21									Number of bays in Y		5					
22									Total number of bays		25					
23									Total Area (m <sup>2</sup> )		1575					
24									V		4065					
25									K		1.683139009					

Archetype 2									
Floor	Loading			Interior Column	Edge Column	Corner Column	Braced Frame Column	Chevron Brace	RS-SCED Brace
	Dead	Snow	Live						
8	2.8	3.0	--					127x127x9.5	E
7	4.8	--	2.4	W200x42	W200x36	W200x36	W310x67	178x178x8	D
6	4.8	--	2.4					203x203x13	C
5	4.8	--	2.4	W250x80	W200x42	W200x36	W310x129	305x305x9.5	B
4	4.8	--	2.4					305x305x9.5	B
3	4.8	--	2.4	W310x107	W250x73	W200x59	W360x216	305x305x13	A
2	4.8	--	2.4					305x305x13	A
1	4.8	--	2.4	W310x158	W310x86	W200x59	W360x347	305x305x13	A

	A	B	C	D	E	F	G	H	I	J	K	L	M	N	O	P
1	Archetype 2															
2	Level	$h_x$	$W_x$	$W_x h_x^k$	$F_x$	$V_{story}$	$V_{brace}$	Brace	$S_t$	$K_1$	$K_2$	$F_{max}$	$P_{col}$	Column	$F_a$	$A_{Chev}$
3		(m)	(kN)	(kN-m)	(kN)	(kN)	(kN)	Type	(mm)	(kN/mm)	(kN/mm)	(kN)	(kN)	Size	(kN)	(mm <sup>2</sup> )
4	RF	32	5355	783169.2	733.6	0.0	N/A	N/A	N/A	N/A	N/A	N/A	N/A	N/A	N/A	N/A
5	R7	28	7560	912428.6	854.7	733.6	183	E	184	138	1.40	350	592		92	4240
6	R6	24	7560	730968.5	684.7	1588.4	397	D	161	313	2.50	600	1285	W310X67	199	5240
7	R5	20	7560	562341	526.8	2273.1	568	C	160	531	3.60	860	2536		284	9260
8	R4	16	7560	407942.2	382.1	2799.9	700	B	176	641	5.10	1250	3850	W310X129	350	11000
9	R3	12	7560	269699.1	252.6	3182.0	796	B	167	641	5.10	1250	5686		398	11000
10	R2	8	7560	150514.9	141.0	3434.7	859	A	173	1407	5.90	1450	7551	W360X216	429	14400
11	R1	4	7560	55534.16	52.0	3575.6	894	A	170	1407	5.90	1450	9906		447	14400
12	GR	0	0	0	0	3627.7	907	A	169	1407	5.90	1450	12266	W360X347	453	14400
13			Total	3872598	3627.7											
14																
15																
16									Number of bays in X	5						
17									Number of bays in Y	5						
18									Total number of bays	25						
19									Total Area (m <sup>2</sup> )	1575						
20									V	3628						
21									K	1.438458713						

Archetype 3									
Floor	Loading			Interior Column	Edge Column	Corner Column	Braced Frame Column	Chevron Brace	RS-SCED Brace
	Dead	Snow	Live						
4	2.8	3.0	--					127x127x9.5	E
3	4.8	--	2.4	W200x42	W200x36	W200x36	W310x67	203x203x13	C
2	4.8	--	4.8					305x305x9.5	B
1	4.8	--	4.8	W250x89	W200x59	W200x52	W360x162	305x305x9.5	B

	A	B	C	D	E	F	G	H	I	J	K	L	M	N	O	P
1	Archetype 3															
2	Level	$h_x$	$W_x$	$W_x h_x^k$	$F_x$	$V_{story}$	$V_{brace}$	Brace	$S_t$	$K_1$	$K_2$	$F_{max}$	$P_{col}$	Column	$F_a$	$A_{Chev}$
3		(m)	(kN)	(kN-m)	(kN)	(kN)	(kN)	Type	(mm)	(kN/mm)	(kN/mm)	(kN)	(kN)	Size	(kN)	(mm <sup>2</sup> )
4	RF	16	5355	133280.9	1055.7	0.0	N/A	N/A	N/A	N/A	N/A	N/A	N/A	N/A	N/A	N/A
5	R13	12	7560	134797.4	1067.7	1055.7	263.92	E	155.74	138	1.40	350	630		132	4240
6	RT2	8	9450	105302.4	834.1	2123.3	530.83	C	165.16	531	3.60	860	1386	W310X67	265	9260
7	RT1	4	9450	47145.05	373.4	2957.4	739.35	B	172.61	641	5.10	1250	3057		370	11000
8	GR	0	0	0	0	3330.8	832.70	B	163.4606	641	5.10	1250	4772	W360X162	416	11000
9			Total	420525.7	3330.8											
10																
11																
12																
13																
14																
15																
16																
17																

Number of bays in X	5
Number of bays in Y	5
Total number of bays	25
Total Area (m <sup>2</sup> )	1575
V	3331
K	1.15936

Archetype 4									
Floor	Loading			Interior Column	Edge Column	Corner Column	Braced Frame Column	Chevron Brace	RS-SCED Brace
	Dead	Snow	Live						
2	2.8	3.0	--					178x178x8	D
1	4.8	--	4.8	W200x59	W200x42	W200x42	W360x91	305x305x9.5	B

	A	B	C	D	E	F	G	H	I	J	K	L	M	N	O	P
1	Archetype 4															
2	Level	$h_x$	$W_x$	$W_x h_x^k$	$F_x$	$V_{story}$	$V_{brace}$	Brace	$S_t$	$K_1$	$K_2$	$F_{max}$	$P_{col}$	Column	$F_a$	$A_{Chev}$
3		(m)	(kN)	(kN-m)	(kN)	(kN)	(kN)	Type	(mm)	(kN/mm)	(kN/mm)	(kN)	(kN)	Size	(kN)	(mm <sup>2</sup> )
4	RF	8	5355	42840	1384.8	0.0	N/A	N/A	N/A	N/A	N/A	N/A	N/A	N/A	N/A	N/A
5	RT1	4	9450	37800	1221.9	1384.8	346	D	171	313	2.50	600	784		173	5240
6	GR	0	0	0	0	2606.7	652	B	181	641	5.10	1250	1711	W360X91	326	11000
7			Total	80640	2606.7											
8																
9																
10								Number of bays in X	5							
11								Number of bays in Y	5							
12								Total number of bays	25							
13								Total Area (m <sup>2</sup> )	1575							
14								V	2607							
15								K	1							

Archetype 5									
Floor	Loading			Interior Column	Edge Column	Corner Column	Braced Frame Column	Chevron Brace	RS-SCED Brace
	Dead	Snow	Live						
2	2.8	3.0	--					203x203x13	C
1	4.8	--	4.8	W200x59	W200x42	W200x42	W360x91	305x305x9.5	B

	A	B	C	D	E	F	G	H	I	J	K	L	M	N	O	P
1	Archetype 5															
2	Level	$h_x$	$W_x$	$W_x h_x^k$	$F_x$	$V_{story}$	$V_{brace}$	Brace	$S_t$	$K_1$	$K_2$	$F_{max}$	$P_{col}$	Column	$F_a$	$A_{Chev}$
3		(m)	(kN)	(kN-m)	(kN)	(kN)	(kN)	Type	(mm)	(kN/mm)	(kN/mm)	(kN)	(kN)	Size	(kN)	(mm <sup>2</sup> )
4	RF	8	3213	25704	830.9	0.0	N/A	N/A	N/A	N/A	N/A	N/A	N/A	N/A	N/A	N/A
5	RT1	4	5670	22680	733.1	830.9	415	C	181	531	3.60	860	816		208	9260
6	GR	0	0	0	0	1564.0	782	B	168	641	5.10	1250	1805	W360X91	391	11000
7			Total	48384	1564.0											
8																
9																
10									Number of bays in X	5						
11									Number of bays in Y	3						
12									Total number of bays	15						
13									Total Area (m <sup>2</sup> )	945						
14									V	1564						
15									K	1						

Archetype 6									
Floor	Loading			Interior Column	Edge Column	Corner Column	Braced Frame Column	Chevron Brace	RS-SCED Brace
	Dead	Snow	Live						
2	2.8	3.0	--					127x127x9.5	E
1	4.8	--	4.8	W200x59	W200x42	W200x42	W360x79	203x203x13	C

	A	B	C	D	E	F	G	H	I	J	K	L	M	N	O	P
1	Archetype 6															
2	Level	$h_x$	$W_x$	$W_x h_x^k$	$F_x$	$V_{story}$	$V_{brace}$	Brace	$S_t$	$K_1$	$K_2$	$F_{max}$	$P_{col}$	Column	$F_a$	$A_{Chev}$
3		(m)	(kN)	(kN-m)	(kN)	(kN)	(kN)	Type	(mm)	(kN/mm)	(kN/mm)	(kN)	(kN)	Size	(kN)	(mm <sup>2</sup> )
4	RF	8	1928	15422.4	498.5	0.0	N/A	N/A	N/A	N/A	N/A	N/A	N/A	N/A	N/A	N/A
5	RT1	4	3402	13608	439.9	498.5	249	E	161	138	1.40	350	738		125	4240
6	GR	0	0	0	0	938.4	469	C	174	531	3.60	860	1580	W360X79	235	9260
7			Total	29030.4	938.4											
8																
9																
10								Number of bays in X		3						
11								Number of bays in Y		3						
12								Total number of bays		9						
13								Total Area (m <sup>2</sup> )		567						
14								V		938						
15								K		1						

Archetype 7									
Floor	Loading			Interior Column	Edge Column	Corner Column	Braced Frame Column	Chevron Brace	RS-SCED Brace
	Dead	Snow	Live						
12	2.8	3.0	--					127x127x8	F
11	4.8	--	2.4	W200x71	W200x52	W200x46	W310x67	127x127x8	F
10	4.8	--	2.4					127x127x8	F
9	4.8	--	2.4	W200x100	W200x71	W200x52	W360x122	127x127x9.5	E
8	4.8	--	2.4					127x127x9.5	E
7	4.8	--	2.4	W250x167	W200x100	W200x71	W360x196	127x127x9.5	E
6	4.8	--	2.4					178x178x8	D
5	4.8	--	2.4	W310x179	W250x101	W200x86	W360x314	178x178x8	D
4	4.8	--	2.4					178x178x8	D
3	4.8	--	2.4	W310x202	W250x131	W200x100	W360x463	178x178x8	D
2	4.8	--	2.4					178x178x8	D
1	4.8	--	2.4	W360x314	W250x167	W250x101	W360x592	178x178x8	D

	A	B	C	D	E	F	G	H	I	J	K	L	M	N	O	P
1	<b>Archetype 7</b>															
2	Level	$h_x$ (m)	$W_x$ (kN)	$W_x h_x^k$ (kN-m)	$F_x$ (kN)	$V_{story}$ (kN)	$V_{brace}$ (kN)	Brace Type	$S_t$ (mm)	$K_1$ (kN/mm)	$K_2$ (kN/mm)	$F_{max}$ (kN)	$P_{col}$ (kN)	Column Size	$F_a$ (kN)	$A_{Chev}$ (mm <sup>2</sup> )
3																
4	RF	48	5355	4683619	203.8	0.0	N/A	N/A	N/A	N/A	N/A	N/A	N/A	N/A	N/A	N/A
5	R13	44	7560	5678345	247.1	203.8	51	F	225	70	1.00	250	530		25.5	3620
6	R10	40	7560	4806105	209.1	450.9	113	F	194	70	1.00	250	1089	W310X67	56.4	3620
7	R9	36	7560	3996936	173.9	660.0	165	F	168	70	1.00	250	2150		82.5	3620
8	R8	32	7560	3252527	141.5	833.9	208	E	176	138	1.40	350	3232	W360X122	104.2	4240
9	R7	28	7560	2574821	112.0	975.4	244	E	163	138	1.40	350	4808		121.9	4240
10	R6	24	7560	1966093	85.5	1087.5	272	E	153	138	1.40	350	6397	W360X196	135.9	4240
11	R5	20	7560	1429070	62.2	1173.0	293	D	181	313	2.50	600	8468		146.6	5240
12	R4	16	7560	967121.6	42.1	1235.2	309	D	178	313	2.50	600	10547	W360X314	154.4	5240
13	R3	12	7560	584607.4	25.4	1277.3	319	D	176	313	2.50	600	13099		159.7	5240
14	R1	8	9450	359460.6	15.6	1302.7	326	D	175	313	2.50	600	15654	W360X463	162.8	5240
15	R1	4	9450	106883.7	4.7	1318.3	330	D	174	313	2.50	600	18678		164.8	5240
16	GR	0	0	0	0	1323.0	331	D	174	313	2.50	600	21701	W360X592	165.4	5240
17			Total	30405589	1323.0											
18																
19																
20									Number of bays in X	5						
21									Number of bays in Y	5						
22									Total number of bays	25						
23									Total Area (m <sup>2</sup> )	1575						
24									V	1323						
25									K	1.749792						

Archetype 8									
Floor	Loading			Interior Column	Edge Column	Corner Column	Braced Frame Column	Chevron Brace	RS-SCED Brace
	Dead	Snow	Live						
8	2.8	3.0	--					127x127x8	F
7	4.8	--	2.4	W200x42	W200x36	W200x36	W310x67	178x178x8	D
6	4.8	--	2.4					203x203x13	C
5	4.8	--	2.4	W250x80	W200x42	W200x36	W310x122	203x203x13	C
4	4.8	--	2.4					203x203x13	C
3	4.8	--	2.4	W310x107	W250x73	W200x59	W360x287	305x305x9.5	B
2	4.8	--	2.4					305x305x9.5	B
1	4.8	--	2.4	W310x158	W310x86	W200x59	W360x463	305x305x9.5	B

	A	B	C	D	E	F	G	H	I	J	K	L	M	N	O	P
1	Archetype 8															
2	Level	$h_x$	$W_x$	$W_x h_x^k$	$F_x$	$V_{story}$	$V_{brace}$	Brace	$S_t$	$K_1$	$K_2$	$F_{max}$	$P_{col}$	Column	$F_a$	$A_{Chev}$
3		(m)	(kN)	(kN-m)	(kN)	(kN)	(kN)	Type	(mm)	(kN/mm)	(kN/mm)	(kN)	(kN)	Size	(kN)	(mm <sup>2</sup> )
4	RF	32	5355	928693.2	233.2	0.0	N/A	N/A	N/A	N/A	N/A	N/A	N/A	N/A	N/A	N/A
5	R7	28	7560	1074889	270.0	233.2	58	F	221	70	1.00	250	533		29	3620
6	R6	24	7560	854616.8	214.6	503.2	126	D	215	313	2.50	600	1098	W310X67	63	5240
7	R5	20	7560	651596.4	163.6	717.8	179	C	214	531	3.60	860	2166		90	9260
8	R4	16	7560	467532.7	117.4	881.5	220	C	208	531	3.60	860	3254	W360X122	110	9260
9	R3	12	7560	304753.6	76.5	998.9	250	C	204	531	3.60	860	4833		125	9260
10	R2	8	7560	166720.7	41.9	1075.4	269	B	219	641	5.10	1250	6420	W360X287	134	11000
11	R1	4	7560	59452.06	14.9	1117.3	279	B	218	641	5.10	1250	8485		140	11000
12	GR	0	0	0	0	1132.2	283	B	217	641	5.10	1250	10552	W360X463	142	11000
13			Total	4508255	1132.2											
14																
15																
16								Number of bays in X		5						
17								Number of bays in Y		5						
18								Total number of bays		25						
19								Total Area (m <sup>2</sup> )		1575						
20								V		1132						
21								K		1.487634						

Archetype 9									
Floor	Loading			Interior Column	Edge Column	Corner Column	Braced Frame Column	Chevron Brace	RS-SCED Brace
	Dead	Snow	Live						
4	2.8	3.0	--	W200x42	W200x36	W200x36	W310x67	127x127x9.5	E
3	4.8	--	2.4						
2	4.8	--	4.8	W250x89	W200x59	W200x52	W310x143	203x203x13	C
1	4.8	--	4.8						

	A	B	C	D	E	F	G	H	I	J	K	L	M	N	O	P
1	Archetype 9															
2	Level	$h_x$	$W_x$	$W_x h_x^k$	$F_x$	$V_{story}$	$V_{brace}$	Brace	$S_t$	$K_1$	$K_2$	$F_{max}$	$P_{col}$	Column	$F_a$	$A_{Chev}$
3		(m)	(kN)	(kN-m)	(kN)	(kN)	(kN)	Type	(mm)	(kN/mm)	(kN/mm)	(kN)	(kN)	Size	(kN)	(mm <sup>2</sup> )
4	RF	16	5355	144536.2	333.5	0.0	N/A	N/A	N/A	N/A	N/A	N/A	N/A	N/A	N/A	N/A
5	R13	12	7560	144956.1	334.5	333.5	83.38	E	220	138	1.40	350	545		42	4240
6	RT2	8	9450	111903.7	258.2	668.0	167.01	D	207	313	2.50	600	1130	W310X67	84	5240
7	RT1	4	9450	49095.34	113.3	926.3	231.57	C	207	531	3.60	860	2561		116	9260
8	GR	0	0	0	0	1039.6	259.89	B	220	641	5.10	1250	4006	W310X143	130	11000
9			Total	450491.4	1039.6											
10																
11																
12																
13																
14																
15																
16																
17																

Number of bays in X	5
Number of bays in Y	5
Total number of bays	25
Total Area (m <sup>2</sup> )	1575
V	1040
K	1.1886

Archetype 10									
Floor	Loading			Interior Column	Edge Column	Corner Column	Braced Frame Column	Chevron Brace	RS-SCED Brace
	Dead	Snow	Live						
2	2.8	3.0	--	W200x59	W200x42	W200x42	W360x79	127x127x9.5	E
1	4.8	--	4.8						

	A	B	C	D	E	F	G	H	I	J	K	L	M	N	O	P
1	Archetype 10															
2	Level	$h_x$	$W_x$	$W_x h_x^k$	$F_x$	$V_{story}$	$V_{brace}$	Brace	$S_t$	$K_1$	$K_2$	$F_{max}$	$P_{col}$	Column	$F_a$	$A_{Chev}$
3		(m)	(kN)	(kN-m)	(kN)	(kN)	(kN)	Type	(mm)	(kN/mm)	(kN/mm)	(kN)	(kN)	Size	(kN)	(mm <sup>2</sup> )
4	RF	8	5355	43812.36	433.7	0.0	N/A	N/A	N/A	N/A	N/A	N/A	N/A	N/A	N/A	N/A
5	RT1	4	9450	38369.83	379.9	433.7	108.43	E	211	138	1.40	350	672		54	4240
6	GR	0	0	0	0	813.6	203.40	C	211	531	3.60	860	1388	W360X79	102	9260
7			Total	82182.19	813.6											
8																
9																
10							Number of bays in X		5							
11							Number of bays in Y		5							
12							Total number of bays		25							
13							Total Area (m <sup>2</sup> )		1575							
14							V		814							
15							K		1.010793							

Archetype 11									
Floor	Loading			Interior Column	Edge Column	Corner Column	Braced Frame Column	Chevron Brace	RS-SCED Brace
	Dead	Snow	Live						
2	2.8	3.0	--	W200x59	W200x42	W200x42	W360x79	178x178x8	D
1	4.8	--	4.8						

	A	B	C	D	E	F	G	H	I	J	K	L	M	N	O	P
1	Archetype 11															
2	Level	$h_x$	$W_x$	$W_x h_x^k$	$F_x$	$V_{story}$	$V_{brace}$	Brace	$S_t$	$K_1$	$K_2$	$F_{max}$	$P_{col}$	Column	$F_a$	$A_{Chev}$
3		(m)	(kN)	(kN-m)	(kN)	(kN)	(kN)	Type	(mm)	(kN/mm)	(kN/mm)	(kN)	(kN)	Size	(kN)	(mm <sup>2</sup> )
4	RF	8	3213	26287.41	260.2	0.0	N/A	N/A	N/A	N/A	N/A	N/A	N/A	N/A	N/A	N/A
5	RT1	4	5670	23021.9	227.9	260.2	130	D	214	313	2.50	600	682		65	5240
6	GR	0	0	0	0	488.1	244	C	205	531	3.60	860	1417	W360X79	122	9260
7			Total	49309.31	488.1											
8																
9																
10									Number of bays in X	5						
11									Number of bays in Y	3						
12									Total number of bays	15						
13									Total Area (m <sup>2</sup> )	945						
14									V	488						
15									K	1.010793						

Archetype 12									
Floor	Loading			Interior Column	Edge Column	Corner Column	Braced Frame Column	Chevron Brace	RS-SCED Brace
	Dead	Snow	Live						
2	2.8	3.0	--	W200x59	W200x42	W200x42	W360x79	127x127x9.5	E
1	4.8	--	4.8						

	A	B	C	D	E	F	G	H	I	J	K	L	M	N	O	P
1	Archetype 12															
2	Level	$h_x$	$W_x$	$W_x h_x^k$	$F_x$	$V_{story}$	$V_{brace}$	Brace	$S_t$	$K_1$	$K_2$	$F_{max}$	$P_{col}$	Column	$F_a$	$A_{Chev}$
3		(m)	(kN)	(kN-m)	(kN)	(kN)	(kN)	Type	(mm)	(kN/mm)	(kN/mm)	(kN)	(kN)	Size	(kN)	(mm <sup>2</sup> )
4	RF	8	1928	15772.45	156.1	0.0	N/A	N/A	N/A	N/A	N/A	N/A	N/A	N/A	N/A	N/A
5	RT1	4	3402	13813.14	136.7	156.1	78	E	222	138	1.40	350	657		39	4240
6	GR	0	0	0	0	292.9	146	D	211	313	2.50	600	1347	W360X79	73	5240
7			Total	29585.59	292.9											
8																
9																
10								Number of bays in X		3						
11								Number of bays in Y		3						
12								Total number of bays		9						
13								Total Area (m <sup>2</sup> )		567						
14								V		293						
15								K		1.010793						

## Appendix D: Earthquake Record Suite and Scaling for FEMA P695

ID No.	Earthquake			Recording Station	
	M	Year	Name	Name	Owner
1	6.7	1994	Northridge	Beverly Hills - Mulhol	USC
2	6.7	1994	Northridge	Canyon Country-WLC	USC
3	7.1	1999	Duzce, Turkey	Bolu	ERD
4	7.1	1999	Hector Mine	Hector	SCSN
5	6.5	1979	Imperial Valley	Delta	UNAMUCSD
6	6.5	1979	Imperial Valley	El Centro Array #11	USGS
7	6.9	1995	Kobe, Japan	Nishi-Akashi	CUE
8	6.9	1995	Kobe, Japan	Shin-Osaka	CUE
9	7.5	1999	Kocaeli, Turkey	Duzce	ERD
10	7.5	1999	Kocaeli, Turkey	Arcelik	KOERI
11	7.3	1992	Landers	Yermo Fire Station	CDMG
12	7.3	1992	Landers	Coolwater	SCE
13	6.9	1989	Loma Prieta	Capitola	CDMG
14	6.9	1989	Loma Prieta	Gilroy Array #3	CDMG
15	7.4	1990	Manjil, Iran	Abbar	BHRC
16	6.5	1987	Superstition Hills	El Centro Imp. Co.	CDMG
17	6.5	1987	Superstition Hills	Poe Road (temp)	USGS
18	7.0	1992	Cape Mendocino	Rio Dell Overpass	CDMG
19	7.6	1999	Chi-Chi, Taiwan	CHY101	CWB
20	7.6	1999	Chi-Chi, Taiwan	TCU045	CWB
21	6.6	1971	San Fernando	LA - Hollywood Stor	CDMG
22	6.5	1976	Friuli, Italy	Tolmezzo	--

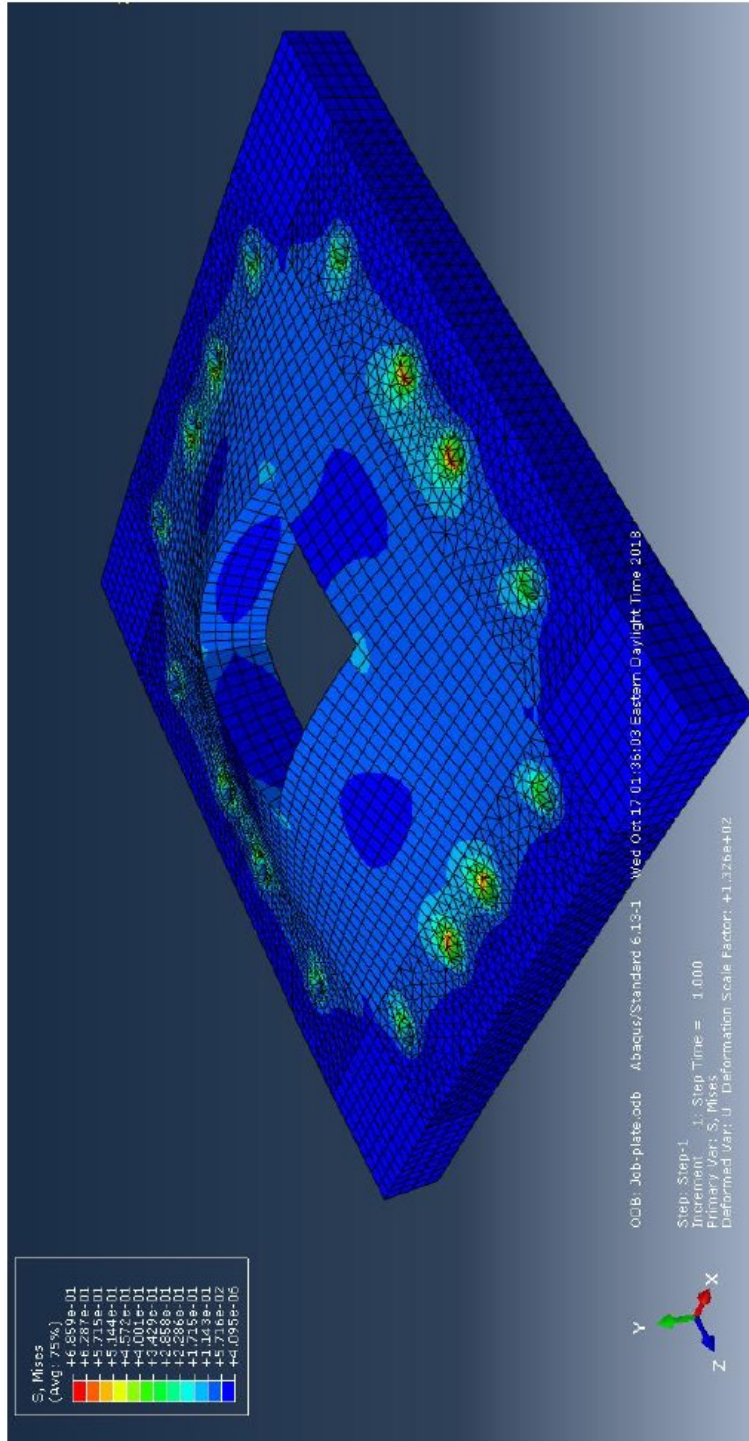
ID No.	Site Data		Source (Fault Type)	Site-Source Distance (km)			
	NEHRP Class	Vs_30 (m/sec)		Epicentral	Closest to Plane	Campbell	Joyner-Boore
1	D	356	Thrust	13.3	17.2	17.2	9.4
2	D	309	Thrust	26.5	12.4	12.4	11.4
3	D	326	Strike-slip	41.3	12	12.4	12
4	C	685	Strike-slip	26.5	11.7	12	10.4
5	D	275	Strike-slip	33.7	22	22.5	22
6	D	196	Strike-slip	29.4	12.5	13.5	12.5
7	C	609	Strike-slip	8.7	7.1	25.2	7.1
8	D	256	Strike-slip	46	19.2	28.5	19.1
9	D	276	Strike-slip	98.2	15.4	15.4	13.6
10	C	523	Strike-slip	53.7	13.5	13.5	10.6
11	D	354	Strike-slip	86	23.6	23.8	23.6
12	D	271	Strike-slip	82.1	19.7	20	19.7
13	D	289	Strike-slip	9.8	15.2	35.5	8.7
14	D	350	Strike-slip	31.4	12.8	12.8	12.2
15	C	724	Strike-slip	40.4	12.6	13	12.6
16	D	192	Strike-slip	35.8	18.2	18.5	18.2
17	D	208	Strike-slip	11.2	11.2	11.7	11.2
18	D	312	Thrust	22.7	14.3	14.3	7.9
19	D	259	Thrust	32	10	15.5	10
20	C	705	Thrust	77.5	26	26.8	26
21	D	316	Thrust	39.5	22.8	25.9	22.8
22	C	425	Thrust	20.2	15.8	15.8	15

ID No.	PEER-NGA Record Information				Recorded Motions	
	Record Seq. No.	Lowest Freq (Hz.)	File Names - Horizontal Records		$PGA_{max}$ (g)	$PGV_{max}$ (cm/s.)
			Component 1	Component 2		
1	953	0.25	NORTHR/MUL009	NORTHR/MUL279	0.52	63
2	960	0.13	NORTHR/LOS000	NORTHR/LOS270	0.48	45
3	1602	0.06	DUZCE/BOL000	DUZCE/BOL090	0.82	62
4	1787	0.04	HECTOR/HEC000	HECTOR/HEC090	0.34	42
5	169	0.06	IMPVALL/H-DLT262	IMPVALL/H-DLT352	0.35	33
6	174	0.25	IMPVALL/H-E11140	IMPVALL/H-E11230	0.38	42
7	1111	0.13	KOBE/NIS000	KOBE/NIS090	0.51	37
8	1116	0.13	KOBE/SHI000	KOBE/SHI090	0.24	38
9	1158	0.24	KOCAELI/DZC180	KOCAELI/DZC270	0.36	59
10	1148	0.09	KOCAELI/ARC000	KOCAELI/ARC090	0.22	40
11	900	0.07	LANDERS/YER270	LANDERS/YER360	0.24	52
12	848	0.13	LANDERS/CLW-LN	LANDERS/CLW-TR	0.42	42
13	752	0.13	LOMAP/CAP000	LOMAP/CAP090	0.53	35
14	767	0.13	LOMAP/G03000	LOMAP/G03090	0.56	45
15	1633	0.13	MANJIL/ABBAR--L	MANJIL/ABBAR--T	0.51	54
16	721	0.13	SUPERST/B-ICC000	SUPERST/B-ICC090	0.36	46
17	725	0.25	SUPERST/B-POE270	SUPERST/B-POE360	0.45	36
18	829	0.07	CAPEMEND/RIO270	CAPEMEND/RIO360	0.55	44
19	1244	0.05	CHICHI/CHY101-E	CHICHI/CHY101-N	0.44	115
20	1485	0.05	CHICHI/TCU045-E	CHICHI/TCU045-N	0.51	39
21	68	0.25	SFERN/PEL090	SFERN/PEL180	0.21	19
22	125	0.13	FRIULI/A-TMZ000	FRIULI/A-TMZ270	0.35	31

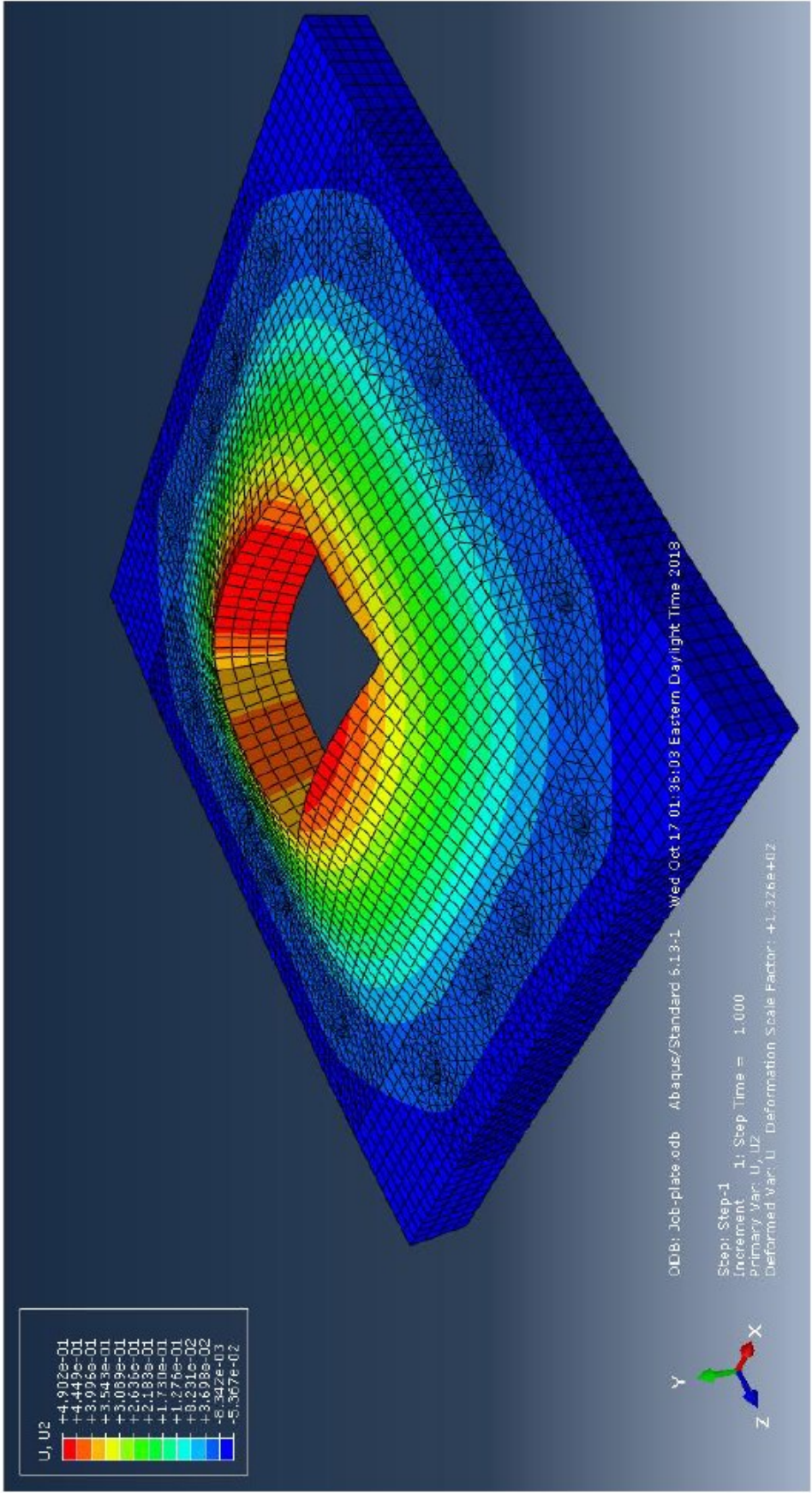
ID No.	As-Recorded Parameters			Normaliz- ation Factor	Normalized Motions	
	1-Sec. Spec. Acc. (g)		PGVPEER (cm/s.)		$PGA_{max}$ (g)	$PGV_{max}$ (cm/s.)
	Comp. 1	Comp. 2				
1	1.02	0.94	57.2	0.65	0.34	41
2	0.38	0.63	44.8	0.83	0.40	38
3	0.72	1.16	59.2	0.63	0.52	39
4	0.35	0.37	34.1	1.09	0.37	46
5	0.26	0.48	28.4	1.31	0.46	43
6	0.24	0.23	36.7	1.01	0.39	43
7	0.31	0.29	36.0	1.03	0.53	39
8	0.33	0.23	33.9	1.10	0.26	42
9	0.43	0.61	54.1	0.69	0.25	41
10	0.11	0.11	27.4	1.36	0.30	54
11	0.50	0.33	37.7	0.99	0.24	51
12	0.20	0.36	32.4	1.15	0.48	49
13	0.46	0.28	34.2	1.09	0.58	38
14	0.27	0.38	42.3	0.88	0.49	39
15	0.35	0.54	47.3	0.79	0.40	43
16	0.31	0.25	42.8	0.87	0.31	40
17	0.33	0.34	31.7	1.17	0.53	42
18	0.54	0.39	45.4	0.82	0.45	36
19	0.49	0.95	90.7	0.41	0.18	47
20	0.30	0.43	38.8	0.96	0.49	38
21	0.25	0.15	17.8	2.10	0.44	40
22	0.25	0.30	25.9	1.44	0.50	44

Period $T = C_u T_a$ (sec.)	Median Value of Normalized Record Set $\hat{S}_{NRT}$ (g)		Scaling Factors for Anchoring Far- Field Record Set to MCE Spectral Demand			
	Near-Field Set	Far-Field Set	SDC D <sub>max</sub>	SDC C <sub>max</sub>	SDC B <sub>max</sub>	SDC B <sub>min</sub>
				SDC D <sub>min</sub>	SDC C <sub>min</sub>	
0.25	0.936	0.779	1.93	0.96	0.64	0.32
0.3	1.020	0.775	1.94	0.97	0.65	0.32
0.35	0.939	0.761	1.97	0.99	0.66	0.33
0.4	0.901	0.748	2.00	1.00	0.67	0.33
0.45	0.886	0.749	2.00	0.89	0.59	0.30
0.5	0.855	0.736	2.04	0.82	0.54	0.27
0.6	0.833	0.602	2.49	0.83	0.55	0.28
0.7	0.805	0.537	2.40	0.80	0.53	0.27
0.8	0.739	0.449	2.50	0.83	0.56	0.28
0.9	0.633	0.399	2.50	0.83	0.56	0.28
1.0	0.571	0.348	2.59	0.86	0.58	0.29
1.2	0.476	0.301	2.49	0.83	0.55	0.28
1.4	0.404	0.256	2.51	0.84	0.56	0.28
1.6	0.356	0.208	2.70	0.90	0.60	0.30
1.8	0.319	0.168	2.98	0.99	0.66	0.33
2.0	0.284	0.148	3.05	1.02	0.68	0.34
2.2	0.258	0.133	3.08	1.03	0.68	0.34
2.4	0.230	0.118	3.18	1.06	0.71	0.35
2.6	0.210	0.106	3.28	1.09	0.73	0.36
2.8	0.190	0.091	3.53	1.18	0.79	0.39
3.0	0.172	0.080	3.75	1.25	0.83	0.42
3.5	0.132	0.063	4.10	1.37	0.91	0.46
4.0	0.104	0.052	4.29	1.43	0.95	0.48
4.5	0.086	0.046	4.34	1.45	0.96	0.48
5.0	0.072	0.041	4.43	1.48	0.98	0.49

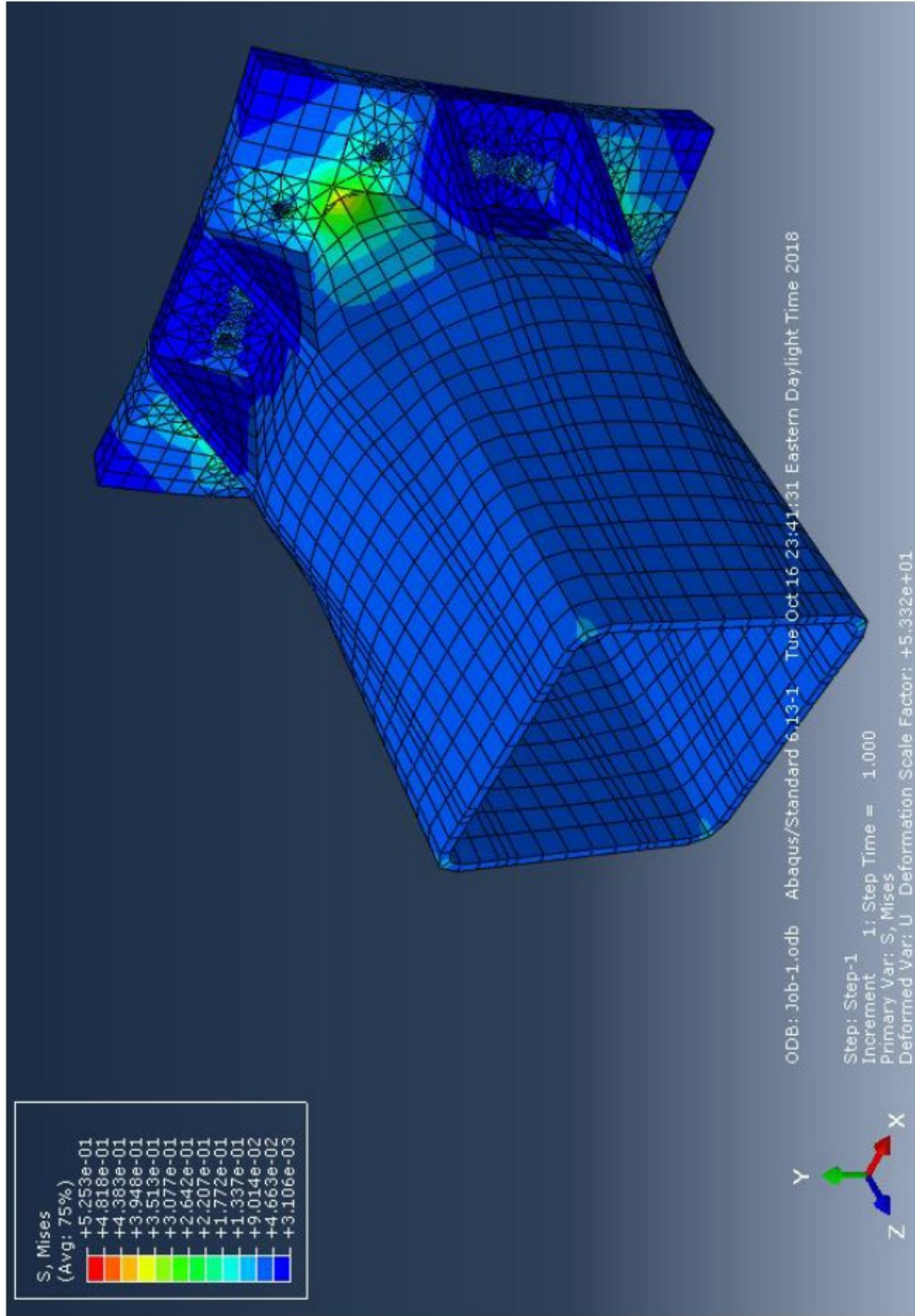
# Appendix E: FEM of RS-SCED Brace Components



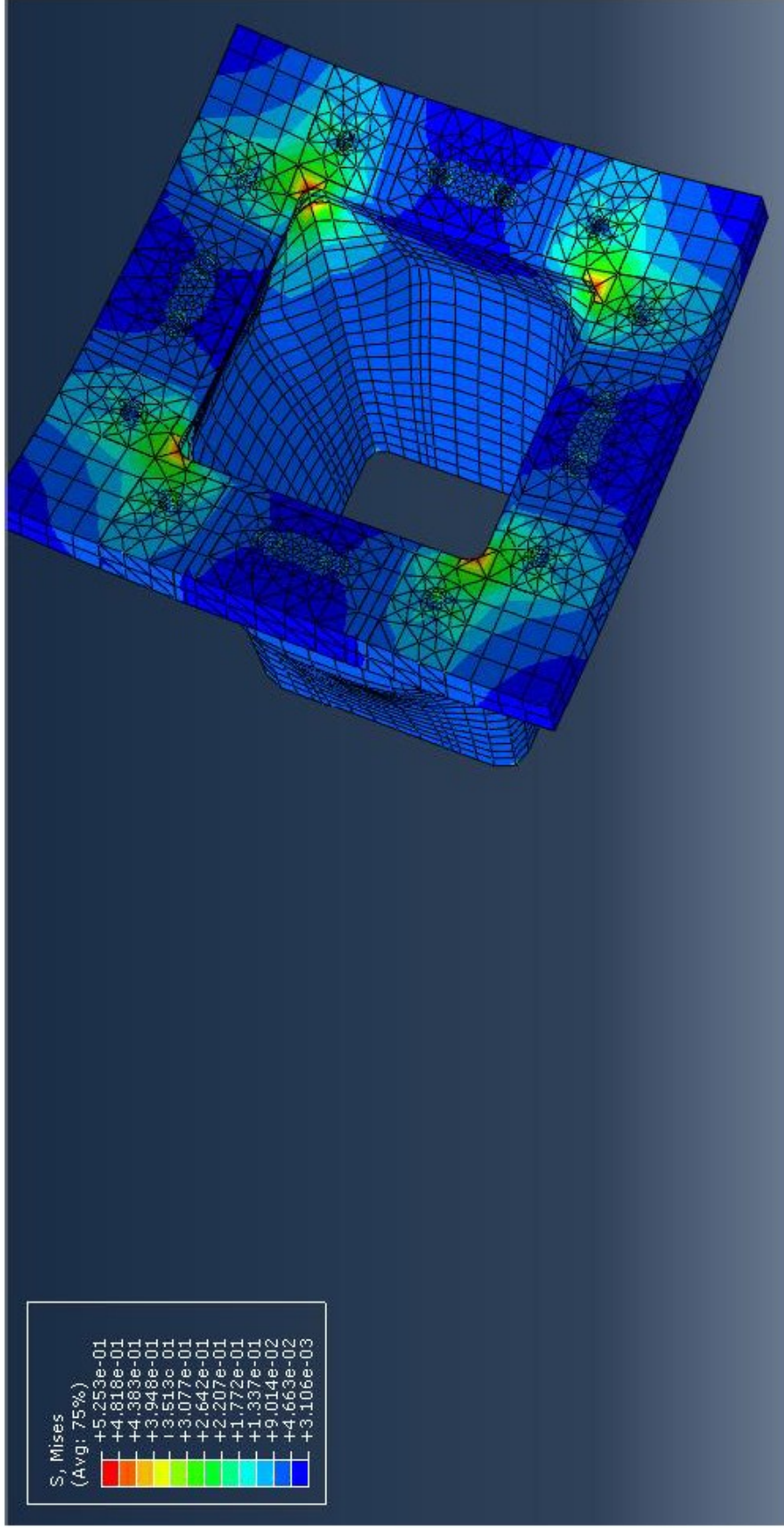
Stresses on plate



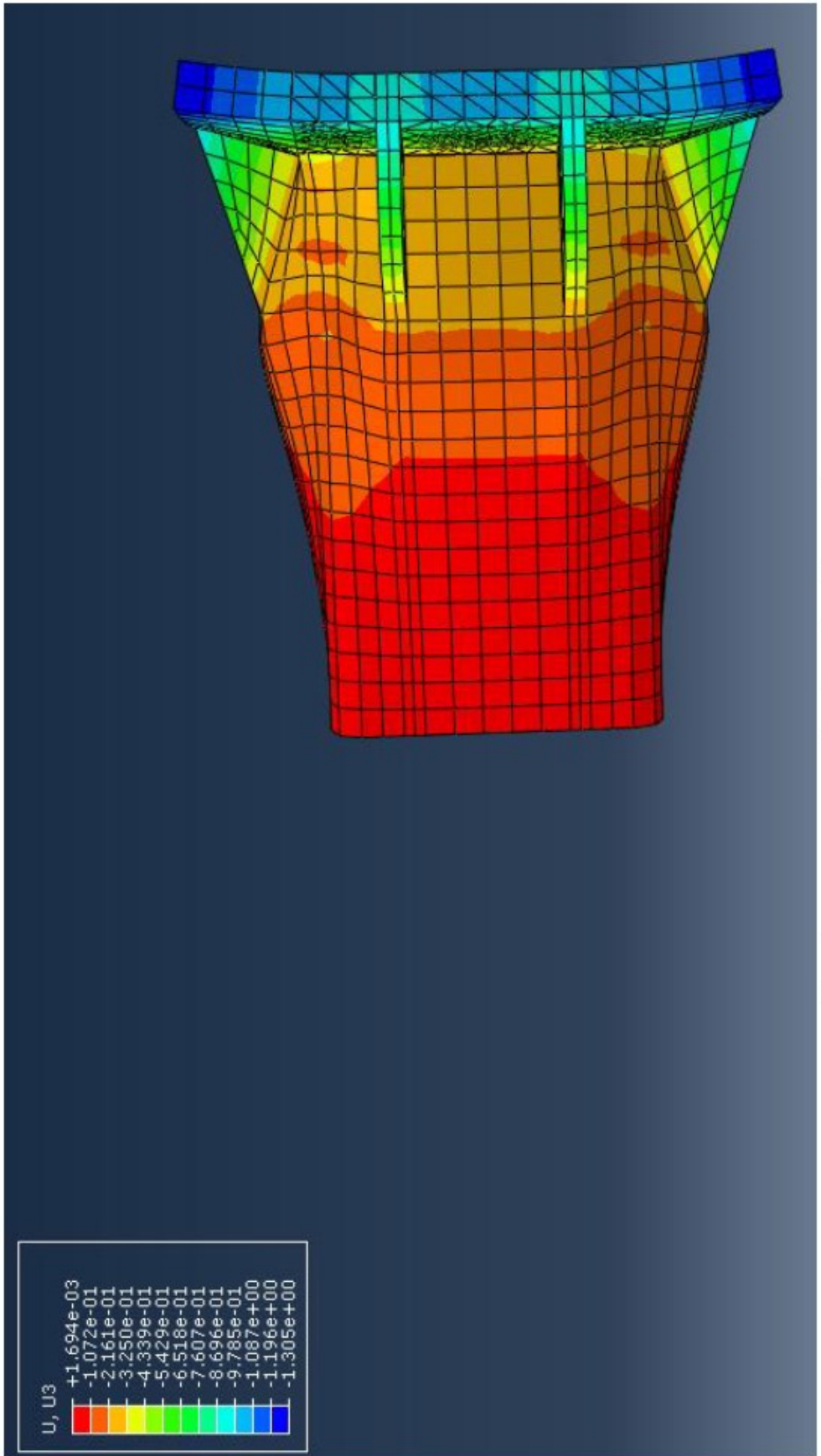
Displacement on plate

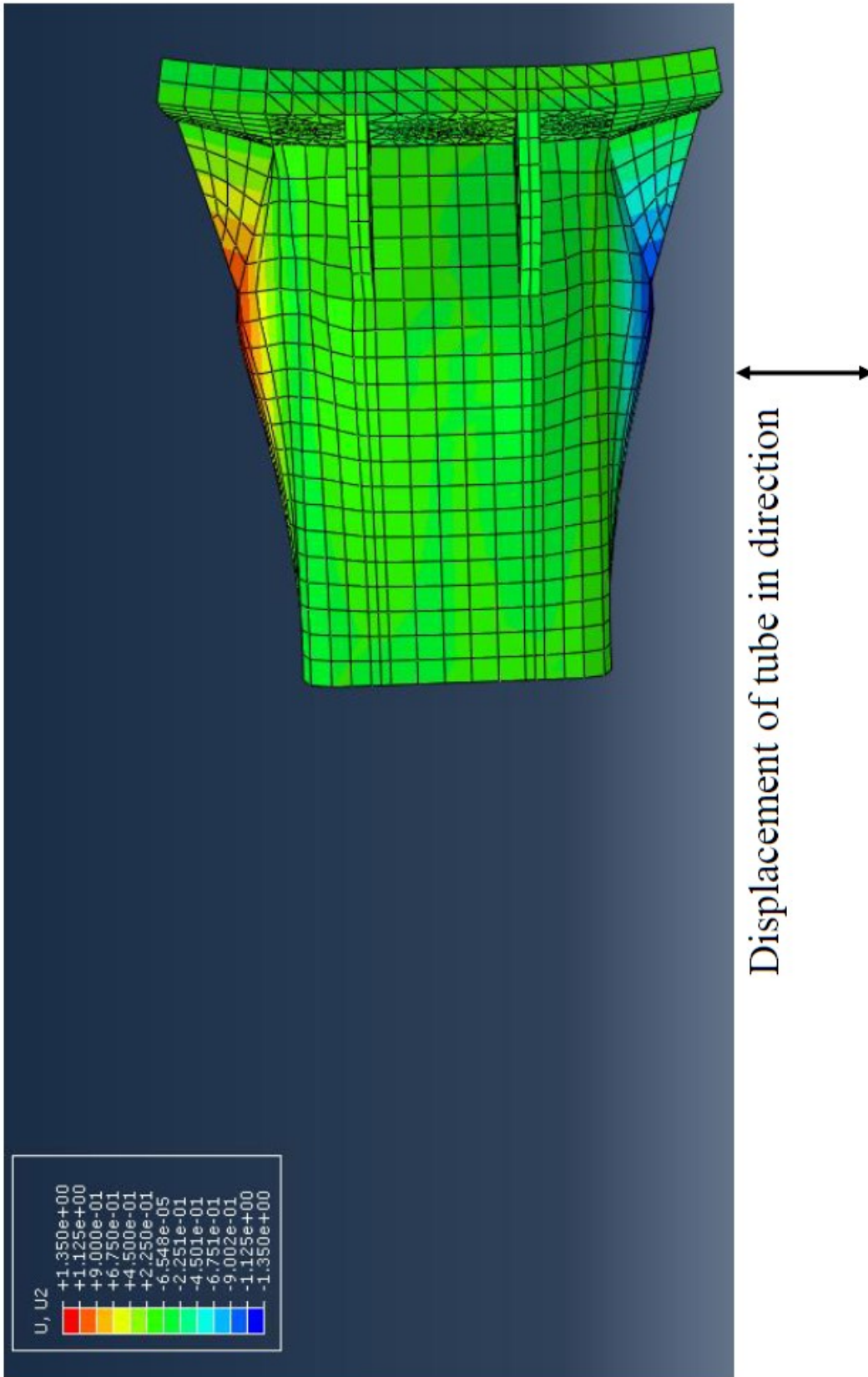


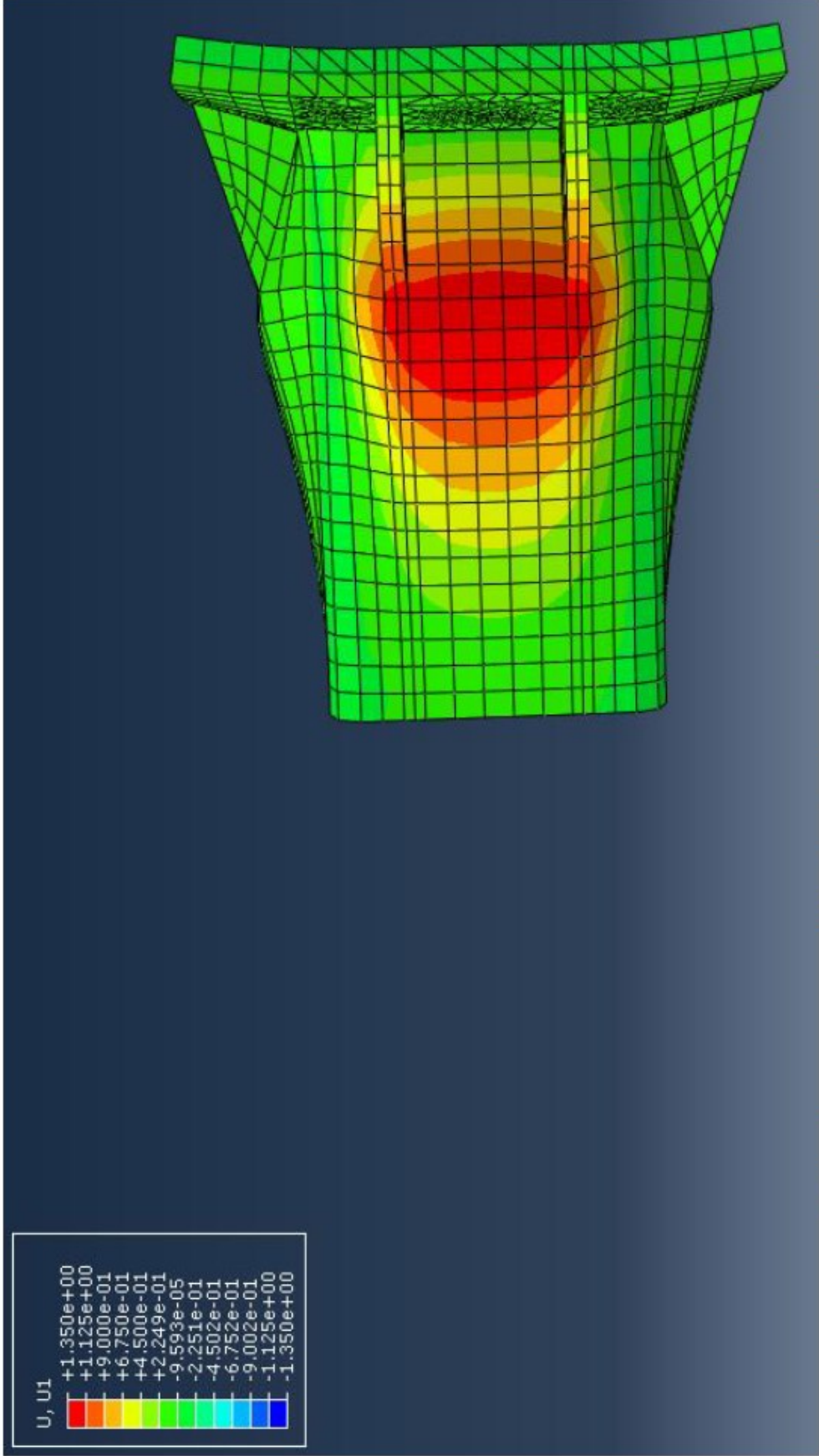
Stresses on Tube view 1



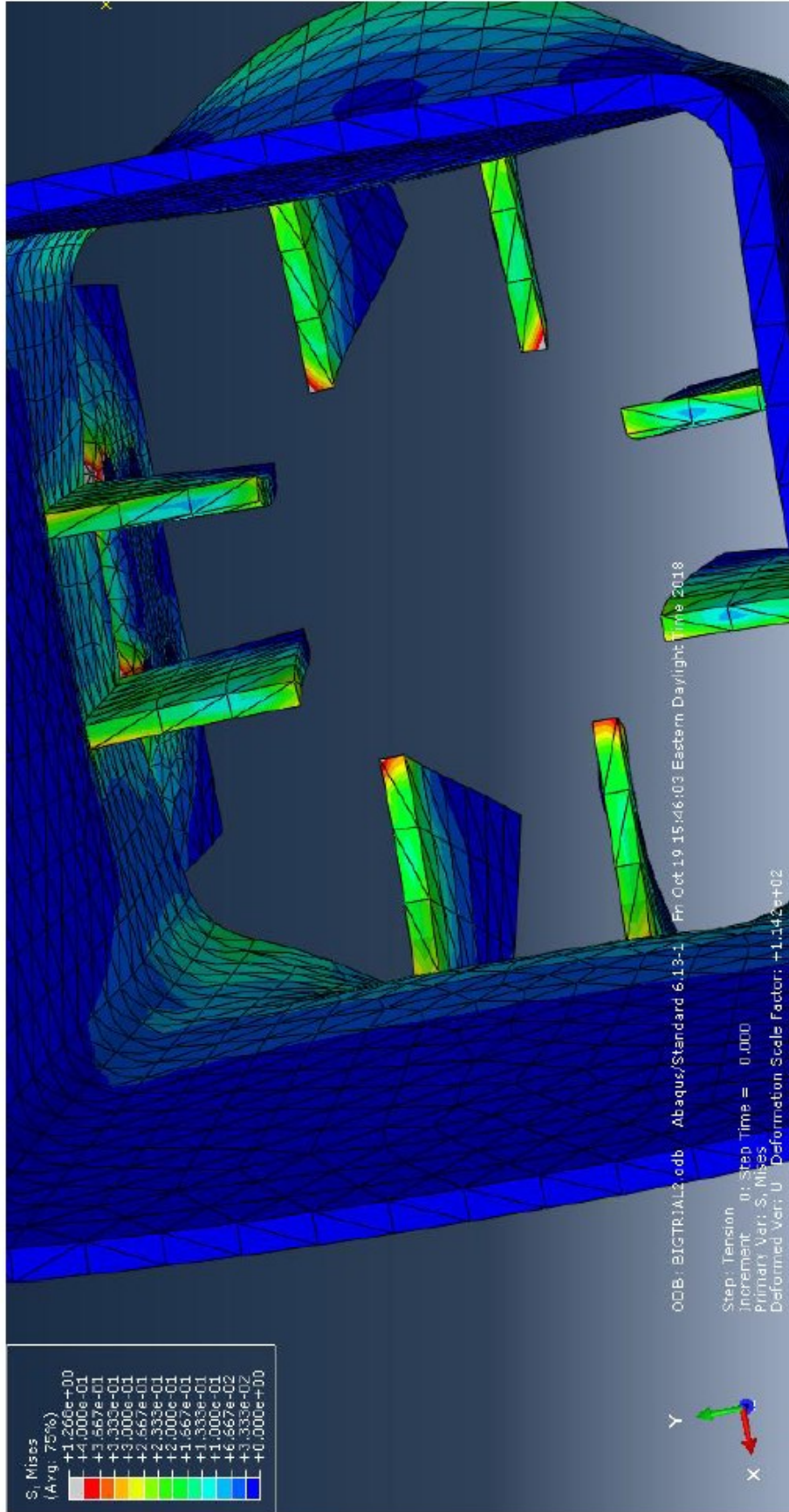
Stresses on Tube view 2



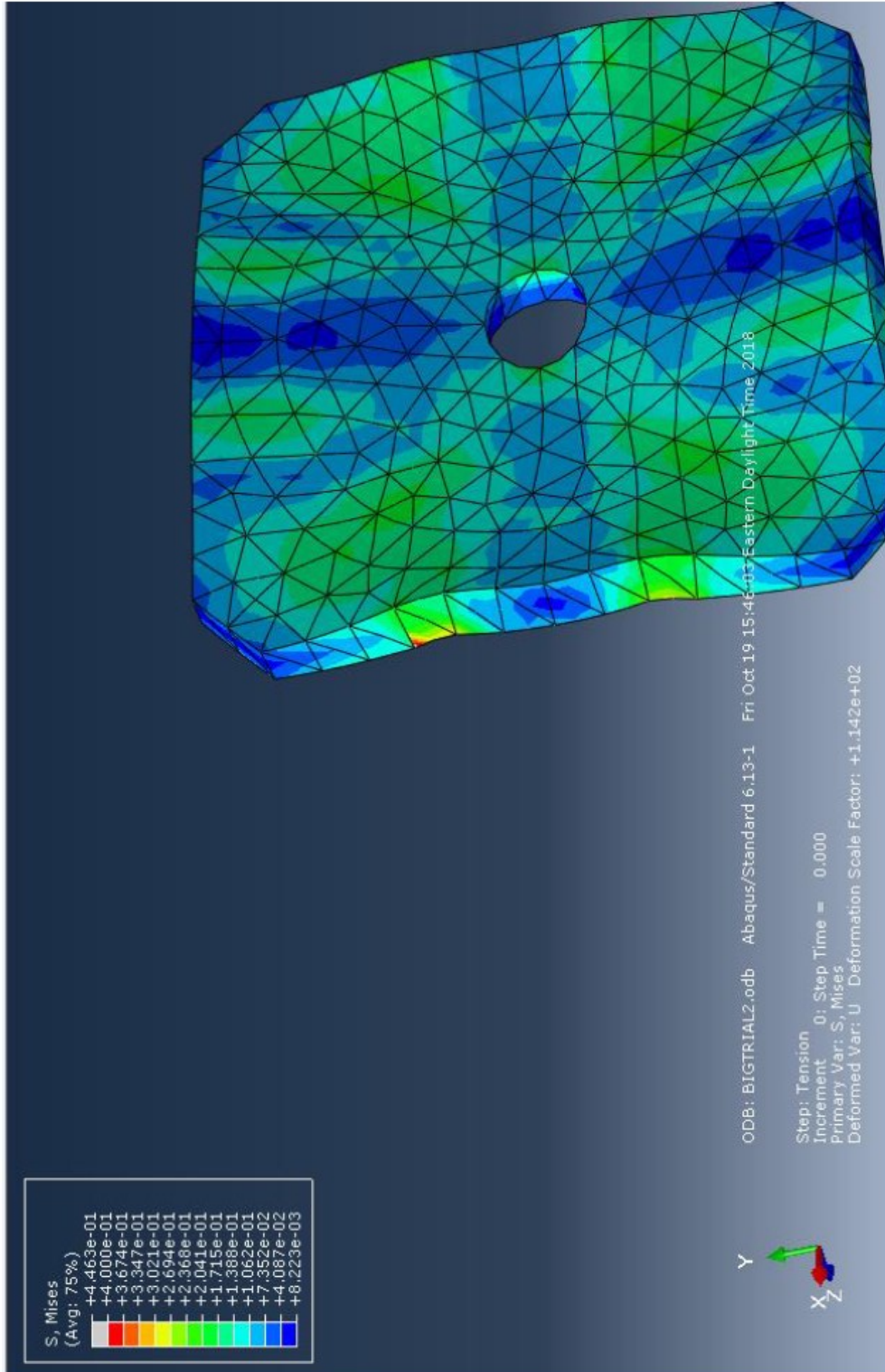




Displacement of tube in in-and-out of plane direction



**Outer Tube Connection Side compression - stress (View 2)**



**Outer Tube Connection Side compression stress (End Plate)**